The University of Iowa, Iowa City, Iowa

17th Annual Meeting
October 21-23, 1993

Conference Proceedings
AMERICAN SOCIETY OF BIOMECHANICS

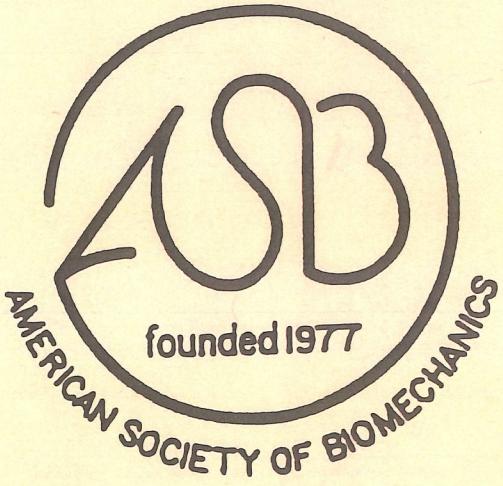

edited by

Andrew A. Biewener, Ph.D., The University of Chicago
Vijay K. Goel, Ph.D., The University of Iowa

EXECUTIVE BOARD
1992-1993

Ron Zernicke
President
Department of Surgery
University of Calgary
3330 Hospital Drive NW
Calgary, Alberta, Canada T2N 4N1
(403) 220-8666

Thomas P. Andriacchi
Past President
Rush-Presbyterian St. Lukes Med Ctr
(312) 942-5813

Thomas D. Brown
President-elect
University of Iowa
(319) 335-7528

Mark D. Grabiner
Secretary/Treasurer
Department of Biomedical Engineering
The Cleveland Clinic Foundation
9500 Euclid Avenue
Cleveland, OH 44195
(216) 444-7276

Robert Gregor
Program Chairperson-elect
University of California at Los Angeles
(310) 825-3910

Vijay K. Goel
Meeting Chairperson
The University of Iowa
(319) 335-5638

M. Melissa Gross
Membership Committee Chairperson
University of Michigan
(313) 764-9663

Mary M. Rogers
Education Committee Chairperson
Wright State University
(513) 259-1326

Andy Biewener
Program Chairperson
University of Chicago
(312) 702-7686

NEWSLETTER EDITOR

Christopher L. Vaughan
University of Virginia
(804) 982-0849

SUSTAINING MEMBERS

Aircast, Inc.
DePuy
DonJoy Orthopedic, Inc.
Electro-Biology, Inc.
Interpore Orthop., Inc.
Kistler Instrument Corp.
Motion Analysis Corp.
MTS Systems Corp.
NICOR
Orthofix SRI
Zimmer, Inc.

1993 CONFERENCE CHAIR

Vijay K. Goel, Ph.D.
The University of Iowa
Department of Biomedical Engineering
1202A Engineering Building
Iowa City, IA 52242
Phone: (319) 335-5638

1993 PROGRAM CHAIR

Andrew Biewener, Ph.D.
Department of Organismal Biology & Anatomy
The University of Chicago
1205 East 57th Street
Chicago, IL 60637
Phone: (312) 702-7686

EXHIBITORS

Advanced Mechanical Technology, Inc.
Artma Biomedical, Inc.
BERTEC Corp.
B&L Engineering Division of Pinsco, Inc.
Innovision Systems
Instron Corp.
Kistler Instrument Corp.
Motion Analysis Corp.
MTS Systems Corp.
Northern Digital, Inc.
Novel Electronics, Inc.
OsteoKinetics Corp.
Peak Performance Technologies, Inc.
Pergamon Press
Therapeutics Unlimited

SPONSORS

The University of Iowa:
Department of Biomedical Engineering, College of Engineering
Department of Orthopaedic Surgery, College of Medicine
Department of Exercise Science, College of Liberal Arts

With Support from

3M
AcroMed Corp.
MTS Systems Corp.
Novel Electronics, Inc.
Stanley Consultants, Inc.
Whitaker Foundation

CME Credit

The University of Iowa College of Medicine is accredited by the Accreditation Council for Continuing Medical Education (ACCME) to sponsor continuing medical education for physicians. The University of Iowa College of Medicine designates this continuing medical education activity for 14.5 credit hours in Category 1 of the Physician's Recognition Award of the American Medical Association. Pre-meeting Tutorials will meet the criteria for 2 credit hours each.

TABLE OF CONTENTS

BONE MECHANICS I

SPORT

HUMAN MOVEMENT & POSTURE I

JOINT BIOMECHANICS

BONE MECHANICS II

HUMAN MOVEMENT & POSTURE II

HUMAN GAIT

ORTHOPAEDIC BIOMECHANICS I

ORTHOPAEDIC BIOMECHANICS II

MUSCLE

SPINE

MOTOR CONTROL

POSTERS

BONE

JOINTS

ORTHODONTICS

SPORT

HUMAN GAIT

HUMAN MOVEMENT & ERGONOMICS

SPINE

FLUID MECHANICS

KNEE LIGAMENTS: TWENTY YEARS AND I HARDLY KNOW YOU

Savio L-Y Woo, Musculoskeletal Research Center, Department of Orthopaedic Surgery, The University of Pittsburgh, Pittsburgh, Pennsylvania

Experimental study of the properties of normal and healing knee ligaments was pioneered by investigators such as Viidik and Tipton. Their findings stimulated an intensive research effort over the past twenty years, primarily focused on the medial collateral and anterior cruciate ligaments. These efforts produced new and more accurate methodology to investigate the structural properties of the ligament-bone complex and the mechanical properties of the ligament substance. In particular, better methods were developed for measuring the cross-sectional area of the ligaments as well as soft tissue strain. As a result, we now know, for example, that temperature and irradiation will change the properties of ligaments, whereas strain rate and proper frozen storage will have a minimal effect. Changes in the properties of knee ligaments following maturation and aging, immobilization, increased tension, exercise, motion and stress dependent homeostatic responses also have been identified. On the analytical side, elastic, linear and nonlinear viscoelastic models for ligaments have been proposed. These mathematical models have contributed significantly to the understanding of ligament behavior. Studies have also been extended to evaluate the biomechanics of ligament healing as well as ligament reconstruction.

As with all good science, the progress made has provided us with some answers but has also led to more questions. Currently, much attempts are being made to measure/estimate the ligamentous forces and strains in the knee (both in-situ and in-vivo). The resulting data are fundamental for further understanding of ligament remodeling and healing processes, which, in turn, may enable provision to be made on an appropriate mechanical environment for optimal healing. The data are also needed for the effective surgical reconstruction and post-surgical rehabilitation secondary to injury of these ligaments. In addition, attention is being directed toward the ligament insertion to bone, known to elongate more than the ligament substance while its structure is incredibly complex. More sophisticated experimental methodology as well as analytical tools are needed here. We must also include the lateral collateral and posterior cruciate ligaments to further our understanding of the ligaments' contribution to knee function. It appears that ample opportunities exist for young and other investigators to emerge in this field and to join efforts in the pursuit of our understanding of ligaments around the knee.

REFERENCES:

1. Ligament and Insertion in Injury and Repair of the Musculoskeletal Soft Tissues. Eds. S. L-Y. Woo and J.A. Buckwalter. American Academy of Orthopaedic Surgeons, Chicago, IL, Chapters 2, 3, and 4, pp. 41-166, 1988.

2. Woo, S.L-Y., Weiss, J.A. and MacKenna, D.A.: Biomechanics and Morphology of the Medial Collateral and Anterior Cruciate Ligaments, in Biomechanics of Diarthrodial Joints. Eds. V.C. Mow, A. Ratcliffe and S.L-Y. Woo, Springer-Verlag, New York, N.Y., Chapter 3, pp. 63-104, 1990.

ACKNOWLEDGEMENTS:

Support by NIH grants AR39683-04 and AR41820-01A1 is gratefully acknowledged.

A COMPETITIVE NEURAL NETWORK MODEL FOR THE CLASSIFICATION OF INDIVIDUAL LUMBAR MUSCLE RESPONSE PATTERNS

M.A. Nussbaum and D.B. Chaffin
Center for Ergonomics, The University of Michigan, Ann Arbor, MI, 48109-2117

INTRODUCTION

When developing and validating biomechanical models, experimental data are usually averaged over a subject pool, but individual values are not considered in detail. Population average values have been used with optimization-based models for the prediction of normative lumbar muscle forces. These models typically generate a single set of muscle forces for a single instance of loading. Sometimes individual anthropometry is included, but the optimization approach attempts to derive an average scheme for muscle recruitment. Therefore, comparing the model with averaged subject data is reasonable. EMG-based models, in contrast, are explicit in their attempt to model muscle responses of individuals. Through the use of subject-specific data, predicted muscle activities should be unique to a subject. These models, though, require EMG measurements for every situation analyzed. Models incorporating artificial neural networks (ANNs) have been proposed as an alternative framework for muscle force prediction models (Nussbaum et al. 1992). ANN models maintain the 'reality-based' advantage of EMG models and the 'predictive' advantage of optimization models.

For static loads applied to the lumbar spine in an upright posture, several studies have shown that, *on average*, lumbar muscle activity generally serves to maintain mechanical equilibrium, although moderate levels of co-contraction are frequently present (Hughes 1991; Lavender et al. 1992). While individual data points might be used in statistical analyses, most studies present averages of individual data for specific conditions of loading in their results. The present work uses a competitive ANN to discriminate between individual subject's muscle responses during static moment loading (flexion, extension, and lateroflexion) of the torso in an upright posture. The competitive ANN model was designed to classify each individual based on their specific patterns of muscle responses to a set of external moment loads. The results suggest that important detail may be lost in treating individual data as random deviants from a mean. This new approach to dealing with individual muscle data should aid future efforts involving muscle prediction models.

REVIEW AND THEORY

In past studies, an average is normally computed using only the individual values obtained for a single exertion. In contrast, it was thought that individual response patterns might fall into discrete categories, yet a method of specifying the number of categories or obtaining exemplars of each was not available. ANN models, because of their ability to recognize patterns and robustness to noisy input (Rumelhart et al. 1988), have the potential to perform such a categorization. A competitive type of ANN model was designed to separate individual muscle responses (represented as vectors of activity levels for single loads across several load orientations) into distinct sets or categories. To allow different loads to have equal influence, each input vector was normalized to unit length.

The model is a continuous version of the discrete competitive model of Rumelhart et al. (1988). It contains two layers of units that are fully inter-connected with variable weights on each connection. The muscle response pattern (vector) is input to units in the first layer of the model while units in the second layer compete to respond to the input. The output unit with the highest activation is chosen as the winner and connection weights are updated using:

$$\Delta w_{ji}(t+1) = \begin{cases} \varepsilon[A_i(t) - w_{ji}(t)] & \text{winner} \\ \kappa[A_i(t) - w_{ji}(t)] & \text{others} \end{cases} \quad (1)$$

where w_{ji} is an element of the weight vector of output unit i connecting it to input unit j, $A_i(t)$ is the activation level of output unit i at time t, and ε and κ are learning rate constants ($\kappa \ll \varepsilon$). The winning output unit is the one whose weight vector most closely matches the input vector, and the learning algorithm acts by moving the weight vector closer to the input. To avoid local minima, and to allow other units to become active (allowing more competition), the second term in (1) modifies the weights connected to the losing units, bringing them slightly closer to the input pattern. Through successive training cycles, during which all the activity vectors of a single muscle are presented, the network classifies the inputs into a small number of distinct sets. The categories are determined by the winning unit for each subject.

PROCEDURES

The data used here were obtained from Lavender et al. (1992). In their experiment, 10 subjects resisted known static moment loads about the lumbar spine while in an upright posture. Five moment magnitudes (10-50 Nm) were applied in flexion, extension, and right lateroflexion at 30 deg. increments. EMG were measured from the Erector Spinae (ES), Rectus Abdominus (RA), External Oblique (EO), and Latissimus Dorsi (LD) bilaterally and normalized using maximal and resting values. Results are presented only for the left ES.

RESULTS

The model was run until the muscle responses of all subjects to all load magnitudes were classified into a stable number of categories. After running the model for ~200 cycles, three distinct categories were found. Within each category are a set of vectors representing similar patterns of muscle activity across the 7 load moment orientations. The model has automatically determined these groupings based on the degree of overlap of the individual vectors. The average left ES responses for each category are shown in Figure 1. Due to the normalization, *relative* activity levels are shown. Five subjects (solid line) were classified together as a single group, four subjects (long dash) into a second group, and a single subject (short dash) into a third group.

The model has grouped subjects such that all subjects within a given category have similar responses across all five load magnitudes. Each group shows peak left ES activity at a load orientation of 30 degrees (combined flexion and right lateroflexion) and decreasing activity as the load orientation approaches 120 degrees. The response of the second group of subjects appears phase shifted relative to the first with higher activity levels for loads composed primarily of lateral bending moments. A notable result from this figure is that the single subject in the third group displays considerable antagonistic co-contraction of the LES, as evidenced by the high activity for applied extension moments (180 degrees). A simple average of all subjects would have indicated ~ 4% activity for this load, but would disguise that the majority occurs from a single subject.

DISCUSSION

The experimental data were derived from simple static loads and unchanging postures. Despite this, it appears that there is a wide range in individual responses to these loads. Although measurement error is certainly a confounding influence, the competitive ANN found that certain subjects were consistently different in their response patterns.

By observing the distribution of subject data about a simple mean it is obvious that there are large variations. In most of the literature there is the implicit assumption that a mean response actually exists and that individual responses vary about it. The results here suggest that a true mean may not exist, rather that individuals cluster around several potential mean responses. Further indications come from Sommerich et al. (1992), who found evidence for clustering of subjects in the timing of muscle responses during asymmetric dynamic lifting. Models assuming a uniform principle (e.g., minimizing spinal compression or muscle intensities), may be unable to fully represent individual behavior, despite continuing efforts to account for subject-specific anthropometry, physiology, etc. These models assume that a consistent strategy is employed by each individual in reacting to or creating exertions through muscle contraction. The differences may lie at a deeper level, however, within individual motor behavior patterns and there may be a number of potential strategies. Further investigations will attempt to elucidate whether the different categories of muscle response result from such alternate recruitment schemes.

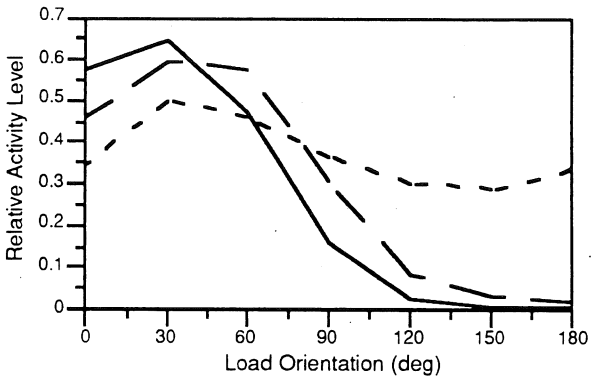

Figure 1. Average left ES responses for the 3 categories found by the competitive ANN model.

REFERENCES

Hughes, R. PhD Thesis, Univ. Michigan, 1991.

Lavender, S. et al. J. Orth Res., 10, 691-700.

Nussbaum, M. et al. Proc. NACOB II, Chicago, (p. 475-6), 1992.

Rumelhart, D. et al. Parallel Distributed Processing, Vol. 1, MIT Press, 1988.

Sommerich, C. et al. Human Factors, 34, 215-230, 1992.

ACKNOWLEDGEMENTS

This work was supported by NIH Grant-1R01-AR39599 in cooperation with Rush Presbyterian-St. Lukes Orthopaedics Department and G.B.J. Andersson and S. Lavender.

THE EFFECT OF IMPACTOR RADIUS ON MUSCLE CONTUSION INJURY

J.J. Crisco, K. Hentel, M.M. Panjabi, P. Jokl
Department of Orthopaedics and Rehabilitation,
Yale University School of Medicine, New Haven, CT, 06510 USA

INTRODUCTION

Injury to muscle tissue can range from muscle soreness after strenuous eccentric exercise to complete disruption of tissue in severe trauma. Muscle contusion injury is defined as the injury produced by the impact of a blunt non-penetrating object, and is the most frequent traumatic muscle injury. We developed a drop-mass technique for the production of muscle contusion injury in the rat. With a constant potential energy, we examined the effect of impactor tip radius on impact response and injury severity. We found that injury severity increased with decreasing impactor radius. A positive correlation existed for all response parameters, indicating trends of increased injury severity with increases in the magnitude of the response parameters.

REVIEW

Previous animal studies have yielded important information on cellular responses of muscle to crush injury (e.g. Allbrook, 1962). However, such injury models were invasive (typically produced with forceps inserted through a skin incision), limiting their ability to model contusion injuries seen clinically. Nonpenetrating and reproducible muscle contusion models have employed a spring loaded hammer (Kvist et al., 1974) and a drop-mass technique (Walton and Rothwell, 1983). Previous studies have not recorded the impact response to muscle. Furthermore, perhaps the best indicator of muscle damage, its ability to contract, has not been studied as function of a contusion injury. Clinically, muscle contusion injuries present with a wide range of severity, possibly due to variations in impact mechanics. The purpose of this work was to determine the effect of impactor tip radius on impact response and severity of muscle contusion injury, quantified by contractile strength.

PROCEDURES

Male Wistar rats (n=83, Charles River Company, Kingston, NY) were anesthetized prior to injury with 0.30 cc Ketamine (100 mg/ml) and 0.20 cc Xylazine (20 mg/ml) intramuscularly, and provided as necessary during the remainder of this experiment. All animal protocols were approved by the Yale Animal Care and Use Committee. Each animal received a single impact in the midsagittal plane to the belly of the gastrocnemius muscle complex (gastrocnemius, soleus, and plantaris). The impact was delivered with one of three spherical tip radii (RI, n=20; RII, n= 56; RIII, n=7). Of these animals, contractile strength in 5, 12, and 5 animals with RI, RII, and RIII, respectively, were studied. The remaining impacted animals were identified for histological study and survival studies not reported herein.

The hind limb of the prone anesthetized animal was exposed by extending the knee and dorsiflexing the foot to 90 degrees. The limb was secured with elastic bands to a plastic support platform. Injury was produced with a mass (171g)dropped from of a height of 102 cm onto the top of an impactor. The impactor was a small T-shaped cylinder fitted on the bottom with a spherical tip (RI = 3.1 mm, 31g; RII = 6.4mm, 30g; and RIII = 31.8 mm,40g) that directly contacted the skin. The support platform was fixed to a load cell (PCB Piezotronics, Depew, NY). The center of the impactor was a displacement transducer (Schaevitz, Pennsauken, NJ). During impact the load transmitted through the limb and the displacement of the impactor were simultaneously recorded (10 kHz) as a function of time by computer.

Maximum force (N) was defined as the maximum of the load-time curve recorded during impact. Maximum displacement (mm) was defined as the maximum displacement of the displacement-time curve. Maximum velocity (m/sec) was defined as the maximum derivative of the displacement-time curve. Impulse (Nsec) of the force of the impact was the integral of the load-time curve. Integration was performed from the time of a nonzero load (t0) to the time of a return to a zero load (t1). Based upon noise consideration we choose a 3 N force as a nonzero load. The energy (J) absorbed during impact was the integral of the compiled load-displacement behavior, integrated from t0 to t1.

Within 2 hours of impact, contractile strength was quantified by determining the maximum tetanic tension in the anesthetized animal. A Kirschner wire (0.45 mm) was placed transversely through the distal femur (0.5 cm above the knee joint) and secured to the testing apparatus. The insertion of the Achilles tendon was exposed and the calcaneus disarticulated. Stainless steel suture wire (22 gauge) was passed through a calcaneal drill hole and attached to a load cell (Entran Devices, Fairfield, NJ). The branch of the sciatic nerve innervating the gastrocnemius complex was exposed and isolated. Maximum tetanic tension for 1 second duration was obtained with stimulation parameters of 120 V, 0.05 msec, 70 Hz, and recorded by computer.

Random specimens were identified for histological study using the stains Hematoxylin and Eosin, Masson's Trichrome, and immunohistochemical markers for vimentin, a single peptide expressed by immature myoblasts. The uninjured contralateral limb was used as the control in all microscopic specimens.

RESULTS AND DISCUSSION

Impact response parameters demonstrated significant differences ($p<0.05$, factorial ANOVA with Fisher LSD post-hoc) with impactor radius. Except for the maximum force which was least with RII, all parameters decreased with increasing radius (Table 1).

The acute effect of impact in all animals was a significant reduction in the maximum tetanic tension as compared to intact contralateral limb ($p < 0.05$, paired Student's t-test). The percentage of loss was greatest with the smallest diameter and decreased with increasing radius (Table 1). Statistics showed that the loss with RI was significantly greater than with both RII and RIII ($p < 0.04$, factorial ANOVA, Fisher LSD post-hoc). Although the average loss continued to decrease with increasing radius, the difference between RII and RIII was not significant at $p < 0.05$.

A positive correlation existed for all parameters, indicating trends of increased injury severity with increases in the magnitude of the response parameters. The average response parameters of energy absorbed, impulse, and maximum velocity had a linear correlation ($R^2 > 0.9$).

Histological evaluation with H&E staining of the RI injury demonstrated a discrete area of severe muscle fiber disruption with evidence of hematoma. For the RII injury, a more diffuse pattern of muscle injury was observed with more extensive hematoma. The RIII histology revealed the most dispersed muscle injury with the least amount of hematoma and muscle fiber disruption. Trichrome staining demonstrated no difference in collagen content when compared with uninjured control specimens. There was no vimentin activity demonstrable in any specimen, indicating muscle regeneration had not yet begun.

REFERENCES

Allbrook D (1962) J. Anat 96:137-152.

Fischer BD, Baracos VE, Shnitka TK, Mendryk SW, Reid DC (1990) Med Sci Sports Exer 22(2):185-193.

Kvist H, Jarvinen M, Sorvari T (1974) Scan J Rehab Med 6: 134-140

ACKNOWLEDGMENTS

THE WHITAKER FOUNDATION for their financial support.

Table 1. For each spherical impactor radius, the mechanics of the impacts were quantified by the average [s.d.] impact response parameters and severity of muscle contusion injury was quantified by the loss in maximum tetanic tension.

Radius (mm)	Force (N)	Displacement (mm)	Velocity (m/s)	Energy (Nm)	Impulse (Ns)	Injury (%)
3.1	371 [124]	9.7 [0.8]	4.15 [0.19]	1.24 [0.37]	0.90 [0.28]	48.7 [12.8]
6.4	223 [66]	8.2 [0.9]	3.80 [0.32]	1.04 [0.30]	0.70 [0.14]	37.4 [6.2]
31.8	314 [43]	5.7 [0.7]	3.42 [0.35]	1.02 [0.19]	0.70 [0.07]	32.0 [14]

THE RELATIONSHIP BETWEEN RUNNING ECONOMY AND THE ACTIVATION PATTERNS OF LEG MUSCULATURE Gary D. Heise, Department of Kinesiology, Louisiana State University, Baton Rouge, LA 70803

Many investigators have reported that the aerobic demand (VO_2) for a given submaximal running speed (i.e., running economy) can be quite different when comparing individuals (e.g., Daniels, 1985). Researchers have reported a 20% to 30% range in economy for several running speeds among age-, gender-, and performance-matched groups of trained runners (Conley & Krahenbuhl, 1980; Daniels, 1985; Morgan & Craib, 1992). Frederick (1985) has described the question of why some individuals use less metabolic energy in performing a given movement than others as "one of the most interesting and fundamental questions confronting biomechanists" (p. 45). Biomechanists have identified several variables describing structural characteristics and running mechanics which are related to running economy (RE). However, Martin and Morgan (1992) summarized their review of the literature by stating that, in general, the relationships between RE and biomechanical variables are weak.

These biomechanical variables describing the running cycle are the result of highly-coordinated neural signals sent to the musculature. Therefore, it is suprising that little is known regarding the association between RE and the electromyographic (EMG) activity of the leg musculature. As McClay et al. (1990) stated in a recent review, research concerning the EMG activity of muscles has been "... a somewhat underrepresented area in the study of biomechanics of running" (p. 161). In addition, it has been shown that the unique action of bi-articular muscles of the leg contribute to more coordinated vertical jumping and cycling (Ingen Schenau, 1989). However, the contribution of these muscle actions to the running stride, particularly to the economy of runners, has not been examined.

Because of the lack of information regarding a potential link between muscle activity and running economy, the purpose of this project is to determine if a relationship exists between running economy and the coordinated activation patterns of leg muscles for several speeds of running. Specifically, the muscles which cross more than one joint and therefore, perform more than one function will be examined. It is hypothesized that the coordinated activity of these two-joint muscles may be related to the amount of energy required for running.

Healthy, physically active subjects, who are fairly homogenous in terms of aerobic fitness, will participate in two test sessions. During the first session, subjects will be oriented to treadmill running, and after accommodation, will perform a test of maximal oxygen uptake (VO_2 max). During three economy runs of the second test session, physiological data, EMG data, and 2-D video data will be collected. For EMG analysis, muscles of interest include rectus femoris, biceps femoris, semitendinosus, and gastrocnemius. Measures of muscle activity onset, duration, and amplitude will be correlated with running economy to determine if a significant portion of the interindividual variability in economy can be explained.

The above project will be a colloborative effort with Don W. Morgan, Ph.D., an exercise physiologist at The University of North Carolina-Greensboro. He has examined the question of economy of locomotion collaboratively with biomechanists in the past and has published numerous articles on the topic including the co-authorship of two reviews.

References

Conley, D.L. & Krahenbuhl, G.S. (1980). MSSE, 12, 357-360.
Daniels, J.T. (1985). MSSE, 17, 332-338.
Frederick, E.C. (1985). MSSE, 17, 44-47.
Ingen Schenau, G.J. van (1989). Human Movt Sci, 8, 301-337.
Martin, P.E. & Morgan, D.W. (1992). MSSE, 24, 467-474.
McClay et al. (1990). In Cavanagh (Ed.) Biomechanics of Distance Running (pp. 165-186).
Morgan, D.W. & Craib, M. (1992). MSSE, 24, 456-461.

RELIABILITY FOR SKIN MARKER USE IN FOOT AND ANKLE INVESTIGATIONS

Norman Murphy, Pediatric Research Center, Sainte-Justine Hospital, Montreal, Que., Can., H3T 1C5. Faculty of Physical Education, University of Montreal, Montreal, Que., Can., H3C 3J7.

Clinical evaluations as well as clinical and fundamental research related to foot and ankle kinematics and kinetics rely on skin, pin and tentalum marker displacements. More specifically, these markers are used to represent bone displacements associated with the respective articulations investigated. Marker displacements are obtained mainly with two data acquisition systems, camera (picture, film and video) and roentgenograms (x-ray). Due to the nature of pin and tentalum marker use as well as ethical considerations, most evaluations and investigations are conducted with skin markers. Presently, the reliability for using skin markers in representing true (bone) movements in the foot and ankle is undefined. Consequently, foot and ankle kinematics and kinetics remain open to question.

The purpose for this study is twofold. Firstly, two data capture systems (video and x-ray) are used to collect skin, pin and tentalun marker three-dimensional (3D) positional data associated with ankle, subtalar joint and first metatarsophalangeal joint motion. The data is then used to determine the reliability for skin marker use in hindfoot and forefoot clinical evalutaions and research investigations. Secondly, it is for the addition of significant knowledge to the understanding of foot and ankle kinematics and kinetics.

The methodology consists of two phases. The first phase is in-vitro and conducted in the Human Motion Laboratory, Pediatric Research Center, Sainte-Justine Hospital, Montreal, Canada. The the second phase is in-vivo and conducted in the Orthopaedic Department, Karolinska Hospital, Stockholm, Sweden.

In the first phase, the Motion Analysis Corporation (MAC) video system is used to collect skin and pin marker 3D displacement data from fresh amputated human lower limbs. Data capture is similar to Allard et al. (1987). Specifically, three non-colinear skin markers are placed over the respective bones of the ankle, subtalar joint and first metatarsophalangeal joint. Through dissected windows exposing bone surfaces, three non-colinear pin markers are then embedded in the bones. The tendons associated with the movements for each articulation are sutured and the lower limb is fixed in an experimental set-up via the tibia. The movements associated to the respective articulations are then induced by a pulley system. The specific movements are dorsiflexion and plantar flexion at the ankle, eversion and inversion at the subtalar joint, flexion and extension at the first metatarsophalangeal joint and finally, combined dorsiflexion and eversion as well as plantar flexion and inversion at the ankle-subtalar joint complex. Data is collected with five lower limbs.

In the second phase, the MacReflex and MAC video systems are used to collect skin marker 3D displacement data while roentgenograms are used to collect tentalum marker 3D displacement data all from five subjects. Data capture is similar to Lundberg (1989). Specifically, three non-colinear skin markers are placed over the respective bones of the ankle, subtalar joint and first metatarsophalangeal joint. The three non-colinear tentalum markers are

already embedded in the bones of subjects. The movements, as defined in the first phase, are induced with the subjects standing on a footplate.

From the skin, pin and tentalum marker 3D positions, the following analysis is carried out. The amplitudes and pattern of motions for each movement of each articulation for each marker set are computed. The computed skin, pin and tentalum amplitudes as well as the pattern of motions are then compared with one another. Additionally, parameters associated with the screw axis (helical angle and translation) as well as the location and orientation of the scew axis will be determined and compared.

The significance for this study is to determine the reliability for using skin markers in foot and ankle investigations. This will eventually simplify and produce quality clinical evaluations as well as clinical and fundamental research. At the present, the confusion regarding ankle and subtalar joint kinematics and kinetics, either isolated or combined, is partially due to an absence of simple and quality lower limb investigations. This study aims to help rectify this unfortunate situation.

Allard, P., Duhaime, M., Labelle, H., Murphy, N. and Nagata, S.D. (1987). Spatial reconstruction technique and kinematic modeling of the ankle. Eng. Med. Bio. 6, 31-36.

Lundberg, A. (1989). Kinematics of the ankle and foot. In vivo roentgen stereophotogrammetry. Acta. Orthop. Scand. 60, Suppl. 233, 1-26.

A BIOMIMETIC APPROACH TO MATERIAL DESIGN

A.H. Heuer and L.T. Kuhn
Department of Materials Science and Engineering, Case Western Reserve University
Cleveland, OH, USA, 44106

Natural hard tissue (shells, teeth, bone, etc.) are a class of ceramic-polymer composites or biological ceramics, which can provide useful insight into materials design of brittle materials. This approach will be illustrated using studies of the fracture of the shell of the large conch *Strombus Gigus*. The organized ceramic/organic interfaces within the cross-lamellar micro-architecture of the conch shell give rise to several toughening mechanisms. During flexure testing, for example, multiple channel cracking, crack bridging, and microstructurally-induced crack branching are observed that increase the fracture resistance of the composite many times above that of its constituents. Finite element analysis has been employed to predict the steady state strain energy release rate as a function of increasing channel crack density. The good agreement between the measurements and the model indicate that multiple channel cracking is a dominant and effective toughening mechanism in the microlaminate architecture of the mollusk shell.

HEMODYNAMIC FORCE TRANSDUCTION MECHANISMS IN THE ENDOTHELIAL CELL

Peter F. Davies*, Andre Robotewskyj*, Kenneth Barbee*, Melvin Griem#, and Ratnesh Lal^
Departments of *Pathology, #Radiation Oncology, and ^Medicine, Pritzker School of Medicine
The University of Chicago, Il., USA

At the interface between the blood and the vessel wall, the endothelium is directly affected by hemodynamic shear stress (frictional) forces that locally regulate vascular tone and are implicated in the localization of atherosclerosis. Thus the endothelium acts as a signal-transduction interface for hemodynamic forces. There are many diverse responses of endothelial cells to hemodynamically-related mechanical stresses ranging from ion channel activation to gene regulatory events. The processes of force transmission from the blood to the cell, and force transduction within the endothelium to electrophysiological, biochemical, and transcriptional responses are poorly understood. This presentation reviews the principal mechanisms currently thought to be involved in flow signalling at the endothelium.

Response mechanisms can be divided into two broad groups: those resulting from direct physical perturbation of the cell, and those arising indirectly from a change in the local concentrations of chemicals that influence endothelial biology. The latter may be altered by flow when the mass transport characteristics close to the cell surface are changed; convective and diffusion kinetics are altered. In contrast, examples of immediate direct effects of flow include alterations of cell tension manifested as cytoskeletal force elements. Conformational changes in membrane proteins also result in specific force-related responses mediated by the cytoskeleton. Imaging of the surface topography of living endothelial cells by atomic force microscopy (AFM) demonstrated significant rearrangement of lumenal surface details in cells exposed to flow. AFM provides high resolution spatial measurements of the cell surface (height, slope, etc.) that facilitate computational analysis of shear stress gradients at different locations of a single cell. Such an approach is essential for studies of force distribution throughout the cell.

Supported by grants from the NIH, National Heart, Lung and Blood Institute HL36028, HL15062, and American Heart Association Grant-in-aid 91-015570.

BIOMECHANICS OF SPEECH

Ingo R. Titze
Department of Speech Pathology and Audiology and
National Center for Voice and Speech
University of Iowa, Iowa City, IA 52242

Speech is produced by setting air and tissue into motion at acoustic frequencies (50 Hz - 10,000 Hz). The human vocal folds, for example, are two biomechanical oscillators coupled by a common airflow that entrains their movements. In addition, acoustic resonance tubes above and below the larynx impose their own resonance modes onto the system. This sets up complicated strategies for control of pitch, loudness, registration, and articulation for speech and singing. Current simulation models employ finite element and finite difference techniques to solve wave propagation in soft tissue and in airways. Examples will be given of recent developments in phonatory and articulatory modeling. In particular, emphasis will be on how viscoelastic and aerodynamic measurements in the laboratory have been incorporated into constitutive equations that govern the movement of air and tissue in vibration. Some validation of results is obtained by stroboscopic imaging of human and canine vocal folds.

THE EFFECTS OF MECHANICAL STRAIN ON MC3T3-E1 OSTEOBLASTS

José A. Morcuende, Neil A. Conti, Clark M. Stanford, Richard A. Brand

Department of Orthopaedic Surgery, The University of Iowa Hospitals and Clinics, Iowa City, IA 52242.

INTRODUCTION

In vivo, strain magnitude, strain frequency, and strain duration have been shown influence bone remodeling, but it is not well understood how the cells integrate these signals. To study these questions at the cell level, we have used the MC3T3-E1 newborn mouse calvarial osteoblast derived cell line grown on mechanically deformable silastic membranes using two models of cell culture, micromass and monolayer. Our work has shown decreases in alkaline phosphatase activity of up to 60 % in monolayer cultures with increased strain magnitude. Also, altering the strain regimes (frequency and time of strain application) has produced significant reductions in alkaline phosphatase activity. Microdot cultures, which are multilayered, show a decrease in alkaline phosphatase activity with -5 to -15 kPa of strain, but a variable effect at -1 kPa. The mineralization response, as measured by the Von Kossa assay, was absent in both strained and control monolayer cultures up to day 16. Conversely, microdot cultures showed pronounced mineralization at day 6 in strained (-1 and -15 kPa) and non-flexed cultures. Thus, because the MC3T3-E1 modifies its cellular response to alterations of strain patterns and intensities, there is the capacity of this cell to interpret and integrate these different signals.

REVIEW AND THEORY

It is known that mechanical strain on bone influences cortical and trabecular architecture, although the exact mechanism is unknown. It is assumed that the loading of bone effects the behavior of the various bone cells by causing changes in their micro-environment (Vandenburg, 1992). Osteoblasts, being the cells responsible for bone formation, have been a focus of study as to their role in the response to strain, although the manner in which this is expressed genotypically and / or phenotypically is not understood well. Also, it is of interest how bone cells time-process signals, responding not to individual strains, but to patterns of strain or strain intensities.

In vivo work by Rubin and Lanyon (1984) with a turkey ulnae model correlated peak strain magnitude, strain frequency, and strain duration with maintenance of bone or new bone formation. Previously, *in vitro* work by Buckley (1988, 1990) and Brighton (1991), and in our lab (ORS, Washington, 1992; AADR, Boston, 1992), showed mechanical strain exerted both phenotypic and proliferative effects on rat calvarial osteoblast cultures. The phenotypic changes seen were alkaline phosphatase activity, osteocalcin production, and 3[H]-Thymidine incorporation. We have reported changes in alkaline phosphatase activity of the MC3T3-E1 mouse embryo osteoblast to mechanical strain (IADR, Chicago, 1993).

PROCEDURES

Cell Culture and Strain Application

MC3T3-E1 osteoblasts were grown on Type I collagen coated silastic membranes as either four microdot (density = 5000 cells / mm^2) or as a monolayer (442 cells / mm^2) with RPMI media (+/- ascorbate, +/- 5 mM β-glycerol phosphate). Cultures were followed for 24 h prior to mechanically being strained 1800 strain reversals per day (SR / d), 0.5 Hz, every 24 h for 6, 8, 10, and 12 days at -1, -5, -10, or -15 kPa with a Flexercell strain unit (Flexcell Corp., McKeesport, PA).

In 12 day experiments to evaluate the time response of culture deformation on alkaline phosphatase activity, monolayer and microdot cultures were strained at -1 or -10 kPa for 7 days (1800 SR / d, 0.5 Hz), then unstrained for the remainder of the experiment, or unstrained for 7 days, then strained daily.

The relationship of strain duration to alkaline phosphatase activity was examined in monolayer cultures by employing different strain regimes of 1800 SR / d at 0.05 Hz (10 sec strain application / 10 sec off), and 0.09 Hz (10 sec strain application / 1 sec off, or 1 sec strain application /10 sec off).

Assays

Alkaline phosphatase activity was determined by the amount of para-nitro phenol (PNP) developed over 30 minutes as measured by absorption at 405 mM on a microtiter plate reader, after cell membranes were homogenated in a lysis buffer via sonication and incubated with para-nitro phenol phosphate (PNPP), an alkaline phosphatase substrate. Values were normalized to the amount of DNA per culture.

DNA levels were quantitated in cell membrane homogenates by a fluorometric assay (emission 365 nm, excitation 460 nm) with Hoechst dye (No. 33258).

Mineralization was determined by the presence of calcified nodules via Von Kossa staining after intact cultures were fixed with 10 % formalin.

RESULTS

Alkaline Phosphatase

Monolayer and microdot cultures showed a decrease in alkaline phosphatase activity when strained at -5, -10, and -15 kPa (1800 SR / d, 0.5 Hz) when compared to controls, with a greater degree of depression with increasing intensity of strain. Cultures showed a variable response to -1 kPa of strain. (data for monolayer shown, fig 1). Media from cell cultures remained free of alkaline phosphatase activity.

Depressions in alkaline phosphatase activity were seen with the different straining regimes (fig 2). A 60% decrease in alkaline phosphatase activity was seen with 10 sec strain application / 10 sec off (0.05 Hz). Also, the 0.09 Hz regimes of 1 sec strain on / 10 sec off and 10 sec on / 1 sec off both produced a lowering of enzyme activity of 30 % when compared to unstrained controls. In microdot cultures, the 0.05 Hz regime produced a 33 % decrease in alkaline phosphatase activity when compared to both 0.09 Hz regimes.

Strain application of -1 and -10 kPa from days 8 through 12 leads to a 25 % reduction in alkaline phosphatase activity in monolayer cultures at day 12 compared to unstrained controls.

Mineralization

Although cultures strained at -15 kPa did show a slight increase in staining at day 4, there was not a visible difference in the mineralization response between strained (-1 and -15) and unstrained microdot cultures at 6, 8, and 10 days, . All monolayer cultures, strained and unstrained, did not mineralize through day 16, despite the addition of β-glycerol phosphate to some cultures.

Figure 1

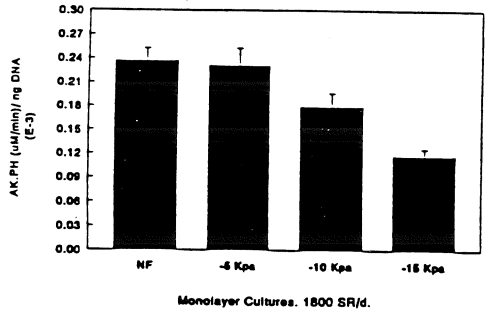

Figure 2

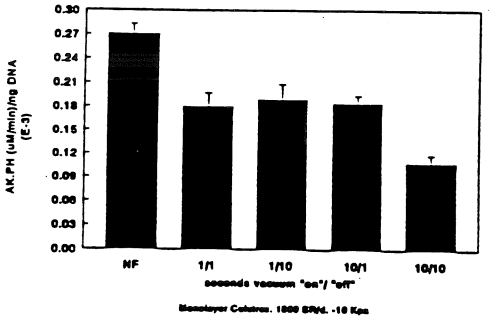

DISCUSSION

The *in vivo* experiments of Rubin and Lanyon as well as *in vitro* experiments suggest a trigger-like mechanism which stimulates new bone formation in response to strain. Our results with the MC3T3-E1 cell line show an alteration of its phenotypic response to changes in strain levels and patterns, as measured by a decrease in alkaline phosphatase activity (fig 1 and 2). These changes of cell response indicates the ability of the cell to somehow interpret and / or process these signals.

The differences in mineralization response of microdot and monolayer cultures may be explained because of the differences in cell density between the two culture systems. Monolayer cultures have a density of 442 cells / mm^2, while microdot cultures are more dense (5000 cells / mm^2) and are multilayered. The increase in cell density and multiple layers of the microdot cultures may allow for enhanced cell-to-cell contact, thus creating unknown cellular changes and / or changes in the local microenvironment and surrounding matrix which are favorable for mineralization to occur.

Although the levels of strain applied to the cultures in this system may be hyperphysiologic, it is not beyond the biological capacity of this cell line to function under these conditions, as the mineralization response in strained and unstrained micromass cultures occurs at similar time points and patterns. However, we can not explain the similar mineralization response between strained and unstrained microdots despite the reduction in alkaline phosphatase activity with strain.

These *in vitro* experiments suggest that the MC3T3-E1 osteoblast interprets mechanical stimuli by modulating its phenotypic expression.

REFERENCES

1) Vandenburg, Am J Physiol, 262: 350-355 (1992).
2) Rubin and Lanyon, Calcif Tissue Int, 37: 411-417 (1985).
3) Buckley, Bone and Mineral, 4: 225-236 (1988).
4) Buckley, J Oral Maxillofac Surg, 48: 276-282 (1990).
5) Brighton, JBJS, 73-A(3): 320-331 (1991).
6) Melitou, 38th ORS, Washington, p. 168 (1992).
7) Madey, AADR, 1992.
8) Conti, IADR, #1381, p. 276 (1993).

ACKNOWLEDGMENTS

This work was sponsored in part by NIH grant AR-0705, a Bristol-Meyer / Squibb / Zimmer Award for Excellence in Research, Funded through the OREF.

SURFACE STRAIN GRADIENTS PREDICT SITES OF SKELETAL ADAPTATION

Ted S. Gross and Clinton T. Rubin
Musculo-Skeletal Research Laboratory, Department of Orthopaedics
State University of New York at Stony Brook, Stony Brook, NY 11794-8181

INTRODUCTION

The intimate association between physical stimuli and skeletal morphology suggests that the cellular population of bone is responsive to some specific component of this stimulus. In this study, we use an *in vivo* model of skeletal adaptation to isolate candidate mechanical parameters correlated to sites of skeletal adaptation, and then validate these relationships by their ability to predict sites of adaptation in the same model under alternate loading conditions. Although several candidate relationships were developed, only one parameter, the circumferential gradient of longitudinal normal strain, was validated by its ability to predict sites of adaptation in the alternate group of animals.

REVIEW AND THEORY

Mechanical parameters such as strain magnitude (1), the strain tensor (2), and strain energy density (3, 4), have been proposed as the stimulus guiding skeletal adaptation. These potential correlates have been identified using theoretical and experimental models, but have not been validated by their ability to predict sites of adaptation under alternative loading conditions *in vivo*. Further, as the distribution of functionally induced strains are highly non-uniform (5), the physiologic relevance of the homogeneous strain stimulus frequently assumed by these models has yet to be determined.

The general hypothesis guiding this work is that the sites and magnitude of skeletal adaptation are related to some specific component of the applied mechanical stimulus. The hypothesis was addressed by relating the sites and magnitude of skeletal adaptation engendered by an exogenous loading regimen to specific components of the externally induced strain environment as defined by finite element modeling. Candidate correlates of skeletal adaptation were then validated by their ability to predict the adaptive response induced in the same *in vivo* model exposed to an alternate loading condition.

PROCEDURES

The right radii of two groups of five adult male turkeys were isolated from their normal functional stimuli via parallel metaphyseal osteotomies. The left radius of each animal served as an intact, contralateral control. The animals underwent a four week daily loading regimen in which external loads were applied to transcutaneous pins using a pneumatic cylinder with custom mating sleeves. The regimen placed the bone primarily in bending (with a small component (< 1%) of axial tension), and consisted of 100 cycles per day of a trapezoidal waveform (2.5s period) calibrated to induce peak longitudinal compressive strains of -2000με and a peak strain rate of 10,000με/s. The two groups of five animals were identical except for the orientation of the loading pins, which were rotated 90 degrees in the transverse plane in the second group of animals (group "B"). As a result, the two groups were exposed to similar magnitude strain environments, but the sites of maximum and minimum strains were located in different portions of the cortex (fig 1).

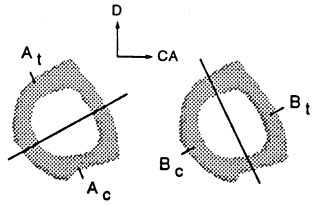

Figure 1. Mid-diaphysis of radius illustrating sites of peak tension and peak compression for loading groups "A" (A_t and A_c) and "B" (B_t and B_c). The group "B" neutral axis (straight line) was rotated 100 degrees clockwise from that of group "A", and spanned the dorsal/ventral cortices.

Upon sacrifice, 125 micron sections were extracted from the midshaft in both the experimental and intact, contralateral control radius. These sections were microradiographed, enlarged (x5), and scanned at 600dpi. Site specific adaptation in the control and experimental sections were assessed by aligning the experimental binary image upon the control image, dividing the cross-sections into 12 equal angle pie sectors through the control centroid, and assessing areal properties within each sector. Adaptive responses within each sector were related to candidate parameters generated by orthotropic finite element models whose meshes were developed from the geometry of each animal's intact control radius. Multiple step-backward regression, in which parameters with high intercorrelation ($r > 0.8$) and non-significant p values ($p > 0.05$) were sequentially eliminated, was used to relate mechanical parameters to measured adaptation. Potential correlates included individual components of the strain tensor, principal

strains, longitudinal shear stress (4), the osteogenic index (6), and strain energy density. The parameters were grouped into five categories (absolute magnitude at the periosteum and endosteum, radial gradients, circumferential gradients, and longitudinal gradients), each of which was independently regressed against periosteal adaptation, endosteal adaptation, and total areal change to yield 15 multiple regressions for each loading group. Any final regression relationship with $r^2 \geq 0.5$ was subsequently validated by its ability to predict the sites and magnitude of adaptation in the second group using a Kendall non-parametric rank correlation.

RESULTS

The four week loading regimen was powerfully osteogenic in both groups of animals, inducing a mean (± S.D.) 20.4 ± 28.8% increase in bone area in group "A", and a 35.2 ± 32.8% increase in group "B". The increased bone mass was achieved primarily via periosteal expansion (78%). The magnitude of the periosteal expansion varied substantially between the 12 sectors, ranging from 6.7 ± 7.4% to 45.1 ± 83.1% in group "A", and from 13.2 ± 23.7% to 80.5 ± 58.1% in group "B". The area of maximal periosteal expansion differed between the two groups, but in both cases was located near the neutral axis (fig 2). In loading group "A", 8 of the 15 regressions developed predictive relationships with $r^2 > 0.50$. Of these, three were distinguished by having one single parameter accounting for nearly all of the predictive power of the relationship. Periosteal adaptation was powerfully predicted by the circumferential gradient of longitudinal normal strain (r^2=0.71). Endosteal adaptation was predicted by both the radial gradient of longitudinal normal strain (r^2=0.59) and the magnitude of longitudinal normal strain on the periosteal surface (r^2=0.50). No single parameter predicted total areal change with r^2>0.40. Only the circumferential gradient of longitudinal normal strain was validated by its ability to predict sites of adaptation in loading group "B" (K=0.56), as no other candidate relationship generated a Kendall coefficient of K≥0.10

DISCUSSION

In both loading groups, the portion of the cortex demonstrating the greatest amount of periosteal bone formation was located near a site of minimum rather than maximum strain. As a result, measures of strain magnitude poorly predicted the observed adaptive response. For example, the predictive power of SED never exceeded r^2=0.20 in group "A". Adaptive activity on the periosteal and endosteal surfaces was more readily related to specific mechanical stimuli than total areal changes, perhaps because total areal change represents the combined activity of two bone surfaces under differing physiologic constraints. Although many candidate relationships were developed, only one, the circumferential gradient of longitudinal normal strain, was validated by its ability to predict sites of adaptation in the second loading group. The predictive power of these strain gradients (i.e. how strain magnitude changes through a volume of tissue in the circumferential direction) is particularly intriguing in light of potential physiologic mechanisms of cellular signal transduction. These include streaming potentials (strain gradients are proportional to fluid flow which in turn would alter streaming potentials), and cellular communication via gap junctions (a potential mechanism for transducing spatial gradients into biochemical signals).

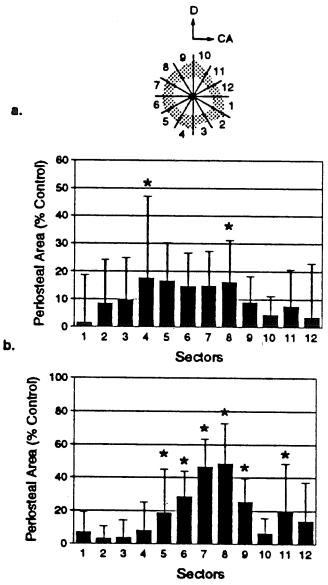

Figure 2. Mean (± S.D.) periosteal area in the experimental radii (% control) for loading group "A" (a) and group "B" (b). The location of maximal new bone formation shifted from the cranial/ventral cortex in group "A" to the dorsal/ventral cortex in group "B". Asterisk denotes difference at p=0.05.

REFERENCES

1. Frost (1987). Bone and Mineral. 2:73-85.
2. Cowin et al. (1989). J. Biom. 22:503-515.
3. Huiskies et al. (1987). J. Biom. 20:1135-1150.
4. Brown et al., (1990). J. Biom. 23:893-905.
5. Gross et al., (1992). J. Biom. 25:1081-1087.
6. Carter (1987). J. Biom. 20:1095-1109.

ACKNOWLEDGEMENTS

This work was supported by NIH AR40411 and AR 39278.

IS BONE SURFACE-STRAIN DISTRIBUTION ALTERED BY EXERCISE-INDUCED REMODELING?

B. Loitz and R. Zernicke
Department of Surgery, University of Calgary, Calgary, Alberta, Canada

INTRODUCTION

Safety factor and relative strain distribution are proposed as being maintained during skeletal remodeling (Biewener *et al.* 1986; Lanyon *et al.*, 1982). We tested this premise in an animal model using exercise as the remodeling stimulus. Adult-rooster baseline controls were evaluated as time-zero controls (30 wk old), while non-exercised age-matched controls and exercised roosters were evaluated at the end of the 9-wk experiment (39 wk old). Strain distribution of the tarsometatarsus (TMT), recorded during fast walking, was similar for the exercise and control (baseline and age-matched) roosters. The safety factor (difference between typical *in vivo* stress and yield stress), however, differed significantly among the groups, suggesting that strain distribution may be a more robust determinant of exercise-related bone remodeling.

REVIEW AND THEORY

Similar *in vivo* strains in the radius and tibia of a variety of species measured at a range of locomotion speeds suggest that at anatomically similar sites, mammalian bone remodels to maintain a similar safety factor between the functional strain/stress generated during activity and the functional strain/stress that occurs at yield or failure. Biewener *et al.* (1986) predicted that strain engendered during maximum-speed running was three-fold less than strain at bone's yield point, suggesting that across a range of animal species and body mass, maintaining safety may be an important determinant of bone remodeling. Here, we tested whether both safety factor and strain distribution are important objectives of exercise-related bone remodeling, and whether both will remain similar in sedentary controls and exercised animals.

PROCEDURES

Thirty-two adult (30 wk) White leghorn roosters were divided into baseline control (n=9), age-matched control (n=11), and exercise (n=12) groups. Baseline controls were euthanized at the beginning of the experiment to establish time-zero data for TMT strains, mechanical properties, and geometry. Exercise roosters ran on a motorized treadmill 1 h/d, 5 d/wk, for 9 wk at 70-75% maximum aerobic capacity. Prior to sacrifice (39 wk), 3 birds per group were implanted with rosette strain gauges on the medial, anterior, and lateral surfaces of the TMT middiaphysis. Strains were recorded during treadmill running 48 h after implantation. Each trial was filmed (100 frames/s) to calculate gait kinematics (TMT orientation, ankle joint angle, and step/stride length). TMTs were mechanically tested in three-point bending with a materials testing system, and geometry was digitized from 1-mm middiaphyseal cross sections. Principal strain magnitude and orientation were computed using standard equations and were synchronized to film data. Peak anterior-surface stress was computed using equations for analysis of strain gauge output of an anisotropic material (Carter, 1979).

RESULTS

The exercised roosters ran a total distance of 150 km during the 9-wk program. Mechanical properties and cortical geometry have been described elsewhere (Loitz *et al.*, 1992). Gait parameters did not differ among the groups, with the TMT following a stereotypical sagittal-plane motion during the step cycle. Despite differences in absolute strain magnitude (Table 1), strain distribution was similar among the groups. Anterior-surface strains, strain distribution across the middiaphyseal cross section, and TMT sagittal-plane orientation were examined at 20% increments of a gait cycle (Fig. 1). Principal compressive and tensile strains on the anterior surface increased as the TMT assumed a more vertical position. Comparison of TMT position and strain vectors throughout the gait cycle suggested that longitudinal compressive loads contributed more to the anterior-surface strains than did bending loads.

In terms of stress, age-matched control (-11.7 MPa) and exercise (-15.4 MPa) principal anterior stress significantly exceeded baseline control stress (-4.6 MPa). Using the rooster-specific elastic modulus measured from the mechanical tests to calculate

safety factor, significant differences in safety factor were noted among the groups, with a factor of 31 for baseline controls, 13 for age-matched controls, and 10 for the exercise group.

Table 1. Peak principal strains averaged over 10 consecutive steps (μstrain; mean±SE).

		Compression	*Tension*
Medial:	Baseline	753±63	319±24
	Age-matched	933±40	378±8
	Exercise	726±13	248±6
Anterior:	Baseline	414±13	260±10
	Age-matched	931±20	291±6
	Exercise	1069±12	291±6
Lateral:	Baseline	466±43	120±9
	Age-matched	727±18	234±17
	Exercise	261±9	363±47

DISCUSSION

Previous data suggested that remodeling attempts to optimize strain magnitude with a site-specific range. Lanyon *et al.* (1982), however, suggested that the parameter optimized was strain distribution rather than magnitude. Our data support their hypothesis, because despite significant differences in absolute strain magnitude and bone mechanical properties, strain distribution was maintained during exercise-induced remodeling.

Calculation of peak surface stresses using our peak anterior principal strains and Carter's equations suggests that the bone safety factor in the rooster decreases with both age- and exercise-related remodeling. At first, our findings appear to contradict the theory that maintaining safety drives bone remodeling (Biewener *et al.*, 1986). The stress used in our calculation of safety factor, however, was not recorded at the bird's maximum running speed, as were the safety factors reported by Biewener, and this discrepancy may account for the difference in values.

REFERENCES

Biewener, A. *et al.* J. Exp. Biol. 123, 283-400, 1986.

Carter, D. J. Biomech. 11, 199-202, 1978.

Lanyon *et al.* J. Biomech. 15, 141-154, 1982.

Loitz *et al.* J. Exp. Biol. 170, 1-18, 1992.

ACKNOWLEDGMENTS

Supported by the California Physical Therapy Fund and the Dorothy & Leonard Strauss Sports Medicine Fund.

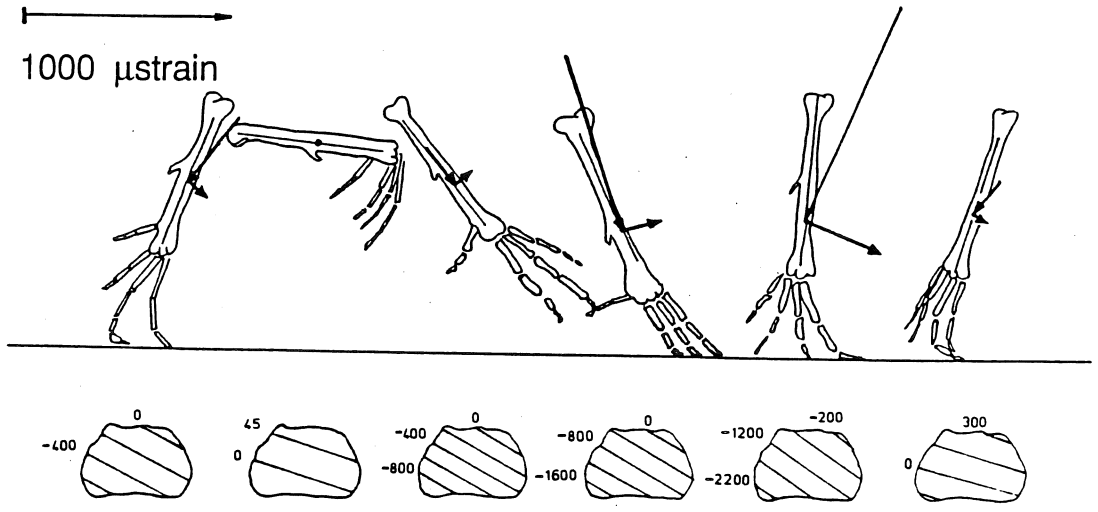

Figure 1. TMT sagittal-plane orientation, anterior-surface strain vectors, and strain distribution across a middiaphyseal section during a representative step cycle (0.37 $m \cdot s^{-1}$) for the right limb. Strain magnitude for each isostrain plane is indicated on the TMT cross sections. Data are presented at 20% increments of a single step cycle, and cross sections are oriented with the anterior cortex down and lateral cortex right.

GROWTH RELATED CHANGES IN HUMERAL AND FEMORAL STRENGTH, RIGIDITY AND STRAIN

D.R. Sumner and T.P. Andriacchi

Department of Orthopedic Surgery
Rush-Presbyterian-St. Luke's Medical Center
Chicago, Illinois 60612

INTRODUCTION

The purpose of this paper was to compare change in strength, rigidity and predicted strain in the human humerus and femur during post-natal growth to test the hypothesis that these changes would be different in bones which have vastly different functions.

MATERIALS AND METHODS

A sample was derived from the Grasshopper Pueblo skeletal collection. This archaeological site is located in east central Arizona and was occupied from A.D. 1275 to 1400. A total of 83 paired femora and humeri, with approximately 5 samples per 1 year age category (i.e., 0-1, 1-2, ... 9-10), 5 samples for the 10-14 age category and 10 samples (5 from female skeletons and 5 from male skeletons) for the 15-19, 20-24, and 25-29 age categories were tested. Age and sex were determined using standard anthropological techniques.

The length (l) of each bone was measured. Midshaft cross-sectional geometric properties were determined based on computed tomographic scans. An automated boundary definition technique was used to define the subperiosteal and endo-cortical surfaces. These data were then used to calculate I_{max}, I_{min}, and the AP and ML subperiosteal diameters (d_{AP} and d_{ML}, respectively). Estimates of Young's modulus (E) were taken from the work of Currey and Butler (1975). From these data, the following parameters were calculated:

average subperiosteal diameter,
$$d = (d_{AP} + d_{ML})/2,$$

average area moment of inertia,
$$I = (I_{max} + I_{min})/2,$$

flexural rigidity, EI, and

bone strength index, $S_B = EI/ld$

(a modification of Selker and Carter's, 1989, bone strength index to include E)

In addition, the maximum strain was calculated:

$$\epsilon = Mc/EI,$$

where M = the applied moment and c was approximated as $0.5*d_{max}$, where d_{max} = the greater of d_{AP} and d_{ML}. To estimate M as a function of l, we determined the peak flexion and extension moments at the hip and knee joints in 11 children, from age 5 to 14 during level walking. As an estimate of l, we used the child's height and then determined the value of the exponent, a, in the allometric equation

$$M = bX^a,$$

where X was the height. The average value for a was 2.75. As a validation, when the child's weight was used as the dependent variable, a = 3.0, as would be expected. For the humerus, we had no direct data and assumed that the moment scaled with bone length similar to the femur (i.e., $M \propto l^{2.75}$). To aid in understanding how these parameters changed during growth, all of the calculated values were expressed as a per centage of the maximum value during growth. Thus, the minimum value for any of the calculated parameters was 0% and the maximum value was 100%.

RESULTS

The basic pattern of change during growth was similar in the femur and humerus (Figs. 1 and 2). The predicted maximum strain increased until age 7-8 in the femur and age 6-7 in the humerus and then declined to ~50% of the maximum in the femur and ~60% of the maximum in the humerus as skeletal maturity was reached. Increase in bone length reached a plateau by 15-20 years, while the area moment of inertia increased until age 20-24 in the femur and age 25-29 in the humerus. The flexural rigidity and bone strength index followed similar trends.

DISCUSSION

It is, of course, well known that the femur and humerus differ morphologically. However, the fact that the post-natal growth-related changes were similar in both bones indicates that the basic morphologic differences were established pre-natally and were maintained during growth. If the loading environments of the humerus and femur were similar *in utero*, then the basic morphologic differences would require a strong genetic component. Alternatively, one could argue that the loading of these 2 bones *in utero* was different enough to establish the morphological differences present at birth.

We anticipated finding a monotonic decrease in strain during growth, but the predicted maximum strain occurred around age 7 in both the femur and humerus and then decreased steadily. Obviously, these predictions are based on estimates of the moments affecting each bone. Dimensionally it can be shown that $M \alpha l^3$ (following Selker and Carter, 1989). This proportionality was tested for the femur and it was found that $M \alpha l^{2.75}$, suggesting that the moment increases less rapidly than expected from purely geometric considerations. Even when the data were analyzed, assuming $M \alpha l^3$, peaks in strain were still predicted to occur between age 5-9 (data not presented).

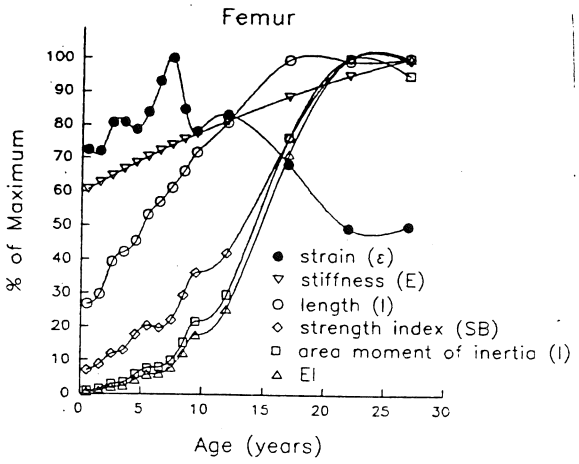

Figure 1.

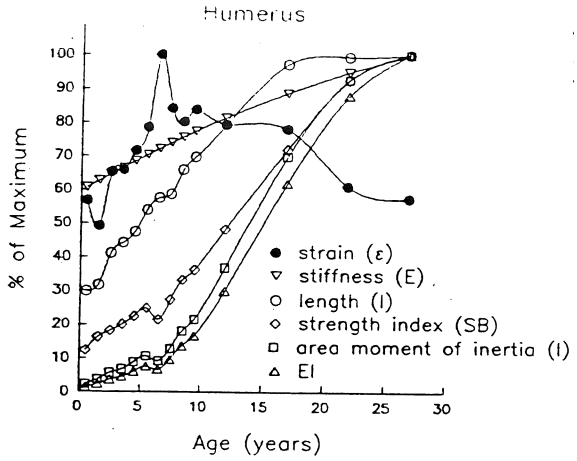

Figure 2.

REFERENCES

Currey JD, Butler G: The mechanical properties of bone tissue in children. *J Bone Joint Surg* 57-A:810-814, 1975.

Selker F, Carter DR: Scaling of long bone fracture strength with animal mass. *J Biomechanics* 22:1175-1183, 1989.

ACKNOWLEDGEMENTS

This projected was supported by a grant from the Wenner-Gren Foundation.

GEOMETRIC SYMMETRY OF THE TURKEY ULNA

D.J. Adams, D. R. Pedersen, M. J. Rudert, R. A. Brand, C.T. Rubin*, and T. D. Brown

Departments of Orthopaedic Surgery and Biomedical Engineering, The University of Iowa, Iowa City, IA 52242.
*Department of Orthopaedic Surgery, State University of New York at Stony Brook, Stony Brook, NY 11794.

INTRODUCTION

Geometric symmetry usually is assumed in long bones with homotypic load histories, in order to compare experimentally induced bony reorganization with contralateral "control" preparations. While intuitively reasonable, it is obvious that such bilateral symmetry cannot be absolute. Thus, quantitation of geometric asymmetry in paired bones is necessary where a size and/or shape change in one bone must be identified. In such experiments, the reliability of conclusions based upon an assumption of absolute geometric symmetry will be compromised by any unappreciated baseline asymmetry.

A series of new techniques devised to analyze three-dimensional geometric asymmetry between paired long bones was applied to the turkey ulna, a frequently used preparation for studies of adaptive remodelling (Rubin and Lanyon, 1987). Serial images of bony cross sectional geometry were captured by transverse milling and subsequent digitization of photographs (6 ulna pairs), or by X-ray computed tomography (1 pair). Following computerized 3-D reconstruction of each bone pair, the right bone was mirrored to allow ipsilateral comparison of two "left" bones. Whole bone voxel-based analysis of total volume and centroidal principal volume moments of inertia demonstrated left-right differences of 4.9 ± 3.5% and 7.2 ± 5.5%, respectively. Following whole bone centroidal and principal axis registration, RMS disparities between paired longitudinal loci of volumetric section centroids were 0.7 ± 0.3 mm.

Longitudinally matched transverse areal properties yielded left-right differences in cross sectional area and principal area moment of inertia of 8.1 ± 3.0% and 10.7 ± 3.8%, respectively. Following centroidal and principal axis alignment, pixel-based discretization of areal intersection fractions and differences in cortical thickness at discrete angular increments revealed left-right disparities of 20 ± 6% and 3.9 ± 3.5%, respectively. Overall, these measurements demonstrated only very modest left-right asymmetry in the turkey ulna. Thus, an assessment of symmetry is desirable when quantifying geometrical remodelling of contralateral long bones (e.g. finite element analysis).

REVIEW AND THEORY

Previous assessments of long bone asymmetry have focused only upon limited attributes of symmetry, rather than upon full three-dimensional geometrical characterization. Various indices of symmetry addressed individually include gross mechanical properties (Currey, 1984; White et al., 1974) and distances between anatomical landmarks, both physically (Helmkamp et al., 1990) and from radiographs. Considerations of cross-sectional parameters have addressed histomorphometric and geometrical symmetry (Miller et al., 1980; Sumner et al., 1988) only at ostensibly corresponding longitudinal sites. Together, all of these studies fall short of elucidating the degree of three-dimensional baseline long bone symmetry desirable for quantifying geometrical remodelling of a contralateral bone. The purpose of this study was to develop a protocol for analyzing geometric asymmetry in bilaterally mated long bones, and to demonstrate its application in quantifying baseline asymmetry in one frequently studied experimental preparation: the turkey ulna.

PROCEDURES

Six pairs of ulnae from commercially-raised male turkeys were embedded longitudinally in rectangular blocks of carbon-black doped PMMA. One end of each block was ablated serially with a milling cutter and color photographed at approximately 1 mm increments. The slides were digitized as grey scale arrays using an Imapro flatbed scanner. Serial transverse images were obtained for one additional pair of ulnae at 1 mm increments with a Siemens Somatom DR/H CT scanner. All images were rendered under maximum magnification and resolution as 512 x 512 pixel arrays, and processed using a threshold-based algorithm which distinguished (bright) bone-containing pixels from surrounding dark pixels. The images comprising the right ulna were reflected about a cardinal plane to produce a mirror image for direct comparison with the anatomical left ulna. Incorporating the "slice" or scan thickness (≈1 mm), each bone was represented as a three-dimensional voxel array in an orthogonal reference frame relative to one corner of the first (distal) cross-sectional image.

The three coordinates of the volumetric centroid of each ulna were computed about the reference origin. Principal volume moments of inertia then were computed at the volumetric centroid. Together, the volumetric centroids and principal axes provided an objective basis for optimal three-dimensional alignment. A further descriptor of whole bone asymmetry was obtained by computing the separation distance between two loci connecting serial section centroids of volumetric "slices" from the left and mirrored right ulnae. This provided an index for assessing global changes in bone curvature, which directly affects the cortex strain field resulting from bending. The two loci were transformed to a common volumetric centroid and principal orientation, and the rectilinear separation distance between the two loci was calculated at 1 mm longitudinal increments (Fig. 1a).

Longitudinally matched comparisons of serial transverse images allowed several additional discriminating indices to be characterized within the central 70% of the ulna diaphysis (Fig. 1b). The metaphyseal regions were excluded from areal comparisons due to the inherent difficulties arising from the predominance of cancellous bone. (Moreover, only the central diaphyseal region is of interest in adaptive remodelling studies using the turkey ulna preparation). Discrete pixel-based differences in cross-sectional area and centroidal principal area moments of inertia were calculated at each longitudinal site. Left and mirrored right cross-sections were aligned at a common centroid and principal orientation to calculate the fraction of cross-sectional area common to both

ulnae (Fig. 1c). Finally, cortical thicknesses were compared at 5^{o} angular increments along rays projected from the common centroid. These latter two indices reflect longitudinally specific differences in cortical surface geometry, which directly influence the strain field for any applied load.

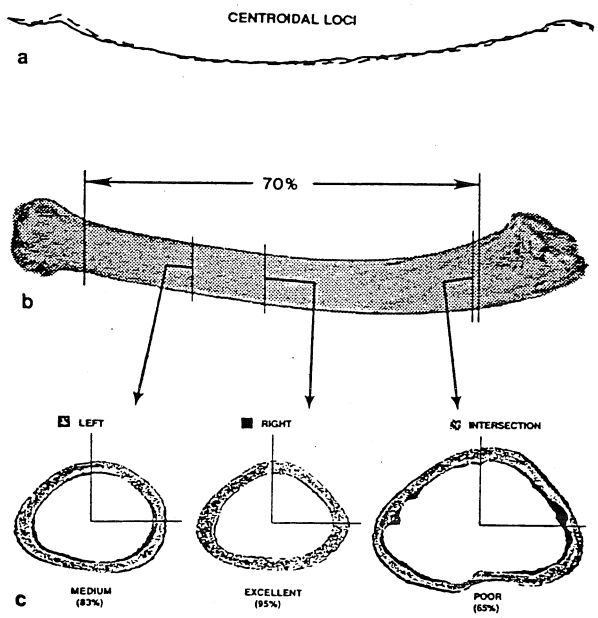

Figure 1. (a) Left-right separation of centroidal loci. (b) Central 70% of diaphysis used for cross-sectional comparisons. (c) Centroidal and principal axes alignment of longitudinally matched cross-sections, demonstrating various degrees of areal intersection.

All left versus right differences were computed as

$$P = 2 (R - L) / (R + L) \times 100\%$$

where P is the percentage difference between the right and left values considered. A pair of machined PMMA testpieces with mirror symmetry was analyzed by serial milling and digitized photographs to provide a standard for comparison of the accuracy of each parameter.

RESULTS

The left-right discrepancy of total ulna volume and principal volume moments of inertia were 4.9 ± 3.5% and 7.2 ± 5.5% (average + SD), respectively, values which were not greater than the difference for the standard (Table 1). The RMS value of separation distance between paired centroidal loci was 0.7 ± 0.3 mm, again not larger than that for the standard .

Volumetric Property	Ulnae Pairs	Standard
Total Volume	4.9 ± 3.5 %	6.9 %
Principal Volumetric I	7.2 ± 5.5 %	7.8 %
Loci Separation	0.7 ± 0.3 mm	0.5 mm

Table 1: Left-right differences in volumetric properties (average ± standard deviation).

Longitudinal differences in cross-sectional area between contralateral images were 8.1 ± 3.0% (Table 2). Likewise, differences in principal area moments of inertia were 10.7 ± 3.8%. Principally aligned cortices intersected to a level of 80 ± 6%, which was less than for the standard. Left-right differences in cortical thickness varied considerably, but tended to cancel out when averaged circumferentially (3.9 ± 3.5%).

Areal Property	Ulnae Pairs	Standard
Cross Sectional Area	8.1 ± 3.0 %	5.0 ± 3.0 %
Principal Area I	10.7 ± 3.8 %	8.8 ± 5.3 %
Area Non-Intersection	20 ± 6 %	6 ± 3 %
Cortical thickness	3.9 ± 3.5 %	-

Table 2: Left-right differences in serial cross section properties (average ± standard deviation).

DISCUSSION

With the exception of areal intersection, all measured parameters of symmetry were similar to these obtained from the standard testpieces. There are several factors which affect the ability to overlay longitudinally matched cross sections. First, the intersection of cross sections was clearly greater in sections near the volumetric centroid, and diminished toward each metaphysis (Fig. 1c). Second, any local anomaly in one image will affect the location of the areal centroid, as well as areal principal moments of inertia, which were used as a basis of overlaying cross sections. Third, whereas the testpieces had a solid cross section, the cortex of the ulna is a thin annulus, inherently degrading the propensity for a high degree of overlap.

For the purpose of contralateral comparisons in adaptive remodelling studies, areal properties of central cross sections are most relevant to assessing symmetry. In all comparisons, the central cross sections demonstrated a higher level of areal intersection than those near the metaphysis, often above 90% and within the margin of systematic error. Thus it is desirable to assess left-right asymmetry when quantitating adaptive remodelling using experimental and analytical tools such as finite element analysis.

REFERENCES

Rubin, C.T. and Lanyon L.E., J Orthop Res, 5, 300-310, 1987.
Currey J.D., The Mechanical Adaptations of Bones, 1984.
White, A.A. et al., Acta Orthop Scand, 45, 328-336, 1974.
Helmkamp, RC et al., A J Phys Anth, 83, 211-218, 1990.
Miller, G.J. et al., J Biomech, 13, 1-8, 1980.
Sumner D.R. et al., J Orthop Res, 6, 758-765, 1988.

ACKNOWLEDGEMENTS

The authors appreciate the technical assistance of Bang-Ling Chang, Nancy Caldwell, and Joni Caplan. Financial support was provided by NIH AR-40411.

LOWER EXTREMITY JOINT KINETICS AND MUSCLE ACTIVATION PATTERNS DURING LANDINGS OF FRONT AND BACK SALTOS

Jill L. McNitt-Gray, Dawn M.E. Irvine, Michelle Welch,
Barry A. Munkasy, Carolyn Barbieri, & David D. Anderson
USC Biomechanics Research Laboratory, Department of Exercise Sciences
University of Southern California, Los Angeles, CA, USA 90089-0652

INTRODUCTION

Although no causal relationship has been proven between load and injury, the high forces and moments encountered during landings of aerial gymnastics skills may be responsible for the high incidence of injury to the lower extremities of gymnasts (McAuley et al., 1987; NCAA, 1986, 1990). Landings of gymnastics skills have produced some of the largest peak reaction forces encountered in sport (Nigg, 1985; Panzer, 1987). The peak magnitude of these forces have been shown to increase as the impact velocity (McNitt-Gray, 1991) and skill complexity increase (Panzer, 1987). For example, landings of a single back tucked saltos have produced peak vertical reaction forces of 8 times the body weight (BW) (Panzer, 1987; Ozguven & Berme, 1988), whereas, double back tucked saltos have produced peak vertical reaction forces exceeding 18 BW (Panzer, 1987). Although no significant differences in peak vertical forces have been observed during landings of front and back saltos (McNitt-Gray, et al., 1991), the differences in rotation, visual conditions and segment configurations prior to contact between tasks may produce differences in joint kinetics and muscle activation patterns (Nigg, 1985; McNitt-Gray & Nelson, 1988; McNitt-Gray, 1989; Sidaway, McNitt-Gray, & Davis, 1989).

The purpose of this study was to determine the influence of forward and backward rotation prior to contact on lower extremity joint kinetics and muscle activation patterns during landing.

PROCEDURES

Six healthy male gymnasts, who were members of a team ranked among the top five of all collegiate gymnastics teams within the United States, volunteered to serve as subjects. During data collection, each subject successfully landed three drop landings (McNitt-Gray, 1991), three front tucked saltos, and three back tucked saltos in a randomized order using their normal competitive landing style. All three tasks were initiated from a height of 0.72 meters above the top surface of two regulation gymnastics mats (100 ILD). These two mats were fully supported by two Kistler force plates. The reaction forces at the mat-plate interface were quantified for each foot using a sampling frequency of 800 Hz. Segment kinematics were recorded simultaneously using high speed video (200 fps; NAC Motion Analysis System). The muscle activation patterns of seven lower extremity muscles -gluteus maximus (GM), Vastus Medialis (VM), Rectus Femoris (RF), Biceps Femoris (BF), Medial Gastrocnemius (MG),Semitendonosis(ST), and Tibialis Anterior (TA) - were quantified, prior to and during the landing, using surface electromyography (1600 Hz; Beckman Silver-Silver Chloride electrodes; Differential Amps, Data, Inc.). The reaction forces, kinematics, and EMG were synchronized at the time of contact. Markers positioned on the body of the subjects were digitized using a video based data acquisition system (Peak Performance, Inc.). Each coordinate of the digitized body landmarks (Zatsiorsky & Seluyanov, 1983) were digitally filtered using a fourth order Butterworth Filter (Saito & Yokoi, 1983) with a cut-off frequency derived by the method of Jackson (1979). The kinematic and reaction force data were synchronized and net ankle, knee, and hip moments were calculated using Newtonian mechanics (Nm/kg). The EMG signals from each muscle were processed using a high and low pass filter, rectified, and normalized to peak amplitude observed during the drop landings (SNIP, 1988, Digital Dynamics, Inc.). The interval of interest, identified as the landing phase, was the time from contact to the time required to bring the vertical velocity of the total body center of mass to zero. Joint kinetics and muscle activation patterns observed during the front and back salto landings were compared within subjects.

RESULTS AND DISCUSSION

Muscle activation patterns of muscles contributing to the ankle, knee, and hip net joint moments observed during front and back salto landings performed by a representative subject have been provided in Figure 1. EMG of muscles contributing to joint extension have been represented by positive magnitudes, whereas, EMG of muscles contributing to joint flexion have been represented as negative magnitudes. Electromechanical delay has been accounted for by shifting the EMG signals (+50 ms) relative to the net joint moments.

Although no significant differences in peak vertical forces were observed between tasks, the orientation of the body relative to the direction of translation produced differences in joint kinetics and muscle activation patterns. For example, when landing a back salto, the horizontal reaction forces opposing translation assist the vertical reaction forces in producing a dorsi flexion moment about the ankle. However when landing a front salto, the horizontal forces opposing translation create a plantar flexion moment counteracting the dorsi flexion moment created by the vertical reaction force. This difference in body position relative to the direction

of translation contributes to the greater plantar flexion net ankle moments observed during back salto landings as compared to front salto landings. In addition, differences in the orientation of the trunk relative to the thigh between tasks contributes to the greater hip flexor moment observed at contact for front salto landings as compared to those observed for back salto landings. More definitive muscle activation patterns observed prior to contact during back salto landings as compared to front salto landings may be associated with differences in surface viewing times between tasks.

REFERENCES

Devita, P. et al. MSSE, 24 (1):108-115, 1992

Jackson, K.M., IEEE Trans. Bio Eng. 26:122-124, 1979.

McAuley, E. et al., AmJ Spts Med,15,558-565, 1987.

McNitt-Gray, J.L., IJSB, 7, 201-224, 1991.

McNitt-Gray, J.L. & Nelson, R.C., MSSE, Sup, 1988.

National Collegiate Athletic Association,1986,1990.

Nigg, B. M., Sprts Med, 2, 367-379, 1985.

Ozguven, et al. J of Biomech.21:1061-1066, 1988.

Panzer, V.P., Doc. Dissert, U of Oregon, 1987.

Saito, S. et al., B Hlth Sprts Sci, 5:201-206, 1982.

Sidaway, B. et al. J of Eco Psych, 3, 1989.

Zatsiorsky, V etal. , Biomech.VIII-B,1152-1159, 1983.

ACKNOWLEDGEMENTS

US Olympic Committee, Carolina Gym Supply, the USC Biomechanics Research Team, and UCLA Gymnastics.

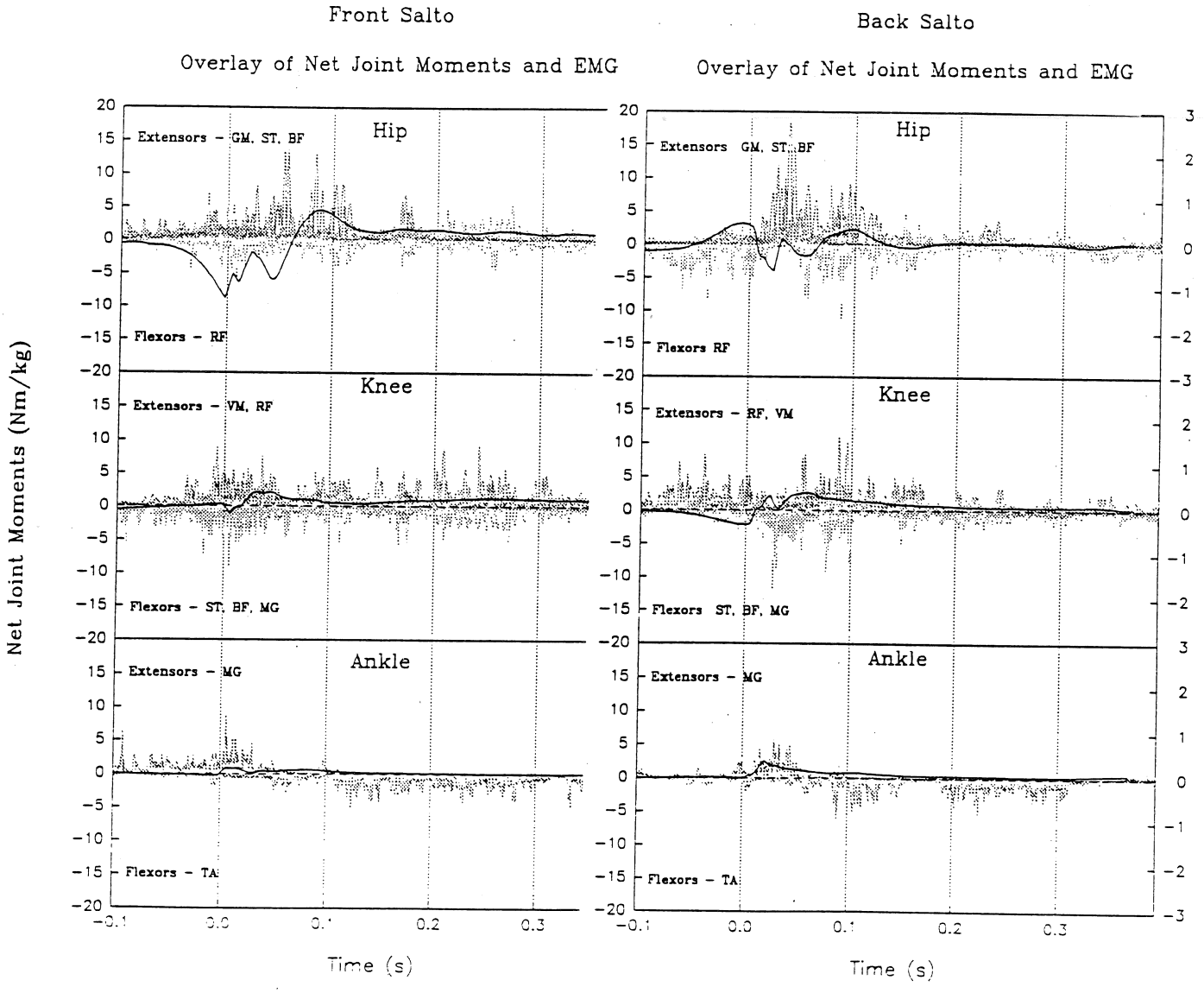

THE CROWHOP: TECHNIQUE FAULT OR UNFAIR ADVANTAGE?

D.I. Miller

Faculty of Kinesiology
University of Western Ontario, London, ON N6A 3K7

INTRODUCTION

In the performance of backward and inward springboard dives, competitors are not permitted to bounce the board before the takeoff. At the discretion of the individual judge, however, an involuntary movement in which the feet lift slightly off the board (i.e., a crowhop) is penalized slightly if at all. The fact that the crowhop is treated by many officials as a technique fault rather than an unfair advantage led to the current study.

An analysis of the performances of female competitors at four international meets revealed that 15% consistently employed crowhops. Results indicated that these divers have the potential for generating approximately 10% greater maximum depression of the springboard thereby gaining an unfair advantage over competitors who maintain continuous contact with the board throughout the takeoff.

PROCEDURES

Backward and inward takeoffs performed in preliminary rounds of the women's 3-m springboard events at the FINA Cup (1989), Dive Canada (1990), World Diving Cup (1991) and Alamo International (1992) which had been videotaped with a stationary and level Panasonic PV-330 camcorder positioned to the side and even with the tip of the 3-m board were reviewed qualitatively. Back 2 1/2 and inward 1/2 takeoffs of 8 divers who used a crowhop and a comparison group of 8 divers exhibiting contact takeoffs were subsequently digitized using a Peak Performance Technologies 2D system and the data processed with custom software. There was no statistically significant difference between the two groups in terms of body weight or average dive score.

RESULTS

Review of the videotapes indicated that, not only were 11 of the 65 women clearly breaking contact with the board with both feet during their standing takeoffs but that an additional 16 were adjusting the position of one or both feet after board oscillation had been initiated. Foot-board interactions in standing takeoffs varied along a continuum. At one end, a firm contact was maintained between almost the entire undersurface of the toes and the board during the takeoff. At the other extreme (operationally defined as a crowhop), there was a distinct separation between both feet and the board while the diver was moving upward. During this noncontact period, the feet began to flatten at the toes and/or ankles in preparation for subsequent contact with and depression of the board.

All but one of the women attempting the inward 2 1/2 pike (the highest degree of difficulty dive) did so with a crowhop.

Detailed quantitative analysis of the crowhop and comparison groups focused on the critical half second interval (30 video frames at 60 Hz) immediately preceding the 0.167 s (10 frames) leading up to maximum depression of the springboard. It was in this half second interval that: the crowhop (if present) occurred; the diver experienced negative vertical acceleration; and maximum downward velocity of the center of gravity was achieved (Figure 1).

Divers employing the crowhop averaged 0.25 s of noncontact, a time which approximated or exceeded that associated with final board recoil. These divers tended to set their fulcrums further back from the board tip than those who maintained continuous contact with the board ($p<0.01$) and the downward velocity of their centers of gravity was, on average, 0.4 m/s greater ($p<0.01$). In addition, their takeoff actions did not disrupt the preliminary oscillation pattern which had been established.

DISCUSSION

Adjustments to standing takeoffs introduced by the crowhop technique have the potential for increasing the kinetic energy which the diver can transfer to the board to depress it and, all else being equal, greater depression of the board will result in better diving performance.

Results of the study indicated that the crowhop is not inadvertent but a well-established pattern of motion employed by certain divers. The crowhop should not be considered a technique fault but rather should be recognized as a method by which unfair advantage can be gained. Judging rules and practices should therefore be revised accordingly.

ACKNOWLEDGEMENTS

Funded by U.S. Diving.

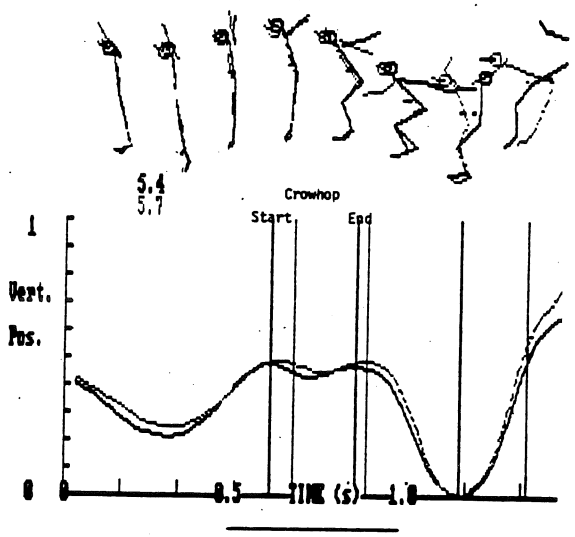

Figure 1. Vertical position of the board tip (m) during takeoffs for the back 2 1/2 somersaults pike (darker line) and inward 2 1/2 somersaults pike (lighter line). Average scores for these dives were 5.4 and 5.7, respectively. The critical half second of analysis is shown below the 'time' caption. Vertical lines during this period indicate the beginning and end of the crowhop for these dives. The final two vertical lines indicate maximum depression and last contact with the springboard.

3-D ANALYSIS OF THROWING PATTERNS OF YOUNG BOYS AND GIRLS

R.N. Hinrichs, J.R. Thomas, P.E. Martin, K.T. Thomas,
M. Marzke[1], T. Joganich, J.K. DeWitt, and C.P. Sherwood

Exercise & Sport Research Institute, Arizona State University, Tempe, AZ 85287
[1]Dept. of Anthropology, Arizona State University, Tempe, AZ 85287

INTRODUCTION

Substantial gender differences in throwing performance have been documented for both children and adults. Little has been done, however, on quantifying the differences in throwing techniques between boys and girls. Ten boys and ten girls between the ages of five and six were selected as subjects. Each subject was instructed to throw a tennis ball in the laboratory with maximum speed. Three-dimensional (3-D) videography was used to obtain 3-D coordinates of the major joint centers and the ball. Several kinematic variables were quantified as functions of time. In addition to the angular kinematics of individual joints, "global arm angular velocity" and "radius of rotation" vectors were defined in 3-D by the motion of a line segment connecting the mid trunk to the ball. There was considerable overlap between boys and girls in specific joint kinematics and radius of rotation vector magnitude at release. No clear differences in individual joint angular velocities were found between boys and girls, however the boys coordinated their joint actions better to produce larger global arm angular velocities and faster ball velocities at release.

REVIEW AND THEORY

Substantial gender differences in throwing performance have been documented for both children and adults. The phrase "throws like a girl" is commonly used to describe a motor pattern used by novice throwers. The throwing patterns of expert male throwers have been quantified and documented in the biomechanics literature (Feltner et al., 1986; Feltner, 1989). Little has been done, however, on quantifying the differences in throwing techniques between boys and girls. Most of what has been published on comparing boys' and girls' throwing patters has been qualitative in nature (e.g., Nelson et al., 1986). The purpose of this research was to study in detail the throwing patterns of young boys and girls in order to detect differences in the 3-D motions of the throwing arm and trunk. Boys were hypothesized to use larger joint angular velocities than girls and release the ball with a greater linear velocity.

PROCEDURES

Ten boys and ten girls between the ages of five and six were selected as subjects. Each subject was instructed to throw a tennis ball in the laboratory with maximum speed. Two 60 Hz Panasonic AG-450 S-VHS video camcorders were used to record the motion. The videotapes were digitized using a Peak Performance video digitizing system. Three-dimensional (3-D) coordinates of the major joint centers on the body and the ball were reconstructed using the NLT algorithm (Dapena et al., 1982). Out of twenty trials performed by each subject, the trials with the six fastest ball velocities were chosen for detailed analysis.

The raw data were smoothed with a Butterworth digital filter with a cutoff frequency of 6 Hz and differentiated using finite difference equations. Several kinematic variables were quantified as functions of time. Among these were trunk shoulder-to-hip (twist) angle, shoulder horizontal ab/adduction and internal/external rotation angles, elbow flexion angle, angular velocities of all these angles, and ball velocity. In addition "global arm angular velocity" and "radius of rotation" vectors were defined in 3-D by the motion of a line segment connecting the mid trunk to the ball.

RESULTS AND DISCUSSION

There was considerable overlap between boys and girls in specific joint kinematics and radius of rotation vector magnitude at release. However, the boys consistently demonstrated a greater global arm angular velocities at release than the girls (see Figure 1). Boys also tended to have greater forward trunk velocity at release than girls (0.5 m/s vs. 0.3 m/s). Radius of rotation magnitudes at release, however, were similar between boys and girls. Overall these differences resulted in faster release velocities of the ball for boys than girls (17 m/s vs. 13 m/s, respectively). Thus even though there were not any clear differences in individual joint angular velocities between boys and girls, the boys coordinated their joint actions better to produce larger global arm angular velocities and faster ball velocities at release.

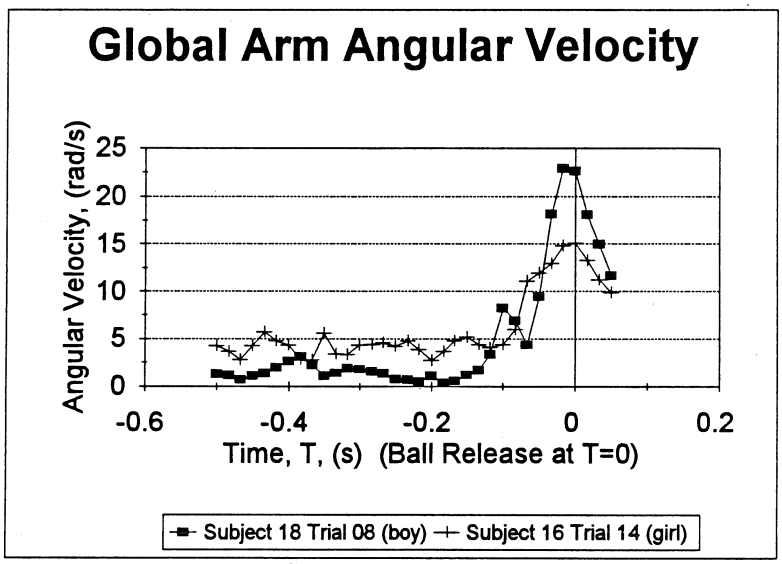

Figure. 1. Comparison of the magnitude of the global arm angular velocity vector for typical trials for boys and girls.

REFERENCES

Dapena J. et al. J. Biomech., 15, 11-19, 1982.
Feltner, M. et al. Int. J. Sport Biomech., 2, 235-259, 1986
Feltner, M. Int. J. Sport. Biomech., 5, 420-450, 1989.
Nelson, J.K. et al. Res. Quart. Ex. Sport, 57, 280-287, 1986.

GENDER DIFFERENCES IN THE LOCATION OF THE CENTER OF BUOYANCY OF COMPETITIVE SWIMMERS

McLean, S.P. and Hinrichs, R.N.
Exercise and Sport Research Institute
Arizona State University, Tempe, AZ 85287-0404

INTRODUCTION

The present study considers the location of the center of buoyancy (CB) as a representative variable of the contributions of the anthropometric characteristics and body composition to performance in an aquatic medium. Males were found to have a CB located cranial to their center of mass (CM) than females. Males also swam faster than females but when performance was limited to kicking there was no statistical difference between genders. The location of the CB relative to the CM was speculated to affect the position of the body in the water by allowing women to float more horizontally.

REVIEW AND THEORY

The center of buoyancy is defined as the centroid of the volume displaced by a floating or submerged body. In a gaseous environment, such as during the airborne phase of a dive, buoyancy effects are negligible so motion is modified only by the action of the gravitational forces through the CM. However, when immersed in a fluid medium a buoyant force acts through the CB in addition to the gravitational force. The CB is theorized to fall cranial to the CM yet its actual position has yet to be quantified. Different locations of these points in a body creates a couple and the body will turn until the moment of this couple has been eliminated (i.e. static equilibrium is achieved).

The location of the CB is affected by the quantity and distribution of water displaced by the body. Gender differences in percentage body fat and distribution of this tissue have the potential to affect the location of the CB by altering the distribution of the displaced fluid. Because females tend to have proportionately more adipose tissue (McArdle, Katch, & Katch, 1981) which is distributed in greater proportion in the lower extremities (Wilmore & Thomas, 1987), they have increased the relative volume of the lower extremities without an equal increase in the relative mass. This distal distribution of adipose tissue in females maintains the CB at a location closer to the CM thus reducing the moment caused by the buoyant and gravitational forces. This logic is demonstrated by the improved ability to float when the arms are placed above the head. Because the arms are relatively more dense compared to the trunk moving the arms above the head will move proportionately more mass than volume thus moving the CM closer to the CB.

Cotton and Newman (1978) applied the concepts of buoyancy to the development of better teaching techniques for swimming. Huijing *et al.* (1988) discussed anthropometric variables as they related to hydrodynamic drag. However, Grimston and Hay (1986) and Von Dõbeln and Holmér (1974) are the only studies relating anthropometric measures directly to aquatic performance. These studies considered anthropometric variables in an individual manner but it is logical that a combined effect of these measures will more directly influence performance. The location of the center of buoyancy is a concise measurement which captures the effect of many components.

The purposes of this investigation were to 1) quantify the CB and CM locations in male and female competitive swimmers in a floating position, 2) relate these parameters to the distribution of adipose tissue, and 3) relate these variables to performance in swimming and kicking. Three hypotheses were tested in this study; 1) females will have relatively more adipose tissue distributed to their lower extremities than males; 2) females will have their CB closer to their CM than males; 3) females will experience a performance advantage due to the reduced drag of a more horizontal position in the water resulting from the location of the CB relative to the CM.

PROCEDURES

Total percent body fat (%BF) was assessed for 16 female (mean age 19.1 yrs) and 15 male (mean age 19.9 yrs) collegiate swimmers using skinfold techniques. A body fat distribution ratio (BFDIST) was defined as the sum of the abdominal and suprailiac skinfolds divided by the thigh skinfold. The CM was located for a "streamlined" position (arms above the head, elbows fully extended, hands clasped) with a maximal inhalation using a reaction board. The CB was located using an "aquatic reaction board." This structure was similar to one described by Carter (1955) and maintained the subject in a horizontal, floating, streamlined position at the surface of the water by supporting the ankles. A two kg weight was added to the ankles to stabilize the scale readings. Measurements of the supporting force at the ankles were taken for a maximal inhalation.

Performance trials were conducted in a 25 yard pool. Four maximal effort sprint swims and four maximal effort sprint kicks were timed for each subject. The kick trials were performed in a streamlined position without the aid of a kickboard. Subjects were instructed to breathe minimally during the trials and to remain near the surface of the water. Warm-up and warm-down were provided and the swim and kick trials were alternated with sufficient rest given between trials.

Two discriminant analyses were conducted to identify group differences in the distance between the CB and CM locations normalized to body height (CB-CM), %BF, BFDIST, swim and kick times. Two separate analyses were required to avoid multicollinearity problems since %BF and BFDIST were both functions of the same measurements. A multiple regression was performed using CB-CM as dependent variable with %BF and BFDIST as independent variables. These data were conditioned first to remove the overlying effect of gender.

RESULTS

Table 1 contains discriminant analysis results. CB-CM was forced into the analysis first based on *a priori* reasoning that this variable accounted for performance differences. Results indicate that the CB is closer to the CM in females versus males. Females also have a smaller BFDIST ratio (more adipose tissue in the lower extremities) and greater %BF compared to males. Males swim faster but may not kick any faster than females.

Figures 1 and 2 are plots of the data with the gender differences incorporated. It is clear that in both graphs there is a parity in the data related to the gender differences. From this it appears that their is a relationship between the CB-CM and %BF or BFDIST. However to examine the pure relationship between these variables the gender difference must be removed. The regression analysis for this indicates no significant relationship.

This can be mentally pictured by overlapping the two groups of data on a given graph. This would lead to a scatterplot of points which has little if any linear trend in it.

Table 1 - Discriminant Analysis Results: Means (± S.E.M.)

	Male	Female	$p <$
CB-CM	0.4451	0.1117	0.01
(% Height)	(0.065)	(0.048)	
BFDIST	2.089	1.315	0.01
	(0.096)	(0.079)	
%BF	11.48	22.91	0.01
	(0.569)	(0.688)	
Swim Time	12.001	13.181	0.01
(s)	(0.176)	(0.143)	
Kick Time	18.891	19.891	NS
(s)	(0.417)	(0.611)	

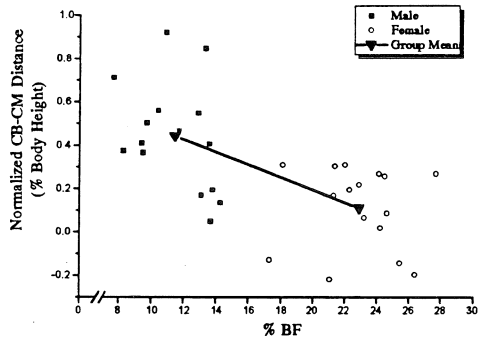

Figure 1 - Plot of CB-CM as a function of %BF.

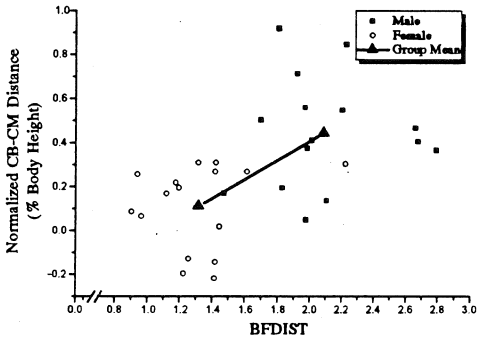

Figure 2 - Plot of CB-CM as a function of BFDIST.

DISCUSSION

The most important result of this study is the quantified location of the CB for one posture. To the authors' knowledge this has not previously been recorded. This point may be very important for future aquatic research as it allows the buoyant force to be accounted for in kinetic analyses. However, this application is limited since a dynamic method for locating this point has not been developed. In addition, a distinct gender difference has been found for this point as the CB is closer to the CM in females than in males. This phenomenon may influence motion in the aquatic environment differently for each gender. Previous literature simply reported thigh skinfolds as an indication that females had more adipose tissue in their lower extremities (Wilmore & Thomas, 1987). This result is not surprising since %BF was significantly higher for females as well. BFDIST provides an alternative measure which describes the relative dimensions of skinfolds above and below the waist. This gives a better description of the distribution of adipose tissue. Based on this measurement it is clear that females store proportionately more adipose tissue on their thighs than males.

No relationship appears to exist between the CB-CM and the distribution of body fat in competitive swimmers from the regression analysis which controls for gender. Upon closer inspection of the raw data (Figures 1 and 2) a relationship as described by hypothesis #1 may exist but is mediated through gender differences in both of these variables. It appears that a lower BFDIST ratio moves the CB closer to the CM (as evident in the females). Perhaps there is a relationship between these variables regardless of gender but in order to find this a less homogeneous group and a greater amount of power (more subjects) would be necessary to identify it.

The performance data indicate that males consistently swim faster than females but they do not consistently kick faster however, there was a large amount of variability in kicking times with much overlap between genders. The potential advantage of a more horizontal, natural floating position for females may have erased much of the presumed strength advantage the men had when kicking. When using the arms, however, the men's presumed strength advantage may have overshadowed the women's body position advantage. No data concerning strength were collected and thus this relationship remains speculative.

This investigation has identified a significant difference in the relative locations between the CM and the CB in competitive swimmers which appears to be related to the distribution of the adipose tissue in the body as this will affect both the CB and CM locations. The effect of these points on performance is less clear. A reduced CB-CM distance should provide a performance advantage for the females due to reduced drag in a more horizontal body position in the water. Evidence of this advantage is provided by a non-significant difference in their kicking times even though the swimming times were significantly faster for the males compared to the females.

REFERENCES

Carter, J.E.L. *New Zealand J. Phys. Ed.*, 6, 14-23, 1955.

Cotton, C.E. and Newman, J.A. *J. Hum. Mvmt. Studies*, 4, 129-143, 1978.

Grimston, S.K. and Hay, J.G. *MSSE*, 18, 60-68, 1988.

Huijing, P.A. *et al.* Swimming Science V, 1988

McArdle, W.D., Katch, F.I., and Katch, V.L. Exercise Physiology. Lea and Fibeger, 1981.

von Döbeln and Holmér *J. Appl. Physiol.*, 37, 55-59, 1974.

Wilmore, J.H. and Thomas, E.L. Ex. Testing and Ex. Prescr. for Special Cases. (pp. 31-46), Lea and Fibeger, 1987.

ACKNOWLEDGEMENTS

The authors would like to acknowledge Deena Harms, Paul Spoor, and Keith Beckett for their assistance with this project.

HAND PRESSURES AS PREDICTORS OF RESULTANT AND PROPULSIVE HAND FORCES IN SWIMMING

Anne M. Thayer

Department of Exercise Science, The University of Iowa, Iowa City, IA 52242

INTRODUCTION

In recent years, there has been an increasing interest in research methods which can provide quantitative data to aid in evaluating technique in swimming. The measurement of the resultant forces exerted by the water on a swimmer's hand has often been the focus of research in swimming involving the analysis of technique. Two very different methods have been used to estimate hand forces. Hydrodynamic analysis, developed by Schleihauf (1979, 1984), involves combining laboratory data on lift and drag forces as a function of angle of attack with a three-dimensional film analysis to obtain an estimate of propulsive forces. Pressure analysis involves the use of pressure sensors located on the hand to estimate hand forces directly. Both methods have underlying assumptions requiring validation. The pressure analysis offers the possibility of being more precise since it is a direct measure and not based on previously obtained laboratory data. It also offers the advantage of being able to provide immediate results, which could be beneficial in future applications. Several problems have been encountered in using pressure transducers to obtain hand forces in swimming. This includes problems of quantifying the results of pressure transducer measurements, of determining the optimum location of the pressure transducers on the hand, and of determining whether the pressure curves accurately represent the resultant and/or propulsive forces. This study was designed to determine if the pressure measured at a single point or at a small number of points on the hand is sufficient to determine the resultant and propulsive hand force. This was done through the use of two full-scale, mechanically-driven hand models instrumented with 127 pressure sensors. It was found that the prediction of the resultant and propulsive forces was dependent on the motion and orientation of the hand, and that a small number of tap locations was inadequate to predict these forces with acceptable accuracy.

REVIEW AND THEORY

The use of pressure sensors is based on the relationship between pressure and force. Surface forces acting on a swimmer's hand are the integrated effects of the normal and shear stresses on the hand surface due to the presence of the surrounding water. For bluff bodies such as a hand, the shear stresses are usually very small and the force due to normal stresses is the primary one (Vogel, 1981). The normal stress at any given point on the hand is equal to the water pressure, p, at that point. Assuming negligible shear stresses, the pressure-dependent resultant force on the hand, $\bar{F}$, can be written as:

$$\bar{F} = \int -p\,\bar{n}\,dA$$

where $\bar{n}$ is the unit vector normal to the surface and directed outward; dA is a differential area on the hand surface; and p is the compressive normal stress (pressure) acting on dA. Note that by convention, the minus sign indicates that a compressive stress is negative and p is a positive number.

In the majority of the studies in which pressure sensors have been used, pressure on the hand has been measured through the use of a single pressure transducer mounted on the palm side of the hand (Van Manen and Rijken, 1975; Boicev and Tzvetkov, 1975; Dupuis et al., 1979). In one study, the difference in pressure between two points -- one on the palm side and one on the back side of the hand -- was measured (Loetz and Reischle, 1986); and in another study, a single differential pressure transducer was used (Havriluk, 1988). The validity of the pressure analysis depends on the validity of the assumption (usually unstated) that the pressure measured at one or two points on the hand is sufficient to determine the resultant hand force.

Research on the pressure distribution over the surface of an airfoil shows that such distributions are not uniform (Prandtl and Tietjens, 1957). The position of the maximum negative pressure on the upper surface of an airfoil depends on the shape of the airfoil and on the angle of attack and moves toward the leading edge as the angle increases. The position of the maximum positive pressure on the under surface of an airfoil is close to the leading edge for positive angles of attack. One might reasonably infer, due to the similarity between the shape of the hand and an airfoil, that the pressure distribution over the hand would also be non-uniform and vary with shape and angle of attack. Pressure measures at one or even two locations on the hand may not, therefore, be sufficient to allow an accurate determination of the resultant hand force. The lack of any form of validation in the studies in which pressure sensors have been used means that the results obtained in these studies must be interpreted with caution.

Another drawback to the pressure method has been that the direction of the pressure-dependent resultant hand force has not been known. Two pressure recordings of equal magnitude may have very different implications if the propulsive component (the component of the force in the direction of the swimmer's forward motion) is much larger in the one than in the other. Consequently, pressures recorded at a single point do not distinguish between hand motions that produce large propulsive forces and those that produce large forces but contribute little to forward propulsion.

The purpose of this study was to determine the extent to which the resultant and propulsive forces acting on the hand of a swimmer can be satisfactorily predicted from measures of local pressure on the hand.

PROCEDURES

Two full-scale hand models, molded out of acrylic plastic and instrumented with 65 pressure taps in one and 62 pressure taps in the other, were used. The data for this study were gathered in a series of dynamic tests conducted in a recirculating water flume with flow velocities of 1.28 and 1.16 m/s. The hand model was moved through the water in a semi-circular path by a mechanical system consisting of a pulley and cable mechanism driven by a falling weight. The hand motions were tested under two conditions which simulated, in a simplified manner, the (a) pull phase of the freestyle stroke, and (b) the propulsive phase of the breaststroke pull. Each condition was tested with the hand model in two different orientations, yielding four test conditions. The total force acting on the hand model was measured using strain gage force transducers mounted on the shaft supporting the hand model. For each of the four test situations, the recorded data included the three components of the force transducer output, the angular displacement of the hand-arm system, and the pressure recordings.

RESULTS AND DISCUSSION

Zero-order correlations were computed between measures of pressure on the hand and (a) the resultant force and (b) the propulsive force. A correlation coefficient, $R \geq 0.92$ ($R^2 \geq 0.85$), was arbitrarily chosen to indicate an acceptable level of prediction. Taps associated with correlations between pressure and the resultant or propulsive force which met this criterion were termed good predictors. Good predictors were found for the resultant and propulsive forces in each of the four conditions. However, the location of the tap varied with each condition and the dependent variable -- the resultant or propulsive force -- tested. A single pressure tap alone was not sufficient to predict the resultant or propulsive forces with acceptable accuracy under changing conditions of motion and orientation.

A forward stepwise regression procedure was used to examine the relationship between pressure and the resultant force, and between pressure and the propulsive force. Several different combinations were found for each condition that yielded an R^2 value of 0.85 or better. However, when all two- and three-variable models that satisfied the criterion measure of $R^2 \geq 0.85$ were compared, no single set of taps appeared in the list for all four conditions. In other words, the stepwise analysis did not produce a single model that predicted with the required accuracy for all four conditions.

All possible combinations of two- and three-variable models which met the criterion of $R^2 \geq 0.85$ were found and compared using an all-possible-regressions procedure. Four sets of two taps were identified which could predict the resultant force for all four conditions; and three sets of three taps were identified which could predict the propulsive force for all four conditions. However, the regression coefficients in the prediction equations differed from one condition to another. No single, generalized equation that could be used to predict the resultant or propulsive force under all conditions could be found using any of these sets of taps.

Combining the data sets and again looking for a set of taps that could be used for all four conditions showed that an adequate prediction could be made if a large number of pressure taps was used. For the resultant force, this required a minimum of eight taps, and for the propulsive force a minimum of eleven taps. This result, although yielding a positive answer to the question of whether an adequate prediction of resultant and propulsive force could be made using measures of pressure on the hand, is not a very practical one. Unless the transducers are very small, instrumenting a swimmer with eight or more pressure transducers would be very cumbersome, and would make it difficult, if not impossible, for him (or her) to perform the stroke normally. The subsequent predictions of the resultant or propulsive force would therefore have little relevance to what the swimmer would normally do.

Another concern that needs to be addressed is how the use of external pressure transducers on a swimmer's hand might alter the flow across the hand, and thus alter the force-producing characteristics of the hand. Pressure measurements may be changed considerably if the flow across the hand is altered, resulting in a measure different than normally produced by a swimmer.

In conclusion, the results of this study demonstrated a strong correlation between pressure measured at specific positions on the hand and the resultant and propulsive forces acting on the hand. However, the prediction of the resultant and propulsive forces was dependent on the motion and orientation of the hand. When the results of different conditions of motion and orientation were considered together, no single prediction equation could be found for the resultant or the propulsive force using pressure measurements from less than eight locations. The findings of this study thus suggest that a small number of tap locations would be inadequate to predict the resultant or propulsive forces on the hand with acceptable accuracy.

REFERENCES

Boicev, K., and Tzvetkov, A. Swimming II, (pp. 80-89), University Park Press, 1975.

Dupuis, R. et al. Swimming III, (pp. 110-117), University Park Press, 1979.

Havriluk, R. J. Swimming Research, 4,4, 11-16, 1988.

Loetz, C., et al. Swimming Science V, (pp. 361-367), Human Kinetics Publishers, Inc., 1988.

Prandtl, L. and Tietjens, O.G. Applied Hydro- and Aeromechanics, (pp. 145-161), Dover Publications, 1957.

Schleihauf, R.E. Ed.D. Dissertation, Teacher's College, Columbia University, 1984.

Schleihauf, R.E. Swimming III, (pp. 70-109), University Park Press, 1979.

Van Manen, J.D., and Rijken, H. Swimming II, (pp. 70-79), University Park Press, 1975.

Vogel, S. Life in Moving Fluids, (pp. 65-80, 191-204, 275), Princeton University Press, 1983.

EFFECT OF AGE AND SPEED ON THE BIOMECHANICS OF SITTING DOWN ONTO A CHAIR

M. Melissa Gross

Department of Movement Science, The University of Michigan, Ann Arbor, MI 48109-2214

INTRODUCTION

Chair transfer is an important activity of daily living that is particularly challenging to the elderly. Although the biomechanics of rising from a chair have been studied for both young and elderly subjects, little is yet known about the biomechanics of sitting down onto a chair. In this study, the biomechanics of sitting down onto a chair were examined in young and elderly women when moving at three different self-selected speeds. Results showed that movement speed affected the biomechanics of sitting down onto a chair in the same way for both age groups, but that the temporal organization of the task was different for the two age groups. Although joint torques were similar for young and elderly subjects during the task, the young subjects generated greater momentum during descent than did the elderly subjects. Differences in the biomechanics of the task between young and elderly subjects may represent a strategy by the elderly subjects to enhance stability at the time of chair contact.

REVIEW AND THEORY

Chair transfer requires the ability to both rise from and sit down onto a chair. Studies of chair rise show that the joint torques required for the task are large, and exceed those used in walking and stair-climbing (Rodosky et al. (1989)). For the elderly, however, maintaining balance during the task may be an even more important performance constraint than diminishing the required muscle torques (Schultz et al. (1992)). Differences in the dynamics of chair-rise between young and elderly subjects depend on movement speed (Pai et al. (1989)) and level of disability (Alexander et al. (1991); Ikeda et al. (1991)). Although sitting down onto a chair is associated with risk for falling (Tinetti et al. (1988)), few studies exist on the biomechanics of sitting down onto a chair (Yoshida et al. (1983)). The purpose of this study was to describe the biomechanics of sitting down onto a chair and how they are affected by age and speed.

PROCEDURES

Fifteen elderly (70±6 yrs) and seven young (24±2 yrs) women participated in the study. The elderly women were community-living and were free of known musculoskeletal or neurological conditions that limited their mobility. Subjects were asked to sit down into a standard height chair at self-selected slow, normal, and fast speeds without the use of their arms for assistance. kinematic data were obtained using a 60 Hz, video-based motion analysis system. Reaction force data were collected using force plates fixed in the floor and chair seat. The motion data were digitally filtered with a low-pas cutoff frequency of 6 Hz. Hip, knee, and ankle muscle torques, as well as the joint torques due to gravity and segmental accelerations and velocities, were calculated using the motion data. The locations of the body center of mass and the center of pressure under the feet were calculated. The effects of age and speed were tested using regression analysis or analysis of variance as appropriate; significant results are reported for $p<0.05$.

RESULTS

Movement times decreased significantly from slow to normal to fast speed trials for both young and elderly subjects (Y=2.88±0.32s, 2.06±0.30s, and 1.41±0.20s; E=2.70±0.39s, 2.16±0.42s, and 1.59±0.21s). Although the young subjects tended to move faster than the elderly subjects at all speeds, the difference was significant only for the fast speed trials. The relative time spent in the descent portion of the movement (*i.e.*, start of movement to chair contact relative to movement time) decreased with movement time for both young and elderly subjects. Although the decrease was significant for both age groups, the elderly subjects showed more variability in relative descent times than did the young subjects (r=.28 and r=.63, respectively). At the same movement speeds, however, elderly subjects took relatively more time to descend than did young subjects (norm=62±14% and 52±11%; fast=51±20% and 45±8%, respectively).

Joint motions were similar at all movement speeds, for both young and elderly subjects. During descent, the knee and hip joints flexed, and were followed by hip joint extension during the "settling" phase (*i.e.*, chair contact to movement end) . Reversal of hip joint motion from flexion to extension occurred at or slightly before chair contact.

Subjects contacted the chair with a decreasing negative (downward) velocity and thus a positive (upward) acceleration. The magnitude of the upward acceleration increased as movement time decreased for both young and elderly subjects (r=.67 and r=.58, respectively). The magnitude of the upward acceleration at chair contact was greater for young subjects than for elderly subjects, even when they were moving at the same rate (normal speed trials) (1.85±1.05 and 1.22±0.72ms^{-2}, respectively). The magnitude of the downward momentum of the body peaked during descent, prior to chair contact. The magnitude of the downward momentum also increased with movement speed for both young and elderly subjects (r=.81 and r=.77, respectively), and was greater for young than for elderly subjects (norm=-28.6±8.6 and -23.5 ± 6.6 $Kgms^{-1}$; fast=-47.6±13.0 and -38.9±7.3 $Kgms^{-1}$, respectively).

Extensor torques at the hip and knee peaked prior to chair contact for young and elderly subjects. Extensor torques

peaked significantly earlier for the elderly subjects than for the young subjects, at both the hip (-0.20±0.35s and -0.06±0.32s, respectively) and the knee (-0.21±0.36s and -0.11±0.15s, respectively). Peak extensor torques at the hip increased significantly as movement time decreased but the relationship was not strong for either young or elderly subjects (r=.27 and r=.33, respectively). Hip torques were the same for young and elderly subjects when moving at the same speed. The magnitude of knee and ankle torques did not depend on movement time or age.

The ratio of hip muscle torque to gravitational torque at chair contact increased significantly with movement speed for both young and elderly subjects (norm=-1.5±0.3 and -1.3±0.3; fast=-1.9±0.6 and -1.6±0.2, respectively). The ratio was significantly greater for the young subjects.

The projection of the center of mass location under the foot was always posterior to the lateral malleolus at the time of chair contact, and did not depend on movement time or age. In contrast, the center of pressure location ranged both anterior and posterior to the ankle joint. The center of pressure position at chair contact tended to move anteriorly as movement time decreased for the elderly subjects (r=.28), but not for the young subjects.

DISCUSSION

The temporal structure of the task was the same for young and elderly subjects. Movement time decreased as speed increased for both groups. Young and elderly subjects had similar movement times, except in fast speed trials in which the young subjects were able to achieve greater speeds than were the elderly. Despite the same overall movement times, elderly subjects were able to move slower during the descent portion of the task by increasing the relative duration of that phase. Thus, the young subjects moved downward faster, and had to generate larger upward accelerations to slow their motion and "soften" chair contact.

The role of muscle torque during the task changed with movement time for both young and elderly subjects. Assuming that velocity torques are negligible (as in this task), the ratio of muscle torque to gravitational torque at a joint indicates the role of muscle in the task dynamics. When the muscle and gravity torques are nearly equal (*i.e.*, ratio is near 1), the muscle torque is acting primarily to counter the effects of gravity. As the ratio increases, the muscle torque is acting increasingly to generate body acceleration. In this task, the increased hip muscle-gravity torque ratio with increased movement speed, and at all speeds for the younger subjects, is consistent with the increased body accelerations during these conditions.

The position of the center of pressure may indicate stability during a task. The anterior precession of the center of pressure position with speed suggests a strategy by the elderly to preserve stability at the time of chair contact as the task becomes more demanding with increased speed.

REFERENCES

Alexander, N. et al., J. Gerontol, 46, M91-98, 1991.
Ikeda, E. et al., Phys. Ther., 71, 473-481, 1991.
Pai, Y-C. et al., Med. Sci. Sport Exerc., 22, 378-384, 1990.
Rodosky, M. et al., J. Orthop. Res., 7, 266-271, 1989.
Schultz, A., J. Biomech., 25, 519-528, 1992.
Tinetti et al., New Eng. J. Med., 319, 1701-1706, 1988.
Yoshida, K. et al., Scand. J. Rehab. Med., 15, 133-140, 1983.

ACKNOWLEDGMENTS

I wish to thank Pamela Stevenson at the Rehabilitation Research and Development Center at the Palo Alto VA Medical Center for her assistance in data analysis. This work was supported by the Department of Veterans Affairs.

EFFECT OF ANKLE SUPPORT ON LEG MUSCLE ACTIVATION, KINEMATICS, AND KINETICS DURING DROP LANDINGS

Jon W. Feuerbach, Thomas M. Lundin, Mark D. Grabiner

Department of Biomedical Engineering
The Cleveland Clinic Foundation, Cleveland, OH 44195

INTRODUCTION

Ankle sprains are one of the most common injuries among physically active people, most frequently affecting the lateral ligamentous complex. The high incidence of ankle injuries and their deleterious impact on participation in athletics and activities of daily living has led to the design of various ankle orthotic supports. The objective of these support systems is to restrict undesirable joint motion without affecting normal joint kinematics or motor performance. Research on various motor tasks such as running and vertical jumping, integral components of many sporting activities, has not yielded a definitive answer as to whether ankle support diminishes motor performance.

Landing from a jump imposes forces on the body that must be absorbed primarily by the musculoskeletal components of the lower extremity. The effects of ankle support on the mechanics of the landing subsequent to a jump are even less delineated than the effects of ankle support on jumping performance. Inappropriate ankle joint orientation (e.g., excessive inversion and plantarflexion) during flight may produce an improper landing position, which in turn may lead to an ankle injury (Peters *et al.*, 1991). No investigators have examined the effect of ankle support on lower limb kinematics or the underlying muscle activation during a drop landing. Furthermore, there has been no research quantifying the effect of ankle support on lower limb kinetics and energetics during a drop landing. An inverse dynamics determination of joint moments of force and joint powers could be used to describe the mechanisms by which the kinetic energy acquired during a free fall can be dissipated. The purpose of this study was to compare the effects of three types of ankle support on lower limb muscle activation, kinematics, and external and internal kinetics and energetics during drop landings.

METHODS

Five uninjured male subjects performed five drop landings under four bilateral conditions: (1) no ankle support; (2) application of tape; (3) application of Aircasts; and (4) application of Swede-O ankle braces. The subjects were instructed to hang from a horizontal bar that was suspended from the ceiling so that the vertical displacement of the lateral malleolus was 50 cm. The subjects initiated the drop by releasing the bar and they were instructed to "land naturally".

Branched electrode EMG signals (Koh and Grabiner, 1993) were collected from the gastrocnemius, peroneus longus, and tibialis anterior of the right leg. The rectified, averaged and normalized EMG signals were analyzed in two phases: (1) descent -- the 20 ms prior to touchdown; and (2) impact -- from touchdown to the time of maximum vertical ground reaction force.

Right foot, shank, and thigh positions were recorded using a Motion Analysis System. The orientation of the foot relative to the shank was specified by Cardan angles of the following order: plantar-dorsiflexion, inversion-eversion, and adduction-abduction. The ankle joint angles and the knee flexion angle were examined 1 ms prior to touchdown.

Ground reaction forces and moments were recorded using two AMTI force plates, one beneath each foot. The maximum vertical and medial ground reaction forces were analyzed. Inverse dynamics were performed to obtain the lower limb joint kinetics and energetics during the impact phase.

The EMG data of each muscle were entered into a 2 by 4 (phase by condition) ANOVA with repeated measures. The other kinematic and kinetic parameters were entered into a 1 by 4 (condition) ANOVA with repeated measures. The level of significance was set at 0.05.

RESULTS AND DISCUSSION

Glick, *et al.*, (1976) suggested that ankle support had a "stimulating effect on the peroneus brevis" which would help prevent inversion injuries. In the present study, increases in peroneus longus activation were seen with each of the ankle supports compared to the no support condition (Table 1). Although the differences in muscle activation level produced by ankle support were not statistically significant, these trends deserve further attention. Surprisingly, the gastrocnemius activation levels tended to be greater during the descent phase compared to the impact phase (only the no support condition was statistically significant) while the tibialis anterior exhibited the opposite trend (n.s.).

Table 1. Mean (SD) of the normalized average EMG.

	Gastrocnemius (%MVE)	Peroneus Longus (%MVE)	Tibialis Anterior (%MVE)
NO SUPPORT			
Descent	41(19)*	38(17)	26(20)
Impact	21(5)	35(23)	61(42)
AIRCAST			
Descent	44(15)	44(42)	20(17)
Impact	20(14)	46(34)	49(50)
TAPE			
Descent	52(31)	49(24)	33(12)
Impact	20(12)	46(35)	51(25)
SWEDE-O			
Descent	32(20)	66(50)	30(22)
Impact	21(17)	48(27)	48(45)

* Significantly different from impact phase ($p<0.01$).

Significantly less plantarflexion was observed prior to touchdown in the ankle support conditions than in the no support condition (Table 2). Inversion and adduction during the descent were not significantly affected by ankle support. An improper ankle joint orientation of excess plantarflexion and inversion during the flight phase of a running stride or jump is a mechanism of ankle joint injury commonly alluded to by clinicians (Peters, *et al.*, 1991). Although the ankle supports did not significantly alter the magnitude of inversion compared to the no support condition, the reduction in plantarflexion could be a mechanism for the decrease in ankle injuries that have been reported with the application of ankle supports (Rovere, *et al.*, 1988).

Table 2. Mean (SD) of the knee and ankle angles prior to touchdown.

	Ankle Plantarflexion (degrees)	Ankle Inversion (degrees)	Ankle Adduction (degrees)	Knee Flexion (degrees)
NO SUPPORT	16.8(3.5)	6.2(3.3)	6.0(5.4)	13.4(4.8)
AIRCAST	9.9(3.2)*	4.6(3.0)	6.1(4.7)	16.7(4.0)
TAPE	9.4(4.3)*	4.9(3.2)	6.3(7.1)	17.5(5.1)
SWEDE-O	9.0(4.7)*	5.0(1.9)	6.1(4.8)	18.4(5.5)*

* Significantly different from no support ($p<0.02$).

Ferguson (1973) suggested that ankle joint support "transmits strain" to the knee joint. Indeed, the trend toward increased knee flexion during the ankle support conditions (Table 2) may have acted in concert with decreased plantarflexion to result in zero net change in the ground reaction forces (not shown here). However, the results of the present study also demonstrate that ankle support had no significant effect on maximum joint moments (Table 3), or joint energetics (not shown here). Thus, these results provide little evidence that application of athletic tape or commercial ankle supports (during a drop landing) increases the risk of knee joint injury.

Table 3. Mean (SD) of the maximum joint moments.

	Ankle Plantarflexion (Nm/kg)	Knee Extension (Nm/kg)	Hip Flexion (Nm/kg)
NO SUPPORT	1.47(0.42)	2.60(0.61)	4.57(0.86)
AIRCAST	1.55(0.30)	2.71(0.33)	4.91(0.34)
TAPE	1.51(0.32)	2.80(0.42)	5.06(0.64)
SWEDE-O	1.40(0.27)	2.67(0.25)	4.77(0.50)

With the exception of knee flexion and plantarflexion angle prior to touchdown, ankle support had few statistically significant effects on lower limb muscle activation, kinematics, and kinetics in normal subjects. A model could be utilized to improve the understanding of the biomechanical significance of factors which influence stress in the lateral ankle joint ligaments.

REFERENCES

Ferguson AB J Sports Med 2:46-47, 1973.

Glick JM, *et al.* Am J Sports Med 4:136-141, 1976.

Koh TJ, Grabiner MD J Biomech 26:S1:151-157, 1993.

Peters JW, *et al.* Foot Ankle 12:182-191, 1991.

Rovere GD, *et al.* Am J Sports Med 16:228-233, 1988.

This work was supported by a grant from Aircast, Corporation.

IMPACTS ON PADDED SURFACES

R.B. Martin, L. Liptai, S. Yerby, and K.R. Williams

Orthopaedic Res. Lab, University of California, Davis CA 95616
Human Performance Lab, University of California, Davis, CA 95616.

INTRODUCTION

Head injury depends more on acceleration than applied force. We show by analysis that when an object impacts a deformable surface, its acceleration is inversely proportional to its mass. To test this prediction, 2.69 and 7.40 kg missiles were dropped onto 3 deformable surfaces, and impact force and acceleration were measured. For each test surface, the smaller mass produced a larger acceleration than the larger mass.

REVIEW AND THEORY

The risk of head injury during a direct impact has been correlated with the linear acceleration which the impacting object experiences (Ommaya 1985). Thus, risk of injury criteria are based on acceleration rather than force. Consider a mass m dropped from a height H onto a deformable surface. The energy to be dissipated is mgH, where g is the acceleration of gravity. If F_{av} is the average force during the impact and z_{max} is the maximum deformation of the surface, then

$$mgH = F_{av} z_{max} \qquad (1)$$

The average acceleration during the impact, in multiples of g, is

$$a_{av} = F_{av}/m = H/z_{max} \qquad (2)$$

Assuming that the deformable surface has a load-deformation behavior described by

$$F = kz^p \qquad (3)$$

where k and p are coefficients,

$$mgH = \int_0^{z_{max}} F\,dz = \int_0^{z_{max}} kz^p dz \qquad (4)$$

$$mgH = \frac{k\, z_{max}^{p+1}}{p+1} \qquad (5)$$

Combining eqs. (5) and (2),

$$a_{av} = \left[\frac{H^p k}{(p+1)mg}\right]^{1/(p+1)} \qquad (6)$$

Eq. (5) implies that a_{av} is inversely proportional to m to a degree dependent on p. For a given H and surface, the average accelerations a_{av}' and a_{av}'', suffered by masses m' and m", respectively, will have the ratio

$$a_{av}'/a_{av}'' = (m''/m')^{1/(p+1)} \qquad (7)$$

Experimentally, it is easier to measure peak acceleration (a_{pk}) than a_{av}. If acceleration-time curve shape is independent of mass, eq. (7) should apply to either a_{av} or a_{pk}.

PROCEDURES

For the first experiment, a missile with a 9.68 cm dia. hemispherical impacting surface was dropped 31.8 cm onto one of 3 test surfaces: moist sod, dry sod, or Astroturf. The missile mass was either 7.40 or 2.69 kg. A Kistler Model 9281B11 force plate was used to record the peak vertical force produced during each impact. a_{pk} was calculated by dividing the force by the missile's mass, and subtracting the acceleration of gravi-

ty. Additionally, the load-deformation characteristics of the three surfaces were measured in an Instron Model 1122 testing machine using the same hemispherically-shaped impactor and a deformation rate of 5 mm/min. Eq.(3) was fitted to the load-deformation curve and k and p were calculated. Eq.-(7) was used to calculate the ratio of the accelerations predicted for the two masses, and this ratio was compared to that for the peak accelerations measured during impact.

RESULTS

ANOVA showed that both mass and surface significantly affected impact acceleration and force, and the interaction between mass and surface was also significant (Table 1, $p < 0.0001$ in each case). Each test surface gave results which were different from the other two ($p < 0.001$ in each case). For a particular test surface, a_{pk} produced by the smaller mass was always significantly greater than that produced by the larger mass ($p = 0.0113$ for the artificial surface and $p < 0.0001$ for both sods). Peak forces produced by the larger mass were greater than those produced by the smaller mass ($p < 0.001$ in all cases), but the increase in force was not in proportion to the increase in mass (e.g., for moist sod, the 2.75x increase in mass only increased impact force 1.49x). Table 2 contains results from the indentation experiment. Predicted and measured acceleration ratios coincide for Astroturf and moist sod, but are not so similar for dry sod.

DISCUSSION

A more massive object deforms a padded surface more than one with less mass, and the velocity is reduced to zero over a longer period of time. Acceleration during the impact depends critically on the load-deformation characteristic of the pad, particularly its nonlinearity. These results have important practical implications in the design of surfaces padded for safety. A child's head hitting such a surface may experience a greater acceleration than an adult's, and the properties of the pad need to be adjusted to match the mass as well as the velocity of the impacting object. Another potential application of these results is with regard to the ability of body tissues to pad the hip during a fall on the greater trochanter. This problem is analogous to that considered here, and could be analyzed similarly.

REFERENCE

Ommaya, A. K. (1985). Biomechanics of head injury: experimental aspects. The Biomechanics of Trauma. Norwalk, CT, Appleton-Century-Crofts.

Table 1: IMPACT TESTING

Mass kg	Pk Accel m/sec^2	Pk Force N	Tests #
Surface: Dry Sod			
2.69	1160±147	3146±396	10
7.40	677±7	5082±51	10
Surface: Moist Sod			
2.69	550±6	1506±15	9
7.40	472±19	3568±143	8
Surface: Astroturf			
2.69	458±81	1260±219	11
7.40	343±29	1875±156	11

Table 2: INDENTATION TESTING

Surface	p	$a_{2.69kg}/a_{7.4kg}$ calc	meas
Dry sod	1.92±0.24	1.41	1.71
Mst sod	3.70±0.33	1.24	1.17
Aturf	2.19±0.41	1.37	1.34

(Mean ± Standard Deviation)

FINGERTIP KINEMATICS AND FORCES DURING TYPING

J.T. Dennerlein, E.R. Serina, C.D. Mote, Jr., D. Rempel

Department of Mechanical Engineering, University of California at Berkeley
Ergonomics Laboratory, University of California at San Francisco

ABSTRACT

Development of a biomechanical model of the upper extremity during typing requires understanding of the finger kinematics and impact forces. In this study, fingertip motion and impact forces were measured during typing. The vertical fingertip motion was characterized by a five-phase 'M' wave pattern consisting of an up swing (A), down swing (B), pulp compression (C), retraction (D), and return to rest (E). DIP extension during phase C was observed in some subjects. Simultaneous occurrence of fingertip peak deceleration and maximum force at impact suggests that the collision of the fingertip with the keyboard, rather than the finger extensors, abruptly decelerates the finger.

INTRODUCTION

Soft tissue injuries of the hand and arms due to work, such as Carpal Tunnel Syndrome and tenosynovitis, have increased in order of magnitude over the past ten years and now account for greater than fifty percent of all occupational illnesses (Rempel, 1992). Studies have linked these injures to prolonged use of computer keyboards (Sauter 1991, Smith 1981, Burt 1990). The associated repetitive finger movements and impact forces are suspected of contributing to injury. Fingertip impact force during keyboard use was investigated by Rempel (1992), yet the biomechanical significance of the forces is still unknown. Understanding how these forces relate to finger motion is essential to the development of a biomechanical model. Therefore it is the goal of this study to further characterize the motion of the finger during typing and correlate the motion with fingertip impact forces.

METHODS

The vertical fingertip impact force was measured using a quarter bridge strain gauge load cell placed above the key switch post below the key cap. The load cell was mounted in the f key of a prototype QWERTY computer keyboard with Apple Extended II keyboard key switches (activation force of 0.6 Newtons (Rempel 1992)). The bridge signal was amplified and filtered before being sampled at 1000 Hz by a National Instruments A/D board in a Macintosh fx computer. The strain gauge was calibrated using weights from 0 to 6.0 Newtons and was linear within 1% of full scale.

Finger motion was measured using a two camera 3-D Selspot motion analysis system with a resolution of 150μm. Four infra-red LED markers were placed on the left index finger. Two markers each were mounted on the dorsal side of the distal and middle phalanges and placed along the axis, approximately 1.5 cm apart. Motion data was collected at 500 Hz and digitally filtered over a two second window. Data acquisition of force and motion data was synchronized by a trigger controlled and activated by the operator. Angles of the phalanges from the horizontal plane were calculated from the Cartesian coordinates of the markers. Fingertip velocities and accelerations were obtained by digital differentiation of the position data. Only kinematic parameters in the vertical direction were considered. Vertical up is defined as positive.

Four touch typists, two male and two female ranging in age from 24 to 40 years were allowed a five minute warm-up period on pangramic text prior to data collection. Subjects then continuously typed special text having a high frequency of the letter f while 10 sets of key force and finger motion data were recorded. The special text was designed such that the f key was preceded and followed by a key that did not require the use of the left index finger, in an attempt to isolate a key stroke cycle. The typing skills ranged from 45 to 60 words per minute. Chair and keyboard heights were adjusted for each subject.

RESULTS

A typical vertical fingertip motion is shown in figure 1. Fingertip position data exhibited an 'M' pattern for all keystrokes among the subjects. During phase A, the finger is pulled back from its resting position to above the key cap in preparation for the keystroke. It is then accelerated downward in Phase B. It comes in contact with the key cap in the later portion of B (-61.5 mm in figure 1). Phase C corresponds to the maximum key travel and pulp compression. The finger is then retracted in phase D and returns to rest in phase E. Average peak-to-peak amplitude of the 'M' wave range from 10.5 to 21.4 mm.

Maximum force, velocity, and acceleration values for the four subjects are presented in table 1. Maximum velocities occurred during phase B, while maximum decelerations coincided with either the maximum force (at the junction of phases B and C) or the initial contact with the keycap in phase B (figure 2). Maximum decelerations were as high as 5g.

Variations in the relative angle between the distal and middle phalanges were observed during phase C. The DIP joint extends approximately 20 degrees in 75% of the keystrokes of two subjects (figure 3). In one subject hyperextension of the DIP joint was observed.

DISCUSSION

The force patterns and finger motions observed support the three-phase force classification reported earlier by Rempel (1992). The force contains the switch

compression (Phase I), finger impact (Phase II), and fingertip pulp compression and release (Phase III). The later part of phase B contains the switch compression, while both phase C and the early part of phase D includes the pulp compression and release. The finger impact occurs at the transition from phase B to C. Kinematic values obtained are comparable to values acquired on a flat piezo-keyboard (Guggenbühl, 1990).

The 'M' wave motion pattern was observed in all subjects. Not all the key strokes were completely isolated. Some patterns showed overlap with motion from other keystrokes including consecutive f key strikes. For these cases the fingertip did not return to or start from rest and followed motion patterns similar to those obtained by Guggenbühl (1990) during continuous single finger keying. The lack of a resting state may contribute to higher heights of the 'M' wave. The average peak-to-peak 'M' wave height is about 15 mm, four times larger than key travel.

The simultaneous occurrence of fingertip deceleration and the maximum force suggests that the maximum impact force is generated only by the abrupt deceleration of the finger by the keyboard base. Additionally, the monotonic relationship between average maximum force and the corresponding deceleration lends credence to this conjecture (table 1). Guggenbühl (1990) suggested that the finger extensors play no role in stopping the finger during a keystroke.

Double-peaked deceleration of the fingertip was observed in 69% of all keystrokes during phase B. Peaks occurred at the contact with the keycap and at the finger impact, the end of phase B. Guggenbühl (1990) results include a double-peaked deceleration.

The observed extension of the DIP joint suggests a complicated finger motion during typing not described before. The extension may be lengthening the tendons and muscles during a keystroke, which in turn would produce unusual force patterns and levels in the flexors tendons.

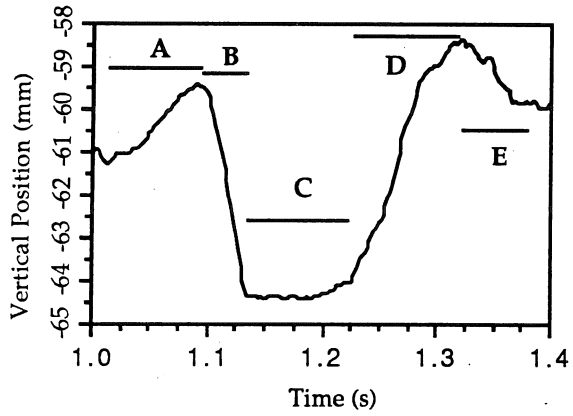

Figure 1: Fingertip motion during a keystroke showing five-phase 'M' wave: up swing (A), down swing (B), pulp compression (C), retraction (D) and return to rest (E) (Subject 1).

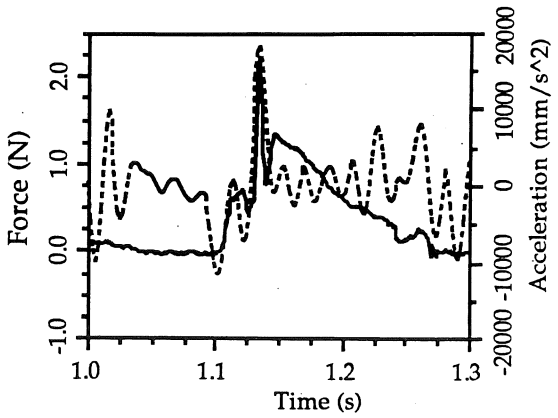

Figure 2: Fingertip force (solid) and acceleration (dashed). Peak deceleration occurs at the end of phase (B) corresponding to the finger impact (Subject 1).

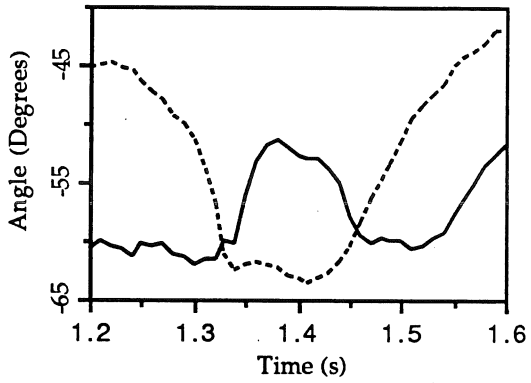

Figure 3: Distal (solid) and middle (dashed) phalanx angles measured from the horizontal during key stroke. The DIP extends during phase C (Subject 2).

Subject	Phase II Peak Force (N)	M wave height (mm)	Peak Velocity (m/s)	Peak Decel (m/s^2)
1	2.3 (.5)	10.6(5)	.27 (.17)	25 (11)
2	2.7 (.9)	20.5 (3)	.53 (.11)	38 (17)
3	1.7 (.3)	10.5 (2)	.31 (.08)	16 (3)
4	2.3 (.4)	21.4 (4)	.52 (.18)	30 (16)

Table 1: Comparison of subject mean force and kinematic values for 10 'f' keystrokes for 4 subjects. Value standard deviation is in parenthesis.

REFERENCES

Burt, et al, HETA 89-250-2046*NIOSH*, Ohio 1990
Guggenbühl U, et al. *Displ ay Units*, 121-128,1990.
Sauter SL, et al. *Human Fact*, 33, 151-167, 1992.
Smith MJ, et al. *Human Fact*, 23, 387-400, 1981.
Rempel D, et al. *JAMA* 267(6), 838-842, 1992.
Rempel D, et al *Proc of NACOBII*, Chicago, Il, 1992.

ACKNOWLEDGEMENTS

This work was done with funding from Apple Computer Inc., Pacific Bell., and Steelcase Inc.

FINGERTIP FORCE HISTORIES FROM MULTIPLE KEYS DURING TYPING

W.P. Smutz, J.T. Dennerlein, C.D. Mote, Jr., D. Rempel

Ergonomics Laboratory, University of California, San Francisco
Department of Mechanical Engineering, University of California, Berkeley

ABSTRACT

Ten keys of a standard keyboard were instrumented to collect fingertip force for five typists to evaluate variability between fingers and between keys during typing. Individual keycaps were instrumented with strain gauges. Maximum force, average force, area under the curve, and duration of the keystroke were used to quantify the force histories. No statistically significant differences were observed between keys for the four summary measures.

INTRODUCTION

The measurement of fingertip force during keyboard usage is an important element in modeling the complex motion of the finger during typing.

Previously, fingertip force during keyboard use has been measured dynamically by placing load cells beneath the keyboard (Armstrong et al. 1993), or instrumenting a single key (Rempel et al. 1992). Rempel et al. instrumented the 'H" key of a standard keyboard by placing a piezoelectric loadcell between the key cap and key switch. They found the following advantages to instrumenting individual keys: 1) Transducer output is not affected by the dynamics of the switch mechanism, circuit board, and keyboard frame. 2) Erroneous forces measurements caused by the hands or fingers resting on the keyboard are eliminated. 3) The difficulty of isolating individual keystrokes is eliminated. The next logical step in the collection of fingertip force data is to instrument multiple keys. The purpose of this study was to instrument multiple keys of a standard alphanumeric keyboard and to collect fingertip force histories from multiple keys and multiple fingers to evaluate variability between fingers and between keys during typing.

METHODS

Ten keys (D,F,H,J,L,M,Q,P,S,V) of a computer keyboard were instrumented with individual strain gauges located between the key cap and the key switch. The instrumented keys were chosen in order to measure force from as many fingers as possible during normal typing. The keys to be instrumented were modified by machining the inside of the keycap to accommodate a metal post and plate. A resistive strain gauge in a quarter bridge circuit was mounted to the top of the plate. The plate was attached to the keycap using cyanoacrylate. The keycap assembly was then placed in the standard key switch. Force on the keycap caused bending of the plate which is measured as strain by the strain gauge (Figure 1). Output from the individual strain gauges was multiplexed before amplification using a dual pole multiplexor integrated chip. Two multiplexors were used, with each multiplexor controlling five strain gauge signals. After passing through the multiplexor, the strain gauge signals were amplified and then sampled at 2000 Hz using a National Instruments A/D board on a Macintosh computer. Four summary measures were used to quantify the finger force impact history: maximum force, average force, area under the curve, and duration of the keystroke (Figure 2).

The characteristics of the instrumented keys were measured before testing to insure that the instrumented keys would accurately measure fingertip force. The linearity, repeatability, strike position sensitivity of the keycaps, and natural frequency of the keycap assemblies were tested. Linearity was determined by placing a series of standard weights (0, 212, 317, and 418 grams) on each instrumented keycap assembly and plotting voltage output versus weight. Repeatability was measured by comparing the voltage output of an instrumented key for ten trials with a 317-gram weight placed on the key. Strike position sensitivity was determined by placing standard weights (0, 212, 317, and 418 grams) in the center of each keycap and in each of the four corners and comparing strain gauge output. Measurement of natural frequency of the keycap assembly, which was performed to determine if it was beyond the range expected during a finger strike, was accomplished by mounting a instrumented keycap assembly on a shaker table and measuring output of the keycap while it was subjected to a constant force input over a frequency range of 100 to 2000 Hz.

Five subjects (3 males, 2 females) were recruited for the study. The subjects were between 18 and 50 years old, capable of typing at least 25 words per minute, and had no history of carpal tunnel syndrome or recent hand or arm surgery.

The chair, keyboard, and monitor height were adjusted to the subject's body dimensions using a standardized protocol. A two minute warmup period preceded the data acquisition to acquaint the subject with the experimental setup. Data acquisition consisted of having the subject type pangramic text (text in which each sentence contains all the letters of the alphabet) until 25 keystrikes for each of the ten instrumented keys was collected. This took from 25 to 40 minutes.

RESULTS

Linearity of the system was ± 3% over the range of 0 to 450 grams, and repeatability of the strain gauge output varied by less than 2%. Strike position sensitivity for each of the instrumented keys varied by less than 10% from the strain gauge output at the center to strain gauge output at any of the corners. Mean corner-to-corner variability was 4.1 %. The natural frequency of the keycap assembly was between 1000 and 1100 Hz, an amount well above the frequency where the energy is concentrated during a keystrike. A power spectrum of a keystrike shows that all of the energy is concentrated well below 200 Hz.

Variability within a key and variability between keys were calculated and are summarized in Table 1. Mean between keystroke values and standard deviations across all keys and subjects and the mean between key values and standard deviations across all subjects for the four summary measures are shown. Between keystroke standard deviations were found to be higher than between key standard deviations for all four summary measures.

A comparison of the four summary measures for five fingers at their home row keys averaged across all subjects is shown in Table 2. An analysis of variance was used to test for differences between the keys. No statistically significant differences were found between the keys for the four summary measures.

DISCUSSION

This paper describes a new system for measuring fingertip force during a keystroke for subjects typing on a keyboard. It is different from previously described systems in that multiple keys have been instrumented.

System validation indicates that the instrumented keys accurately and repeatably measure fingertip force. Mean peak force for the "H" key was found to be similar to mean peak values for the "H" key as reported by Rempel et al. (2.35 N, SD 0.49 vs. 2.99 N, SD 0.62). Although values for the force histories are similar, the advantages of the strain gauges are less drift than the piezoelectric load cell used in that study and and the strain gauges are less expensive.

Fingertip force differences between fingers was observed by Armstrong. Highest forces were measured in R2, R3, with the next highest in L2, L3. Lowest forces were seen in digits 4 and 5. Similar trends were observed in this study but they were not significant. This may be due to small sample size.

In order to characterize an individual during typing, sample size calculations show that the number of keystrokes needed for each key varies from 10 to 28 and the number of keys needed varies from 7 to 14, depending on which summary measure is used. This is for an error rate of 10 percent of the mean value of the summary measure.

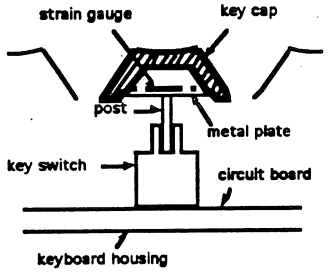

Figure 1. Cut away of instrumented keycap. A resistive strain gauge is mounted on top of the plate. Force on the keycap causes bending of the plate which is measured by the strain gauge. The instrumented keycap fits into the standard key switch on the keyboard.

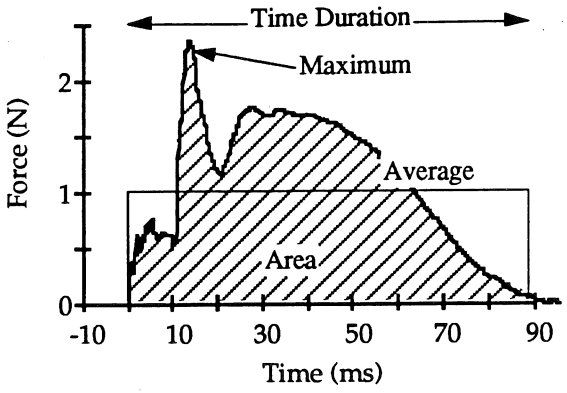

Figure 2 Summary measures were used to quantify the finger force impact history: Maximum force, Average force, Area under the curve, Duration of the keystroke.

		Max Force (N)	Average Force (N)	Curve Area (N ms)	Duration (ms)
I	Mean	2.32	1.10	122.7	110.9
	SD	0.56	0.22	33.4	18.3
II	Mean	2.33	1.10	123.0	111.1
	SD	0.44	0.15	21.6	16.7

Table 1. Summary measures for: (I) Between keystroke values across all keys and subjects, (II) Between key values across all subjects.

FINGER		Max Force (N)	Average Force (N)	Curve Area (N ms)	Duration (ms)
L2 (F)	MEAN	2.05	1.04	104.0	99.3
	SD	0.34	0.05	12.6	9.2
L3 (D)	MEAN	1.91	0.95	100.5	104.3
	SD	0.26	0.10	14.3	7.4
L4 (S)	MEAN	2.19	1.17	133.4	112.8
	SD	0.33	0.17	27.6	13.0
R2 (K)	MEAN	2.48	1.04	109.5	106.0
	SD	0.80	0.11	9.3	5.4
R4 (L)	MEAN	2.20	1.05	122.4	115.5
	SD	0.51	0.27	33.6	9.4

Table 2. Comparison of summary measures of five fingers for the home row averaged across all subjects.

REFERENCES

Armstrong TJ, et al. *American Industrial Hygiene Journal*, In Press, 1993

Rempel DM, et al. *Proceedings of North American Congress on Biomechanics*, Chicago, 1992

ACKNOWLEDGMENTS

This study was supported financially by Apple Computer, Inc., Pacific Bell, and Steelcase Inc.

THE QUANTIFICATION OF INTRA-ARTICULAR CONTACT STRESSES IN DISPLACED FRACTURES OF THE DISTAL RADIUS

J. Des Jardins†, M. Baratz‡, D. Anderson†, and J. Imbriglia‡

†Biomechanics Research Laboratory, Allegheny-Singer Research Institute, Pittsburgh, PA, 15212
‡Department of Orthopaedic Surgery, Allegheny General Hospital, Pittsburgh, PA, 15212

INTRODUCTION

Post traumatic osteoarthritis is a common sequela of injuries that result in residual displacement of the articular surface. The mechanical factors that may predispose an incongruous joint to degenerative processes are still unclear, and limited biomechanical research has been done thus far to investigate them. A simple in vitro fracture model of the wrist has been developed to explore relationships between the degree of fracture malreduction and contact stress aberrations in the radio-carpal joint. Results of this study indicate that there exists a strong correlation between increasing residual articular incongruity and altered kinetics of the radiocarpal joint.

REVIEW AND THEORY

Displaced fractures of the distal radius can, if untreated, lead to post-traumatic osteoarthritis (OA). Persistent malreduction following fracture reduction can also result in OA. Knirk and Jupiter (1986) observed that fractures healing with any residual intra-articular incongruity led to arthritis in 91% of their cases. Offsets of 2 mm or more resulted in post-traumatic OA in 100% of affected patients. Fernandez and Geissler (1991) reported that an adequate reduction of these fractures prevented the development of arthritis in 95% of cases. They also provided evidence that the lunate fossa is involved in a majority of these fractures. We know of no biomechanical study that has provided an explanation for these clinical observations. Brown et al. (1991) studied intra-articular contact stresses as a function of circular defect size in the vicinity of canine knee osteochondral defects. They found only a mild relationship between spatial mean stress and defect size. The present study was intended to explore relationships between fracture malreduction and contact stress aberration in the radio-carpal joint.

PROCEDURES

Intra-articular contact stresses were measured after simulating displaced fractures of the lunate fossa in the distal radius of human cadaver specimens. Eight human cadaver arms were transected at the midhumeral level. Specimens were dissected free of skin and muscle preserving the wrist and elbow capsule and supporting ligaments. Specimens were mounted in a custom designed jig that applied 100N of load through the wrist flexor and extensor tendons. Contact stresses were measured with low and superlow Fuji pressure-sensitive film. Packets of the film were inserted into the joint space through a dorsal capsulotomy. The dorsal radioluno-triquetral ligament was repaired, in order to prevent mid-carpal instability during testing. Contact stresses were measured with the wrist in 0° of extension, with neutral forearm rotation.

After testing the intact specimen, precision osteotomies were performed to simulate an intra-articular fracture. Contact stresses were measured with 0, 1, 2 and 3 mm displacements of the fracture fragment. During loading, the packets of 4 specimens were marked by an indenter, mounted on the dorsal aspect of the radius, so that each packets' orientation relative to the specimen could be determined. Pressure distributions were analyzed by entering the image into a Macintosh IIci computer using an eight bit grey scale scanner (resolution ≈ 12 pixels/mm). Image analysis was performed using Image Analyst® and PASCAL programs. Analysis has included measurement of mean stresses and "overloaded" areas, defined as regions on the scaphoid fossa that saw a 2-fold or greater increase in contact stresses. Measurement of maximum stress concentrations and their locations with respect to the intra-articular fracture have also been determined.

RESULTS

The variations in mean contact stress for increasing fracture displacement were normalized for each specimen to the mean for the anatomically reduced fracture. Mean contact stresses in the reduced specimen averaged 1.61 MPa. Mean stress following a 1 mm step-off increased 1.13-fold. After 2 and 3 mm step-offs mean stress increased 1.27 and 1.29-fold, respectively; values that were statistically significant when compared to the reduced specimen ($p=0.0005$ and $p=0.00004$, respectively).

"Overloaded" areas of the joint surface were defined as areas

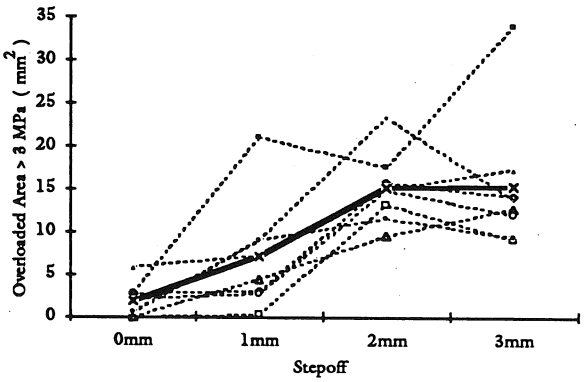

Fig. 1. Overloaded Area (with stress > 3.0 MPa)

experiencing stresses of 3 MPa or more following a displaced fracture of the lunate fossa. The change of this overloaded area for increasing fracture displacement is shown in Figure 1. With a 1 mm step-off, overloaded areas increased 3.9-fold ($p=0.048$). After creating 2 and 3mm step-offs, overloaded

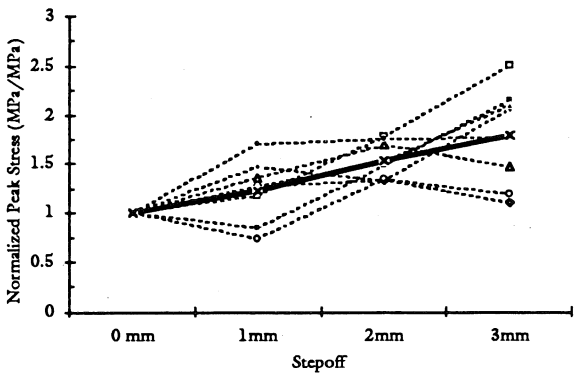

Fig. 2. Normalized Peak stress vs. Stepoff

areas of the joint increased 8 and 8.5-fold, respectively. These increases were found to be statistically significant when compared to the anatomically reduced fracture (p=0.00005 and p=0.001).

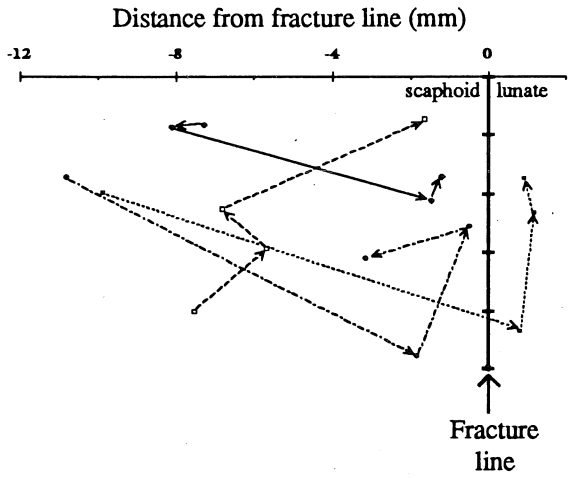

Fig. 3. Locations of Maximum stress with fracture displacements of 0, 1, 2, and 3 mm for each specimen.

Maximum stress concentrations were determined from regions in which the highest concentration of forces were recorded. These are shown in Figure 2. Maximum stresses in the reduced specimen averaged 4.79 MPa. With a 1 mm step-off, maximum stress increased 23% (p=0.08). After 2 and 3 mm step-offs, maximum stress increased 53 and 79%, respectively; values that were statistically significant when compared to the reduced specimen (p=0.0001 and p=0.002). The migration of the maximum stress with increasing fracture displacement is plotted with respect to the fracture line orientation for each of 4 specimens in Figure 3. It is clear that the location of maximum stress approaches the fracture line with increasing step-off magnitude.

DISCUSSION

The factors involved in the development of post-traumatic arthritis are thought to include primary injury to cartilage, intra-articular incongruity and associated joint instability. In this model we have attempted to isolate the mechanical effects of the most commonly involved fracture pattern in displaced intra-articular fractures of the distal radius. Previous studies examining contact stresses following displaced intra-articular fractures have reported only modest increases in mean and peak local contact stresses (Brown et al. 1991). While the changes in mean stresses observed here were statistically significant, their magnitude was relatively small. The observation that there may be fairly dramatic shifts in what we have defined as "overloaded" areas may help to reconcile the apparent disparity between observed clinical results and our experimental model. Further, the significant increases in maximum stresses and their migration towards the fracture with increasing displacement raise new questions about altered joint stability. The ability of the articular cartilage at the defect lip to withstand these increased loads without lateral support is unknown, and is a topic which needs to be addressed in future work. Another parameter which remains to be quantified in the Fuji stains is the peak gradient of contact stress in the vicinity of the fracture line, a parameter which Brown et al. found increased with increasing defect size.

REFERENCES

1. Knirk and Jupiter: J Bone Joint Surg 68A:647, 1986.
2. Fernandez and Geissler: J Hand Surg 16A:375, 1991.
3. Brown, et al.: 37th ORS:361, 1991.

ACKNOWLEDGMENT

Supported by a grant from the Allegheny-Singer Research Institute.

THE DIFFERENTIAL EFFECTS OF A QUADRICEPS-DOMINANT AND HAMSTRING-DOMINANT LOAD ON THE INTERNAL MECHANICS OF THE KNEE

E. A. Giron, R. P. Mikosz, and A. G. Rosenberg
Department of Orthopedic Surgery, Rush-Presbyterian-St. Luke's Medical Center, Chicago, Ill.

INTRODUCTION

Gait changes following total knee replacement (TKR) have been described in terms of changes in the flexion-extension moments at the knee (1). Two abnormal moment patterns were identified during level walking in patients following TKR. The two patterns can be related to a more quadriceps-dominant moment pattern or a more hamstring-dominant moment pattern. Although several explanations for these changes have been proposed, the effects of the abnormal gait patterns and their relationship to the mechanics of the knee are not well understood. The objective of this study is to investigate the changes in the internal knee mechanics resulting from the two gait loading patterns.

METHODS

Six fresh-frozen cadaver knees were obtained for mechanical testing. Each knee was fitted with a posterior cruciate retaining TKR. Two instrumented spatial linkages were used to record the tibiofemoral and patellofemoral kinematics ($\pm$.5 deg, $\pm$.5 mm accuracy). A buckle force transducer was used to measure tension in the patellar ligament ($\pm$9 N accuracy). Each implanted knee was tested under a total load of approximately 340 N. under two load conditions. A quadriceps-dominant load applied a quadriceps to hamstring force ratio of 2:1 while a hamstrings-dominant load applied a quadriceps to hamstring force ratio of 1:2. An axial load of 25% of the dominant force was applied to the tibia in both conditions. Muscular forces were directed along the femoral anatomical axis. The knees were placed in full extension and data taken in 10 degree increments to 100 degrees of flexion. A repeated measures ANOVA was performed to determine statistical significance.

RESULTS

There was a net posterior shift in the position of the tibia in the hamstring-dominant condition relative to the quadriceps-dominant condition for all angles of knee flexion tested. The maximum average difference in the tibial position between the two load states was approximately 2 mm. between 10 and 50 degrees. These differences were not statistically significant ($p>.05$). Statistically significant changes ($p<.05$) in the position of the patella towards a more flexed orientation, coincident with the posterior shift of the tibia, occurred in the hamstring-dominant runs relative to the quadriceps-dominant runs (Fig. 1). A statistically significant inferior patellar shift ($p<.05$) also occurred in the hamstring-dominant load state

compared to the quadriceps-dominant load state (Fig. 1).

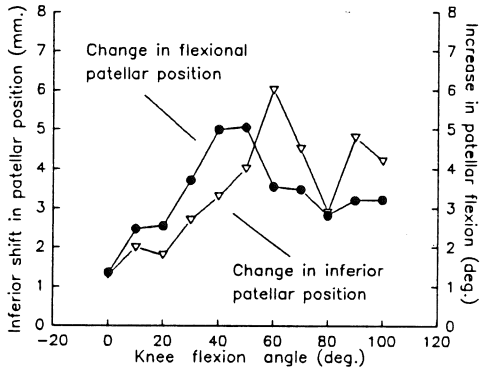

Figure 1 The graph illustrates the positional changes of the patella which result from a hamstring-dominant load when compared to a quadriceps-dominant load.

Analysis of the patellar ligament force to quadriceps force ratio suggests an increase in the mechanical advantage of the extensor mechanism in the hamstring dominant condition relative to the dominant quadriceps condition (Fig. 2). The extensor mechanism transmitted a

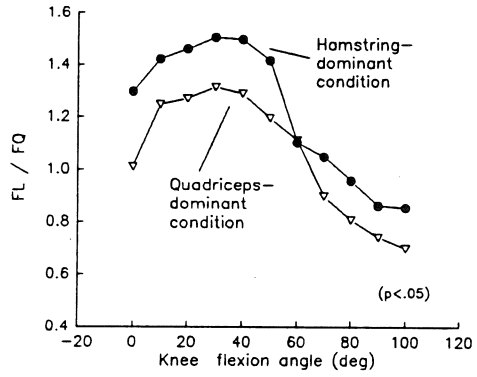

Figure 2 The graph shows the differences in the ratio of the patellar ligament force (FL) to the quadriceps force (FQ) resulting from the two applied load states.

greater force per unit quadriceps load to the ligament when the hamstring dominant condition was applied compared to the quadriceps dominant load condition.

DISCUSSION

The increased force transfer from the quadriceps to the ligament appears to be a result of the altered tibiofemoral and patellofemoral orientations. The two load cases produced subtle changes in the relative bone positions that produced relatively substantial changes in the mechanical advantage of the extensor mechanism. The posterior tibial shift modifies the patellar orientation to either displace the retropatellar contact point inferior or change the geometric configuration of the extensor mechanism to generate a more efficient force transfer from the quadriceps to the ligament. Thus, the two types of gait patterns seen in patients following TKR can produce substantial differences in the internal mechanics of the knee which may influence function as well as implant longevity.

REFERENCES

1. Andriacchi et al. JBJS 64A:1328, 1982.

ACKNOWLEDGEMENTS

NIH/NIAMS GRANT: #20702, Zimmer
The assistance from Dr. T.P. Andriacchi is gratefully acknowledged.

Principal author: Edwin A. Giron, Department of Orthopedic Surgery, Rush-Presbyterian-St. Luke's Medical Center, 2242 W. Harrison, Suite 103, Chicago, Ill., 60612, U.S.A.

GLENOHUMERAL REACTION FORCE AND MUSCLE LOADS IN SCAPULAR PLANE ABDUCTION WITH ROTATOR CUFF ACTIVITY AND SUPRASPINATUS DEFICIENCY

M. C. Miller, D.A. Deddo
Department of Mechanical Engineering
University of Pittsburgh

INTRODUCTION

Knowledge of the joint reaction forces and the forces in the shoulder muscles is an important consideration in shoulder reconstruction and rehabilitation. The activity of the shoulder muscles has been considered by Inman[1] and Perry[5]., but the estimation of the loads imposed and the exact purpose of each muscle's activity remains unexplained, especially in the understanding of muscular stabilization of the gleno-humeral joint.

The determination of necessary muscle forces and joint reaction forces depends on the orientation of the humerus in the glenoid and on the lines of action of all muscles and ligaments across the joint. Additionally, the muscle, ligament and joint force form an overdetermined system so that many combinations of muscle activity can effect the same motion. Solution for muscle and joint forces, therefore, depends on eliminating the redundancy or application of a method that accommodates this difficulty, such as linear programming.

Recent works by Karlsson and Peterson[7] and van der Helm[8] have used published data on muscle insertions and origins and linear programming to compute joint reaction forces and estimate muscle activity. This work used all shoulder muscles and a specially determined fit of relative motions of the elements of the shoulder girdle. Other previous work has estimated the forces in the shoulder[1,2] but has not incorporated published values of muscle origins and insertions or accurate joint kinematics.

In order to estimate the maximum relative importance of each of the rotator cuff muscles, a model using only rotator cuff and primary abductors permits an easy reference to determine changes occurring due to rotator cuff injury.

METHOD

A computer model of the rotator cuff musculature insertions and origins was constructed using published values[4], including the possibility of muscles wrapping around intervening structures. The relative motions of the scapula, humerus and clavicle were taken from the works of Inman[2] and Perry[5]. The glenohumeral joint was modeled as a spherical joint and values for the arm mass was chosen to reflect standard anthropometric values.

A standard linear programming package in the IMSL library was used to determine the optimal muscle activities for scapular `lane abduction. The functional objective of the human body for the linear programming method was taken to be a minimization of a linear combination of the sum of the necessary muscle forces and of the force acting to move the humerus out of the plane of scapular abduction.

Two cases of muscle activity were run: 1) normal musculature and 2) a simulated rotator cuff tear. Omission of the supraspinatus from the available muscles, models the rotator cuff tear. That is, the supraspinatus force is set to zero for all times for the second muscle activity case.

RESULTS

Resulting muscle and joint forces are shown in the figures. The figure shows only the middle deltoid activity rather than the posterior, anterior and middle deltoid portions included in the model. Subscapularis and infraspinatus forces also increase, with a particular increase in activity during the initial phase of abduction.

DISCUSSION

The deltoid activity peaks slightly before 90° abduction and the early activity of the infraspinatus (not shown) and subscapularis fits well with the known need for activity of these muscles to permit abduction without subluxation of the humerus. The increase in deltoid activity when the supraspinatus is inactive requires approximately 20% more muscle strength. The joint reaction forces are a cost of supraspinatus inactivity, however.

CONCLUSION

Surgical repair of rotator cuff injuries without restoring supraspinatus function can lead to satisfactory results if the deltoid is strong enough to compensate for the lack of supraspinatus strength. The additional joint reaction force may cause future arthritic degeneration or lead to pain and increased wear at the joint.

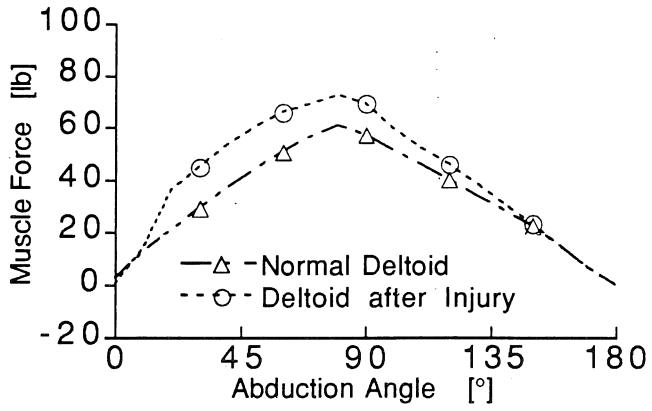

Deltoid Activity Before and After Cuff Tear

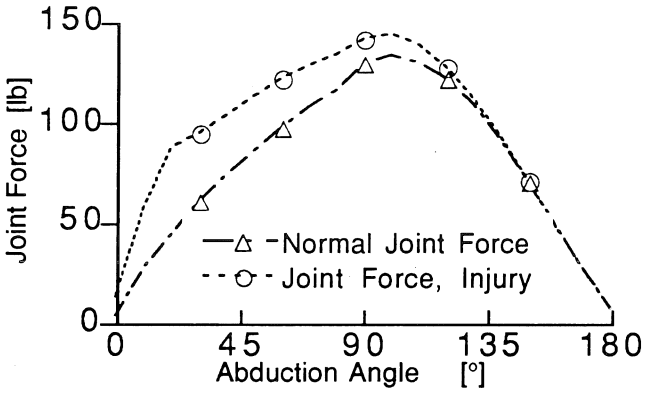

Joint Force Before and After Cuff Tear

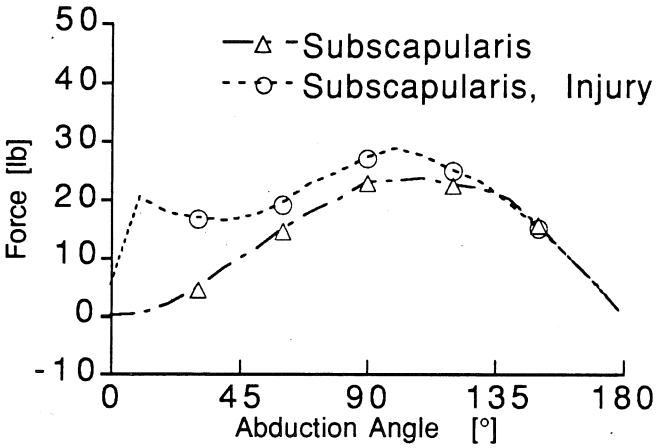

Subscapularis Force Before and After Injury

References

1) Poppen, Walker, Clinical Orth., No135, 1978
2) Inman, et al., JBJS, XXVI, No1, 1944
3) Sidles, et al Trans.37th ORS, p209
4) Högfors, et al, J.Biomech.,V20, 1987.
5) Perry ,J,Biomechanics of the Shoulder, 1988
6) Deluca and Forrest, J. Biomech.,V6, 1973
7) Karlsson, D., Peterson, B., J. Biomech., 1992.
8) van der Helm,F., PhD Dis., 1991.

ACUTE AND CHRONIC CHANGES IN KINEMATICS AND VERTICAL GROUND REACTION FORCES OF THE ACL LESIONED CANINE.

A.J. Threlkeld †, R. Shapiro‡, R. Stine‡, and K. Ferris‡

†Dept. of Physical Therapy, Creighton University, Omaha, NE 68178

‡Biodynamics Laboratory, University of Kentucky, Lexington, KY 40506-0070

INTRODUCTION

One of the most widely used experimental models of osteoarthrosis (OA) is the canine anterior cruciate ligament lesion (ACL-X). Although much information is available on the biochemical and morphologic changes in the articular tissues of the canine ACL-X tibiofemoral joint, very little is known of the changes in gait associated with the ACL-X model. Gait is a common clinical indicator of OA disability and of functional changes in response to therapeutic intervention. This study examined the acute and chronic changes in the gait of beagle dogs due to ACL-X through the kinematics of treadmill gait and through the peak vertical ground reaction force (VGRF) during free gait. Utilizing 3-D motion analysis and a force platform, the gait of 44 dogs was examined prior to surgical ACL-X and at 4 weeks postop. A subset of 12 dogs were also evaluated at 18, 24, 36 and 52 weeks postop. The kinematic indicators that changed most strongly in response to the ACL-X were vertical excursion (VEx) of the distal tibia and the angular excursion of tibiofemoral joint flexion (FLx). Kinematic and VGRF changes were most pronounced acutely (4 weeks postop) but improved at 24, 36 and 52 weeks. Tibiofemoral joint FLx tended to worsen again at 52 weeks. By documenting the kinematic changes in the gait of the ACL-X canine model, the functional response of the model to therapeutic intervention can in turn be investigated.

REVIEW AND THEORY

The canine ACL-X model has provided much information about the anatomical (Adams; Marshall et al) and biochemical (McDevitt et al; Vignon et al) changes in articular cartilage associated with OA. Some recent research using force platform analysis has shown that vertical loading during gait is actually reduced in the ACL-X limb (Budsberg et al; O'Connor et al) which implies that joint instability induced degeneration of the cartilage may be caused by biomechanical changes other than vertical ground reaction forces. However, no kinematic data are available for this model to correlate with the force plate studies. Kinematic studies have been useful and sensitive in describing OA in humans (Murray et al; Stauffer et al) as well as documenting the response to intervention for OA (Chao et al; Ivarsson et al). The purposes of this research were to describe the acute and chronic changes in gait kinematics and peak VGRF of the canine in response to ACL-X.

PROCEDURES

Purpose-bred adult beagles (n=44, 9-12 mos. old, 8-10.7 Kg, both genders, no tibiofemoral OA detectable by X-ray) were trained to trot on a treadmill at 1.8 m/sec. Reflective markers were placed bilaterally on the skin overlying the lateral aspect of the distal tibiae, lateral femoral epicondyles, greater trochanters, and on the dorsal sacrum. A typical three second epoch of treadmill gait was collected with 4 high speed video cameras (200 Hz) as the dogs trotted in a pre-defined calibrated space. Mean kinematic data were calculated for each dog. Dogs were also trained to trot at about 1.6 m/sec across a force platform embedded in a runway. Three isolated strikes for each paw were collected at 2000 Hz and a mean peak VGRF calculated. Following the collection of normal data, the left anterior (cranial) cruciate ligament of each dog's left tibiofemoral joint was surgically transected. Dogs were permitted cage activity, gradually resumed treadmill and free gait activity after three weeks and were retested at 4, 18, 24, 36 and 52 weeks postop. Dogs had unrestricted cage activity (~1.0x1.5m pens). Enforced activity was limited to minimum training periods (½ hr/day x 5-10 days prior to each test session). All data from this repeated measures design were compared by ANCOVA.

RESULTS

The strongest kinematic indicators of change after ACL-X were VEx of the distal tibia and the angular range of FLx (Fig. 1,2). The VEx of both the intact right and ACL-X left limbs were different from preop values at 4 wks ($p<.0009$ R; $p<.0001$ L). The right limb VEx remained higher than normal at 18 wks ($p<.02$). The range of FLx diminished bilaterally at 4 weeks ($p<.01$ R; $p<.0001$ L) and remained less on the left at 18 weeks ($p<.03$) before returning to normal. Although not statistically significant, the lesioned knee tended to have diminishing FLx at 52 weeks. The peak VGRF was significantly decreased in the ACL-X left limb at 4 wks and 18 wks but returned to near normal levels by 52 wks (Fig 3).

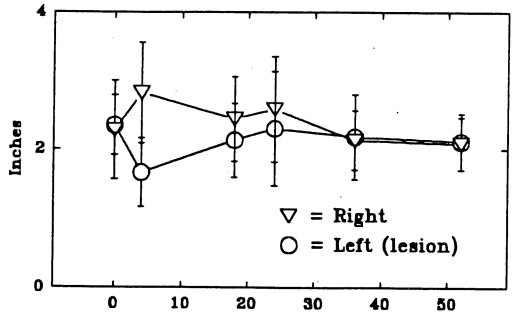

Vertical Excursion of the Distal Tibia

FIGURE 1

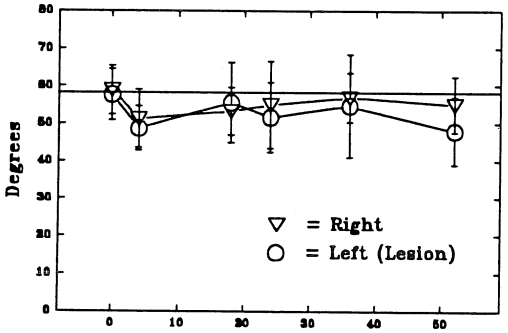

Tibiofemoral Flexion Range of Motion

FIGURE 2

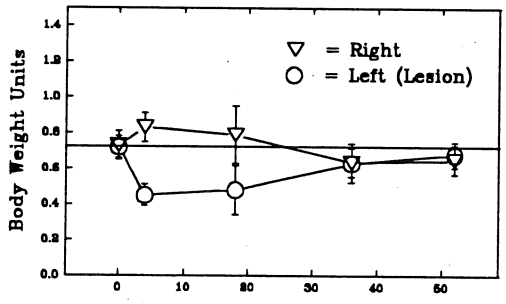

Peak Vertical Ground Reaction Force

FIGURE 3

DISCUSSION

The kinematic responses to ACL-X were detectable with 3-D motion analysis. Kinematic changes occurred bilaterally and were most pronounced in the hindlimbs. The response is most marked during the acute phase when little arthritic change is expected in the articular cartilage (Marshall et al) therefore this acute lameness are primarily attributable to compensations for joint instability. As the gait response matured in the 18 to 36 week timespan, the limping behavior became less pronounced, signalling that sufficient motor learning had occurred to provide secondary restraints to the joint instability. At 52 weeks, the gait was probably more typical of OA than joint instability. The response of VGRF was consistent with other reports and indicates that vertical loading remains reduced for an extended period after ACL-X.

We concluded that: 1) kinematic and peak VGRF changes were bilateral; 2) acute changes at 4 wks postop reflected a gait response to uncompensated joint instability rather than OA; 3) notable motor learning occurred between 18 and 36 weeks that permitted a more normal gait pattern during the chronic phase; 4) functional changes in the canine ACL-X model are detectable with 3-D motion analysis and force platform techniques. These findings may permit the objective evaluation of clinical intervention strategies for joint instability and for studying ways to limit OA.

REFERENCES

Adams M.E. J. Rheumatol. 16, 818-824, 1989.

Budsberg S.C. et al Am. J. Vet. Res. 49, 1522-1524, 1988.

Chao, E.Y. et al. Arch. Orthop. Traumat. Surg. 97, 309-317, 1980.

Ivarsson I. et al. Clin. Orthop. Rel. Res. 239,185-190, 1989.

Marshall J.L. et al. J. Bone Jt. Surg. 53-A, 1561-1570, 1971.

McDevitt C.A. et al J. Bone Jt. Surg. 58-B, 94-101, 1976.

Murray M.P. et al. Clin. Orthop. Rel. Res. 199, 192-200, 1985.

Stauffer R.N. et al. Clin. Orthop. Rel. Res. 126, 246-255, 1977.

O'Connor B.L. et al. Arth. Rheum. 32, 1142-1147, 1989.

Vignon E. et al. J. Rheumatol. 11, 202-207, 1984

Geometry Dependent Changes in the Biomechanics of Osteochondral Defect Repair

J. E. Hale† and T. D. Brown‡

† Department of Biomedical Engineering, The University of Virginia, Charlottesville, VA 22903
‡ Department of Orthopaedic Surgery, The University of Iowa, Iowa City, IA 52242

INTRODUCTION

Local articular defects disrupt the natural congruency of a joint surface and presumably alter the normal biomechanics of the joint. Aberrations of contact stress distribution, intrinsic material properties, and histologic response associated with the repair process can be assessed using experimental models. However, these studies provide relatively little information about the fluid-phase kinematics and solid-phase stresses of normal cartilage or repair tissue.

REVIEW AND THEORY

Analysis of articular cartilage behavior has been greatly facilitated by the development of biphasic finite element formulations. Computational solutions for uniaxial confined and unconfined compression of cylindrical plugs of articular cartilage have demonstrated excellent agreement with experimental findings. Application of biphasic FE analysis to the indentation problem of a hydrated soft tissue layer has helped characterize the stress-relaxation response of articular cartilage (Spilker et al., 1992) and the intrinsic material properties of both normal cartilage and repair tissue (Athanasiou, 1989; Hale, 1991). Wayne et al. (1991) extended this technique to study the response of a repaired articular surface to a uniformly distributed applied load.

The current study employs the continuum linear biphasic finite element formulation developed by Spilker et al. [1990], and uses a geometrically simplified model of full-thickness circular (axisymmetric) defects. This particular model corresponds to the experimental canine (in vitro/ in vivo) models for which contact stress data had already been collected (Brown et al., 1991; Hale, 1991; Mohler et al., 1992). Nonuniformly distributed loads, based on contact stress data for an intact articular surface and surrounding local articular defects, afford a realistic model of physiologic joint loading. In addition, a full factorial parametric evaluation of both intact and defect cases is performed, to assess the dependence of computed field variables on defect size and cartilage layer thickness.

PROCEDURES

The behavior of both an intact articular surface and graded osteochondral defects was modeled using a two-dimensional, axisymmetric mesh (Figure 1) with 576 4-node, isoparametric, quadrilateral elements (2500 degrees of freedom). Four distinct material regions, each modeled as linear biphasic, are designated. Material properties (permeability k, aggregate modulus H_A, solid-phase Poisson's ratio ν_s, and solid volume fraction ϕ_s) for articular cartilage and for defect repair material are set equal to the apparent constitutive coefficients derived from indentation analyses of the in vivo canine series (Hale, 1991; Hale et al., in press 1993). Material properties for the subchondral plate ($k=0.1\times10^{-19}$ m^4/N-sec, $H_A=2.79\times10^9$ Pa, $\nu_s=0.3$, $\phi_s=0.99$) and dense cancellous bone ($k=0.1\times10^{-12}$ m^4/N-sec, $H_A=10\times10^6$ Pa, $\nu_s=0.3$, $\phi_s=0.99$) were chosen to achieve physiologic (quasi-elastic) behavior. The dependence of the algorithm solution on mesh resolution and loading rate (i.e. spatial and temporal convergence) was assessed over a wide range of mesh refinements (8-648 elements) and ramp times (0.1 - 1000 seconds).

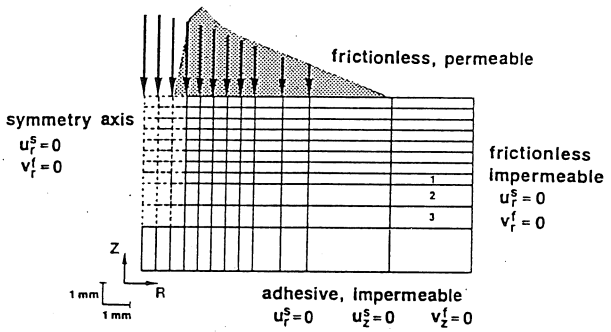

Figure 1. Schematic representation of the finite element mesh for biphasic analysis of osteochondral defects. Profiles of the surface traction distribution are depicted for the intact case (arrows) and for a 3 mm diameter defect (shading). Elements in or above layer 1 comprise articular cartilage, layer 2 is subchondral bone, and elements in or below layer 3 are modeled as dense cancellous bone. Elements near the symmetry axis (dashed lines) identify the region occupied by repair tissue.

Based on convergence testing, an input loading history (force-controlled creep) consisting of a 500 second linear upramp from zero to maximum load was applied. The distribution of surface traction for intact and graded defect cases (1, 3, and 5 mm diameter) closely approximated the nonuniformity of experimentally determined (series-average) contact stress distributions from the in vitro canine series (Brown et al., 1991). However, to obtain strains consistent with the linear FE formulation, the resultant load (area under the contact stress profile) for all cases was attenuated to a value of 12.0 N. The boundary conditions imposed for the model are intended to be representative of the corresponding biological conditions - the contact surface is assumed to be frictionless and permeable; nodes along the symmetry axis and at the peripheral border of the mesh are designated as frictionless and impermeable; and adhesive, impermeable restraints are applied at the bottom

layer of the mesh. Solid/fluid load allocation for the model is directly proportional to the surface area fractions of the biphasic mixture.

Parametric variations in defect size (intact, 1 mm, 3 mm, and 5 mm diameter defects) and cartilage layer thickness (1 mm, 2 mm, 3 mm, and 4 mm) were readily affected by reassigning material properties for appropriate elements of the mesh; the physical dimensions of the element layers (i.e. mesh zoning) remained constant. Field variables including fluid velocity, fluid pressure, and solid phase principal stress and maximum shear stress, were computed either at the nodes or at the centroid of each element.

RESULTS and DISCUSSION

All defect parametric series were performed within the documented limits of the FE code reliability. Because this involved sub-physiologic surface tractions and load rates, data interpretation should emphasize relative rather than absolute magnitudes. In addition, rather obvious limitations are associated with the geometrically simple FE representation of the highly complex anatomical structure. Nonetheless, this representation provides a reasonable first approximation of the macroscopic geometric features associated with full-thickness osteochondral defects.

Computed field variables responded in varying degrees to parametric variations in defect diameter and cartilage layer thickness. Perturbations related to cartilage layer thickness, however, tended to be rather minor compared to defect-size-dependent changes. All results are reported for a time corresponding to the attainment of peak applied load (t = 500 seconds).

Deformed mesh plots for the specified surface tractions consistently exhibited well-behaved displacements and strains. Local anomalies (specifically, disproportionate straining of surface layers) were not observed for any combination of defect size and cartilage layer thickness. With increasing defect diameter, the unbuttressed lip of cartilage at the defect rim exhibited a tendency to move ever farther into the defect. Huber-Betzer et al. (1990) noted a similar phenomenon for elastic FE contact simulations of articular surface step-off incongruities.

Consistent with experimental results for contact stress at the articular surface, solid phase principal stresses showed only modest elevations over the intact case, regardless of defect size. In 5 mm dia defects, the occurrence of tensile stresses at the interface between repair tissue and intact cartilage correlates well with poor gross appearance and histologic findings. Tensile stresses in this region potentially disrupt whatever fragile bonding may exist during the early stages of repair.

Peak maximum shear stress for all three defect cases exceeded that of the intact case, and progressively increased with defect diameter (Figure 2). Peak shear stress magnitude within the cartilage layer consistently occurred at the contact surface. In the presence of a defect, this point was at or near the defect lip, and moved radially outward in accordance with increasing defect diameter. Low shear stresses within the defect (consistent with the inability of repair tissue to contribute to loading bearing) led to severe shear stress gradients at the defect/cartilage interface.

Although fluid pressures in the cartilage surrounding the defect were not substantially altered versus the intact case, high fluid pressure gradients were evident at the cartilage/defect interface, with the most obvious consequence being a large efflux of interstitial fluid from the surrounding normal cartilage into the defect. Volumetric flow rates based on fluid velocity data indicate a net depletion of interstitial fluid from the cartilage immediately surrounding the defect, most notably for the 3 mm and 5 mm defects (Table 1).

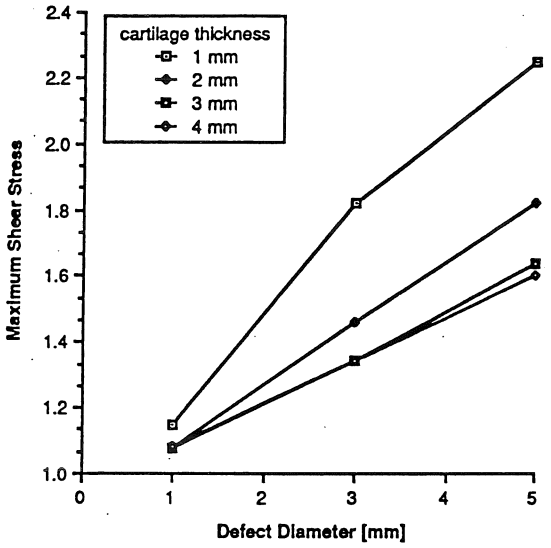

Figure 2. Peak maximum shear stress as a function of defect diameter and cartilage layer thickness. Shear stress values are normalized to the intact case.

Table 1. Net interstitial fluid depletion during load application as a percentage of initial fluid volume fraction for normal cartilage surrounding the defect periphery.

Cartilage thickness [mm]	1	2	3	4
1 mm defect	0.3	0.2	0.1	0.1
3 mm defect	2.3	2.2	1.7	1.4
5 mm defect	1.6	2.1	1.8	1.6

REFERENCES

Athanasiou, K. PhD Thesis, Columbia University, 1989.
Brown, T. et al. J Orthop Res 9:559-567, 1991.
Hale, J. PhD Thesis, University of Iowa, 1991.
Hale, J. et al. J Biomech, in press, 1993.
Huber-Betzer, H. et al. J Biomech 23:811-822, 1990.
Mohler, C. et al. Trans Orthop Res Soc, p. 208, 1992.
Spilker, R. et al. J Biomech Engg 112:138-146, 1990.
Spilker, R. et al. J Biomech Engg 114:191-201, 1992.
Wayne, J. et al. J Biomech Engg 113:397-403, 1991.

ACKNOWLEDGEMENTS

The FE algorithm and technical guidance on its operation were provided by Dr. R. L. Spilker. Financial support provided by NIH Grant AR-38916.

A HYDROSTATIC COMPRESSION TECHNIQUE TO MEASURE FEMORAL HEAD STRUCTURAL COMPLIANCE

Melvin J. Rudert and Thomas D. Brown

Departments of Orthopaedic Surgery and Biomedical Engineering
The University of Iowa, Iowa City, IA, 52242.

INTRODUCTION

An experimental apparatus was designed to apply hydrostatic compressive loading to the surface of a cartilage-denuded cadaveric femoral head. Radially directed surface deformations due to this loading were measured for four normal femoral heads and compared to those predicted by FEM.

REVIEW AND THEORY

Prevention of collapse and thus preservation of the natural femoral head is the ideal treatment goal for osteonecrosis. To that end, finite element models have proven useful for studying how generic pathomechanical phenomena and alternative treatments affect collapse propensity. Most recently, in vivo delineation of lesion involvement patterns by MRI has enabled patient-specific stress analysis (Baker et al., 1991). To date, however, complex mathematical models of this type have lacked direct physical validation. This study describes the design and performance of a testing fixture developed specifically for that purpose.

PROCEDURES

The pressure vessel test fixture is shown schematically in Figure 1. It consists of a hemispherical dome, a base plate, and a specimen holder, all machined from 6061-T6 aluminum. The dome bolts to the base plate, forming a closed vessel capable of sustaining internal pressure with very small deformation. A port in the dome wall connects the vessel to a precision regulator (0-7 MPa) and high pressure air cylinder.

Femoral heads that are obtained for testing, either at autopsy or at resection for total hip arthroplasty, usually have only a short length of femoral neck remaining. This neck serves as a support for the head when it is mounted inside the vessel. The head is placed in the center cup of the specimen holder and potted with PMMA, shown crosshatched in the figure. A small vent tube allows marrow egress to prevent nonphysiologic buildup of pressure inside the head.

Threaded through the wall of the dome are 3 linear variable displacement transducers (LVDTs). They lie on a single meridian and are radially directed toward the center at 0, 30, and 60 degrees elevation relative to the equator of the dome. When a head is mounted concentrically inside the vessel, the tips of the LVDTs very lightly spring load against its surface, and transduce deformation when the vessel is pressurized.

Through position indexing of both the dome and the specimen, it was possible to sweep the LVDTs around the surface of the head at 15 degree increments of rotation, re-pressurizing the dome at each position and recording deformations. This allowed sampling of 72 discrete sites per head.

RESULTS

Head surface radial deformations measured with this equipment were found to be highly reproducible and very nearly pressure-linear ($r > 0.99$). Series average results for four normal femoral heads are presented in Figure 2 as radial microstrain contours. The conversion to microstrain (using head radius for the gage length) was done to facilitate calculation of average values. The infero-medial surface positions (toward the fovea) were consistently more compliant than corresponding supero-lateral positions. This is consonant with the underlying cancellous bone density and orientation, since the principal (compressive) trabecular system aligns to preferentially reinforce the superior portions of the subchondral plate. In addition to infero-medial bias, anterior-posterior deformation symmetry about the coronal plane is evident. These results are in good agreement with corresponding FEM-predicted deformation (Baker et al.,1989).

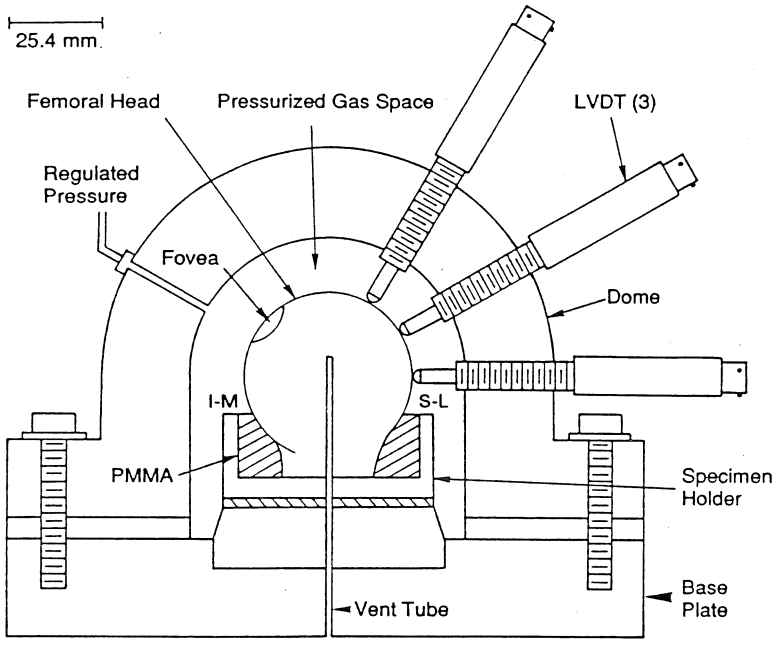

Figure 1. Cross section schematic of pressure vessel showing LVDT and femoral head mounting. I-M and S-L denote infero-medial and supero-lateral positions in the coronal plane of the head.

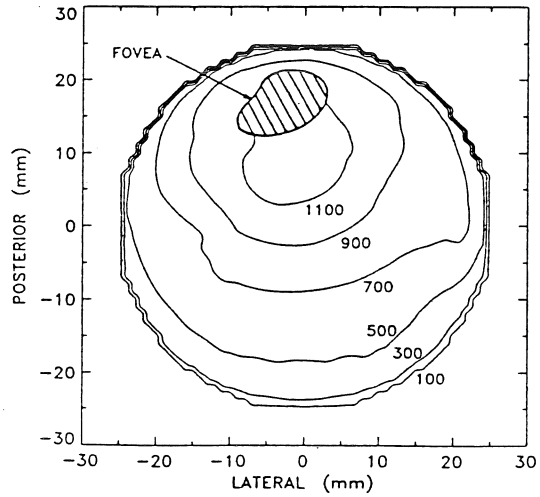

Figure 2. Radial Compression Microstrain under 0.67 MPa Pressure. Average of four normal femoral heads.

DISCUSSION

The application of hydrostatic pressure loading to the cartilage-denuded articular surface of a resected femoral head is experimentally tractable. Deformations recorded were reproducible, nearly pressure-linear, and corresponded to the architectural features of the underlying trabeculation. Results reported herein provide valuable preliminary corroboration for our analytical models, and constitute a baseline against which osteonecrotic head deformation patterns can be interpreted.

REFERENCES

Baker, K. J. et al. Pgh. Orthop. J., 2, 101-106, 1991.

Baker, K. J. et al. Clin. Orthop. Rel. Res., 249, 183-198, 1989.

ACKNOWLEDGEMENT

NIH Grant AR35788

THE EFFECT OF SPECIMEN END SUPPORT ON EXPERIMENTAL MEASUREMENT OF CANCELLOUS BONE MECHANICAL PROPERTIES

TE Wenzel, DP Fyhrie, MB Schaffler, and FR Brodie

Breech Research Laboratory, Bone and Joint Center, Case Western Reserve University/Henry Ford Health Science Center, Detroit, MI 48202

Introduction

The way in which the ends of a cancellous bone specimen are supported during a compression test has been shown to have a significant effect on the measured material properties. In this study, thirty-six cores of bovine cancellous bone were destructively tested to 15% strain in compression. Eighteen of the specimens were restrained at the ends by adhering them to aluminum disk supports with glue and the remaining eighteen were not. It was found that end restraint had no significant effect on maximum modulus, ultimate stress, or ultimate strain, but had a significant effect on modulus at 0.6% strain and residual strain.

Review and Theory

Previous work done to determine material properties of cancellous bone from compression testing [1,3] was done without end support. Recently, the influence of end effects on the measurement of material properties was investigated and found to be important. Linde and Hvid [5] showed that fixing the ends of the specimen to the test column resulted in a 40% increase in elastic modulus at 0.8% strain and reduced the energy dissipation to 67% of unconstrained values. To reduce end effects, Keaveny et al. [4] machined cancellous bone test specimens with a dumbbell (waisted) shape and measurements were recorded by a mini extensometer attached directly to the gage length region. Neither of these studies looked at the effects of end restraint on ultimate properties. Our work was done to investigate the effect that gluing the ends of the specimens to aluminum disks had on ultimate properties, as well as to compare non-destructive material property data reported by other investigators.

Procedures

Thirty-six cylinders of trabecular bone (diameter=8mm) were cored from bovine proximal tibiae and distal femora using a diamond core drill. Coring was done while the samples were immersed in saline to prevent dehydration and overheating. The cores were trimmed to a 10mm height using a low-speed diamond saw. Parallel faces were ensured by using a gang-cut method. Specimens were assigned into one of two test groups. The ends of the cores of one group were glued to 1mm thick aluminum disks with cyanoacrylate adhesive (Krazy Glue). After allowing a few seconds for the glue to set, specimens were compression tested between unpolished, unlubricated steel platens. Preliminary studies showed that glue penetration was consistently less than 250 microns. Cores from the second group were compressed between the platens with no additional preparation of the bone-platen interface. All specimens were preconditioned with a 5N force and then strained 15% in compression at 1%/sec. Specimens were then returned to zero strain at 15%/sec. Tests were conducted using an Instron 8501 servo-hydraulic test system. Loads were monitored using the system load cell and displacements were measured using an extensometer mounted on the load platens. Elastic modulus at each data point was calculated as the slope of the least-squares regression line of the stress vs. strain data of that point plus the ten previous data points and the ten after it. Ultimate stress was measured where the slope of the stress-strain diagram was zero and ultimate strain as the strain at the ultimate stress (Figure 1). Residual strain was defined as the strain during unloading when the stress returned to zero (Figure 1). A Student's t-test was used to compare the data from the two protocols. Significance is reported at $p<0.05$.

Results and Discussion

Ultimate stress, ultimate strain, and maximum modulus were not significantly different between the glued and non-glued groups (Figure 2). The modulus at 0.6% strain was more than 2.5 times greater for the glued specimens than for the non-glued specimens. Residual strain was 23% higher for the glued group than for the non-glued group. In examining the changes in modulus over the course of the test, note that both the glued and non-glued specimens reached approximately the same maximum modulus, but that the glued specimen became stiffer faster (Figure 3). We propose that the constraint imposed by the adhesion of the end trabeculae to the aluminum disks limits the amount of bending in these end surface trabeculae. Accordingly, they were subjected to a more direct axial compression, whereas the end trabeculae of the non-glued specimens could bend and slip before finally compacting as the test progressed. This may explain why the glued specimens were stiffer at 0.6% strain than the non-glued specimens. When comparing data from tests with different end restraints, it may be more accurate to compare the maximum modulus obtained rather than the modulus at a given strain level.

If gluing the ends to a support had the proposed effect of not allowing bending of surface trabeculae, both groups should have similar mechanical behavior once the specimen has settled in. This is supported by the fact that we found no differences in maximum modulus, ultimate stress, or ultimate strain between groups.

All specimens recovered more than 90% of their original height when loading was removed, consistent with the work of Fyhrie et al. [2] on human cancellous bone. However, there were significant differences in amount of residual strain between glued and non-glued groups. When unloaded, the non-glued cores recovered more of their original height than the glued cores. We suspect that this was again due to limited bending of the surface trabeculae. The surface trabeculae of the glued specimens would tend

to break due to the more direct axial compression load, at which point the specimen's height would be unrecoverable. Those of the non-glued specimens, however, would have more of a tendency to bend when loaded and thus the specimen would have a greater chance of returning to its original height.

Our results have important implications for compression testing of cancellous bone. The significant difference in residual strain showed that more permanent damage was sustained by the glued specimens in a destructive test. Also, providing no end support results in a delay in the onset of stiffness in a non-destructive test. Thus the modulus measured at a given strain was greater. The maximum modulus, ultimate stress, and ultimate strain, however, were not affected by end restraints.

References

[1] Ciarelli, MJ et al., J Ortho Res, 9(5), 674-682, 1991.
[2] Fyhrie et al., Transactions of the 39th Annual Meeting of the Orthopaedic Research Society, 18(1), p. 199.
[3] Goldstein, SA et al. J Biomechanics, 16(12), 965-69, 1983.
[4] Keaveny et al. Transactions of the 39th Annual Meeting of the Orthopaedic Research Society, 18(2), p. 586.
[5] Linde, F and I Hvid, J Biomechanics, 22(5), 485-490, 1989.

Acknowledgements

The authors would like to thank Dr. Susan Hoshaw for her assistance in preparing this abstract. This work was supported by NIH grants AR40776 and AR41210.

Material Property	Group	Mean (SD)	P-value
Utimate Stress (MPa)	Glued	9.32 (4.30)	.604
	Non-glued	8.59 (4.03)	
Ultimate Strain	Glued	.034 (.008)	.248
	Non-glued	.037 (.007)	
Maximum Modulus (MPa)	Glued	541 (302)	.451
	Non-glued	477 (192)	
Modulus at .6% Strain (MPa)	Glued	437 (344)	.004
	Non-glued	169 (141)	
Residual Strain	Glued	.059 (.015)	.022
	Non-glued	.048 (.011)	

Figure 2: Test results. $p < 0.05$ indicates significance

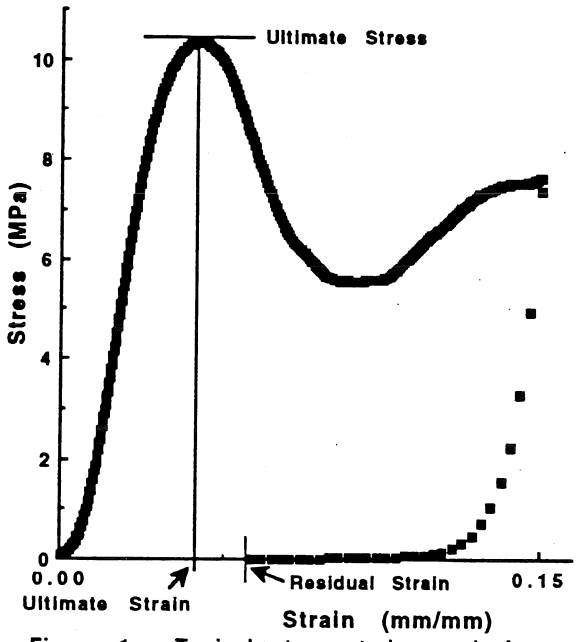

Figure 1: Typical stress-strain graph for compression test of bovine cancellous cores. Specimens were loaded to 15% strain and then unloaded to zero strain. Positive stress and strain indicate compression.

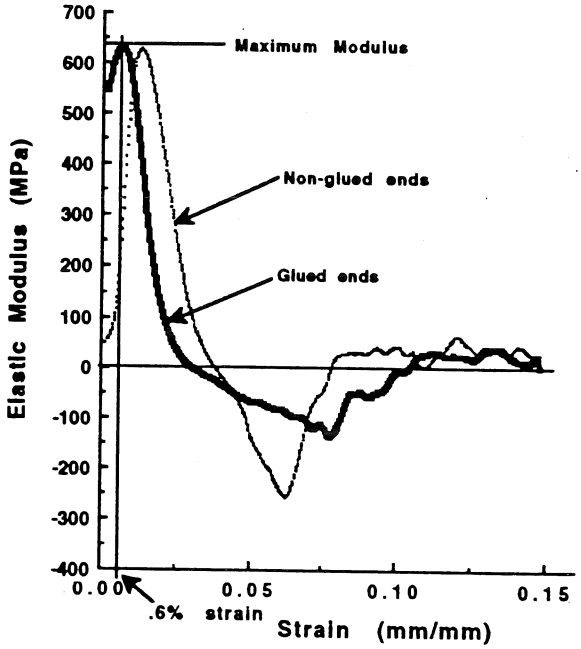

Figure 3: Graph of elastic modulus vs. strain for loading portion of compressive test. Positive stresses and strains indicate compression. The maximum modulus and the modulus at the 0.6% strain level were compared between the two groups.

QUANTIFICATION OF MATRIX COLLAGEN ARCHITECTURE IN MURINE CORTICAL BONE TO ASSESS THE EFFECT OF A TYPE I COLLAGEN MUTATION ON BONE MECHANICAL PROPERTIES

K. J. Jepsen, M. B. Schaffler*, S. A. Goldstein

Orthopaedic Research Labs, The University of Michigan, Ann Arbor, MI 48109
*Bone and Joint Center, Henry Ford Hospital, Detroit, MI 48202

INTRODUCTION

The composite nature of the extracellular matrix (ECM) plays a fundamental role in defining the mechanical properties of cortical bone, particularly in regard to fracture mechanisms. Our approach to investigating ECM structure-function relationships involved the use of type I collagen mutations to disrupt the composite nature of the ECM. The transgenic mouse, Mov13, has a genetic mutation altering the synthesis of type I collagen and has been shown to exhibit increased bone brittleness. In the current study, we employ a birefringence method to quantify matrix collagen architecture in order to explain the increased bone brittleness observed in Mov13 mice. We found that in addition to reduced collagen content, the type I collagen mutation also appeared to disrupt collagen packing in a significant manner which may have compromised the fracture properties of Mov13 femurs.

REVIEW

We have recently undertaken a series of investigations using models of type I collagen mutations as a new approach to characterizing ECM structure function relationships in cortical bone. In a previous study (Jepsen et al, 1992) we reported the mechanical properties of femurs from a strain of transgenic mice (Mov13) which has a retroviral mutation shown to result in a loss of one functioning proα1(I) collagen gene (Hartung, et al, 1986)). The mechanical properties of eight week male Mov13 femurs were found to be identical to their littermate controls (C57 Bl/6) in regard to stiffness and failure load but exhibited a significant reduction in post-yield deformation (taken here as a measure of bone brittleness). Given the nature of the genetic perturbation, we hypothesized that the increased brittleness of Mov13 cortical bone was a consequence of altered tissue composition and/or structure. We recently demonstrated (Jepsen et al, 1993) that the collagen content of Mov13 femurs was significantly reduced compared to littermate controls. To complete this tissue level assessment of matrix perturbations, the current study presents the results of an investigation which quantifies the matrix collagen architecture of Mov13 femurs and discusses how perturbations in collagen packing may account for altered whole bone mechanical properties.

PROCEDURES

Study Design: Femurs from 8 week male Mov13 mice (n=5) and 8 week male littermate controls (C57 Bl/6) (n=4) were examined. Prior to sacrifice, the mice were labeled with fluorescent dyes using a triple pulse of double IP injections. Oxytetracycline (30 mg/kg), xylenol orange (90 mg/kg), and calcein green (10 mg/kg) were administered starting at six weeks of age with five days between labels and four days between the last label and sacrifice.

Tissue Structure: After harvest, left femurs were fixed in Bouin's reagent, decalcified in formic acid/sodium citrate, and embedded in paraffin. Five micrometer (μm) transverse serial sections were obtained at 200 μm intervals. The sections were stained with Picrosirius Red F3BA according to the protocol described by Sweat et al (1964) and examined using Nomarski Differential Interference Contrast (DIC) microscopy. Picrosirius Red has been shown to enhance the birefringency of type I collagen and DIC enhances the contrast between tissue structures. Using this contrast method, it was possible to quantify matrix architecture for each cross-section. Four tissue types were identified with regard to collagen fiber orientation:

1. Transverse/lamellar bone (lamellar bone with collagen fibrils running transversely in alternate lamellae),
2. Longitudinal/lamellar bone (lamellar bone with collagen fibrils running predominantly in longitudinal direction),
3. Transverse/nonlamellar bone (fine fibered bone; fibrils exhibiting long range structure but without lamellar appearance), and
4. Woven bone.

These tissue types were similar to those described by Ascenzi and Bonucci (1967). Area fractions occupied by specific tissue types were measured using a standard point counting technique at 400x magnification for 3 random diaphyseal sections.

Lamellar Thickness: Average lamellar thickness was determined by counting the number of bright lamellae using a reticule micrometer. Because apparent differences bright and dark lamellar thicknesses were observed, the reported lamellar values represent an average of the two lamellar types. Lamellar thickness measures were corrected for tissue shrinkage.

Mineral Apposition Rate (MAR): Undecalcified samples from the contralateral limbs were used to assess MAR. Right femurs were fixed in 70% EtOH, embedded in methyl methacrylate, and serially sectioned using a metallurgical saw. Three random transverse sections spanning 3 mm of the diaphysis were polished to 100 μm thickness, mounted, and examined under UV light at 400x magnification. MAR was determined from the average interlabel distances for each quadrant using a video image analysis system.

Statistics: Differences in structural properties between Mov13 and C57 Bl/6 femurs were determined using the Wilcoxon-Mann-Whitney rank sum test. Significance is reported at $p<0.03$.

RESULTS

Table 1 summarizes the matrix collagen architecture results for Mov13 and C57 Bl/6 femurs. Mov13 femurs exhibited a 35% reduction in the area fraction of longitudinal/lamellar bone and a 30% increase in the area fraction of woven tissue. No significant differences were noted in the area fractions of the other tissue types. A significant reduction in average lamellar thickness was noted in the Mov13 femurs.

Table 1: Area fractions (%) of tissue types and lamellar thickness (μm).

Tissue Type	Mov13	C57 Bl/6
Trans./lamellar	30.4±5.8	27.6±4.1
Long./lamellar	21.4±5.9*	32.8±2.5
Trans/nonlamellar	13.8±6.0	13.2±4.0
Woven	34.4±3.8*	26.4±3.0
Lamellar Thickness	1.27±0.12*	1.44±0.01
Cortical Area (mm^2)	0.60±0.03	0.67±0.03

Table 2 summarizes the MAR results. Fluorescent labels were observed on the endosteal surface, primarily in the anterior region and extending into the lateral and medial quadrants, and on the periosteal surface, primarily in the lateral and posterior quadrants. This pattern of bone mineralization indicated that an antero-medial to postero-lateral modeling drift was occurring and this was evident for both Mov13 and C57 Bl/6 femurs. No difference in average MAR was found along the periosteal surface. However, Mov13 femurs exhibited a 34% increase in MAR on the endosteal surface.

Table 2: Mineral appositional rate (μm/day).

Cortical Surface	Mov13	C57 Bl/6
MAR-Endosteal	2.54±0.45*	1.89±0.29
MAR-Periosteal	1.79±0.28	1.95±0.37

* $p<0.03$ by Wilcoxon-Mann-Whitney rank sum test.

DISCUSSION

The results suggest that the type I collagen mutation of the Mov13 transgenic mouse significantly altered cortical bone structure. The reduced area fraction of longitudinal/lamellar bone and the increased area fraction of woven bone indicated that collagen packing was different in the Mov13 femurs. This was further supported by the significant reduction in lamellar thickness of the Mov13 femurs. The reduced lamellar thickness is line with the nature of the mutation and supports the observation that collagen content is reduced in Mov13 femurs (Jepsen et al, 1993). Thus, the type I collagen mutation appeared to disrupt both the amount of collagen and the organization of collagen in Mov13 femurs.

Differences in the way collagen is incorporated into the extracellular matrix has been shown to have profound effects on the elastic (Ascenzi and Bonucci, 1967) and fracture properties (Simkin and Robin, 1974) of cortical bone. Since no differences in whole bone stiffness were noted between Mov13 and C57 Bl/6 femurs (Jepsen et al, 1992), the changes in matrix architecture may not have been severe enough to alter cortical stiffness. However, the increased proportion of woven tissue and the loss of longitudinally oriented collagen fibrils in Mov13 may have contributed to the loss of post-yield deformation observed in Mov13 femurs by reducing the resistance to transverse crack propagation. This may account for a large portion of the apparent brittleness of Mov13 femurs when tested in bending. Tissue level fatigue tests are currently underway to better characterize the mechanical effects of the alterations in tissue structure and composition.

REFERENCES

Ascenzi, Bonucci; Anat. Rec., 158(4):375-386, 1967.
Bonadio et al; PNAS, USA, 87:7145-7149, 1990.
Hartung et al; Nat., 320:365-367, 1986.
Jepsen et al; Trans. Orthop. Res. Soc., 17(1), 1992.
Jepsen et al; to be presented at the ASME Summer Bioengineering Conference, Breckenridge, June 1993.
Simkin, Robin; J. Biomech. 7:183-188, 1974.
Sweat et al; Arch. Path., 78:69-72, 1964.

ACKNOWLEDGMENTS

The authors wish to thank R. Jaenisch, R. Curry, and J. Bonadio for their assistance. Support provided by NIH AR41349, AR20557 and University of Michigan Graduate School Pre-Doctoral Fellowship.

THE THREE-DIMENSIONAL MORPHOLOGY AND MECHANICAL PROPERTIES OF HUMAN VERTEBRAL CANCELLOUS BONE

S.M. Lang and D.P. Fyhrie

Breech Research Laboratory
Case Western Reserve University/Henry Ford Health Sciences Center
Henry Ford Hospital
Detroit, MI 48202 USA

INTRODUCTION

The three-dimensional (3D) morphology of human vertebral cancellous bone cubes was digitized at a 50 micron resolution using the technique of microcomputed tomography. Mechanical tests were performed to determine the compressive strength and stiffness of the bone. The structural and mechanical properties were then compared to determine their relationships. Results indicate that bone specific intercept count is proportional to bone volume fraction. Bone's ultimate strength and stiffness are also correlated to its volume fraction. Residual strains following unloading reveal that crushed bone cubes regain much of their original height; however, this parameter is unrelated to any structural properties examined.

PROCEDURES

One hundred and ten cubes of cancellous bone eight millimeters on a side were prepared from T12 or L1 human vertebrae obtained during routine autopsy of 6 women (ages 49, 56, 64, 74 and 81) and 1 man (age 62). The specimens were cut so that their vertical axis coincided with the anatomical (infero-superior) axis of the vertebra. They were stored frozen at -20C until they could be scanned using microcomputed tomography (MCT), a technique which allows direct 3D analysis of trabecular bone microstructure (1,2). The structural parameters examined were bone volume fraction (BV/TV), and the specific intercept count (P_I) along each principal axis, measured by counting the number of intersections an array of straight lines makes with the bone-marrow interface per length of line. Invariant functions of the tensor defined by using the principal intercept counts as the diagonal of a matrix were also calculated. The invariants were combined into the functions (3):

a) $I/3 = (P_{I1}+P_{I2}+P_{I3})/3$

b) $(II/3)^{1/2} = ((P_{I1}*P_{I2}+P_{I2}*P_{I3}+P_{I1}*P_{I3})/3)^{1/2}$

c) $III^{1/3} = (P_{I1}*P_{I2}*P_{I3})^{1/3}$

The specimens were then refrozen until mechanical testing. Using an INSTRON 8500 hydraulic testing system, the bone cubes were compressed between unlubricated steel platens in the infero-superior direction to 15% strain at either 15%/sec ("fast") or 1%/sec ("slow") using a havertriangle displacement waveform. The mechanical parameters examined were the ultimate stress, residual strain upon unloading and Young's modulus, determined as the maximum slope of successive regression lines plotted along the pre-failure portion of the stress-strain curve.

RESULTS

The failure curves of the bone cubes showed the typical behavior of a porous foam in compression (FIG. 1) with an initial linear region, a clear ultimate stress, and a post-failure plateau region. When the load was removed, the bone cubes did not remain fully compressed, but regained an average of 95% of their original height.

The data was pooled to combine specimens tested at both fast and slow rates. Strong correlations were found between each principal value of P_I and BV/TV, but overall, the P_I invariant functions produced much better relationships than the raw data ($R^2=0.91$, FIG. 2). The mechanical parameters of ultimate stress and Young's modulus were also related to BV/TV, with $R^2=0.64$ and 0.42, respectively (FIGS. 3,4). The residual strains, however, were unrelated to any of the microstructural parameters measured ($R^2<0.01$). Significance in the above relationships was taken as $p<0.001$.

DISCUSSION

The relationships between the raw data indicate that P_I is essentially proportional to bone volume fraction, which is consistent with the findings of Snyder and Hayes (4). The results for the invariants (FIG. 2) show that these functions of the intercept tensor are strong linear functions of bone volume fraction (BV/TV). Since none of these measurements are related theoretically, their close relationship implies that the

trabecular structure of vertebral cancellous bone is strongly constrained. This is consistent with the hypothesis that different bone volume fractions are formed by the removal of trabeculae from a primal structure in a programmed way. The prediction of mechanical strength and stiffness from BV/TV is to be expected, as an increase in the amount of material present enhances its ability to resist applied loads. The residual strain reflects cancellous bone's ability to "spring back" from a damaging compressive load, which may be fundamental to the tissue's ability to heal itself and restore function. The lack of a relationship between residual strain and structural properties implies that the mechanisms responsible for the "rebounding" properties of cancellous bone may lie more at the ultrastructural rather than microstructural level.

ACKNOWLEDGEMENTS

Our appreciation to Dr. Susan Hoshaw and Ms. Traci Wenzel for their assistance. This work was supported in part by NIH AR40776 and the Whitaker Foundation.

REFERENCES

1. Feldkamp et al., J Bone Min Res, 4(1):3-11, 1989.
2. Kuhn et al., J Orth Res, 8:833-842, 1990.
3. Fyhrie et al., Proc, 38th Annual ORS Meeting, 112, 1992.
4. Snyder, Biomechanics of Diarthrodial Joints, Springer 1990.

FIG. 1: FAILURE CURVE
Stress vs. Strain

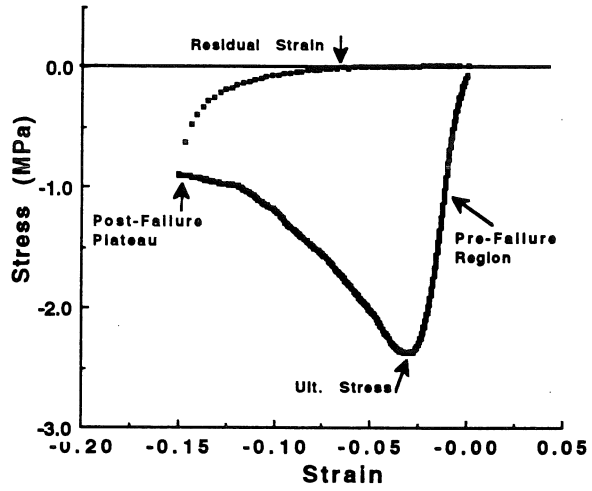

FIG. 2: Invariant Functions vs. Bone Vol. Fraction

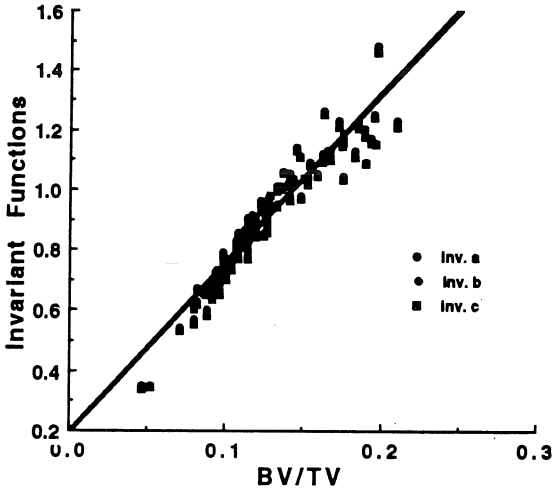

FIG. 3: Ultimate Stress vs. Bone Vol. Fraction

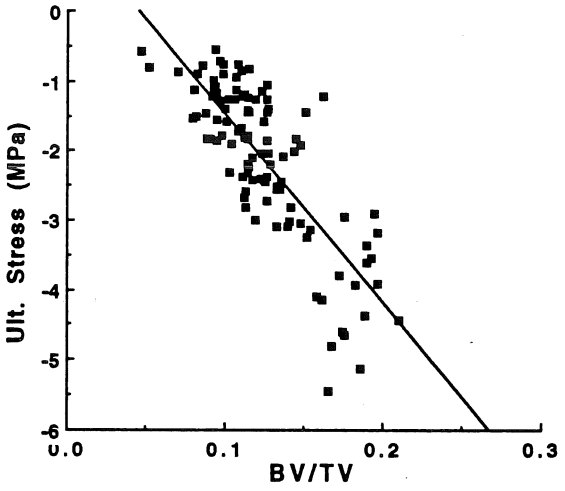

FIG. 4: Young's Modulus vs. Bone Vol. Fraction

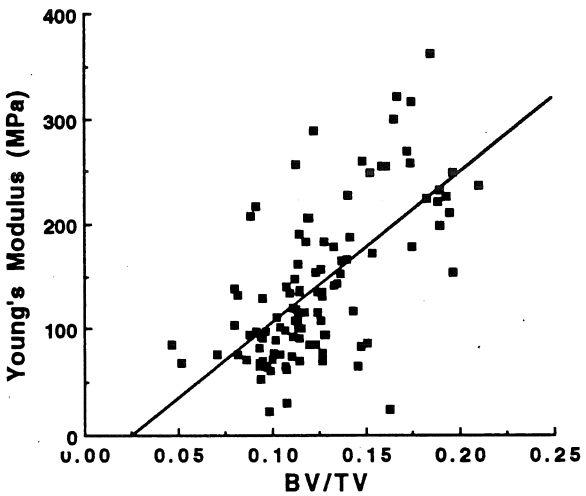

A BIOMECHANICAL STUDY OF THE EFFECTS OF AGE ON RECOVERY FROM IMPENDING LATERAL FALLS

X. Zhang, J.A. Ashton-Miller, A.B. Schultz and N.B. Alexander

Biomechanics Research Laboratories, Department of Mechanical Engineering and Applied Mechanics,
University of Michigan, Ann Arbor, MI 48109-2125

INTRODUCTION

Falls are the second leading course of accidental death in the United States, with 75 percent of all falls occurring in the elderly (for example, Kelsey et al.). Commonly associated factors include environmental factors such as trips and slips, reactions to prescribed drugs, visual impairments, and dementia (for example, Morgan et al.). Although falls can occur forward, backward, or to one side, it is the falls to one side that are increasingly being identified as being associated with the highest risk of one of the more serious outcomes of a fall, a hip fracture (Robinovitch et al.). In earlier studies we have examined the effects of age on the ability to recover from an impending backward fall caused by a perturbation consisting of an impulsive force applied to the pelvis (for example, Luchies et al.). Those studies showed that balance was recovered using sway and, when necessary, step-taking in the direction of the disturbing force. When stepping was necessary elderly subjects took multiple steps to recover from a disturbance that in the young would only require only a single step. In the present paper, we will test the hypothesis that age has no effect on the strategies used to recover from an impending lateral fall caused by a laterally-directed impulse to the pelvis. Specifically, we tested the null hypotheses (a) that there is no difference in biomechanical parameters describing how young and elderly recover from a lateral fall; and that their response is not significantly affected by (b) the magnitude of the disturbance, or (c) by whether the feet are placed together or apart; or (d) with eyes open or closed.

METHODS

Subjects – Twenty four healthy adult female volunteers gave their informed consent to participate in these studies. Twelve young adults adults (YA) with a mean (standard deviation, SD) age of 23.4 (2.7) years were recruited from university staff and students. Twelve elderly (OA) adults with a mean age of 71.7 (4.3) years were recruited from social support and recreation programs sponsored by a university-affiliated geriatrics clinic. Examined by a physician-geriatrician (NBA) no subjects had histories of significant head trauma, otologic or neurologic disease, limb fracture, musculoskeletal impairments, or persistent problems with vertigo, lightheadedness, unsteadiness, or falling. There were no significant differences in height and body weight between the two groups.

Apparatus – Subjects stood upright without shoes, with arms folded across their chests, and exactly half their weight supported by 6 channel force plates as indicated by a visual display at the instant of the lateral disturbance. The force plates were sampled at 100 Hz. Subjects wore a torso safety harness, suspended from the ceiling, adjusted to safely arrest the subject before any major fall could occur. A snug semirigid harness was worn just below the level of the iliac crests. This allowed a laterally-directed force to be imparted to the pelvis from either side via a computer-actuated dropped weight system, cables, pulleys and series force transducers (which were used to measure the time course of the impulse). The magnitude and duration of the lateral pull (approximately 20 % of body weight) was adjusted to produce initial broom-stick whole body lateral sway equivalent disturbance angles (EDA) of 1, 2 or 3 degrees subtended at the ankle. Subjects were instructed that they would be pulled randomly from either side and could use any method that was comfortable to recover their balance. After the drop mechanism was triggered five seconds of data were collected in each trial. Twenty four trials, in a fixed randomized sequence, were conducted per subject, 12 to each side. At each EDA the subject stood: (a) with eyes open and feet together (three trials); (b) with eyes open and feet apart by one foot length (three trials); (c) with eyes closed and feet together (one trial); and (d) with eyes closed and feet apart (one trial). A two camera Watsmart optoelectronic motion analysis system was used to track (at 100 Hz) the 3-D locations of five infrared emitting diode (IRED) markers placed on each heel, the low back, neck and one force plate, respectively. The force transducers were used to measure the time history of the disturbance force exerted on the subject, specifically, the disturbance onset time, the time and magnitude of maximum force and the overall disturbance time. The force plates were used to measure the time course of the vertical and horizontal reaction forces, the foot reaction onset time, and the time of maximum force.

Data Analysis - The Watsmart data were used to characterize the stepping patterns as follows: when pulled suddenly to the side subjects exhibited one of four patterns of kinematic responses to recover their balance. Pattern I: a sway response; Pattern II: stepping the ipsilateral (pull-side) foot in the pull direction; Pattern III: stepping the contralateral foot opposite to the pull direction; or Pattern IV: stepping the contralateral foot across the pull-side foot in the pull direction. We used the force plate data to analyze the time course of the ground reaction. Analysis of variance (ANOVA) was used to examine the effects of age, disturbance levels, and foot placement and visual feedback. P values < 0.05 were considered statistically significant. Post-hoc comparisons were conducted using independent t tests and Boneferroni's correction.

RESULTS

There were no significant age differences in the time from pull onset to maximum pull force. For the EDA 1 this time averaged 45 msec, for EDA 2 it averaged 65 msec, while for EDA 3 it averaged 76 msec. Thus for the largest EDA the disturbance force acted approximately 70% longer duration than the smallest EDA.

The disturbance levels significantly affected the frequency of use of the four different response patterns as well as the value of the maximum vertical ground reaction. There were,

however, no significant age differences in the frequency with which the four different patterns were used to resist the three levels of postural disturbance (ANOVA, P=0.31). The presence or absence of visual feedback did not significantly influence subject responses. None of the disturbances caused a subject to actually fall sideways. Subjects usually resisted an EDA=1 with a sway response not needing to take a step: for example, in 40/48 OA trials and 30/43 YA trials subjects used a Pattern I strategy to resist the disturbance. At an EDA 2 with feet together, only 13/47 OA trials showed continued Pattern I usage, and the OA needed to use each of the other Patterns II-IV strategies in approximately equal measure. YA essentially abandoned the Pattern I sway strategy, mostly (22/37 trials) adopting a Pattern II response. When the feet were separated to give a larger base-of-support, both groups again mostly adopted Pattern I. Finally, when resisting an EDA 3 disturbance, a bimodal distribution showed that most OA either adopted Pattern IV (24/45) or Pattern II (16/45), while most YA (31/46) adopted a Pattern II response. With feet apart, most OA adopted Patterns III and IV, while most YA adopted Patterns II and III. The mean pelvic lateral velocity of the young group was higher than that of the elderly group at every EDA level, despite there being no significant differences in young-old disturbance magnitudes, perhaps reflecting a less conservative pattern of use of joint torques and stiffnesses. At EDA 1 the step lengths, when used, ranged from 3 cm to 19 cm in the YA and from 5 cm to 22 cm in the OA. The reaction time as evidenced in the foot reaction ranged from 200 ms to 400 ms in the YA but from 390 ms to 470 ms in the OA. It was apparent that the YA were quicker to start and finish their response to an EDA=1 than OA. At an EDA=3, which seldom resulted in a sway response, foot reaction onset times were again significantly quicker in the YA (200-270 ms) than the OA (360-410 ms).

Effects of Age - A significant slowing in foot response onset time (P=0.002) and time to maximum foot vertical reaction force (P=0.005) was found with age (ANOVA). However, the distance subjects stepped, when they did step, did not change significantly with age.

Effect of Size of Base-of-Support - When compared to standing with a narrow base-of-support, the use of a broad base-of-support significantly affected the choice of response pattern used (P=0.001), the onset time for the reaction foot (P=0.000) the time for the reaction foot step (P=0.003), the time for the stance foot peak force (P=0.000) and the normalized peak vertical force on the pull-side force plate (P=0.003, ANOVA).

DISCUSSION

This is one of the first studies reporting how healthy subjects recover from an impending lateral fall. Subject used fairly stereotyped sway/stepping responses to the disturbance depending upon the EDA magnitude. Interestingly, these responses could involve the use of either foot to step, a behavior we did not initially anticipate. Such alternative strategies allow the threat of having one foot obstructed by an obstacle to be circumvented if recognized early enough. The study suggests that a sway response is used until the perturbation is recognized as being of sufficient magnitude that a sway response will no longer suffice. This may be partially mediated through proprioception and vestibular estimates of linear and angular head accelerations. Even though such information takes on the order of 40 msec to reach the cerebellum and brain stem, and efferent commands another 40 msec to travel down the appropriate pathways to the limb muscles, significant trunk/lower extremity joint torques, however, are not generally avaliable for 300 to 400 msec after the perturbation due to the central processing latencies and finite rates-of-developing joint strength. Significant age differences were found, but even though a large step will arrest more momentum than a small step, the elderly did not employ a more conservative stepping strategy than the young as evidenced by longer steps or multiple steps. It is possible that had we used larger EDA's, we might have observed multiple step taking by the OA. But the absence of multiple stepping behavior in OA differs from the use of such behavior by OA when arresting impending backward falls initiated using identical EDA values (Luchies et al. 1992). This suggests impending lateral falls are not perceived to be as threatening as lateral falls.

REFERENCES

Luchies, C.W., Alexander, N.B., Schultz, A.B., and Ashton_Miller, J.A., "Stepping Responses of Young and Old Adults to Postural Disturbances: Kinematics ", Submitted to *J. Gerontology*, 1992

Robinovitch, S., W.C. Hayes, and T.A. McMahon, "Prediction of Femoral Impact Forces in Falls on the Hip", *J. Biomech. Eng.* Vol. 113, Nov. 1991, pp. 333-374

Overstall, P.W. et al.,"Falls in the Elderly Related to Postural Imbalance", *British Med. J.* 1977, 1, pp.261-264

Morgan, K, et al., "Falls by Elderly People at Home: Prevalence and Associated Factors", *Age and Aging*, Vol. 17, No.6, 1988, pp.365-372.

Kelsey, J.L. and Hoffman, S., "Risk Factors for Hip Fracture", *New England J. Med.*, Feb. 12, 1987, pp. 404-406

ACKNOWLEDGEMENTS

We gratefully acknowledge the assistance of Janet Grenier, Julie Akers and Youda He and the support of PHS grants AG 06621 and 8808,

DYNAMIC BALANCE RECOVERY: STEPPING RESPONSES TO POSTURAL PERTURBATIONS

Michael R. Carhart, Gary T. Yamaguchi, and Jonathan I. Green

Department of Chemical, Bio & Materials Engineering
Arizona State University, Tempe, AZ 85287-6006

INTRODUCTION

The question of interest is whether or not paraplegics can utilize functional neuromuscular stimulation (FNS) to maintain a standing posture in the presence of unexpected postural perturbations. It is hypothesized that the time lags in (i) sensing and processing the disturbance information, (ii) determining and implementing control actions, and (iii) developing force in muscles and tendons, coupled with strength and fatigue limitations in muscles excited via FNS, may make it impossible to correct for large postural perturbations during FNS induced standing, regardless of postural recovery strategy. In order to study the limitations of FNS technology and explore the feasibility of using FNS to restore a *working stance* to paraplegics, i.e., a stable standing position in which a paraplegic can perform a vocational task (such as lifting, machining, etc.), we have begun a dual track study (experimentation and computer simulation) of stepping responses to postural perturbations.

REVIEW AND THEORY

While postural responses of the young and old to small perturbations of standing position have been studied in some detail (Nashner et al., 1985, 1989; Keshner et al., 1988; Woollacott et al., 1986), the biomechanics of responses to large perturbations of stance which require stepping movements remain largely unstudied. Likewise, dynamic analysis and modeling of FNS used to effect standing postures has been restricted to small perturbations and planar movements. Khang and Zajac (1989) developed optimal control algorithms utilizing sagittal-plane and frontal-plane models with a sophisticated musculotendon actuator set; however, perturbations were small and easily corrected using ankle and/or hip strategies.

In order to restore the ability of a paraplegic to work safely in the presence of real-world perturbations, one would need to enable them to take steps to restore their balance. Thus, it would be desirable to utilize both computational and experimental approaches to explore multi-directional non-planar balance recovery stepping movements. Because of the 3-D asymmetric nature of these movements, sagittal plane analyses coupled with frontal plane analyses are inadequate. Though complex, experimental measurement and dynamic modeling analysis of these movements can be employed synergistically to explain (a) how normals effect balance recovery by taking a step and (b) whether or not FNS will be a feasible means of restoring stepping as a means of balance recovery in paraplegics. In this paper, we restrict our discussion to the first topic, normal balance recovery via stepping.

PROCEDURES

Model Development. A 9 segment, 16 degree-of-freedom (DOF) dynamic musculoskeletal model has been developed (Green, 1992). This model has separate stance and swing legs (2 DOF ankles, 1 DOF knees, and 3 DOF hips), a three segmented torso (with 2 DOF between the pelvis and low trunk, and 1 DOF between the low trunk and upper trunk), 46 musculotendon actuators, and is capable of analyzing and simulating asymmetric 3-D motions.

Experimentation. Our experimental facility consists of a 16 channel custom manufactured electromyographic (EMG) detection and recording system, a four-camera motion tracking system, dual Bertec 4080H six-component force platforms surrounded by raised a experimental platform, and an electro-pneumatic perturbation system. The perturbation system is comprised of: (i) four Speedair 1.25" bore pneumatic cylinders, each mounted on metal frames located in front of, behind, and laterally to each side with respect to the force platforms, (ii) an adjustable cabling, pulley, and release system to transmit the forces developed in the pneumatic actuators to the subject, (iii) Interface tensile loadcells to measure the applied perturbation force, and (iv) a Festo electro-pneumatic controller card to provide remote control of pneumatic cylinder activation.

Thus far, experimentation has been performed on two male subjects, age 23 and 25. The subjects were asked to stand comfortably in the center of the force sensing area, with one foot on each force platform, looking straight ahead with the eyes open and arms folded across the chest. A belt was tightly secured over the subject's anterior superior iliac spines, and cables from the pneumatic cylinders were connected to the belt anteriorly, posteriorly and bilaterally. Three of the four cables were then partially released so that only one could sustain a sizable force, yet all appeared to be similarly connected. Upon actuation of the appropriate cylinder, a waist level horizontal force (approximately 25 pounds peak) was applied to the subject via one of the four cables in either the forward, backward or lateral direction, while the other three cables released. In this way, neither the timing nor the direction of the perturbation force was evident to the subject prior to its application.

Each subject was perturbed 4 times in each of the 4 possible directions (forward, backward, left, and right) for a total of 16 trials per subject, with the sequence of directions being randomly determined. For each trial, 3-D body segment kinematics were measured using spherical reflective markers (3 per rigid-body-segment) and a four camera motion tracking system. Additionally, 16-channel EMG activity, ground reaction forces, and the perturbation force were simultaneously measured.

RESULTS AND DISCUSSION

Preliminary results include recordings of 16 channel bilateral EMG, ground reaction force, perturbation force, and 3-dimensional kinematic data for multiple trials in each of the four directions (forward, backward, right and left). An EMG recording for subject #1 during a forward perturbation is included below in Figure 1.

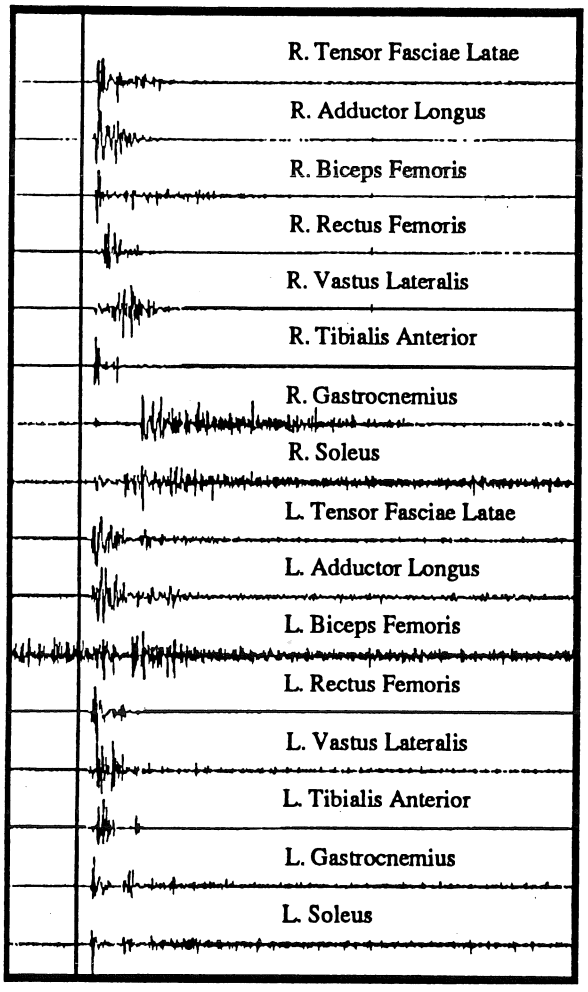

Figure 1. EMG record for subject #1 during a forward perturbation. The vertical line in the figure denotes the initiation of the perturbation force. The subject responded by stepping forward with his right foot.

The EMG recording in Figure 1, coupled with the corresponding ground reaction and kinematic results, indicates an assistance reflex type response with the latency period between the initiation of the perturbation force and onset of response muscle activity being approximately 80 ms.

Complete detailed analysis of the results is pending the collection of data from additional subjects.

REFERENCES

Green, J.I., *Masters Thesis*, Arizona State University, 1992.

Keshner, E.A., et al., *Exp. Brain Res.*, **71**, 455-66, 1988.

Khang, G. et al., *IEEE Trans. Biomed. Engrg.*, **36**, 885-984, 1989.

Nashner, L.M., et al., *Behavioral Brain Sci.*, **8**, 135-172, 1985.

Nashner, L.M., et al., *Progress in Brain Research*, **80**, 411- 423, 1988.

ACKNOWLEDGEMENTS

The authors wish to thank the National Science Foundation for its support through grants BCS-9110658 and BCS-9257395 as well as Dan Moran for his assistance.

THE EFFECT OF IMPAIRED LOWER LIMB JOINT FUNCTION ON POSTURAL BALANCE AND FALLS

Ge Wu

Biobehavioral Health Program and Center for Locomotion Studies
The Pennsylvania State University, State College, PA, 16801

INTRODUCTION

The balance of upright stance has been hypothesized to be maintained primarily by the ankle joint [1], and to be modulated mainly by the activity of lower limb muscles [4]. However, the evidence based on the biomechanical studies of posture suggested that joint strength might not be the primary risk factor to elderly falling [2].

It is the aim of this study to investigate the role of the lower limb joints in maintaining balanced upright posture, and to investigate how people react to a fall provoking stimulus when constraints are placed on movement at the lower limb joints.

BACKGROUND

Many studies have been conducted to determine the changes in the musculoskeletal system with age, and the extent to which these changes are associated with decreased balance abilities. The results suggest that declines in lower limb strength and joint range of motion in the elderly may account for postural instability; and extreme dorsiflexion weakness may be particularly responsible for backward falls [3]. However, a recent study has shown that the strength required at the ankle to maintain body balance is much less than the maximal strength that the joint is able to generate [2], suggesting that joint strength might not be the primary risk factor to elderly falling. Overall, it is not clear yet exactly how elderly falls are related to the decline in lower limb muscular functions due to aging.

This study investigated the effect of impaired lower limb joint function on balance and falls. It is hypothesized that: (1) the incidence of falls will increase when the ankle joints are immobilized; (2) muscular response to the perturbation will show significant differences in the magnitude and response latency between normal and ankle immobilization conditions.

METHOD

Four healthy young subjects participated in this study. Each subject was asked to stand on the platform of the perturbation device, with arms located at the sides of the body. A well illuminated, solid colored screen was placed in front of the subject to control the visual field. A headphone was worn by the subject to avoid environmental disturbance. The postural perturbation was applied to the subject through an unexpected, electromagnetic motor driven toe-up rotation. The speed was set at 50*deg/sec*, and the total angular rotation was varied from 5 to 14 degrees. The acceleration of the platform was measured by an accelerometer to record the on-set of the perturbation.

The movements of the ankle and knee joints were restrained by commercially available joint immobilizers. Such joint restraint device was able to eliminate completely the joint motion. Six electromyography (EMG) electrodes were attached to tibialis anterior, gastrocnemius, rectus femoris, hamstring, erector spinae, and rectus abdominus on the left side of the body, respectively. Raw EMGs were digitized at 500 Hz and were processed to calculate the mean magnitudes and latencies to the perturbation through visual inspection.

One controlled and three immobilized conditions were conducted. For each condition, multiple trials at three angular rotations (5, 10 and 14 deg) were collected. The sequence of these perturbations was random, but it was the same for every subject. In response to the platform perturbation, the subject was asked to maintain a balanced posture, that is not to reposition the foot (or feet) and not to support the body by hand(s). If either of the above responses occurred, that trial was considered to be fall trial and was recorded.

RESULTS AND DISCUSSION

First, it was found that the total number of falls increased dramatically when the ankle joints were completely immobilized compared to when they were not, regardless of the constraints at the knee joints (Fig. 1). For example, during 10 and 14 degree toe-up perturbations the rate of falls was higher than 80% under ankle immobilization while the rate of falls was less than 6% under the control condition. This result supported the hypothesis that the ankle is the primary joint in the lower limb for maintaining balanced upright posture.

Second, the number of falls under smaller perturbation angles (e.g. 5 degrees) was much less (17%) than that under larger perturbation angles (>80%); and the rate of falls was similar for both 10 and 14 degree perturbations (Fig. 1). This suggested that a perturbation threshold might exist below which the human body is able to maintain balanced upright posture even though the ankle joints are completely immobilized.

Third, it was found that under the ankle restraint condition, about all the six muscles monitored tended to activate earlier than they did under the normal condition (see Fig. 2). Furthermore, it was observed that the decrease in the response time was independent of the level of perturbation among the lower limb muscles, except for the RF muscle, whereas the amount of

decrease in latency was increased as the degree of perturbation was increased for the trunk muscles. This finding suggested that the central nervous system might have regulated postural control strategy, to a certain extent, in coping with the physical changes at the lower limb.

Last, it was found that the level of muscular activities after the ankle joints were immobilized were suppressed for the agonist muscles of the ankle and knee joints (i.e. the TA and RF), whereas it was enhanced for the rest of the muscles (see Fig. 3). Moreover, the amount of the enhancement tended to increase for the more proximal muscles. This finding suggested that (1) the responses of the muscles around the ankle joint to the perturbation were initiated in part by the joint receptors; (2) the inhibition in the ankle joint muscles resulted in the increase in the activation of the proximal joint muscles in order to maintain the postural balance.

CONCLUSION

Despite the earlier responses and the enhanced level of muscle activation after the ankle joints were immobilized, the fact that the incidence of falls was increased significantly under ankle immobilized condition suggested that the proper function of the ankle joint is vital in maintaining balanced posture upon perturbation. Although the postural strategy may be altered by utilizing more of the other muscles, it may not be effective, especially when the perturbation is large.

REFERENCE

[1] Nashner, LM. and McCollum, G The Beh. and Brain Sci., 8:135-172, 1985
[2] Schultz, AB J. of Biom., 25(5):519-528, 1992
[3] Whipple, RH et al. J. Am. Geriatr. Soc. 35:13-20, 1987
[4] Woloszko, J. et al. Proc. of The 2nd North Am. Con. on Biom. pp147-148, 199

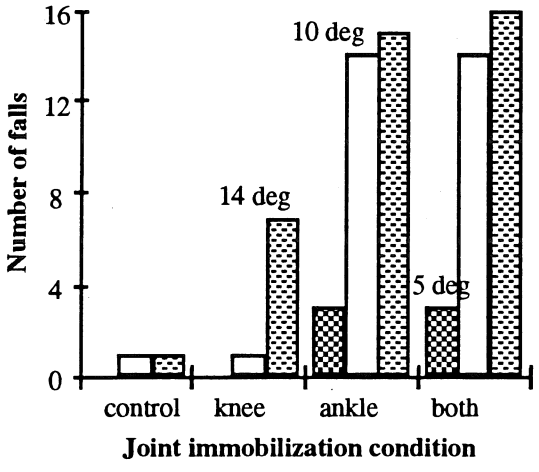

Figure. 1 Total number of falls (out of 16 trials) under control, knee immobilized, ankle immobilized, and both joint immobilized conditions.

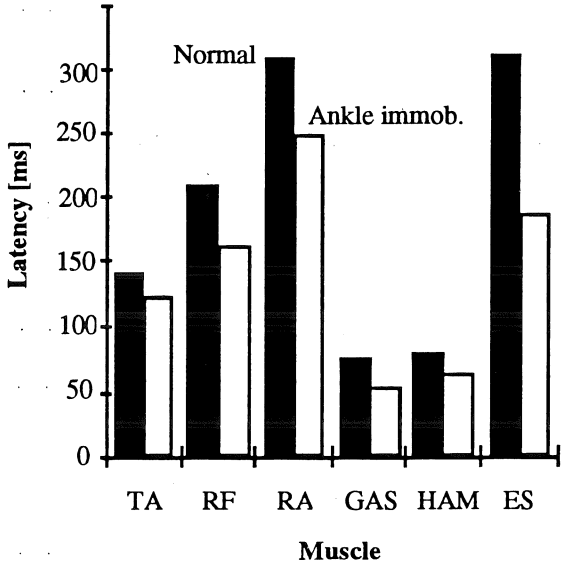

Figure. 2 Mean latencies of six muscle responses under control and ankle immobilized conditions. The platform rotation was 14 degrees.

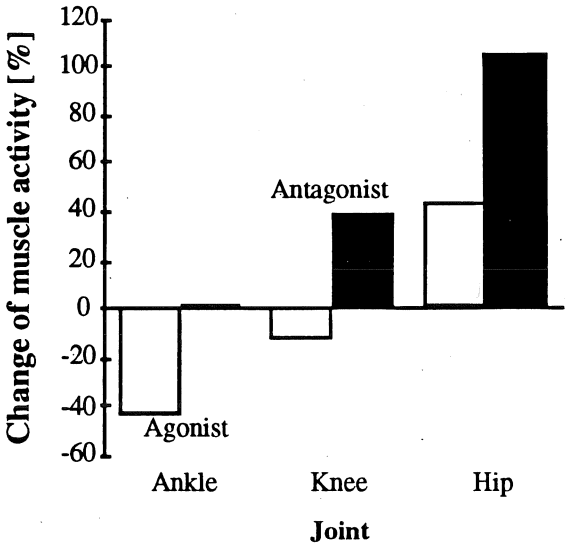

Figure. 3 Relative changes of the mean muscle activity under ankle immobilized condition with respect to that under control condition. The agonist muscles include TA, RF and RA, and the antagonist muscles include GAS., HAM. and ES. The platform rotation was 14 degrees.

ANTICIPATORY REACTIONS DURING DROPPING AND CATCHING WEIGHTS

Alexander S. Aruin, John J. Nicholas, Gerald L. Gottlieb, Kyung C. Lee, and Mark L. Latash

Departments of Physical Medicine & Rehabilitation and of Physiology,
Rush-Presbyterian St.Luke's Medical Center, Chicago, IL 60612, USA.

INTRODUCTION

In healthy adults, activity of postural muscles is observed prior to fast voluntary movements. This anticipatory activity provides a quick albeit crude postural correction prior to the perturbation introduced by the movement. Certain neuromotor disorders (in particular, Parkinson's disease, PD) and normal aging are associated with decreased or even absent anticipatory postural activity. However, such individuals usually demonstrate slower voluntary movements that are likely to give rise to smaller postural perturbations and cannot be compared to those in young healthy adults. We have attempted to elaborate a method of testing anticipatory postural reactions that would be independent of the ability of a person to perform fast voluntary movements.

REVIEW AND THEORY

Voluntary limb movements are virtually always associated with changes in the activity of postural muscles (Cordo & Nashner, 1982; Bouisset & Zattara, 1983; Brown & Frank, 1987). Some of these changes occur prior to the movement and can be described as anticipatory. Their assumed role is to minimize perturbations of the vertical posture that would otherwise be induced by the movement. Bouisset & Zattara (1987) have suggested that these reactions initiate an acceleration of the body that would oppose the expected perturbation due to an intended limb movement. Anticipatory postural corrections before a voluntary movement have been observed in only a small fraction of patients with PD (about 5%) as compared with 100% among control subjects (Bazalgette et al., 1986). Postural reactions in patients with PD occurring in the course of a voluntary movement are not specific to the movement and occur bilaterally in cases of both uni- and bilateral voluntary movements (Bouisset & Zattara, 1987).

PROCEDURES

Five healthy adults stood on a biomechanical platform (OR-65 AMTI). The subjects performed either fast voluntary shoulder flexion and extension movements, or were required to drop or catch weights (2 or 5 lb) with arms extended. Forces and moments of forces in three directions were calculated from the signals recorded by the platform. Surface electromyograms (EMGs) of the following muscles from the right side of the body were recorded: Shoulder flexor (m.pectoralis major) and extensor (m.deltoideus posterior), and also 6 postural muscles (mm. erector spinae, rectus abdominus, rectus femoris, biceps femoris, tibialis, and gastrocnemius). Besides that, markers (infrared diods) were placed on the right hip, shoulder, elbow, wrist, fingertip, and the load. Their movements were recorded and analyzed by an OPTOTRAK system. All the signals were sampled at 500 Hz and later processed with a 386 IBM computer. The trials were aligned according to the first visible agonist EMG increase in trials with voluntary movements and to the load kinematics in the trials with load dropping and catching. The final stage of data processing and plotting was performed on a Mac-IIci.

RESULTS

Anticipatory reactions in all the subjects were seen prior to the beginning of the agonist activity during voluntary movements and prior to the load impact or release. They represented changes in the postural muscle activity, force in the anterior-posterior direction, moment in the saggital plane, displacement of the center of mass of the body and the center of pressure. Their mechanical effect was always directed to compensate for a displacement of the body center of mass induced by the movements or interaction with the weight.

Figure 1 shows the averaged trials for one of the subjects during 5 lb load dropping (dashed traces) and catching (solid traces). Note considerable changes in the background activity of biceps femoris and erector spinae that start about 100-150 ms prior to the load impact or release (two upper graphs). Load dropping was also associated with anticipatory displacement of the center of pressure (the third graph). Anticipatory finger displacements were seen in the trials with load catching and dropping (the lower graph). Catchcing and dropping the light load (2 lb) was associated with qualitatively similar but less pronounced anticipatory patterns.

Generally, anticipatory reactions occurred about 50 ms earlier, were more pronounced and reproducible during weight dropping and catching than prior to fast voluntary movements.

DISCUSSION

Our most important finding is that dropping and catching a load is accompanied in healthy subjects by a reproducible pattern of anticipatory changes in activity of postural muscles. These changes lead to an alleviation of the effects of the interaction with the load upon vertical posture.

This simple method can be used for testing patients with suspected absence or deficiency of anticipatory reactions. Note that the method is independent of the subject's ability to perform fast voluntary movements and therefore can be used in aged subjects and in patients with slow voluntary movements (e.g., PD).

REFERENCES

Bazalgette, D. et al. Adv. Neurol., 45, 371-374, 1986.

Bouisset, S. & Zattara, M. Physiologie Spatiale, (pp. 137-141) Cepadues Editions, 1983.

Bouisset, S. & Zattara, M. J. Biomech., 20, 735-742, 1987.

Brown, J.E. & Frank, F.S. Exp. Brain Res., 67, 645-650, 1987.

Cordo, P.J. & Nashner, L.M. J. Neurophysiol., 47, 287-302, 1982.

ACKNOWLEDGEMENTS

The study was supported by NIH grants HD-30128 and NS-28176.

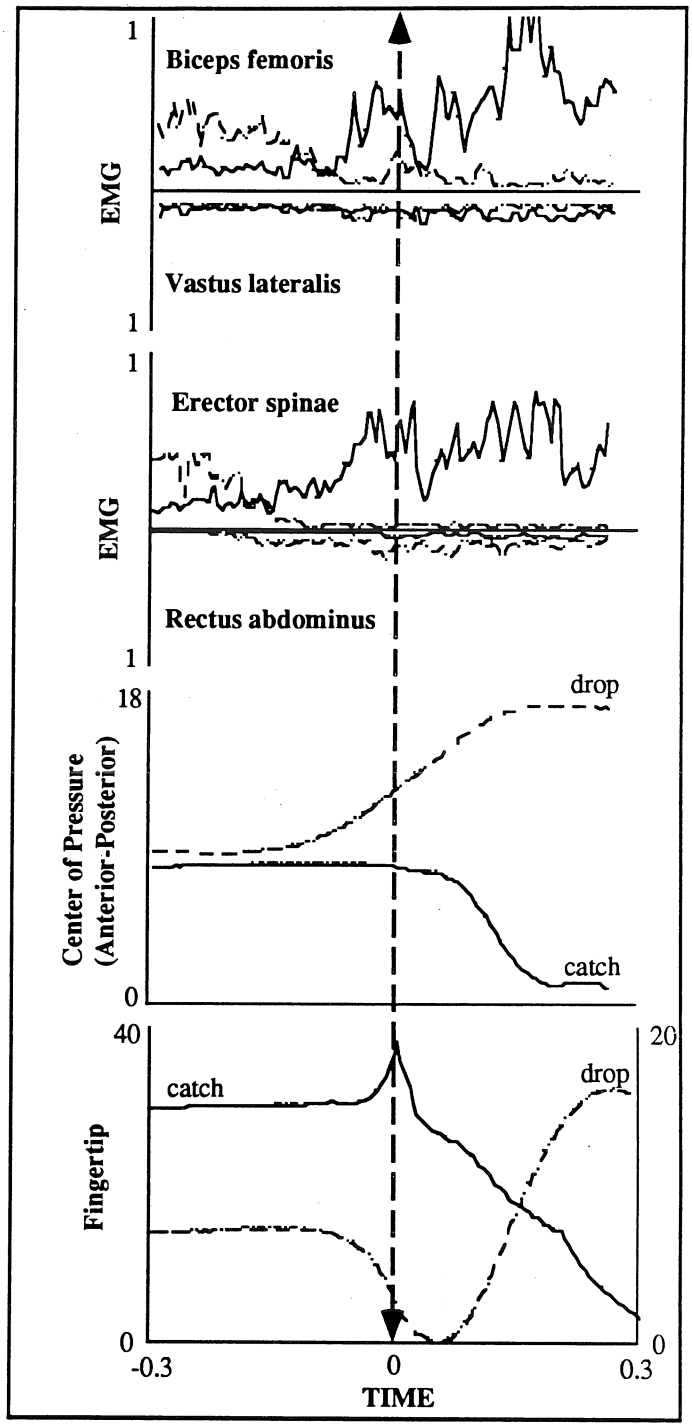

Figure 1.
EMG patterns, displacement of the center of pressure, and fingertip movements in the anterior-posterior direction during 5 lb load dropping (dashed traces) and catching (solid traces). Averaged trials (n = 5) for one subject are shown. Time "zero" corresponds to the load release or impact. Time axis is in s, EMG axes are in arbitrary units, center of pressure and fingertip axes are in mm (an increase corresponds to a backward movement).

IN-SHOE HEEL PRESSURE DISTRIBUTION AND IMPACT GROUND REACTION FORCE DURING RUNNING.

M. A. Lafortune, M. J. Lake, G. A. Valiant *

School of Human Biology, University of Guelph, Ontario.
*Sport Research Laboratory, Nike, Oregon.

INTRODUCTION

Each running foot contact generates impact ground reaction forces (GRF) which are modulated through the shoe sole and transmitted to the body. Although different cushioning properties of midsoles with distinct material characteristics can readily be perceived, and confirmed with mechanical impact testers, few authors have shown significant changes in impact GRF that result from running in shoes with different midsole hardness. Simultaneous GRF and heel in-shoe pressure measurements during running demonstrated that cushioning differences between midsole densities are found in the very initial phase of foot ground contact as the rear border of the shoe is compressed. Differences were revealed predominantly by pressure information in specific heel areas while GRF variables provided limited discriminatory ability between shoe hardnesses.

REVIEW AND THEORY

In vivo cushioning properties of footwear have been extensively studied with variables derived from measured GRF during running (Bates et al., 1983; Clarke et al., 1983; Snel et al., 1985; Nigg et al., 1987). For footwear with midsole material having different physical properties, peak impact forces of similar magnitude were found for groups of individuals during running. This was explained by a concurrent difference in internal forces (Nigg et al., 1987) and adaptations in the neuromuscular control system to the changing sole hardness (Snel et al., 1985). Yet, Bates et al., (1983) using a single subject approach found a considerable subject-shoe interaction and implied that the GRF was sufficiently sensitive to discriminate between running shoes. Recently, discrete plantar pressure sensors have been used to provide information relevant to reduction of symptoms associated with overloading of the foot (Hennig & Milani, 1989). This study compares the cushioning properties of different midsole materials during running with in-shoe pressure distribution and GRF information.

PROCEDURES

Ten male recreational runners (mean: 70.7 kg and 174.7 cm) were asked to run at 3.83 m/s along an 18m runway so that their left leg landed naturally on a force platform (AMTI). Center of pressure data confirmed that each subject was a rearfoot striker. Subjects wore three experimental shoes differing only in midsole density (hard, 0.4 g/cm^3; medium, 0.3; and soft, 0.25). Heel pressure distribution was monitored with 25 h.a.l.m. discrete pressure sensors located in specific areas. To overcome point loading discussed by Lake and Lafortune (1991), the pressure sensors (size: 5 mm by 4 mm by 2.5 mm) were encapsulated in a thin layer of silicone rubber material to form an insole which fitted tightly in the shoes. The pressure sensors were linked to charge amplifiers (1 kg mass) carried in a belt bag by the subjects. Pressure and force platform signals were simultaneously sampled at 500 Hz by a MicroVax/GPX II computer for ten trials in each experimental shoe. Power spectra were used to determine the 62.5 and 50 Hz cutoff frequencies for digital filtering of the force and pressure signals, respectively.

RESULTS

Group mean GRF results are summarized in Table 1. Peak impact force was not statistically different between shoes for this group of subjects. ANOVA's revealed that the rate of loading (ROL) and the time to 0.2 bw (T2) were different across shoes. Post hoc comparisons indicated that ROL and T2 were different between hard and low midsole density.

Table 1. Means (± SD) of the GRF variables (* - significantly different from soft, ** - different from soft and medium).

Variable	SOFT	MEDIUM	HARD
Initial Peak F_Z (BW)	**2.01** (0.40)	**2.02** (0.33)	**1.96** (0.39)
Loading rate (BW/s)	**60.4** (17.6)	**63.3** (15.7)	**67.4** * (17.5)
Time to 0.2 BW (ms)	**7.5** (1.0)	**7.3** (0.7)	**6.5** ** (1.1)

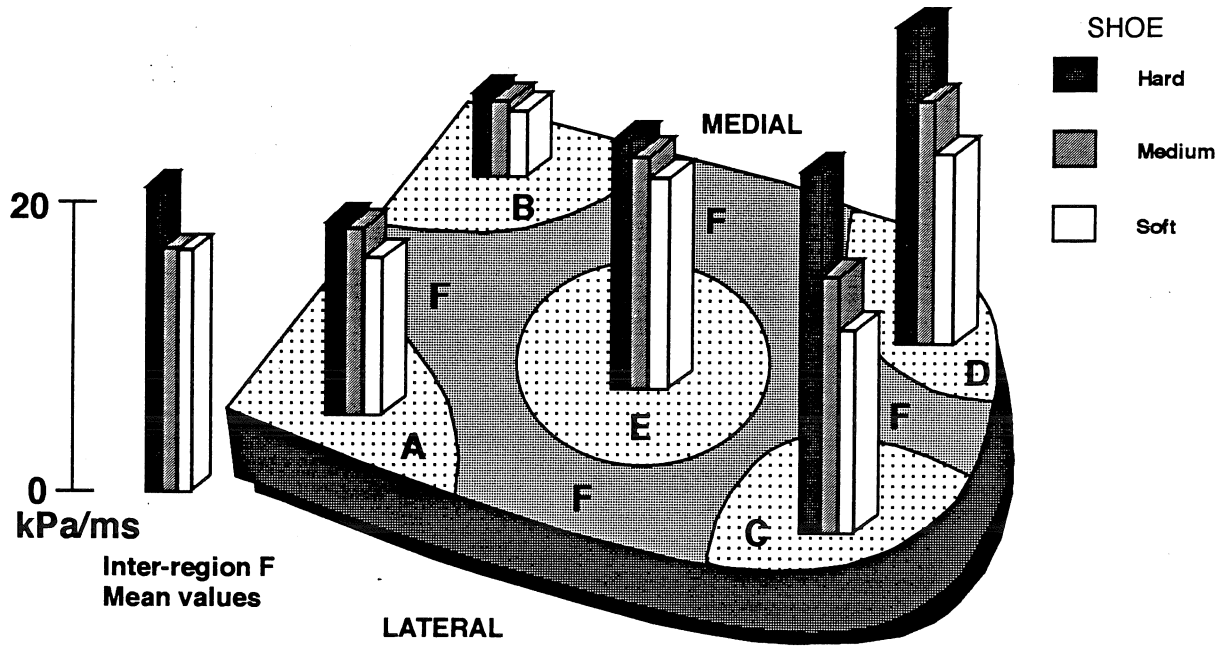

Figure 1. Mean rate of loading for each region and shoe condition.

Figure 1. shows the six heel areas monitored for in-shoe pressure. The peak and rate of loading of the in-shoe pressure were similar to those measured in the heel by Gross and Bunch (1989). The test shoes did not produce even peak pressures or loading rates across the heel. Independently of the shoe used, the peak pressures nearer the arch region were significantly lower than under any other regions of the heel. Substantial increases in peak pressures and rate of loading with midsole density were seen in areas C and D. In contrast, minor differences between shoes were seen in areas A, B, E and F. Rate of loading was the variable which best illustrated midsole density differences especially in areas C and D (Fig. 1). Every shoe comparison in these areas proved to be significant. The peak pressure distribution followed a similar pattern in the different heel regions, although in areas C and D the comparison between the medium and soft density shoes was found to be non-significant.

DISCUSSION

The lack of difference in peak impact GRF between shoe types was in agreement with the findings of previous researchers mentioned. Some individuals responded differently to shoe midsole hardness, as acknowledged by Bates et al. in 1983, and this could have led to the absence of group trends. An alternative explanation could be that the cushioning effects of the shoe midsoles are mainly demonstrated by temporal rather than force magnitude changes. This is supported by the GRF rate of loading and the time to 0.2 BW variables which showed a significant difference between low and high density midsoles. A larger group of subjects or trials per shoe condition may have shown significant differences between all levels of midsole density. The pressure differences found particularly in the rear area of the heel are likely related to the area of the sole in contact with the ground being initially small. At that time the stiffness of the sole appeared to have a greater effect than later when the heel is flat on the ground. The in-shoe pressure measurements were found to be sensitive to midsole density and they indicated that shoe hardness influences the loading of specific areas of the foot.

REFERENCES

Bates, B. et al. J. Biomech., 16, 181-192, 1983.
Clarke, T. et al. Biomech. aspects of sports shoes & surfaces, (pp. 25-34), Univ. Calgary. Press, 1983.
Gross, T. & Bunch, R. J. Biomech., 22(6), 699-703, 1989.
Hennig, E. & Milani, T. Proceedings of First World Congress on Sport Science, Colorado Springs (pp. 183-184), 1989.
Lake, M. & Lafortune, M. Proceedings of ISB meeting, Perth, (pp. 370-372), 1991.
Nigg, B. et al. J. Biomech., 21, 951-959, 1987.
Snel et al. Biomechanics IX-A, (pp. 133-138), Human Kinetics, 1985.

FOOT PLACEMENT DURING A GAIT PERTURBATION.

Mark S. Redfern, Timothy Schumann, and James DiPasquale
Human Movement Analysis Laboratory, University of Pittsburgh

INTRODUCTION

This study investigates the role of foot placement in balance during gait after perturbations. Foot trajectories and placements were measured before and after perturbations. The data were then analyzed to determine if foot placement can be predicted from the position of the stance foot with respect to the pelvis as proposed by Redfern and Schumann (1992, 1993) for non-perturbed gait..

REVIEW AND THEORY

Foot trajectories have been studied in terms of toe clearances and heel velocities (Redfern, et al., 1993; Strandberg and Lanshammer, 1981) and energy expenditure (Holt, et al., 1991). The control of foot placement is not well understood even though placement is critical to balance during gait. Winter (1992) found that both toe clearance and joint angles during swing phase had very low variability, indicating that foot trajectory and placement is a precisely controlled task. Further, this control is multi-segmental probably including muscles in both the swing and stance leg. Redfern and Schumann (1992, 1993) proposed a model for foot placement during walking which stated that the objective is to minimize the sum of the right and left leg angles at heel contact in order to maintain balance. This control strategy has the property of maintaining a stable base of support at heel contact with the center of mass of the body being approximately at the mid-point between the two feet in double support phase. They also demonstrated this model for normal gait at varying speeds.

The full three dimensional foot placement model is described in Redfern and Schumann (1992, 1993). A two-dimensional version investigating frontal plane leg trajectories is used in this study. Foot trajectories are described in relation to the pelvis. Hip abduction angle and the distance from the trochantor to the foot are measured. This is performed on both legs throughout the gait cycle.

EXPERIMENTAL METHODS

Four normal subjects participated in the study. All subjects presented with negative histories for neurologic, orthopedic, and vestibular disease. Small spherical reflective markers were placed on the subjects' legs bilaterally at lateral malleoli, lateral femoral epicondyles, and greater trochantors. Pelvic markers were placed at right and left anterior superior iliac spines (ASIS), and midway between the posterior superior iliac spines (PSIS).

Four high shutter speed video cameras were used to acquire motion data at 60 Hz while subjects walked at a self selected speed. Five steps of gait data were collected for each trial. All trials were collected without vision (eyes closed). Four perturbation conditions were presented: push from right during left swing, push from left during left swing, push from right during right swing, and push from left during left swing. A control of no push was also run. Three repetitions per each condition were performed for a total of 15 trials. The push was given to the lateral pelvis just inferior to the iliac crest in the frontal plane using a padded rod. The subject did not know when or where the push was being applied during the trials.

The video data was analyzed with a Peak Performance motion analysis system using a discrete linear transformation matrix to calculate three dimensional coordinates, as well as custom software. The accuracy of the measurement system for the recording window was approximately 3mm for linear displacements.

The evaluation of foot placement during these trials was performed by computing the hip abduction angles with respect to the pelvis (Θ) and the length (R) for each leg over the full trial for all subjects. Θ was calculated such that right leg abductions were positive in Θ and left leg abductions were negative in Θ. Only Θ was analyzed in this study.

RESULTS

Changes in body position in response to the perturbation were approximately 0.5 m laterally. Figure 1 shows the changes in body position due to the perturbation during right swing phase. Three separate trials are plotted to show the differences in response. Pushes from the side contra-lateral to the swing leg caused slightly more rapid lateral movements of the body. The path of the body then realigned to the original direction by the second step after perturbation. The ipsi-lateral push, however, showed a more gradual lateral change in position which did not realign to a direction parallel to the original path until after the second step, if at all.

Figure 2 shows a representative plot for one gait trial along with the timing of the perturbation. The trial shown is a perturbation to the left side during right swing. Also included in the graph is the sum of the right and left angles over time. An X denotes the time when the perturbation began. The total time of the push was approximately .5 s. Note that the curve representing the sum of the right and left leg angles was approximately zero at heel contact before and after perturbation. Changes in the trajectory of the swing leg in response to the perturbation occurred. This can be seen by comparing the pre- to post-perturbation data in the figure. Also worth noting is that the first derivative of the sum curve also appears to go to zero just prior to heel contact after the perturbation.

Values of the Θ sum curves at heel contact were calculated for all subjects, both before and after the perturbations. The mean sum angles at heel contact before the perturbation across subjects was 0.8(0.6) degrees. Thus, the pre-perturbation data are consistence with the stability hypothesis. Post-perturbation steps were found to have different responses, depending upon the condition. Perturbation contra-lateral to the swing leg created a sum angle near zero (1.5 (3.1) degrees), indicating symmetry w.r.t. the pelvis in the frontal plane. Perturbations ipsi-lateral to the swing leg created a sum angle of 5.1 (3.0). This asymmetry in leg angles at heel contact was due to adduction of the swing leg further than the stance leg. Thus, the swing foot was placed beyond frontal plane symmetry. The second step during these trials did return to frontal plane symmetry at heel contact.

Variability in the angles at heel contact was due not only to spatial differences in foot placement, but also to slight temporal variations. The minimum of the sum curve sometimes occurred slightly before or after heel contact. A small change in the temporal relationship caused variations in the spatial sum values at heel contact.

DISCUSSION AND CONCLUSIONS

In the present study, swing trajectory compensations in response to frontal plane perturbations were found. Contra-lateral perturbations (stance side) produced zero sum angle responses in the following steps. Ipsi-lateral perturbations (swing side), however, had non-zero sums on the first step after perturbation. The swing foot travelled beyond the symmetry point at heel contact. The sum angles on the second step post-perturbation, however, were zero.

Foot placement control is necessary to maintain stability from step to step by establishing a new base of support. This study supports the concept that foot placement is determined by the position of the stance leg with respect to the pelvis. Thus, the establishment of the new base of support is based upon the spatial relationship between the stance foot and the pelvis.

REFERENCES

Holt, et al., Med. Sci. Sports Exerc. 23:491-498, 1991..

Redfern and Schumann, Proc. ASB, 1992.

Redfern and Schumann, J Biomechanics, (In Press).

Redfern, et al. Ergonomics (In Press).

Strandberg and Lanshammer J. Occup. Accidents 4:153-162, 1981

Winter, DA Physical Therapy 72(1), 45-53, 1992.

ACKNOWLEDGEMENTS

This research was supported by a grant from the Whitaker Foundation and the NIA, Grant # AG00463.

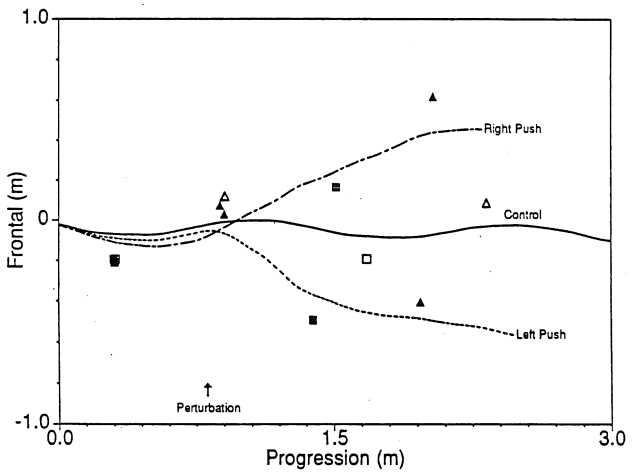

Figure 1: Changes in the path of the body in response to perturbations to the right and left side. The pushes occurred just after toe off of the right foot. A control trial without a perturbation is also shown. Squares and triangles represent right and left heel contact, respectively.

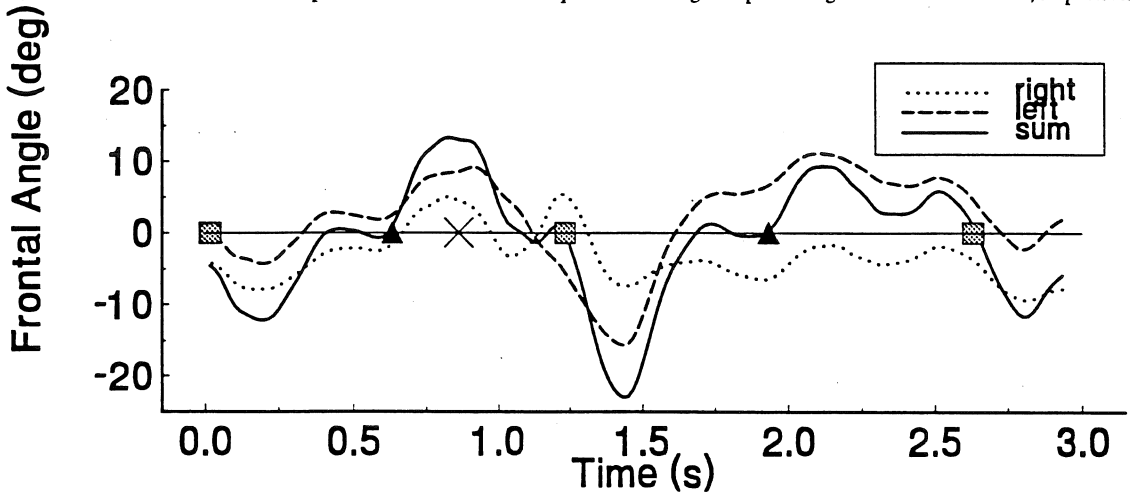

Figure 2: Representative abduction angles (Θ) from one gait trial with a perturbation from the right during left swing phase. The squares and triangles represent right and left heel contact time, respectively. The timing of the push is indicated by the X on the axis.

RELATION OF JOINT MECHANICAL WORK TO CHANGES IN WALKING CADENCE AND STRIDE LENGTH

Scott C. White, Ph.D.
Department of Physical Therapy & Exercise Science
State University of New York at Buffalo, Buffalo, NY 14214

INTRODUCTION

The role of lower limb muscles in propelling the body during walking is contentious. The purpose of the present study was to examine changes in the work done by different muscle groups while walking at variable speeds with the two determinants of walking speed, cadence and stride length, systematically varied. Significant changes in the work profile of some muscle groups depended upon whether speed varied as a function of cadence or stride length. The present study elucidates the predominant role of different muscle groups in locomotion.

REVIEW AND THEORY

Different locomotor roles have been ascribed to various lower limb muscle groups by different investigators. For example, Sutherland et al. (1980) contend that the ankle plantarflexors (Pflex) work primarily to restrain forward motion of the body during stance. Winter (1991) claims that this muscle group is the main source of energy propelling the body. Acceleration of the swing limb has been attributed to energy generation by the ankle Pflex (Robertson, et al., 1980); yet amputees accomplish swing limb mechanics without the benefit of ankle musculature. The present investigation examines changes in the work done by lower limb muscles during variable speed walking. The experimental design involved changing either cadence or stride length independent of each other in order to delineate the role of different muscle groups in effecting a cadence or stride length change.

PROCEDURES

Nine variable walking speeds were documented for six subjects walking at three different cadences (97, 117, 134 steps/min) at each of three stride lengths (1.25, 1.43, 1.60 meters). Cadence was matched to an audio metronome and stride length was controlled using floor markings. Subjects were videotaped and foot-ground reaction forces were monitored with force plates (Kistler Instrument Corp.). A sagittal plane rigid body, linked segment analysis was used to determine joint power profiles for calculating the lower limb joint mechanical work values commonly used to characterize gait (Winter, 1991). Segment anthropometrics and spatial orientation were defined from the cartesian coordinates of anatomical markers determined by digitizing the video records (Peak Performance Technologies). The coordinates were filtered and synchronized with ground reaction force records for calculation of mechanical work values (Winter, 1990). Work values were normalized to subject mass. A one-way repeated measures ANOVA with Post-hoc was used to test for significant effects ($p<.05$) between: the slowest, normal and fastest speeds; the different stride lengths; and, the different cadences.

RESULTS AND DISCUSSION

Significant speed effects were present for nearly all lower limb work values when evaluated across the three speeds. Stance phase energy absorption at the ankle for the slowest walking speed (1.01 m/s) was significantly greater than the normal (1.39 m/s) and fastest (1.87 m/s) speeds but there was no significant difference between the normal and fastest speeds. The results underscore the importance of the ankle Pflex in restraining forward motion but the insignificant results when comparing the normal and faster walking speeds bring into question the contention that this is their major role in locomotion (Sutherland et al., 1980).

Independent changes to stride length and cadence had varying effects on different muscle groups. Positive work by the ankle Pflex during push-off, was the only measure that was significantly different across the three different cadences when the subject maintained a normal (1.43 m) stride length (Fig. 1). The results support the assertion that the ankle Pflex muscle group has a major role in propulsion (Winter, 1991) since they are the primary contributors to extending the stride.

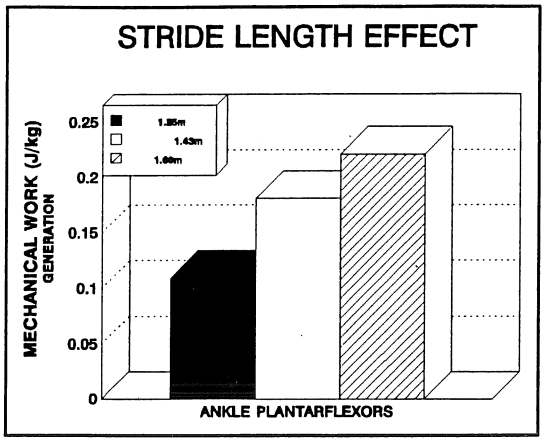

Fig. 1: Effect of changing stride length on ankle plantarflexor work at 117 steps/min cadence.

The relative importance of Pflex energy generation that has been attached to acceleration of the swing limb (Robertson et al., 1980) is contentious. Acceleration and deceleration of the swing limb reduces swing time thereby increasing cadence. The present results show that cadence changes are primarily achieved through energy generation and absorption at the hip and knee (Fig. 2). Significant increases in work values with increased cadence were noted during three phases of the gait cycle: generation by the hip extensors at the end of swing and the first half of stance, generation by hip flexors as they accelerate the limb through toe-off; and, absorption by the hamstrings in the last half of swing as they slow forward rotation of the lower leg in preparation for stance. Each of these muscle groups has the primary role of changing the energy level of the free limb during swing and not the ankle Pflex.

Different muscle groups appear to have different roles in gait. Mechanical work generated at different joints depends upon whether variable speed walking is accomplished with a cadence or a stride length change. Adjustments to metabolic cost in gait is probably accomplished through optimal combinations of muscle work demands via cadence and stride length changes.

REFERENCES

Robertson, D. et al. *J. Biomech.* 13, 845-854, 1980.
Sutherland, D. et al. *J. Bone Joint Surg.* [Am] 62,354-363, 1980.
Winter, D. *Biomechanics and Motor Control of Human Movement*, Wiley, 1990.
Winter, D. *Biomechanics and Motor Control of Human Gait*, U. Waterloo Press, 1991.

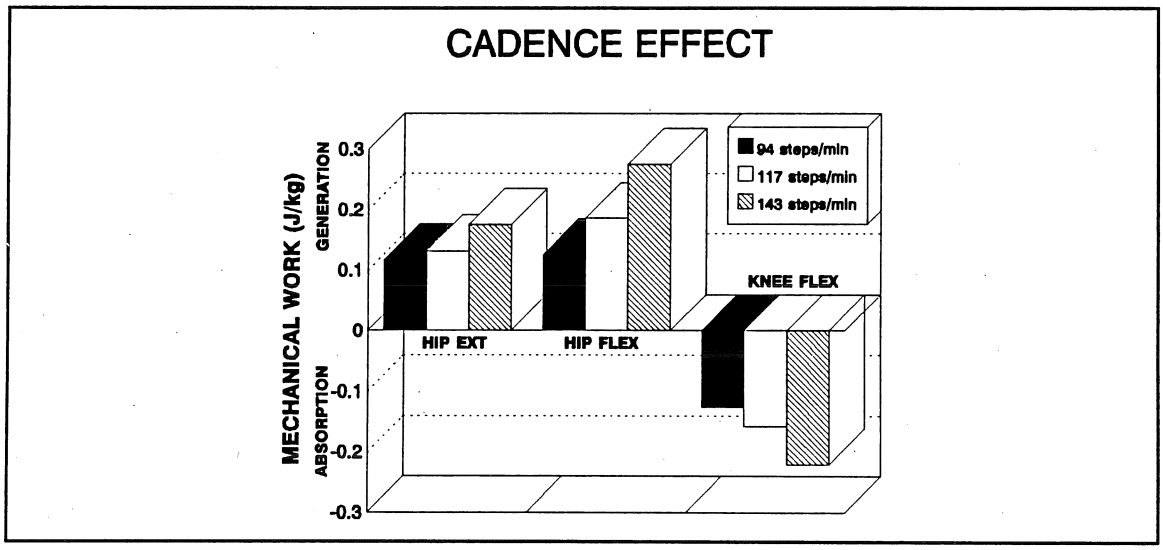

Fig. 2: Effect of changing cadence on hip and knee work values for a stride length of 1.43 m.

EFFECT OF STRENGTH IMPROVEMENT ON POSTURAL CONTROL AND PREFERRED WALKING SPEED OF ELDERLY AND YOUNG ADULTS

P.E. Martin, A. P. Marsh, D. Burton and D.D. Larish

Exercise and Sport Research Institute
Arizona State University, Tempe AZ 85287-0404.

INTRODUCTION

Impaired gait and postural stability have frequently been observed in elderly adults. In order to assess the importance of lower extremity muscular strength on postural stability and preferred walking speeds of elderly and young adults, subjects performed one leg balance and forward leaning tasks on a force platform and normal and fast walking before and after a 16-week strength training program. Muscular strength, postural stability, and preferred walking speed were generally higher for the young subjects compared to the older group prior to training. Strength improved significantly in all muscle groups except the dorsiflexors for both old and young adults as a result of the 16-week program. Strength improvements were accompanied by modest improvements in many of the postural stability descriptors for both old and young adults but the majority of changes were not statistically significant. Preferred normal and fast walking speeds failed to increase significantly following strength increases. These results suggest that the lower levels of muscular strength of the older adults was not a limiting factor for the tasks under investigation. It is speculated that this is related in part to the general well being of the subjects. Future research might include examination of a more impaired group of elderly subjects and a wider range of tasks to gain further insight to the functional benefits of strength improvement through resistive training.

REVIEW AND THEORY

Impaired gait and postural stability have frequently been associated with advancing chronological age (Hadley *et al.*, 1985; Himann *et al.*, 1988; Sabin, 1982; Woollacott *et al.*, 1988). It is also apparent that muscle mass and strength decline with age after approximately 30 yrs of age (Aniansson *et al.*,1978; Larsson *et al.*, 1979; Murray *et al.*, 1985). It is not clear whether declines in strength play an important role in the development of gait and postural stability impairments. Whipple *et al.* (1987) reported that individuals who had a history of falls were significantly weaker than non-fallers. Impairments in overall ankle strength, particularly the dorsi-flexors, were especially apparent. Vandervoort and Hayes (1989) reported that maximal isometric plantar flexor torques of elderly women were 71% lower than those of young women. They suggested that the plantar-flexors of the elderly show considerable impairment in the ability to provide stabilizing torques about the ankle. With respect to walking, Winter (1983) noted that at push-off the plantar flexors produce over 80% of the mechanical power generated during the gait cycle.

While elderly adults respond favorably to strength training (e.g., Frontera *et al.* 1988), there is a lack of information on the effects of a strength training program on postural stability and walking mechanics. The purposes of this study were to examine the effect of strength improvement on postural stability and self-selected walking speeds of the elderly and to compare the response to training of old and young adults.

PROCEDURES

Seventeen elderly subjects (7 male, 10 female; $\overline{X}_{age}$ = 72.5±4.3 yrs, $\overline{X}_{height}$ = 165.8±10.5 cm, $\overline{X}_{mass}$ = 70.9±10.1 kg) and 6 young (3 male, 3 female; $\overline{X}_{age}$ = 27.4± 3.2 yrs, $\overline{X}_{height}$ = 173.6±10.8 cm, $\overline{X}_{mass}$ = 67.4±9.0 kg) who had no major orthopedic, neurological or cardiovascular disorders served as subjects. Every effort was made to recruit generally healthy individuals in order to minimize confounding effects due to disease. None of the subjects had participated in a strength training program within the previous two years and no subjects had extensive strength training experience prior to this study.

All subjects completed a 16-week progressive resistance strength training program that included exercises for 12 major muscle groups of the body using Hydrafitness equipment (Hydra-Gym Fitness Inc., Belton, TX), with the exception of training about the ankle. Plantar flexor training was performed on a calf raise machine while dorsiflexor training utilized a Footdeck system (Life Plus Inc., Ann Arbor, MI).

Pre- and post-training assessments of lower extremity strength, postural stability, and walking speed were identical. Peak isokinetic (60 deg s^{-1}) torque (normalized to body mass) were determined for the ankle dorsi- and plantar flexors (DFLEX, PFLEX, respectively), knee flexors and extensors (KFLEX, KEXT), and hip flexors and extensors (HFLEX, HEXT). Postural stability was assessed using descriptors of center of pressure (CP) migration, quantified from force platform recordings (sampling frequency=100 Hz, 10 s duration, digitally filtered at 3 Hz) during a) a forward leaning task and b) balancing on one leg (5 trials for each). For the first task, subjects leaned forward from a relaxed standing position as rapidly and as far as possible by dorsiflexing at the ankle and then maintained that position. Dependent variables included the anterior shift of the CP (CPSHIFT) normalized to foot length, average and peak CP velocity during the forward shift (AVCPVEL, PKCPVEL, respectively), and the total CP migration per second (TOTCP) and anterior-posterior variability in CP position (APSD) while the forward leaning position was maintained. For the one leg balance test, dependent variables included TOTCP and the variability about the mean CP position in anterior-posterior (APSD) and mediolateral (MLSD) directions.

Averages of four trials of self-selected normal and fast walking speeds (NRMWLK and FSTWLK) were quantified over 20 m along a 30 m walkway. Results were statistically analyzed using a 2 factor (age x pre/post) repeated measures design.

RESULTS

Muscular strength was generally higher for the young subjects compared to the older group prior to training (Table 1). Strength improved considerably for both old and young adults with the exception of DFLEX. PFLEX torque increased

	Old		Young	
	Pre	Post	Pre	Post
PFLEX* ** ($N \cdot m \cdot kg^{-1}$)	0.71 (0.23)	0.92 (0.17)	1.29 (0.24)	1.61 (0.41)
DFLEX* ($N \cdot m \cdot kg^{-1}$)	0.13 (0.05)	0.12 (0.06)	0.24 (0.08)	0.25 (0.08)
KFLEX* ($N \cdot m \cdot kg^{-1}$)	0.89 (0.23)	0.93 (0.23)	1.44 (0.41)	1.50 (0.37)
KEXT* ** ($N \cdot m \cdot kg^{-1}$)	1.56 (0.42)	1.75 (0.40)	2.89 (0.54)	3.13 (0.54)
HFLEX* ** ($N \cdot m \cdot kg^{-1}$)	0.79 (0.28)	0.86 (0.24)	1.40 (0.37)	1.50 (0.52)
HEXT* ** ($N \cdot m \cdot kg^{-1}$)	2.27 (0.59)	2.55 (0.58)	3.20 (0.60)	3.61 (1.10)
NRMWLK ($m \cdot s^{-1}$)	1.36 (0.10)	1.38 (0.13)	1.47 (0.30)	1.36 (0.26)
FSTWLK ($m \cdot s^{-1}$)	1.84 (0.27)	1.86 (0.26)	2.01 (0.36)	1.93 (0.36)

Table 1: Peak isokinetic joint torques for ankle, knee and hip flexors and extensors, and preferred normal and fast walking speeds. (* Significant age effect, ** significant training effect).

	Old		Young	
	Pre	Post	Pre	Post
TOTCP* ($mm \cdot s^{-1}$)	9.54 (2.71)	9.27 (2.13)	8.18 (3.33)	6.26 (1.91)
MLSD* (cm)	0.86 (0.26)	0.80 (0.18)	0.54 (0.11)	0.55 (0.10)
APSD* (cm)	0.98 (0.37)	0.86 (0.19)	0.61 (0.14)	0.62 (0.09)

Table 2: Center of pressure migrations descriptors for the one leg balance task (*significant age effect).

	Old		Young	
	Pre	Post	Pre	Post
TOTCP ($mm \cdot s^{-1}$)	7.71 (2.84)	6.87 (1.53)	7.47 (2.98)	5.43 (1.99)
APSD* (cm)	0.89 (0.19)	0.78 (0.17)	0.68 (0.15)	0.59 (0.08)
CPSHIFT* (% ft length)	27.48 (4.75)	27.50 (5.22)	37.75 (7.94)	39.97 (5.50)
AVCPVEL** ($cm \cdot s^{-1}$)	6.45 (1.82)	5.59 (1.87)	3.97 (1.25)	8.32 (1.34)
PKAPVEL ($cm \cdot s^{-1}$)	25.13 (6.84)	21.70 (5.87)	20.83 (4.12)	29.07 (10.55)

Table 3. Center of pressure migrations descriptors for the forward leaning task (*significant age effect, **significant training effect).

approximately 30% in the old and 25% in the young as a result of training. Improvements in the remaining muscle groups other than DFLEX were approximately 10%. Neither the preferred normal nor fast walking speeds improved significantly in either group due to training. Young adults actually reflected a decline in these measures (Table 1). In general, young subjects displayed better postural stability than the older subjects during both one leg balance and forward leaning tasks (Tables 2 and 3). Strength improvements were accompanied by modest changes in many of the postural stability descriptors in the expected direction but the majority of changes were not statistically significant.

DISCUSSION

We had anticipated that both old and young adults would respond positively to strength training. This was confirmed by the isokinetic strength assessments and was consistent with previous research (Aniansson *et al.*, 1978; Larsson *et al.*, 1979; Murray *et al.*, 1985). Only the dorsiflexor muscle group failed to respond to training. Strength of the young adults was higher than that of the older adults prior to training but the two age groups showed similar improvements over the 16-week program.

Also confirmed was our expectation that young adults would reflect less CP migration than older adults during the forward lean and one leg balance tasks, suggesting better postural stability in the young. This was consistent with the higher levels of strength possessed by the young adults but does not provide convincing evidence that strength is an important determinant of the stability differences between the old and young adults. More convincing would be improvements in stability following improvements in muscular strength due to training. We had anticipated that strength improvements would result in decreases in CP migration (TOTCP, APSD, MLSD) while posture was being maintained in both the forward leaning and one leg balance tasks and increases in the amount and velocity of the forward CP shift (CPSHIFT, AVCPVEL, PKCPVEL) during the leaning task. Changes in CP migration characteristics for both age groups were generally in the expected direction for most dependent variables, but few of these changes were statistically significant.

Preferred normal and fast walking speeds of the young adults were higher than those of the older adults which was consistent with previous observations (Himann *et al.*, 1988; Martin *et al.*, 1992). Walking speed, however, did not increase in either age group with strength improvements. The absence of speed increases and the modest improvements in postural stability, particularly for the elderly adults, suggests that muscular strength was not a critical determinant of performance for the tasks under investigation. It is speculated that this is related in part to the general well being of the subjects. Future research might include examination of a more impaired group of subjects and a wider range of tasks to gain further insight to the functional benefits of strength improvement for elderly adults.

REFERENCES

Aniansson, A. *et al.*, *Scand. J. Rehabil. Med.*, 6, 43-49, 1978.
Frontera, W.R. *et al.*, *J. Appl. Physiol.*, 64, 1038-1044, 1988.
Hadley, E. *et al.*, *Clin. Geriatr. Med.*, 1, 497-500, 1985.
Himann, J.E. *et al.*, *Med. Sci. Sports Exerc.*, 20, 161-166, 1988.
Larsson, L. *et al.*, *J. Appl. Physiol.*, 46, 451-456, 1979.
Martin, P.E. *et al.*, *J. Appl. Physiol.*, 73, 200-206, 1992.
Murray, M.P. *et al.*, *J. Gerontol.*, 40, 275-280, 1985.
Sabin, T.D. *J. Am. Geriatr. Soc.*, 30, 51-58, 1982.
Vandervoort, A.A. *et al.*, *Eur. J. Appl. Physiol.*, 58, 389-394, 1989.
Whipple, R.H. *et al.*, *J. Am. Geriatr. Soc.*, 35, 13-20, 1987.
Winter, D.A. *Clin. Orthop. Rel. Res.*, 197, 147-154, 1983.
Woollacott, M. *et al.*, *Annals N.Y. Acad. Sci.*, 515, 42-53, 1988.

ACKNOWLEDGMENTS

Supported by NIH grant AG-07352

POSTURAL CONTROL AND PREFERRED WALKING SPEED OF ACTIVE AND SEDENTARY ELDERLY ADULTS: RELATIONSHIP WITH PLANTAR AND DORSI FLEXOR STRENGTH

A.P. Marsh, P.E. Martin, D. Burton and D.D. Larish

Department of Exercise Science and Physical Education
Arizona State University, Tempe AZ 85287-0404.

INTRODUCTION

In order to determine the influence of dorsi- and plantar-flexor strength on the postural stability and preferred walking speed of elderly adults, active and sedentary subjects performed forward leaning and one-leg balance tasks on a force platform and their normal and fast preferred walking speed were timed over a 20 m distance. In addition the effects of a 16 week strength training program on strength, postural stability and preferred walking speed were also examined. Plantar-flexor strength improved 40% in the active group and 21% in the sedentary group after training, however there were no improvements in dorsi-flexor strength. In general, our hypothesis that increases in plantar-flexor strength would be reflected in improved postural control and an increase in preferred walking speeds was not supported. However, the active group preferred a significantly faster normal walking speed compared to the sedentary group and had a faster average anterior-posterior center of pressure velocity during the forward leaning task. The one-leg task did not discriminate between the groups nor reflect any changes in postural control due to improvements in plantar-flexor strength. We speculate that the general well being of these subjects may have resulted in the lack of significant differences between the groups. Future studies might use a wider variety of tasks and examine a more impaired group of individuals.

REVIEW AND THEORY

There is general agreement among researchers that postural stability in the elderly is a significant problem. It has been estimated that a third to a half of the population aged ≥ 65 years fall each year (Horak *et al.* 1989). Further, it has been projected that by 2020 there will be 52 million US residents ≥ 65 years, up from 28 million in 1987 (Schultz, 1992). Within this special population there are several frequently reported trends associated with advancing age which may impact the likelihood of falls. Himann *et al.* (1988) reported a decline in the preferred walking speed in the elderly, while numerous researchers have shown a decline in postural stability with aging (e.g., Straube *et al.* 1988; Woollacott *et al.* 1988). Aniansson *et al.* (1978), Larsson *et al.* (1979) and Murray *et al.* (1980, 1985) have also shown a decline in isometric and isokinetic strength of the lower extremities of the elderly. Whipple *et al.* (1987) attempted to classify individuals into faller/non-faller groups. They stated that fallers were significantly weaker than non-fallers with severe impairments in overall ankle strength, in particular the dorsi-flexors. These authors suggested that the lack of strength in the dorsi-flexors may be an important factor in backwards falls. Vandervoort and Hayes (1989) have also suggested that the plantar-flexors of the elderly showed considerable impairment in the ability to generate stabilizing torques about the ankle. Related to these observations, Winter (1983) suggested that at push-off during walking the plantar-flexors produce over 80% of the mechanical power generated during the gait cycle.

While elderly adults appear to respond favorably to strength training (e.g., Frontera *et al.* 1988), there is a lack of information on the effects of a strength training program on postural control and preferred walking speed. Considering the suggested importance of the plantar-flexors (Vandervoort and Hayes, 1989; Winter, 1983) and dorsi-flexors (Whipple *et al.* 1987), the purposes of this study were to: a) compare the relationship between plantar- and dorsi-flexor muscle strength, postural sway and the self-selected walking speeds in active and sedentary elderly subjects and b) determine the effects of a 16-week strength training program on postural control and walking speed in these two groups.

PROCEDURES

Eight physically active (3 male, 5 female; $\overline{X}_{age}$ = 73.0±4.9 yrs, $\overline{X}_{height}$ = 166.9±13.7 cm, $\overline{X}_{mass}$ = 70.2±25.8 kg) and nine sedentary (4 male, 5 female; $\overline{X}_{age}$ = 72.0± 4.9 yrs, $\overline{X}_{height}$ = 164.90±7.3 cm, $\overline{X}_{mass}$ = 71.6±9.2 kg) adults who had passed a medical screening and who had no major orthopedic, neurological or cardiovascular disorders served as subjects. None of the subjects had participated in a strength training program within the previous two years.

Prior to strength training, assessments of strength, postural control and walking speed were conducted. Plantar-flexor (PFLEX) and dorsi-flexor (DFLEX) strength were quantified as the peak torque (normalized to body mass) produced during three maximal voluntary isokinetic (60 deg s^{-1}) trials. Movement of the center of pressure (CP) was assessed using an AMTI force platform (sampling frequency=100 Hz, 10 s duration) during a forward leaning task and a one-leg balance task. During the forward leaning task subjects, on a command, leaned forward from a relaxed standing position (hands placed on the hips) as rapidly and as far as possible by dorsi-flexing at the ankle and then maintained that position for 8-9 s. Force platform data were digitally filtered at 3 Hz and subsequently used in the computation of CP position with respect to time. For the forward leaning task the dependent variables were the total migration of the CP (TOTCP), average CP velocity (AVCPVEL) during the anterior movement, the magnitude of the anterior shift of the CP (CPSHIFT) expressed as a percentage of foot length and the anterior-posterior (AP) variability in CP position (CPAPVAR) while the forward lean was maintained. Dependent variables on the one-leg balance were TOTCP and the variability of CP movement, medio-laterally (ML) and AP (MLSD, APSD). Averages of four trials of self-selected normal and fast walking speeds (SPDNORM and SPDFAST) were quantified over 20 m along a 30 m walkway. The dependent variables were analyzed using a 2 factor (activity group x pre-/post-test score) repeated measures design. Correlations between the combined active and sedentary pre-test PFLEX and DFLEX scores and the pre-test score on the dependent variables were also calculated.

Following a 16-week progressive resistance strength training program subjects were re-tested on the same battery of tests used in the pre-testing. Although we only focus on ankle strength measures in the results the program incorporated exercises for the entire body using Hydrafitness machines (Hydra-Gym Fitness Inc., Belton, TX). However, ankle strength training was

performed on a seated calf raise machine and the Footdeck system (Life Plus Inc., Ann Arbor, MI).

RESULTS

The results are summarized in Tables 1-3. Correlations between pre-training PFLEX and DFLEX torques and the dependent variables were low. PFLEX torque increased approximately 40% in the active group and 21% in the sedentary group from the pre- to post-test however the DFLEX torque failed to show any improvement. The active group had a significantly higher average velocity of the CP during the forward leaning task, however postural stability was not affected by the increase in PFLEX strength. There were no improvements in postural control during the one leg balance task in either group nor were the groups different. There were no significant changes in the walking speeds pre- and post-training, although there was a trend for speeds to increase after training in all but the active fast condition.

	Active		Sedentary		r	
	Pre	Post	Pre	Post	PF	DF
PFLEX* ($N \cdot m \cdot kg^{-1}$)	0.65 (0.18)	0.91 (0.12)	0.77 (0.26)	0.93 (0.22)		
DFLEX ($N \cdot m \cdot kg^{-1}$)	0.14 (0.05)	0.14 (0.07)	0.13 (0.05)	0.11 (0.05)		
SPDNORM# ($m \cdot s^{-1}$)	1.41 (0.10)	1.45 (0.15)	1.31 (0.09)	1.32 (0.06)	-.11	.12
SPDFAST ($m \cdot s^{-1}$)	1.90 (0.24)	1.87 (0.24)	1.79 (0.30)	1.84 (0.29)	-.17	.18

Table 1: Peak plantar-flexor (PF) and dorsi-flexor (DF) torques and preferred normal and fast walking speeds. Values are means with standard deviations in parentheses.
* Significant training effect.
# Significant activity level effect.

	Active		Sedentary		r	
	Pre	Post	Pre	Post	PF	DF
TOTCP ($mm \cdot s^{-1}$)	7.99 (3.05)	6.81 (1.39)	7.47 (2.79)	6.93 (1.73)	.05	-.28
AVCPVEL* ($cm \cdot s^{-1}$)	7.15 (1.87)	6.64 (1.79)	5.83 (1.63)	4.66 (1.47)	-.24	.24
CPSHIFT (% ft length)	27.15 (3.85)	26.91 (5.03)	27.77 (5.65)	28.01 (5.63)	.19	.16
CPAPVAR (cm)	0.92 (0.15)	0.84 (0.19)	0.86 (0.23)	0.73 (0.13)	-.15	.14

Table 2: Dependent variables in the forward leaning task.
* Significant activity level effect.

	Active		Sedentary		r	
	Pre	Post	Pre	Post	PF	DF
TOTCP ($mm \cdot s^{-1}$)	9.86 (2.61)	9.43 (1.99)	9.26 (2.93)	9.12 (2.36)	-.05	-.31
MLSD (cm)	0.85 (0.22)	0.83 (0.21)	0.88 (0.30)	0.77 (0.15)	.06	-.20
APSD (cm)	1.07 (0.46)	0.91 (0.24)	0.90 (0.27)	0.82 (0.13)	-.42	.09

Table 3: Dependent variables in the one-leg balance task.

DISCUSSION

We had expected a positive correlation between speed of walking and PFLEX strength as well as increases in the preferred walking speed with increases in PFLEX strength. Correlations for normal and fast walking speeds were in the expected direction with respect to DFLEX but in the opposite direction with respect to PFLEX. Further, DFLEX and PFLEX strength explained little of the variation in speed. Improvements in the strength of the ankle musculature were also expected to be reflected in improvements in postural control during the balance tasks. We were unable to significantly improve the DFLEX strength in either group. Despite a significant increase in PFLEX strength there were no significant changes in postural stability during the one-leg balance task. During the forward leaning task improvements in postural control due to the training program were expected to be reflected by increases in AVCPVEL and CPSHIFT and a decrease in CPAPVAR. The data, however, did not support these hypotheses. Interestingly, the AVCPVEL was higher in the active group compared to the sedentary group. This was the only stability variable indicating that the active group may have somewhat better postural control due to a higher daily level of activity. In addition, the active group had a slightly faster preferred walking speed in the normal condition. Despite our efforts to stress the ankle musculature via the two balance tasks and the fast walking speed it appears that PFLEX and DFLEX strength were not limiting in these tasks. The lack of significant improvements in postural control and walking speed may also be related to the general well being of the subjects used in this study. Excluding people with significant motor and sensory impairments potentially resulted in two groups that were quite homogeneous and this may have been one reason why only two of the dependent variables (SPDNORM, AVCPVEL) showed significant group effects. Future work might include examination of a more impaired group of subjects and a wider range of tasks to gain further insight to the functional effects of a strength training program on dorsi- and plantar-flexor strength.

REFERENCES

Aniansson, A. *et al.*, *Scand. J. Rehabil. Med.*, 6, 43-49, 1978.
Frontera, W.R. *et al.*, *J. Appl. Physiol.*, 64, 1038-1044, 1988.
Himann, J.E. *et al.*, *Med Sci Sports Exerc.*, 20, 161-166, 1988.
Horak, F.B. *et al.*, *Neurobiology of Aging*, 10, 727-738, 1989.
Larsson, L. *et al.*, *J. Appl. Physiol.*, 46, 451-456, 1979.
Murray, M.P. *et al.*, *Phys. Ther.*, 60, 412-419, 1980.
Murray, M.P. *et al.*, *J. Gerontol.*, 40, 275-280, 1985.
Schultz, A.B., *J. Biom.*, 25, 519-528, 1992.
Straube, A. *et al.*, *Posture and gait: Development, adaptation and modulation*, (pp. 105-114), Elsevier Science Pub., 1988.
Vandervoort, A.A. *et al.*, *Eur. J. Appl. Physiol.*, 58, 389-394, 1989.
Whipple, R.H. *et al.*, *JAGS*, 35, 13-20, 1987.
Winter, D.A., Clin. *Orthop. Rel. Res.*, 197, 147-154, 1983.
Woollacott, M. *et al.*, *Annals of the New York Academy of Sciences*, 515, 42-53, 1988.

ACKNOWLEDGMENTS

Supported by NIH grant AG-07352

THE DIABETIC FOOT WITH PARTIAL AMPUTATION - A BIOMECHANICAL STUDY

Peter R. Cavanagh, Jan S. Ulbrecht, Ge Wu, Mary B. Becker, John C. Garbalosa, Ian J. Alexander[#], and James H. Campbell[*].

Center for Locomotion Studies, Penn State University, University Park, PA 16803, [#]The Crystal Clinic, Akron, OH, and [*]The Cleveland Clinic Foundation, Cleveland, OH.

INTRODUCTION

Plantar pressure measurements during barefoot walking were made on the feet of 14 diabetic patients with transmetatarsal amputations. Peak regional pressures were analyzed and compared, where possible, to the pressures on the intact contralateral side. Peak forefoot pressures were significantly higher ($p<0.05$) in the feet with partial amputations compared to the contralateral foot (n=10). Heel pressures tended to be lower on the amputated side. These findings reflect the altered forefoot mechanics and effect of equinus resulting from partial amputation. The data suggest that enhanced post-operative care including therapeutic footwear is vital to successful long term management of diabetic patients with partial foot amputation.

REVIEW AND THEORY

Diabetes Mellitus accounts for over half of the non-traumatic lower extremity amputations in the US. The majority of primary amputations are performed at the below knee level even for forefoot lesions because it is commonly believed that partial amputation of a foot will only provide a temporary respite from inevitable amputation at a higher level (Kacy et al 1982).

However, a below knee procedure carries a guarded prognosis together with a distinct decline in the quality of life for the amputee (Bild et al 1989). Although there is a growing realization that many foot problems in the diabetic patient can be successfully treated by partial amputation, very little is known about the function of the foot after partial procedures. In particular, there is concern that altered mechanics and progressive deformity will render the foot "at risk" for further ulceration.

The purpose of this study was, therefore, to examine the function of partially amputated feet during gait to determine what therapeutic intervention might be needed for successful management.

PROCEDURES

Fourteen patients average age 60.1 years (sd 15.6), duration of diabetes 21.5 years (sd 12.1), duration from first surgery 4.5 years (sd 4.6) with 15 transmetatarsal amputations (one bilateral) without Achilles tendon tenotomies were studied (figure 1). The surgical procedures were graded from 1 to 4 according to the residual length of the metatarsals (1 = MTH resection only; 4 = almost a Lisfranc amputation). Only one patient had bilateral surgery but two had evidence of previous Charcot changes contralaterally. Comparisons to a contralateral limb without surgery or Charcot fracture were, therefore, available in 10 patients.

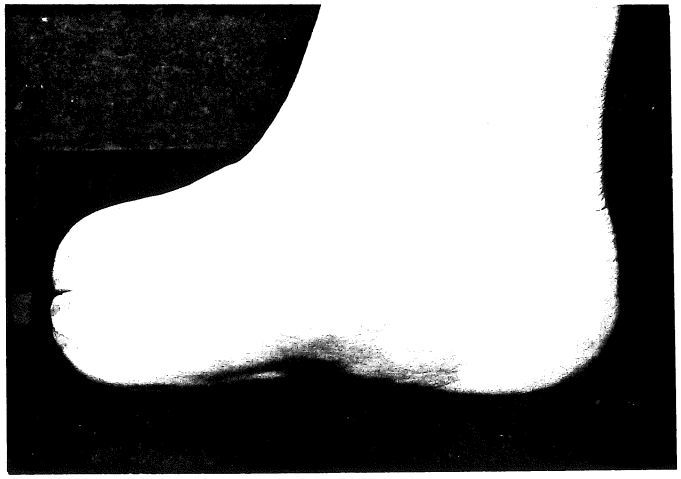

Figure 1: Patient with a transmetatarsal amputation graded as 2 based on radiographically measured length of the residual metatarsals.

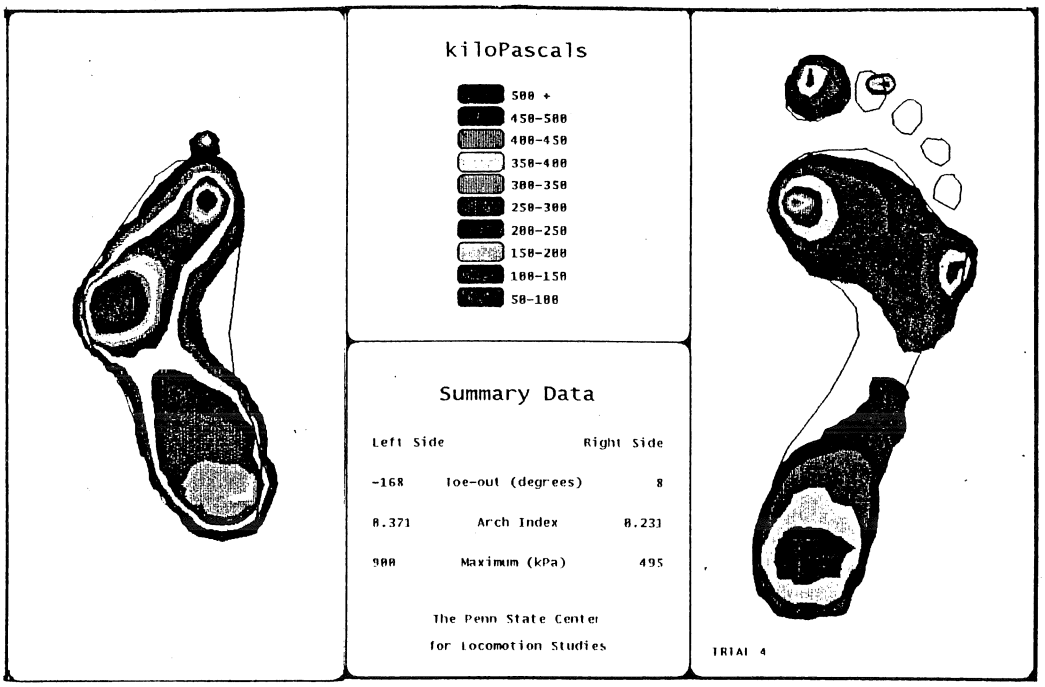

Figure 2: Peak plantar pressures under both feet of a patient in the study.

Bilateral plantar pressure distribution data were collected during first step gait using a Novel EMED Pressure platform. Mean peak pressures from the five trials were calculated in four regions of the feet - the heel and the medial, central and lateral regions of the anterior margin of the foot (the metatarsal remnants in amputated feet and metatarsal heads in contralateral feet). Three dimensional kinematic information on surface mounted target clusters was also obtained but these data are not reported here.

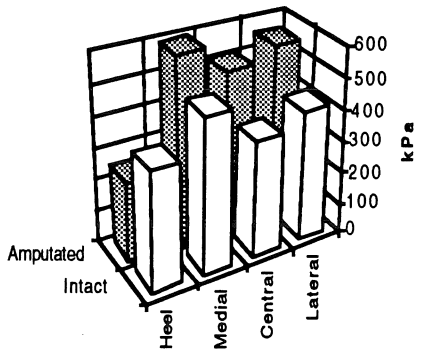

Figure 3: Peak regional pressures in kPa under the amputated and intact feet.

RESULTS

Four feet were classified as grade 2, six as grade 3 and five as grade 4. An example of a peak pressure distribution from both feet of one of the patients in the study is shown in figure 2. Mean peak pressure in the feet with partial amputation was 705 kPa (sd 233 kPa) while in the contralateral feet it was 28% lower at 551 kPa (sd 202 kPa) (Sig p=0.05). The trends in the mean regional pressures (Figure 3) indicated that heel pressures were less while forefoot pressures tended to be greater in the group with amputations (NS p>0.05).

DISCUSSION

The trend towards reduced heel loading suggests that tenotomy could have been beneficial for these feet while the significantly elevated pressure under the metatarsal remnants highlights the need for enhanced foot care and special footwear in the long term management of feet with partial amputation. It is likely that transmetatarsal amputation can be a successful procedure in the long term only if such care is provided.

ACKNOWLEDGMENT

This research was supported by a grant from the Veterans Administration.

REFERENCES

Kacy SS, Wolma FJ, and Flye MW (1982) Factors affecting the results of below knee amputation in patients with and without diabetes. Surgery, Gynecology, & Obstetrics.155: 513-518.

Bild DE, Selby JV, Sinnock P, Browner WS, Braveman P, Showstack JA (1989) Lower-extremity amputation in people with diabetes - epidemiology and prevention. Diabetes Care. 12(1): 24-31.

A FINITE ELEMENT ANALYSIS OF THE RADIOCARPAL JOINT

D. Anderson

Biomechanics Research Laboratory, Allegheny-Singer Research Institute, Pittsburgh, PA 15212

INTRODUCTION

It is clear from a survey of current literature that the relationship between malreduced intra-articular fracture of the distal radius and the subsequent onset of radiocarpal osteoarthrosis (OA) is clinically important, yet poorly understood. Nonlinear contact finite element analysis of the juxtarticular region is a feasible computational option well-suited for investigation of local tissue stresses in the radiocarpal joint. It provides a useful tool for investigating the mechanical implications of imprecise reduction of intra-articular fracture of the distal radius. The broad objective of this research is the development of a well-verified computational model of the radiocarpal joint, which, in concert with experimental models previously developed, will be capable of providing guidance toward rigorously grounded improvements in distal radius intra-articular fracture management techniques. A plane strain finite element model of the radiocarpal joint has been developed and verified through comparison with previously developed experimental and analytical models of the joint.

REVIEW AND THEORY

Intra-articular fractures of the distal radius are a significant clinical problem. In a large number of such fractures, the normally smooth articular surface is greatly disrupted. It is a clinical impression that if the articular surface is not closely restored to its normal congruence there is an increased likelihood that the joint may develop post-traumatic OA. Several authors have suggested in clinical studies that radiographically-evident "step-offs" following fracture are highly correlated with the onset of early OA (Knirk and Jupiter (1986), Bradway et al. (1989), Fernandez and Geissler (1991)). While clinical study may help to identify broad relationships between fracture management and clinical outcome, it provides little information regarding relations between the details of fracture management, the resulting alterations in joint loading, and the eventual clinical outcome. In order to begin to understand these relationships, more information must be obtained regarding the nature of stress distributions in the vicinity of the articular surfaces. Laboratory research into the biomechanics of these intra-articular fractures offers an alternative means of investigating the mechanical implications of residual incongruity.

A considerable amount of experimental work has been presented using Fuji Pressensor® to characterize contact stress distributions in the radiocarpal joint (Viegas et al.(1987),Viegas et al.(1990), and Short et al.(1987)). In recently completed experiments, we have measured contact stress distributions in a cadaver model of malreduced intra-articular distal radius fractures (Baratz et al. (1993)). While useful in terms of establishing the details of surface loading, these data provide only limited insight into potential initiating factors in the degenerative sequence of events, since they yield little direct information regarding the full juxtarticular stress distribution. The mechanisms of deterioration associated clinically with post-traumatic OA seem to point toward initial tissue failure beneath the articular surface (Radin et al. (1985)). Experimentally, work by Donohue et al. (1983) and Vener et al. (1991) has suggested that failure begins in the zone of calcified cartilage/ subchondral bone and subsequently involves the deeper subchondral bone and overlying cartilage. Hence, the details of stress distributions in regions beneath the surface are especially of interest.

Analytical modeling of the distal radius is an avenue of investigation which can provide useful information about the reliance of radiocarpal load transfer upon a number of physical parameters. Horii et al.(1990) presented an alternative contact formulation to model force transmission through the wrist. Their generalized method used discrete spring elements to solve the articular joint pressure distribution problem. The inherent simplicity of their analytical approach made feasible the computation of contact stress distributions in the radiocarpal joint. While useful for estimating the stress distribution at the articular surface, their method yields no information regarding stresses throughout the remainder of the tissues.

Once established and validated, a finite element model would represent a source of detailed information regarding both the nature of radiocarpal stress transmission and the relationship between system parameters and the associated distributions of stress. Thus, it would provide a vehicle for estimating the mechanical implications of alterations in joint geometry or associated changes in the material properties of the biological tissues. Huber-Betzer et al. (1990) developed a generic two-dimensional, finite element contact model of the tibio-femoral joint to investigate local stress aberrations near imprecisely reduced intra-articular fractures. They found that increasing step-off was associated with the development of local stress states markedly at variance with those in the intact joint.

We have developed a finite element contact model to study static juxtarticular stress distributions specifically in the radiocarpal joint. The model includes the distal radius and two primary load-bearing carpal bones (the lunate and the scaphoid), as well as the articulations and ligamentous connections between these bones.

PROCEDURES

The distal radius, lunate, and carpal bones of a scaled anatomical drawing were digitized and zoned to create a 1270 degree-of-freedom plane strain finite element contact model of the radiocarpal joint. The mesh consisted of 536 isotropic continuum elements, 8 nonlinear spring elements, and 27 sliding surface contact elements. Six distinct linearly elastic material regions were included in the model. Their material properties were based on those reported in the literature. (Material regions modeled were articular cartilage (E=10MPa), subchondral bone (2.8GPa), cortical bone (13.8GPa), and three regions of differing density cancellous bone (1.4GPa, 690MPa, and 345MPa); the Poisson's ratio was 0.45 for cartilage, and 0.3 for all other materials.) This simplified treatment of material properties (esp. of those for articular cartilage) was chosen to provide a first level approximation of their behavior while allowing for a tractable solution of the three-body contact problem.

Nonlinear spring elements were used to model ligamentous attachments between the three bodies (palmar radio-scaphoid, palmar radio-lunate, and combined palmar/dorsal scapho-lunate ligaments), and were designated so that they were only capable of providing tensile forces. The stiffness values for these spring elements were based on those reported by Horii et al. The surface contact elements were arrayed across three distinct surfaces, between the radius, lunate, and scaphoid. Frictionless interfaces were assumed for all articular surfaces.

Simplified boundary conditions based on values reported by Horii et al. were used to constrain the separate bones in a static analysis. The distal radius was fixed against both displacement along its long axis and rotation proximally, while quasi-physiologic distributed loadings were applied to the distal surfaces of the lunate and scaphoid. The total applied load was equivalent to 100N. The ulna was modeled as a boundary condition on the lunate, fixed against proximal-distal translation, while allowing radio-ulnar translation. The scaphoid was further constrained distally against radio-ulnar translation, while still allowing rotation of the body, so as to simulate the constraint represented physiologically by the scapho-triquetral ligament.

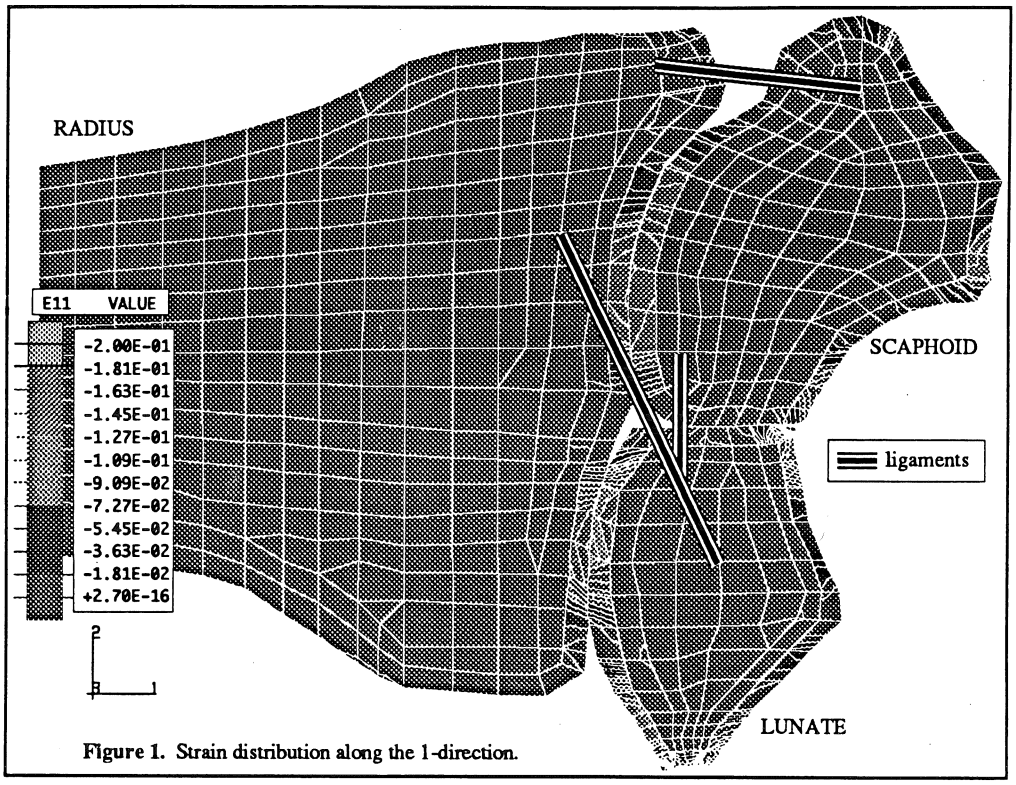

Figure 1. Strain distribution along the 1-direction.

Preliminary validation of the model has involved comparing the contact stress distributions obtained with the finite element model to those reported by Horii et al. and Baratz et al. The loads calculated in each of the ligaments has also been compared to those computed by Horii et al.

RESULTS AND DISCUSSION

In general, the stress distributions obtained with the finite element model were consistent with results previously published for other articular joints. Strains in the centrally loaded articular cartilage were on the order of 15 to 20% (see Figure 1). The contact stress distributions computed in the finite element model between the radius and the ulna were in general agreement with those previously reported. (see Table 1 below).

Table 1. Comparison to previously reported work.

	Present	Horii et al.	Baratz et al.
Max Stress (MPa)			
Radio-scaphoid	4.7	7.0	4.8
Radio-lunate	5.9	6.0	4.8
Scapho-lunate	2.4	2.0	*
Mean Stress (MPa)			
Radio-scaphoid	3.0	*	1.6
Radio-lunate	3.5	*	1.6
Scapho-lunate	1.8	*	*
Ligament force (N)			
Radio-lunate	8.5	16	*
Scapho-triquetral	5.8	14	*

* indicates data is not available

In assessing discrepancies between the work of Horii et al. and the present results, one must keep in mind that different load magnitudes were applied in the two models. The total load across the radiocarpal joint in Horii et al's work was approximately 1.5 times as large as those applied in the current model. This difference was not present between Baratz et al's experimental model and the current FEM model.

A finite element model of the radiocarpal joint has been developed and validated through comparison with existing analytical and experimental models. Continuing work with the finite element model must focus on including a more accurate representation of the ulna, as well as on pursuing more complete agreement with the experimental model. The model holds promise for providing new insight into the relationships between juxtarticular load transmission and altered surface geometry in malreduced intra-articular fracture of the distal radius.

REFERENCES

Viegas, S. et al. J Hand Surg, 12A(6), 971-8, 1987.
Viegas, S. et al. J Hand Surg, 15A, 268-78, 1990.
Radin, E. et al. Osteoarthritis, Current Clinical and Fundamental Problems, (pp. 90-99), CIBA-Geigy, 1985.
Huber-Betzer, H. et al. J Biomechanics, 23(8), 811-22, 1990.
Knirk, J. and Jupiter, J. J Bone Joint Surg (Am), 68, 647-59, 1986.
Bradway, J. et al. J Bone Joint Surg (Am), 71, 839-47, 1989.
Fernandez, D. and Geissler, W. J Hand Surg, 16A, 375-84, 1991.
Short, W. et al. J Hand Surg, 12A, 529-34, 1987.
Baratz, M. et al. Trans of the 39th ORS, (p.106), 1993.
Donohue, J. et al. J Bone Joint Surg (Am), 65(7), 948-57, 1983.
Vener, M. et al. Trans of the Combined Meeting of the Orthop Research Societies of USA, Japan, and Canada, (p. 82), 1991.
Horii, E. et al. J Hand Surg, 15A(3), 393-400, 1990.

ACKNOWLEDGMENTS

This project was funded in part by the Arthritis Foundation, Western Pennsylvania Chapter and by the NIH BRSG program.

THE EFFECT OF HALLUX SESAMOID RESECTION ON FLEXION MOMENT ARMS OF THE MTP JOINT

Rhonda L. Aper, Charles L. Saltzman, and Thomas D. Brown

Departments of Orthopaedic Surgery and Biomedical Engineering, The University of Iowa, Iowa City, IA 52242.

INTRODUCTION

Intrinsic disorders of the great toe sesamoids (e.g., fracture, osteochondritis, avascular necrosis) can become a chronic source of considerable disability. There is no consensus, however, as to the optimal surgical treatment. The wide variation in the treatment of such disorders points to a fundamental lack of understanding of the functional biomechanical significance of the hallux sesamoids. In this study, the functional significance of the hallux sesamoid bones was quantified by measuring the effective tendon moment arm (ETMA) of the flexor hallucis brevis (FHB) force. The intact case was compared with three levels of progressive sesamoid resection: distal half of the medial sesamoid excised, entire medial sesamoid excised, and both the medial and lateral sesamoids excised. The experimental method consisted of applying a known active functional load to the FHB muscle of fresh frozen cadaver specimens (the great toe being maintained at specific angles of dorsiflexion) while recording corresponding resisting force from three orthogonally mounted transducers. Results showed the ETMAs to decrease significantly ($p < 0.05$) only with dual excision.

REVIEW AND THEORY

The optimal treatment for disorders intrinsic to the sesamoids is not agreed upon. Among many others, recommended surgical procedures include partial sesamoid resection, removal of an entire sesamoid, and excision of both the medial and lateral sesamoids. However, no previous investigation has attempted to biomechanically quantify the surgical effect of these treatment options on normal FHB flexion moment.

The equation used to calculate the ETMA of the FHB arose from a vectorial (three-dimensional) equilibrium analysis of the MTP joint (Fig. 1). The external force-couple system acting on the MTP joint included an active functional force input to the FHB,

$$\mathbf{F}_b = F_{by}\mathbf{j} + F_{bz}\mathbf{k}, \qquad (1)$$

and a transduced resisting force,

$$\mathbf{F}_t = F_{ml}\mathbf{i} + F_{si}\mathbf{j} + F_{ap}\mathbf{k}. \qquad (2)$$

The condition necessary for moment equilibrium about the MTP center of rotation point C (taken to be at the center of the metatarsal head) could be expressed as

$$\mathbf{r}_{CS} \times \mathbf{F}_b = \mathbf{r}_{CM} \times \mathbf{F}_t, \qquad (3)$$

where the operator × designates a (vectorial) cross product. In this equation, values for the resisting force components (F_{ml}, F_{si}, F_{ap})

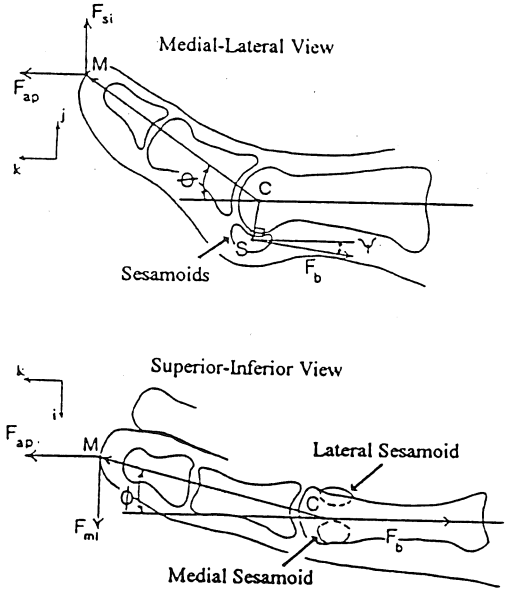

Figure 1.

and the force input to the FHB ($\mathbf{F}_b$) were obtained from the respective load cells. $\mathbf{r}_{CM}$ was measured directly, as simply the position of the tracking point M relative to the center of the metatarsal head. The cross product of the position vector $\mathbf{r}_{CM}$ and the transduced resisting force vector $\mathbf{F}_t$ resulted in the transduced resisting moment vector. The magnitude of this moment vector, divided by the magnitude of the input FHB load vector, yielded the ETMA magnitude of $\mathbf{r}_{CS}$ of the FHB. This effective tendon moment arm represents the functionally equivalent moment arm of the tendon force about the center of rotation point, rather than the apparent anatomic moment arm (Tolbert et al., 1985).

PROCEDURES

The prepared specimen was mounted in a fixation device, which held rigid the metatarsal. Cables sutured to the ends of the relevant intrinsic muscles and tendons ran through adjustable tracking guides and a series of pulleys, allowing each muscle/tendon to be statically loaded (by hanging weights) along its physiologic line of pull. As the FHB muscle was chosen to provide the main impetus for sesamoid motion, a specially designed clamp (rather than a suture attachment) was used, and the cable connected to a load cell mounted on the ram of an MTS machine. The clamped FHB muscle was preloaded through manual control of ram displacement. To determine reasonable concurrent static loads for the respective muscles and

tendons, physiologic cross-sectional areas (PCSAs) were measured (Aper, 1992). The PCSA-based static loads and FHB preload were used to establish a balance between the flexors and extensors, such that the great toe was in equilibrium at the desired angle of flexion. A ramp-controlled displacement of the MTS ram supplied a functional load input force (recorded by the ram load cell) to the preloaded FHB, ranging from 50 N to 155 N. The corresponding changes in the outputs of force transducers mounted orthogonally in the medial-lateral, superior-inferior, and anterior-posterior directions were recorded. Additionally, the distance from the center of the head of the metatarsal (the assumed nominal center of rotation) to the tracking point M on the great toe was measured, as was the angle between the metatarsal and the hallux while the great toe was dorsiflexed. The initial test configuration was 50°. Dorsiflexion angles of 35°, 25°, 15°, and -10° were sequentially obtained, and the above procedures replicated at each MTP angle. Subsequently, three progressively more extensive sesamoid resections were performed, with the above described testing protocol being repeated for each case. These resection stages were 1) partial sesamoidectomy in which the distal half of the medial sesamoid was removed, 2) sesamoidectomy in which the remaining proximal half of the medial sesamoid was removed (so that the entire medial sesamoid was excised), and 3) sesamoidectomy where the lateral sesamoid was also removed (so that both sesamoids were excised).

RESULTS

Eleven specimens were tested, each immediately after preparation, in order to minimize deterioration and the likelihood of tearing the FHB muscle. Two specimens in which the FHB tore prior to completion of the protocol were excluded from the final analysis. ETMA data for the remaining nine successfully completed specimens are shown graphically in Fig. 2, as a function of the angle of dorsiflexion. Statistical analysis (two-factor ANOVA without replication) found a significant difference ($p < 0.05$) in the moment arms with the successive resections, and with the changes in the angle of dorsiflexion. Further analysis (paired t-tests comparing each sesamoid resection to the normal) showed a significant decrease ($p < 0.05$) in the moment arms only when both the medial and lateral sesamoids had been excised.

DISCUSSION

Three simplifying assumptions were made in the modeling of the MTP joint. First, in the moment equilibrium analysis, the center of rotation for the resisting moment was taken to be at the apparent geometric center of the metatarsal head. Strictly speaking, the true center of MTP joint rotation (point C in Fig. 1) will not be coincident with the geometric center. However, the difference between the two (estimated to be < 3 mm) was small enough as to seem negligible, compared to the relatively large distance (typically about 80 mm) from the center point C to the force monitoring site M. Therefore, the associated error in the calculated resisting moment, $(r_{CM} - r_{GM}) \times F_t$, will be only a small fraction (< 5 %) of the true

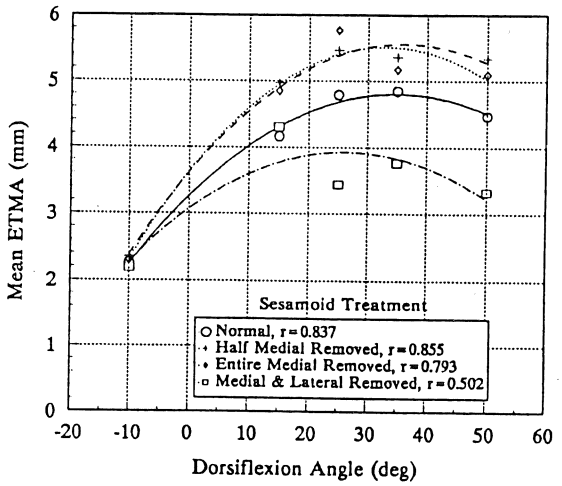

Figure 2.

resisting moment, $r_{CM} \times F_t$. Second, also in the equilibrium analysis of the MTP joint, forces present in the soft tissue structures (as applied through the concurrent static loads and FHB pre-load) were assumed to be relatively insignificant. Third, in the current testing configuration, the effects of contact force from the plantar surface (i.e., ground) is not included. This effect would presumably be to add a modest amount of apparent "rotating friction" at the MTP joint.

Interestingly, the functionally measured ETMA values of the FHB were less than expected, given the overall physical size of the MTP joint. This occurs because the ETMA values represent the distance between the effective centroid of the tendon pull (which lies relatively close to the plantar surface of the metatarsal head) and the actual center of rotation in the head. The ETMA values obtained in this study suggest that the true center of rotation is located plantarwards of the geometric center, close to the tendon centroid.

The clinical significance of the results of this study is that the excision of the distal half of the medial sesamoid, or indeed the excision of the entire medial sesamoid, is unlikely to cause appreciable MTP flexion power deficit. However, when contemplating the removal of both the medial and lateral sesamoids, it would be prudent to take into consideration the resulting MTP flexion power deficit, at least for individuals in whom maximal push-off strength is critical.

REFERENCES

Aper, R.L. M.S. Thesis, The University of Iowa, 33-35, 1992.
Tolbert, J.R. et al. J. Biomech., 18, 887-897, 1985.

ACKNOWLEDGEMENTS

The authors are grateful for the helpful technical assistance of Mr. M. James Rudert.

THE EFFECTS OF AN ARTICULATED EXTERNAL FIXATOR ON ANKLE JOINT KINEMATICS

Daniel C. Fitzpatrick, J. Lawrence Marsh, and Thomas D. Brown

Departments of Orthopaedic Surgery and Biomedical Engineering, The University of Iowa, Iowa City, IA 52242

INTRODUCTION

High energy fractures of the distal tibia (tibial plafond fractures) present particularly difficult clinical management problems due to extensive comminution of the articular surface of the ankle and significant soft tissue injury. Since the early 1970's, open reduction and internal fixation (ORIF) with early motion and prolonged non-weight bearing has been the preferred method of treatment. However, the high rate of serious soft tissue complications involved with ORIF has led to the investigation of new, less invasive treatment methods. The Orthofix articulated ankle external fixator has been proposed as a treatment alternative to ORIF. This fixator allows tibial plafond fractures to be reduced and fixed without major soft tissue disruption. Clinical studies show significantly decreased rates of soft tissue infection with no significant bony deformities [Bonar et al]. However, it is unclear what effect this fixed-hinge external fixator has on normal ankle kinematics and fracture site motion. A biplanar kinematic analysis of ankle and subtalar joints was performed for the normal ankle and three alternative fixator applications. The fixator applications simulated a horizontal axis (the configuration currently used), an axis coincident with that described by Inman [1976], and an axis located using a new mechanical axis finder. The motion most closely matched that of the normal ankle for the axis finder application. The amount of fracture motion was found to be insignificant for all fixator positions in both stable and unstable fracture models.

REVIEW AND THEORY

Tibial plafond fractures typically occur as the result of falls from heights, resulting in a high energy axial compression fracture of the distal tibia. Until recently, the accepted treatment method has been ORIF, which allowed early ankle joint motion, but required wide surgical approaches. Due to the extensive soft tissue injury and the precarious blood supply in the region, serious complication rates as high as 50% have been reported. These figures have led to the introduction of external fixation as a possible treatment modality. Unfortunately, most external fixation methods are either difficult to apply (ring-wire) or involve the immobilization of the hindfoot (cross-ankle). The Orthofix articulating ankle external fixator (Fig. 1) places two proximal screws in the tibia, and two distal screws in the hindfoot (one in the talus and one in the calcaneus). A hinge attaches the hindfoot screws to the fixator body. The subtalar joint is effectively immobilized in this application technique. Clinically, the hinge is released one week after application and the patient performs passive, non-weight bearing motion. As healing progresses, active motion is encouraged. The current clinically recommended application technique involves placing the fixator hinge along a horizontal ankle axis. However, the ankle has been described by Inman to move about a simple hinge axis oriented along a line connecting the distal tips of the malleoli. There is a significant amount of variation in the location of this axis between individuals. Many authors have also described ankle axes that change as the foot is moved.

The biplanar radiographic method for kinematic analysis is commonly used for the study of three dimensional motions in joints. In this method, two orthogonal radiographs of the test specimen and a calibration frame are exposed. The images of the calibration frame are used to reconstruct the three dimensional locations of the x-ray sources. Using a linear transform, the locations of bones may then be reconstructed in three dimensions. Once the locations of the bones are known, the Cardan rotation angles between neutral position and any other position may be calculated.

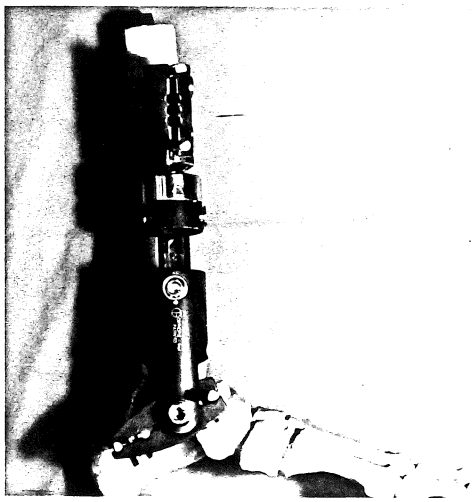

Figure 1. The Orthofix articulating ankle external fixator.

This study investigated the effect of three different fixator hinge orientations on normal ankle kinematics. Three fracture models (stable tibia, unstable tibia, and unstable tibia and fibula) were simulated to quantify the ability of the fixator to control fracture motion.

PROCEDURES

Nine fresh frozen cadaver below-knee specimens were prepared by inserting at least three 1.0 mm diameter chrome beadlets in the talus and calcaneus. The specimen was mounted in a specially designed apparatus which allowed three degrees rotational freedom in the ankle joint. The apparatus and specimen were placed in a wire calibration frame designed for biplanar radiographic analysis (Fig. 2). Biplanar radiographs were exposed at 10° intervals, from 30° plantar flexion to 10° dorsiflexion, for an unfixed ankle. The fixator was then applied in three different hinge orientations and radiographs were exposed over the same range of motion.

The first application technique was the current clinical method, which assumes a horizontal axis. The second application

oriented the fixator hinge along Inman's ankle axis, located posterior to the distal tips of the malleoli. For the third

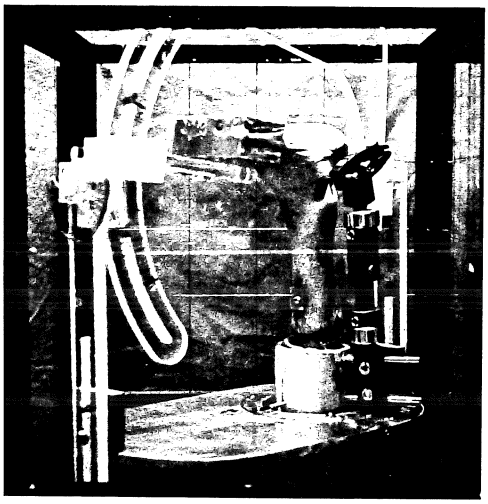

Figure 2. The test apparatus in the calibration frame used for biplanar radiographic analysis.

application, a specimen-specific ankle axis was located using a mechanical device termed an axis finder. The fixator hinge was then oriented along this axis. All fixators were applied under fluoroscopic control by an experienced trauma surgeon.

After the joint kinematics testing was complete, fractures were modeled on four of the specimens with the fixator in the axis finder orientation. A stable fracture was modeled by a transverse osteotomy 2.5 cm proximal to the articular surface. After collecting data over the same range of input foot motion previously tested, another cut was made and a 5 mm segment of bone was removed, to simulate an unstable fracture. A fibular fracture was modeled by a 5 mm gap osteotomy at the same level as the tibial fracture. Data were also collected for the unstable tibia/fibula fracture with the fixator in non-axis finder configurations.

The radiographs were encoded into an on-line computer program using a sonic digitizer. This program computed the three dimensional locations of the beadlets with respect to the center of the cage. The locations of these beadlets were transformed into a tibial-based coordinate system and used to calculate the Cardan rotation angles about a plantar/dorsiflexion axis, followed by an ab/adduction axis and then an in/eversion axis, relative to the neutral ankle position.

RESULTS

The average Cardan rotation angles of the talus and calcaneus increased approximately linearly through the dorsi/plantar flexion interval. The data were therefore fit by regressions which were representative of the talar and calcaneal motion. The slopes of the regression lines for each fixator hinge orientation were compared to those for the normal (unfixed) ankle, using the regression analysis t-statistic ($p = 0.05$). The results are reported in Table 1, where the motions which are significantly different from normal are marked with an asterisk.

Motion of the fracture fragment was small in all directions and for all fracture models. The maximum rotation observed (6°) was for the tibia/fibula fracture in the non-axis finder application at 30° plantarflexion.

Table 1. The slopes of the regression lines for bone motion versus foot position.

calcaneus	normal	clinical	Inman's	axis finder
P/D	.772	.522*	.531*	.633
A/A	.373	.267*	.267*	.366
I/E	.183	.120	.175	.176
talus				
P/D	.639	.547*	.646	.601
A/A	.321	.200*	.319	.269
I/E	.146	.209*	.125	.108

* statistically significant ($p=0.05$) difference from normal ankle motion.

DISCUSSION

Motion at the ankle joint has been described by various authors to occur about either a fixed axis or an axis which changes as the ankle is flexed. In this study, it was assumed that ankle joint motion occurred about a fixed axis, and that it was possible to align the axis of a hinged external fixator along that axis, thus allowing undisturbed motion at the ankle joint. The current clinical application technique, which approximates a horizontal ankle axis, significantly disturbs normal ankle joint motion. Aligning the fixator with the average ankle axis described by Inman results in significant differences from normal motion about only two of six rotational axes. This is most likely due to the high amount of variability in the orientation of the true ankle axis among individuals. The axis finder was able to reliably find the ankle axis in each specimen. With the fixator hinge applied along this axis, normal ankle motion was not significantly disrupted.

With the fixator applied, there appeared to be no physiologically significant fracture fragment motions for any of the fracture simulations. The amount of motion was noted to be highest in the unstable tibia/fibula fracture model. However, it should be noted that, clinically, the fixator hinge is not released for free movement until soft tissue healing has begun (usually 1-2 weeks). During this time, significant callus will begin to form, which will have the effect of reducing the already small fracture motion reported in this study.

REFERENCES

Bonar, S.K. and Marsh, J.L., Foot and Ankle 14:57-64, 1993.
Inman, V.T., Joints of the Ankle. Williams and Wilkins, 1976.

ACKNOWLEDGMENTS

The authors appreciate the technical assistance of D.R. Pedersen and M.J. Rudert and the axis finder suggestions of Dr. C.L. Saltzman. Financial support provided by Orthofix Srl., Verona, Italy.

A BIOMECHANICAL EVALUATION OF THE EFFECTS OF THE BANKART RECONSTRUCTION ON THE EXTERNALLY ROTATED SHOULDER

L. McGrady, K. Black, T. Lim, D. Fagan, and W. Raasch

Department of Orthopaedic Surgery, Medical College of Wisconsin, Milwaukee, WI 53226

INTRODUCTION

The Bankart reconstruction is a well accepted surgical technique involving shortening of the glenoid humeral capsule to repair anterior shoulder dislocations and subluxations. Although the literature suggests the vast majority of patients continue to have a full range of motion postoperatively (Rowe, 1978), it is our hypothesis that this is achieved at the expense of increased torques impressed across the capsule. This study investigated the effects of the capsular shortening on the resisting torque (about the vertical axis) of the externally rotated cadaveric shoulder at 0° of abduction. The zone of high flexibility (ZHF), in which an external rotation can be produced with a minimal internal resistance (Panjabi, 1991) was determined based on the measured torque-rotation curves (TRC). Significant reductions in the ZHF were found to be approximately 40% and 67% due to shortening the capsule by 2 and 7 mm, respectively.

REVIEW AND THEORY

The inherent instability of the minimally constrained glenohumeral joint is generally accepted to be directly related to the extreme mobility of this joint (Turkel, 1981). This lack of intrinsic passive stability makes the shoulder joint susceptible to a host of pathological lesions. The Bankart lesion has been found in approximately 70-85% of all anterior dislocations (Rowe,1978 & 1981). It is described as the avulsion of the capsule and labrum from the anterior glenoid rim. In the Bankart reconstruction, the labrum is not repaired back on the bone, but rather a capsular shortening is done in which the labrum becomes an extrarticular reinforcement. Biomechanically speaking, this shortening of the capsule should affect the tensile forces induced across the capsule and possibly external rotation. The purpose of this study was to investigate the affects of the reconstruction on the externally rotated shoulder in 0° of abduction.

PROCEDURES

The six fresh-frozen cadaveric shoulder specimens used in this study were prepared as follows. With the arm in 0° of abduction and the elbow flexed 90°, a pin was placed through the humerus, at approximately 5 cm. above the medial and lateral epicondyles and in line with the forearm, to serve as a pointer for angular measurements. A second pin was placed through the humerus at the same level to manually apply external rotation torque. The arm was then amputated 1 cm. proximal to the epicondyles. Using dental cement, a bone screw was embedded in the exposed medullary cavity of the humerus to serve as a pivot point about which the humerus was rotated. The vertebral border was positioned and embedded in the load cell container so it would be perpendicular to the floor when mounted on the load cell (AMTI Multi-component transducers, AMTI Inc., Newton, MA). The prepared specimen was then mounted in the test frame (Fig. 1).

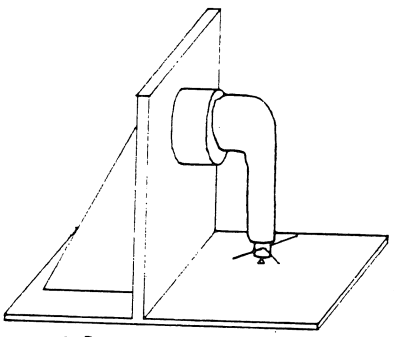

Figure 1 Set-up for the mechanical test.

Resisting torques about the vertical axis were measured at specific increments of external rotation. This testing procedure was repeated three times, and the mean of measured torques was used to obtain the TRC. TRC's were generated for each of the following cases: 1) *shoulder intact;* 2) *capsule vented with 18 gauge needle;* 3) *subscapularis removed (capsule intact);* 4) *capsule cut;* 5) *2 mm shortening of*

capsule; and 6) *7 mm shortening*. The capsule shortening using the Bankart reconstruction techniques included making a capsular incision adjacent to the glenoid. Anchors were placed as close as possible to the articular surface and sutures were put through the capsule 2-3 mm from the incision.

RESULTS

All 6 shoulder joints demonstrated a highly nonlinear load-displacement behavior (Fig 2) for all 6 test conditions. The TRC can be divided

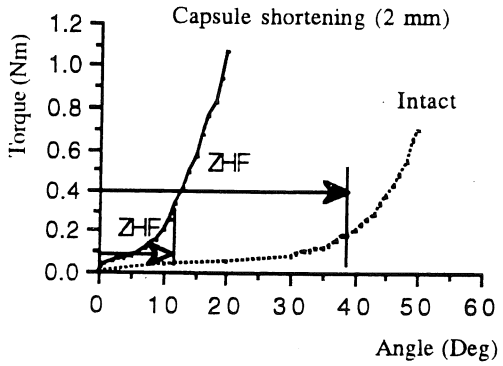

Figure 2 Typical TRC's for shoulder specimen and corresponding ZHF's.

into two parts: a ZHF and an elastic zone, which is defined as the region of high stiffness. The transition point (angle) between the ZHF and the elastic zone was determined as the point at which the slope of the TRC became at least two times greater than the slopes at the previous points (Fig 2). The transition points for all 6 test conditions were normalized with respect to the intact specimen. Their means and standard deviations are listed in Table 1.

Wilcoxon's Rank Sum Test was used to analysis the data. There was no significant change found in the ZHF between the intact and vented, or the vented and the removed subscapularis. There was a significant change ($p<0.05$) when comparing the intact capsule (subscapularis removed) and the cut capsule. The ZHF of both capsular shortenings (2 mm and 7 mm) were found to be significantly different ($p<0.01$) from the following cases: intact shoulder, intact capsule, and capsule cut. There was also a significant difference ($p<0.01$)in the ZHF of the two capsular shortenings.

Table 1 Normalized ZHF's (% change) of the 6 shoulders, their means, and standard deviations.

Case	2	3	4	5	6
shld1	8.7	8.7	15.2	-73.9	-93.5
shld2	1	1	12.7	-60.6	-91.6
shld3	2.7	8.7	18.4	-13.5	-37.8
shld4	2.7	8.7	18.4	-13.5	-37.8
shld5	-5	27.8	26.9	-29.6	-24.8
shld6	28	28.6	38.1	-28.6	-38.1
Mean	6.1	15.5	21.5	-40.4	-66.6
STD	11.9	11.2	9.3	22.5	24.7

2=Capsule ventilated; 3=Subscapularis removed; 4=Capsule cut; 5=Capsule shortened 2 mm; 6=Capsule shortened 7 mm.

DISCUSSION

This study specifically looked at the affect of the Bankart reconstruction on the ZHF of the externally rotated shoulder in 0° abduction. There was no significant change found in the ZHF until the capsule was cut. However, a significant increase in the ZHF was found once the capsule was cut, and a significant decrease in the ZHF was found in the two capsular shortenings. This would indicate that the anterior glenohumeral capsule plays an important part in resisting external rotation (with respect to torque about the vertical axis).

Bigliani, L et al. J Orthop Res. 10:2,187-192, 1992

Rowe, C.: Orthopedic Clinic of N Amer, 11:2, 253-269, 1980

Rowe, C et al: JBJS, 60A:1-16, 1981

Terry, G.: Amer J Sports Med, 19:1, 1991

Turkel, et al: JBJS, 63A:1208-1217, 1981

Panjabi, J Spinal Disorders, 5:390, 1991

An In Vitro Kinematic Analysis of the Pennig Dynamic External Fixator for Distal Radius Fractures

Erika L. Skaro, William F. Blair, Howard W. Popp, and Thomas D. Brown

Departments of Orthopaedic Surgery and Biomedical Engineering, The University of Iowa, Iowa City, IA 52242.

INTRODUCTION

Fractures of the distal radius account for almost 20 percent of fractures in general, and over 80 percent of all radius fractures. The mechanism of injury is most often an axial compressive load on the radius, such as a fall on an outstretched hand, which tends to result in substantial comminution and dorsally displaced fracture fragments. Maintenance of the reduction of these fractures is difficult; they often regress towards the initial deformity due to the lack of fragment support, especially in the elderly whose rate of healing is relatively slow. External fixation provides an adequate method of fixation for this type of fracture, but persistent pain and loss of motion of the wrist are frequently seen complications. The Pennig dynamic external fixator is capable of allowing 90°-100° of early wrist motion, while continuing to maintain traction. A biplanar kinematic analysis was undertaken to determine the effects of the Pennig fixator on normal carpal kinematics and on fracture stability. The recommended frontal plane application of the device was investigated, along with several clinically relevant deviations from this position: three alternate frontal plane positions and two non-frontal plane positions. It was found that in the normal (unfractured) wrist, with the fixator applied in any of the four frontal plane positions, the flexion/extension range of motion was only slightly reduced, and the motions of the carpal bones were essentially unchanged, as compared to the situation without the presence of the fixator. In contrast, the non-frontal-plane applications of the fixator severely restricted the range of motion of the wrist. Carpal kinematic data were not obtained for non-frontal-plane applications due to the limitation in the range of achievable positions. Wafer osteotomies of 3 and 5 mm thicknesses were performed to simulate a distal radius fracture. Fracture fragment motion was found to be significant for all fixator positions, with as much as 20° of rotation occurring over the range of hand motion. A proximal, frontal plane fixator application was found to be significantly less effective than the recommended application, although the recommended application still failed to provide adequate immobilization of a free fragment. However, simulation of a superimposed callus mass strikingly reduced fragment motion.

REVIEW AND THEORY

Several techniques have been used to treat fractures of the distal radius, including closed reduction with a plaster cast, internal fixation, and pins and plaster. These fractures are often comminuted, and maintenance of the reduction can be difficult. Pain, loss of motion at the wrist joint, and decreased grip strength are commonly seen when distal radius fractures are treated by the previous methods. Effective treatment of these injuries requires fracture reduction and fixation, as well as early range of motion exercises for the wrist[Melendez, Sisk] and free forearm rotation[Leung]. Current devices for external fixation of the distal radius offer many advantages over the previously mentioned techniques of fracture management. Along with free forearm rotation and motion of the adjacent joints, some designs allow early motion of the wrist while continuing to maintain traction. One of these designs is the Pennig dynamic external fixator. This fixator has a central ball joint articulation which allows early mobilization during healing. The effects of these dynamic external fixators on normal carpal kinematics and on fracture stability are critical to their success, yet few hard data exist to either support or refute their performance in that regard. The present paper reports the effects of the Pennig dynamic external fixator on normal carpal kinematics and on fracture fragment kinematics for distal radius fractures simulated in a cadaver model. These influences were studied both for the recommended position of the fixator as well as for clinically relevant deviations from the recommended configuration.

PROCEDURES

A biplanar radiographic technique, based on the Roentgen Stereophotogrammetric (RSPG) method developed by Selvik[1989], was used to determine Cardan rotation angles for the capitate, the scaphoid, the lunate and the fracture fragment. Seven fresh cadaver upper extremities(average age 77 years), transected at the mid-humeral level, were used in this study. The absence of abnormalities was verified radiographically. At least three tantalum or chrome metallic markers, 0.8-1.0 mm diameter, were inserted into each of the three carpal bones and the distal radius (i.e. the future fracture fragment) with the assistance of fluoroscopy (Fig. 1).

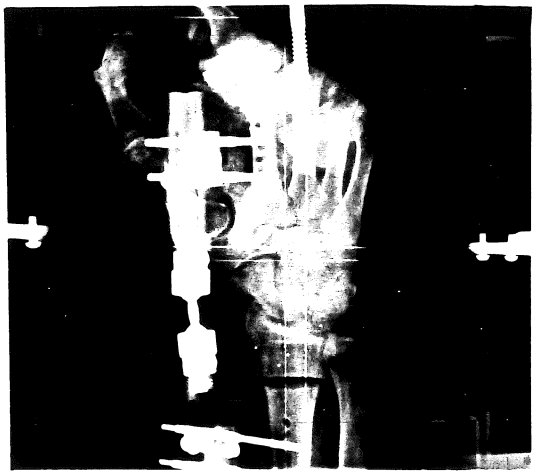

Figure 1. Specimen with markers in the carpal bones and distal radius. Fixator applied as recommended by the manufacturer.

Specimens were then fixed midway between pro/supination by two threaded rods passed through both the radius and the ulna. Polymethylmethacrylate was molded around the bone/rod system to provide additional rigidity. The specimen was mounted in an upright position in the forearm fixation apparatus, with the fixator applied in the frontal plane as recommended by the manufacturer. This position aligns the distal ball joint with the capito-lunate junction, and uses a 2 cm transverse offset of the fixator. Tendon loads were applied to the five major wrist motors through calibrated springs. A motion guide consisting of a base ring and an arc was used to measure the positions of the hand (Fig. 2). The hand was then passively positioned from 50° flexion to 50° extension, in 25° increments. This was the range of motion allowed by the fixator. The entire apparatus was placed inside a calibration cage, and biplanar radiographs were taken at each hand position. The radiographs were digitized and the three-dimensional locations of the markers were determined, at each position, with respect to a global coordinate system based in the cage. Cardan rotation angles relative to a right-hand anatomic reference coordinate system were then calculated. The Cardan angle order of rotation was chosen to be flexion/extension, followed by radioulnar deviation, and then pro/supination. Alternate frontal plane fixator positions, namely 1 cm proximal and 1 cm distal to the recommended position, and an additional 2 cm of transverse offset, were also investigated. Two non-frontal plane positions, 30° and 60° dorsal to the frontal plane,

were also studied. After completing measurements for the intact case, 3 mm and then 5 mm wafer osteotomies were performed to simulate distal radius fractures. These osteotomies were intended to simulate comminution and the resulting instability of the fracture site. The fixator was then reapplied as for each of the intact cases, and the previous experimental procedure was repeated. Finally, since wafer osteotomy represents a probably more unstable situation than would prevail clinically at the time of fixator mobilization, selected trials were run using compliant foam inserts to flexibly couple the proximal and distal fragments, simulating callus effects.

Figure 2. The forearm fixation apparatus and motion guide in the calibration cage used for biplanar radiographic analysis.

RESULTS AND DISCUSSION

The data in Figure 3 are typical of the relationships seen for the primary flexion/extension rotation of each carpal bone of interest. The four frontal plane fixator positions are shown, with linear regressions fit to each fixator position data set. Statistical analysis of the slopes of the linear regression lines found that none differed significantly from unity, indicating that the fixator has no effect on the normal flexion/extension motions of the carpal bones in the unfractured situation. However, frontal plane application of the fixator was found to severely restrict radioulnar deviation in the intact situation.

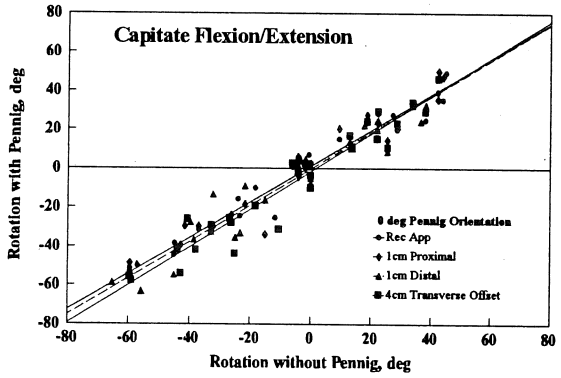

Figure 3. Capitate flexion/extension with versus without the Pennig fixator.

The non-frontal plane applications of the fixator were found to significantly reduce the range of motion of the hand. Both the 30° and 60° positions restricted flexion to a minimum in the unfractured case. Figure 4 shows a mapping of the range of motion of the hand without the fixator, as well as the range of motion allowed with the recommended application of the fixator and with the two non-frontal plane fixator applications.

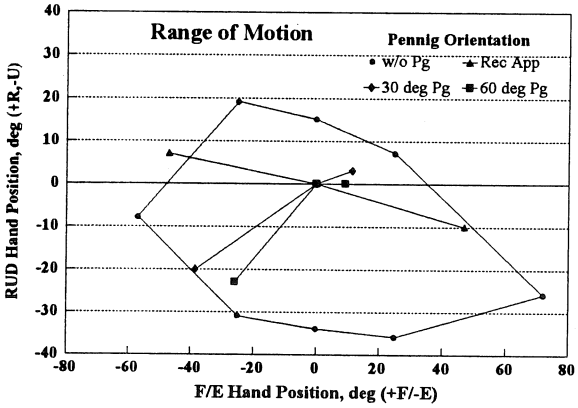

Figure 4. Range of motion of the hand without the Pennig fixator and with various fixator applications.

Fracture fragment motion was analyzed as a function of hand position and as a function of fixator position. The dorsal/volar rotation of the 3 mm fracture fragment (without callus simulation) is shown in Figure 5. Linear regression lines were fit to the data. Statistical analysis (paired t-test at the extremes) determined that proximal placement of the fixator provided significantly less stability than the recommended application. However, appreciable fragment motion occurred even for the recommended application. Fragment rotation in the medial/lateral and pro/supination directions was insignificant.

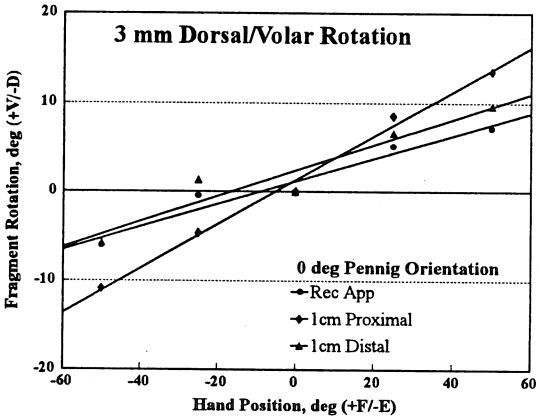

Figure 5. 3 mm fracture fragment dorsal/volar rotation versus hand position. Four frontal plane fixator positions shown.

REFERENCES

Leung, K. J. Hand Surg., 15A, 11-17, 1990.
Melendez, E. J. Hand Surg., 14A, 807-811, 1989.
Selvik, G. Acta. Ortho. Scand. Suppl. 232, 60, 1989.
Sisk, T.D. Clin. Orthop. Rel. Res., 180, 15-22, 1983.

ACKNOWLEDGMENTS

The authors wish to thank Mr. Doug Pedersen for his programming assistance and Ms. Denise Hammen for her assistance with fluoroscopy. Financial support for this study was provided by Orthofix Srl, Verona, Italy.

THE EFFECT OF PERIODIC RETIGHTENING OF A LACE-UP ANKLE BRACE

Michael J. Askew, Ph.D., Donald A. Noe, B.S.
Donald N. Marshall, M.S., A.T.C.*, E. Herbert Thompson, M.D.,
George J. Mallo, M.D., Thomas Teater, M.D.

Musculoskeletal Research Laboratory, Department of Orthopaedic Surgery, Akron City Hospital, Summa Health System, 525 East Market Street, Akron, OH 44309 and *Sports Medicine Center, Childrens Hospital Medical Center of Akron
300 Locust Street, Akron, OH 44302

INTRODUCTION

The stability provided to the ankle by a lace-up brace (Swede-O-Universal, North Branch, MN) was compared to that provided by taping before and after exercise and after retightening of the brace. Both taping and the brace significantly reduced the passive ranges of rotational motion of the ankle. These ranges were increased following exercise for both stabilization techniques. Retightening of the lace-up brace reduced these ranges to and beyond those seen after initial brace application.

REVIEW AND THEORY

It has been suggested that the effectiveness of a lace-up ankle brace can be maintained during athletic activities by periodic retightening (2,7). This practice may negate the detrimental effects of exercise that occur with taping and other ankle stabilization techniques (1,4,6). The objective of this study was to test the hypothesis that retightening of a lace-up brace restores the passive ranges of motion of the stabilized ankle to their pre-exercise levels and to those seen after initial taping.

PROCEDURES

Following pre-conditioning ankle exercises, each of ten male subjects was seated on an elevated bench with the thigh horizontal, the knee flexed at 90^{o}, and the foot on a rotating foot plate. Torques were applied to the foot plate in each of the six rotation directions: Dorsiflexion, 21.4 N-m; Plantar flexion, 16.4 N-m; Internal rotation,4.9 N-m; External rotation, 3.3 N-m; Inversion, 4.5 N-m; and Eversion, 9.0 N-m.

These tests were conducted on each ankle before and after tape or bracing, following an exercise period, and again following retightening of the brace. One ankle of each subject was taped while the other was stabilized with the brace. The taping method involved Tuf-Skin spray (Cramer Products, Inc., Gardener, KS), a layer of pro-wrap, and a Universal Taping (combination heel stirrup, basket-weave and figure 8) (5). The lace-up stabilization involved a properly sized Swede-O-Universal ankle support (Swede-O-Universal, North Branch, MN) over a cotton sock. The stabilization, the left/right order of the tests, and the torque applications were randomized for each

subject. The exercise period consisted of 10 minutes of walking on a treadmill at 1.34 m/s (3 mph) up a 15% incline.

The data were analyzed non-parametrically using Friedman two-way rank order analysis, followed by a post-prior Tukey test ($p<0.05$), on the ranges of motion and the percent changes in motion relative to the no support condition.

RESULTS

Inversion-Eversion Ranges of Motion (degrees)

No support	68.5 ± 12.3
Taped	39.4 ± 6.8
Taped/Post Exer.	44.0 ± 12.7
Laced	53.4 ± 10.7
Laced/Post Exer.	55.6 ± 12.5
Laced/Retighten	41.1 ± 11.9

Ranked Order of Inversion-Eversion Ranges of Motion for Lace-Up Stabilization

- No Support
- Post Exer
- Laced
- Retighten

Ranked Order of Percent Changes in Inversion-Eversion Ranges of Motion

- Laced/Post Exer
- Laced
- Taped/Post Exer
- Taped
- Laced/Retighten

(Groupings at the $p<0.05$ level)

DISCUSSION

Both the taping and lace-up stabilizations resulted in significant decreases in the passive ranges of motion. In agreement with Bunch et al (1) and Gross et al (3), the taping was initially superior. Exercise caused increases in the passive ranges of ankle motion for both the taped and lace-up braced ankles. The increases in inversion-eversion (13% for taping and 6% for the brace) agreed with changes reported by others (1). Retightening of the lace-up brace after exercise reduced the passive ranges of motion to their original dorsiflexion-plantar flexion levels and to levels below their original inversion-eversion and internal-external rotations.

REFERENCES

1. Bunch, R.P., et al. Phys. Sports Med., 13, 59, 1985.
2. Greene, T.A., et al. Am. J. Sports Med., 18, 498,1990.
3. Gross, M.T., et al. J.O. S.P.T., 13, 11, 1991.
4. Hughes, L.Y., et al. Phys. Sports Med., 11, 99, 1983.
5. Miller, E.A., et al. Ped. Clin. N. Am., 37, 1175,1990.
6. Myburgh, K.H., et al. Am. J. Sports Med., 12, 441,1984.
7. Rovere, G.D., et al. Am. J. Sports Med., 16, 228,1988.

ACKNOWLEDGEMENTS

This work was supported, in part, by The Foundation for Sports Medicine Education and Research of The American Orthopaedic Society for Sports Medicine, The Summa Health System Foundation, and The Robertson-Hoyt Fund.

CONTACT STRESSES ON MACHINED VS. MOLDED UHMWPe INSERTS IN TOTAL KNEE ARTHROPLASTY

R.E. Bristol, D.C. Fitzpatrick, T.D. Brown, J.J. Callaghan

Departments of Mechanical Engineering, Orthopaedic Surgery, and Biomedical Engineering,
The University of Iowa, Iowa City, IA 52242

INTRODUCTION

UHMWPe wear is arguably the largest factor contributing to the failure of total knee replacements. Wear debris can provoke a hostile immune response, in which macrophages and giant cells secrete enzymes that stimulate bone resorption. Due to the lack of any suitable replacement for UHMWPe as a bearing material, the best current solution for minimizing wear debris appears to lie with design optimization. This paper discusses the use of Fuji PresSensor film to examine the contact stresses produced on the articulating surface of total knee replacements possessing machined vs. molded UHMWPe tibial tray inserts. Machining produces fine anterior/posterior grooves on the PresSensor film that may cause higher shear stresses due to reduced (Poisson effect) transverse compression. Furthermore, at physiological load levels, the surface contact stresses are consistently in excess of the safe working range for UHMWPe.

REVIEW AND THEORY

Most previous research involving stresses on UHMWPe has been aimed simply toward determining a spatial mean pressure, found by dividing the applied force by the apparent contact area. Unfortunately, such measurements can be misleading because they give no information about the peak stresses or the amount of surface area experiencing deleteriously high stress levels. By contrast, whole surface contact stress distribution mappings provide a wealth of detail pertinent to rational design improvements, and provide a gold standard against which finite element models [1] can be explicitly validated.

PROCEDURES

PresSensor film stains were made using a specially designed apparatus in conjunction with a closed-loop servo-hydraulic materials testing machine. The apparatus allowed physiologic knee flexion angles to be input into the system. The Johnson & Johnson PFC Total Knee System, the Zimmer Miller/Galante I and II Total Knee System, and the Zimmer Insall/Burstein II Modular Knee System were all tested, with various UHMWPe tibial tray insert designs. Contact stains were collected for several flexion angles and loading regimes, including one series in which the magnitude of loading was varied from 500 N to 3000 N at a constant flexion angle of 90°. Contact stains were also collected for a series wherein the magnitude of the load and the angle of flexion were held constant (2000 N and 90°) while the duration of loading was varied from 0.1 to 100 seconds. All stains were optically scanned, and interactively analyzed using the P-V Wave (Precision Visuals, Inc., Boulder, CO) programming language, first converting the varying levels of stain intensities to 8-bit gray levels. Gray levels for known indentation stress standards were used to construct calibration curves relating gray levels to compressive stresses. Each stain was numerically integrated to verify load recovery, and then processed to determine the pressure distribution, total area of contact, pressure profile smoothness in both M/L and A/P directions, maximum pressure on the component, and pressure at the 99th percentile of pixel loading intensity. Additionally, a histogram of the pressure distribution (Fig. 1) and 3-D surface plots of the pressures over the entire contact areas (Fig.2 & 3) were examined for each study case. Both Fig.1 and Fig.2 correspond to a Johnson & Johnson PFC Total Knee System with a 10 mm Curved UHMWPe articulating surface. Fig. 3 corresponds to a Zimmer Miller/Galante Total Knee System with a Regular 11 mm A/P Lipped UHMWPe articulating surface.

RESULTS

Under realistic physiological loading, typical peak contact stress on the UHMWPe was approximately 30 MPa, which is about twice the yield strength [2], and three times the recommended compressive working stress for the polymer. Confirmation of this is given by Fig. 1, which indicates that the largest engaged area corresponding to any single contact stress range belongs to the 25-27 MPa range.

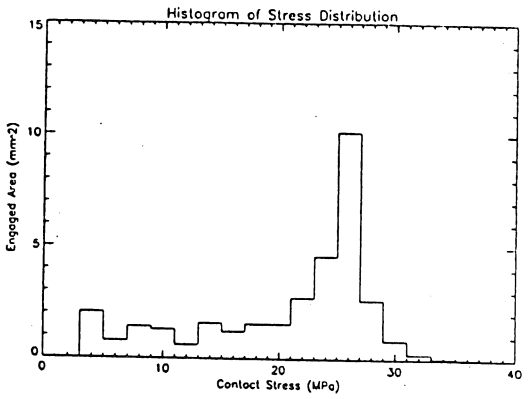

Figure 1: Histogram of Stress Distribution

The anterior/posterior surface grooves from machining left grossly visible tracks in the PresSensor stains. Akin to conventional surface roughness measures, the difference in pressure profile smoothness (Fig.2) for the A/P and M/L directions for each stain was reflected by large differences in the root-mean-square (RMS) variability in pressures among adjacent pixels. For the machined articulating surface components, the M/L RMS variability

(111 MPa/mm, in this case) was typically as high as four to five times the A/P RMS variability (here, 26 MPa/mm).

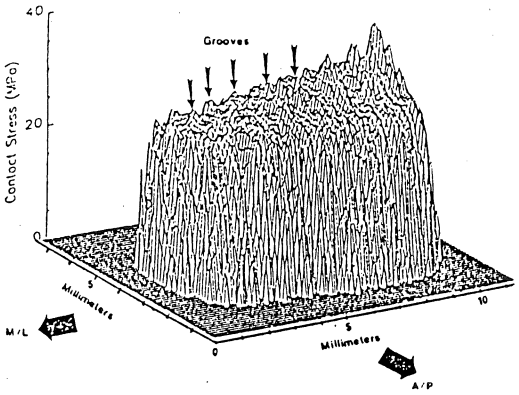

Figure 2: 3-D Surface Stress Plot for J&J PFC.
--Note the A/P machining grooves

By contrast, the Zimmer Miller/Galante I (molded) UHMWPe articulating surface components showed little difference between M/L (30 MPa/mm) and A/P (25 MPa/mm) RMS variability values. Furthermore, the magnitude of the M/L RMS was appreciably greater for the machined components than for the molded ones.

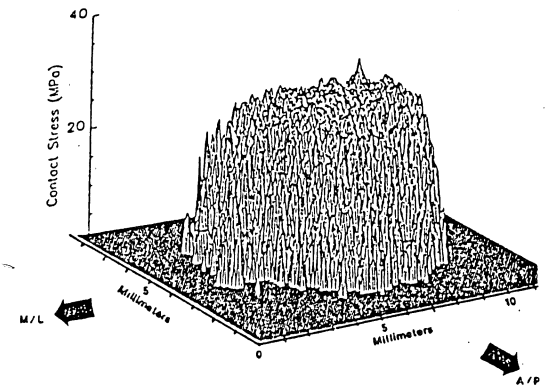

Figure 3: 3-D Surface Stress Plot for Zimmer M/G I

Typically, only 30-40 mm^2 of the total available surface area for each condyle (approximately 900 mm^2) was detectably in contact at any given instant. There was no apparent loading rate effect over the range of upramp loading durations from 0.1 to 100 seconds.

DISCUSSION

Stress levels measured in the present series are consistent with recent data [3] showing that the typical surface compressive stress for the polyethylene was approximately twice the yield strength, and three times the recommended stress of 10 MPa.

In most instances, the global stress distribution on the UHMWPe surface was very spatially uniform. This could be indicative of "plastic flow". However, the effect of machining on the local surface stresses for UHMWPe was surprisingly pronounced. By creating grooves that run in the A/P direction, machining may cause a reduced (Poisson effect) local transverse compression. Because of this reduced transverse compression, contact with the condyles may produce an abnormally high local shear stress within the UHMWPe. Therefore, the presence of these grooves may prove to be very detrimental to the life of the implanted UHMWPe component because these asperities may be a source of early wear debris, and even possibly the cause of premature implant failure.

The ratio of actual contact area to the total surface area available for each condyle indicates that typically less than 5% of the available surface area is used for load bearing at any instant.

REFERENCES

[1] Bartel, D.L. et al. Journal Bone and Joint Surg., 68-A, 1041-1051, 1986.

[2] Rimnac, C. et al. Proc. VIth Intl. Conf. on Polymers in Medicine and Surgery: 5/1-5/6, 1989.

[3] Hayes, W.C. et al. Proc. 39th ORS: 421, 1993.

ACKNOWLEDGMENTS

The authors appreciate the technical assistance of Ms. NJ.Caldwell, Mr. D.J. Adams, Mr. M.J. Rudert, and Mr. D.R. Pedersen. Financial assistance was provided by Zimmer, Inc.

THE EFFECTS OF FIXATION TECHNIQUES ON DISPLACEMENT INCOMPATIBILITIES IN CEMENTED AND CEMENTLESS TKA

A. Berzins, D.R. Sumner, T.M. Turner and R.N. Natarajan

Department of Orthopedic Surgery
Rush-Presbyterian-St. Luke's Medical Center
Chicago, Illinois 60612

INTRODUCTION

One of the factors contributing to relative motion between an implant and bone is the mismatch in elastic properties of the bone and implant material. In total knee arthroplasty this mismatch can cause displacements in the tangential direction (i.e., within the transverse plane) because of the transverse expansion of the tibia under axial loading. In this study, we test the hypothesis that the magnitude of the initial transverse expansion of the proximal tibia (and associated tangential displacement) depends upon the fixation design of the tibial component.

MATERIALS AND METHODS

The transverse expansion of the canine proximal tibia was measured 2.3 mm (±0.4) distal to the level at which the bone was resected for implantation of a tibial component[1]. Five proximal tibiae from adult male mongrel dogs were tested in the following sequence:
(1) intact,
(2) flat porous coated component,
(3) flat porous coated component with 4 screws,
(4) pegged porous coated component,
(5) pegged porous coated component with 4 screws,
(6) cemented pegged component,
(7) cemented pegged component with 4 screws.

Configurations 2-5 were cementless and 6-7 were cemented. The transverse expansion along a posterior-lateral to anterior-medial diagonal (41 ± 1.6 mm) was measured with linear variable displacement transformers (LBB-375-TA-100-1, Schaevitz), which were accurate to $< 1\mu m$.

Load to the intact tibia was applied through the distal femur. Load to the tibial component was applied to it's geometrical center. Axial load from 0 to 900 N was applied with displacements registered at 300, 600 and 900 N, corresponding to approximately 1, 2, and 3 body weights (BW). The transverse expansion of each test configuration was compared with the intact bone using paired t-tests. The effects of pegs and screws in cementless components (test configurations 2-5) and the effects of cement and screws (test configurations 4-7) were tested with multivariate analyses of variance for repeated measures.

RESULTS

The greatest average expansion (10 $\mu m \pm 4$) was recorded at 3 BW with the flat porous coated component (configuration #2) followed in order by configurations #4, #3, #6, #5 (Fig. 1). The smallest expansion (6 $\mu m \pm 1$) at this load was detected with the cemented interface in combination with 4 cortical screws (configuration #7). None of the fixation designs significantly affected the measured expansion when compared to the intact tibia. The magnitude of the deformation increased with higher applied loads ($p < 0.001$). Statistically, addition of 4 cortical screws significantly decreased the measured expansion with a cementless interface at 1 BW and 3 BW ($p < 0.05$) and with a cemented interface at 2 BW and 3 BW ($p < 0.05$). Pegs did not reduce the transverse expansion in the presence of a cementless interface. Cementing of the interface significantly reduced deformation at 1 BW and 3 BW only in the absence of additional screw fixation

($p<0.05$); with screws present, cement had no significant effect.

DISCUSSION

Screws were as effective as cementing the interface in constraining transverse expansion of the proximal tibia in the canine model. Pegs provided no transverse constraint. This implies that for cementless fixation tangential displacements can be reduced by screws but not by pegs. This is in contrast to a 2-dimensional finite element model prediction[2].

The magnitudes of the transverse expansion of the present study were smaller than reported for a previous study in the human knee[3]. The smaller size and higher bone stiffness of the canine knee combined with a thinner cortical shell in humans probably contribute to this interspecific difference.

The transverse expansion was similar in the intact and resected tibia. Obviously, the natural transverse constraint in the proximal tibia must be provided by the surrounding cortical ring more than by the subchondral bone.

REFERENCES:

(1) Turner et al., *J Orthop Res* 7:893-901, 1989
(2) Natarajan et al., *Trans ORS* 13:331, 1988
(3) Dujovne and Wevers *Abstracts of XII International Congress of Biomechanics*, 26-30 June 1989, Los Angeles, 265.

ACKNOWLEDGEMENTS

NIH Grant AR39827

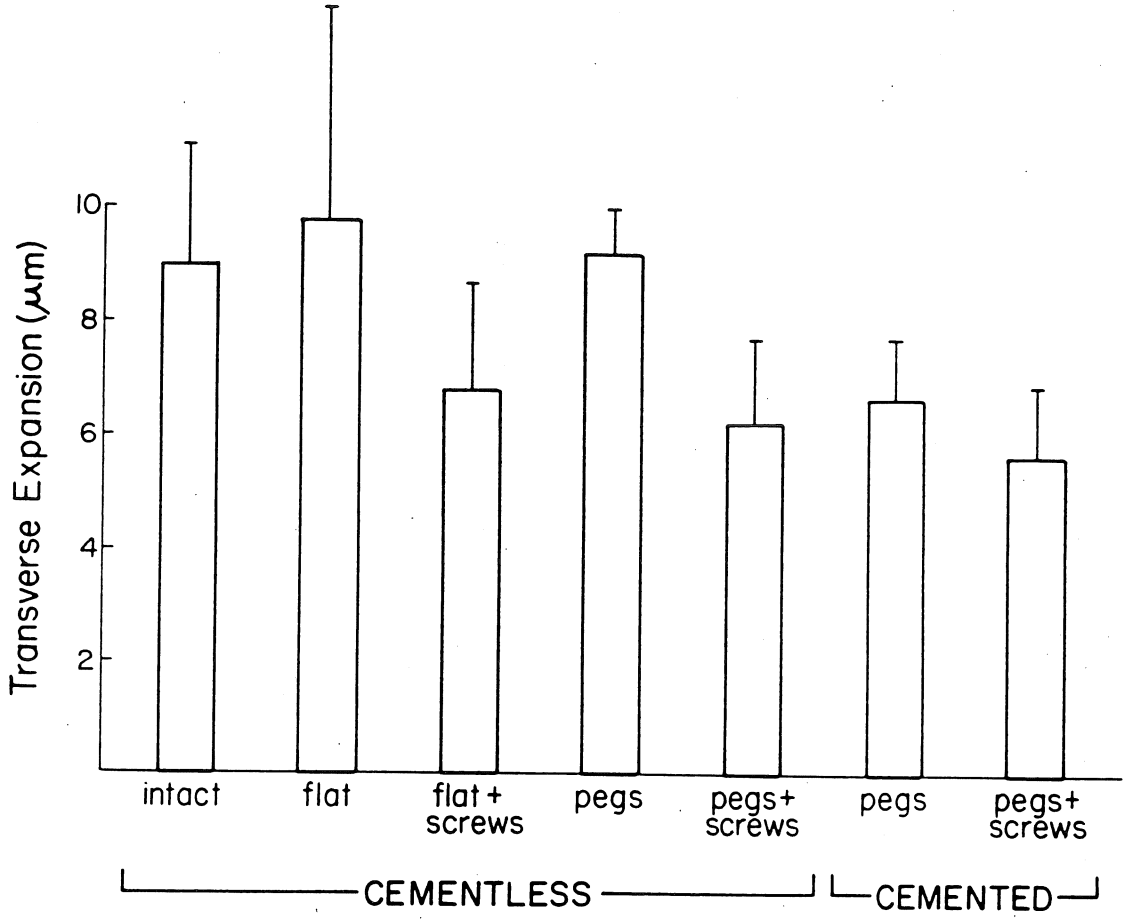

Figure 1. Transverse expansion at a load of 3 times body weight.

QUASI-PHYSIOLOGIC LOADING OF THA FEMORAL COMPONENTS USING A DUAL ACTUATOR SYSTEM

F. C. Barich, T. D. Brown, J. J. Callaghan, S. H. Elder

Departments of Orthopaedic Surgery and Biomedical Engineering, The University of Iowa, Iowa City, IA 52242.

INTRODUCTION

Laboratory studies of the micromotion of femoral components in total hip arthroplasty (THA) necessarily involve simplifications of in vivo loading. Most commonly, compression and torsion are applied separately. Another frequent idealization is the use of simple ramp or sinusoidal loading, cycling from no load to peak load and back to no load, as opposed to following the complex patterns of in vivo dynamic loading. A new procedure herein described uses both axial and torsional loading simultaneously, to apply quasi-physiologic three-dimensional load patterns to cadaveric specimens. Dynamic loading regimes simulating both level walking and stair climbing were programmed and used to study in situ micromotion of a newly-designed THA noncemented femoral component.

REVIEW AND THEORY

In situ testing of THA components began with the study of fixation strength in cemented arthroplasty. The development of cementless prostheses created a need for testing micromotion between the prosthesis and femur, the amount of motion being critical to bone growth into porous coatings on the prosthesis. The complexity of forces acting on the hip makes precise simulation of physiological loading difficult, especially with use of conventional (biaxial) materials testing machines incorporating co-linear axial and torsional actuators. Most investigators have separated axial and torsional loading, although a few recent studies applied more complicated loading schemes. Both Burke et al. (1991) and Maloney et al. (1989) applied axial and torsional loads simultaneously, but only statically. Schneider et al. (1989) did use time variant loads, but, applied them only sinusoidally and in an anatomically imprecise manner, since the "axial" load was aligned with the femoral shaft.

The consensus of current clinical opinion is that torsional loading is probably more critical to prosthesis loosening than is axial loading. Stair climbing generates a large posterior component of femoral head loading, which in turn creates large torques about the prosthesis shaft. Level walking, however, is also of clincal interest due to the much larger number of loading cycles and the generally higher resultant magnitudes involved.

As part of a broader micromotion study, a new procedure was developed to more realistically simulate level walking and stair climbing dynamic cyclic loads on a femoral component. A modification of an established hemi-pelvis simulation fixture was used in conjunction with a biaxial test machine to apply three-dimensional loads. The load histories were based on the in vivo data obtained by Kotzar et al. (1991).

PROCEDURES

The test system is depicted in Figure 1. Medial-lateral (ML) and superior-inferior (SI) (frontal plane) forces were assumed to act independently of anterior-posterior (AP, or out-of-plane) forces.

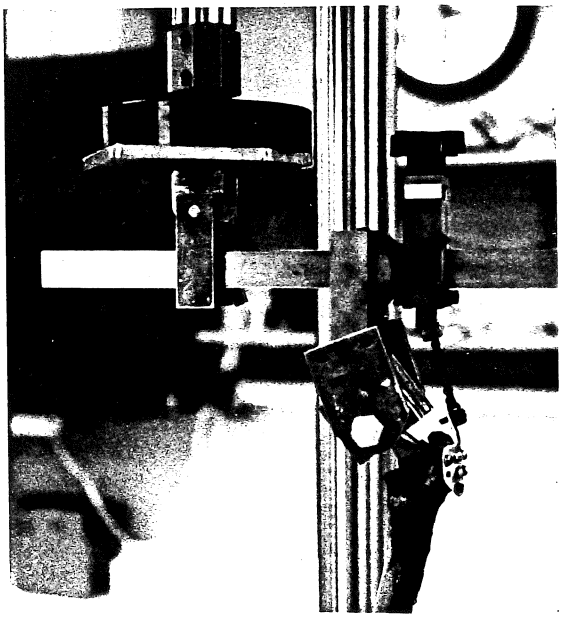

Figure 1. Test System Setup

The system was analyzed to determine the relationship between the applied loads and the resulting joint reaction forces. The relationship between applied axial load, L, and the frontal plane joint reaction load, J, was inferred from planar free body analysis of the hemi-pelvis loading fixture shown in Figure 2. At eleven specific instants during stance phase for which J and its inclination angle, ß, were inferred from Kotzar's data, static equilibrium was invoked to obtain three equations with the three unknowns: L, the abductor force A, and the length from actuator to prosthesis head, d_1. A horizontal reaction force is developed by the actuator if the bottom of the specimen does not lie directly below the actuator. This force is proportional to L and is represented by qL in Figure 2. While this equation system is well behaved mathematically, as a practical matter it is not feasible to repeatedly make the necessary adjustments in d_1

to achieve equipollence of this force system at all instants. Therefore, at most instants in the cycle there will be some error in replicating both J and ß.

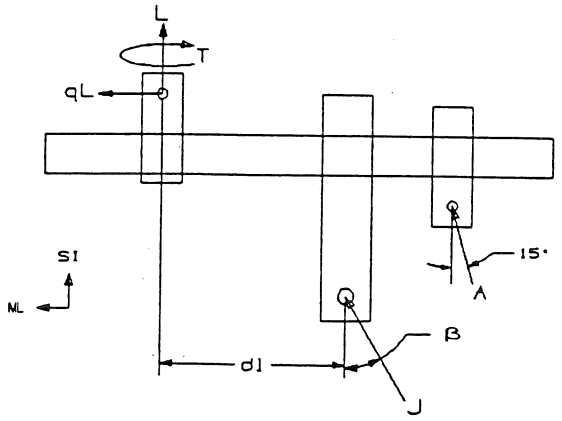

Figure 2. Free Body Diagram of Hemi-Pelvis Loading Fixture

Out-of-plane load was applied using the torsional actuator. Torque values were determined by multiplying the AP load times d_1. The simple relation between torque and the out-of-plane load component allows an identical match with the AP component of the Kotzar data, throughout the cycle.

Initial analysis of the frontal plane force system matched the joint reaction force magnitude and allowed the application angle ß to vary. Since d_1 could be matched at one load only, the instant corresponding to the maximum resultant joint reaction force was chosen so that the model would match the data at high loads, which are more critical in prosthesis loosening. This also has the benefit of ensuring that the specimen will not experience loads unexpectedly larger than a specific preset level at any time in the test cycle. A spreadsheet data file was created to perform the required calculations. The results from the spreadsheet are then input to vendor-supplied testing machine control software. After the specimen is adjusted to the appropriate d_1, the test is run. The AP, ML, and SI forces for the eleven instants were extracted from the Kotzar data. The data consisted of a continuous curve for each of three prosthesis oriented force components. Data values were digitized for each component at each point along the curve where significant magnitude changes occurred. These values were then converted to the test system reference frame.

RESULTS AND DISCUSSION

To determine the accuracy of the model, the error between the model and the data force components was calculated. The error was normalized with respect to the peak SI load. Figure 3 shows the error history for the SI component for both stair climbing and level walking. All errors were within five percent of the peak SI load. Interestingly, waveform simulations replicate the in vivo stair climbing data even better than the level walking data. The SI component was chosen for comparison because it is the largest component of the joint reaction force, ranging from two to ten times the magnitude of the ML or AP components.

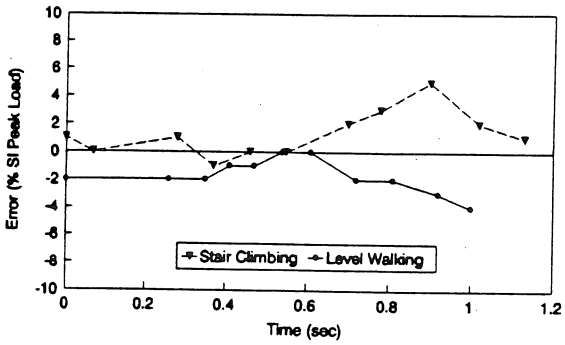

Figure 3. Error Between SI Component of Model Load and In Vivo Load

To our knowledge, this is among the first prosthesis fixation tests to use "irregular" load and torque histories patterned after actual gait data. Accurately modeling gait dynamics is important in matching the loading experienced by the prosthesis. A comparison of cycle-integrated impulse is shown in Table 1.

Table 1. Gait Cycle Impulse Calculations (%BW-s)

		AP	ML	SI
Stair Climbing	Kotzar	.358	.301	1.180
	Present	.358	.402	1.155
	Ramp	.458	.350	1.003
	Sinusoid	.583	.446	1.273
Level Walking	Kotzar	.293	.372	1.356
	Present	.293	.236	1.400
	Ramp	.236	.227	1.386
	Sinusoid	.299	.293	1.757

As expected, the new procedure exactly matches the AP component of impulse. The resultant impulse is matched within 1.0% by the new procedure. The simple ramp and sinusoidal have errors up to 8.8% and 25.8% respectively. The cumulative effects of such discrepancies would be magnified when large numbers of gait cycles are studied.

REFERENCES

Burke, D. et al. JBJS, 73-B:33-37, 1991.
Kotzar, G. et al. J. Orth. Res., 9:621-633, 1991.
Maloney, W. et al. Clin. Orth., 249:129-140, 1989.
Schneider, E. et al. J. Biomech., 22:735-744, 1989.

ACKNOWLEDGEMENTS

The authors wish to thank Zimmer for their financial and equipment support and BIOMET for supplying the prostheses.

THE EFFECT OF REALISTIC COATING PROPERTIES ON INTERFACIAL STRESSES IN POROUS COATED HIP ENDOPROSTHESES

E.A. FRIIS AND D.L. HAHN

Orthopaedic Research Institute, Inc.
929 N. St. Francis
Wichita KS 67214 USA

INTRODUCTION

Porous coatings on orthopaedic implants provide a network into which tissue may grow. The extent to which ingrowth is achieved (or not achieved) may depend on the interfacial conditions of the bone-coating interface. The effect of the coating properties on interfacial stresses in the bone has been a topic of study for several investigators. Most studies on this subject have concentrated on the effect of the coating thickness and elastic modulus on interfacial conditions.(1,2) A new porous structural material exists which exhibits an apparent negative Poisson's ratio. A previous study compared the effect of Poisson's ratio of coatings of equal stiffness on interfacial stresses in a fully-ingrown idealized finite element model of a porous coated hip endoprosthesis.(3) In this study, the effect of both Poisson's ratio and coating modulus on interfacial shear stresses are examined.

REVIEW AND THEORY

All currently used porous coatings for orthopaedic implant devices exhibit a positive apparent Poisson's ratio. A structural material has been developed which exhibits a controllable apparent negative Poisson's ratio.(4) This structure, referred to as the re-entrant structure, is formed by partial buckling of the struts of a regular open-celled foam. It can be formed from both polymeric and metallic materials.(5) Metallic re-entrant structures have been shown to exhibit apparent Poisson ratios as low as -0.8.(6) The negative Poisson's ratio materials, however, have a much lower initial apparent stiffness in comparison to the original foam structure (around 0.1 to 1.0 GPa). In addition, both the apparent Poisson's ratio and stiffness of the re-entrant structure increase with increasing applied strain.

Both the apparent negative Poisson's ratio and low initial stiffness of the re-entrant structure coating may have an effect on the interfacial stresses between the coating and adjacent bone. Foam structures of higher relative densities and therefore higher modulus (around 2 to 5GPa) and positive Poisson's ratios (around +0.3) would be typically used for a porous coating. The objective of this study was to determine the combined effect of the coating Poisson's ratio and elastic modulus by comparing maximum interfacial shear stress components in the bone at the bone-coating interface in an idealized fully ingrown porous coated hip endoprosthesis. Realistic values of coating modulus for the corresponding Poisson's ratios are examined.

PROCEDURES

A three-dimensional finite element model of one-half of a fully-ingrown idealized porous coated hip endoprosthesis was developed and analyzed with ANSYS 5.0. A hemispherical tube of 30 mm outer diameter and 20 mm inner diameter with a total length of 150 mm and linear elastic and isotropic modulus of 17 GPa was used to model the femoral diaphyseal bone. The prosthesis stem was modeled as one half of a straight cylinder with a diameter of 17 mm and modulus of 110 GPa. The porous coating filled the gap between the prosthesis and bone

with a thickness of 1.5 mm. The coating was assumed to be intimately attached to the bone. The distal end of the model was fully constrained and a unit pure bending moment of 0.5 Nm was applied at the proximal end of the prosthesis.

The apparent Poisson's ratio of the coating was varied between +0.30 and -0.5. Coating apparent modulus was varied between 0.1 and 5.0 GPa. Maximum values of the interfacial shear stress components in the bone at the bone-coating interface were determined at the distal, midsection, and proximal locations along the prosthesis. Models with regions of coatings of different properties were also analyzed.

RESULTS AND DISCUSSION

The maximum values of R-θ shear stresses in the bone at the bone-coating interface are shown in Figure 1. As shown in this graph, the R-θ shear stress is dependent on both the coating apparent Poisson's ratio and the modulus of elasticity (E). There is a trend shown in which each value of coating stiffness has a unique corresponding Poisson's ratio which yields a minimum value of R-θ shear stress. The pattern displayed with E = 2.0 GPa clearly shows this trend.

Figure 2 illustrates the maximum values of R-Z interfacial shear stress components with varying coating apparent Poisson's ratios and stiffnesses. As shown in this graph, R-Z interfacial shear stress is primarily a function of only the coating stiffness; the R-Z shear stress is decreased by increasing coating stiffness.

The final interfacial stress, radial stress, was a function of both the coating stiffness and Poisson's ratio. The direction of the radial stress, which may be important for bone ingrowth, also varied with coating properties. Results of models with regions of coatings of different properties showed that the interfacial stress magnitudes and directions could be altered by changing coating properties. Future work will include attempts to optimize coating property distribution to minimize interfacial shear stresses along the entire implant interface.

The next step in finite element analysis will be to examine the effect on interfacial stresses of non-displacement constraint boundary conditions at the interface. Mechanical testing of biocompatible foams with properties in the ranges examined in this study is underway.

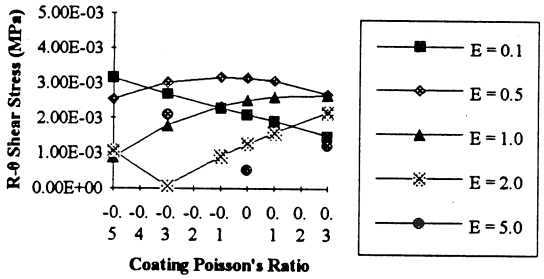

Fig. 1 R-θ Shear Stress vs Coating Poisson's Ratio, Proximal Region

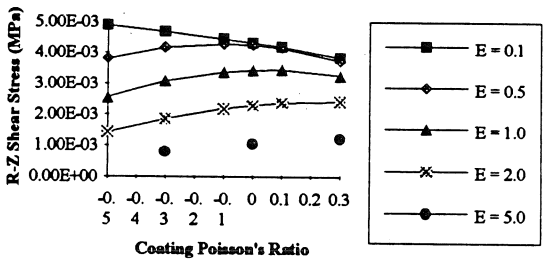

Fig. 2 R-Z Shear Stress vs Coating Poisson's Ratio, Proximal Region

REFERENCES

1. Rohlmann, A., et al. J Biomech, 21(7):695-611 (1988). 2. Ducheyne, P. et al. J Biomech, 11:297-307 (1978). 3. Friis, E.A. et al, Tran ASB, Tempe AZ, (pp. 162-63), 1991. 4. Lakes, R.S. Science, 235:1038-1040 (1987). 5. Friis, E.A. et al. J Mater Sci, 23:4406-4414 (1988). 6. Choi, J.B. and Lakes, R.S. J Mater Sci, 27:5375-5381 (1992).

RESORBABLE PARTICLE PRE-COATED CEMENT FIXATION OF IMPLANTS: AN *IN VITRO* STUDY

Y.S. Kim, J.K. Kim, S.S. Kim, and J.B. Park

Department of Biomedical Engineering
The University of Iowa, Iowa City, IA, 52242, USA

INTRODUCTION

Bone particle impregnated bone cement is one of the promising developments in bone cement fixation technique.[1] However, bone particle impregnated bone cement decreased ultimate tensile strength and impact strength of the bone, and decreased the interfacial shear strength between the prosthesis and bone mineral particle impregnated bone cement.[2] Therefore, restricting the application of the bone mineral particle impregnated bone cement next to the areas in contact with bone would appear to be more desirable.

The purpose of this study is to evaluate the effectiveness of our newly developed method in *in vitro* condition.

REVIEW AND THEORY

Bone mineral particle impregnated bone cement fixation technique has a dual-purpose:The implant is fixed immediately and later as particles are resorbed, thereby leaving space for tissue to grow into. This is similar to the biologic porous implant fixation method. Recent studies indicate that the resorbable particle impregnated bone cement can be used effectively for the rabbit and canine model.[3,4]

PROCEDURES

The canine femur was osteotomized through base of lesser trochanter at a right angle to the long axis. The intramedullary cavity was drilled and reamed to a diameter of 12mm, with a depth of 11cm. The cavity was irrigated with a saline solution. A solid PMMA tube(10cm long, 11mm diameter and 1mm thickness) was filled with bone cement and a 4mm diameter 10cm long stainless steel rod simulating prostheses was inserted in the middle. After the cement had cured, bone particles were mixed thoroughly with the powder portion of a commercially available PMMA bone cement(Zimmer, USA, Warsaw, IN). The standard powder to momomer ratio(2:1) was maintained. The mixture was stirred for 2 minutes and the dough was kneaded for an additional 2 minutes. The medullary canal was then filled with the bone mineral particle impregnated bone cement(10%, 20%, 30%), and the PMMA tube was inserted as shown in Figure 1.

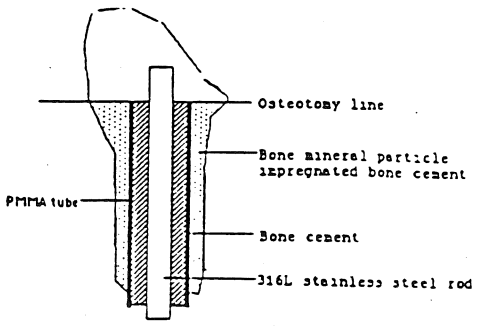

Figure 1. Schematic illustration of the longitudinal cross-section of the femur after implantation of the bone cement, bone mineral particle impregnated bone cement, prosthesis and PMMA tube.

The mechanical disc push-out tests of the prepared specimens were performed at room temperature.

Interfacial shear strength between PMMA tube and bone cement, prosthesis and bone cement, and bone and bone cement were determined by mechanical "push-out" test on a hydraulically controlled material testing machine(MTS, model 812, Minneapolis, MN). All interface were observed with SEM and confocal laser electroscanning microscope(MRC 600, Biorad Co., England).

RESULTS

The results of interfacial shear strength are plotted in Figure 1. The average interfacial shear strength between PMMA tube and bone cement was high and the values decreased linearly according to bone particle content. The average interfacial shear strength between PMMA tube and 30% bone mineral particle impregnated bone cement was more than ten times that of prosthesis and bone interface. The average interfacial shear strength between bone and bone cement was decreased linearly also as the amount of bone particles are increased.
The confocal laser scanning microscopic examination showed solid contact among PMMA tube, pure bone cement, and bone mineral particle impregnated bone cement.

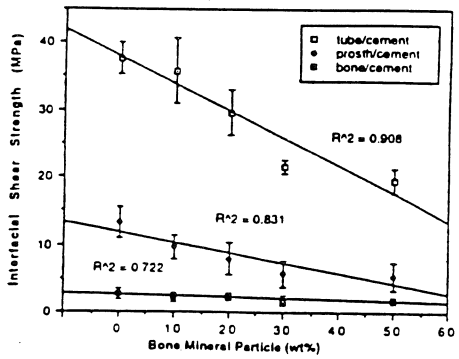

Figure 1. Comparison of interfacial shear strength.(bone-PMMA tube-prosthesis)

DISCUSSION

Using a PMMA tube would make two more interface which possibly make it more susceptible to loosening on the interface. Our results showed that the interfacial shear strength between PMMA tube and bone cement and bone mineral particle impregnated bone cement have much higher shear strength than the bone cement stainless steel rod (prosthesis) interface and closer to the shear strength values of PMMA cement. The bond between PMMA tube and bone cement is a chemical bond, rather than a mechanical bond although the degree of chemical reaction between PMMA tube and bone cement can not be measured at this time. However, EPR(electron paramagnetic resonance) studies on bone cement showed the chemical reactions takes long time and a lot of free radicals are present for long time.[5] It is clearly demonstrated that the use of thin PMMA tube can isolate the bone particle impregnated bone cement into the bone surface rather than distributed throughout the bone cement. This technique has advantages in that the resorbable particles can be in intimate contact with bone ensuring tissue ingrowth. Another advantage is that the weakening of bone cement by resorbable particles can be minimized and the delivery of the particle is very simple and effective by using the PMMA tube.

REFERENCES

1. Park, J.B. Ann. Biomed. Eng., 20, 583-594, 1992.
2. Liu, Y.K.,et al. J. Biomed. Mat. Res.,21, 247-261, 1987.
3. Park, J.B. et al. Tissue integration in oral and maxillo-facial reconstruction., D. Van Steenberghe(ed), Excerptu Media, Amsterdam, 118-124, 1986.
4. Dai, K.R. et al. J. Biomed Mater Res., 25, 141-156, 1991.
5. Park, J.B. Ann. Biomed Eng., 11, 297-312, 1983.

FORCE-VELOCITY RELATION OF THE WRIST FLEXORS AT VARIOUS ACTIVATION LEVELS

John W. Chow and Warren G. Darling

Department of Exercise Science, The University of Iowa, Iowa City, IA 52242-1111

INTRODUCTION

The purpose of this study was to quantify the force-velocity (FV) relation of the wrist flexors at various activation levels, measured as a fraction of the maximum isometric strength (F_{max}). Using the quick-release method, FV data were gathered at five different activation levels from four subjects. The FV data at different activation levels were fitted remarkably well with Hill's characteristic equation -- $F = (F_{max}b - av)/(v + b)$, where F is muscle force, v is shortening velocity, a and b are Hill constants (Hill, 1938). In general, the shortening velocity decreased with activation. Most of the a/F_{max} values at 100% and 80% activation levels lay between 0.5 and 0.6, which are somewhat greater than those obtained from isolated muscles and muscle fibers. Using normalized data, first order polynomials relating the Hill constants and activation levels were obtained. Both a and b were found to increase with increasing activation. When the FV curves were forced to converge at the maximum velocity of shortening(V_{max}), there were drastic changes in the shape of the curves, especially when v was greater than 20% of V_{max}.

REVIEW AND THEORY

One of the problems that has to be addressed when using Hill-type muscle models in movement control studies is how to modify the FV relation at sub-maximal activation. The major issue is V_{max} at different activation levels. Some investigators assume that V_{max} is constant while others assume that V_{max} decreases with activation. In other words, the former group assumes that the Hill constants are constants regardless of the activation and the later group considers the Hill constants are functions of activation.

Recent efforts have been made to quantify the force-velocity-activation (FVA) relation of skeletal muscles to provide muscle parameters for modeling purposes. Zahalak et al. (1976) attempted to relate surface electromyographic (EMG) measurements to the FV relation of the forearm flexors. Petrofsky and Phillips (1979 & 1981) and Phillips and Petrofsky (1980) expressed Hill constants as functions of activation, based on the results of quick-release (QR) experiments performed on cat muscles, In view of the limited quantitative data available on the FVA relation on human muscles, it was the purpose of this study to quantify the FVA relation of the wrist flexors.

PROCEDURES

Four paid volunteers (three male and one female) served as subjects (age 18 - 25 years) of this study. The device used for data collection is shown in Figure 1. During the trials, the subject's left forearm was constrained by the plastic polymer cast. There were two openings in the cast so that bipolar surface EMG electrodes could be placed over the medial and lateral surfaces of the forearm. The center bore of the motor pulley was fitted to the shaft of a potentiometer located underneath the table top. The weight plate holder was located directly above an electromagnet fixed to the floor.

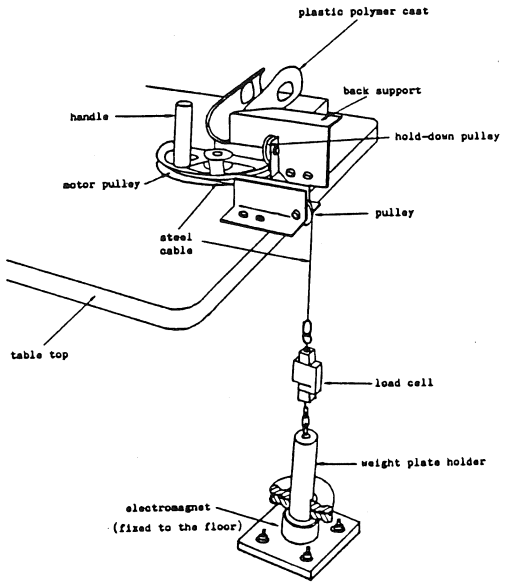

Figure 1. A custom-made device for data collection.

The tension of the steel cable and the angular position of the handle were measured by a load cell and by the potentiometer, respectively. Including the EMG signals, four channels of analog signals were filtered and amplified using a bridge amplifier before being digitized (12-bit A/D convertor) at a sampling rate of 500 Hz. The signals from the load cell were branched off to an oscilloscope stationed on the table top and displayed to the subject as a horizontal line (force line) on the CRT screen.

The data collection session started with three trials of maximum isometric flexion and three trials of maximum isometric extension contractions, from which the F_{max} and maximum rectified integrated EMG (IEMG) were established. In each of the subsequent QR trials, the load (weight plates and holder) was initially held down by the active electromagnet and the subject was asked to apply force on the handle such that the force line on the CRT screen remained at a specific position. Once the force line stayed at a target position, the load was released by switching off the electrical supply to the electromagnet. Five activation levels from 20% to 100% at intervals of 20% were employed in this study. Six different loads were used for each activation level. A total of 30 QR trials (5 activation levels x 6 loads) were conducted in each data collection session. Trials of the same activation level were conducted as a group from heavy to light loads and progressed in an order of 100%-20%-80%-40%-60%.

To compute the angular velocity, the time instant when the handle was 5° away from the release position (5° instant) was identified. The angular positions of the handle at the instants 4 ms before and after the 5° instant were then identified. The angular velocity was obtained by dividing the change in angular position by 8 ms.

Hill's characteristic equation was fitted to each set of FV data using the least-squares technique. By setting F equalled to zero, V_{max} of each subject was obtained. The force and velocity data were then normalized as a fraction of the F_{max} and V_{max}, respectively. The normalized data were pooled and Hill's hyperbolic curves were fitted to the data of the same activation level. The coefficient of determination (R^2) for each fitted curve was computed.

RESULTS AND DISCUSSION

The forces attained before QR were examined and it was found that, on average, the recorded forces of all subjects deviated from the expected forces by 2.36% (SD = 2.90%) of their F_{max}. In all trials, the angular velocity increased gradually after the release of load and started to decrease before the motion was completed. There was no noticeable duration of constant velocity.

The IEMG of the wrist extensors at different activation levels indicated that the degree of cocontraction before QR increased linearly with the activation of the agonist. On average, the normalized IEMG of the wrist extensor at maximal activation of the flexors was about 7%. Without further investigation on the effect of cocontraction, it was assumed in this study that the torque contribution of the wrist extensors was relatively small when compared with the flexors and was considered negligible.

The FV curves at different activation levels obtained from the normalized data are shown in Figure 2. As indicated by the R^2 values (0.915 - 0.998), the FV data at different activation levels for each subject could be fitted remarkably well with Hill's characteristic equation. In general, the shortening velocity decreased with activation. These findings are in agreement with those obtained for isolated muscle (Phillips and Petrofsky, 1980), but contrary to those obtained for muscle fibers (Edman, 1979). A constant V_{max} at different activation levels is not found in the whole muscle because muscles are usually formed by both fast (FT) and slow twitch (ST) fibers and ST fibers are recruited at low-force output. Therefore, the wrist flexors which have approximately equal numbers of FT and ST fibers are expected to contract slower as the activation decreases.

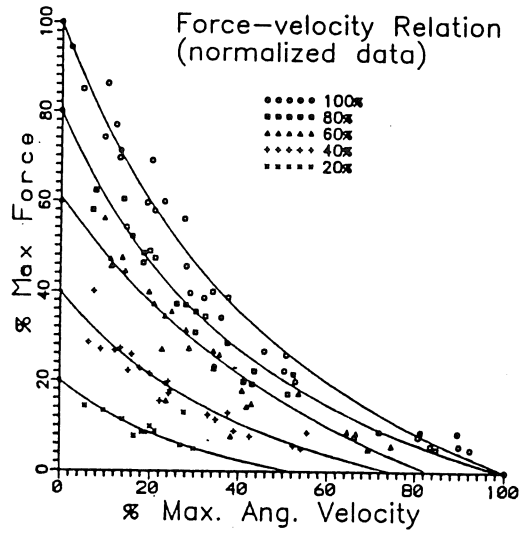

Figure 2. Normalized force-velocity curves.

Although individual difference were apparent in most of the characteristic parameters (i.e., a, b, a/F_{max}), it is worth noting that, for all subjects, most of the a/F_{max} values at 100% and 80% activation levels were in the neighborhood of 0.5 to 0.6. These values are greater than those obtained for isolated muscles and muscle fibers. (Note: The smaller the a/F_{max} value the greater curvature is the curve.)

To relate Hill constants with the activation levels, the following equations were obtained:

$$a = 0.441A + 14.94 \quad (1)$$

$$b = 0.044A + 54.72 \quad (2)$$

where A is the activation level expressed in percentage.

The FV curves at different activation levels generated by the mathematical model (Eqs. 1 and 2) fitted the normalized data very well ($0.837 < R^2 < 0.990$), indicating that the mathematical model is capable of making accurate predictions. By setting the constants $a = b$ in the parameter searching process, the FV curves were forced to converge at V_{max}. Although there were no obvious changes in the R^2 values when V_{max} was assumed constant, drastic changes were observed in the shape of the curves (indicated by the changes in a/F_{max} values), especially when the shortening velocity was greater than 20% of V_{max} (Figure 3). These results suggest that unless the movement being modeled involves a low shortening velocity of the muscles, V_{max} should be scaled with activation.

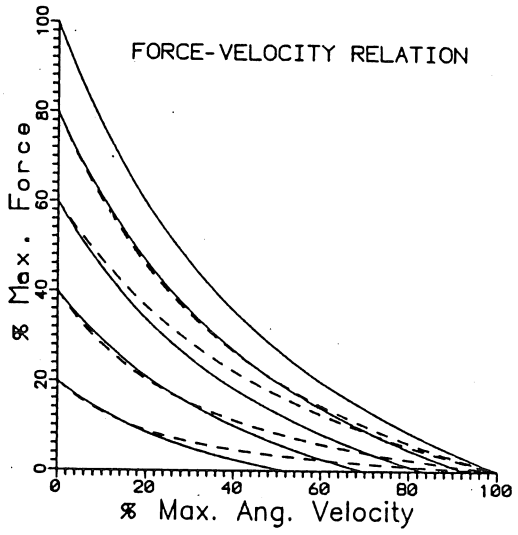

Figure 3. Comparison of force-velocity curves obtained by the mathematical model (solid line) and when the maximum shortening velocity was assumed constant (dashed line).

REFERENCES

Edman, K. *J. Physio.*, 291, 143-159, 1979.
Hill, A. V. *Proc. Royal Soc. B*, B126, 136-195, 1938.
Petrofsky, J. et al. *Med. Biol. Eng. Comp.*, 17, 583-592, 1979.
Petrofsky, J. et al. *J. Biom.*, 14, 297-306, 1981.
Phillips, C. et al. *J. Biom.*, 13, 549-558, 1980.
Zahalak, G. et al. *J. Appl. Mech.*, 1, 81-86, 1976.

RELATIONSHIPS BETWEEN MAXIMUM EFFORT ISOMETRIC AND CONCENTRIC-ECCENTRIC ISOKINETIC TRUNK EXTENSION FORCES

M.D. Grabiner
Department of Biomedical Engineering
The Cleveland Clinic Foundation, Cleveland, OH, 44195.

INTRODUCTION

The changes affecting today's health care system may further increase an already present need for valid and accurate quantitative tests of motor function. Isokinetic testing has been suggested as having "considerable inferential value" with regard to muscle function (Sapega, 1990). However, isokinetic technology as a clinical tool to rehabilitate and evaluate trunk muscle function has been limited not only by a lack of standardized procedures but by a lack of agreement as to the proper method to assess muscle function as well as the appropriate muscle function to assess (Garrett et al., 1989). The historical trunk muscle functions that have been studied are strength and endurance. The general methods of assessment include static vs. dynamic muscle contraction. The relationships between static and dynamic measurements of trunk muscle function have not been clearly defined.

Isokinetic evaluation requires selection of various test parameters. Because muscle function variables are sensitive to the selected test parameters the selection will directly influence the results of the assessment. Test parameters include isokinetic velocity (speed and contraction type), the range of motion, and the joint angles at which performance measurement will be made.

Isometric testing of the trunk extensors provide numerous measurement benefits in a clinical testing and rehabilitation environment but there are conflicting opinions as to the functional relationships between isometric and dynamic strength (Sapega, 1990, Andersson et al, 1989). The purpose of this study was to characterize functional relationships between trunk extensor function as measured by peak force during isometric, isokinetic concentric and isokinetic eccentric conditions.

PROCEDURES

Ten male and female recreationally active subjects without recent history of low back pain volunteered for participation. Maximum effort isometric and isokinetic trunk extension strength were measured using a Kin-Com isokinetic dynamometer. Maximum isometric trunk extension strength was measured at five trunk angles: vertical (relative to the room), 15 and 30 degrees of extension and flexion, respectively from vertical. Isokinetic measurements were extracted at the same angles as the subjects executed maximum effort contractions through a 70 degree range of motion; 35 deg on either side of vertical. Isokinetic trunk extension was performed concentrically and eccentrically at 30, 60, 90, 120, 150, 180, 210, and 250 deg/s. The contractions were performed individually and alternated between concentric and eccentric. The order of isokinetic velocity was fixed, beginning at 30 and subsequently progressing to 250 deg/s. Each isokinetic effort was preceded by a brief isometric trunk extension generating 25 percent body weight. The peak trunk extension force from each trial was extracted for each angle from the digitzed data and expressed as a percentage of body weight. The isometric data were first analyzed using a 5-way repeated measures ANOVA in which the analyzed factor was trunk angle. For each of the five trunk angles measured, stepwise forward regression was used to characterize the relationships between peak isokinetic trunk extension force and isokinetic velocity (-250 to 250 deg/s). Independent variables used were the maximum isometric trunk extension force, and linear, quadratic, and cubic representations of isokinetic velocity. The presence of functional redundancies was investigated using correlation and regression analyses.

RESULTS AND DISCUSSION

Maximum isometric trunk extension force was significantly affected by trunk angle ($p<0.05$). Post hoc multiple comparisons revealed that the maximum trunk extension force at 30 degrees trunk extension was significantly less than that at other trunk angles which were not significantly different from one another. The results of the multiple regression revealed that for each trunk angle, statistically significant predictions of peak concentric and eccentric trunk extension forces could be calculated using only the independent variables related to isokinetic velocity. The stepwise regression rejected maximum isometric trunk extension force as a predictor variable in all cases. Notably, the level of statistical strength of the regressions performed on the 30 degree flexion and extension data was less than that of the predictions from the middle of the range of motion.

With a singular exception, the correlations between maximum isometric trunk extension force and peak isokinetic trunk extension force at all trunk angles and isokinetic velocities were nonsignificant and of weak to moderate amplitude (-0.52 to 0.43). Regression analysis revealed that significant prediction of peak trunk extension force at the vertical trunk angle (the middle of the range of motion) could be obtained for concentric speeds up to 150 deg/s using only the peak trunk extension force value from the 30 deg/s condition (all adjusted $R^2 > 0.73$). Peak eccentric trunk extension forces could not be predicted using the 30 deg/s concentric contraction peak trunk extension value. Regression was less successful, although still statistically significant, in predicting peak eccentric forces for speeds up to 150 deg/s using the 30 deg/s eccentric contraction peak trunk extension value (adjusted R^2 0.33 to 0.56).

The results of the present study highlight several points relative measurement of trunk extensor function. Most notably, the results demonstrate an independence between maximum effort isometric and isokinetic trunk extension performance, and within isokinetic performance, an independence between concentric and eccentric performance. In part, this independence reflects the findings that with the exception of the 30 degree extension angle maximum isometric trunk extension force remained constant through the range of motion. The data tend to support increases in maximum effort during eccentric contractions but these increases are modulated by both trunk angle and speed.

Thus, the results of the present study demonstrate a statistical independence and suggest a functional independence of maximum effort isometric and isokinetic trunk extension force. Maximum effort concentric and eccentric trunk extension efforts also seem to be somewhat independent. These relationships may be useful in designing and interpreting outcomes of rehabilitation protocols.

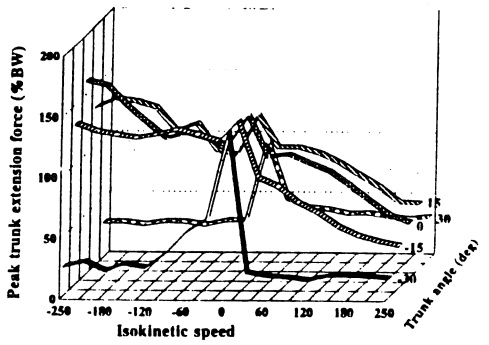

Mean data for 10 subjects performing maximum effort isokinetic and isometric trunk extension (negative velocities are eccentric contractions)

REFERENCES

Andersson et al: New Perspectives in Low Back Pain, Frymoyer and Gordon, 1989.

Garrett et al: New Perspectives in Low Back Pain, Frymoyer and Gordon, 1989.

Sapega: JBJS, 72-A:1562-1574, 1990.

ACKNOWLEDGMENTS

This work was supported by **Chattecx Corporation**
The author would like to express appreciation to L. vonHafen who assisted in the data collection

STRETCH-SHORTENING CYCLE KINEMATICS AND MUSCLE FORCE POTENTIATION OF THE RAT TIBIALIS ANTERIOR MUSCLE

David Hawkins

Department of Physical Education
University of California
Davis, California 95616

INTRODUCTION

A study of the rat tibialis anterior (TA) muscle-tendon (MT) complex was conducted to investigate the relationship between muscle force and stretch-shortening cycle variables of stretch rate, stretch amplitude, and initial muscle length. Stretch amplitudes of 1 mm, 2 mm, 3 mm, and 4 mm were imposed on active muscle at rates of 1 mm/s, 10 mm/s, and 100 mm/s. Stretches were initiated from MT lengths ranging from 4 mm less than the optimum length, to 2 mm greater than the optimum length. Muscle force recorded at the end of each stretch was compared to the isometric force generated by the muscle at a length equal to the previously stretched MT length.

REVIEW AND THEORY

There are many factors which affect a muscle's ability to generate force, some of which are muscle length, shortening velocity, activation level, architecture, and contraction history. The first four of these factors have been considered in numerous mathematical muscle models derived to predict muscle force (Coggshall et al., 1970; Pell et al., 1972; Hatze, 1981; Caldwell et al., 1989; Hawkins, 1990). However, the effects of contraction history on muscle force have not been well defined and as a result these effects have been ignored in mathematical models. Contraction history refers to a muscle's previous activation level, duration of contraction, and kinematics. If a stretch-shortening cycle (SSC) (i.e. eccentric contraction followed by a concentric contraction) takes place, then the muscle force may be potentiated during shortening compared to a similar contraction executed without the preceding eccentric contraction (Edman et al., 1978). The objective of this study was to investigate the relationship between muscle force potentiation, initial MT length, and the kinematics of the SSC in rat skeletal muscle.

PROCEDURES

The work station used to collect the data for this study consisted of several components. The hardware included an arbitrary waveform generator (Model 75 supplied by WaveTek), an ergometer lever system (Model 305B supplied by Cambridge Technologies), a video-based motion analysis system (Motion Analysis Corporation), and a microcomputer containing a Lab Master DMA data acquisition board (Scientific Solutions).

The TA muscle-tendon complexes of five female Holtzman rats (avg. wt. 3.18 $\pm$ 0.26 N) were tested. The rats were anesthetized by an intraperitoneal injection of pentobarbitone sodium (50 mg/kg body wt.). Tissue covering the TA was carefully removed and a small electrode cuff was positioned around the TA nerve. The distal end of the TA-bone complex was dissected free and attached to the lever arm of an ergometer. Three small black silicone markers were located along the muscle-tendon complex, one at the proximal end of the muscle, one at the muscle-tendon junction, and one at the bone-tendon junction. The tibia was secured in a fixture with the TA positioned in front of a video camera. All mechanical tests were conducted at room temperature 24 $\pm$ 2 °C with a saline drip system used to maintain the TA moist at all times.

Two tests were required to determine the muscle's optimum length (lo). Muscle force was recorded while the MT complex was passively stretched, and again while the muscle was stimulated maximally at different initial MT lengths. "lo" was identified as the length at which the active force (i.e. total force minus passive force) reached a maximum. After determination of "lo", a series of active stretch and hold cycles were imposed on the MT complex. The MT complex was stretched from initial lengths ranging from 4 mm less than "lo" to 2 mm greater than "lo". Stretch amplitudes of 1 mm, 2 mm, 3 mm and 4 mm were used. Stretches were performed at rates of 1 mm/s, 10 mm/s, and 100 mm/s. Each stretch cycle was recorded on video tape at 200 Hz while the muscle force was sampled by a computer at 1400 Hz. The muscle force at the end of a stretch was divided by the isometric force generated by that muscle while held at a length equal to the stretched MT length. Force potentiation was defined to exist if this ratio was greater than one.

RESULTS

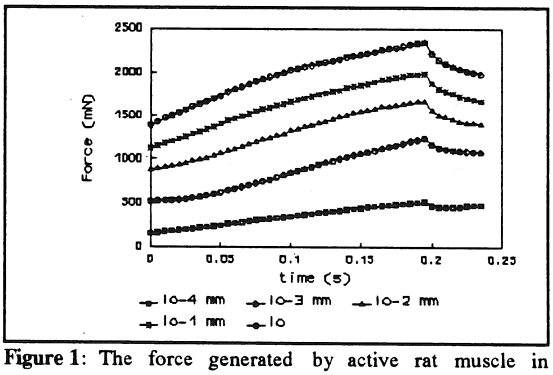

Figure 1: The force generated by active rat muscle in response to five stretches of 2 mm performed at 10 mm/s.

Examples of the data collected during five stretch and hold trials are illustrated in Fig. 1. The five stretches were initiated from initial MT lengths of lo-4 mm, lo-3 mm, lo-2 mm, lo-1 mm and lo. The stretch rate was 10 mm/s and the stretch amplitude was 2 mm. During each trial the force generated by the muscle at the end of a stretch was greater than or equal to the force generated at the beginning of the stretch.

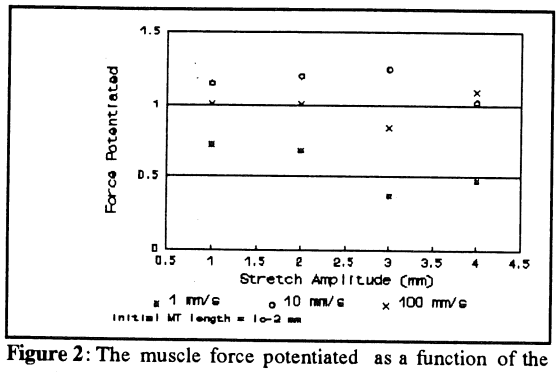

Figure 2: The muscle force potentiated as a function of the stretch amplitude and stretch rate for an initial MT length of lo-2 mm.

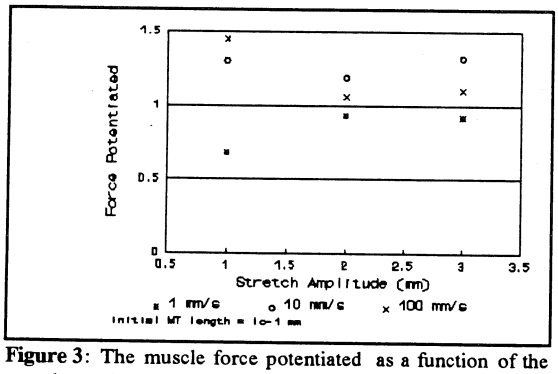

Figure 3: The muscle force potentiated as a function of the stretch amplitude and stretch rate for an initial MT length of lo-1 mm.

However, the force at the end of a stretch was not always greater than the isometric force generated by the muscle at that same final length. Thus, the amount of force potentiation was dependent on the stretch conditions.

The averaged force potentiation data were more sensitive to the initial MT length and to the stretch rate than to the stretch amplitude. For initial MT lengths less than lo-3 mm the force was potentiated very little and only during stretch rates of 10 mm/s. There was no force potentiation for all trials at the slow stretch rates of 1 mm/s. The average force potentiated during stretch cycles initiated from initial MT lengths greater than lo-3 mm increased with increased initial MT length and was greatest for a stretch rate of 10 mm/s. At this rate, the force potentiation increased from approximately 15 % to 25 % as the initial MT length was increased from lo-2 mm to lo-1 mm. For a stretch rate of 100 mm/s, very little force potentiation occurred for an initial MT length of lo-2 mm, but some did occur for an initial MT length of lo-1 mm. Fig. 2 and Fig 3. illustrate these results for initial MT lengths of lo-2 mm and lo-1mm respectively.

DISCUSSION

Cavagna et al. (1985) theorized that force potentiation created by a stretch-shortening cycle is primarily due to an increased force per attached cross-bridge. If the site of force potentiation resides in the cross-bridges, then it follows that the amount of force potentiation would be affected by the initial MT length, the stretch amplitude, and the stretch rate. For MT lengths less than the optimum length, fewer cross-bridges can be formed and hence less force would be available for potentiation. Further, a cross-bridge can withstand only a finite amount of stretch before breaking, hence large stretch amplitudes would not be expected to produce significant amounts of force potentiation. Also, since cross-bridges can break or yield at high stretch rates, the force potentiated would be expected to decrease for fast stretch rates.

Data from this study indicate that two of the three variables tested do influence the muscle force potentiation. The greatest force potentiation occured for initial MT lengths of 1 mm and 2 mm less than "lo" and at a stretch rate of 10 mm/s. The relative independence of the amount of force potentiated relative to the MT stretch amplitude observed may be due to interaction of the muscle and tendon. It may be that during an active stretch of the MT complex, the muscle stretches very little while the tendon accounts for most of the MT stretch. This idea is currently being investigated through analysis of the video data which allows length changes in both the muscle and tendon to be quantified.

REFERENCES

Caldwell, G. et al. *Comp. in Biol. and Med.* 19, 17-434, 1989.
Cavagna, G., et al. *J. Exp. Biol.* 115, 79-87, 1985.
Coggshall, J. et al. *Math. Biosci.* 7, 405-419, 1970.
Edman, K. et al. *J. Physiol.* 281, 139-155, 1978.
Edman, K. et al. *J. Gen. Physiol.* 80, 769-784, 1982.
Hatze, H. Myocybernetic control models of skeletal muscle. Muckleneuk, Pretoria, 1981.
Hawkins, D., Ph.D. Dissertation, UCD, 1992.
Pell, K. et al. *Am. J. Physiol. Med.* 51, 23-28, 1972.

ACKNOWLEDGEMENTS

The author is grateful to Michael Bey for conducting the experiments in this study, James Vannes for his technical assistance, and the Whitaker Foundation for their financial support.

MUSCLE AND TENDON STRUCTURAL PROPERTIES AND THEIR INTERACTIONS IN-VIVO: A STUDY OF THE RAT TIBIALIS ANTERIOR MUSCLE

David Hawkins

Department of Physical Education
University of California
Davis, California 95616

INTRODUCTION

An experimental study was conducted to determine the range of structural properties experienced by muscle and tendon in-vivo and to determine the effect that tendon compliance has on muscle force generation. The rat tibialis anterior (TA) muscle-tendon (MT) complex was used as the experimental model. Muscle and tendon lengths as they occurred in the body during ankle joint motion ranging from 20° to 90° of flexion were determined for both passive and maximally stimulated muscle. Structural properties (i.e. force-length relationships) for the tendon, passive muscle, and active muscle were determined from a partially isolated MT preparation.

REVIEW AND THEORY

The passive and active structural properties of isolated muscles, fibers and tendons have been well documented (Huxley et al., 1954; Gordon et al., 1966; Huxley, 1969; Herzog et al., 1992; Gareis et al., 1992; Lieber et al., 1992). However, very little is known about these properties and their interactions in-vivo. The objectives of this study were to determine the normal in-vivo operating range of structural properties of tendon and both passive and active muscle and to evaluate the functional significance of (MT) interactions.

PROCEDURES

The work station used to collect the data for this study consisted of several components. The hardware included an arbitrary waveform generator (Model 75 supplied by WaveTek), an ergometer lever system (Model 305B supplied by Cambridge Technologies), a video-based motion analysis system (Motion Analysis Corporation), and a microcomputer containing a Lab Master DMA data acquisition board (Scientific Solutions).

The TA muscle-tendon complex of six female Holtzman rats (average wt. 2.90 $\pm$ 0.08 N) were tested. The rats were anesthetized by an intraperitoneal injection of pentobarbitone sodium (50 mg/kg body wt.). Tissue covering the TA was carefully removed and a small electrode cuff was positioned over the TA nerve. Two small black silicone markers were located on the muscle, one at the proximal end and the other at the muscle-tendon junction. The TA, in both a passive and an active state, was recorded on video tape while the foot was held first in a fully extended position (approximately 20° of flexion) and then in a 90° flexed position. The distal end of the TA-bone complex was then dissected free and attached to the lever arm of an ergometer. The TA was again positioned in front of the video camera and the tibia secured to a fixture to minimize movement of the limbs during testing. An additional silicone marker was placed at the distal tendon-bone junction. All mechanical tests were conducted at room temperature 24 $\pm$ 2 °C with a saline drip system used to maintain the TA moist at all times.

The force generated by the TA was determined during both a passive and a series of active test. The tests were initiated from a lever arm position at which the stimulated muscle transmitted minimal force to the lever arm. During the passive test, the non-active MT complex was stretched 10 mm at a rate of approximately 2.0 mm/s. During the active test, the muscle was stimulated to contract isometrically at 0.2 mm increments over the same 10 mm range used in the passive test. During both tests, force, lever arm position, and video data were collected at 60 Hz. Muscle and tendon lengths were determined from the video data and an automated digitizing system, and then consolidated with the muscle force data.

RESULTS

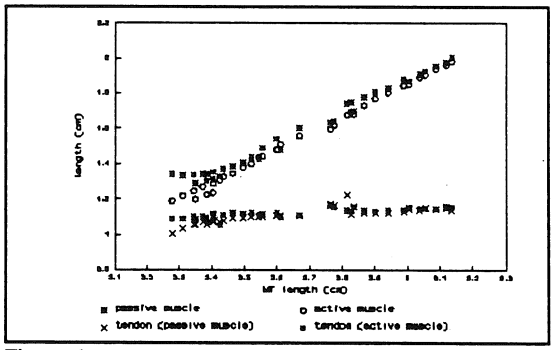

Figure 1: The relationship between MT length, muscle length, and tendon length for both passive and active muscle.

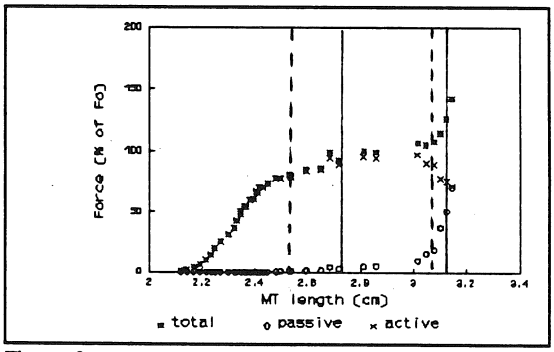

Figure 2: The relationship between MT length in-vivo and total, passive, and active muscle force.

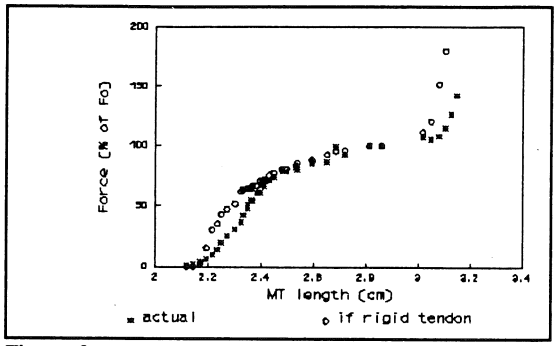

Figure 3: The effects of tendon compliance on the force generated by a muscle in-vivo.

Data obtained from all rat muscles were similar to those illustrated for a single muscle in Fig. 1, Fig. 2, and Fig. 3. Fig. 1 illustrates the relationships between MT length, muscle length, and tendon length for both passive and active muscle. With the exception of short MT lengths, changes in MT length were achieved primarily by changes in muscle length.

Fig. 2 illustrates the normalized total, passive, and active muscle forces. Active force was calculated by subtracting the passive force from the total force. Total muscle force was zero for MT lengths less than 2.1 cm and increased for lengths between 2.2 cm and 2.5 cm. The total muscle force had a plateau for MT lengths between 2.5 cm and 2.9 cm and increased rapidly for longer lengths. The muscle's passive and active MT lengths in-vivo are identified with the solid and dashed vertical lines respectively, for both the foot flexed 20° and 90°.

Fig. 3 illustrates the effects that a compliant tendon has on the force generating potential of the TA in-vivo. For purposes of comparison, a rigid tendon was modeled with a length equal to the tendon length under zero load. Tendon compliance does not affect the muscle force over the normal ROM experienced in-vivo, however, it does have an effect at the extremes of motion. During full extension, the compliant tendon allows greater motion before the rapid increase in passive force occurs. During extreme flexion, the compliant tendon reduces the force generating potential of the muscle.

DISCUSSION

The foot ROM examined in this study was 20° to 90° of flexion, however, the normal ROM of the rat foot is approximately 35° to 135° of flexion. Based on estimates from intact MT complexes the additional flexion from 90° to 135° would cause a MT length change of 2 mm. Therefore, for the foot fully flexed, the muscles's average minimum passive and active MT lengths in-vivo would be about 2.64 and 2.44 respectively. For normal foot extension the MT length would be about 3 cm for both a passive and an active muscle. It is evident from Fig. 1 and the lengths just cited, that very little passive force and nearly constant total force is developed over the normal ROM. Outside of this range, the force decreases for joint flexion, and increases rapidly for joint extension. This type of response appears to facilitate the muscle's function within the body. It can generate maximum active force and minimal passive force over a normal ROM. Thus, the muscle can generate forces to move the limb, yet not produce forces to inhibit motion produced by antagonist muscles. For extreme joint extension, the passive force increases rapidly to assist in stabilizing the joint.

The benefit of tendon compliance to muscle function is not readily apparent form the results of this study. For the rat TA muscle, tendon compliance does not alter the force generated by the muscle over a normal joint ROM. However, it does effect the muscle's ability to generate force at the extremes of joint motion; allowing greater joint extension before large passive muscle forces are developed, and reducing the muscle force potential for extreme joint flexion.

REFERENCES

Gareis, H. et al. *J. Biomech.*, 25, 903-916, 1992.
Gordon, A. et al. *J. Physiol.*, 184, 170-192, 1966.
Herzog, W. et al. *J. Biomech.*, 25, 945-948, 1992.
Huxley, A.F. et al. *Nature*, 173, 971-973, 1954.
Huxley, H.E. *Science*, 164, 1356-1366, 1969.
Lieber, R. et al. *J. Biomech.*, 25, 421-428, 1992.

ACKNOWLEDGEMENTS

The author is grateful to Michael Bey for conducting the experiments, James Vannes for his technical assistance, and the Whitaker Foundation for financial support.

A MODELING APPROACH FOR DETERMINING LOWER EXTREMITY JOINT ANGULAR VELOCITIES WHICH MAXIMIZE THE POTENTIAL FOR MUSCLE POWER PRODUCTION

David Hawkins

Department of Physical Education
University of California
Davis, CA 95616
USA

INTRODUCTION

A computer program was developed to calculate lower extremity joint angular velocities which allow specific muscles, if activated, to generate their greatest power. This program is modular in structure, allowing the use of either generic musculoskeletal information, or information specific to a given individual. Additionally, the joint configurations to be studied can be specified directly or read from a file containing actual movement analysis data. The program outputs a set of joint angular velocities which satisfy the maximum power based criterion for each muscle considered in the simulation. To test this approach, theoretical knee angular velocity data were determined for a simple knee extension task and compared to experimental results.

THEORY AND REVIEW

Maximizing the power output of the human body is often a primary objective in sport and work related activities. Power is defined as the rate at which energy is transferred, generated, or used. Thus, power represents the capacity of a machine, or for studies of human movement, the body, to do work or deliver energy. Power output is a critical consideration in physical activity requiring large amounts of work to be done over a short period of time.

To maximize the power output of the human body, the coordinated power output of individual muscles must be maximized. The power developed by a skeletal muscle is the product of the force it generates and its shortening velocity. Further, muscle force depends on its shortening velocity which depends on gross limb kinematics. Thus, muscle kinematics are coupled to limb kinematics through tendon compliance and musculoskeletal geometry.

The purpose of this study was to develop a method for determining lower extremity joint angular velocity profiles which allow individual muscles, if activated, to generate their greatest power. This was accomplished by developing an interactive computer program which utilizes a musculoskeletal modeling scheme. A summary of this program and methodology is given below followed by an example of its utility.

PROCEDURES

The software used to determine joint angular velocities which allow a muscle to shorten at a rate conducive to maximizing its power output involves four input stages, two analysis stages, and one output stage. The four input stages require 1) gross subject anthropometrics, 2) muscle specific parameters, 3) gross limb kinematics, and 4) muscle origin/insertion attachment location data. The two analysis stages involve 1) the determination of individual muscle-tendon lengths for each joint angle configuration, and 2) the determination of joint angular velocities which are most conducive for individual muscles to generate their greatest power. Joint angles and angular velocity data are written to a file in the output stage.

A subject's gross anthropometric parameters must be quantified in the first stage. This can be accomplished through the procedures described by Hawkins (1992). Anthropometric data are used to calculate limb masses, center of gravity locations, and moments of inertia based on regression equations derived for men by Plagenhoef (1983). Anthropometric data are also used to scale muscle-tendon origin/insertion location data according to the procedures outlined by Brand et al. (1982).

The power developed by a muscle depends on its relative shortening velocity, and this velocity depends on architectural features of the muscle. Therefore, parameters related to a muscle's architecture must be defined. These parameters include the average rest length (Lfo) of the muscle fibers and the angle of pinnation (β) that these fibers make relative to the line of pull of the muscle-tendon complex. These parameters, for the 47 muscles modeled by Brand et al. (1982), were defined in a file for use with this program. Parameter values were taken from several sources summarized by Yamaguchi et al. (1990). The user of this software may utilize these generic values or choose to modify them to reflect subject and muscle specific information.

The lower extremity joint angle configurations that may be considered in an analysis can be specified in two ways. The user can specify either that a range of joint angles be simulated for each joint (i.e. hip, knee, ankle), or that a set of joint angles be read from a file created from an actual movement analysis. Method one allows either individual joints to be considered, for example by limiting the range of other joints, or specific joint configuration combinations. The second method is particularly useful in the study of constrained movements in which the range of joint motion remains fairly consistent and independent of the cadence (e.g. cycling, rowing).

Muscle origin/insertion attachment locations may also be specified using two methods. Either muscle origin/insertion attachment location data are defined using the scaled data from Brand et al. (1982) and anthropometric scaling factors, or they are expressed as absolute values relative to local coordinates. The second approach provides more accurate information, but it requires that the user determine these muscle attachment locations for the subject being studied (e.g. using magnetic resonance imaging). Once the above input data are specified, then muscle-tendon lengths are calculated using a straight-line approximation. The details of this calculation are described in Hawkins (1992).

Several steps are involved in determining the optimal joint angular velocity, for each muscle, joint, and joint angular position. First, the shortening velocity which allows a muscle to generate its greatest power must be identified. The maximum power produced by skeletal muscle is achieved for a shortening velocity equal to about 30 % of the muscle's maximum shortening velocity (Edgerton et al., 1986). Further, the maximum shortening velocity ($Vmax_m$) of a muscle has been estimated to be ten times the average resting length (Lfo) of the fibers within the muscle (Close, 1973). Thus, the optimal muscle shortening velocity ($Voptimal_m$) for power production was defined to be $3(Lfo_m)$.

In the second step, a finite difference technique Is used to express muscle velocity (V_m) in terms of muscle length (L_m) for each instantaneous joint angle configuration. It was assumed that the tendons act as rigid links so that changes in MT length equal changes in muscle length.

In the third step, the optimal time between successive joint angle configurations is determined. If the muscle shortening velocity is defined to be equal to the optimal shortening velocity, then the time (dt) between successive joint angle configurations can be expressed as:

$$dt = [L_{m,(i+1)} - L_{m,i}]/Voptimal_m \quad (1)$$

where:

i - represents the ith joint position
m - represents the mth muscle

In the fourth step, joint angular velocities (ω) which maximize the power potential for each muscle and each joint configuration are calculated using a finite difference technique and the time (dt) defined above. Joint angular position and velocities are output as the final step in the program.

The program described above can be used to determine joint angular velocities for the hip, knee and ankle which provide specified muscles the greatest potential for power production. However, for the sake of brevity, only a simple knee extension task was considered here. The primary muscles responsible for knee extension are the rectus femoris, vastus lateralis, vastus intermedius, and the vastus medialis. Therefore, these four muscles were modeled and the knee extension angular velocities which provide these muscles their greatest potential for power production were calculated. A subject was modeled to have anthropometric parameters similar to those described by Hawkins (1992). Theoretical knee extension angular velocity data were compared to experimental data presented by Perrine (1986).

RESULTS AND DISCUSSION

Results from the theoretical analysis of the knee extension movement are illustrated in Fig. 1. The optimal joint angular velocity remains constant for each muscle across the range of motion considered (140° to 0° with 0° being full extension). However, the magnitude of the joint angular velocity is different for each muscle due to differences in the modeled muscle geometries. The rectus femoris was modeled to have the shortest fibers (5.54 cm) hence the slowest optimal knee angular velocity (143 °/s). The vasti muscles were modeled to have similar fiber lengths (7.3 cm - 7.9 cm), hence the optimal joint angular velocities for them were similar at about 205 °/s.

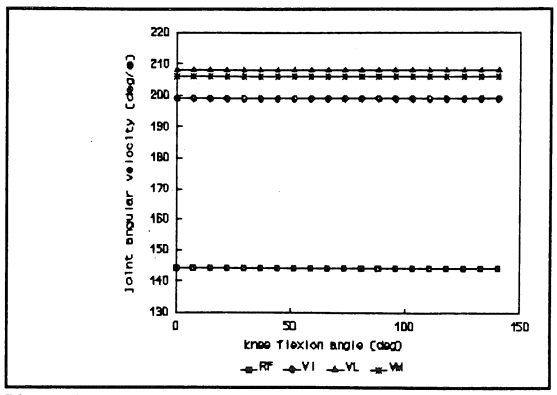

Figure 1: Illustrated are the theoretical knee joint angular velocities for maximizing the power produced by the rectus femoris (RF), vastus lateralis (VL), vastus intermedius (VI), and vastus medialis (VM).

Maximum power production during a simple knee extension task was reported by Perrine (1986) to occur for a knee extension angular velocity of 245 °/s. This value is comparable to the theoretical value of 205 °/s based on the vasti muscles. Discrepancies between the theoretical and experimental data are likely the result of variations between the modeled and the actual subject's musculoskeletal geometry. Subject anthropometric data were not reported by Perrine (1986) and hence could not be accurately modeled in the computer simulation.

The modeling and computer simulation program described above provides a useful tool for predicting joint kinematics which produce the most favorable muscle kinematics for maximizing muscle power. The program allows the utilization of either generic musculoskeletal parameter values or subject-specific ones. The utilization of generic values is appropriate for studying and identifying fundamental relationships between musculoskeletal form and function. The utilization of subject-specific quantities allows the most appropriate limb kinematics for a given subject and movement task to be determined.

REFERENCES

Brand, R. et al. *J. of Biomed. Eng.*, 104, 304-310, 1982.

Edgerton, V. et al. Chp. 4 in *Human Muscle Power*, (pp. 43-64), 1986.

Hawkins, D. *Comp. in Biol. and Med.* , 22, 59-71, 1992.

Perrine, J. Chp. 2 in *Human Muscle Power*, (pp. 15-25), 1986.

Plagenhoef, S. *Res. Quart. for Ex. and Sport*, 54, 169-178, 1983.

Yamaguchi, G. et al. Appendix in *Multiple Muscle Systems: Biomechanics of Movement*, (pp. 717-773), 1990.

Measuring Intervertebral Kinematics Using A Videofluoroscope System

Raymond R. Brodeur, DC, PhD and Daryl Hansmeier, BS
Research and Graduate Studies, Palmer College of Chiropractic, Davenport, Iowa

INTRODUCTION

Videofluoroscope (VF) technology has the potential to provide enormous amounts of information regarding the kinematics of the spinal column. However, little work has been done to quantify the accuracy and reliability of measuring intervertebral motion from VF images. The variability of the angle calculations from VF images of an in-vivo lateral cervical spine examination were compared to those of a dry spine model. Video frames were captured from VF images of the dry spine model in 11 positions. For the in-vivo study, we captured video frames at 3 Hz (every 10th video frame) for a total of 25 frames over an entire flexion-extension-flexion cycle. The variability of the angle calculations were determined by repeating the measurements of landmarks on each of the captured video frames four times. The absolute errors in the angles calculated from the images of the dry spine model ranged from 0.0° to 2.0° with an average absolute error of 0.89° and an overall standard deviation (SD) of 1.03°. For the in-vivo study, more than 85% of the angle calculations had a SD of less than 1.5° and an overall average SD of 1.1°. Our results indicate that in-vivo angle calculations can be determined with sufficient accuracy to study the intervertebral motion of the cervical spine. The intervertebral angles from a single VF lateral cervical spine examination are presented.

REVIEW AND THEORY

The in-vivo study of cervical spine intervertebral kinematics has been done with plain film radiography. Dvorak, et al (1991, 1993) investigated cervical spine intervertebral ranges of motion (ROM) using flexion/extension radiographs. They studied asymptomatic subjects and subjects with functional disorders of the cervical spine. The subjects with functional disorders of the cervical spine had differences in intervertebral ROM as well as in the location of the center of rotation (CR) when compared to asymptomatic subjects. Kraemer and Patris (1989, 1990) also studied the patterns of cervical mobility using flexion/extension radiographs. They compared subjects with cervical trauma to a control group. The injured subjects had a statistically significant decrease in the global ROM as well as having far more frequent "locked" joints (intervertebral joints with a ROM less than 2°) compared to the control group.

Plain-film x-rays provide an excellent means of studying the end ranges of motion, but they are not well suited to the study of mid-range motion. Videofluoroscope technology provides a means for studying intervertebral kinematics through the entire range of motion. Cholewicki, et al (1991) used a videofluoroscope system to measure the intervertebral motion of L3/L4 during specific movements. They used a vertebral model to assess digitizing error and found a mean absolute error of 0.69° (SD = 0.43°). In an effort to expand the study of intervertebral motion of the cervical spine, we examined the accuracy and repeatability of angle measurements for our VF system and present the results of an in-vivo cervical spine flexion-extension-flexion examination.

PROCEDURES

Dry Spine Study

Intervertebral motion was simulated using a model constructed from two dry lumbar vertebrae. Videofluoroscope images of the model were acquired for 11 positions, ranging from (+)14° extension to (-)14° flexion, and recorded on super-VHS video tape. The position of two landmarks on each vertebra were measured for all 11 images. This procedure was repeated four times for each of the 11 images, providing a means of determining the variability of the digitizing process. The angles were calculated for changes in the position of the top vertebra relative to the bottom vertebra. These calculations were made for all possible permutations of angle changes for the 11 positions. Thus, there were several measurements made for each angle, with the angles ranging from 2° to 28°.

In-Vivo Cervical Spine Study

A single subject was asked to flex and extend her head while being given a videofluoroscope examination. A time-code generator was used to label each video frame. Radiolucent spheres were attached to the skin at the occiput level to provide landmarks for measuring positional changes. The VF images, with time-code labels, were recorded on super-VHS videotape. A video capture board was used to import select video frames for display on a computer monitor. The flexion/extension motion of the subject was approximately eight seconds long, with more than 240 video frames. In order to reduce the volume of data, we captured video frames at 3 Hz (ie, every 10th video frame) for a total of 25 frames over a complete flexion-extension-flexion cycle. Since the motion was at approximately 0.125 Hz, sampling at 3 Hz is sufficient to describe the vertebral kinematics. The positions of the two anterior corners of the vertebral bodies and two points on the lamina-spinal junction were measured for C3-C7. For C2, the radiographic image of the junction of the facet with the dens was used in place of the anterior-superior corner of the body. For C1 two points were measured at the anterior tubercle and two at the posterior tubercle. The radiolucent spheres were digitized as landmarks for the occiput. The 25 frames were digitized four times each. The variability in the angle calculations were compared to those from the dry spine study.

RESULTS AND DISCUSSION

Dry Spine Study

The average changes in the angles calculated from the four measurements of each of the dry spine positions were compared to those measured by the goniometer attached to the two vertebra. The absolute value of the average error ranged from 0.0° to 2.0° with an overall absolute error of 0.89° (SD = 0.58°). The standard deviations (SD) of the error ranged from 0.1° to 2.3° with an overall standard deviation of 1.03°.

In-Vivo Cervical Spine Study

The variability of the in-vivo intervertebral angle calculations are comparable to those from the dry spine study. The vast majority of the angle calculations had SD below 2.0° (6 out of 182 had SD greater than 2.0°, 29 had SD greater than 1.5°). Thus, the variability was on the same order as that determined for the dry spine model. More than 85% of the angle calculations had a standard deviation below 1.5°.

It might be argued that the cervical spine data cannot be compared to the vertebral model since our dry spine model used two lumbar vertebra. However, the landmarks that were digitized on the cervical vertebra for the in-vivo study (the anterior vertebral body and the spinal-lamina junction) are approximately the same distance apart as the landmarks used in the dry spine study (anterior and posterior corners of the lumbar vertebral body).

The intervertebral angles from a single VF lateral cervical spine examination are presented in the figures below. The largest ROM was 25.7° for the C0-C1 joint and the smallest ROM was 6.7° for the C1-C2 joint. All other joints varied between 10.7° to 16.5°. The standard deviations for all of the angle calculations for each joint were averaged. The C0-C1 joint had the largest average SD (1.5°). The other joints had average standard deviations between 0.9° and 1.1°. The larger SD for the C0-C1 joint may be due to the blurring the VF image on certain frames. Thus, in spite of having radiolucent markers on the skull, these markers were blurred on several frames, making it difficult for the digitizer to find the true center of the marker. This would increase the SD for the angle calculations for C0-C1.

The results of our study indicate that using a VF system for the kinematic analysis of intervertebral motion has a resolution of approximately 1.5° for C0-C1 motion. This resolution increases to approximately 1.1° for the remaining vertebra.

REFERENCES

Cholewicki, et al, Clin. Biomech., 6:73-78, 1991.
Dvorak, et al, J. of Ortho. Res., 9:828-34, 1991.
Dvorak, et al, Spine, 18:120-27, 1993.
Kraemer M, Patris A, J. Neuro-radiol, 16:48-64, 1989.
Kraemer M, Patris A, J. Neuro-radiol. 17:125-34, 1990.

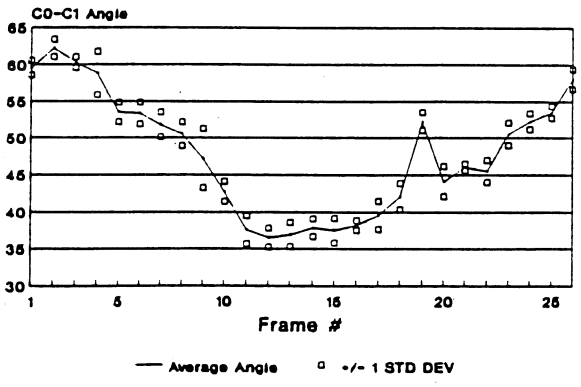

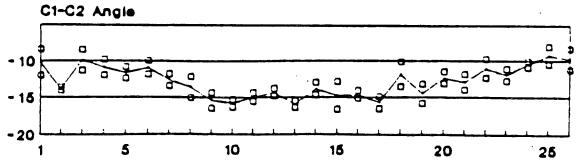

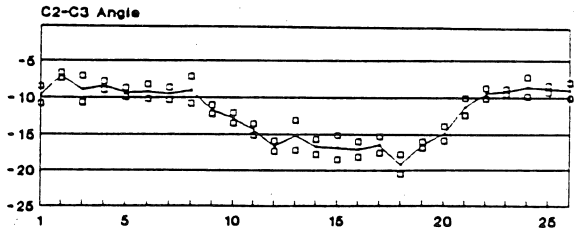

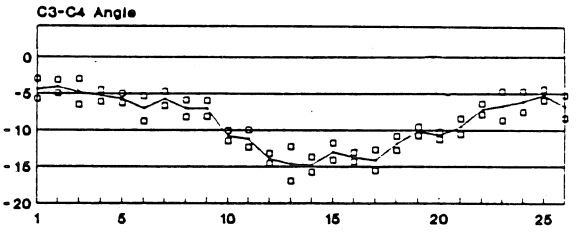

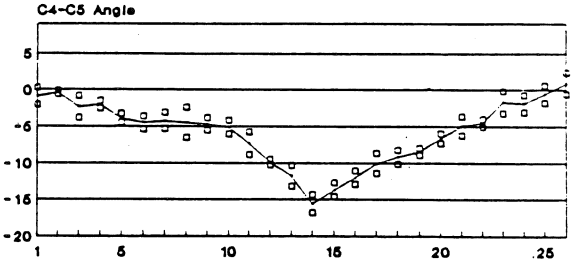

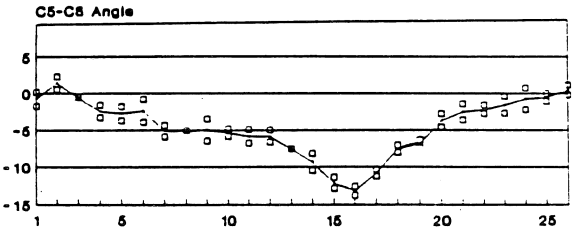

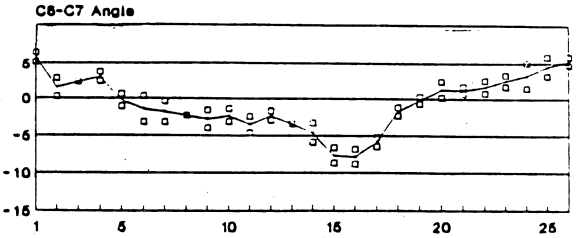

3-D GEOMETRIC MODELLING AND COMPUTER GRAPHIC REPRESENTATION OF PERSONALIZED SPINAL DEFORMITIES

Dansereau, J.[1,2], Labelle, H.[2], de Guise, J.[2], Aubin, C.-É.[1], Bellefleur, C.[1,2]
1. Dept. of Mech. Eng., École Polytechnique, P.O. Box 6079, Stat. "A", H3C 3A7
2. Pediatric Research Center, Hôpital Sainte-Justine
Montréal, Québec, Canada

INTRODUCTION

Several stereoradiographic or biplanar reconstruction techniques have been developed and used in order to obtain computed three-dimensional (3-D) representations of scoliotic spines [1,2,3] to evaluate geometrical spinal deformities. Such representations are difficult to be interpreted by clinicians because of their inability to represent the realistic geometrical shape of vertebral structures and also because reconstruction errors on landmark coordinates may generate a resulting distorted image. In order to obtain an adequate and a realistic representation of the 3-D shape of scoliotic spines which can be visually and easily analyzed by clinicians, a personalized spinal parametric model was developed based on our stereoradiographic reconstruction technique. This paper presents the methods used to obtain such geometric model as well as validation techniques and results.

MODELLING METHODS

Three-dimensional stereoradiographic reconstruction of the spine is obtained by taking conventional postero-anterior (PA) X-ray films and 20 degree angled down PA films. Six anatomical landmarks per vertebra (center of the endplates and inferior and superior tips of both pedicles) are reconstructed using the DLT program [4]. It is from these reconstructed coordinates and from spinal anthropometric measurements reported in the literature [5,6] that the parametric model was built. The computer methods used to generate personalized parametric models of scoliotic spines are the following:

1) The pedicle midpoint of each vertebra is computed from the four reconstructed pedicle landmarks.
2) A smoothed 3-D curve (Fourier series optimized by least squares) is fitted through the pedicle midpoints to compensate for errors on reconstructed coordinates. Corrected pedicle midpoint coordinates are then computed.
3) The frontal and lateral orientations of each vertebra are corrected by using the slope of the smoothed curve evaluated at the new pedicle midpoint coordinates. The axial rotation of each vertebra is incorporated into the model using the method reported by Stokes et al. [7].
4) The centroid of vertebral bodies is corrected so as to be centered with respect to the line joining midpoints of both pedicles.
5) In order to consider variations in patient size and height, a generalized dimension coefficient for the whole spine is calculated based on the mean ratio of the projected frontal length between the center of the right and left pedicles to the interpedicular distance obtained from the reported anthropometric study of Berry et al. [5].
6) Based on this dimension coefficient and on the reported anthropometric data, the transversal and PA diameters of the vertebral bodies are calculated to model them as elliptical cylinders. Tips of both pedicles are realigned with respect to their midpoints and their corresponding corrected vertebral body 3-D orientations. They are modelled as solid blocks. Spinous and transverse processes are angled and extrapolated as volumetric tetrahedrons.
7) The vertebral body heights are optimized in such a way that the intervertebral distances fit as well as possible the anthropometrical disc height data published by Schultz et al. [8] without changing the location of vertebral body centroids. This is done in order to compensate for reconstructed errors made on vertebral endplate landmarks.
8) Finally, an output file (MOVIE.BYU) adapted to the 3-D computer graphic software running on an INDIGO workstation (Silicon Graphics) is created as well as a file containing the corrected anatomical landmark coordinates.

Figure 1 shows the resulting representation of a scoliotic spine.

VALIDATION METHODS AND RESULTS

Dimensional and positional validation of the model on the frontal plane was done by comparing the standard PA X-ray image projected into the posterior view of the 3-D parametric model using, in the inverse way, the equations of the DLT program. For each vertebra, the projection was done on a plane parallel to the frontal plane and passing through the centroid of the vertebral body. On PA X-ray films of 28 patients with scoliosis (mean Cobb angle of 30°), the four corners of the vertebral bodies and the tips of both pedicles were digitized. Height and frontal diameters and the frontal angulation of the vertebral bodies as well as the interpedicular distances were

compared between projected digitized informations and the model corresponding coordinates.

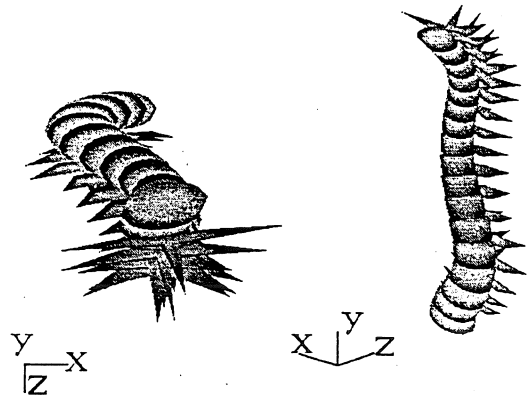

Figure 1. Graphical representations of the parametric model for a scoliotic spine: apical and 3-D views.

The results show that the mean difference in vertebral frontal angulation is $0.3^0 \pm 2.6^0$ over the 17 vertebrae composing the thoracic and lumbar spines. The standard deviation of the difference of the interpedicular distances is ± 1.7 mm. The width of vertebral bodies is over-estimated by 1.0 mm ± 2.1 mm and their height is slightly under-estimated by 0.4 mm ± 0.8 mm. It can be estimated that the difference in the AP diameter is of the same order. Finally, mean positioned difference of vertebral bodies in the horizontal and vertical directions are respectively 1.1 mm ± 2.5 mm and 1.7 mm ± 2.2 mm.

Validation on lateral plane was also done to evaluate the corrected effect of the model on the plane where reconstruction errors are greater (due to the 0° - 20° PA stereoradiographic set-up). Lateral projections of three modelled spines were compared to their corresponding lateral radiographs on which the same anatomical landmarks were digitized. A least square algorithm was programmed to fit the different lateral views. The residual least square values were used as a validation index. Best fits were done, first, between digitized coordinates of the lateral X-ray film and lateral projection of reconstructed coordinates (on which no landmark correction was done) and secondly, between digitized coordinates and the lateral projection of the modelled (corrected) coordinates. Table 1 presents the mean values and standard deviations of these results. Student T-tests show that there is a significant improvement in the resulting representation for the modelled spines compared to the reconstructed spines. Figure 2 shows the lateral radiographic projection as well as the improvement on the graphical representation between reconstructed and corrected (modelled) lateral views for one of the three spines.

Table 1. Means and standard deviations (in parentheses) of residual least square values (mm^2) for lateral reconstructed and modelled spines compared to the lateral radiographic views.

	Spine 1	Spine 2	Spine 3
RECONSTRUCTION [no correction]	1.84 (1.05)	3.27 (1.05)	2.93 (1.27)
PARAMETRIC MODEL [corrections]	1.75 (0.91)	1.42 (0.68)	1.72 (0.61)

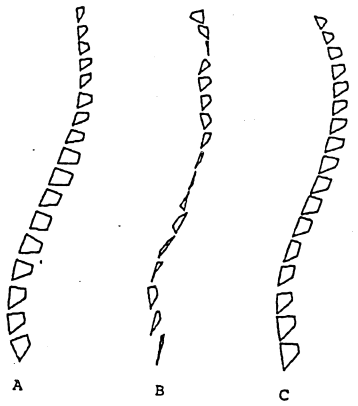

Figure 2. a) Lateral radiographic view, b) lateral reconstructed view, c) lateral corrected view.

CONCLUSION

The small differences presented above indicate that the modelling and correction techniques give valid, adequate and realistic representations of 3-D scoliotic deformities. It also indicates that corrections done by the parametric model improve the quality of the 3-D graphical representation of scoliotic spines. This parametric model is now used to give input geometric data to a finite element model in order to study the biomechanics of scoliosis. It is also used as a tool to help clinicians in the understanding of the 3-D deformity of each scoliotic patient and to characterize its evolution as well as suggesting better planning for its treatment.

REFERENCES

1. Brown, R.H. et al., J. Biomech., 9:355,1976.
2 Hindmarsh, J. et al., J. Biomech., 13:279, 1980.
3. Stokes, I. et al., J. Orthop. Res., 5:102, 1987.
4. Marzan, G.T., Ph.D. Thesis, University of Illinois at Urbana-Champaign, 1976.
5. Berry, J.L. et al., Spine, 12:362, 1987.
6. Scoles, P. et al., Spine, 13:1082, 1988.
7. Stokes, I.A.F. et al., Spine, 11:213, 1986.
8. Schultz, A.B. et al., J. Biomech., 6:373, 1973.

ACKNOWLEDGEMENTS

This research was funded by NSERC and FCAR.

INTERFACE PRESSURES IN THE BOSTON BRACE TREATMENT FOR SCOLIOSIS

D.L. Hill, H. X. Jiang, V. J. Raso, and M. J. Moreau

Department of Rehabilitation Technology, Glenrose Rehabilitation Hospital, Edmonton, AB, Canada, T5G 0B7

INTRODUCTION

The rationale for brace treatment for children with scoliosis is based on the application of corrective mechanical forces on the trunk by the brace. The degree of support and the correction of the curve depend theoretically on the location, magnitude and direction of the forces exerted by the pressure pads on the brace. The objective of this study was to determine the magnitude and direction of pressures exerted by the corrective pads of Boston braces on children with idiopathic scoliosis. The average pressure in the frontal plane was 4.4 KPa coupled with an average sagittal plane pressure of 3.6 KPa. To ensure effective scoliosis corrective pressures, it is essential to tighten the strap; however, this tension also applies undesirable pressures that induce lordosis.

REVIEW AND THEORY

The Boston brace is a prefabricated rear-opening orthosis constructed of polypropylene with a 7 mm polyethylene foam liner. Additional pads are placed in the brace to balance and correct the scoliosis. The brace is fitted firmly and is secured by two or three posterior straps.

The effectiveness of the Boston brace has been traditionally evaluated by assessing radiological changes of the spine curvature in the frontal plane. The magnitude, locations and directions of forces generated by the brace have not been defined. Aaro et al. (1981) suggested that the Boston brace derotates the spine but based this conclusion on radiographic analysis of spinal alignment with the patient lying (an unloaded spine). Weisz et al. (1989) found that 13 of 32 patients treated with a Boston brace demonstrated an improved surface shape whereas only 3 showed radiographic improvement. Willner (1984) showed that elongation forces were not as important as lateral forces for the correction of spinal deformities. Chase et al (1989) measured forces that the pads exerted on the trunk in 14 subjects and found a negative correlation between brace force and curve correction.

PROCEDURES

Nine female adolescents (age range 9 to 14 years; mean 12.5) with right thoracolumbar idiopathic scoliosis participated. Braces were worn for an average of 14 hours per day over a 21 month period. The pre-treatment Cobb angle ranged from 24^{o} to 38^{o} (mean 33^{o}).

An Oxford Pressure Monitor (Talley Group Ltd.) was used to measure the pressure exerted by the Boston brace (Bader et al., 1985). Interface pressures between the brace and the skin were determined with air filled pillows inflated to equalize the external pressure exerted by the brace on the trunk. Pressures were measured at the lateral buttock, the lateral lumbar crests, the thoracic pads and the axillary pads. The force exerted by each strap that secured the brace was measured using a strain gauge mounted on an aluminum insert connecting the strap with the hoop on the brace. Pressures were measured with the patient standing, sitting and lying.

Posterioanterior (PA) and lateral radiographs were taken with the subject in the brace. Radio-opaque markers, attached to each transducer, were located on PA and lateral radiographs and digitized to calculate the direction and the location of the pressure. Vertebral body centroids and points along the pelvic crests were digitized to document the applied pressure with respect to the spine. Pressure was subdivided into components acting in the frontal (scoliosis inhibiting) and the sagittal (lordosis promoting) planes.

RESULTS

Pressures in the buttock area were relatively low and symmetric, directed towards the midline of the pelvis with a mean value of 3±4 KPa on the left and 3±2 KPa on the right. Higher pressures were found around the lumbar crests: 6±5 KPa on the left versus 6±4 KPa on the right. The axillary pad exerted a pressure of 4±2 KPa. There was no statistically significant difference between pressures in standing, sitting and lying positions. Average scoliosis inhibiting pressure was 4.4 KPa coupled with a lordosis promoting pressure of 3.6 KPa. The medial part of the posterior thoracic pad exerted an anterior pressure averaging 5±5 KPa and the lateral part of the pad produced a pressure directed anterior medially averaging 9±7 KPa.

Strap forces were less than 20 N in five subjects and greater than 50 N in four subjects. Mean maximum pressures exerted by the brace were less than 8 KPa with low strap forces to over 13 KPa with high strap forces.

DISCUSSION

Strap tensions and brace pressures were variable in the group tested. The pressures exerted by the brace depended on the strap tension. Tightening the straps of the Boston brace increased corrective lateral and derotation forces produced by the thoracic and axillary pads. Pressures exerted by the Boston brace in the buttock and crest areas were coronal to the midline of the body and well balanced on both sides, effectively 'holding the trunk'. Posterior thoracic pads on the convex side provided scoliotic correction, derotation and lordotic promoting forces. The medial part of the posterior thoracic pad was located posterior to the scoliotic segment of the spine and exerted a lordotic promoting force. The lateral aspect of the posterior thoracic pad applied pressure in an anterolateral direction in the sagittal plane. The lateral component usually acted on the rib attached to the vertebrae at the curve apex to provide scoliosis correction. The sagittal component was about 10 cm lateral from the spine which created a derotation moment. The axillary pad on the concave side exerted lateral force on the rib attached to the upper end vertebrae of the curve. This force, coupled with the contra-lateral force of the thoracic pad, may play a role in keeping the trunk from leaning laterally.

REFERENCES

Aaro S. et al. The Derotating Effect of the Boston Brace: A Comparison Between Computer Tomography and a Conventional Method. *Spine*, 6:477-482, 1981.

Bader D.L. et al. Pressure Measurements at the Patient Support Interface *Biomechanical Measurement in Orthopedic Practice.* Edited by MW Whittle, JD Harris, Oxford, Oxford University Press, 1985.

Chase A.P. et al. The Biomechanical Effectiveness of the Boston Brace in the Management of Adolescent Idiopathic Scoliosis *Spine*, 14:636-642, 1989.

Weisz, I. et al. Back Shape in Brace Treatment of Idiopathic Scoliosis *Clinical Orthopaedics and Related Research* 240: 157-163, 1989.

Willner, S. The Effect of the Boston Brace on the Frontal and Sagittal Curves of the Spine. *Acta Orthop Scand*, 55:457-460, 1984.

THE CONTINUOUS MEASUREMENT OF PRESSURES EXERTED BY BRACES IN THE TREATMENT OF SCOLIOSIS

E. Lou, V. J. Raso, N. G. Durdle, D. L. Hill, M. Moreau
Department of Electrical Engineering, University of Alberta, Edmonton, AB Canada
Department of Rehabilitation Technology, Glenrose Rehabilitation Hospital, Edmonton, AB Canada
Division of Orthopedic Surgery, University of Alberta, Edmonton, AB Canada

INTRODUCTION

A battery powered microcomputer system was developed to monitor pressures exerted by braces used to treat children with spinal deformities. The test subject was a young man, age 18 years, with a 37^{o} right thoracic curve who was approaching the end of treatment. Sixteen transducers were mounted on the brace to measure either brace pressure or strap forces. Data acquisition was controlled by a MC68HC11 microcontroller. To minimize power consumption, CMOS circuits are used and the microcomputer and analog circuit are kept in a low power mode except at the specific times when the measurements are taken. Data was sampled every minute for two days. Average of the pressure at the right top axillary is 75 mmHg and the average of the strap forces at the top buckle is 27.5N.

REVIEW AND THEORY

Scoliosis is an abnormal curvature of the spine with vertebral rotation. Clinicians have few non-surgical treatment tools at theirdisposal for children with this type of potentially progressive spinaldeformity. Historically, braces have been used to support mechanically the spine when risk of progression is greatest (Asher et al. (1986)) and are often prescribed despite poor compliance and much uncertainty as to effectiveness (Houghton et al, 1986, Patwardhan et al, 1986 and Ylikoski et al., 1989). All braces are designed to provide mechanical support; the degree of support and the extent of corrective action depends on the location, magnitude and direction of the pressures exerted by the brace relative to the spine (Wynarsky et al.,1989). Although the support that is provided has been described in the frontal plane, the three dimensional action of the brace on the spine has not been well investigated.

Brace treatment for children with spinal deformities has been based largely on instinct with very little scientific data to support treatment decisions. By examining in-brace curvatures, Willner (1984) showed that elongation forces are not as important to the correction of spinal deformities as are lateral forces. To examine the biomechanical impact of Boston brace treatment for idiopathic scoliosis, Cote (Cote et al. (1992)) used thin polymeric resistors to measure the pressure distribution generated by the brace. They found that the Boston brace did not generate a uniformdistribution of pressure and that the distribution depended greatly on the quality of each brace. Jiang, et al. (1992) measured the magnitude, location anddirection of pressures generated by the brace as well as forces imposed by the straps and found that there is considerable variation in how the brace was worn by patients. Some children secured the brace very aggressively and imposed high loads on their trunks; other children wore the brace loosely imposing low pressures. These measurements were taken at a single time under laboratory conditions and may not be true indicators of the pressure exerted by braces during the treatment. A small, light weight and rugged microcontroller system was developed to measure and record the pressure and forces exerted by braces during normal wear. Small size and low power consumption were achieved by using CMOS integrated circuits (ICs), minimizing the number of ICs and turning off the power to any IC not in use. The data collection period, the sampling frequency and the number of channels supplied under software control. Thirteen pressure transducers may be placed at the acting surface of each pad and in the foam liner of the brace. Three force transducers may be used to measure the tension of the straps used to secure the brace.

PROCEDURES

A nighttime Charleston being woren by a young man (18 yrs) with a 37^{o} right thoracic curve was instrumented. Three transducers were place the left and right axillary lines, four on each of the front and back surfacesof the brace. Three transducers measured the forces in the three straps that secured the brace. Measurments were made every minute over 2 days.

RESULTS AND DISCUSSION

The pressure at the top right axillary ranged between 50mmHg to 100mmHg. The maximum pressure was found at the top left axillary ranged between 80mmHg to 125mmHg, and the lowest pressure was found to be 10mmHg to 35mmHg. The force in the top strap ranged from 20N to 35N. Peak loads which occured when the brace was first donned was 104N for the middle strap, 76N for the bottom strap and 74N for the top strap. A method has been developed that will permit studies of the mechanical effects of braces used to treat children with idiopathic scoliosis .

REFERENCES

Asher, W. et al. Orthotics for Spinal Deformity, in Orthotics Etcetera Edited by JB Redford, Williams and Wilkins, Baltimore, 1986.

Cote, D. et al. Proceedings Int'l Symposium on 3-D Scoliotic Deformities, (ed J. Dansereau) Montreal, (pp81-88), June 27-30, 1992.

Houghton, M. et al. Proceedings of the 21st. Meeting of the Scoliosis Research Society, Hamilton, Bermuda, September, 1986.

Jiang, R. et al. Proceedings Int'l Symposium on 3-D ScolioticDeformities, (ed J Dansereau) Montreal, (pp395-399), June 27-30, 1992.

Patwardhan, D. et al. Proceedings ofthe 21st. Meeting of the ScoliosisResearch Society, (eds S.A. Lantzand A.I. King) Hamilton, Bermuda,(pp50-51), September, 1986

Willner S: The effect of the Bostonbrace on the frontal and sagittal curves of the spine. Acta Orthop Scand 55:457-460, 1984.

Wynarsky, S. et al. Trunk Muscle Activities in Braced Scoliosis Patients, Spine, 14:1283-1286, 1989.

Ylikoski, P. et al. Biological Factors and Predictability of Bracing in Adolescent Idiopathic Scoliosis, J Pediatric Orthopedics, 9:680-683, 1989.

BIOMECHANICAL CHARACTERISTICS OF CASPAR AND SYNTHES PLATES USED TO STABILIZE CERVICAL SPINES BEFORE AND AFTER CYCLIC LOADING

V. Goel, J. Clausen, T. Ryken, V. Traynelis, Z. Zheng

Department of Biomedical Engineering, The University of Iowa, Iowa City, IA 52242

Division of Neurosurgery, University of Iowa Hospitals and Clinics, Iowa City, IA 52242

INTRODUCTION

The load-displacement (flexibility) data in various clinically relevant loading modes for twelve fresh, intact ligamentous cervical spine C2-T1 specimens were recorded. These specimens were divided into two groups of six each. In each group, a load-displacement experiment was sequentially repeated for the intact, injured-stabilized, and injured-stabilized-fatigued cases. The injury consisted of a total C5-C6 disco-ligamentous disruption. The injured specimens were stabilized using Caspar plate systems in one group and Synthes plate systems in the other group. The flexibility results indicate that both devices are effective in restoring stability to that of intact levels across the injured segment when evaluated in quasi-static loading modes prior to cyclic loading. However, following cyclic loading the performance of the Caspar plate system surpassed the Synthes plate system.

REVIEW AND THEORY

Several treatment options are available to restore spinal function in case of disc disorders with and without posterior bony and/or ligamentous injury. Rigid external immobilization, posterior cervical fusion, and anterior plate stabilization have been used separately and in combination to support the injured spine while healing occurs. Recently the use of anterior plates with interbody bone graft has received prominence because decompression, grafting, and plating may be performed through single exposure. In order to understand the mechanics of anterior plates a biomechanical study was initiated to determine stability characteristics of the Caspar and Synthes plate systems used to impart stability to injured fresh ligamentous cervical spines. The methodology developed and results obtained are described next.

PROCEDURES

Fresh human cadaveric ligamentous cervical spines (C2-T1) were procured and radiographed to ascertain any significant amount of degeneration. Using this process twelve specimens were selected for biomechanical testing. Each specimen was cleaned of all paravertebral musculature and the base (C7 & T1) was secured in a plastic resin so that the C5-C6 interspace was horizontal. A loading frame designed to provide pure moments to the specimen was rigidly fixed to C2, and a set of three infrared LEDs (light emitting diodes) was secured to the posterior aspect of each vertebra (C2-C7). The prepared specimen was sequentially tested in the following manner: (1) The load-deformation behavior of the intact (INT) specimen was determined by applying clinically relevant loads to produce flexion, extension, lateral bending, and axial rotation and measuring the resulting displacements of the LEDs through a Selspot II® motion measuring system (Goel et al., 1987, 1988). Pure moments in four equal steps of 0.25 Nm each were applied for this purpose. (2) A total discectomy was performed at the C5-C6 disc space from the anterior aspect. An iliac graft was inserted and the motion segment was stabilized using either the Caspar or the Synthes plate system. The tightening torque of the screws employed to secure the plates to the motion segment was measure using a torque wrench. All of the posterior elements were subsequently dissected. In summary, a total disruption of the C5-C6 interspace was created and the disrupted segment was stabilized using an interbody iliac graft and a plate system. The injured-stabilized (I-S) specimen was tested for its load-displacement behavior once more, using the motion measuring system. (3) The stabilized specimen was fatigued in flexion-extension for 5000 cycles at 0.5 Hz. A total of 20 to 30 degrees of motion (flexion - 10 to 15°; extension - 10 to 15°) was achieved by applying an off-center cyclic axial load. An MTS machine was used in conjunction with a special loading apparatus designed to create flexion and extension without constraining natural motions. (4) The injured-stabilized-fatigued (I-S-F) specimen was tested once again for its load-displacement behavior using the Selspot II® system. The degree of screw looseness was recorded and the screws were tightened to initial torque levels. Finally, (5) the specimen was tested to failure in an off-center axial compression load and the degree of screw looseness was noted again. The primary difference between the Caspar and the Synthes plate systems is that the former uses bicortical screws and the later uni-cortical screws for fixing the respective plate to the vertebral bodies. In addition Synthes incorporates a locking hub into the uni-cortical screw system whereas the Caspar system does not.

RESULTS

Using the principles of rigid body mechanics the load-displacement data were processed to obtain three rotations for each vertebral body with respect to C7 for the intact (INT), injured - stabilized (I-S), and then following cyclic loading of the stabilized (I-S-F) specimen. Typical flexion/extension rotations at various vertebral levels for the three cases with a specimen stabilized using the Caspar plate system are shown in Figure 2. The flexion rotation across the C5-C6 level decreased following injury and stabilization (Figure 2B) as compared to intact case (Figure 2A). The results for the 'I-S' and 'I-S-F' cases were normalized with respect to the 'INT' case to calculate the percent change in rotations following the procedure as a function of the spinal level, the type of plate system used for stabilization, and the type of loading modality. The results listed in Table 1 for the stabilized specimen indicate that in flexion both devices increased the stability of the injured motion segment from the intact levels. However, in extension the Caspar plate system showed a significantly greater stabilization effect while the Synthes plate was less effective. The results after cyclic fatigue loading in Table 2 indicate that in extension the Caspar plate system continued to be more stable than the intact spine. In flexion, the Synthes plate showed a significant decrease in stability. The screws used for both plates stripped out at a rate of 25% following fatigue loading. The Caspar screws which were tight prior to fatigue showed a higher rate of remaining tight when compared to the Synthes. Screws in both plates that were tight prior to fatigue loading did not strip out following cyclic loading. The failure moment did not differ significantly for the two systems (Average 5.1±1.9 Nm @ 30.1° for Caspar vs. 7.7±3.4 Nm @ 29.2° for Synthes). A typical failure curve is shown in Figure 3 for a Caspar plate system.

TABLE 1 Average % decrease in rotation of the 'I-S' specimens w.r.t. the 'INT' case.*

Plate Type	Flexion	Extension
Caspar	-38.5 (45.1)	-47.1 (28.7)
Synthes	-31.7 (26.8)	15.8 (37.1)

*Results based on six specimens in each group. Standard deviation is indicated in parenthesis. A negative sign indicates an increase in stability from the intact case.

TABLE 2 Average % decrease in rotation of the 'I-S-F' specimens w.r.t. the 'INT' case.*

Plate Type	Flexion	Extension
Caspar	-18.5 (57.1)	-42.4 (28.3)
Synthes	93.2 (95.5)	5.1 (41.8)

*Results based on six specimens in each group. Standard deviation is indicated in parenthesis. A negative sign indicates an increase in stability from the intact case.

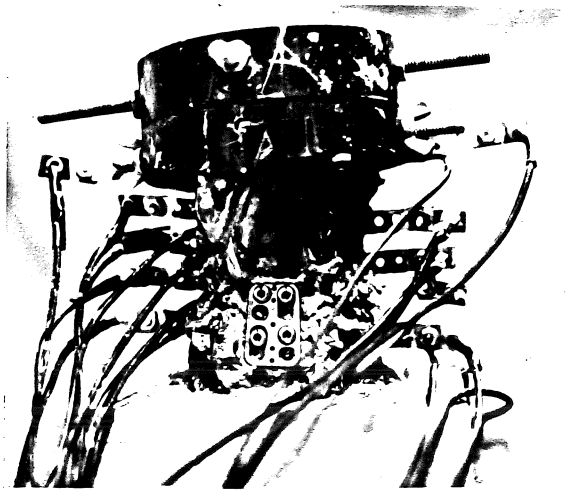

Figure 1. Ligamentous specimen stabilized with a Caspar plate system mounted in the testing rig.

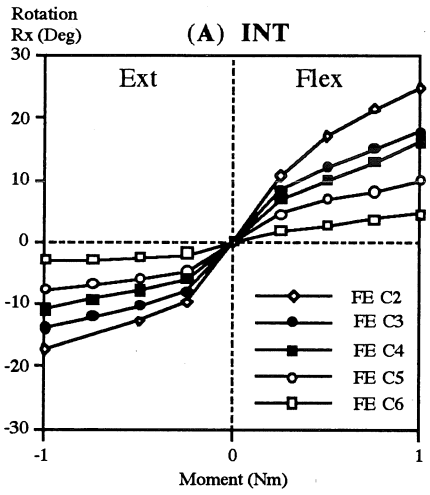

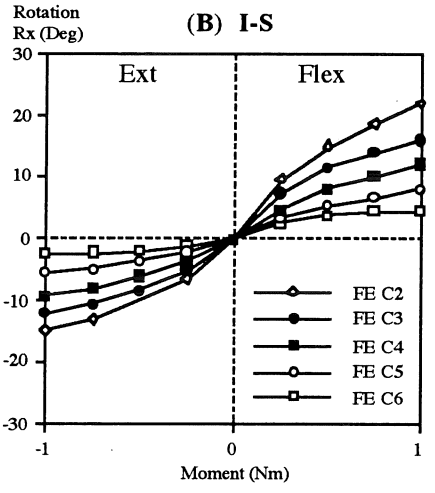

Figure 2. The flexion/extension rotations at various levels of the specimen in response to the applied moments for the segment of interest. (A) For intact (INT), (B) for intact-stabilized (I-S), and (C) for injured-stabilized-fatigued (I-S-F).

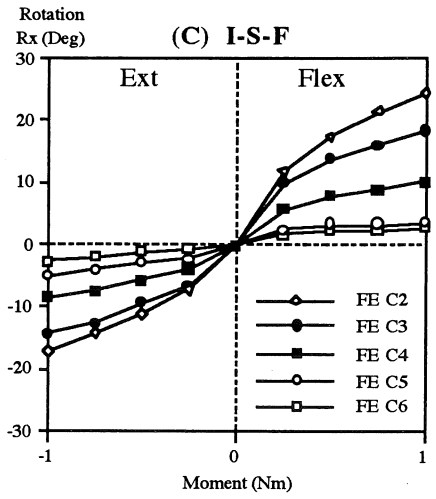

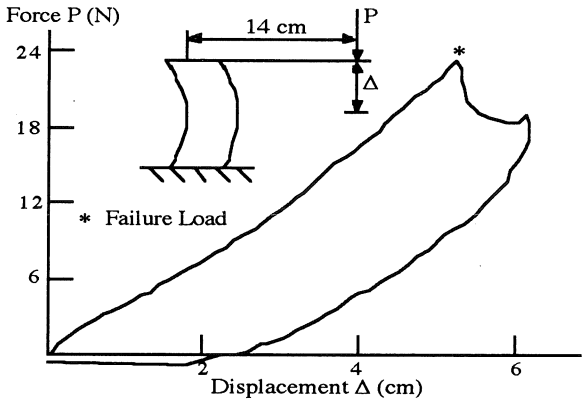

Figure 3. Failure curve of a specimen stabilized with a Caspar plate system.

DISCUSSION

The results indicate that in flexion the Caspar and Synthes plate systems are equally effective in restoring stability across the completely disrupted C5-C6 motion segment. In extension however, the Caspar system shows a significantly greater ability to stabilize the motion segment. Following cyclic loading the results indicate a decreasing stabilization potential for the Synthes system, whereas the Caspar system shows an increase in stabilization potential from the intact case. This may be due to the use of bicortical screws in the Caspar system as opposed to the uni-cortical screws used to attach the plate to the vertebral body in the Synthes system. One may extend the hypothesis, based on our results, that once the Caspar system is implanted correctly at the time of surgery, there is lesser likelihood of a significant decrease in stability over time. These findings become significant since screw loosening does occur with cyclic loading.

REFERENCES

Goel VK,. et, al. "Moment-rotation relationships of the ligamentous occipito-atlanto-axial complex." *J Biomechanics*, Vol.21, pp. 673-680, 1988

Goel VK, et, al. "A technique to evaluate an internal spinal device by use of Selspot II® system-an application to luque closed loop." *Spine*, Vol.12, pp. 150-159, 1987

ACKNOWLEDGMENTS

Work supported in part by grants from Aesculap Inc., and NIH (AR 40166-02).

MUSCLE RECRUITMENT PATTERNS IN LANDINGS WITH REDUCED VERTICAL REACTION FORCES

Dawn M.E. Irvine and Jill L. McNitt-Gray
Biomechanics Research Laboratory, Department of Exercise Sciences
University of Southern California, Los Angeles, CA 90089-0652, USA.

INTRODUCTION

Peak vertical reaction forces experienced during landings have been reduced by modifying joint kinematics (Devita & Skelly, 1992; Dufek & Bates, 1990; Gross & Nelson, 1988; McNitt-Gray, 1990; Mizrahi & Susak,1982). Landings with reduced peak vertical force have also resulted in reductions in peak ankle, knee and hip extensor moments (McNitt-Gray et al., 1990). From the observed joint kinetics, inferences have been made to the expected muscle activation patterns, however, EMG and joint kinetics have not been examined together. The purpose of this study was to compare muscle recruitment patterns between subjects during self selected normal and softer than normal landings.

PROCEDURES

Six healthy male collegiate gymnasts performed six drop landings using normal and softer than normal landing strategies. Self selected softer than normal landings produced reductions of peak vertical forces of 1-2 BW. Each landing was performed by stepping from a stationary platform positioned 0.72 meters above two gymnastics landing mats (12cm) fully supported by two force plates. The reaction forces acting at the mat-plate interface were quantified using the force plates (800Hz). Segment kinematics were recorded simultaneously using high speed video (200fps). The muscle activation patterns of seven lower extremity muscles, Gluteus maximus (GM), Vastus Medialis (VM), Rectus Femoris (RF), Biceps Femoris (BF), Medial Gastrocnemius (MG), Semitendonosis (ST), and Tibialis Anterior (TA), prior to and during the landing were quantified using surface electromyography (1600Hz; Beckman Ag/AgCl electrodes; Differential Amps, Data, Inc.). The reaction forces, kinematics and EMG were synchronized at the time of contact. Markers positioned on the body of the subjects were manually digitized using a video based data acquisition system (Peak Performance, Inc.). Each coordinate of the digitized body landmarks (Zatsiorsky & Seluyanov, 1983) were digitally filtered independently using a second order Butterworth Filter (Saito & Yokoi, 1983) with a cut-off frequency derived by the method of Jackson (1979). Net ankle, knee and hip moments were calculated using Newtonian mechanics (Nm/kg). The EMG signals were initially band pass filtered with cut off frequencies of 30-800Hz, then rectified (SNIP, 1988, Digital Dynamics, Inc.). EMG amplitude was normalized to the peak value observed during all trials (Yang & Winter, 1984). The temporal characteristics and the relative adjustments of muscle activity and ankle, knee and hip kinetics during the landings were compared within subjects.

RESULTS AND DISCUSSION

A within subject comparison of the normal and softer than normal landings revealed similar temporal muscle activation patterns and similar muscular coactivation. Significant reductions were observed in peak vertical joint reaction forces during the softer than normal landing. No significant differences in peak flexor and extensor moments were observed between normal and softer than normal landings (Irvine et al., 1992).

Across subject comparisons indicate two primary muscle recruitment patterns. These two patterns will be referred to as the bi-uniarticular recruitment pattern and the bi-biarticular recruitment pattern.

Figure 1 shows the lower extremity net joint moments and muscle activity of a normal landing from one subject using the bi-uniarticular recruitment pattern (a) and another subject using the bi-biarticular recruitment pattern (b). When visually shifting the EMG to the right 50 by ms, to account for electromechanical delay (EMD), a relationship between net joint moment and muscle activity can be seen. The primary differences between the two strategies were the selective mechanisms of control used in accommodating the knee and hip moment.

The two recruitment patterns were different in the following ways. First, subjects using the bi-uniarticular EMG recruitment pattern were able to minimize hip extensor activity when the hip moment approached zero. The biphasic burst of the GM allowed them activate the GM along with the ST and BF, then decrease all hip extensor activity when the hip extensor moment approached zero. The decrease in hip extensor moment was not accompanied by a decrease in hip extensor muscle activity in the subjects using the bi-biarticular recruitment pattern. The temporal EMG patterns reveal that these subjects had continuous GM, ST or BF activity during this phase.

The second difference observed between recruitment patterns was the inhibition of both hamstrings during the second hip extensor moment in the bi-uniarticular recruitment pattern. Subjects using the bi-uniarticular recruitment pattern accomplished this by the sole use of the GM for the second hip extensor moment as they were able to minimize or inhibit the use of the ST and BF during this time, hence the name bi-uniarticular. The subjects using the bi-biarticular recruitment pattern used the hamstrings along with the GM to accommodate the first and second hip extensor moment, hence the name bi-biarticular. The use of the ST and BF in the first hip extensor moment is quite efficient since there is also a knee flexor moment present. This allows these biarticular muscles to function at both hip and knee. The second hip extensor moment is however coincident with a knee extensor moment, therefore, use of these biarticular muscles during this portion of the landing is counterproductive due to their function as knee flexors.

The third difference in recruitment pattern was a distinct onset of the MG prior to contact observed in the bi-uniarticular recruitment pattern. In contrast, subjects using the bi-biarticular recruitment pattern activated MG continuously prior to contact. This observation is consistent with results reported by McKinley & Pedotti (1992).

Subjects using the bi-uniarticular EMG recruitment pattern were gymnasts with more than 12 years experience, where as, subjects using the bi-biarticular EMG recruitment pattern had less than 7 years experience in gymnastics. In summary, subjects with less experience used a bi-biarticular recruitment pattern which was characterized by counterproductive muscle recruitment patterns in controlling knee and hip joint moments.

REFERENCES

Devita P. & Skelly, W.A. (1992). *MSSE*, **24** (1), 108-115.
Dufek, J.S. & Bates, B.T. (1990). *MSSE*, **22** (2), 370-377.
Gross, T.S. & Nelson R.C. (1988) *MSSE*. **20**, 506-514.
Irvine, D.M.E.I., et al. (1992). In *Proceedings of the 2nd NACOB*, (p.547-548).
Jackson, K.M. (1979). *IEEE Transactions on Biomedical Engineering*, **26**, 122-124.
McKinley, P. & Pedotti, A. (1992). *Exp. Brain Res.*, **90**, 427-440.
McNitt-Gray, J.L. (1991). *IJSB*, **7**, 201-224.
McNitt-Gray, J.L., et al. (1990). In *Proceedings of 14th Annual American Society of Biomechanics*, (pp. 75 - 76).
Mizrahi, J. & Susak, Z. (1982). *Eng. Med.*, **11** (3), 141-147.
Saito, S., & Yokoi, T. (1982). (Tech. Rep. No. 5). Ibaraki, Japan: Univ. of Tsukuba, Inst. of Health and Sports Sciences.

Yang, J.F. & Winter, D.A. (1984). *Arch. Phys.Med.Rehab.*, **65**, 517-521.
Zatsiorsky, V., & Seluyanov, V. (1983). *Biomechanics VIII-B*, (pp. 1152-1159). Champaign, IL: Human Kinetics Publishers.

Acknowledgements: USC Faculty Research and Innovation Fund, the US Olympic Committee and USC Biomechanics Research Team.

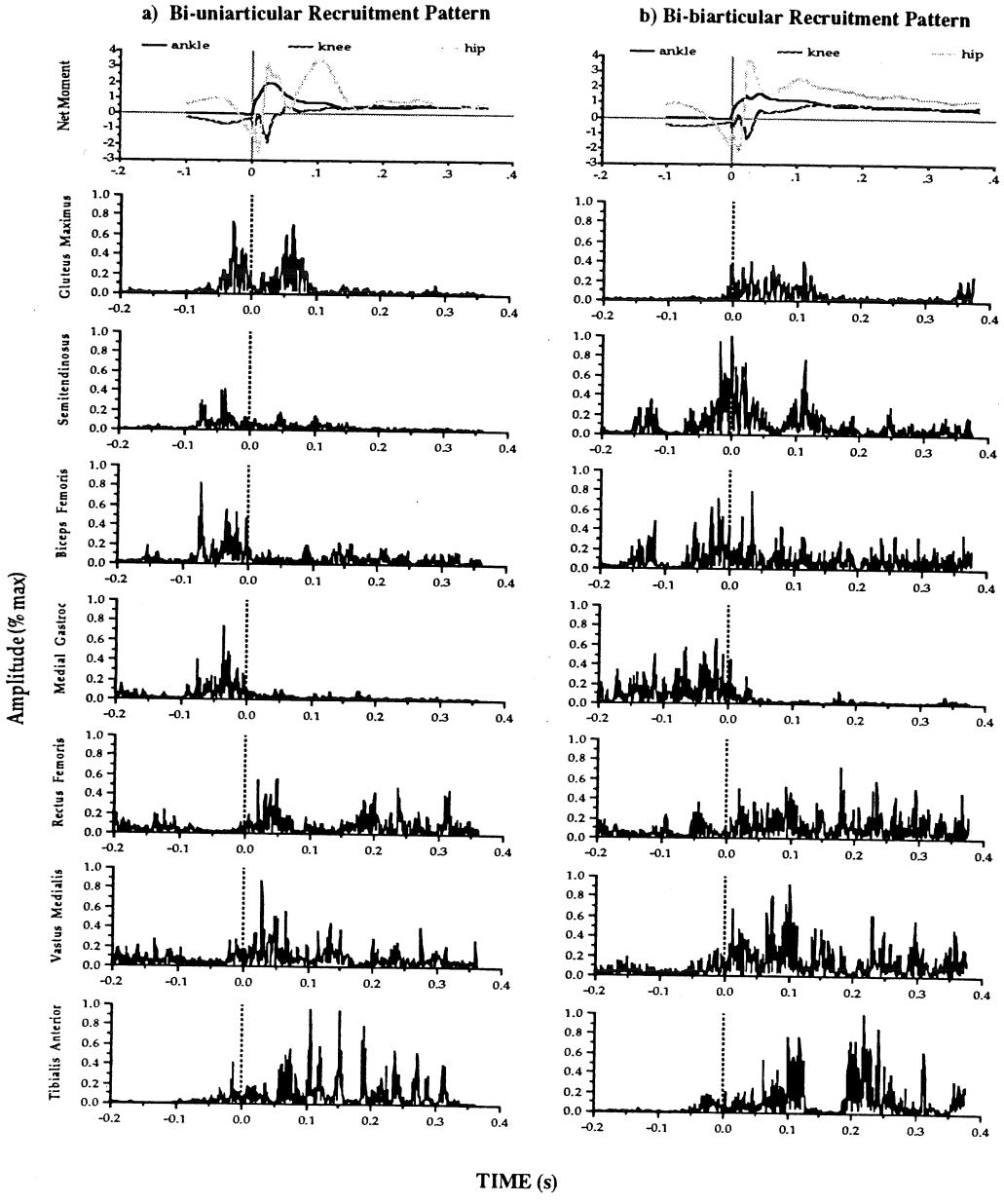

FIGURE 1. Ankle, knee and hip net joint moments and EMG of a normal landing from one subject using the bi-uniarticular strategy (a) and another subject using the bi-biarticular strategy (b).

PERCEPTION OF VERTICAL TRUNK ALIGNMENT

J.M. Hondzinski and W.G. Darling

Department of Exercise Science,
University of Iowa, Iowa City, IA 52242

INTRODUCTION

Awareness of trunk alignment to the gravitational axis is important in everyday situations and in athletic activities such as gymnastics, springboard diving and dancing. However, little research has been devoted to perception of vertical trunk alignment. The purpose of this experiment was to compare the accuracy of such perceptions in divers and normal healthy individuals without experience in diving or related activities while manipulating the presence of visual information, head orientation and knee angles. Subjects' abilities to achieve a full turn on a beam were assessed to determine if this ability was related to perceptions of trunk alignment.

There were no significant differences between divers and controls during trunk aligning tasks. Subjects made greater errors when their head was not aligned with the trunk and the knees were flexed; lack of vision further increased such alignment errors ($p=.0077$). Divers performed much better than controls on the full-turn task when vision was allowed but the performance gap was reduced when the subjects were blindfolded.

REVIEW AND THEORY

The trunk, because it is less confounded by constant errors, is the most accurate indicator of orientation ability (Ross et al. 1969). In previous research the accuracy of frontal plane trunk positioning has been shown to be very good (Jakobs et al. 1985). Knowing that visual perception of the vertical is influenced by head and body orientation (Parker et al. 1983), we chose to manipulate these orientations to exam their effects with and without vision. Diving performance is also affected by head alignment to the trunk and leg positioning. Thus, we expected divers to show lower errors in trunk alignment under these conditions.

PROCEDURES

Four healthy college-age male subjects and four university team male divers performed the task of voluntarily aligning their trunk to the gravitational axis under four different conditions: (1) head and trunk aligned (HA), (2) head tilted to various angles relative to the trunk (HT), (3) legs straight (STR) or (4) knee flexed (FLX) both with (V) or without vision (NV) (8 conditions total). The trunk, head and/or leg orientations were manipulated by the experimenter prior to the movements by the subject to align his trunk to gravity. Positional data was collected optoelectrically with infrared light emitting diodes (ireds) connected to a device that attached firmly to the trunk, directly to the subject's right thigh to define it's horizontal angle and to goggles, both clear and opaque, to control visual input and define head orientation.

Upon completion of the perceptual tasks each subject attempted to complete 20 full turns on a 6' x 5" x 6" beam, the first ten with vision and the second ten without vision. One diver had gymnastics experience but all other subjects were novice on a balance beam. Completion of turns was determined objectively and scored using the following system: full-turn (4), full-turn fell off (3), half-turn (2) and half-turn fell off (1). A full-turn was marked if the foot of the subject touched the beam after a complete turn. It should be mentioned that this technique did not discriminate among those who did full turns but did not put their foot down before falling and those who barely completed a half turn and fell.

RESULTS

The errors in trunk alignment were larger in the FLX and HT conditions, but greatest when the conditions of HT, FLX, and NV were used simultaneously. Note the conditions with no vision often had lower

alignment errors than their visual counterparts (fig. 1). Surprisingly there were no significant differences in perceptual abilities of divers and controls, though it should be mentioned that errors by divers were generally lower (p=.104).

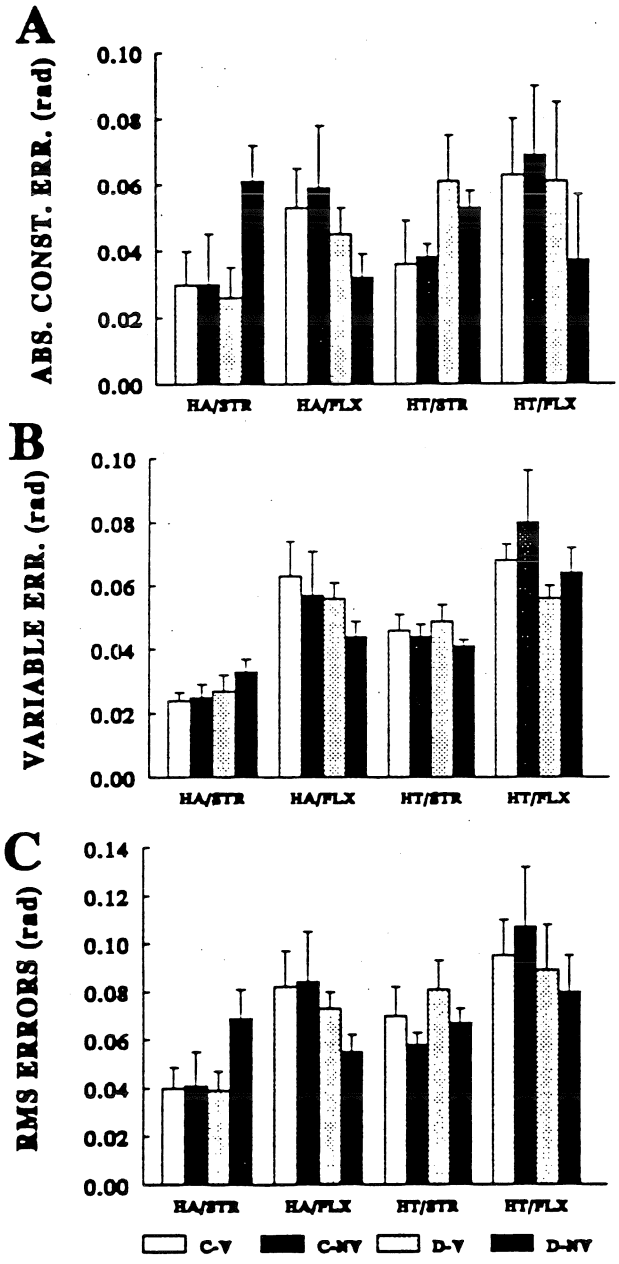

Figure 1. The absolute constant (A), variable (B) and RMS (C) errors for perception of trunk alignment to the gravitational axis in both groups are shown. The experimental conditions are shown on the abscissa.

The divers performed substantially better on the full turn task with vision. Differences between groups were not as prominent when subjects were blindfolded. Table 1 depicts the average turn completed.

Table 1 Average Completed Turn

	vision	no vision
Divers	3.15	1.90
Controls	1.35	1.45

Numbers were computed by use of ordinal values: 1-half-turn-fell, 2-half-turn, 3-full-turn-fell, and 4-full-turn, and averaged across groups.

DISCUSSION

Tilting the head and flexing the legs negatively affected the subjects' perceptions of trunk alignment to the gravitational axis as hypothesized. Misalignment of the head causes perception of trunk orientation to depend on integration of neck joint angle receptors with otolith inputs, which are the most sensitive to body orientations relative to gravity, presumably causing increased errors in perception of trunk orientation. Flexing the knees to varying angles requires subjects to alter the hip angle appropriately to align the trunk to gravity. Larger errors in trunk alignment may result from inaccurate perceptions of knee and hip angles in this condition.

Turning performance on the beam was not related to perceptions of trunk alignment. A possible contributor to the diver's alignment errors was their rapid performance during trunk alignment tasks. It is likely that the diver's twisting experience and use of head alignment led to their better beam performance.

REFERENCES

Jakobs, T.et al. Exp Brain Res,90,129-138, 1985.

Parker, D.E. et al. Percept & Psychophys, 33, 139-146.

Ross, H.E. et al. Aerospace Med,40, 728-732, 1969.

Wade, N.J. Percept-Psychophys, 3, 215-219, 1968.

KINESTHETIC PERCEPTION OF THE ANTERIOR DIRECTION

W.G. Darling and T.E. Williams

Department of Exercise Science, University of Iowa, Iowa City, IA 52242

INTRODUCTION

Recent research in the motor control field has focussed on the issues of transformations among visual and kinesthetic coordinate systems that are necessary for accurate reaches to visually specified targets. However, the actual axes of the these coordinate systems have not been experimentally determined. The purpose of this experiment was to determine the preferred anterior direction for a kinesthetic coordinate system. We examined subjects' abilities to specify anterior directions perpendicular to the head or trunk frontal planes by moving their forearm at the elbow under kinesthetic guidance while varying the angles of the head and trunk. Perceptual errors were larger when specifying head-fixed anterior direction. In addition, regression analysis showed that the perceptual errors for specifying the head-fixed anterior direction were highly dependent on the difference in head and trunk orientations (i.e., neck rotation angle). In contrast, perceptual errors for the trunk-fixed anterior direction were much less predictable from differences in body orientations. Together, these data show that the kinesthetic coordinate system for the upper limb is fixed in the trunk as expected. Thus, we concluded that the preferred kinesthetic anterior direction at the perceptual level is parallel to the anterior axis of the trunk.

REVIEW AND THEORY

Transformation of visually defined target location coordinates into a kinesthetic coordinate system is necessary to specify the upper limb orientation for target acquisition in reaching movements (Flanders et al. 1992). However, the axes used to specify the visual and kinesthetic coordinate systems have not been identified. It has been implicitly assumed in past research that visual axes would be fixed in the head while kinesthetic axes would be fixed in the trunk. Thus, the coordinate transformation for reaching would involve transformations between head and trunk fixed coordinate systems. Recent studies of preferred kinesthetic coordinate systems for the upper limb have shown that segment angles in space relative to gravitational and anterior body axes are perceived with either greater or similar accuracy to that for perception of joint angles between adjacent body segments (e.g., Soechting 1981, Soechting and Ross 1984, Darling 1991). A kinesthetic system using segment angles in space would simplify coordinate transformations for reaching because the axes of the kinesthetic system axes would be fixed rather than variable as in the case of joint angles. However, in most previous studies of kinesthetic perception the trunk and head have remained in fixed, aligned positions. Thus, the true axes of the kinesthetic system have not been determined because earth, head and trunk-fixed vertical axes are aligned and the anterior directions of the head and trunk are aligned. Manipulations of head and trunk orientations are necessary to determine whether the preferred kinesthetic axes are specified relative to the head or trunk. We hypothesized that the preferred anterior axis would be fixed in the trunk.

PROCEDURES

Six normal healthy college-aged individuals served as subjects for this research. The general procedure involved subjects flexing or extending their forearm under kinesthetic guidance to place its long axis parallel to the direction of their head-fixed or trunk-fixed anterior axis which were independently varied by the experimenter rotating the head or trunk about their longitudinal axes. The experimenter also manipulated the arm and forearm to various positions prior to the movement by the subject to place their forearm parallel to the desired axis. The upper limb motion and the anterior axes of the head and trunk were maintained primarily in the horizontal plane. Subjects performed the task under 5 different conditions: (1) manipulate arm orientation (trunk and head orientation aligned), orient the forearm parallel to the trunk anterior, (2) manipulate arm and head orientation (trunk orientation constant), orient the forearm parallel to the trunk anterior, (3) manipulate arm and trunk orientation (head orientation maintained nearly constant by the experimenter moving the head to its standard position after manipulating trunk orientation), orient the forearm parallel to the trunk anterior, (4) same as condition 2 except orient forearm to head anterior and (5) same as condition 3 except orient the forearm parallel to the head anterior. Subjects performed 30-40 consecutive trials in each condition.

Orientation of the longitudinal axis of the arm and forearm and of the anterior axes of the head and trunk were recorded optoelectronically using a WATSMART system (Northern Digital, Waterloo, Canada). Infrared emitting diodes were attached directly to the arm and forearm to define their longitudinal axes and to two aluminum bars, one attached to a weight belt worn about the thoracic region of the trunk and another to translucent goggles which were also used to blindfold the subject.

Constant, variable and RMS errors were used to evaluate the accuracy of placing the forearm parallel to the desired axis. It was assumed that errors would be lowest for the preferred direction. In addition, multiple regression analysis was used to determine whether the errors in forearm placement were predictable from differences in head, trunk and arm orientation. Such errors should be nearly random for the preferred direction but may depend on body orientation for the non-preferred direction.

RESULTS

Variable errors in placing the forearm parallel to the trunk-fixed anterior axis were significantly lower than for placement of the forearm parallel to the head-fixed anterior axis ($p < .05$). This is shown in Fig. 1 which displays the mean absolute constant (Fig. 1A) and variable errors (Fig. 1B) for all 5 conditions. RMS errors were also lower for perception of the trunk-fixed anterior direction. Thus, the experimental hypothesis that a trunk-fixed anterior direction would be preferred was supported.

It was also observed that errors in forearm positioning relative to the head-fixed anterior were highly predictable from differences in head and trunk orientation (neck rotation angle). This is shown in Fig. 2A which contains the mean coefficients of determination (R^2 values) for the multiple regression analysis. Furthermore, the coefficients for the differences in head and trunk orientations in the regression equation were similar for all six subjects when positioning the forearm parallel to the head-fixed anterior direction

(Fig. 2B). This indicates that all the subjects erred in a uniform manner on the basis of the difference in head and trunk orientations when perceiving the head-fixed anterior direction but not when perceiving the trunk-fixed anterior direction. Thus, these data also support the conclusion that the kinesthetic anterior direction is specified relative to the trunk rather than the head.

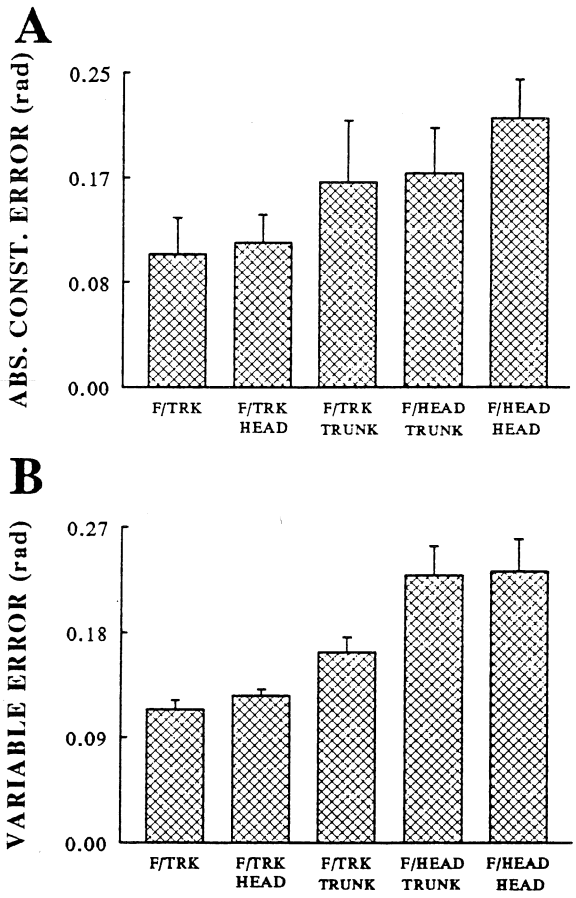

Figure 1: Constant (A) and variable (B) errors for kinesthetic perceptions of trunk-fixed and head-fixed anterior axes. Each bar is them ear error for six subjects. The labels on the abscissae represent the anterior axis to which the forearm was matched (trunk - F/TRK, head - F/HEAD) and, below those labels, whether head or trunk orientation was manipulated. Error bars represent 1 S.E.

DISCUSSION

The results of this experiment confirm the implicit assumption of most previous research that the kinesthetic anterior direction is specified relative to the trunk and not to the head. Thus, transformation of visually specified target coordinates into a kinesthetic coordinate system requires rotation of the head-fixed coordinates at least in terms of the anterior direction. Additional research is needed to specify whether the vertical axis of the kinesthetic system is earth-fixed (gravitational vertical) as assumed in previous research (e.g., Soechting 1981, Darling 1991), trunk-fixed (body longitudinal axis) or head-fixed (head longitudinal axis).

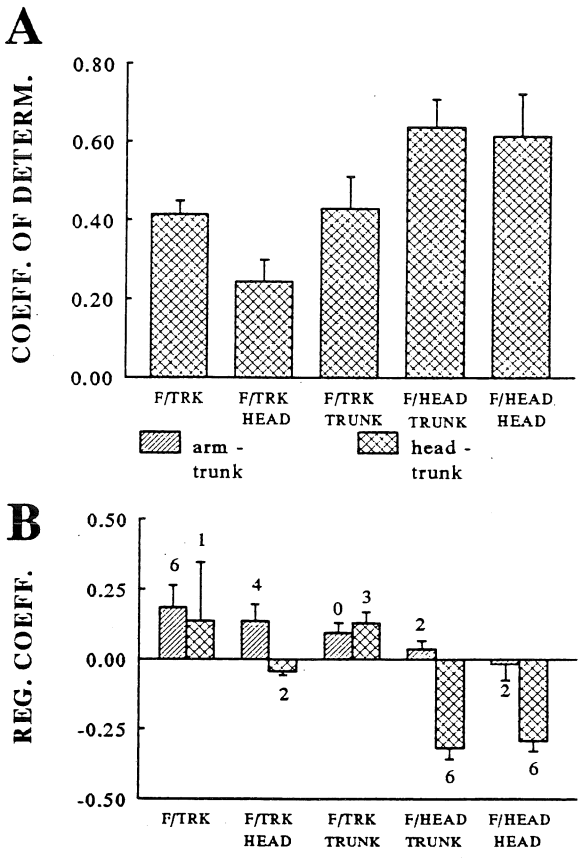

Figure 2: Mean coefficients of determination (A) and regression coefficients (B) for prediction of errors in kinesthetic perception of the anterior direction from differences in arm and trunk and head and trunk orientations. Each bar is the mean value for six subjects. The number above or below each bar in B represents the numberof subjects for whom the coefficient differed significantly from zero ($p < .05$). The labels on the abscissa of each graph are as described in Fig. 1.

REFERENCES

Darling W.G. Exp. Brain Res., 87, 445-456, 1991

Flanders M. et al. Behav. & Brain Sci., 15, 309-362, 1992

Soechting J.F. Brain Res., 248, 392-395, 1982

Soechting J.F., Ross B. Neurosci., 13, 595-604, 1984

FACTORS RESPONSIBLE FOR FORCE-SHARING BETWEEN SOLEUS AND GASTROCNEMIUS MUSCLES DURING CAT LOCOMOTION

B.I. Prilutsky*, W. Herzog, T.L. Allinger and T.R. Leonard

Human Performance Laboratory, The University of Calgary, Calgary, Alberta, Canada, T2N 1N4.
*Permanent address: Central Institute of Physical Culture, Moscow, Russia, 105483.

INTRODUCTION

Forces in cat soleus (SO) and gastrocnemius (GA) muscles were measured using tendon force transducers of the 'buckle'-type, and EMGs were recorded using bipolar, indwelling fine wire electrodes during normal locomotion. Muscle-tendon and fiber lengths, as well as the corresponding velocities, were derived from the hindlimb kinematics, anthropometric measurements, and a muscle model. SO force vs. GA force (force-sharing) and SO IEMG vs. GA IEMG (IEMG-sharing) relationships were analyzed for every step cycle. It was shown that the loop-like shape of the force-sharing relationship between SO and GA and the counterclockwise direction of formation of the force-sharing loops were determined primarily by differences in the contractile properties and the force-length relations of both muscles. Differences in normalized velocities of shortening of fibers of SO and GA during a step cycle were associated with the change in orientation of the force-sharing loops with increasing speeds of locomotion. The changes in activity of SO and GA were associated primarily with the decrease in width of the force-sharing loop with increasing speeds of locomotion.

REVIEW AND THEORY

Musculoskeletal systems of animals and humans are mathematically redundant. The advantages of this redundancy are not clear, but a disadvantage may be that motor control is complex (Bernstein, 1947). In order to gain an understanding of the biological significance of the musculoskeletal redundancy, it may be useful to study force- and activity-sharing between synergistic muscles during natural movements. The cat SO and GA are convenient models for studying force-sharing (Walmsley et al., 1978; Hodgson, 1983; Herzog and Leonard, 1991). The relationship between SO and GA forces during a step cycle has a loop-like shape. The direction of formation of the loop is counterclockwise. When speed of locomotion increases, the orientation of the force-sharing loop changes, because peak SO forces do not change much as a function of speed of locomotion, whereas peak GA forces increase substantially with increasing speeds of locomotion (Walmsley et al., 1978; Hodgson, 1983; Herzog et al., 1991). Hodgson (1983) assumed that force-sharing between SO and GA was determined primarily by the activation of these muscles, whereas differences in properties and structure of SO and GA did not influence force-sharing much. This explanation was based on the observation that force- and IEMG-sharing between SO and GA had a similar shape and that the absolute contractile conditions of the two muscles were similar. However, the fact that the normalized contractile conditions of SO and GA were dramatically different during locomotion was neglected.

The aim of this study was to identify factors that are responsible for the force-sharing between SO and GA: the counterclockwise direction of formation of the force-sharing loop, and the change of orientation of the loop with increasing speeds of locomotion.

PROCEDURES

Forces and EMG of soleus (SO) and gastrocnemius (GA) muscles, and the kinematics of five cats were recorded simultaneously during treadmill locomotion at nominal speeds of 0.4 m/s. 0.8 m/s, 1.2 m/s, 1.5 m/s and 1.8 m/s (Herzog and Leonard., 1991). Lengths of muscle-tendon complex and lengths and velocities of fibers of SO and GA in absolute and relative terms were calculated throughout the step cycle using a geometric muscle model (Allinger and Herzog, 1992), kinematic data and anthropometric measurements from the animal after sacrifice. The fiber velocities were normalized to the optimal length and maximum shortening velocity of fibers of SO and GA (Spector et al., 1980). Force values of SO and GA corresponding to each one percent of every step cycle were selected from raw force recordings, and were averaged over all step cycles available for a given speed. Raw EMG signals of SO and GA were rectified and integrated over time intervals of 50 ms for all step cycles. Discrete IEMG values were connected using an interpolation cubic spline, and IEMG values were then determined for each one percent of every step cycle and averaged over all step cycles available for a given cat and speed. In order to analyze force- and IEMG-sharing between SO and GA, force and IEMG of SO vs. force and IEMG of GA plots were constructed.

RESULTS

Figure 1 shows a force-sharing between SO and GA of a cat during step cycles at four different speeds. The direction of formation of the loop was counterclockwise except at a speed of 1.5 m/s. The angle of inclination of the loop decreased with increasing speeds of locomotion. When speed of locomotion increased, the descending portion of the force-sharing loop shifted to the right. This shift caused a decrease in width of the loop, a twist of the loop at a speed of 1.2 m/s and a change in the direction of formation of the loop at a speed of 1.5 m/s.

Figure 2 shows typical IEMG-sharing loops between SO and GA. The direction of formation of the IEMG-sharing loops was clockwise. The inclination of the loop was virtually independent of the speed of locomotion. The width of the loop increased as speed of locomotion increased due to a shift of the descending portion of the loop to the right.

Figure 3 shows the normalized velocity of fibers of SO and GA as a function of normalized step cycle time. The normalized fiber velocities of SO during elongation and shortening were consistently larger than those of GA, possibly with the exception of the slowest speed studied (0.4 m/s), where they were about the same. Differences between normalized fiber velocities of SO and GA increased with increasing speeds of locomotion. The peak forces of SO and GA occurred during the shortening phase of the muscle fibers.

DISCUSSION

The SO and GA have a different architecture and different

mechanical, morphological, and biochemical properties which affect the force output of these muscles. Twitch contraction time and twitch half-relaxation time of GA are shorter than those of SO (Spector et al., 1980) because of the different fiber type composition of these muscles (Burke et al., 1973, 1974). The difference in architecture of SO and GA [different fiber lengths and angles of pinnation (Spector et al., 1980)] is associated with a steeper ascending limb of the force-length relation of GA compared to SO (Walmsley and Proske, 1981). When relative rates of increase and decrease in IEMG of SO and GA are almost the same (Figure 2, speed 0.4 m/s), one may expect that relative rates of increase and decrease in the force of GA are higher than those of SO, because of the differences in the contractile properties and the force-length relations of these muscles. The experimental results obtained in this study support these expectations (Figures 1 and 2, speed 0.4 m/s).

Despite similar changes in the absolute length of the muscle-tendon complex, SO and GA had different relative shortening velocities of the fibers, particularly at speeds exceeding 0.4 m/s (Figure 3). This difference in relative velocities is primarily associated with the higher maximal velocity of shortening of fibers from GA compared to fibers from SO (Spector et al., 1980). At a speed of 0.4 m/s, the relative velocities of shortening of the SO and GA fibers were low. Therefore, the contractile abilities of both muscles were near their isometric values. When the speed of locomotion increased beyond 0.8 m/s, differences in the contractile abilities of SO and GA muscles increased substantially (Figure 3), with the contractile abilities of GA remaining closer to optimum than those of SO. This differential increase in contractile abilities may explain why GA forces increased steadily with increasing speeds of locomotion whereas peak SO forces did not.

With increasing speeds of locomotion, a decrease in the width of the force-sharing loop, a twist of the loop at a speed of 1.2 m/s, and a change in direction of formation of the loop was observed (Figure 1). We speculate that these changes in the shape of the force-sharing loops are associated with the shift of the descending portion of the IEMG-sharing loop to the right (Figure 2) and the more pronounced change of the normalized contractile abilities of SO compared to GA (Figure 3) with increasing speeds of locomotion.

In conclusion, the results of this study suggest that force-sharing between SO and GA muscles is determined by activity, mechanical and morphological properties, architecture, and kinematics of the muscles. Activity of SO and GA appears to be primarily responsible for the changes in the width of the force-sharing loops; mechanical and morphological properties of these muscles appear to be primarily responsible for the counterclockwise direction of formation of the force-sharing loops, and muscle kinematics and architecture of SO and GA are primarily associated with changes in the orientation of the force-sharing loops and their width.

REFERENCES

Allinger, T. and Herzog, W. Proceedings of The Second North American Congress on Biomechanics, Chicago, (pp. 81-82), 1992.

Bernstein, N.A. On construction of movements, Medgiz, Moscow (in Russian).

Burke, R.E. et al. J. Physiology, 238, 503-514, 1974.

Burke, R.E. et al. Physiology, 234, 723-748, 1973.

Herzog, W. and Leonard, T.R. Journal of Biomechanics, 24, 31-39, 1991.

Hodgson, J.A. J. Physiology, 337, 553-562, 1983.

Spector, S.A. et al. Journal of Neurophysiology, 44, 951-960, 1980.

Walmsley, B. et al. Journal of Neurophysiology, 41, 1203-1216, 1978.

Walmsley, B. and Proske, U. Journal of Neurophysiology, 46, 250-259, 1981.

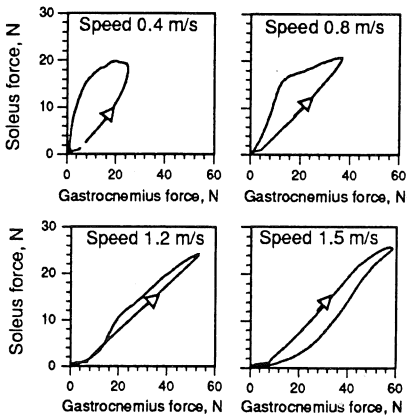

Figure 1. Force-sharing between SO and GA.

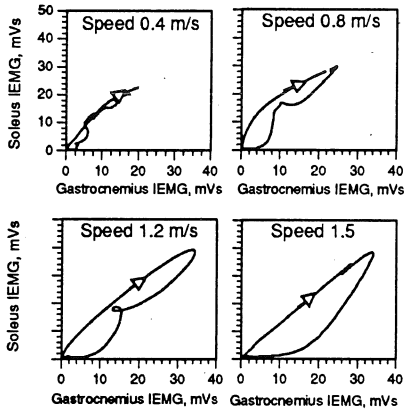

Figure 2. IEMG-sharing between SO and GA.

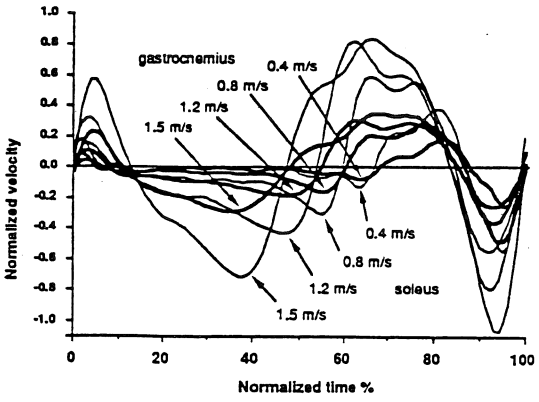

Figure 3. Normalized velocity of fibers of SO and GA as a function of normalized step cycle time.

IS THE PATTERN OF MUSCLE ACTIVITY IN HUMANS OPTIMAL DURING WALKING?

B.I. Prilutsky* and L.M. Raitsin

Central Institute of Physical Culture, Moscow, Russia, 105483
*Present address: Human Performance Laboratory, The University of Calgary, Calgary, Alberta, Canada, T2N 1N4.

INTRODUCTION

Muscle forces during walking, calculated using recorded movement characteristics of the subject and the optimization approach, were compared with integrated EMG (IEMG) of those muscles for which forces were determined. Six optimization criteria were used for the calculation of the muscle forces. Five criteria (the minimum sum of muscle forces, the minimum of the maximum stress among all muscles, the minimum sum of muscle powers, the maximum total muscle endurance, and the minimum of the maximum fatigue among all muscles) agreed with the hypothesis about optimal organization of the muscle activity, and one criterion (maximum sum of muscle forces) did not. It was shown that there was a qualitative agreement between IEMGs and muscle forces computed using the first five criteria. Forces computed using the sixth criterion clearly did not agree with the IEMG pattern. It was concluded that the pattern of muscle activity in humans during walking could be considered optimal.

REVIEW AND THEORY

Some researchers would argue that movements of animals and humans are optimal in terms of energy expenditure (Nubar et al., 1961), optimal time control (Clark et al., 1975), and so on. In support of this opinion, researchers point to the qualitative similarity between kinematic and joint moment patterns of humans (or animals), and anthropomorphic mechanisms, the movement characteristics of which are computed using an optimization approach (Formalsky, 1982). However, this comparison does not consider that the same kinematic and joint moment patterns of human (or animal) movement can be realized by an infinite number of muscle activity patterns because musculoskeletal systems of humans and animals are redundant: the number of muscles is higher than the number of mechanical degrees of freedom. Each muscle activity pattern can be associated with a different value of a cost function (for example, mechanical expenditure of muscles). Therefore, kinematic and joint moment patterns of human and animal movement do not determine completely the mechanical efficiency of a movement. To decide whether humans move in an optimal way, it is not enough to compare human kinematics and joint moments with optimal ones. It is necessarily also to determine if the muscle activity pattern is optimal.

The aim of this study was to try to answer the question: is the muscle activity pattern in humans optimal during walking?

PROCEDURES

In order to answer the above question, the following approach was used. The muscular forces which induce a given movement were determined from a recorded movement, walking. Muscular forces were calculated from the solution to the optimization problem, as described below. In other words, among all possible combinations of muscular forces that induce a given movement, the combination providing the minimum total muscular force or, minimum any other cost function, was found. Then a comparison was made between calculated muscular forces and integrated electrical activity of the same muscles (IEMG) recorded for the same movement. If there was an agreement between the forces and the IEMG, one could consider the organization of muscle activity optimal.

Recording of the electrical muscle activity. Ten young, healthy males took part in the experiments. Two 4-channel electromyographic amplifiers (MG-400, Medicor, Hungary) recorded electrical potentials of the muscles with surface bipolar silver electrodes 8 mm in diameter. Eight muscles of the right lower limb (Figure 1) were studied. After the electrical muscle potentials were amplified, they were fed into a computer (Robotron, Germany) at a sampling frequency of 2083 Hz for 2.8 s. The electrical activity of the muscles was recorded during the walking test on a treadmill operated at a speed of 1.82 m/s. The EMGs were rectified and integrated for every 40 ms. Discrete IEMG values were connected by an interpolation spline function from which IEMG values for each percent of the walking cycle were determined. The IEMG amplitude for each muscle was normalized to its maximum level in a single cycle of locomotion. For each per cent of the walking cycle, the average IEMG and its standard deviation over all walking cycles available for all subjects were calculated. A total of 20 walking cycles were processed.

Determination of forces generated by separate muscles during locomotion. Muscular forces during walking were determined from recorded movements by solving the inverse problem of dynamics using a musculoskeletal model of a lower limb (for more details see Prilutsky et al., 1989; Prilutsky, 1991). The model consisted of four links (foot, shank, thigh and pelvis) and 11 muscles. One subject walked at various speeds on a podium which had built-in force platforms (PD-3A, USSR). The coordinates of the metatarsophalangeal, ankle, knee, hip, and shoulder joints were recorded by an optoelectronic system (SELSPOT, Sweden). The trial of the subject walking at about 1.8 m/s was selected for further analysis. Joint moments were determined from coordinates of the appropriate joints and ground reactions (Prilutsky, 1991). The forces of separate muscles were determined by solving the optimization problem, formulated as follows: at each instant, find the minimum of the objective function depending upon all muscle forces

$$\Phi[F_1, F_2, ..., F_{11}] \rightarrow \min$$

under the constraints

$$M_j - \sum_i d_{ij} F_i = 0,$$

$$F_{imax} \geq F_i \geq 0,$$

$$(j=1,2,..., 3;\ i=1,2,..., 11),$$

where M_j is the joint moment relative to the j-th joint, F_i is the force of the i-th muscle, d_{ij} is the moment arm of the i-th muscle relative to the j-th joint, F_{imax} is the maximal muscle force of the i-th muscle ($F_{imax} = KA_i$, where $K = 40$ H/cm^2 is the muscle force constant, A_i is the average physiological cross-sectional area (PCSA) of the i-th muscle). The following optimization criteria were used: 1) the minimum sum of muscle forces (Yeo,1976); 2) the minimum of the maximum stress among all muscles (An et al., 1984); 3) the minimum sum of muscle powers (Prilutsky et al., 1989); 4) the maximum total muscle endurance (Crowninshield et al., 1981); and 5) the minimum of the maximum fatigue among all muscles (Dul et al., 1984). To prove

the hypothesis that muscle activity during walking is optimal, it is not enough to show an agreement between muscle forces calculated using the above criteria and IEMG of the same muscles. Hatze (1981) argued against the feasibility of determining muscle forces by the optimization method, noting that different objective functions give similar muscle forces that agree with their electrical activity. In other words, according to Hatze, this approach for the determination of muscle forces is not valid. Therefore, it is essential to prove that the deliberately 'non-optimal' criterion results in muscular force time histories that dramatically differ from IEMG patterns. We have chosen criterion 6), the maximum sum of the muscle forces as the 'non-optimal' criterion. The following method was used to solve the optimization problem. Each cycle of locomotion was divided into 20 instants. For each instant and optimization criterion, the sought-for muscle forces were determined. Discrete values of muscle forces for each particular criterion were connected by an interpolation spline function, from which muscle forces for each percent of walking cycle were obtained. The optimization procedure was carried out according to the standard algorithm, flexible simplex method, with an SM-1420 computer. The moment arms of muscles and their elongations necessary for computations were obtained from the recorded characteristics of the movement (joint angles) and with the use of empirical regression equations (Aruin et al., 1988). The percentage of slow muscle fibres needed to calculate criterion 5 were taken from Johnson et al. (1973). PCSAs of the muscles were taken from Pierrynowski (1982).

RESULTS AND DISCUSSION

Figure 1 presents the forces of the main muscle groups of the lower extremity which have been obtained using the optimization criteria 1 - 5 (A) and 6 (C), and mean IEMGs from the same muscles (B) during walking. The muscle forces obtained from criteria 1 - 5 are in agreement among themselves and with the IEMG patterns. Similar results were obtained by other authors (for example, see Crowninshield et al., 1981). For example, at higher electric muscle activity, muscular forces have higher values. When the electric activity is low the muscular forces approximate zero. As well, the forces and IEMGs of respective muscles have similar patterns (Figure 1, A, B). The muscular forces determined from criterion 6 clearly do not agree with IEMG. For example, TA and RF muscles (see Figure 1, C) demonstrate their maximum forces during the entire walking cycle. SO and GLM muscles do not produce any force. The patterns of muscular force in the other muscles differ dramatically from those of IEMG (Figure 1, B, C). Taking into account the close relation between muscle force output and IEMG, and that the muscle forces obtained using optimization criteria 1-5 are in agreement with the registered IEMGs for corresponding muscles (Figure 1, A, B), one might suppose that the muscle activity pattern during walking appear to be near optimal. The pattern of muscle activity is similar to the pattern of muscle forces obtained using different objective criteria, 1-5. All of those criteria are a function of muscle forces, and optimization of criteria 1-5 decreases the total muscle force. However, there is no well-grounded support for the conclusion that CNS controls locomotion by keeping the total muscle force minimal, although information about muscle forces can be obtained by CNS from the Golgi tendon organs. The obtained results do not allow us to formulate a hypothesis about the objective function which can be used by CNS to control locomotion. Apparent optimal organization of muscle activity during walking could be an 'accessory effect' of some kind of different principle of control.

REFERENCES

An, K.N. et al. Trans. ASME: J. Biomech. Eng., 106, 364-367.

Aruin, A.S. et al. Arch. Anat. Histol. Embriol., 94, 52-55, 1988 (in Russian).

Clark, M.R. et. al. IEEE Trans. Automat. Contr., 20, 345-248, 1975.

Crowninshield, R.D. et al. J. Biomechanics, 14, 793-801, 1981.

Dul, J. et al. J. Biomechanics, 17, 675-684, 1984.

Formalsky, A.M. Movement of anthropomorphic locomotor machines. Nauka, Moscow, 1982 (in Russian).

Hatze, H. IEEE Trans. Automat. Control., 25, 375-385, 1980.

Johnson, M.A. et al. J. Neurol. Sciences, 18, 111-129, 1973.

Nubar, Y. et al. Bull. Math. Biophys., 23, 377-390, 1961.

Pierrynowski, M.R. Ph.D. Thesis. Simon Fraser University, Vancouver, 1982.

Prilutsky, B.I. et al. Biophysics, 34, 1126-1131, 1989.

Prilutsky, B.I. Mathematical computer modelling of human movements (description of the model and software). Central Institute of Physical Culture, Moscow, 1991 (in Russian).

Yeo, B.P. J. Biomechanics, 9, 413-416, 1976.

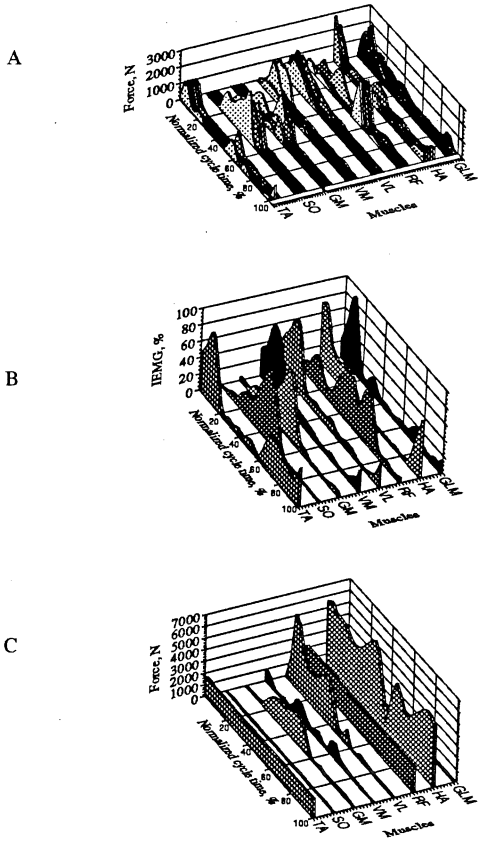

Figure 1. Muscle forces and IEMG during walking. TA is tibialis anterior muscle; SO is soleus muscle; GM is gastrocnemius medialis muscle; VM and VL are vastus medialis and vastus lateralis muscles, respectively; RF is rectus femoris muscle; HA is hamstrings; GLM is gluteus maximus muscle. A: The forces of eight muscles (each muscle force is represented by five force curves obtained using the optimization criteria Φ_1, Φ_2, ..., Φ_5, respectively). B: The averaged IEMG of eight muscles. C: The forces of eight muscles obtained using the optimization criterion Φ_6.

A 3-D, NONLINEAR, FINITE ELELMENT ANALYSIS OF THE EMBALMED HUMAN TIBIA

M. Cooper, J. Wasserman Phd., R. Krieg Phd., J. Snider Phd.

Graduate student, Univ. of TN, Knoxville, TN 37996
Dept. of Engineering Science, Univ. of TN, Knoxville, TN 37996
Dept. of Engineering Science, Univ. of TN, Knoxville, TN 37996
Dept. of Industrial Engineering, Univ. of TN, Knoxville, TN 37996

INTRODUCTION

Over the past seven years, the University of Tennessee, has conducted research in the area of high-speed impact of human, animal, and artificial leg bones for the Japanese Automobile Manufacturers Association (JAMA). This research involves an in-depth study concerning the mechanisms of failure in leg bones. The thrust of the study has been to quantify the damage to hard and soft tissues that undergo loading conditions similar to an automobile impact upon a human leg. The study has given insight into the design and development of protective mitigating devices as well as providing input data for modeling of the event.

The research reported here shows initial results of an application of a dynamic impact load to a 3D, nonlinear, finite element model of a human tibia. Experimental verification of the finite element model was conducted to ensure accuracy of results. Two main areas of interest in the computer model were fracture propagation and fracture force in the tibia.

REVIEW AND THEORY

The majority of previous research involving automobile accidents and biomechanics focused on injuries of the head and neck. Anthropomorphic dummies were generally reported as indicators of human body dynamics. In the present study, rather than considering the overall response of an assemblage of major body parts, we consider the detailed response of a single bone.

There is a vast amount of literature on material properties of human and animal tissue. This research uses material properties documented by such researchers as Yamada (1973), McElhaney (1966), and Fung (1981). Note the fact that these material properties were found at low strain rates instead of the preferable high strain rate data that is not available in the literature.

In 1972, FEM was introduced for use in the biomedical community to evaluate stresses in human bones; since then it has been used almost exclusively for orthopaedic applications. With the development of nonlinear, 3D, transient, dynamic finite element codes and powerful computer workstations, it is possible to use the FEM for complicated analyses of impact/injury predictions. Also with state-of-the-art impact facilities at the University of Tennessee, the computer model can be easily verified through experimental means.

PROCEDCURES

A 7.47 m./sec. midshaft impact of a dry embalmed human tibia was modeled computationaly through the FEM and experimentally to represent pedestrian/auto impact situations.

The FEM was conducted using a 3D, nonlinear, transient dynamic, finite element code developed by Taylor and Flanagan (1989). The finite element model consists of 13352 elements and 18669 nodes. Gravitational effects are neglected. The model is considered to be freely suspended and closely models the experimental test setup. Figure 1 shows the finite element mesh used for modeling purposes.

The experimental testing consisted of eleven tibia specimens potted at the proximal and distal ends in steel cups with woods metal. This weighting was considered appropriate for modeling the inertia of connecting body masses. Three crack gages instrument the diaphysis of the tibia to measure crack propagation. The tibia is impacted midshaft by an impact cart mounted with a force transducer to measure fracture force. All data was recorded on an HP3562A digital signal analyzer.

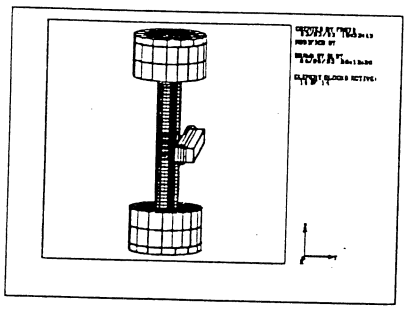

Figure 1. Finite Element Mesh

RESULTS AND DISCUSSION

The experimental results show that the fracture propagates in the posterior to anterior direction for four of the five tibial specimens on which the crack gages functioned properly. Average peak fracture force for all eleven tibias was found to be 5.73 KN with a standard deviation of 1.45 KN.

The finite element model showed that the crack propagated longitudinally along the anterior face of the tibia and from exact lateral-medial position propagating to the posterior midshaft region. However, when looking at interior slices of the tibia model, the crack propagated longitudinally at the anterior face but now propagates along the interior posterior wall of the cortical bone or in a longitudinal direction. The fracture results indicate longitudinal intact pieces of bone similar to that observed in the experiments. The fracture force was found to be 7.12 KN. This value is about 24% higher than the average experimental peak force but within one standard deviation of the experimental result. Although the FEM overpredicts the average experimental force, it should be noted that the computational model was based on an average human tibia and that the experimental force values are specimen dependant. There were tibia specimens that broke in the 7.12 KN range however using an average fracture force value lowered this number drastically. Table 2 shows the comparative results between the experimental and computational models.

TABLE 1 Comparative Study

Category	Experiment	FEM
Crack Direction	posterior to anterior	anteriorly longitudinal and middle midshaft to posterior midshaft
Fracture Geometry	Longitudinal Splinters	Longitudinal Splinters
Peak Fracture Force	5.73 KN	7.12 KN

A weakness of the finite element model is that the constitutive model approximated the region of failure but did not calculate the direction of each fracture.

The experimental testing showed problems with the crack gages. The crack gages adhered poorly to the bone and often the leads were pulled from their solder joints thus giving faulty readings.

REFERENCES

Fung, Y.C. Biomechanics Mechanical Properties of Living Tissues, Springer-Verlag, 1981.

Taylor, L. and D.P. Flanagan. PRONTO 3D a Three-Dimensional Transient Solid Dynamics Program, Sandia National Laboratories, 1989

Yamada, H. Strength of Biological Materials, Robert E. Krieger, 1973.

Acknowledgements

The authors acknowledge Kevin Brown, Tyler Kress, Jim Cain, Winston Holmes, Faye Muley.

DETERMINATION OF THE ACTUAL ULTRASONIC PATHWAY AND THE WAVELENGTH DEPENDENCE IN RELATION TO THE BONE SPECIMEN AND MICROSTRUCTURAL DIMENSIONS

Jae-Young Rho* and Kenneth P. Wagener§
*Department of Orthopaedic Surgery and §Department of Mechanical Engineering
State University of New York at Buffalo, Buffalo, NY 14214

INTRODUCTION

Ultrasonic methods have been used to measure properties intrinsic to bone's structure that are not necessarily dependent on bone mass[1]. However, one of the difficulties in applying these techniques is the unknown actual pathway of the wave through bone. Also, specimen dimensions must be taken into account when measuring a particular velocity. The purpose of this study was to determine the actual pathway and wavelength dependence in relation to the bone specimen and microstructural dimensions.

REVIEW AND THEORY

Elastic wave propagation theory predicts a relationship between the elastic modulus, density and acoustic velocity of the form

$$v = (E/\rho)^{1/2}$$

Whether this is true in a porous material like cancellous bone is critically dependent on the wave length of sound in relation to the bone specimen and microstructural dimensions[2]. Using low frequency ultrasound, Ashman and Rho (1988)[3] have found a good agreement between the ultrasonically determined and macroscopically measured elastic moduli. However, Martin (1991)[2] who doubts the ability to predict the results for high frequency ulrasonic velocity in relation to the microscopic modulus (i.e., for the bone within the trabeculae), suggests that the theory must be modified to deal with cancellous bone structure, and to describe the relationship of high frequency clinical measurements to bone microstructure.

It is well known that the velocity of propagation is dependent on the dimensions of the specimens and the wavelength. The specimen dimensions transverse to the direction of wave propagation are larger than the wavelength of the longitudinal wave propagated by the transducers so that the compressional wave propagates with the bulk wave speed. The other case, in where wavelengths are larger than the specimen dimension transverse to the direction of wave propagation is called bar velocity. In this case, the entire cross section is excited by the passing wave. Ashman *et al.*[4] mentioned that a theory does exist which describes stress wave propagation in the range between bulk and bar propagation. Although this is inconsistent with the theory, it is often exactly what is measured experimentally.

Therefore, the issue of actual pathlength and the wavelength dependence should be addressed. The distinction must be made with small samples if the measured value is the bar velocity or bulk wave velocity.

PROCEDURES

The pulse trasmission ultrasonic technique was used to measure the velocity. The pulse was excited with a Panametrics Model 5055UA pulser/receiver and time measurement were obtained by a Tektronix 2230 oscilloscope.

Twenty individual trabeculae (0.3 mm diameter by 2 mm length) and fifty cylindrical specimens (5mm diameter by 15 mm length) were obtained from the proximal region of a human tibia to examine the actual pathlength for cancellous bone. In addition, Plexiglass cylinders, 3.2, 6.5, 9.6 and 15.7mm in outer diameter, some solid and some with central holes ranging from 1.5 to 11mm were machined to simulate cortical bone cross-sections. The circular central hole will be filled with water that simulates bone marrow transmitted with a velocity of 1500 m/s. Also, 10 mm cubes of Plexiglass with regular space or irregular holes (1-5mm) was used to simulate the porous cancellous bone. Measurements taken with air in the central cavity confirmed that the pathway for the minimum time of flight was only through the Plexiglass. After the central cavity was filled with water, the two distinct pathways were verified.

In order to examine the effects of the specimen dimensions and the wavelength in the direction of wave propagation, a group of experiments was performed by using aluminum cylinders of varying diameters and lengths.

RESULTS

Transverse cortical bone velocity can be estimated by using the second order polynomial equation in Fig 1 which allows estimation of the path length as follows: $y=1.002+1.236e\text{-}2x+0.226x^2$, where x=pathlength, and y=ratio of medulla to cortex diameter.

The average velocity through a single trabecular bone was 2893.8 m/s (SD 152.1), while the mean velocity through cylindrical specimens was 2704.7 m/s (SD 142.3). Therefore, the velocity through the cylindrical specimens was underestimated as 6.5 percent of the velocity through a single trabecular bone.

The bar and bulk velocities of aluminum calculated from tabulated elastic coefficients were found to be 5083 m/s and 6320 m/s, respectively[4]. The bulk velocities in this experiment were found to be 6100 m/s. However, a transition between the bulk and bar wave velocity as Ashman *et al.* showed was not exhibited in Fig 2.

DISCUSSION

In this study transverse cortical bone velocity can be determined rather than the apparent transverse velocity because it is less subject to geometrical effects. This allows an estimation of the modulus of elasticity and should provide better correlation between individuals.

Inhomogeneity of cancellous bone may contribute to velocity measurement error. Acoustic waves travel faster through denser regions of bone; therefore, in an inhomogeneous sample, acoustic waves arrive at slightly different times. The variation in anisotropy of cancellous bone may also be taken into account to the calculation of velocity. However, the actual pathway of cancellous bone measurement was slightly longer than the length of the specimens (6.5%). It can be postulated that ultrasonic energy has propagated through the smallest passway.

The results of this study substantiated that dimensions should be carefully considered so the specific velocities and the associated elastic constants can be calculated.

REFERENCES

1. Turner and Eich *Cal Tissue Int* **49**, 116-119, 1991. 2. Martin, B. *J. Biomechanics* **24**, 79-88, 1991. 3. Ashman and Rho *J Biomechanics* **21**, 177-181, 1988. 4. Ashman *et al. J Biomechanics* **17**, 349-361, 1984.

ACKNOWLEDGMENTS

This work was supported by the SUNY at Buffalo Orthopaedic Research Fund.

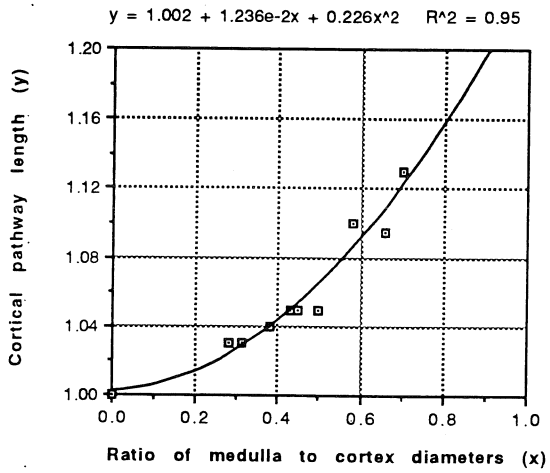

Fig1. Empirical formula for ultrasound pathway length for transverse cortical bone.

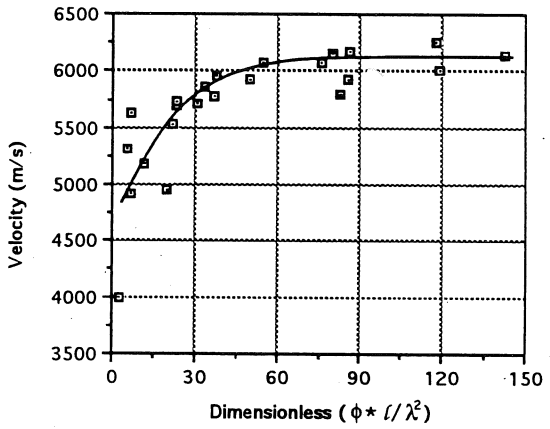

Fig2. Experimentally derived curves of velocity vs dimensionless (diameter*length/wavelength^2) for an aluminum rod.

NON-INVASIVE DETERMINATION OF LONG BONE STRUCTURAL PROPERTIES

T. M. Cleek and R. T. Whalen
NASA/Ames Research Center, Moffett Field, CA, 94035

INTRODUCTION

The cross-sectional asymmetry and curvature found in long bones are related to musculoskeletal forces present during development and maintenance of bone. Bone densitometry has been used to obtain cross-sectional properties of bone in the scan plane (Martin and Burr, 1984; Beck et al., 1990). It would be useful to have a non-invasive method to determine three-dimensional structural properties that would reflect the growth and loading history of an individual. Such a technique could effectively monitor effects of disuse, as with space flight or spinal cord injury, overuse with intense exercise, and be useful in clinical assessment of fracture risk in paraplegics, quadriplegics, and osteoporotics.

We have developed a non-invasive method that can be applied to produce non-uniform structural beam models of long bones. Principal second moments of area and orientation of the principal axes of the mineralized tissue at each scan cross-section along the length of a bone are determined by combining attenuation data from three non-coplanar dual-energy x-ray absorptiometry (DXA) scans. Whole bone models are generated by combining section properties from each scan cross-section.

We have investigated this new technique to determine its sensitivity and accuracy to (1) scan resolution, (2) cross-sectional shape, (3) orientation to the scan plane, (4) included angle of the non-coplanar scans, and (5) isotropy index, I_{min}/I_{max}. Axi- and non-axisymmetric aluminum phantoms of known cross-sectional properties and geometries were designed and used to validate our approach and algorithms.

REVIEW AND THEORY

Cross-sectional area, centroid, and the second moment of area of the phantom or mineralized tissue in the plane of the x-ray beam can be computed by integrating pixel bone mineral content or aluminum thickness across the scan width as proposed by Martin and Burr (1984). The discretized equations are

Cross-sectional area, A_t: $A_t = \Sigma\, t_i\, \Delta x$
Centroid, x^*: $x^* = (1/A_t)\, \Sigma\, x_i\, t_i\, \Delta x$
Second moment of area, I_y: $I_y = \Sigma\, (x_i^2 - x_i\, x^*)\, t_i\, \Delta x$.

The summation is across the phantom or bone width, t_i is the phantom or bone mineral thickness at the ith pixel obtained from raw attenuation data, and Δx is the pixel width (see fig. 1).

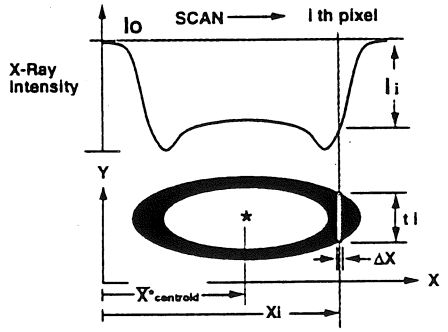

Figure 1: Method of Martin and Burr (1984) applied to an aluminum phantom cross-section

Independent analyses of 3 non-coplanar scans are used to obtain principal moments and orientations at each cross-section. Maximum and minimum second moments of area are calculated by the diagonalization of the moment matrix. Components of the transformation matrix are direction cosines of the principal axes which are orthogonal to each other. Section properties from cross-sections along the length of the phantom are then combined.

PROCEDURES

Beam calibration
Scans were taken with a Hologic QDR-1000/W bone densitometer in whole body, normal, and high resolution spine scan modes. Areal (pixel) resolutions for whole body, normal, and high resolution spine scans are 26.7, 0.95, and 0.47 mm^2, respectively. An aluminum phantom comprised of twenty 0.050" incremented steps was scanned to obtain linear calibration equations for the air, bone, and tissue segments of Hologic's internal calibration wheel. The regressions were used to convert beam attenuation data to equivalent thicknesses of aluminum. Only the high energy beam attenuation was used since all scans were done in air.

Phantom designs
Aluminum phantom designs included various tubes with a tapering outer diameter, an elliptical cross-section, an off-center circular cross-section, and a tapering double helical groove (fig. 2). An entire cadaver femur was also scanned and analyzed to explore the application of these methods to bone.

Expected values of sectional properties were computed from micrometer measurements and digitized cross-sections of the aluminum phantoms or were set by the machining operation (e.g., helical pitch angle).

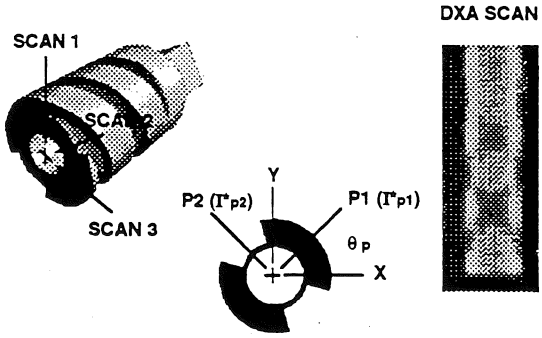

Figure 2: Aluminum double helical phantom

Scanning procedure
Objects were scanned along their entire length with the scan direction perpendicular to the phantom long axis. The tapered tube was scanned only once in whole body, normal, and high resolution spine modes, due to its symmetry. The helix was scanned 7 times in both whole body and normal spine modes by rotating the phantom axially from 0 to 90 degrees in 15 degree increments. The elliptical and off-center circular tubes were scanned in 15 degree increments, -45 to 135 and 0 to 90 degrees, respectively, in normal spine mode. A cadaver femur was scanned at 0, 45, and 90 degrees also in the normal spine mode.

Analysis
Computer programs accessed raw attenuation data, converted data to equivalent thicknesses, and computed section properties from the 3 registered scans. No special filtering or edge detection algorithms were used.

Section properties of the helix were calculated with 3 scans of various included angles. The planes used in the analysis included an initial position and ±45, ±30, or ±15 degrees from that angle yielding included angles of 90, 60 and 30 degrees at different cross-sectional orientations along the phantom length. Section properties of the off-center circular and elliptical phantoms were calculated similarly.

In this preliminary study, cadaver scans were not calibrated to bone tissue. Calculated values are proportional to second moments of the bone mineral attenuating the beam.

RESULTS

Influence of scan resolution
Aluminum thickness profiles across a scan line at the largest cross-section of the externally tapered tube were computed in whole body, normal spine, and high resolution spine modes. The greatest errors in thickness occurred at the edge of the internal diameter where the attenuation (thickness) gradient was the largest. There was no appreciable difference between the normal and high resolution spine scan measurements. The overall width of the phantom cross-section was overestimated in all scan modes mainly due to limitations of pixel width resolution and partial volume effects.

Cross-sectional areas and second moments of area computed over the length of the tapered tube were underestimated by an average of ~2% and ~4% respectively, in normal spine mode. Surprisingly, in the coarser whole body mode, cross-sectional areas were underestimated by an average of only ~2.5% and second moments of area were overestimated by ~3%. All calculated measurements were independent of phantom width and wall thickness.

Influence of included angle
The computed principal moments and orientations for both the ellipse and off-center circular tubes were extremely accurate for included angles of 90, 60, and 30 degrees. Angular position and changing cross-sectional shape of the helix also did not affect calculated section properties for all included angles investigated.

Principal major axis orientations of the helix were in excellent agreement with the expected angle from phantom design (fig. 3). There were slight increases in error with the 30 degree included angle, but the results were still within ~2 degrees of the expected value. Only minor errors were introduced as the helix approached a circular cross-section with no unique principal orientation.

The calculated principal angles from whole body scans were linear for all 3 included angles. When scanned at 0, 45, and 90 degrees, the maximum error in the computed principal axis orientation was 10 degrees. The highest errors were found at the ends of the phantom where areas of air and collet insertion may have been included in the wide scan lines.

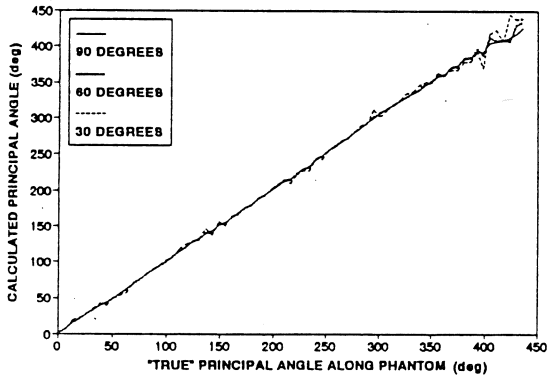

Figure 3: Principal axis orientation of double lead helix using spine scan mode

Influence of isotropy
The calculated principal second moments of area were expressed as an isotropy index, the ratio I_{min}/I_{max}. The isotropy index for the helix scanned in spine mode steadily increased from ~0.5 to 1.0 with included angles of 90, 60, and 30 degrees, as expected by design. With included angles of 30 and 60 degrees, slightly more noise was exhibited.

With the whole body mode, the isotropy index increased from ~0.6 to 1.0 for an included angle of 90 degrees. The isotropy index increased from 0.7 to 0.8 for included angles of 30 and 60 degrees. Overestimations of isotropy were due to errors in the calculations of both principal moments. Errors in computedmoments may have been caused by including air and unwanted metal sections at the ends, and the rapid changes in the cross-sectional area and orientation compared to line width.

Application of method (cadaver specimen)
Calculated sectional properties (proportional to mineralized tissue) along the femur length are shown in figure 4. As expected, the principal moments of the femur were larger at the proximal and distal ends with the major axis oriented in the medial/lateral plane. Large variations in the computed principal angle along the length were observed indicating changes in mass distribution. Small principal angles at the proximal and distal ends suggest flatter bone in this region. The principal major axis rotates 90 degrees to the anterior/posterior plane in the mid-diaphysis, although the bone cross-section is nearly isotropic in this region since I_{max} and I_{min} are nearly equal to each other.

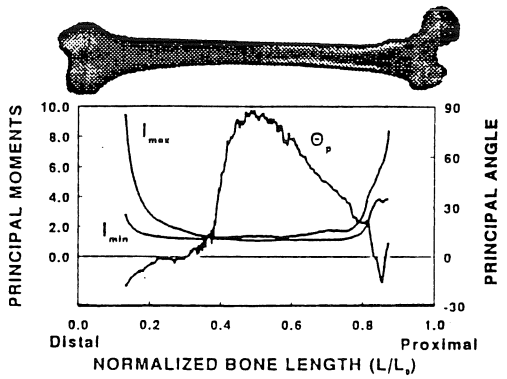

Figure 4: Femur sectional properties

DISCUSSION

Our initial efforts have concentrated on validating our approach and algorithms using phantoms of known material properties and geometries covering the normal range of long bone. Excellent agreement was found between experimentally determined and true section properties of axi- and non-axisymmetric phantoms. The high resolution spine scan mode did not prove to be more accurate than normal spine scans in computing section properties. The whole body scan was also found to be quite good in computing the properties of the tapered tube and helix, though its pixel resolution was much lower than either spine scan mode. Further investigation is needed to explore the limitations of this coarse mode. Errors in all scan modes were introduced in regions of high thickness gradients.

Calculated section properties were accurate and insensitive to cross-sectional shape and isotropy when 3 non-coplanar scans were taken with an included angle of 90 degrees. Minimal errors were introduced when the included angle was reduced. This finding is important for future *in vivo* studies of bones such as the tibia, which must be scanned without interference from the fibula.

Significant changes in principal moments and orientations along the length of the femur were observed, although this femur was nearly isotropic in the mid-diaphysis with respect to sectional properties. For bones with irregular cross-sections, a single scan or even 2 scans may be insufficient in the determination of whole long bone structural properties.

We believe this method of analysis will provide a useful link between changes in bone mineral distribution with changes in daily activity patterns, space flight, age, and spinal cord injury.

REFERENCES

Martin, B. and Burr, D. *J Biomech*, 17,195-205, 1984.
Beck et al. *Invest Radiol*, 25, 6-18, 1990.

A METHOD OF MEASURING THE CROSS-SECTIONAL AREA OF SOFT CONNECTIVE TISSUES DURING MECHANICAL TESTING

J. Lehneman, T.S. Keller, and † L.A. Ekström
Department of Mechanical Engineering, The University of Vermont, Burlington, VT. 05405
†Department of Orthopaedics, The University of Gothenburg, Gothenburg, Sweden

INTRODUCTION

A new method, incorporating two optocator scanning laser sensors, was used to determine the cross-sectional area of a rubber specimen and ligamentum flavum *in vitro* during mechanical testing. A rubber specimen and several plastic objects were used to determine the height precision (0.08 mm) and accuracy (0.21 mm) of the method. Mechanical tests were conducted on bone-ligament-bone preparations of the ligament in order to determine the sensor's reproducibility (5% of the field of view, FOV). This non-contact area measurement method allows the true stress of the specimen to be calculated and therefore provides a means to better understand the properties and behavior of soft connective tissues.

REVIEW AND THEORY

Soft connective tissues have been studied extensively in an attempt to develop a better understanding of their mechanical properties which will help in the diagnosis and treatment of soft connective tissue injuries. Of central importance to understanding soft tissue mechanical behavior is how the cross-sectional area changes as it is loaded in tension. However, measuring the cross-sectional area is not an easy task since the tissues are highly compliant, and their surfaces quite irregular.

Several non-contact[4,12] and contact[7,8,10] electronic and mechanical devices for measuring original cross-sectional area of soft tissues have been developed, and each offer certain advantages in terms of precision and accuracy, but none can be used to measure the cross-sectional area during mechanical testing. Shrive et al. (1988)[7] reported an area accuracy of 5% for their mechanical contact device. Schönström and Hansson (1991)[6] reported a thickness accuracy of 0.2 % for their non-contact thickness measurement method. An area precision of 0.71 mm^2 was reported by Torzilli et al. (1988)[8] for their mechanical area gage device, and 0.2 mm^2 by Woo et al, (1990)[12] for their laser micrometer device. Based on data provided by Vanderby et al. (1991)[10], an area accuracy of 0.22 mm^2 to 1.2 mm^2 was calculated for their TRAC device. The purpose of this study was to determine the accuracy, precision, and reproducibility of a laser based contour mapping and area measurement system modified to provide thickness and width measurements.

The area measurement equipment used includes two Selcom Optocator Scanner S001 lasers manufactured by Selcom AB, Partille, Sweden, originally developed for adaptive real-time robotic seam tracking of welds by measuring two dimensional height profiles and contours. The scanners emit an infrared laser beam which is swept (using a galvanometer) through a 30 mm range at the center of a 72 mm height measurement range which lies at a mounting stand-off distance of 190 mm from the back side of the laser head. The scanning frequency is 20 Hz, and the height of the object in the measurement range is determined by optical triangulation. The manufacturers precisions are 0.02 mm for the height and 0.12 mm for the width.

PROCEDURES

In order to facilitate simultaneous measurements of the surface contours of opposite sides of the mechanical test specimens, the laser scanners were mounted to opposite arms of a C-frame attached to a photostand. The photostand and C-frame were positioned such that the sweep range of the laser scanners was centered with respect to the mechanical test system cross-head (Figure 1). A Tektronics digital oscilloscope was used as a monitor for observing the signals from both lasers. Sweep and height data are output by the laser microprocessor as 12 bit digital data. This 12 bit digital data was converted to an analog signal using an 8 bit D/A converter (using the 8 least significant bits). The analog data was again converted to digital data using a 12 bit data acquisition system (Tecmar LabMaster) with a gain set to 4x, and stored as a binary data file on a personal computer. The height, sweep (width), invalid, load, and displacement signals were collected at an acquisition rate of 2400 Hz, resulting in ten cycles of 1200 points per channel, per load or distraction increment. The invalid signal provided a means to determine when the laser beam was not in contact with the specimen.

The binary data files were analyzed using a computer program (AreaCalc) that aligned and calibrated the width, height and invalid data from the two laser scanners. Since the lasers faced each other, their coordinate systems were different, so a coordinate transformation was performed. The scanner system was calibrated by placing a thin plate in the measurement range. The calibration gave an offset value which represented the difference in the calculated thickness and the known thickness of the plate. The thickness (T) of the specimen was calculated by adding the right height to the left height values, and subtracting the offset. The cross-sectional area was calculated from the X,Y (sweep width, height) using a successive approximation algorithm based on the method of Nagurka and Hayes (1980).[5]

For **accuracy** determinations, plastic objects with precise prismatic dimensions were scanned by the lasers, and the results were then compared to digital caliper measurements (0.025 mm resolution). The accuracy was determined using the digital caliper measurements as the 'gold standard', and calculated as the percent difference between the gold standard and the laser measured heights[11], based upon the height measurement range (72 mm).

For **precision** determinations, a rubber specimen, of gage length 98 mm, 6.52 mm thick and 23.87 mm wide was placed in a tensile testing machine using a clamp on both ends so that the specimens width was approximately perpendicular to, and in the center of the measurement range for both scanners. Fine adjustments were made until the laser emitting diode visible spots of both lasers were superimposed on each other. The specimen was then distracted through a series of 2 mm displacements up to 24 mm and then back down to zero displacement. The height and width profiles of the specimens were recorded simultaneously by both lasers at each displacement

increment. The precision was expressed as the standard deviation of the height measurements of the rubber specimen obtained from each laser scanner.[1],[2]

For **reproducibility** determinations, a spinal ligament specimen (ligamentum flavum), which had a width of approximately 19.5 mm at a load of 20 N, was obtained from the lumbar spine of a human cadaver. The ligamentum flavum and the bony processes where the ligament attaches were carefully dissected from the lumbar spine. The bone-ligament-bone preparation of the ligamentum flavum was placed in the tensile test machine and preconditioned by 20 load cycles from 20-100-20 N, followed by a series of 5 repetitions of a quasi-static distraction protocol of 20-100-20 N with load increments of about 20 N. The height and width profiles, sweep invalid, load and displacement signals were recorded at each increment. The reproducibility of the repeated measurements at each load increment were expressed as the coefficient of variation (COV) of the thickness and area values:[4],[13]

RESULTS

The laser sensors tended to underestimate the height and width of the plastic specimens used for the assessment of measurement accuracy (Table 1). In terms of the 72 mm field of view (FOV), the method had an average accuracy of 0.11%. Using the manufacturers precision value for the sweep width (≈ 0.1 mm), the effective area accuracy was approximately 0.025 mm^2 or < 0.01 % of FOV. Both lasers exhibited very precise height measurements for the rubber specimen at all elongation values. The average precision for both lasers was 0.08 mm (0.11% of FOV). The cross-sectional area of the rubber specimen was slightly overestimated after 10 mm elongation (Fig. 2). The reproducibility of the testing method ranged from 1.86 to 7.81% of the mean for the LF cross-sectional area with an average reproducibility of 4%, and from 3.07 to 8.08% for the thickness of the LF with an average reproducibility of 5%. There was a non-uniform change in the calculated area and average thickness values for increasing load and elongation.

DISCUSSION

All of the existing non-contact methods of measuring the cross-sectional area of soft connective tissues are limited to measurement of the original cross-sectional area. The scanning laser micrometers used in this study can measure the height variations of two surfaces on the specimen during testing, from which the cross-sectional area can be determined. These values compare favorably with that reported previously for other measurement devices. Some of the inaccuracies of the system may have been due to movement of the cross-section during testing, since the lasers were not repositioned during distration.

Table 1. Micrometer Shape Measurements used to Determine Accuracy. The accuracy (Acc) is expressed as a percentage of the height (H) measurement range (72 mm).

Specimen Shape	Caliper H (mm)	Scanner H (mm)	Acc (%)
White Nipple	1.78	1.72	(1.33)
Blue Ramp	3.46	3.25	(4.67)
Paper step	0.17	0.16	(0.22)
Gray Rack	1.85	1.81	(0.89)

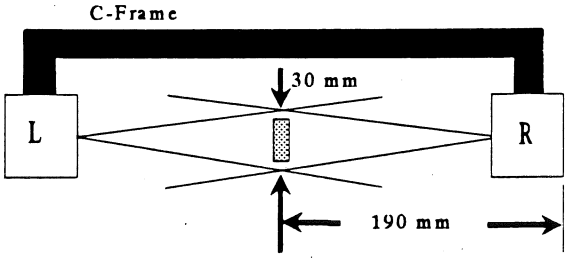

Figure 1. Top view of the scanners with a specimen in the measurement range. This figure shows the mounting stand-off distance (190 mm) and the width sweep range (30 mm).

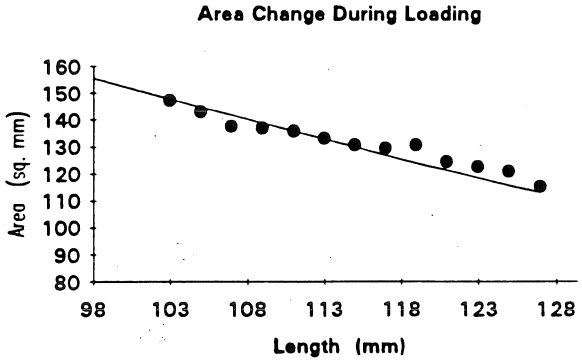

Figure 2. Cross-sectional area change during loading for the rubber specimen. The experimental results represent the theoretical curve very well, with only a slight overestimation after 10 mm elongation.

REFERENCES

[1] Annual Book of ASTM Standards, General Methods and Instrumentation, Vol. 14.02 1990.

[2] Barford,N. C. Experimental Measurements: Precision, Error and Truth, 2nd edition,John Wiley & Sons Ltd., 1985.

[3] Dillard,J. et al., *Spine*, **16**, :321-323, 1991.

[4] Lee,T.Q. et al., *J. Biomech. Eng.*, **110**, :110-114, 1988.

[5] Nagurka,M.L. et al., *J. Biomech.*, **13**, :59-64, 1980.

[6] Schönström,N.R. et al., *Clinical Biomech.*, **6**, :19-24, 1991.

[7] Shrive,N.G. et al., *J. Biomech. Eng.*, **110**, :104-108, 1988.

[8] Torzilli,P.A. et al., *J. Biomech. Eng.*, **110**, :208-212, 1988.

[9] Torzilli,P.A. et al., *J. Orthop. Research*, **9**, :730-736, 1991.

[10] Vanderby, R. Jr. et al., *IEEE Trans. Biomed. Eng.*, **38**, :1040-1042, 1991.

[11] Walton,J.S., *Proceedings of SPIE*, **693**, :14-25, 1988.

[12] Woo,S.L-Y. et al., J. *Biomech. Eng.*, **112**, :426-431, 1990.

THE USE OF BONE CONTOUR REGISTRATION TO INVESTIGATE CARPAL KINEMATICS

J.J. Crisco, K. Hentel, J. Duncan, L. Katz, S.W. Wolfe

Biomechanics Laboratory, Department of Orthopaedics and Rehabilitation
Yale University School of Medicine, 333 Cedar St., New Haven, CT, 06510

INTRODUCTION

Previously, accurate measurement of joint motion, important for applications ranging from implant design to instability assessment, required the attachment or implantation of markers, limiting detailed investigations of joints primarily to cadaveric studies. We propose that planar joint kinematics can be accurately determined non-invasively by matching, or registering, curvatures of bone contours obtained from imaging techniques. The goal of this work was to develop, validate, and apply such a method. The Curvature method was developed and validated *in vitro* by comparing its accuracy with the classical Two-Point method. The Curvature method was then used *in vivo* to investigate normal carpal kinematics.

REVIEW AND THEORY

Applications of registration algorithms have ranged from sorting manufactured assembly parts to identifying friendly and hostile aircraft. An extensive review of such may be found in the paper by Besl and Mckay (1992). The algorithm developed below is based on a technique developed to measure non-rigid deformations of the human heart. (Duncan et al., 1991a,b).

For the Curvature method, consider contour images of a bone at different positions, represented digitally with varying segment lengths and number of points. For each contour, the curvature as a function of length is determined. Because, curvature is invariant for rigid bodies, it is possible to register, or obtain a point for point correspondence, between two images. Such registration defines a field of displacement vectors (Fig 1) from which kinematic parameters are determined by a least squares minimization.

PROCEDURES

In Vitro
A sagittal section (1mm thick) was taken from the distal end of a dried cadaveric femur. Two steel balls (diam. 1.2 mm) were glued to the bone section. An apparatus was constructed to rotate the bone in a plane about a fixed axis. Thirteen different positions of the femur were recorded by an angular transducer and plane lateral radiographs. The two steel balls, bone contours and center of rotation were then manually digitized from the radiographs. The angle of rotation and the instantaneous center of rotation (CRi) were determined by both the classical Two-Point Method using the steel balls and the Curvature Method. Both methods were compared to the angle recorded by the transducer and the digitized CRi.

In vivo
As part of an ongoing study, 8 healthy subjects without history of wrist injury underwent CT scanning of the wrist with the elbow flexed such that a sagittal image could be obtained through the distal radius, lunate, capitate and third metacarpal using 1.5 mm thick sections and a field of view of 16 cm. The hand and the forearm were positioned in a custom Plexiglas device that fixed the wrist in ten degree increments from flexion to extension. The CT images were then digitized manually to obtain the bone contours. The relative motion between the radius and the capitate, the lunate and capitate, and the capitate and metacarpal were determined using the Curvature method. From this, the LC/LR ratio, defined as the number of degrees of capitolunate motion for each degree of radiolunate motion, was calculated.

RESULTS

The *in vitro* accuracy of the Curvature method was comparable to that of the Two-Point Method (Table 1). For both methods, the error in rotation angle was approximately constant, whereas the error in the CRi was inversely proportional to the angle of rotation.

Table 1. Mean [s.d.] error in both methods for the fixed-axis, rigid-body rotations (n=13) of the *in vitro* femur experiment.

	Rotation (deg)	CRi (mm)
Two-Point	0.23 [0.13]	4.51 [4.91]
Curvature	0.44 [0.19]	6.61 [8.86]

For the *in vivo* carpal motion, the average LC/LR ratio was 1.9 (0.27) in flexion defined from -20 to -60 degrees and 0.8 (0.21) in extension defined from 20 to 60 degrees. In both flexion and extension the LC/LR ratio tended to increase as the wrist moved away from the neutral position.

DISCUSSION

Accurate and non invasive motion measurement has important and widespread applications in biomechanics. The Curvature method was shown to be comparable in accuracy to the Two-Point Method with several advantages. One significant advantage is its non invasive nature. A second advantage is that for images that are partially obscured, the Curvature method is still applicable. Furthermore registration provides a full field of contour displacement vectors that can easily be adapted to determine soft tissue strains.

This method was applied to a *in vivo* study of wrist kinematics. The average LC/LR ratios were determined for flexion and extension, omitting the points around the neutral position as error was shown to be inversely proportional to angle size. The values obtained for the LC/LR ratio for normal carpal kinematics are similar to those determined by a Two-Point method (Wolfe et al, 1993). The same paper also reported significantly different LC/LR ratios may indicate wrist pathology. The Curvature method now offers a non invasive method to quantify joint motion using common imaging modalities which can lead to both classification and early diagnosis of abnormal joint motion.

Currently, the major limitation of the Curvature method is that it is only applicable for two-dimensional motion. Even so, the method presented above allows *in vivo* motion studies that previously were limited to cadaveric studies, making it a potentially valuable scientific and clinical tool.

REFERENCES

Besl, P.J. and Mckay, N.D. (1992) *IEEE Trans. Pattern Anal. Machine Intell.* 14, 239-256.

Duncan, J. et al.(1991) *Proc. Comput. Vision Patt. Recogn.* (Hawaii) pp.318-324.

Duncan J. et al. (1990) Proc. Comput. Cardiology (Chicago) pp.41-44.

Wolfe S.W. et al. (1993) Adavances in the Biomechanics of the Hand and Wrist, Plenum Publishing Corp. New York 1993.

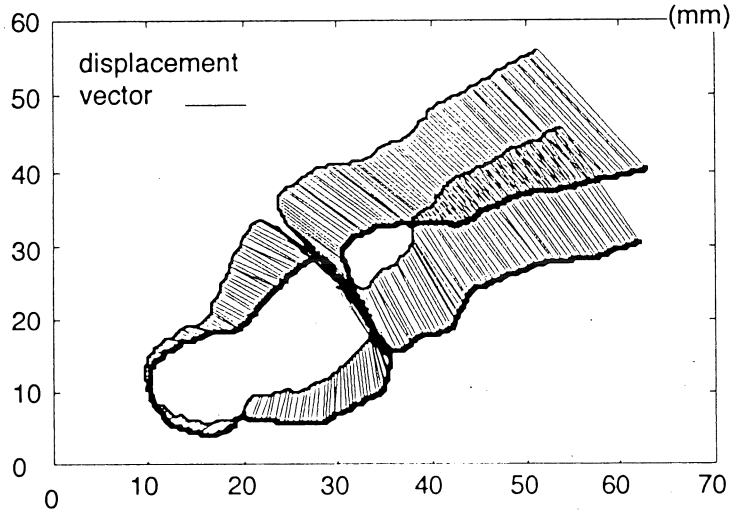

Figure 1 - Displacement vectors of the capitate and third metacarpal defined by registration of two contour images. Radius and lunate are not shown.

CRINKLE ARTIFACT COMPENSATION IN PRESSURE-SENSITIVE FILM RECORDINGS

N. J. Caldwell, J. E. Hale*, M. J. Rudert, and T. D. Brown

Departments of Orthopaedic Surgery and Biomedical Engineering, The University of Iowa, Iowa City, IA 52242
*Rehabilitation Engineering Center, University of Virginia, Charlottesville, VA 22903

INTRODUCTION

An objective, empirically based image-processing technique was devised to compensate for the presence of crinkle artifact in Pressensor pressure-sensitive film recordings. A spherical indentor was used to produce film stains which deliberately included radially directed artifact streaks, superimposed upon otherwise smooth, nearly axisymmetric stain recordings. An interactive, threshold-based search algorithm was developed to delineate explicitly the perimeters of specific artifacts present within manually (cursor) circumscribed regions where crinkle features were visually apparent. Three mathematical artifact transformation operators were parametrically evaluated in terms of their ability to approximate objectively the corresponding artifact-free axisymmetric pressure fields. All three operators were found to reduce substantially the quantitative deviation from the idealized distributions. When appropriately tuned transformation operators were applied to typical *in vitro* intraarticular contact stains, the visual prominence of crinkle artifact features was markedly reduced.

REVIEW AND THEORY

The use of commercially available pressure-sensitive film (Pressensor Film, Inteque Resources Corp., P. O. Box 2112, Fort Lee, NJ 0702) has come to be almost standard practice for measuring contact pressure distributions in articular joints. While adequate for many applications, the film's performance is problematical when the contact surface under study possesses two principal planes of substantial curvature. Because the paired acetate film sheets can freely bend only in one curvature plane, conformation to a bicurvilinear surface requires that the sheets locally fold or crinkle. This gives rise to high local stresses at the fold edges, causing artifactual streaks in what otherwise would be smooth gradations of staining intensity.

A means to retroactively compensate for such crinkle stain artifacts could potentially extend the range of feasible film application. This paper reports on the development of an objective, empirically based image processing technique devised for that purpose.

PROCEDURES

A family of Pressensor stains, containing deliberately induced crinkle artifacts of various intensities, was produced by spherical platen indentation of a rubber substrate layer. The raw stains were converted to quantitative contact stress distributions using the digital image analysis protocol of Hale et al. (1992).

Artifact features were delineated manually by a cursor-input m-sided circumscribing polygon Γ, drawn slightly outside the visually apparent margin of each involved region (Fig. 1). To provide for objective and consistent designation of the artifact perimeter, inwardly directed local surface normals $\mathbf{n}_i$ were constructed through the midpoint of each line segment of Γ. Along each $\mathbf{n}_i$, grey levels were sequentially sampled at regular increments. The corresponding $\mathbf{m}_i$ points on the artifact perimeter polygon Π were defined as those points at which the apparent local grey level gradient $\delta g/\delta n_i$ (determined by a Lagrange-polynomial-based differencing formula) exceeded a discontinuity threshold ε.

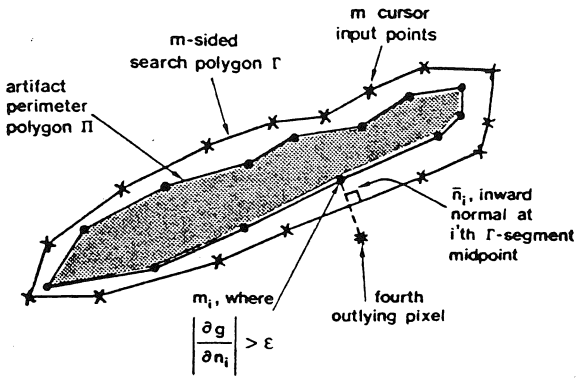

Figure 1. Definition schematic diagram for the geometric parameters used to identify the margins of a typical crinkle artifact.

The perimeter polygon, Π, enclosed a large number of pixels, for each of which the 'true' pressure, p_j, was assumed to have been overwritten by an artifactual value p°_j apparent in the raw image. Artifact compensation consisted of invoking an empirical transformation operator Φ within Π, so as to change each overwritten pixel pressure p°_j to a compensated value p^c_j. Departures from the ideal radial pressure variation were indexed in terms of a residual error function Ψ.

Three candidate forms of the Φ operator were investigated: one involving power-weighted averaging of grey scales within Π, one involving an exponential transformation of pressures within Π, and one involving proximity-weighting based on pixels immediately outside the perimeter of Π. These respective operator forms are given by:

$$\Phi_1:\ g^c_j = g_{min}\sqrt[k]{(1/q)\sum_{j=1}^{q}(g^\circ_j/g_{min})^k} \qquad (1)$$

$$\Phi_2:\ p^c_j = (1/q)\sum_{j=1}^{q}(p^\circ_j)\, e^{-[(\beta/100)p^\circ_j]} \qquad (2)$$

$$\Phi_3:\ g^c_j = \{\,1/\sum_{i=1}^{m}[1/(r_{ij})^\gamma]\,\}\sum_{i=1}^{m}\{\,1/[(r_{ij})^\gamma]g^\circ_{i*}\} \qquad (3)$$

where k is a positive integer value, β is a positive real value, r_{ij} is the distance from internal pixel j to perimeter pixel i, g°_{i*} is the

grey level in the fourth outlying (i.e. non-overwritten) pixel along n_4, and γ is a proximity weighting factor.

RESULTS

All three transform operators proved successful in substantially reducing the discrepancy, Ψ, between the expected axisymmetric pressures and those initially present. The compensatory power of the two homogenizing transforms (Φ_1 and Φ_2) was a strong function of the features of the specific image. The error reductions of these two transforms as a function of their respective weighting parameters, k and β, are shown in Fig. 2 for one representative artifact pattern stain (#4M). For this particular stain, both the Φ_1 and Φ_2 operators show a decrease of the error as the weighting parameter is increased, albeit with progressively diminishing returns. The maximum error corrections were about 54% for this stain.

The dependence of Ψ upon the proximity weighting factor γ for the Φ_3 operator was also investigated. The results for a typical stain are also shown in Fig. 2. This operator produced much more visually striking artifact compensation than could be achieved for either of the homogenizing operators, despite only slightly improved objective (Ψ) residual error reductions.

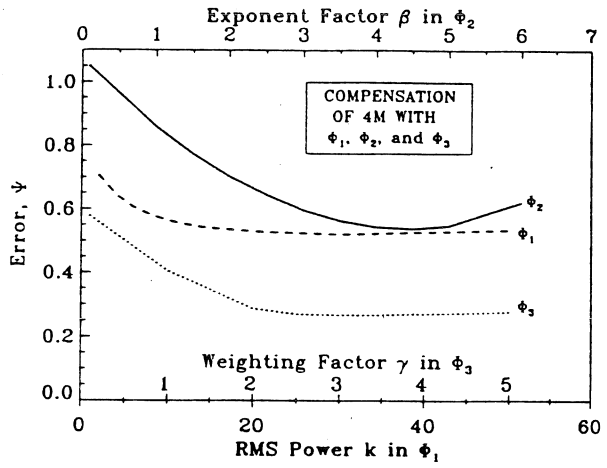

Figure 2. Representative residual error reductions obtained with the artifact homogenizing operators Φ_1, Φ_2, and Φ_3, as a function of the k, β, and γ, factors, respectively. Increasing the k and β factors corresponds to increasing the relative weighting to less densely stained regions, while increasing γ corresponds to increasing the relative weighting of the closest perimeter pixels.

DISCUSSION

While the objective error reductions available with each of the alternative Φ operators lie within the same general range (50-80%), Φ_1 and Φ_2 are restricted to homogeneous artifact smoothing, based ultimately on artifactual information that has been written over the original pressures. By contrast, Φ_3 has the intuitive appeal of allowing graded blending of artifacts, and is ultimately based on noncorrupted information. Figure 3 demonstrates the striking effectiveness of the Φ_3 operator in reducing the visual dominance of artifact features in a typical *in vitro* film recording of contact pressures from a human ankle (talar plafond).

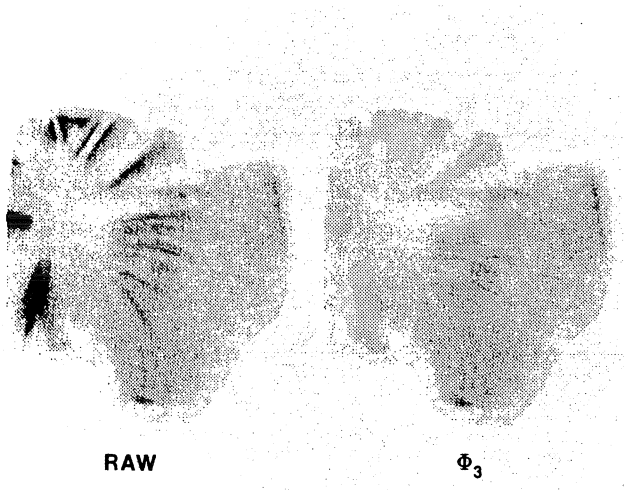

Figure 3. An illustration of the effectiveness of the Φ_3 operator in reducing the dominance of the crinkle artifact in an *in vitro* contact pressure recording from a human ankle. In this particular application, talar plafond contact pressures were mapped as a function of residual offset in a displaced Weber type-C fracture. The salient features of the recording are preserved essentially intact, whereas most of the crinkle artifact is removed. Such an image is thus rendered much more amenable to automated analysis of contact area, peak and spatial mean pressures, histograms of area loading intensity, etc.

Obviously, many other Φ expressions are conceivable, some of which may improve upon the present performance. And, it is important to bear in mind that the use of these operators should be limited to noncritical areas of a stain. Nevertheless, given the essentially empiric nature of this approach to artifact compensation, and given the relatively modest goal of first-order image correction, this approach to artifact approximation should suffice for a great many practical applications.

REFERENCES

Hale, J. et al. J. Biomech. Eng., 114:352-357, 1992.

ACKNOWLEDGMENTS

The authors appreciate the technical assistance of Mr. Douglas R. Pedersen. Financial support was provided by NIH Grant AR-38916, and by the University of Iowa Undergraduate Scholar Assistantship Program.

A Calibration Technique for Measurements from Photographs of Sliced Specimens.

H.Wang*, J. Ryu, and J.S. Han
Orthopedic Research Laboratory, Department of Orthopedic Surgery
West Virginia University, Morgantown, WV 26506-9196
*Orthopedic Research Laboratory, Department of Orthopedic Surgery
Texas Tech Health Science Center, El Paso, TX 79912

INTRODUCTION

Photographs of sliced specimens (PSS) is a technique widely used in determining three-dimensional human joint geometry. It consists of four procedures: slicing, photographing, projecting and digitizing. It is simple in principle, easy to implement, and probably the most effective way to evaluate *closed-surface* geometry. However, a number of inherent errors, such as lens distortion, film deformation, and non-parallelity between the lens and the surface of an object, may influence the reliability of PSS measurements.

This study attempts to improve PSS measurement accuracy by developing a calibration technique consisting of a mathematical model linked to a precise plastic grating. Three tests were conducted to verify calibration effectiveness; resultant accuracies are reported.

METHOD

Calibration Principle: Define $\boldsymbol{Po}(x, y)$ to be a position vector of an observation point in the observed plane denoted by xy, and $\boldsymbol{Pi}(u, v)$ to be the counterpart of that point in the image plane represented by uv, both relative to an affixed local reference system (Figure 1). Then in the photographic procedures of PSS, the two position vectors can be related as:

$$\boldsymbol{Po}(x, y) = \frac{1}{m}[\boldsymbol{Pi}(u, v) - \Delta \boldsymbol{P}(u, v)] \qquad (1)$$

where m is a magnification factor, $\Delta \boldsymbol{P}(u, v)$ is defined as a deviant position vector with two equal components expressed by:

$$\Delta P_u = \Delta P_v = A + Bu + Cv + \sum_{k=1}^{N} Z_k(u, v) \qquad (2)$$

in which A, B, and C are three constants, and

$$Z_k(u, v) = D_k[(u - x_k)^2 + (v - y_k)^2] \ln[(u - x_k)^2 + (v - y_k)^2]$$

in which coefficients D_k are subjected to the following three constraint equations:

$$\sum_{k=1}^{N} D_k = 0, \quad \sum_{k=1}^{N} D_k u_k = 0, \quad \sum_{k=1}^{N} D_k v_k = 0 \qquad (3)$$

By substituting values of N sampling points into equation (2) and combining equation (3), $N + 3$ coefficients in the two equations can be solved, and $\boldsymbol{Po}(x, y)$ in equation (1) are therefore determined.

Calibration implementation: A plastic grating, consisting of orthogonal lines that form grating mesh points (GMPs), was utilized to define the above calibration mathematical model by selecting a number of GMPs at an area being studied. A computer program based on the model was developed to implement calibration. In the three calibration tests, slides, taken of the grating were projected onto the graphics table of a two-dimensional digitizer (Scriptel Translucent Digitizer: Model RDT 2436) with measurement accuracy of $0.05mm$. GMPs in a photographed area were selected and digitized. Data obtained facilitated calibration. Calibration accuracy of the GMPs examined was obtained by comparing their calculated coordinates, both before and after calibration, with their original coordinates, which were readily determined by known grating intervals.

RESULTS

Test A: A Nikon camera ($120mm/f3.5$), was used to photograph a $100 \times 100mm$ section of grating. Fifteen GMPs in that section were chosen to define a calibration model, and 25 GMPs were examined to test their calibration accuracies. Results show that, after calibration, average accuracy of the 25 GMPs for x and y coordinates was $0.07 \pm 0.05mm$ and $0.08 \pm 0.06mm$, respectively; while before calibration, the accuracy was $15.03 \pm 8.49mm$ and $14.53 \pm 8.62mm$, respectively.

Test B: The same Nikon camera, mounted with a fish-eye lens, was used to photograph a $250 \times 200mm$ section of grating. In that section, 45 GMPs were chosen to define a calibration model. An additional 48 GMPs were randomly selected to examine calibration accuracy. It was found that, average accuracy of the 48 GMPs for x and y coordinates after calibration was $0.28 \pm 0.23mm$ and $0.30 \pm 0.27mm$, respectively; while before calibration, the accuracy was $5.90 \pm 2.56mm$ and $3.68 \pm 2.10mm$, respectively. Figure 2 shows total error and nonlinear distribution for x and y coordinates. Shapes of the two types of nonlinear distortions were even greater than the total errors. This illustrates that the error due to lens distortion using the fish-eye lens has greater influence on the results than the parallelity between medias.

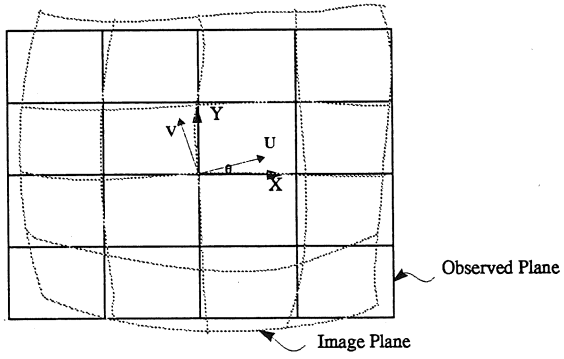

Figure 1

Test C: A third simulated test was performed on a template, bearing several circles whose diameters were measure using a Vernier caliper with a measurement accuracy of $50\mu m$. The area photographed covered approximately $60 \times 35mm$, and contained $23, 18, 17, 6.5, 6,$ and $5.5mm$ in diameter circles. Marked lens distortion in the field was evident even to the naked eye. (Figure 3). Calibration results gave an excellent approximation of the original coordinate, with average accuracy of 0.07 and $0.05mm$ for x and y, respectively, which is also close to the two-dimensional mechanical digitizer measurement accuracy of $50\mu m$. Table 1 presents diametric values for six templates circles, as well as samplings densities along their peripheries. Differences between diameters before and after calibration and their measurements determined with Vernier caliper were compared.

Figure 2

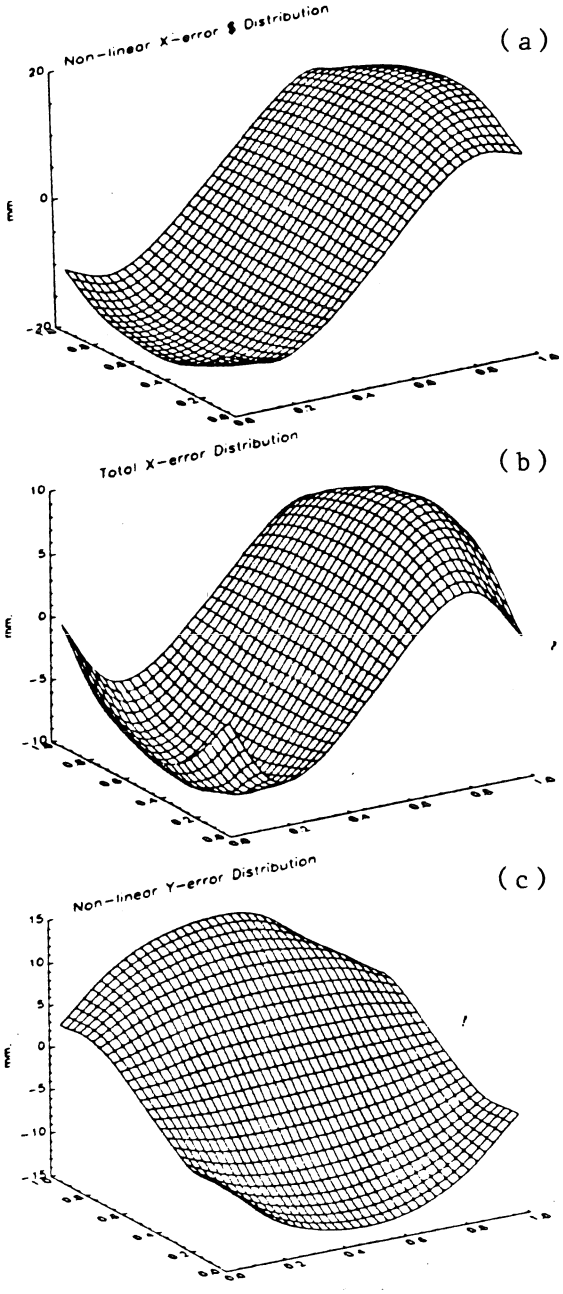

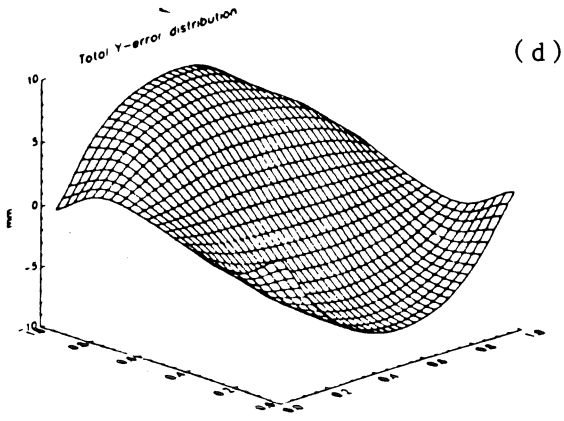

Figure 3

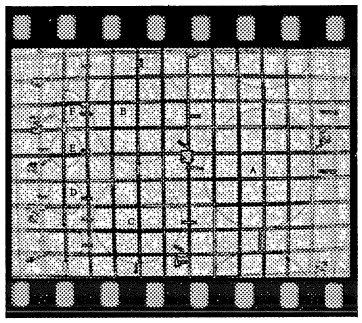

DISCUSSION

A mathematical model for calibrating errors involved in the photographic procedures of PSS is described here. The model consists of linear and nonlinear functions capable of reflecting overall and local error distribution in an area being investigated. It is therefore believed to be an effective calibration technique.

In the three tests, parallelity between projector and digitizer table was purposely left unadjusted. Thus, error distribution in test A was basically linear in the calibrated area because a standard lens with little image distortion was used. Measurement accuracy after calibration in this test A was close to that of the digitizer. In test B, however, the fish-eye lens generated a large image distortion dominated by a nonlinear error component. As a result, measurement accuracy was lower than in test A, although it was still greatly enhanced. This seems reasonable, because nonlinear error is quite complicated, thus making it much more difficult to deal with mathematically than linear error.

CONCLUSION

The calibration technique described here demonstrates effective calibration of errors involved in the PSS technique, yielding a good assessment of accuracy. Our method, therefore, can enhance the reliability of PSS measurements and extend the possibility of an accurate description of the articular surfaces of human joints, where high accuracy in measurement is essential for defining geometric parameters.

REFERENCES

1. Szilard R. (1974) Theory and Analysis of Plates, PRENTICE HALL, INC., Englewood Cliffs, New Jersey

ACKNOWLEDGEMENTS

Partially supported by a Whitaker Bioengineering Research Grant and the Orthopedic Research and Education Foundation Fund

CAN THE TEKSCAN SENSOR ACCURATELY MEASURE DYNAMIC PRESSURES IN THE KNEE JOINT?

J.L. Pavlovic, Y. Takahashi, J.E. Bechtold, R.B. Gustilo, R.F. Kyle

Orthopaedic Biomechanics Laboratory, Hennepin County Medical Center,
701 Park Ave. S., Minneapolis, MN, 55415

INTRODUCTION

Thin mylar conductive paint sensors (Tekscan, Inc., Boston, MA) were evaluated for their effectiveness in measuring dynamic pressures in the human knee joint. The sensor measurements were repeatable, but demonstrated hysteresis and inaccuracy. The results indicated that the sensors can be effective in this application if they're calibrated at an appropriate load and if the output is carefully analyzed.

REVIEW AND THEORY

A six degree-of-freedom dynamic knee simulator has been developed to move a human cadaver knee through a specified range of motion while applying muscle and ground reaction forces. The simulator provides realistic conditions for measuring pressures in the knee joint. A sensor that can accurately measure dynamic pressure magnitude and distribution is needed to measure normal knees and reconstructed knees, which may have high pressure concentrations that can cause pain and excessive wear on prostheses. Static joint pressures have previously been measured with Fuji film (Liggins, *et al.* (1991)). However, Fuji film does not allow dynamic measurement and quantification of pressure distributions.

Tekscan, Inc. developed a thin (0.10 mm), flexible sensor that can be inserted into the joint (Fig. 1). This computer-controlled sensor is made of a mylar substrate enveloping a 10x10 conductive paint grid consisting of 100 "sensels". The sensor measures force and pressure distributions, and the computer displays the pressure distributions in real time. The purpose of this project was to determine how accurately and consistently the Tekscan sensor can measure pressure under dynamic loading conditions. The data were evaluated at three loading rates to determine (*i*) Repeatability: how consistently the sensor measured the loads over ten trials, (*ii*) Hysteresis: how well the unloading curves matched the loading curves, and (*iii*) Accuracy: how well the sensor force matched the applied force.

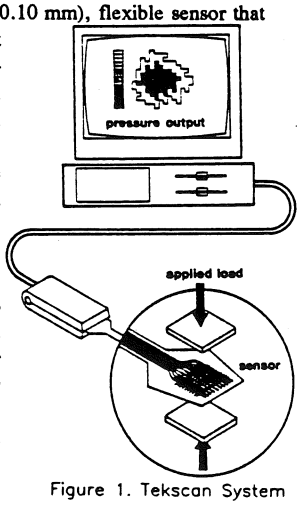

Figure 1. Tekscan System

PROCEDURES

To simulate conditions for intra-articular testing, one layer of 3M #5480 tape (3M, St. Paul, MN) was applied to each side of the sensor. The sensor was then sandwiched between two polished metal squares made to fit the sensor area (Fig. 1), and loads were applied by a servohydraulic materials testing machine.

Tekscan reports a need for sensor "conditioning", which requires at least twelve loading cycles to prevent changes in the calibration with use (Cranmer (1992)). Before testing, the sensor was conditioned by loading it to 1,334 N (300 lb.) fifteen times. Each time, the sensor was loaded for one minute, then unloaded for one minute before the load was applied again.

Loading and unloading of the Tekscan sensor were tested at three rates, in this order, to simulate human walking (Inman (1981)), knee simulator speed, and a medium rate halfway between the first two (Fig. 2-Fig. 4). For each rate, the sensor was calibrated at 1,334 N, then tested ten times, allowing at least two minutes between tests. During each test, the entire area of the sensor was loaded once to 1,334 N, to represent the maximum patellofemoral force in level walking (Fulkerson, *et al.* (1990), Hsu, *et al.* (1989), and Koshino (1991)), then unloaded.

RESULTS AND DISCUSSION

The results are reported in terms of total force read by the sensor, which is the sum for all sensels of the pressure detected by each sensel times the sensel area. The pressure varied in direct proportion to the force because the same loading area was used throughout the study.

Repeatability: Figures 2 through 4 show that the sensor measurements were very repeatable over each set of ten trials. On closer inspection of these curves, Figures 5 through 7 show that the sensor force increased with each additional trial, and increased by almost 20 N over ten trials. It is important to note that over all thirty trials, the sensor force increased by almost 30 N, which is 2.3% of the total load range (0-1,334 N).

Hysteresis: Figure 8 shows that, for each loading rate, the sensor forces were higher and less accurate for unloading (2) than for loading (1). The amount of hysteresis varied, with maximums of 75 N (5.6% of the load range) at the walking rate, 106 N (8.0%) at the medium rate, and 113 N (8.5%) at the knee simulator rate. The sensor had the least amount of hysteresis at the fastest loading rate.

Accuracy: The sensor force curves followed the patterns of the applied force curves well for all three test rates. But the sensor readings (355-400 N) were very high for the 111 N applied load at the beginning and end of each test (Fig. 2-Fig. 4). Did this error occur because the sensor was calibrated at a 1,334 N load? To answer this question, the same sensor was calibrated at two lower loads and tested at all three rates. At 111 N calibration, the sensor was accurate at the 111 N load, but measured 470-495 N at the 1,334 N load (Fig. 2-Fig. 4). At 890 N calibration, the sensor force was 260 N at the 111 N load and 1,040-1,070 N at the 1,334 N load. These results indicate that the error at the low 111 N load in the original tests was due to the high calibration load (1,334 N). Since the sensor could not measure up to 1,334 N when calibrated at 111 N or 890 N, it is important to note that the sensor must be calibrated at the

maximum load to be measured, and will only be accurate for a small range of loads.

In Figure 8, the sensor force curve would follow the diagonal line if the sensor were perfectly accurate. For all three loading rates, the sensor force was high, except near the calibration load (1,334 N). The greatest difference between the applied force and the sensor force for loading was 320 N (24% of the load range) for the walking rate, 295 N (22%) for the medium rate, and 280 N (21%) for the knee simulator rate. This is unsatisfactory. However, if the difference between the applied force and the sensor force is known and consistent, this offset value can be used to calculate the true force from the sensor reading. Also, since the sensors are thin, it may be possible to insert two sensors, calibrated for different load ranges, into the joint to obtain accurate measurements over a larger range.

CONCLUSIONS

Clinically, we're interested in locating and reducing high pressure concentrations which cause pain and degradation in the knee joint. Since we want to compare pressure distributions in the normal knee and the reconstructed knee, and we're looking for high pressure areas, the Tekscan sensor is useful for this application. The sensor measurements were repeatable over many loadings. The results were best, with the least amount of hysteresis, at the fastest loading rate. Sensor accuracy was poor, but comparable for all loading rates. The sensor should be calibrated at the maximum load to be measured. Sensor readings low and high relative to the calibration load will not be accurate. This must be accounted for by a using a known offset, or simultaneously using two sensors calibrated for different load ranges, to obtain accurate output.

REFERENCES

Cranmer, H. *et al.* RESNA International, 1992.

Fulkerson, J.P. *et al.* Disorders of the Patellofemoral Joint, (pp. 27-29), Williams & Wilkins, 1990.

Hsu, *et al.* Clinical Orthopaedics, 246, 260-265, 1989.

Inman, V.T. Human Walking, (p. 28), Williams & Wilkins, 1981.

Koshino T. Clin. Orthop. Rel. Res., 266, 133-138, 1991.

Liggins, A.B. *et al.* Trans. First Combined Meeting of U.S.A., Japan, and Canada, Banff, 1991.

ACKNOWLEDGEMENTS

The Whitaker Foundation is gratefully acknowledged for their support of this project.

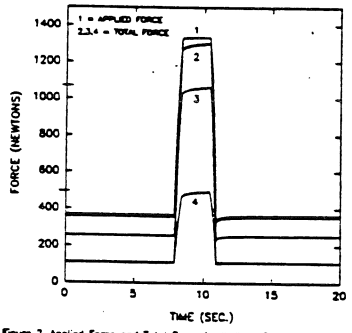

Figure 2. Applied Force and Total Force for Walking Rate Load. Sensor Calibrated at 2) 1334 N (10 trials), 3) 890 N, and 4) 111 N.

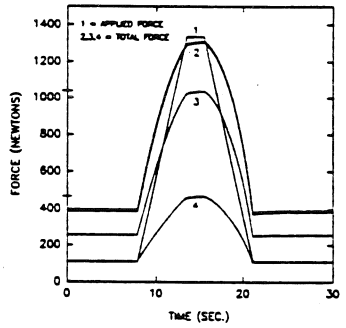

Figure 3. Applied Force and Total Force for Medium Rate Load Sensor Calibrated at 2) 1334 N (10 trials), 3) 890 N, and 4) 111 N.

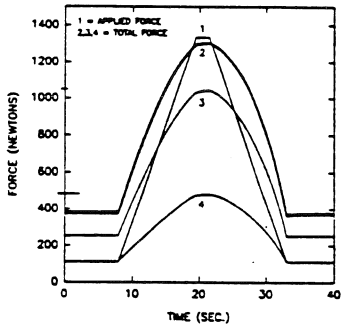

Figure 4. Applied Force and Total Force for Knee Simulator Rate Load. Sensor Calibrated at (2) 1334 N (10 trials), (3) 890 N, and (4) 111 N.

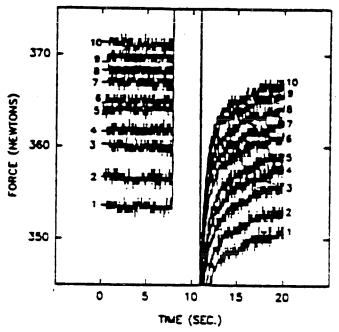

Figure 5. Close-Up of Total Force for Walking Rate Load. (10 trials)

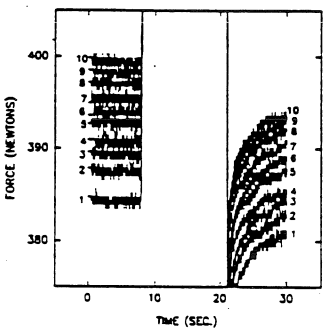

Figure 6. Close-Up of Total Force for Medium Rate Load (10 trials)

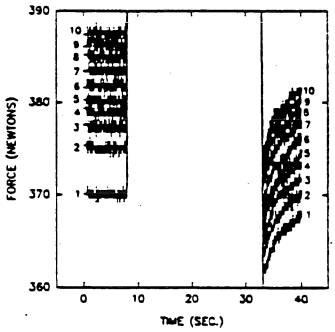

Figure 7. Close-Up of Total Force for Knee Simulator Rate Load (10 trials)

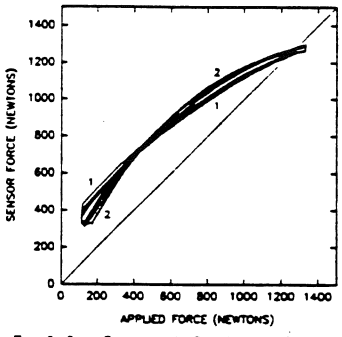

Figure 8a. Sensor Force vs. Applied Force for Walking Rate Load

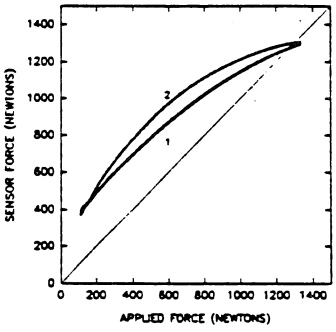

Figure 8b. Sensor Force vs. Applied Force for Medium Rate Load

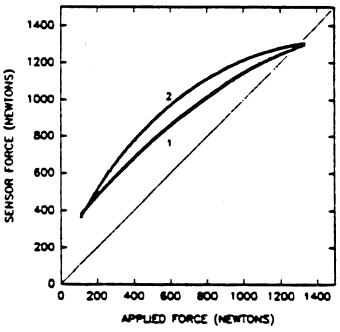

Figure 8c. Sensor Force vs. Applied Force for Knee Simulator Rate Load

THE EFFECT OF REARFOOT STRUCTURE ON RELATIVE TIBIAL-TO-REARFOOT ROTATIONS OF THE COMBINED TALOCALCANEAL AND TALOCRURAL JOINTS

D.A. Nawoczenski, T.M. Cook, and C. L. Saltzman*
Physical Therapy Graduate Program, The University of Iowa, Iowa City, IA 52242
*Department of Orthopedic Surgery, The University of Iowa Hospitals & Clinics, Iowa City, IA 52242

INTRODUCTION

Musculoskeletal injuries of the lower extremity have been linked to alterations in kinematic behavior resulting from abnormal structures of the foot. The focus of many investigations has been directed to the subtalar joint (STJ) because of its assumed role in force attenuation and transfer of axial rotation from the weight-accepting leg to pronation/supination of the foot during stance. While biological differences have been reported to account for much of the inter-subject variability in the results of kinematic investigations, few studies have attempted to categorize foot structures when studying movement behavior of the LE.

This study examined the effects of foot structure on relative tibial-to-rearfoot rotations during the stance phase of running. Ten subjects were identified for each of two distinct foot groups based on radiographic measurement criteria. The three-dimensional kinematics were recorded during treadmill running. A Cardan angle system of three ordered rotations was used to define the relative orientation between the lower leg and rearfoot.

The results of the kinematic analysis indicated significant rotational differences between groups for selected dependent variables. The coupling ratio, which described the proportion of tibial abduction/adduction (AB/AD) rotations relative to internal/external rotation (IR/ER), demonstrated group differences for different periods of stance analyzed. The rotation patterns unique to each group may provide a better understanding of injury mechanisms associated with foot structures similar to those studied in this investigation.

REVIEW AND THEORY

Musculoskeletal injuries in the lower extremity (LE) are common in activities that are highly repetitive in nature. These injuries have also been linked to abnormal structures of the foot. Recently, an abnormal coupling between inversion/eversion movement of the foot and the axial rotation of the leg has been described to be a contributing factor to LE musculoskeletal injuries (Siegler et al., 1988; Nigg et al., 1992). This coupling has been indirectly related to the orientation of the STJ axis, which is determined, in part, by the structure and shape of the articulating surfaces of the foot. The biological differences in foot structures have been reported to account for much of the variability between subjects and investigations that have studied the kinematic behavior of the STJ complex (Engsberg et al., 1988; VanLangelaan, 1983). However, there have been few studies that have categorized foot structures when examining LE kinematic behavior. The purpose of this investigation was to determine the effect of rearfoot structure on relative tibial-to-rearfoot rotations of the combined talocalcaneal (STJ) and talocrural (TC) joints during the stance phase of running.

PROCEDURES

Ten recreational runners were identified for each of two foot groups based on radiographic measurements of the lateral calcaneal inclination, lateral talometatarsal, and anterior-posterior talometatarsal angles. The groups were identified as either a low rearfoot profile group, or a high rearfoot profile group. Prior to the test session, each subject was issued a pair of sport sandals that allowed for direct visualization of the rearfoot target markers without imposing any motion-control constraints.

Three markers were placed on each of the lower leg and rearfoot segments. Three high-speed, high resolution cameras, sampling at 60 Hz. were used to film the subjects during treadmill running at self-selected speeds. Following the filming session, the target markers and selected anatomical markers were digitized using the Metrecom Skeletal Analysis System (3D digitizer). Using these data, an anatomical coordinate system (ACS) and a target marker coordinate system (MCS) were constructed for each of the lower leg (tibia) and foot segments. A transformation matrix, which related the assumed constant orientation of the target MCS to the ACS was determined during a standing neutral calibration position. This matrix was used to transform the MCS to the ACS of each segment for each frame of a digitized running trial.

Two additional transformation matrices were determined at each time instant of the stance period, and were based on the target marker data measured in the laboratory coordinate system. A final computation described the orientation of the lower leg ACS with respect to the rearfoot ACS. A Cardan angle system of three ordered rotations was used to define the relative orientation of the two body segments. The Z-Y-X rotation sequence described internal/external (IR/ER), abduction/adduction (AB/AD), and dorsiflexion/plantarflexion (DF/PF) rotations about coordinate axes embedded in the lower leg. These coordinate axes were assigned the orientation of the laboratory coordinate system such that the X axis was directed medial-lateral, the Y axis anterior-posterior, and the Z axis vertical. The focus of this investigation was directed to the IR/ER and AB/AD rotations. IR/ER was calculated as a rotation of the lower leg relative to a fixed rearfoot about the Z axis of the tibia. AB/AD described the rotation of the lower leg with respect to the rearfoot about the Y axis of the tibia.

The Peak Performance Motion Analysis System was used to acquire two dimensional coordinate data. The DLT method (Abdel-Aziz, 1971) was applied to compute the 3D marker coordinates using customized software programs.

The dependent variables were the magnitudes of α and ß rotations describing IR/ER (max-min) and AB/AD (max-min), respectively, as well as the coupling relationship of ß/α. The coupling relationship was assessed for the entire stance period (ßmax/αmax), as well as for the period of stance from heel contact to peak AB and IR ($ß_{HCAB}/\alpha_{HCIR}$). Means and standard deviations were obtained for all dependent variables describing α and ß rotations about Z and Y, respectively. Independent sample t-tests were used to evaluate group differences for each independent variable. The mean of three successive stance trials of one extremity was used in the analysis. The significance was set at $p < 0.05$.

RESULTS

Means, standard deviations and results from the t-tests are summarized in Table 1. Figures 1 and 2 represent the kinematic patterns of the coupling relationship for representative subjects in the low and high rearfoot groups, respectively. In these figures "hc" represents heel contact and "to" signifies toe-off. The groups were significantly different for the ratio ßmax/αmax (1.5 for low rearfoot; 0.91 for high rearfoot). The low rearfoot group demonstrated greater AB/AD to IR/ER rotation for the entire stance period. Conversely, the high rearfoot group showed greater IR/ER rotation to AB/AD for this period of stance. Although it did not test significant, the ratio increased for both groups for the period of stance between heel contact and maximum AB and IR (1.8 for low rearfoot; 1.1 for high rearfoot). Both groups demonstrated similar magnitudes for AB during this period of gait.

Table 1. Means, (standard deviations) and t-test results of IR/ER, AB/AD rotations and ratios for all dependent variables

Variable	Low Rearfoot Profile Group N=10	High Rearfoot Profile Group N=10	t-test p
α max	10.4 (5.5)	14.6 (7.6)	0.23
ß max	12.2 (5.0)	10.2 (4.2)	0.90
ß max/α max	1.5 (1.3)	.91 (0.65)	0.04*
α HCIR	6.4 (4.1)	10.4 (7.6)	0.04*
ß HCAB	8.8 (4.4)	8.2 (3.9)	0.85
ß HCAB/α HCIR	1.8 (1.1)	1.1 (0.7)	0.29

NOTE: All means and standard deviations are presented in degrees.
*Significant group differences

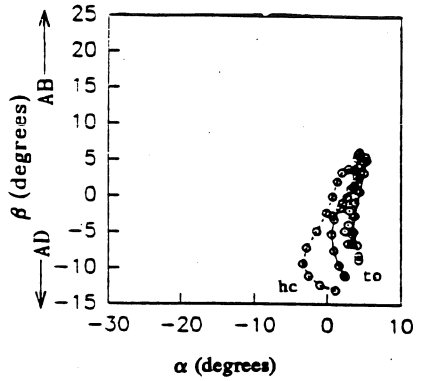

Figure 1. Representative Subject - Low Rearfoot.

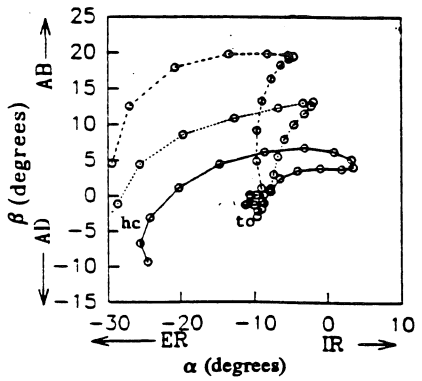

Figure 2. Representative Subject - High Rearfoot

DISCUSSION

In this investigation lower leg to rearfoot rotations were described without the confounding effects of motion-control footwear. Furthermore, to our knowledge, this is the first report of the 3-dimensional kinematic behavior of foot subtypes classified according to strict radiographic criteria. The kinematic analysis demonstrated both descriptive and statistical differences between groups for α and ß rotations. The predominant rotations demonstrated by each foot group suggested an effective, combined STJ/TC axis orientation that favored AB/AD rotation for the low rearfoot structure, and IR/ER for the high rearfoot structure.

The coupling ratio, which describes the proportion of rotation of AB/AD to IR/ER, has been considered by some investigators to be an important indicator of injury potential in the LE. Nigg et al. (Nigg et al., 1992) found a difference in this ratio between high- and low- arch subject groups. The investigators used the term "transfer coefficient" to describe the coupling of foot in-eversion to axial leg rotation.

In the present study the ratio demonstrated characteristic kinematic behavior for the groups that was not obvious when making individual axis rotational comparisons. The ratio also varied according to the period of stance analyzed. Subjects in the high rearfoot group not only displayed greater magnitudes of α rotations about Z, but also displayed a coupling relationship having greater proportion of IR/ER to AB/AD than subjects in the low rearfoot group, measured over the entire stance period (0.91 for high group; 1.5 for low group). For the period of stance between heel contact and maximum IR and maximum AB, the ratios increased for both subject groups, but most markedly for subjects in the low rearfoot group (1.1 for high group; 1.8 for low group). There was no difference between the groups for the magnitudes of ß rotation from heel contact to maximum AB; the primary difference occurred in the amount of associated, or coupled IR.

These findings indicate that different strategies may be necessary for the effective treatment of musculoskeletal symptoms related to foot structures represented in this study. Mechanisms for injury prevention may be better directed to the loading response of stance for individuals in the low rearfoot group. For the high rearfoot group, injury prevention becomes more challenging when trying to affect the IR/ER component of tibial motion.

REFERENCES

Abdel-Aziz, Y. and Karara, H. ASP Symposium on Close Range Photogrammetry, 1971.

Engsberg, J. et al. J Orthop Res 6;749-757, 1988.

Nigg, B.M., et al. Proceedings of the NACOB, (pp 233-234), 1992.

Siegler, S. et al. J Biomech Eng, 110, 364-373, 1988.

ACKNOWLEDGEMENTS

This project was supported in part by a grant from the Foundation for Physical Therapy.

THE EFFECT OF BONE MINERAL PARTICLES ON THE POROSITY OF BONE CEMENT

Y.S. Kim, J.K. Kim, and J.B. Park

Department of Biomedical Engineering
The University of Iowa, Iowa City, Iowa, 52242

INTRODUCTION

The cemented total hip arthroplasty creates three areas of concern:cement mantle itself, cement-metal interface and cement-bone interface. Therefore, maximizing the strength of the bone cement itself by reinforcement with additives or reduction of pores is not enough for a successful total hip arthroplasty.

Bone mineral particle impregnated bone cement have a dual-purpose in bone-cement fixation technique:(1) it is used to fix the implant immediately, (2) later the particles can be resorbed while new tissues grow into the resorbing space resulting in "biologic or tissue ingrowth fixation".[2] Our previous results showed that bone mineral particle impregnated bone cement decreased the tensile strength but increased the crack propagation rate.[1]

The present study was undertaken to elucidate the effect of bone mineral particles on the porosity of bone cement *in vitro* by using laser confocal electron microscopy and computer assisted image analysis.

REVIEW AND THEORY

There have been two different approaches in improving strength of acrylic bone cement. One approach has been to increase cement strength by making it a composite by incorporating reinforcing materials. Due to application difficulties in clinical situations and/or a marginal improvement in properties, this method has not been successful. The other approach has been to reduce the porosity of bone cement by centrifugation and vacuum mixing.

PROCEDURES

Fresh canine cadaver femora were osteotomized through the base of a lesser trochanter at a right angle to the long axis. The intramedullary cavity was drilled and reamed to a diameter of 10mm, with a depth of 11cm. The cavity was irrigated thoroughly with a saline solution. The medullary was injected with the prepared bone cement(Zimmer regular bone cement®, Zimmer, USA, Warsaw, IN) containing 0, 10, 20, and 30% bone mineral particles. Bone mineral particles(150-300μm) were made from canine femora according to the method described earlier. A 4mm diameter 10cm long stainless steel rod was inserted to simulate an implant. Distal and proximal portions of the specimen with stainless steel rod was cut into ten 2mm thick disc(three each for the two portions) for pore analysis. Five canine cadaver femurs were used for each group(0, 10, 20, and 30% bone mineral particles).

The representative surface of each specimen was observed with a confocal laser scanning microscope(MRC 600, Biorad Co., England) and pictures were taken randomly in the cement region. Pores were traced with a black pen on a transparent paper and an image was obtained using a high-resolution television camera. Digital images were processed by using a personal computer(Macintosh Quadra 950, Apple Co), from which distribution and size of detectable pores were measured by counting them in a

15.8mm^2 area an the pore size was measured from the digitized images directly. Pore distribution was analyzed by using a linear analysis method.
In order to evaluate the tensile strength, bone cement was introduced into a 9mm(inside diameter) cylindrical glass tube. After the bone cement hardened, the glass tube was removed. The samples were cut with a diamond blade into 2mm long for diametral mechanical testing on a hydraulically controlled machine(MTS, Minneapolis, MN) using 12mm/min cross-head speed at room temperature between two self-aligning plates.

RESULTS

The mean and standard deviation of the porosity and size of the pores are summarized in Table 1 and the diametral tensile strength are plotted in Figure 1.

Table 1. Summary of the results.

Part (%)	Pore Size(μm)	Porosity (%)	Ten stren(MPa)
0	154.7±72	7.2±2.5	23.2±2.3
10	160.6±68	5.0±1.7*	22.6±2.0*
20	172.9±52*	4.9±1.5*	20.1±1.1*
30	218.0±92*	2.4±0.7*	19.7±1.1*

* 15 specimens for each group.
* Stastically significant vs control($p<0.05$)

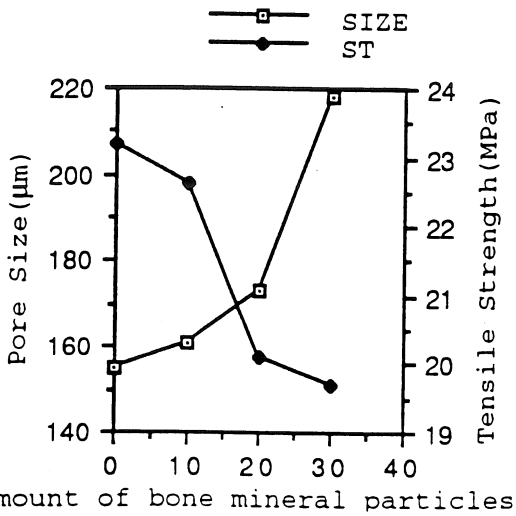

Figure 1. pore size vs strength

The 10, 20, and 30% specimens had statistically significantly lower($p<0.05$) number of pores and porosity than the pure bone cement. The 10% bone mineral particle-impregnated bone cement had a slightly larger pore size than the pure bone cement but it was not statistically significant. However, the 20% and 30% specimens had statistically significantly larger($p<0.05$) pores than the pure bone cement. The bone cement and bone particle impregnated bone cement showed no specific porosity distribution. Addition of bone mineral particles decreased the porosity and tensile strength of bone cement linearly.

DISCUSSION

It is believed that the bone mineral particles are quite porous by themselves and absorb monomers which will be released later. The absorbed monomer will be released later as the cement is polymerized which may increase the pore size. Another reason for the reduced porosity of bone mineral particle impregnated bone cement is due to less amount of monomers used than the pure bone cement.
However, it is not clear that the reduced strength of the bone cement by bone particle impregnation could limit clinical application of this material. Further, the ingrowth of tissue can only occur for the 30% since continuous porosity can only be created by intimate contact of bone paticles which poses further challenges with the present material.

REFERENCES

1. Park, J.B. et al. Tissue integration in oral and maxillo-facial reconstruction., D. Van Steenberghe(ed), Excerptu Media, Amsterdam, 118-124, 1986.
2. Liu, Y.K. et al. J. Biomed. Mat. Res.,21, 247-261, 1987.

EFFECT OF SHOCK WAVE TREATMENT ON CEMENT AND PROSTHESIS EXTRACTION IN HUMAN CADAVER MODEL

J. K. Kim, J. B. Park, S. A. Loening*, J. L. Marsh**,
Y. S. Kim, and J. N. Weinstein**

Department of Biomedical Engineering, College of Engineering

*Department of Urology, College of Medicine

**Department of Orthopaedic Surgery, College of Medicine

The University of Iowa

Iowa City, IA 52242

INTRODUCTION

The most difficult and time consuming step in revision arthroplasty is the extraction of well fixed distal cement. Infection, perforation, and fracture of femur are common complications. The distal portion of the bone cement is very difficult because it is hard to reach with currently available instrument.

A method to loosen the bone and bone cement interface without adverse consequences could simplify cement removal and incidence of complications may be decreased by shortening the operation time and reducing trauma to the bone. This may be achieved by applying shock waves to the bone-cement interface. The efficacy of extracorporeal shock wave lithotripsy (ECSWL) to aid on removal of bone cement before revision of cemented hip joint has been reported by many researchers.[1-4] Most of studies have focused on the interfacial strength of bone-cement interface. It is predictable that a loosening effect of ECSWL on the bone-cement interface could remove the well-fixed cement more easily, however, how much the shock waves affect on the extraction of bone cement in revision operation have not been reported yet.

We have investigated the efficacy of the extracorporeal shock waves on the removal of bone cement and prosthesis in human cadaver femora simulating the clinical setting. Especially, we have tried to focus on the bone cement extraction time, the number of strokes needed to remove the prosthesis, and the cleanliness of the medullary canal after removing of cement with and without shock wave treatment.

METHODS

Nine pairs of human cadaver femora were used for this study. Average age of patients was 79.7±9.1 years. The femoral specimen was prepared as same manner as clinical situation. Simplex P bone cement (Howmedica Inc.,Rutherford, NJ) was used for this study. The bone cement was prepared and injected into the medullary cavity for fixing hip prosthesis (Aesculap Well, West Germany).

Each pair of femora were prepared at the same time in order to ensure the specimen uniformity. The shock wave treatments were made with a Dornier HM-3 lithotripter(Dornier Medizintechnik GmbH,Germany). The shock wave was applied to the specimen at four points, in the circumference at 90° apart, with four-hundred shocks on each point at three levels with an intensity level of 25kV. The first level was 2.5±0.5cm below the top of the specimen as shown in Fig.1.

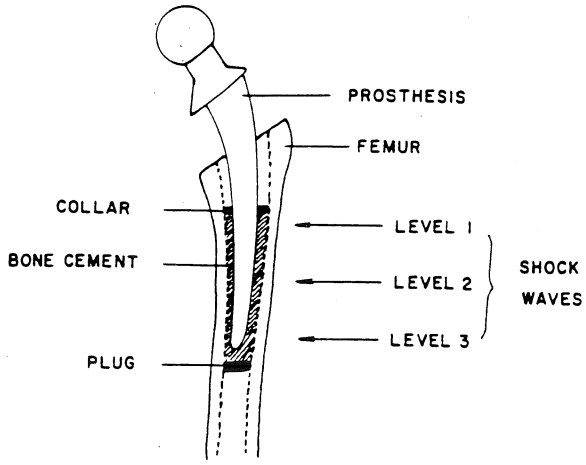

Fig.1. Schematic diagram of the test specimen after implantation into the femur with bone cement and 3 levels of shock wave treatment.

The fixed prostheses and bone cement were removed by two orthopedic surgeons. Blind test had been done. Operation time was recorded. The specimen diameter and thickness were measured. The weight of remaining cement after extracting them from the surface of cut bone was measured.

RESULTS

The mean and standard deviation of total time consumed for removal of bone cement, remained cement, and number of strokes for extracting prosthesis of control and treated specimen are given in Table 1.

Table 1. Summary of results.

	Control	Treated
Time (sec)	650 ±140	433 ±148
Weight(g)	4.58 ±3.11	2.53 ±2.33
Strokes	7.11 ±4.46	1.44 ±2.19

The result show an average of 32% decrease in cement extracting time after treatment($p<0.002$). The amount of average value of the weight of remained cement is given in Table 1. The difference was statistically significant ($p<0.006$) for the treated compared with control. The significance of the number of strokes to remove femoral prosthesis represent 0.001.

DISCUSSION

The ultimate goal of ECSWL is shortening of actual operation time, reduction of trauma to the bone. In this study, cement extraction time, amount of cement remaining in the cavity, and the number of strokes to extract prosthesis were reduced. For better revision results, old cement in the cavity should be removed more thoroughly.

REFERENCES

1. Park, S.H., et al. J. Appl. Biomat. 2: 115-126, 1991.
2. Park, J.B., et al. J. Appl. Biomat. 2: 161-170, 1991.
3. Weinstein, J.N., et al. Clin. Orthop. 235: 261-267, 1988.
4. Weinstein, J.N., et al. J. Appl. Biomat. 2:171-182, 1991.

ACKNOWLEDGEMENT

The help of Dr. S. H. Park, Department of Orthopedics, University of Southern California, Los Angeles, California and Dornier Medizintechnik GmbH, Germany is gratefully acknowledged.

FINITE ELEMENT ANALYSIS OF RAPID MAXILLARY EXPANSION IN THE RABBIT MIDPALATAL SUTURE

K.J. Baker, R.C.L. Sachdeva*, L.A. Crawford*, and R.B. Ashman

Texas Scottish Rite Hospital for Children, Dallas, TX 75219
*Dept. of Orthodontics, Baylor College of Dentistry, Dallas, TX 75246

INTRODUCTION

Rapid maxillary expansion is a common therapeutic technique used to correct transverse maxillary deficiency in preadolescent and adolescent patients by disarticulation of the midpalatal sutural complex. The nature of the force system required to split the suture remains empirical, with little concern for biological and physical variables presented by the patient. To achieve both a predictable and desirable biological response during expansion, characterization of interactions between applied load, mechanically-related biological variables, and resulting displacement is a necessary prerequisite. Finite element analysis was thus utilized to examine the load/ displacement behavior of, and stresses created within, the rabbit midpalatal suture.

METHODS

Two 2D finite element models (FEM) were generated: a macrostructural model and a microstructural model. The macrostructural model was created to analyze overall displacement of the suture as compared with experimental data. Seven 30- and 45-day-old New Zealand rabbit midpalatal sutures were transversely loaded to at least 7N using bone screws attached to a microtensile apparatus. Resulting displacements at the anterior and posterior edges of the suture were measured using extensometers. Specimens were later examined histologically to determine the amount of ossification present.

The macrostructural model was generated with an 11mm x 11mm mesh having 484 elements, 529 nodes (1058 d.o.f.), and a 1mm-wide, 7mm-long idealized suture, as derived from average specimen measurements. Material properties of the intact suture (E=20 MPa, ν=0.45), ossified suture and surrounding cortical bone (E=13 GPa, ν=0.3, for both) were inferred from literature. A 7 N load was applied on opposite sides of the suture to simulate experimental conditions of expansion. Experimentally-matched FEM displacements were computed using ALGOR software, accounting for ossifications and load offsets seen in each specimen, for model validation. A parametric series was then undertaken to assess displacements occurring with various degrees of sutural ossification (7, 14, 28, 50, 78%), material properties of the intact suture (20, 10, 5, 1 MPa) and ossified suture (13, 11, 5.3, 0.2 GPa), and load magnitudes (7, 15, 25, 35 N).

The microstructural model was created to analyze stresses occurring at three isolated areas of the sutural complex (non-ossified, partially ossified, and fully ossified regions), regardless of overall suture ossification. A 1.56 mm x 1.56 mm mesh having 1079 elements, 1144 nodes (2288 d.o.f.), and a 1mm-wide convoluted suture (3 'waves' per 1.56 mm), was generated. The same material properties were used, except that the ossified suture was characterized as 30% cortical bone (or E=5.3 GPa, ν=0.3). The 7N-load/7mm-suture was equally distributed as 1.56 N along the 1.56 mm lateral edge nodes. The model was tested for convergence with two additional FEM mesh densities (d.o.f. = 3742, 6220). Maximum principal stresses were computed using ALGOR software.

RESULTS AND DISCUSSION

In 5 of 7 specimens, the posterior edge of the suture separated (0.0191 to 0.0457 mm), while the anterior edge compressed (0.00977 to 0.0372 mm), indicating a pivot point, probably near the site of ossification. In the remaining two specimens, both edges were separated, implying an absence of a pivot point, although

histologic examination of all specimens showed some evidence of ossification. Anterior and posterior displacements computed with the specimen-matched macrostructural FEM models (0.0117 to 0.0182 mm, and 0.0071 to 0.0093 mm, respectively) fell within the range of experimental data.

With increasing suture ossification, the amount of anterior and posterior displacement computed in the macrostructural model declined, with minimal displacement (less than 0.0025 mm) occurring beyond 50% ossification. As intact suture stiffness was reduced, displacement increased proportionately, although the effect was diminished as ossification was increased and only minimal at 50% ossification or greater (Fig. 1). As ossified suture stiffness was reduced, the effect was negligible until ossification reached 28% or higher, where only the 0.2 GPa stiffness produced increased displacement (Fig. 2). As load magnitude was increased, displacement increased proportionately, regardless of the ossification. Thus, the most important overall parameter was the amount of ossification, but for a given ossification level, sutural stiffness and applied expansion load could dramatically effect the amount of sutural expansion achieved.

Stresses computed in the microstructural model were similar for each of the three mesh densities, indicating model convergence. The non-ossified and fully ossified suture produced relatively low to moderate stresses within the suture (~0.5 MPa and ~1.6 MPa, respectively) and surrounding bone (~1.0 MPa). The partially ossified suture, or ossification juncture site, exhibited very low sutural stresses (~0.1 MPa) but elevated stresses (~3.5 MPa) at the interdigitation near the ossification juncture. In addition, stress gradients at the suture-bone interface of the partially ossifed suture were substantially elevated. This suggests that fracture can occur at the base of an interdigitation regardless of the degree of ossification. However, a minimally ossified suture, such as in the pre-adolescent patient, could be more easily expanded than one that has a definite ossification juncture point, such as in the adult.

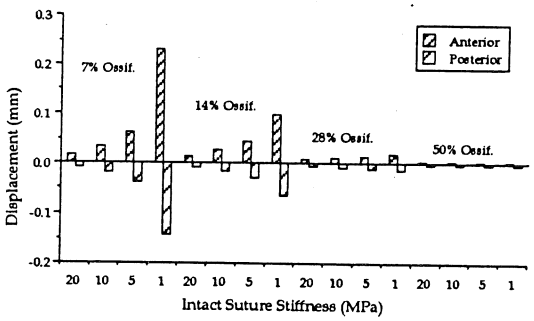

Figure 1. The effect of intact suture stiffness on anterior and posterior sutural displacement.

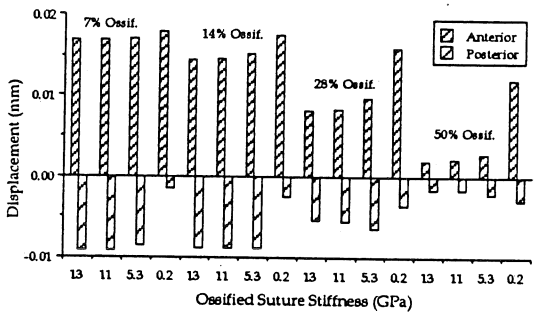

Figure 2. The effect of ossified suture stiffness on anterior and posterior sutural displacement.

Clearly, the amount of achievable expansion is dependent upon a number of biological variables, with ossification being the single most important. Beyond ossification, material parameters of different age groups or disease states and the chosen applied load could dramatically affect expansion. Increased stresses at the intact/ossified sutural junction produce the undesirable effects of initial fracture of the interdigitation, not the suture itself. Since greater ossification appears to produce more difficult expansion, and thus greater trauma to the sutural complex, the best results are probably attained with younger patients.

ACKNOWLEDGEMENTS

The authors acknowledge the support of the Research Fund of Texas Scottish Rite Hospital for Children, and Baylor University Medical Center College of Dentistry.

TOOTH CUSP DEFORMATION DUE TO SHRINKAGE OF COMPOSITE RESIN RESTORATIONS

A.A. Suliman¶, D.B. Boyer* and R.S. Lakes§

¶Department of Conservative Dentistry, College of Dentistry, University of Mosul, Mosul, Iraq,
*Department of Operative Dentistry, College of Dentistry and §Department of Biomedical Engineering and Center for Laser Science and Engineering, The University of Iowa, Iowa City, Iowa 52242, USA

INTRODUCTION

Polymerization shrinkage is one of the most important limitations of dental composite resins. Shrinkage results in stresses in teeth restored with composite resins and in the material itself (Davidson and De Gee, 1984). Shrinkage stresses may cause such clinical problems as post-operative pain, fracture of the tooth, and opening of the margins of restorations which may result in microleakage of fluids as well as recurrent caries (Eick and Welch, 1986). Polymerization contraction of composite resins ranges from 0.6 to 2 linear % and from 1 to 6 volume %.

Several studies have demonstrated that the cusps of molars and premolars are deflected inward after placement of class II composite restorations (Causton et al., 1985). The amount of contraction ranged from 18 to 45 microns in these studies and was similar to linear setting shrinkage of the composites. Most of the deformation occurred in the first 15 minutes after placing the composite, however, in one study shrinkage continued for at least for 2 days.

Cusp movement was observed to be sporadic by some (Causton et al., 1985), indicating stress relief in the tooth due to microfracturing.

This investigation was conducted to determine (i) what amount of cusp movement results from composite resin polymerization shrinkage; (ii) whether the size of the cavity preparation influences the amount of cusp deflection; (iii) the effect of choice of composite; (iv) the effect of hydration on tooth deformation.

METHODS AND MATERIALS

Two composites with substantial differences in inorganic filler loading and properties were selected. The low resin composite, P-50 (3M Co. Dental Products Division, St. Paul, MN) has filler loading of 87 wt% (77 vol%). The high resin composite, Heliomolar R. O.(Vivadent-USA, Tonawanda, NY) has filler content of 77-79 wt% (65-67 vol%).

Forty extracted non-carious maxillary premolars were randomly assigned to eight experimental groups. The experimental variables were cavity size (small, large), hydration (dry, wet) and composite (P-50, Heliomolar). Small (approximate volume = 0.10 cm3) and large (approximate volume = 0.16 cm3) standardized mesio-occlusal-distal (MOD) cavities were prepared under water spray with #55 fissure burs in a high speed handpiece. The apical third of the root was removed using a fissure bur. The pulpal tissue was removed and the canal was reamed with endodontic files to facilitate the implantation of a 21 gauge disposable needle (Monoject, St. Louis, MO) to supply the tooth with water and to simulate intrapulpal fluid pressure. Panavia dental adhesive (Kuraray Co. Ltd, Osaka, Japan) was used to seal the needle to the apex of the tooth. The tooth was tested for sealing under pressure, then the root was embedded in acrylic resin. All cavities were restored in the same manner.

The lingual cusp of each tooth was etched for 10 seconds, rinsed, and air dried. The etched cusp was fixed to a textured aluminum plate using Scotchbond 2 dental adhesive (3M Co.). The movement of the buccal cusp relative to the fixed lingual cusp was measured in this study. The root of the tooth with its acrylic block was unrestricted in movement. A small notch was prepared at the tip of the buccal cusp to which a 6 X 6 mm mirror was glued using cyanoacrylate adhesive. The aluminum plate was affixed to an optical bench.

A Michelson interferometer was used to measure movement of the buccal cusp following restoration of the tooth with composite. Changes in the position of the mirror upon the tooth (Fig. 1) were measured by counting the number of fringes that passed a reference point on a target screen. The Michelson method does not give the sign of the displacement. The direction of movement, which was the buccal cusp toward the lingual cusp, was determined by microscopic measurement of the intercuspal distance. Tilting of the cusp was determined from the fringe spacing in either x- or y-directions.

Fringes were located on the target screen, then the composite resin was cured and fringe counting was started. The number of fringes passing the reference point on the screen was counted for 60 minutes. Fringe spacing in both x- and y-directions was measured every 5 minutes. The number of fringes counted was converted into cusp displacement in μm. The average displacement (d) of the buccal cusp was calculated from $d = n\lambda/2$, where n is the number of fringes and λ is the laser wavelength (0.633 μm). The tilt (ξ) of the cusp in bucco-lingual direction and mesio-distal direction was obtained via $\xi = \lambda/2D$, where D is the distance between fringes.

RESULTS

Movement of the buccal cusp was detected in all experimental groups during the first 60 minutes after placement of the composite resin. The mean cusp movement after 1 hour was statistically significant in all experimental groups ($p < 0.05$). Most of the deformation took place within the first 5 minutes. Fig. 2 shows cusp movement for teeth restored with Heliomolar. Large cavities restored with either Heliomolar or P-50 under dry conditions had the largest

displacement of the buccal cusp (40-45 μm). The least amount of movement (10 microns) was found in small cavities in hydrated teeth restored with Heliomolar.

Small cavities had less cusp movement than large cavities; teeth restored with Heliomolar were not statistically different from those restored with P-50; and hydrated teeth had less cusp movement than dry teeth.

The tilt of the buccal cusp relative to the lingual cusp in the x-direction (bucco-lingual direction) was found, as expected, to be more than that in the y-direction (mesio-distal direction).

DISCUSSION

Interferometry permitted real-time measurement of cusp movement as it occurred. Contraction occurred very rapidly, about 1\3 of the 60 minute amount occurred during the first 2 minutes while the composite was exposed to the curing light.

The amounts of deformation measured, 10.8-45.7 μm, were similar to previous studies using other methods. Movement of cusps was smooth rather than interrupted and indicated no microfracturing at these deformations. This agrees with some previous work but disagrees with others.

Cusp movements expressed as a percentage of cavity width were very similar to literature values of linear shrinkage of the resins: Heliomolar, 2.8 vol% (0.93 lin%), P-30 (forerunner of P-50), 3.6 vol% (1.2 lin%). Our values were 0.94 % and 1.21 %, respectively.

It was found that the larger the cavity size the greater the cusp movement. This can be explained by two points. First, there was less tooth structure left in large cavities which meant more flexibility of the cusps. As the cavity preparation becomes wider and deeper, the strength and stiffness of the prepared tooth is considerably reduced and the tooth becomes more flexible. Secondly, the greater total volume of composite resin needed to restore large cavities results in higher shrinkage force .

Hydration of teeth may potentially influence the deformation of teeth restored with composite resins in several ways. A hydrated tooth may be more flexible and this would lead to higher deformation. Hydration interferes with bonding to dentin of some bonding agents. Absorption water by composite is known to offset polymerization shrinkage to some extent. Hydrated teeth deformed less than dry teeth in this study. It was hypothesized that this was due to decreased bonding between the composite and wet teeth and to absorption of water by the composite.

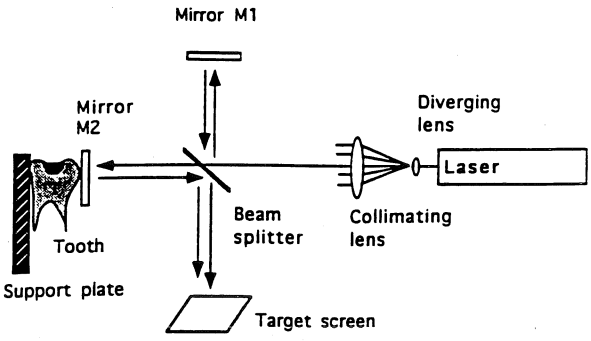

Figure 1. Michelson interferometer configuration for measuring cusp movement.

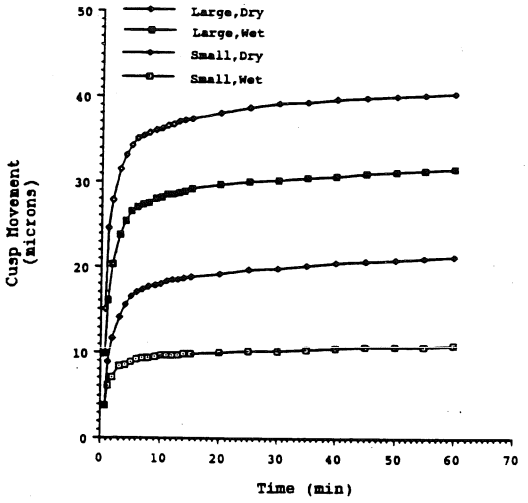

Figure 2. Cusp movement vs time caused by polymerization shrinkage of Heliomolar MOD restorations in premolars.

REFERENCES

Causton, B.E, Miller, B., Sefton, T., The deformation of cusps by bonded posterior composite restorations: an in vitro study. Br Dent J 159: 397-400, (1985)

Davidson, C.L., De Gee, A.J., Relaxation of polymerization contraction stresses by flow in dental composites. J Dent Res 63:146-148, (1984).

Eick, J.D. and Welch, F. H., Polymerization shrinkage of posterior composite resins and its possible influence on postoperative sensitivity. Quintessence Int 17:103-111, (1986).

Hegdahl, T., Gjerdet, N.R., Contraction stresses of composite resin filling materials. Acta Odontol Scand 35:185-195, (1977).

CALCULATION OF THE TRUE VALUE OF A HIGH JUMP USING A COMPUTER GRAPHICS MODEL

J. Dapena

Department of Kinesiology, Indiana University, Bloomington, IN 47405.

INTRODUCTION

The true value of a high jump is the maximum height that the athlete would have been able to clear cleanly, and its value generally is not known. If the bar is knocked down, the jump is ruled a foul and the athlete receives no credit, although a hypothetical bar set at a lower height would have been cleared successfully. If the bar stays up, the athlete is credited with the height of the bar. This is also misleading: If the bar is cleared with room to spare, the height of the bar is an underestimate of the true value of the performance; if the bar is bent down during the bar clearance but does not fall, the height of the bar is an overestimate of the maximum height that would have been cleared cleanly. This is an important shortcoming for the evaluation of high jumping technique, because the researcher is left without the most important criterion measure for the value of the performance. A method involving three-dimensional (3D) film analysis, curvilinear interpolation and computer graphics was devised for the solution of the problem. A test showed that the method yielded reasonably close estimates.

DEVELOPMENT OF THE MODEL

General description

The upper arms, forearms and hands were modeled by pyramidal frustra; each thigh and each shank by two serially-linked pyramidal frustra; the neck by a prism; the feet by irregular polyhedrons; the head by three quarters of a sphere (cranium), with an irregular polyhedric surface (face and chin) replacing the fourth quarter; the trunk was modeled by six serially-linked pyramidal frustra connected to an irregular polyhedric pelvis and buttock; hemispheroid breasts were added to the trunk in the female version of the model.

The model required as input the mass, standing height and sex of the subject, and the 3D coordinates of 21 body landmarks (vertex, chin-neck intersect, suprasternale, and left and right shoulders, elbows, wrists, knuckles, hips, knees, ankles, heels and toes).

Anthropometry

The anthropometric parameters for the model were obtained from still photographs of 14 male and 11 female college varsity high jumpers. Most anatomical measurements were taken from a side view photograph; supplementary measurements were taken from frontal and diagonal views.

Scaling

Knowing the thickness t_{s1} of a segment in the average subject (mass m_1; standing height h_1), its thickness t_{s2} in a subject of different mass (m_2) and standing height (h_2) can be estimated using the following equation:

$$t_{s2} = t_{s1} [(m_2 h_1) / (m_1 h_2)]^{1/2}$$

Trunk arch

Between the hips and the suprasternale there is no intermediate landmark that can be identified reliably in film analysis. Because of this, the trunk is kept straight in most computer graphics models. However, the trunk is known to arch markedly during the high jump bar clearance, and therefore it was decided to incorporate a flexible trunk into the model. Anecdotal evidence suggested that the trunk tends to arch backward when the thighs are hyperextended at the hip, and forward when the thighs are flexed at the hip. Sports magazines and books were searched for action photographs of sports activities showing a wide variety of hip flexion-extension angles. The main criteria for selection of a photograph were: a view as close as possible to the perpendicular to the sagittal plane of the trunk, tight-fitting clothes, and little or no obstruction of the view of the trunk by the arms or other objects. A total of 19 photographs were selected for analysis. This included 7 male and 12 female subjects (4 high jumpers, 1 triple jumper, 3 long jumpers, 2 hurdlers, 5 sprinters, 2 distance runners and 2 divers). The curved midline of the trunk and a straight line from the suprasternale to the hip joint were drawn on each photograph (see Fig. 1). The deviation of the trunk midline curve from the line was measured at five equally spaced cross-sections (d_1 through d_5). Positive deviations corresponded to a forward

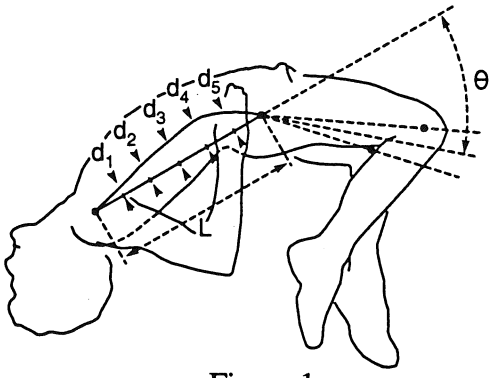

Figure 1

position of the trunk midline (hollow-back arch). For normalization purposes, each deviation was divided by the distance L between the suprasternale and the hip. The average flexion-extension angle of the two thighs with respect to the longitudinal axis of the trunk (θ) was also measured. This angle was measured in degrees, relative to the fully aligned neutral position; positive values corresponded to hip hyperextension. For each of the five intermediate cross-sections of the trunk, the normalized deviation values (d/L) obtained from the 19 photographs were plotted against the values of the hip angle θ. The statistical relationships were modeled using linear regression (Table 1).

Trunk twist

Due to axial rotations at the various intervertebral junctions, the upper trunk generally does not face the same direction as the lower trunk. This is reflected in the difference between the orientations of the shoulder and hip axes in the transverse plane. Table 2 shows the maximum amounts of accumulated axial rotation (twist) within each of the six equal-length serially-linked pyramidal frustra of the

Table 1.

$d_1/L = 0.000914\,\theta + 0.030$
$d_2/L = 0.001564\,\theta + 0.059$
$d_3/L = 0.001957\,\theta + 0.078$
$d_4/L = 0.002052\,\theta + 0.081$
$d_5/L = 0.001526\,\theta + 0.054$

Table 2.

	absolute	relative
$\Delta\phi_{0\text{-}1}$ =	33°	37.9 %
$\Delta\phi_{1\text{-}2}$ =	31°	35.6 %
$\Delta\phi_{2\text{-}3}$ =	8°	9.2 %
$\Delta\phi_{3\text{-}4}$ =	6°	6.9 %
$\Delta\phi_{4\text{-}5}$ =	9°	10.3 %
$\Delta\phi_{5\text{-}6}$ =	0°	0.0 %
Total =	87°	100.0 %

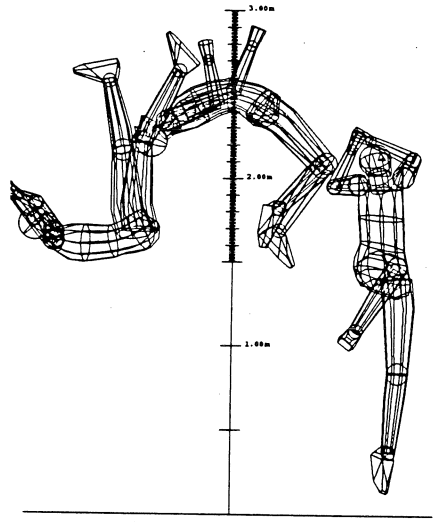

Figure 2

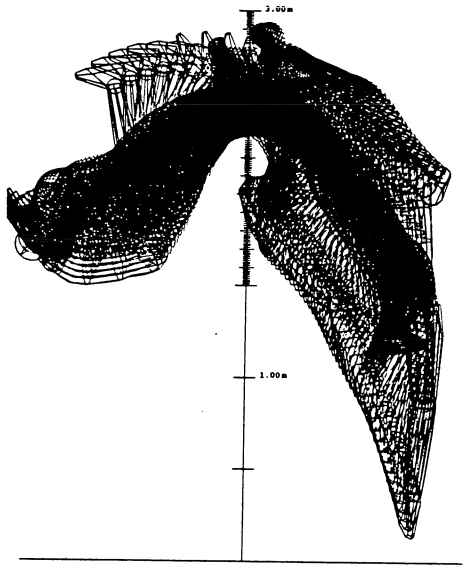

Figure 3

trunk ($\Delta\phi$), estimated from the maximum possible amount of twist at each intervertebral junction (White and Panjabi, 1978) and the number of intervertebral junctions included in each frustrum (Hollinshead, 1974). For the model it was assumed that the amounts of twist within the six frustra are always proportional to the maximum values given in Table 2.

TESTING THE MODEL

A set of 32 jumps (20 by males; 12 by females) was selected from a large pool of high jumps previously analyzed for other purposes at our laboratory. In the selected jumps, the bar was bent down during the bar clearance, but did not fall immediately. Film analysis provided the 3D coordinates of the standard 21 body landmarks at instants separated by 0.06-second intervals during the bar clearance. The coordinates of the body landmarks were input to a computer program that implemented the graphics model. Fig. 2 shows three selected images from one jump. Curvilinear interpolation with quintic spline (Wood & Jennings, 1979) was then used to generate landmark positions at 0.01-second intervals. With the addition of these interpolated positions, the computer graphics model produced a saturated plot (Fig. 3) which yielded an estimate (h_{ce}) of the maximum height that the athlete would have been able to clear cleanly. This value was compared with the true value of the jump (h_d) as indicated by the minimum height of the bent bar, measured in the films.

RESULTS

The error in the predicted value of the maximum height cleared cleanly was $\Sigma\,(h_{ce} - h_d) / N = 0.010 \pm 0.032$ m (men); 0.024 ± 0.018 m (women). Considering absolute error values, the difference was $\Sigma\,(|h_{ce} - h_d|) / N = 0.027 \pm 0.017$ m (men); 0.024 ± 0.018 m (women).

DISCUSSION

The results indicated that the proposed method yields a reasonably close prediction of the value of a high jump. The remaining errors are due to errors in the 3D coordinates of the body landmarks and in the shapes and thicknesses of the segments.

The method will be most useful in computer simulation analysis. In this approach, the researcher makes alterations in factors that control the motions of a high jumper; the resulting motions are predicted by a computer program. The method described here will provide estimates of the true values of any two simulated jumps. The method will be particularly accurate for the calculation of the *difference* between the values of the two simulated jumps, since the amount and direction of the error will be similar for both.

REFERENCES

Hollinshead, W.H. *Textbook of Anatomy* (p. 300), Harper and Row, 1974.

White, A.A. and M.M Panjabi. *Spine* 3:12-20, 1978.

Wood, G.A. and L.S. Jennings. *J. Biomech.* 12:477-479, 1979.

ACKNOWLEDGEMENTS

The author thanks the subjects for their cooperation, and E. Cole, P. De Leva, T. Durham and T. Yanai for their technical help.

OPTIMAL CURVES IN SLALOM SKIING AS A FUNCTION OF COURSE VARIABLES

G.R.Hamilton
Human Performance Laboratory,
University of Calgary, 2500 University Drive N.W.
Calgary, Alberta, Canada, T2N 1N4

INTRODUCTION

The optimal curve down a slalom course is one which minimizes the time to complete the course. This paper found an approximation of the optimal curve as a function of several course variables. The near-optimal curves were also described.

REVIEW AND THEORY

Empirical studies on the optimal slalom curve have been reported by Kashiwa (1986). He proposed that the optimal curve should approach the gate wide.

A truncated Fourier series was used to approximate the optimal curve down a simplified slalom course. The curves were calculated as a function of six course variables: amplitude of gate placement; distance between gates i and i+2; slope inclination; coefficient of snow friction; drag coefficient; and centre of mass displacement towards the fall line. These six variables will henceforth be referred to as course variables.

The simplified slalom course was assumed to have both a constant inclination and a periodic gate placement. The interval time for a curve was defined as the time required to ski from one gate to the next.

The optimum curve down the periodic slalom course was also assumed to reach a periodic steady state after an initial transitory period. The periodic solution was the one solved in this paper. It was assumed that the optimal and near-optimal periodic curves could be described by a Fourier series, $FS(\theta)$, where θ is the distance down the hill.

The Fourier series was constrained to intersect each gate and have an amplitude of exactly A. One truncated Fourier series which satisfied these constraints is:

$$FS(\theta) = a_1 Sin(\theta) + (a_1 - A)Sin(3\theta) + b_1 Cos(\theta) - \frac{b_1}{3} Cos(3\theta)$$

Therefore, for a specific amplitude of gate placement, A, there exist two variables which describe the set of potentially optimal curves. These variables will henceforth be referred to as the sine and cosine coefficients.

The equation of motion for the skier was calculated to be

$$M\ddot{\theta} = \frac{\left(F_g - F_\mu - F_\delta\right)}{\sqrt{1+\left(\frac{dFS(\theta)}{d\theta}\right)^2}}$$

where the denominator originated from the projection of the forces onto the fall line axis, θ, and the forces in the numerator are gravitational, frictional and drag respectively.

Both the coefficient of friction for snow and the drag coefficient were taken from the range of values reported in the literature (Spring et al. (1985) and Ingen Schenau (1982) respectively).

PROCEDURES

For a specific set of both the course variables and the sine and cosine coefficients, the interval time for the Fourier series was calculated iteratively as follows: First, the skier's velocity at a gate was guessed. Secondly, the skier was allowed to move down the curve as dictated by the equation of motion. When the next gate was passed, the skier's velocity was checked; if it was within 0.25% of the velocity at the previous gate then the interval time was recorded otherwise a new guess at the initial velocity was made.

RESULTS AND DISCUSSION

Four general trends were extant for all realistic changes in the course variables:

First, the interval time was much more sensitive to the sine coefficient than the cosine coefficient.

Secondly, the sine coefficient of the curves with low interval times were always larger than the amplitude. This meant that these curves had pronounced rounding of their turns.

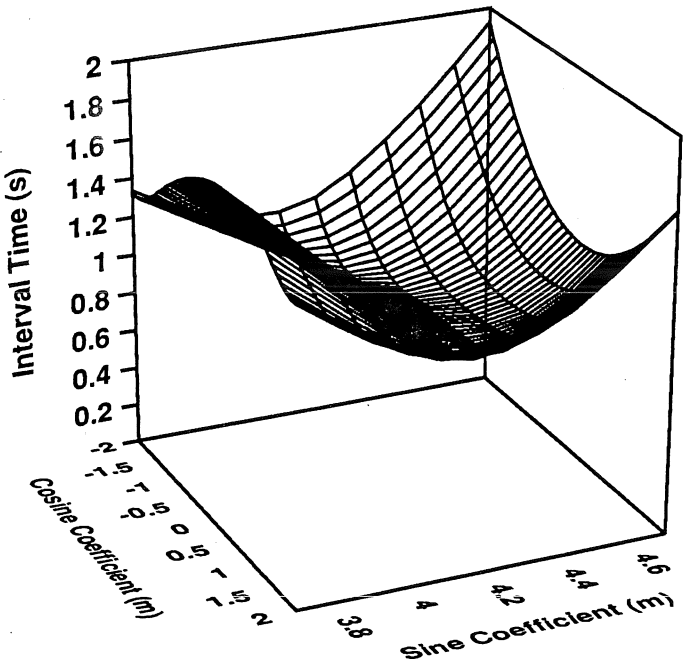

Figure 1. Interval times as a function of both the sine and cosine coefficients for an amplitude of gate placement of 4m, a distance between gates i and i+2 of 2π m, a slope inclination of 22.5 degrees, a coefficient of friction of 0.05, a drag coefficient of 0.092 and no displacement of the centre of mass.

Thirdly, the curve with the lowest interval value often had a cosine coefficient close to zero. This meant that the phase of the optimal curve was approximately the same as the phase of the gates. A decrease in the cosine coefficient resulted in a relatively better solution than an increase in the coefficient. This result meant that curves in which gates were exited widely were favoured over curves in which gates were approached widely. This contradicted Kashiwa (1986).

Lastly, the two dominant terms in the equation of motion were the gravitational force which invoked motion and the centripetal force component of the frictional force which opposed motion. The centripetal force was responsible for about 95% of the opposition to motion during an interval:

$$CT\left(\theta,\dot{\theta}\right)=\frac{M\left(\dot{\theta}\right)^2\left(\frac{d^2FS(\theta)}{d\theta^2}\right)^2}{\left(1+\left(\frac{dFS(\theta)}{d\theta}\right)^2\right)^{1.5}}$$

An additional two results came from observing the effects of modifying the course variables:

An increase in the amplitude of the gate placement resulted in an increase of the difference between the sine coefficient and the amplitude of the optimal curve. An increase in the amplitude of the gate placement also increased the interval time of the optimal curve.

An increase in the coefficient of friction increased the sensitivity of the optimal solution to the cosine coefficient, although this sensitivity was still a magnitude less than that of the sine coefficient. An increase in the coefficient of friction also increased the the interval time of the optimal curve.

REFERENCES

Ingen Schenau, G.V. van, J. Biomechanics, 15, 449-458, 1982

Kashiwa, H. Skiing, 12, 38, 1986

Spring, E.et al. Acta Polytechnica Scandinavica; applied physics series No. 148, 1985

THREE-DIMENSIONAL VIDEOGRAPHY OF SWIMMING TECHNIQUES

Toshimasa Yanai and James G.Hay

Department of Exercise Science, The University of Iowa, Iowa City, IA. 52242

INTRODUCTION

Two-dimensional cinematography has been used frequently in the analysis of swimming strokes. A two-dimensional approach is not sufficient, however, for the analysis of complex multiple-joint movements that take place in three-dimensional (3D) space. The purpose of this study was to develop a method to record the 3D motions of a swimmer above and below the surface of the water. Sample analyses of the body roll angle and shoulder joint angles of beginning and elite freestyle swimmers are presented.

REVIEW AND THEORY

The DLT algorithm (Abdel-Aziz and Karara. 1971) was applied to determine 3D coordinates from video recordings. The method requires that at least two video recordings be taken by stationary cameras. Two periscope systems were used to satisfy these requirements. Several periscope systems had been designed, constructed, and tested in our laboratory (McIntyre and Hay, 1975. Hay and Gerot, 1991). The periscope system employed in the present study was the one with the latest design, which consisted of four parts, (a) a tripod with a horizontal beam which held a camcorder, (b) a frame which could be fixed to a pool deck and which supported a large underwater mirror (0.91 x 1.22m), (c) a rectangular plexiglass box which served as a wave deflector, and (d) a small mirror (0.3 x 0.6m) which could be attached to the front edge of the plexiglass box and which provided an above-water view. Each mirror provided an independent view of the motion in the fluid in which the mirror was placed. With this arrangement, the views from the mirrors in the periscope system were recorded by a single camcorder, so that a total of four independent views were recorded by two camcorders.

A major limitation of the DLT method is that accurate 3D reconstruction is limited to the size of the control object. The volume a competitive swimmer goes through in one complete stroke cycle is much greater than the volume of a typical control object. The required space could be roughly estimated as follows:

(a) Length = (Stroke length) + (Height of the swimmer) + (Arm length)
(b) Width = (Arm length) x 2 + (Shoulder width)
(c) Height = (Arm length) x 2

This volume is roughly (5 x 2 x 1.5)m^3 for freestyle competitive swimmers. A large control object was constructed mathematically, by calibrating a standard control object at several adjacent locations in the required volume.

PROCEDURES

The method was tested in the University of Iowa indoor swimming pool. Two periscope systems were placed on the pool deck so that a front view and a side view of a swimmer could be recorded. The optical axes of the two cameras were perpendicular to each other. Each camcorder was connected to a television monitor, which enabled the recorded image to be observed on-line. A control object with 72 points (1.2 x 1 x 2m) was used for calibration. The upper and lower halves of the control object were used for the above- and below-water calibration, respectively. The object space was in the middle of the farthest lane from the side-view camera.

A former world record-holder and a beginning swimmer served as subjects. Each subject was asked to swim 25yd (22.86m). Two Panasonic AG450-SVHS camcorders, with exposure time set at 1/250s and a frame rate of 60Hz, were used for the data collection. A Peak Motion Measurement System (Peak Performance Technologies, Denver, CO) was used to extract coordinate data from the video recordings. Data files were created and stored in a micro-computer, and four sets of 11 camera parameters (one set for each independent view) were then computed. Twenty one body landmarks, defining a fourteen segment model of the human body, were digitized. The computed 3D coordinates were smoothed using a digital filter (Yu, 1991).

RESULTS

Calibration error was estimated by the sum of the squared differences between the coordinates of known control points and the computed coordinates for these same points. The mean square errors (MSE) and the standard deviations (SD) in each single control volume and the total object space are listed in Table 1.

Table 1: Estimated Calibration Errors

	Positions of Calibration Volume						Total Calibration Volume	
	1		2		3			
	Air	Water	Air	Water	Air	Water	Air	Water
Points	28	27	28	22	18	16	74	65
MSE (mm)	7.56	10.01	7.24	11.41	7.91	11.81	12.06	18.85
SD (mm)	3.30	5.11	2.73	5.42	3.63	5.88	4.47	6.92

The magnitudes of the calibration errors were quite large. These errors were probably due to one or more of the following:

(a) the limited resolution of the monitor;
(b) the insufficient brightness of the underwater view;
(c) the presence of some distortion in the mirror; and
(d) the relatively small size of the projected size of the control object.

Errors in the use of a video technique were investigated by Angulo and Dapena (1992). They stated that "a larger field of view (8m) makes the accuracy of video analysis clearly inferior to that of film analysis." Although it was not concluded in their study where the difference in accuracy came from, it would be reasonable to point out the possibility of the error due to the limited resolution of the monitor, particularly when the size of the recorded image of the body of interest was small. The second problem could be solved by using some extra lights positioned in the pool or by videotaping in an outdoor pool. The third problem could be minimized by constructing the frame and mirror with more rigid material. The last problem could not be solved with the present method.

SAMPLE ANALYSES

One complete stroke without breathing was digitized for each subject. The lower body motion of the subject was obscured by the upper body motion in the front view, and was thus excluded from the analysis.

Two rotational motions were derived from the motion of shoulders, which were assumed to move as a unit defined as the upper-trunk -- the rotation of the trunk about its longitudinal axis (the body roll) and the rotation of shoulder about the frontal axis of the trunk (the shoulder tilt). The computed results for the elite swimmer are

shown in Figure 1, with the body roll (BR) indicated by the solid line and the shoulder tilt (ST) by the dashed line. Three shoulder joint angles were defined: (a) the ab/adduction angle -- the angle between the projected line of the longitudinal axis of the upper arm on the frontal plane of the upper-trunk and the transverse axis of the upper-trunk; (b) the horizontal ab/adduction angle -- the angle between the projected line of the longitudinal axis of the upper arm on the transverse plane of the upper-trunk and the transverse axis of the upper-trunk; and (c) the int/external rotation -- the angle between the longitudinal axis of the forearm and the longitudinal axis of the upper-trunk projected on the transverse plane of the upper arm. The computed result for the elite swimmer is shown in Figure 2 and that for the beginner is in Figure 3, with ab/adduction (AB) indicated by the dotted line, horizontal ab/adduction (HA) indicated by the dashed line, and int/external rotation (IR) indicated by the solid line.

DISCUSSION

Two interesting results were obtained. First, asymmetry was observed in the BR and ST patterns for both subjects. A difference in the maximum BR was observed even in the elite swimmer, where the maximum was greater on the right side than on the left side (35° vs 25°). This asymmetry was probably associated with the subject's breathing side --the right side. The computed BR's were somewhat smaller than previously reported (Counsilman, 1968. Beekman, 1986). There are at least two possible reasons: (1) the elite swimmer had a more efficient stroke technique than the subjects of previous studies, and (2) the computation method applied in the previous studies had some errors associated with the limitations of 2D cinematography.

Second, a technique fault known as "dropped-elbow" was observed in the beginner. The elite swimmer had a peak IR (160°) and a relatively constant HA (20° to -35°) during the initial press. This matched exactly what Counsilman described (1968) as an "elbow-up pull", in which the "elbow is bent and held higher than the hand throughout the first part of the pull." The beginner's IR fell to less than 0° immediately after entry. Although IR was increased and then held at around 35° during the first part of the stroke, the low IR and the accompanying low HA (min. -70°), made it impossible for him to keep the "elbow higher than the hand." These observations suggest that the internal rotation of the shoulder is critical to the attainment of an "elbow-up pull."

The amount of shoulder tilt is of some practical importance in this regard. At the end of the initial press, the arm reaches the farthest forward position in the stroke, and AB may approach the maximum possible anatomically. In the stroke of the elite swimmer, a relatively large amount of shoulder tilt (max. 31° on the right side) served to moderate the AB required (max. 65°), and thus facilitated the attainment of the needed internal rotation. The beginning swimmer, however, did not use this mechanism. His maximum ST was only 12° in the first half of the stroke phase. To achieve the desired forward hand position from which to begin the pull, he thus had to attain a relatively large abduction of the arm (max. 78.8°). This, in turn, served to impede the attainment of an effective internal rotation, and may have contributed to the "dropped-elbow."

To overcome the methodological problems identified here, a 3D videography procedure with panning periscopes is currently in the process of development in our laboratory. The larger image size attained with this method should ensure more accurate digitizing. The lower body analysis will become possible, as well. With the new method, more detailed analysis should permit an increased understanding of the mechanics of swimming techniques.

REFERENCES

Abdel-Aziz,Y.I.& Karara,H.M. ASP Symposium on Close Range Photogrammetry, American Society of Photogrammetry, Church, VA. 1971.

Angulo,R.M.& Dapena,J. International Journal of Sport Biomechanics, 8, pp 145-151, 1992.

Beekman,K.M. Journal of Swimming Research, 4, pp 15-21, 1988.

Counsilman,J.E. The Science of Swimming, pp 49-50, Prentice-Hall, Inc., Englewood Cliffs, New Jersey, 1968.

Hay,J.G. & Gerot,J. International Journal of Sport Biomechanics, 7, pp 392-399, 1991.

McIntyre,D.R. & Hay,J.G. Swimming II, pp 51-57. University Park Press, Baltimore, 1975.

Yu,B. Unpublished Computer Software, Biomechanics Lab. Dept. of Exercise Science, The University of Iowa, Iowa City, 1991.

Figure 1: Bodyroll and Shoulder Tilt Angles of Elite Swimmer

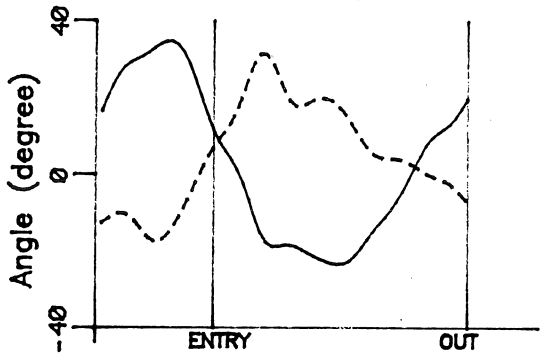

Figure 2: Shoulder Joint Angles of Elite Swimmer

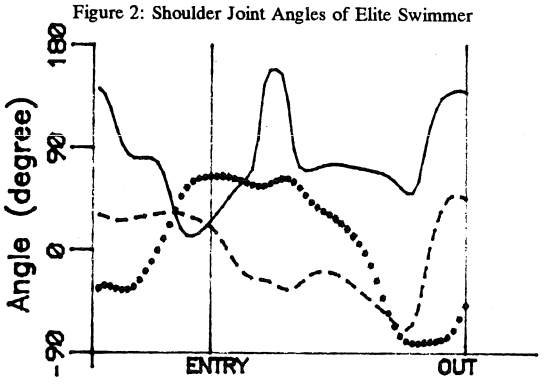

Figure 3: Shoulder Joint Angles of Beginner

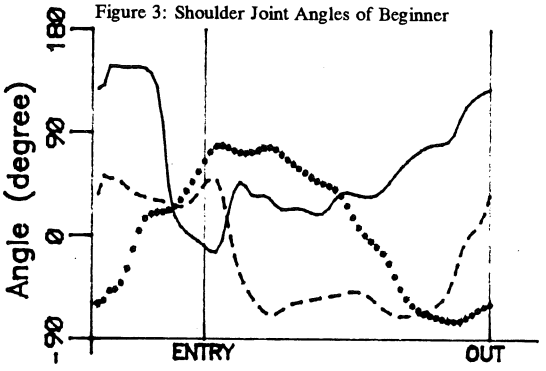

ANGULAR MOMENTUM AND PERFORMANCE IN THE TRIPLE JUMP

Bing Yu and James G. Hay

Department of Exercise Science, The University of Iowa, Iowa City, IA 52242

INTRODUCTION

In the last decade, the techniques employed by elite triple jumpers have received increased attention from researchers in biomechanics. However, a recent review of the literature (Hay, 1992) revealed that most of the biomechanics studies on triple jump were two dimensional in nature and focused on those linear motions which determined the distance of a triple jump. Only one of the papers located for this review contained data on the angular momentum of the triple jumper -- and that about only one of the three principal axes of the body.

The angular momentum of the whole body about each of the three principal axes through the center of gravity of a triple jumper seems likely to have an influence on his or her ability to maintain balance during the execution of the triple jump, and thus to affect the official or actual distance. The purposes of this study were (a) determine the magnitude of the angular momentum elite triple jumpers possess during each of the three phases of a triple jump, and (b) to identify those characteristics of the angular momentum that are closely related to the actual distance of the triple jump.

PROCEDURES

The subjects were the 13 finalists in the men's triple jump event at the 1992 United States Olympic Trials in New Orleans, Louisiana. For each subject, the trial in which the longest official distance was recorded was selected for analysis.

Two video camcorders and a Direct Linear Transformation procedure with panning cameras (Yu, *et al.*, 1993) were used to collect three-dimensional coordinates of 21 body landmarks. The videotape records of the events of interest were digitized at a sampling frequency of 60 Hz. The coordinate data were smoothed using a second-order, low-pass, recursive digital filter (Winter, *et al.*, 1971) at a optimum cutoff frequency of 7.4 Hz determined from sampling frequency.

The side-somersaulting, somersaulting, and twisting angular momenta of the body in each frame during each of the flight phases of the last stride, hop, step, and jump were calculated using the method described by Dapena (1978). The mean of the angular momentum about each principal axis of the body during each flight phase was considered to be the best estimate of the corresponding angular momentum at the takeoff to the flight phase. The angular momenta were normalized for body mass (m_b) and standing height (h_b) by dividing by $m_b\, h_b^2$.

The data analysis procedure consisted of the computation of means and standard deviations and the performance of linear and non-linear regression analyses. If the magnitude of the correlation coefficient obtained in the non-linear analysis was significantly higher than that obtained in the linear analysis, the non-linear correlation coefficient was used. Such use was consistent with the expectation that an optimum value existed for many of the independent variables considered. The 0.1 level of confidence was chosen to indicate overall statistical significance after considering the consequences of Type I and Type II errors. The 0.0015 level of confidence was used with each individual test to guarantee the overall level of confidence.

RESULTS AND DISCUSSION

The mean value of the side-somersaulting angular momentum at the takeoff of each of the last stride and step was significantly different from zero (Table 1). The magnitude of the side-somersaulting angular momentum at these two takeoffs reflected the technical demand of the following flight phases. During each of the flight phases of the last stride and step, a triple jumper has to position the legs for the support phase to follow. A side-somersaulting angular momentum towards the side of the free leg at each of these two takeoffs is essential to accomplish the downward motion of the free leg and upward motion of the takeoff leg without rotating the upper body (or perhaps the whole body) towards the opposite side during the subsequent flight phase.

Table 1
Mean (standard deviation) of angular momenta at each takeoff (Nms)

	Takeoff			
Axis	Last stride	Hop	Step	Jump
Side-somersaulting	3.71* (1.17)	-0.40 (0.83)	-3.58* (1.56)	0.70 (2.04)
Somersaulting	6.37* (2.31)	8.27* (2.28)	2.16* (1.65)	5.63* (2.33)
Twisting	1.00 (3.04)	0.94 (1.64)	0.78 (1.31)	0.17 (1.51)

* Significantly different from zero ($P < 0.0015$).

The mean values of the somersaulting angular momentum (Table 1) were qualitatively consistent with those reported by Hillman (1981) in a study of 15 male subjects. The mean values reported by Hillman were 13.0, 11.5, 1.3, and 6.9 Nms at the takeoff of the last stride, hop, step, and jump, respectively. The low magnitude of the somersaulting angular momentum of the body at the takeoff of the step might be related with the low activeness of the motion of the landing foot at the end of the succeeding flight phase (Koh and Hay, 1989).

None of the mean values of the twisting angular momentum was significantly different from zero (Table 1), suggesting that, on average, elite male triple jumpers tend to minimize the twisting angular momentum at each takeoff.

No significant relationship was found between any angular momentum value and the actual distance, except the side-somersaulting angular momentum at the takeoff of the step. A significant, non-linear correlation ($r = 0.86$) with the actual

distance was obtained for the normalized side-somersaulting angular momentum at the takeoff of the step. The best regression equation was

$$D_a = -6087\ H'_{x(step)}{}^2 - 84\ H'_{x(step)} + 17$$

where D_a is actual jumping distance and $H'_{x(step)}$ is the normalized side-somersaulting angular momentum at the takeoff of the step. From this equation, it was found that the optimum value of the side-somersaulting angular momentum at the takeoff of the step was 0.0069 $m_b\ h_b^2$ Nms towards the side of the free leg.

It was found that the mean value of the change in the side-somersaulting angular momentum during each of the support phases of the hop, step, and jump was significantly different from zero, and that the mean value of the change in the somersaulting angular momentum during the support phases of the step and jump were significantly different from zero (Table 2).

Table 2
Mean (standard deviation) of the change in the angular momentum during each support phase (Nms)

	Support phase		
Axis	Hop	Step	Jump
Side-somersaulting	-3.75* (1.10)	-3.54* (1.93)	4.28* (3.26)
Somersaulting	1.90 (2.81)	-6.11* (2.35)	3.47* (2.54)
Twisting	-0.07 (1.53)	-0.16 (1.53)	-0.61 (1.31)

* Significantly different from zero ($P < 0.0015$).

A significant, positive correlation ($r = 0.91$) was found between the side-somersaulting angular momentum of the body at the takeoff of the step and the change in the corresponding angular momentum during the support phase of the step. This result suggested that the change in the side-somersaulting angular momentum during the support phase of the step was the major determinant of the corresponding angular momentum at the succeeding takeoff.

Significant correlations were also found between (a) the twisting angular momentum at the takeoff of the last stride and the corresponding angular momentum at the takeoff of the hop ($r = 0.82$), and (b) the side-somersaulting and somersaulting angular momenta at the takeoff of the jump and the changes in the corresponding angular momenta during the preceding support phase ($r = 0.92$ and $r = 0.79$, respectively). These results suggested that the twisting angular momentum at the takeoff of the hop was determined primarily by the corresponding angular momentum at the takeoff of the last stride, and that the side-somersaulting angular and somersaulting angular momenta at the takeoff of the jump were determined primarily by the changes in the corresponding angular momenta during the preceding support phase.

No significant relationship was found between any value of the change in angular momentum and the actual distance, except the change in the side-somersaulting angular momentum during the support phase of the step. A significant, non-linear correlation ($r = 0.86$) with the actual distance was obtained for the change in the normalized side-somersaulting angular momentum during the support phase of the step. The best regression equation was

$$D_a = -2360\ \Delta H'_{x(step)}{}^2 + 17$$

where $\Delta H'_{x(step)}$ is the change in the normalized side-somersaulting angular momentum during the support phase of the step. From this equation, it was found that the optimum value for the change in the side-somersaulting angular momentum during the support phase of the step was zero. This suggested that the change in the side-somersaulting angular momentum during the support phase of the step should be minimized, and that the side-somersaulting angular momentum needed for the flight phase of the step should be obtained during the support phase of the hop.

No significant relationship was found between a change in a normalized angular momentum value and the change in either of the other two normalized angular momentum values during the same support phase. This suggested that each component of the angular momentum can be adjusted independently during each support phase.

No significant relationship was found between the change in a normalized angular momentum value and the change in any of the three components of the velocity of the center of gravity of the body during the same support phase. This suggested that the angular momentum of the body was adjusted without affecting the linear motion of the body, and vice versa.

The findings suggesting that the side-somersaulting angular momentum at the takeoff of the step is important in determining the actual distance of a triple jump, and that this side-somersaulting angular momentum should be obtained during the support phase of the hop have some relevance in practice. The initial vertical impact force of the support phase of the step may be as high as 12 to 22 times body weight (Amadio, 1985, Ramey and Williams, 1985). This extremely high force appears to be due primarily to the braking of the support foot and lower leg. A side-somersaulting angular momentum towards the side of the free leg at the takeoff of the hop tends to decrease the vertical velocity of the support foot and lower leg at the touchdown of the step by rotating the body towards the side of the free leg. Decreasing the initial vertical impact force serves not only to make it easier for a triple jumper to position the body during the support phase of the step to maintain horizontal velocity and produce vertical velocity but also to protect him or her from injury.

REFERENCES

Amadio, A.C., Deutsche Sporthochschule, Köln, 1985.
Dapena, J., J. Biomechanics, 11, 251-256, 1978.
Hay, J.G., *et al.*, J. Biomechanics, 10, 269-277, 1977.
Hay, J.G., J. Sports Science, 10, 343-378, 1992.
Hillman, K., Universität Frankfurt, 1981.
Koh, T.J. and Hay, J.G., Int. J. Sport Biomechanics, 6, 361-373, 1990.
Ramey, M.R. and Williams, K.R. Int. J. Sport Biomechanics, 1, 233-239, 1985.
Yu, B, *et al.*, J. Biomechanics, 1993 (in press).
Winter, D.A., J. Biomechanics, 7, 157-159, 1974.

Kinetic Analysis of the Luge Start Technique

P.F. Vint*, S.D. Betty, L.M. Gorsky, and S.L. Smith.

*Arizona State University, Department of Exercise Science, Tempe, AZ 85287-0404
Converse, Inc., Biomechanics Laboratory, North Reading, MA 01864
United States Olympic Committee, Athlete Performance Division, Colorado Springs, CO 80909

INTRODUCTION

The purpose of this investigation was to quantify the temporal phases of the luge start, determine the magnitudes and relative effectiveness of applied forces and impulses, and estimate bilateral asymmetries which might have deleterious effects on the initial sled trajectory.

Both males and females were highly symmetric in the application of forces throughout the luge start, especially during the propulsive (DRIVE) phase. Kinetic effectiveness scores indicated that only about 75% of the force applied during the DRIVE phase contributed to the forward propulsion of the sled. Male athletes demonstrated significantly higher absolute impulse and force magnitudes during the start which facilitated greater initial sled speeds. Average initial sled speeds for males and females were 3.15 m/s and 2.87 m/s, respectively. Among all athletes, DRIVE phase kinetics were highly correlated with sled speed. It was also determined that greater kinetic output during the preparatory (BLOCK) phase enhanced the forward propulsion of the sled during the DRIVE phase. The results of this study suggest that fast luge start performances are a function of both an explosive eccentric loading of the shoulder, trunk, and hip musculature during the BLOCK phase and a vigorous forward propulsion of the sled during the DRIVE phase.

REVIEW AND THEORY

In Winter Olympic luge and bobsled competitions, the start technique at the beginning of the race is critically important to the overall race performance. During the luge start, the slider pushes, then vigorously pulls on a pair of fixed handles in preparation for racing down the track. In luge events, timing of the race does not begin at the instant the handles are released, but rather, several meters down the track when the athlete is already moving. Therefore, the goal of the luge start is to develop and maintain as high an initial sled speed as possible.

PROCEDURES

Twelve senior members of the US elite luge team were tested in controlled conditions on the ice rink of the World Arena in Lake Placid, New York. Eight men and four women participated in the testing sessions. All of the athletes were tested during the Elite Luge pre-Olympic training camp in September, 1991. Seven of the twelve athletes who participated in the testing sessions went on to compete in the 1992 Winter Olympic Games in Albertville, France.

Kinetic data were collected for all athletes competing in the singles sliding event. The Peak Performance Technologies, Inc., Analog Sampling Module (ASM) was employed to collect analog force signals from a pair of instrumented start handles. The handles were constructed to meet competition design specifications, but were equipped with surface mounted piezo-electric strain gauges to detect vertical and horizontal forces. The specially made handles were calibrated on dry land using known loads applied in vertical and horizontal directions. Four channels of analog force data were collected at 300 Hz for a 6 second duration during each start trial.

The luge start sequence was defined by three distinct temporal phases: the BLOCK, BRAKE, and DRIVE phases. The BLOCK phase described the time when the athlete pushed backwards on the handles to eccentrically load the shoulder, trunk, and hip extensor musculature prior to the DRIVE phase. The BRAKE phase defined a relatively brief transition period when the athlete stopped the backwards motion of the sled. The DRIVE phase corresponded to the actual propulsion of the sled in the forward direction. The DRIVE phase began at a time which was coincident with the application of the peak horizontal force, and ended with the release of the handles. Figure 1 illustrates typical horizontal and vertical force-time profiles and the three major temporal phases of the luge start. Custom software was developed to compute kinetic performance parameters of the luge start. Impulse values were computed by numerical integration of the force-time curves using Simpson's Approximation (Edwards *et al.*, 1982). Initial sled speeds were estimated using idealized impulse-momentum methods. Asymmetry and effectiveness values were expressed as percent scores and are defined in Equations 1 and 2, respectively.

$$\% \text{ Asymmetry} = |(\text{right} - \text{left}) / \text{right}| * 100 \quad (1)$$

$$\% \text{ Effectiveness} = \text{horizontal} / (\text{horizontal} + \text{vertical}) * 100 \quad (2)$$

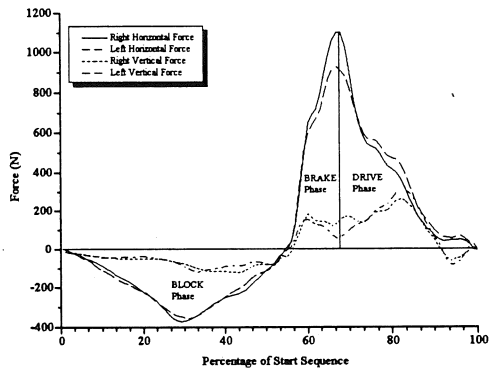

Figure 1. Typical Force-Time Curves for the Luge Start

RESULTS

The force-time profiles were very consistent among all athletes during the luge start (Figure 1). Among all athletes, about 44% of the total force output in the luge start was applied during the DRIVE phase, while about 32% was developed during the BLOCK phase. The transitional BRAKE phase accounted for 24% of the total kinetic output.

Table 1 summarizes average phase durations for all groups tested. The female luge athletes demonstrated consistently longer phase durations than did the males. Average phase duration asymmetries ranged 6.1 to 11.7% during the BLOCK phase; 6.9 to 10.6% during the BRAKE phase; and 3.0 to 7.8% during the DRIVE phase.

Table 1. Average Phase Durations of the Luge Start (±S.E.M.)

	BLOCK Phase (s)	BRAKE Phase (s)	DRIVE Phase (s)
Males	1.313 (0.305)	0.227 (0.030)	0.558 (0.060)
Females	1.496** (0.202)	0.275* (0.047)	0.605 (0.041)

** statistically significantly at $p < 0.002$
* statistically significantly at $p < 0.001$

Analysis of variance tests revealed that males produced significantly higher output for all kinetic parameters when compared to their female counterparts (Table 2). Initial sled speed was significantly faster for males than for females ($p < 0.002$). Average initial sled speeds for male and female athletes were 3.15 (±0.25) m/s, and 2.87 (±0.32) m/s, respectively.

Table 2. Mean Values for Selected Kinetic Parameters of the Luge Start (±S.E.M.)

	Block Imp. (N*s)	Brake Imp. (N*s)	Drive Imp. (N*s)	Block Force (N)	Drive Force (N)
Males	-253.1*	185.8*	354.5*	-459.7*	1852.5*
	(57.7)	(37.8)	(32.4)	(48.8)	(311.3)
Females	-198.5	150.7	287.9	-352.8	1341.9
	(28.5)	(26.7)	(33.4)	(32.4)	(184.9)

* statistically significant at $p < 0.001$ level.

Bilateral asymmetries were highest in the BLOCK phase, ranging from 9.0 to 17.8% difference between right and left side kinetic output. BRAKE and DRIVE phase kinetics were more symmetric, averaging 6.5% and 9.2%, respectively. Asymmetry values were not statistically different between males and females.

Correlation coefficients were computed between selected kinetic and temporal variables and initial sled speed from pooled male and female data. All impulse and maximum force values were significantly related to initial start speed (Table 3).

Table 3. Kinetic and Temporal Correlates of Initial Sled Speed

Luge Start Parameter	Correlation Coefficient (r)
BLOCK Impulse	-0.6272*
BRAKE Impulse	0.5593*
DRIVE Impulse	0.9084*
Max. BLOCK Force	-0.5095*
Max. DRIVE Force	0.7606*
Ave. BLOCK Duration	-0.1695 *ns*
Ave. BRAKE Duration	-0.5386*
Ave. DRIVE Duration	0.2576 *ns*
DRIVE Effectiveness (Impulse)	0.1968 *ns*
DRIVE Effectiveness (Max. Force)	-0.2605 *ns*

* statistically significant at $p < 0.001$ level

Female athletes demonstrated slightly higher kinetic effectiveness scores, although these differences were not significant. Effectiveness measures indicated that, on the average, between 68 and 82% of the total DRIVE impulse, and between 70.5 and 79.1% of the peak force during the DRIVE was actually applied in a direction which would contribute to the forward propulsion of the sled. However, kinetic effectiveness was not significantly associated with initial sled speed.

DISCUSSION

Bilateral DRIVE phase asymmetry in horizontal impulse and peak force application averaged 8.89% across all groups. Intuitively, the more symmetric the application of forces during the start, the straighter the sled will travel in its initial descent. However, it is not known how much kinetic asymmetry would induce a significant deviation of the initial sled trajectory.

Male athletes demonstrated significantly higher absolute impulse and force magnitudes throughout the entire luge start sequence which facilitated greater initial sled speeds. DRIVE phase kinetics were highly correlated with sled speed (Table 3). This association may be readily understood by examination of the idealized impulse-momentum equation used to calculate initial sled speed (Equation 3).

Initial Sled Speed = DRIVE Impulse / Sliding Mass (3)

Linear regression analysis demonstrated a highly significant association between DRIVE phase impulse and sled speed ($p < 0.001$). The R^2 value indicated that 76.7% of the variability in luge start speed could be explained by the magnitude of the horizontal DRIVE phase impulse alone.

It appeared that greater kinetic output during the BLOCK phase enhanced the forward propulsion of the sled during the DRIVE phase (Figure 2). Regression analysis revealed a highly significant linear relationship between total block impulse and initial sled speed ($p < .001$). BLOCK phase impulse alone accounted for 45.36% of sled speed variation.

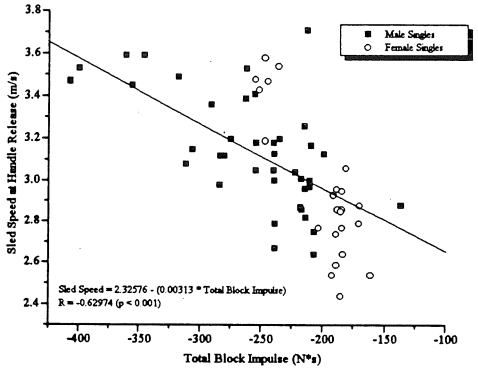

Figure 2. Linear Regression of Total Block Impulse and Sled Speed

The association between BLOCK phase impulse and initial sled speed may be explained by a more effective utilization of stored elastic energy during fast start performances (Cavagna *et al.*, 1965; Cavagna *et al.*, 1968). Intuitively, the BLOCK-BRAKE-DRIVE phase sequence may be considered analogous to that of the counter-movement vertical jump whereby an eccentric phase precedes a concentric phase in an alternating cycle. Komi and Bosco (1978) demonstrated that vertical jump performance increased with increased drop jumps heights (i.e. increased eccentric loads), and that the rate of the eccentric load was significantly related to concentric force output. The results of this study suggest that fast luge start performances are a function of both an explosive eccentric loading of the shoulder, trunk, and hip musculature during the preparatory BLOCK phase and a vigorous forward propulsion of the sled during the DRIVE phase.

In the future, an integrated analysis including force, EMG, and motion analysis measurements should be performed to further enhance the understanding of luge start mechanics.

REFERENCES

Cavagna, G.A. et al. *J. Appl. Physiol.*, **20**, 157-158, 1965.
Cavagna, G.A. et al. *J. Appl. Physiol.*, **24**, 21-32, 1968.
Edwards, C.H. et al. *Calculus and Analytical Geometry* (pp. 231-233), Prentice-Hall, 1982.
Komi, P.V. et al. *Med. Sci. Sports Exerc.*, **10**, 261-265, 1978.

ACKNOWLEDGMENTS

The authors wish to thank the staff of the USOC Athlete Development Computer Science Department and the Engineering Technology Division for their assistance with this project. Thanks also to Marge Hartfel of the 3M Corporation for her assistance with the data reduction.

KINEMATIC AND KINETIC CHANGES IN CYCLING DURING AN EXHAUSTING STEADY-RATE RIDE

Annita Amoroso[1], David J. Sanderson[1] and Ewald M. Hennig[2]

[1]UBC Biomechanics Laboratory, University of British Columbia, Vancouver, Canada
[2]Sportsmedizinisches Institut, Universität Essen, Essen, Germany

INTRODUCTION

The purpose of this study was to investigate the kinematic and kinetic changes that may occur during the final stages of an exhausting steady-rate ride. Subjects rode at 300 watts and 80 rpm until they were unable to maintain the required cadence. Angular displacements of the hip, knee, and ankle joints, along with normal and shear pedal forces were analysed for differences between the first and last minutes of the ride. Significant differences were found for the peak joint angles, with the largest differences seen at the ankle joint (greater dorsiflexion). The peak pedal forces for both the normal and shear components also showed differences between the first and last minutes. These results suggest major adaptations occurring primarily at the ankle as the rider fatigues which as shown, has consequences on the force application to the pedal. Further study looking at joint moments would contribute to a greater understanding of the roles played by the lower limb muscles in compensating for the fatiguing conditions.

REVIEW AND THEORY

Although in the scientific literature, fatigue is defined as the inability to maintain a certain workload, this study was only concerned with the ride prior to the point of fatigue, where constant power output and cadence were maintained despite the increasing challenge of the workload as the ride progressed. Fatigue is sometimes described as a progressive condition where certain metabolic and physiological changes take place and eventually lead to a cessation of the activity. In this context therefore, the need to continue to perform optimally contributes to the cyclist experiencing some form of fatigue. As a consequence, the muscles driving the legs may function differently resulting in changes to the kinematics and kinetics of cycling. Kinematic and kinetic changes resulting from fatigue have already been reported in running (Williams, 1985). The consequences may be the result of a failure to maintain optimal mechanics, or they may be the necessary adaptations to maximize efficiency under stressful circumstances. Investigating whether kinematic and kinetic changes occur as one fatigues, is the first step in trying to gain a better understanding of the underlying mechanisms involved in producing these changes. The objective of this study is two-fold; first to provide information on specific kinematic and kinetic changes that occur in cycling during an exhausting ride, and second, to infer from the results some possible strategies the human body adopts to optimize movement patterns under fatiguing conditions.

METHODS

Eleven male competitive cyclists (CCA Cat. I - Cat. III) volunteered as subjects for the study. The subjects rode an instrumented bicycle mounted on a Schwinn Velodyne, an electronically braked cycle ergometer that simulates inertial characteristics of road riding and can modulate given power outputs based on cadence. The Velodyne was set at 300 watts, and subjects were asked to maintain a cadence of 80 revolutions per minute (rpm). The cyclists rode until they were no longer capable of maintaining this cadence. The first and last minutes of the ride were termed 'non-fatigue' (NF) and 'fatigue' (F), respectively. The bicycle was equipped with two triaxial piezo-electric force transducers mounted in the right pedal, a continuous output potentiometer to measure pedal angle, and two optical sensors; one to locate crank position and one to indicate top dead centre (TDC). Force data were collected at 15° intervals for 600 msec at a rate of 1 KHz, every 45 seconds during the ride. Two gen-locked video cameras, oriented perpendicular to one another, recorded the movement of highly reflective markers placed on specific anatomical landmarks of the subject's right leg. The three dimensional coordinates of the markers were determined by direct linear transformation after digitization of the points recorded by each of the two cameras. From these data, the movement of lower extremity body segments and angles between these segments were determined, in addition to the joint angular velocities. In order to compare the 'non-fatigued' and 'fatigued' data, paired Student's t-tests, with $p<0.05$ set a priori, were performed on the minimum and maximum angles, and on the percent cycle at which the two occurred.

RESULTS AND DISCUSSION

Fatigue resulted in greater peak hip extension by an average of 1.5°. There were

significant differences for both the minimum (NF=104.65°; F=106.16°) and maximum (NF=144.77; F=146.72) hip angles between the NF and F trials. Although the knee showed a similar trend towards greater extension, the differences were not significant. The more noticeable changes brought on by fatigue were seen at the ankle joint (Figure 1). The curve showed a significant shift towards greater dorsiflexion, by an average of 4.13°. Significant differences were found for both the minimum (NF=84.97; F=89.91) and maximum (NF=108.26; F=111.88) angles between the two trials.

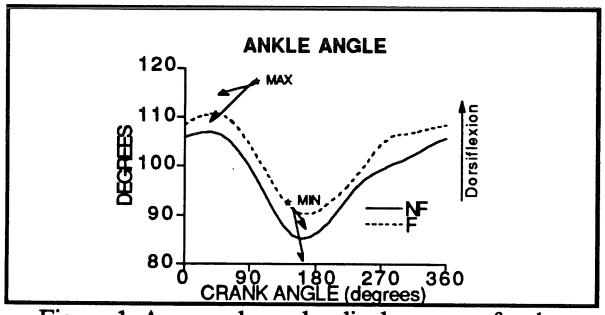

Figure 1. Averaged angular displacements for the ankle. Statistical significance denoted by *.

The increased dorsiflexion is produced by dropping the heel thus altering the pedal angle. Changes in pedal angle, termed 'ankling', have been documented in the cycling literature (Kautz et al., 1991). Such changes are thought to be related to the pedaling effectiveness of the rider by favouring more pulling across at the bottom of the pedal stroke, pulling up during the recovery phase, and pushing forward across the top. The averaged angular pedal displacements (Figure 2) demonstrated an altered pedal orientation with fatigue, with a shift towards a smaller angle between the pedal and the vertical axis.

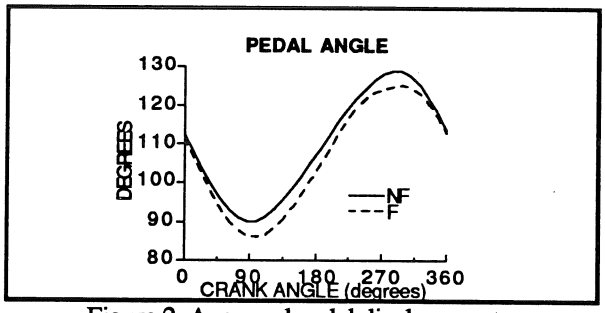

Figure 2. Averaged pedal displacements.

The resultant force profiles are similar in magnitude and pattern for both the NF and F trials. The component of the resultant force applied perpendicular to the crank, known as 'effective force', also showed no significant differences between trials. Calculated 'indices of effectiveness' (integral of effective force divided by integral of resultant force) revealed no difference between trails (NF, F=0.57).This implies that the rider does not overcome fatigue by becoming more effective in pedaling strategy.

There were however, observed changes in the two components of the applied force, normal (Fz), which is perpendicular to the pedal surface, and shear (Fy), which is anterior/posterior to the pedal (Figure 3A, B). Fatigue resulted in an increase in the normal force within the firsthalf of the pedal cycle (0-180°), with peak forces being significantly different (NF= 339.44; F=369.48). The shear force demonstrates an obvious shift with fatigue, prominent between 45-225°. There were significant differences between the maximum forces (NF=79.06; F=68.24) and the percent of the cycle in which the minimum and maximum forces occurred. These changes also coincide with the observed changes in pedal angle (Figure 2).

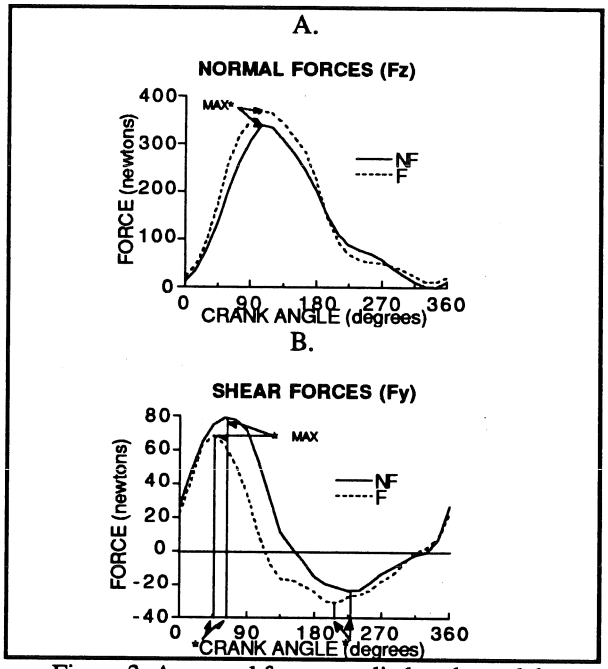

Figure 3. Averaged forces applied to the pedal. Statistical significance denoted by *.

The changes seen in the kinematic and kinetic variables with fatigue reflect adaptations in the body's mechanical response to the increasing demands placed on it. The reasons for these changes may be better understood by looking at joint moments and EMG.

REFERENCES

Kautz, S. A. et al. (1991). *Int J Biomechanics* 7, 29-53.

Williams, K. R. (1985). *Exercise & Sport Sciences Reviews*. 13, 389-441.

GAIT ANALYSIS OF PATIENTS ONE YEAR AFTER CALCANEAL FRACTURES

D. V. Skvortsov, I.V. Fishkin
Orthop. Hosp.and The Med. Inst. in Ivanovo, Russia, 153000.

INTRODUCTION

Patients often have disturbances of Gait after Calcaneal Fractures. Investigation of biomechanics of the Gait of the foot after injury may be useful for understanding the causes of of Gait disturbances. This paper is a study of Gait and foot function after Calcaneal Fracture.

PATIENTS AND METHODS

The 65 patients (56 male, 9 female, ages 21-50) were all investigated after calcaneal fracture on one side using clinical and biomechanical methods. All patients were treated by perosseus apparatus. For 6 patients with complicated interjoint fracture we used a special device Fishkin et al, 1989. The state of health of each patient was determined by exhaustive method including estimates of clinical and biomechanical conditions. Each parameter had its own ball value. Patients were separated in accordance with their rehabilitative potential. There were 32 persons that had good results, 26 had satisfactory results and 7 had bad results. Gait was measured by a special goniometer system for Ankle and Subtalar joints developed by the authors of this work Fishkin et al (1989), and a special walking floor for measuring the step length, width and toe-out angle. The timing of walking was measured simultaneously with angles of rotation by shoe switches. The active range of motion of all joints was also measured. The control group was that of 30 normal adult men.

RESULTS

The motion at the Subtalar joints while walking on the affected side was characterized by decreased supination in the terminal stance and early swing phase according to the results of treatment. The range of motion of supination decreased in the group with the bad result as compared to that with satisfactory or good results. Patients with a bad result also had a decreasing range of pronation motion in the weight acceptance phase. These differences were statistically significant, $p<0.05$ for the groups with good and satisfactory results and $p<0.02$ for the group with bad results. The goniograms of the Subtalar joint showed accompanying increasing amplitude of supination on the normal side. The motion at the Ankle joint had decreasing amplitude in weight acceptance and toe-out phase according to clinical result. The worse result of treatment had the less amplitude, ($p<0.05$). The goniograms of the Ankle joint on the normal side was significantly different also. In all groups the step length on the affected side was more than of normal side ($p<0.05$), but it was statistically significant only for the group with the satisfactory result. In all groups the step length on the normal and affected side was less than the control group, ($p<0.001$). The toe-out angle decreased on the affected side in all groups ($p<0.05$), but it was only significant for groups with good results. The step width was increased gradually according to the state of the patient's health. Patients with bad results had the widest step width. The active motion at the Ankle and Subtalar joints was decreased on the affected side in the groups with good and satisfactory results ($p<0.001$). Patients with bad results on the treatment were unable to execute the active motion tests.

The worse clinical results were accompanied by gradual increasing

heel contact time and gradually decreasing swing phase on the affected side. Time of the heel contact was increased on the normal side, $p<0.05$ for groups with good and bad results and $p<0.001$ for groups with satisfactory results. The increasing time of the heel contact on the affected side was combined with unchanged time of the support phase ($p<0.02$ for groups with satisfactory results and $p<0.05$ for groups with a bad result). The double stance time decreased with the worst clinical result for both sides.

DISCUSSION

All patients after calcaneal fracture had decreasing range of supination on the affected side and simultaneous increasing range of supination on the normal side. We assume this was a compensation process. The function of the Ankle joint on the affected side was characterized by decreasing range of rotation at the weight acceptance and toe-out phases. Probably it depends on insufficiency of triceps sure muscle because the height of calcaneus remains shorter after surgery than normal, particularly in patients with bad and satisfactory results. The cause of decreasing toe-out angle on the affected side is probably, a consequence of decreasing range of motion in a Subtalar joint. Axis of rotation of the Subtalar joint stays approximately in line with the walking direction in normal walking. The Ankle and Subtalar joints work together. The foot with abnormal Subtalar joint realigns along the walking direction, decreasing the toe-out angle. This decreases the functional load on the Subtalar joint (less range of motion), because the Subtalar joint movement causes pain and the lower leg movement is dictated by the Ankle joint. In our study, the average active range of motion in the Ankle joint was determined to be 36 degrees. This value differs significantly from that of the known literature ranging 50-70 degrees, Langelaan (1983, Scott et al. (1991), Wrght et al. (1964). We measured Ankle range of motion on 18 roentgenograms of normal adult people. The average range of motion was measured at 37.4+1.0 degree. This is the same result When measured by active range of motion. We explain this discrepancy in the literature and our study results the fact that the midtarsal and Lisfranc joints were included in their measurements. These joints have small range of motion like in the Ankle joint itself Langelaan (1983), Scott et al.(1991). We think that increasing time of heel contact and decreasing the toe support time is a result of the disturbance of the muscles balance between the font and back muscle groups of the calf. After Calcaneal Fractures, the uneffected leg executes mainly a support function and the affected leg, mainly a swing function. This increase in step length on the affected side compared to normal supports our hypothesis.

Reference

Fishkin I.V. and Skvortsov D.V. The Device for Measuring Angle of Rotation in the Ankle and Subtalar Joints while Walking. Bulletin of Inventions n. 6, 1989. N 1489722

Fishkin I.V. and Skvortsov D.V. The Device for Reposition of Complication Fracture of the os Calcaneus. In the Book: The III International Congress by the Developing of Methods Extrabones Fixsation, p. 232, Riga 1989.

Langelaan E. J. A Kinematical Analysis of the Tarsal Joints. An X-ray Photogrammetric Study. Acta Orthop Scand (Suppl 204) 1983; 54: Munksgaard 1983.

Scott S. H. Winter D. A. Talocrural and Talocalcaneal Joint Kinematics and Kinetics During the Stance Phase of Walking. J. Biomechanics,24, 743-52, 1991.

Wright D. G., Desai S. M., Henderson W. H. Action of the subtalar and ankle joint complex during the stance phase of walking. J. Bone Joint Surg. (Am) 46, 361-382, 1964.

CLINICAL AND BIOMECHANICAL CORRELATIONS IN PATIENT'S WITH LOW BACK PAIN USING FORCEPLATE

D. V. Skvortsov, V. N. Larina,
The Medical Institute in Ivanovo, Russia, 153000

Introduction

Very little information has been published about the biomechanics of recovery in patients with clinical pathology. This paper presents data of the biomechanics of gait and standing at different period of recovery of Low Back Pain.

Patients and methods

The 49 patients with Low Back Pain were investigated by clinical and biomechanical methods. The patients were 25-52 years of age, the average being 39. There were 32 men and 17 women. The Back Pain were characterized by spasm in the spinal column, radiculopathies of L5 and S1, and neurodystrophies with ischialgia. At the time of investigation, the rehabilitative potential of each patient was examined by a method known as the four ball system. The first ball corresponded to a grave condition, two ball to acute form Low Back Pain syndrome, three ball to subacute form, and four ball showed a a good general state of health.

Gait was measured as forceplate Ground Reaction Force, measured in vertical (Z1 weight acceptance phase, Z2 single support phase, Z3 push off phase), and horizontal directions, (Y1 weight acceptance, and Y2 push off). The results of measurement were calculated as percentage of body weight. The weight distribution on each leg was measured in standing position on the forceplate and calculated according to body weight. Stabilometry was made with patient standing quietly for 3-4 minutes on the forceplate. The center of the forceplate corresponded to the center line connecting the apex of the medial malleolus of the ankles. The projection on the ground of the center of the pressure was measured in centimeters in anterior-posterior "S" and medial-lateral "F" direction with their deviations "s" and "f" accordingly. Positive range for "S" is anterior and negative is posterior, relatively to the center line connecting the malleolus. The distance between the patient's feet was a constant.

Results

The patients were found to fall into four groups based on the results of the biomechanical and clinical conditions. There were three basic gait abnormalities and a fourth group who had finished treatment and had good clinical outcomes. The first group consisted of five patients having significant decreases in amplitude in the weight acceptance phase, Z1 and Y1 accordingly. The second group of 29 patients showed a decreased amplitude at the weight acceptance and push off phases; Z1 and Z3, and Y1 and Y2. The third group of 8 patients had a decreased amplitude mainly in push - off phase of vertical component of Ground Reaction Force Z3. The fourth group of 7 patients, having finished treatment with good results, only differed in the single support phase Z2. The difference between the affected and normal leg was statistically significant ($p<0.05$).

The patients in the first group had an acute form of the Low Back Pain, the average ball group was 2.13. In the second group, with less disability than the acute form ball group of ball 2.71. The third reconvalescention group had subacute form, ball 3. The fourth had a ball group of 3.10 and finished treatment with good results.

The results of weight distribution in standing position measurements is presented in graph from in Graph 1. At the first group had a weight bearing on the affected side approximately 13% less, whereas the remainder of the groups really had no statistical difference between the affected and normal sides.

Center of pressure has a tendency to shift back with increasing state of severity of the patient's condition, see Graph 2. Medial-lateral position of stabilometry showed very little change. Variability of the center of pressure was high in all groups. The average mean was 5.47 cm. for sagittal plane and 2.27 cm. for the frontal plane.

The first group was characterized by decreasing Ground Reaction Forces in both directions, see Graph 3 and 4. However, Ground Reaction Force during weight acceptance phase was less than the other groups. The vertical component of Ground Reaction Force at weight acceptance phase Z1 was less than the body weight 94% and Z3 was 103% of body weight. The second group had identical value weight acceptance and push off (103%), but this was less than normal. The third group had normal values at weight acceptance, but lower during push off (101%). Finally, the fourth group had normal values of Z1, Z2 and Z3.

We have a decreasing Z2 from group one 84% down to a normal range of 75.3% from group to group. These differences are statistically significant between the first and fourth groups with $p<0.05$. Thus, loading on the single leg did correspond to clinical result.

The horizontal component of Ground Reaction Force on the affected side was characterized by lower values Y1 and Y2, see Graph 4. The Y1 or weight acceptance is considerably less than Y2 to push off for all groups ($p<0.05$). We can see gradual increase in both Y1 and Y2, but the Y1 does not achieve the normal range, even in fourth group.

The dynamics of change on the normal side are presented in Graphs 6-7. These changes were similar to that of the affected side and were not statistically significant.

Discussion

As we see, investigation of weight distribution in Standing position had useful information only in patients with acute form of Low Back Pain. This was not a specific test for Low Back Pain.

The patient's trunk at acute low back pain had bending not only to the side, but also to the back. The movement of the center of pressure of position backwards possibly could be explained by first, the patients having a decrease in their lumbar lordosis, and the second being that of possible neuropathic groups of muscles at the ankle, knee flexors and hip extensors. This position provides a load on the extensor group of muscle. In position of posterior trunk bending, the Ground Reaction Force vector is behind the ankle, knee, and hip joints axis. Ankle, knee flexors, and hip extensors remain relaxed. The diminished center of pressure had a large range of motion in both directions as sagittal as frontal with more expressions in the sagittal plane (s). These do not depend on degree of disease and remain the same in group with good results of treatment, see group 4. In spite of right position of the center of pressure, S

and F. These results show a decreased ability to maintain balance in standing position in patients as with acute forms of Low Back Pain as without clinical manifestation of disease. Thus, motor control of posture was insufficient, particularly in the sagittal plane, i.e. for flexor and extensor groups of muscles.

Ground Reaction Force patterns were characterized by identical changes for both sides having a decrease in the force in the weight acceptance phase. We suppose that a symmetrical process in humans is a manifestation of general biological function and is necessary for normal gait. If asymmetry increases, the patient will use a cane. The additional support of body weight while walking will help to decrease the walking asymmetry.

As we can see, acute forms ofLow Back Pain are characterized by general decreasing of Ground Reaction Forces, but more expressed in the weight acceptance phase. Dynamics of recovery of walking for different degrees of disease (groups 1-3) was characterized by increasing gradual Ground Reaction Forces according to the clinical condition except in Z3 in the push off phase which remained approximately at the same level. At push off phase, the basic activity localized in the ankle flexors of muscles group Perry J. (1992). Obviously, these muscles have had recovery in the latest phase. It was confirmed by results of group 4, where push-off phase reached the normal values. We shall be able to have a more detailed answer after clinical and EMG investigation.

Dynamics of Z2 reflect only cadence of walking Winter D.A. (1992) which increased gradually from group number 1 to 4. The important phenomenon is the decreasing horizontal Ground Reaction Force in weight acceptance phase, relative to push off phase. At this time we can assume the following: It was result of the disturbances oft he function of the gluteus maximus, and painful lumbar part of the erector spinae muscle on the affected side. As we know, the erector spinae have two peaks of activity. The first is associated with weight acceptance phase of the ipsilateral limb, the second with the contralateral limb, Winter D.A. (1992). They both accomplish control of the forward acceleration of the trunk in weight acceptance phase. The gluteus maximus assists in controlling trunk forward acceleration with peaks during weight acceptance phase as correspond to the first peaks of the horizontal Ground Reaction Force Winter D.A. (1992). Horizontal Ground Reaction Forces just reflect this process. Generally, Stabilography and Ground Reaction Forces reflect pathology in motor control groups of muscles in the ankle, knee flexors and hip extensors.

References

Perry. J. Gait Analysis. Normal and Pathological Function. Copyright 1992 by SLACK Incorporated 1992.

Winter D.A. The Biomechanics and Motor Control of Human Gait: Normal, Elderly and Pathological. Second Edition. University of Waterloo Press, 1992.

GRAPH 1. Weight Distribution on Each Leg at Standing Position.

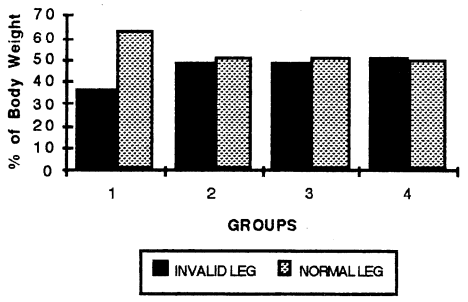

GRAPH 2. Stabilometry Data.

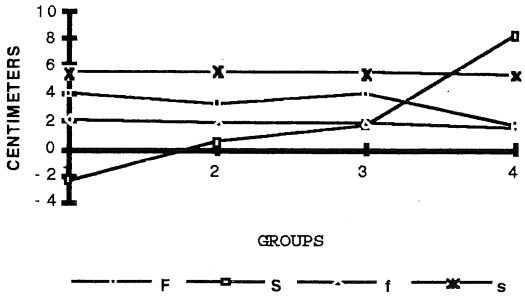

GRAPH 3. Vertical Forceplata Data on Invalid Side.

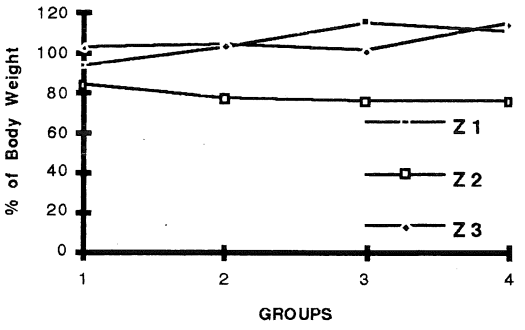

GRAPH 4. Horizontal Forceplata Data on invaiid Side.

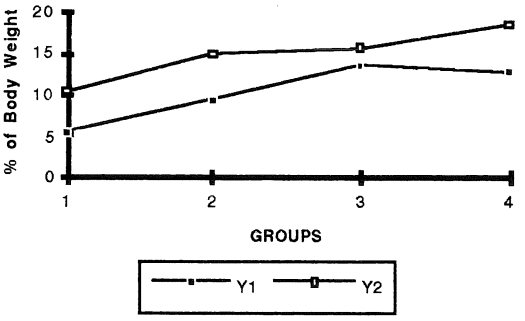

GRAPH 5. Vertical Forceplata Data on Normal Side.

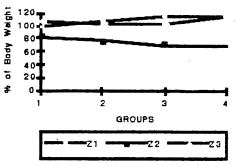

GRAPH 6. Horizontal Forceplata Data on Normal Side.

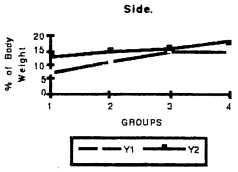

ETIOLOGIC FACTORS ASSOCIATED WITH ACHILLES TENDINITIS IN RUNNERS

Stephen P. Messier, Jean L. McCrory, David F. Martin, Robert B. Lowery, Walton W. Curl, and D. Monte Hunter

J.B. Snow Biomechanics Laboratory and the Bowman Gray School of Medicine, Wake Forest University, Winston-Salem, NC 27109.

INTRODUCTION

The purpose of this study was to determine whether relationships exist between selected training, anthropometric, muscular strength and endurance, and biomechanical variables and runners afflicted with Achilles tendinitis (AT). Specifically, we examined differences in selected measures between a non-injured cohort (C) of runners (N = 58) and a cohort of injured runners with AT (N = 31). Separate discriminant function analyses were performed on each of the five sets of variables to identify the factors that best discriminate between the AT and C groups. Years running, training pace, stretching habits (injured runners were less likely to incorporate stretching into their training routine), touchdown angle, plantar flexion peak torque at 180 deg/s, and arch index were found to be significant discriminators. Discriminant analysis revealed no significant kinetic discriminators between the AT and C groups. A combined discriminant analysis using the above mentioned significant variables revealed that plantar flexion peak torque, touchdown angle, and years running were the strongest discriminators between runners afflicted with AT and runners who had no history of overuse injury.

REVIEW AND THEORY

Injuries to the Achilles tendon, the most common overuse syndrome of the lower leg (Nelen et al.,1989), account for 5% to 18% of the total number of running injuries (Brunet et al., 1990; Clement et al., 1984; Clement et al., 1981; Krissoff et al., 1979).

Current knowledge concerning the etiology of Achilles tendinitis in runners has been based on surveys of injured runners (Brunet et al., 1990; Jacobs et al., 1986; Janis, 1986) or expert opinion (James et al., 1978). Excessive rearfoot motion (Clement et al., 1984) and gastrocnemius - soleus insufficiency (Nelen et al., 1989; Smart et al., 1980) are the most common mechanisms believed to precipitate the onset of Achilles tendinitis.

Prevention and treatment of runners afflicted with Achilles tendinitis is inhibited by the lack of definitive evidence concerning its etiology. Hence, the purpose of this study was to extend our knowledge of running related injuries by determining whether relationships exists between selected kinematic, kinetic, anthropometric, muscular strength, and training variables and runners afflicted with Achilles tendinitis.

PROCEDURES

The subjects for this investigation were male and female recreational and competitive runners who had been running a minimum of 10 miles per week for at least one year. A non-injured control group (N = 58) and an Achilles tendinitis injury group (N = 31) were analyzed. The control group consisted of runners who had no history of an overuse injury. Achilles tendinitis was defined as inflammation and irritation of the Achilles tendon 2 to 6 cm above its insertion into the calcaneus.

Non-injured runners and runners afflicted with Achilles tendinitis (as diagnosed by an orthopedic surgeon) were evaluated during two testing sessions. On the first visit to the clinic a runners' history questionnaire was completed, and anthropometric and isokinetic strength measurements were collected. On the second visit, kinematic and kinetic analyses were performed. Three trials of each measurement were taken and averaged to yield representative values.

Inked prints of both feet were used to calculate an arch index. With the subject in the supine position, relative leg length, absolute leg length, Q-angle and ankle and knee flexibility were assessed.

A Cybex II+ isokinetic dynamometer was used to determine the strength and endurance of the subject's ankle dorsiflexors and plantar flexors. The subject performed seven repetitions at an angular velocity of 60 deg/s to determine muscular strength. Subsequently, the subject performed 32 repetitions at an angular velocity of 180 deg/s to evaluate muscular endurance. The first leg tested was randomized to limit any practice effects.

Rearfoot movement was analyzed using a Motion Analysis high speed video system (200 fps). Joint markers were placed on the posterior leg and running shoe heel counters according to the method outlined by Clarke, et al. (1984).

Ground reaction force data were obtained while subjects ran along a 22.5 m runway and struck an A.M.T.I. Model OR-6-5-1 force platform (500 Hz). Running speed was monitored with a photoelectric control system.

Bilateral muscular strength and endurance, anthropometric, kinetic, and kinematic variables, as well as running history data, were analyzed statistically. The injured side was used for each subject afflicted with with Achilles tendinitis and a

random side (with percentages of left to right foot equal to that of the injured group) was chosen for each control subject. Five discriminant function analyses, each employing a backward elimination variable selection procedure, were performed. These analyses were used to select the most important discriminators between injury and control groups separately for muscular strength and endurance, anthropometric, force, rearfoot, and training data. Significant variables from these analyses were entered into a final discriminant analysis to identify the factors that best discriminate between the injured and control groups. Variables significant to the 0.05 level in the final analysis were considered good predictors.

RESULTS AND DISCUSSION

A Runners' History Questionnaire was used to collect the subjects' training histories. Stretching habits (MAT = 0.89 ± 0.62; Mc = 0.62 ± 0.06; note: 0 = does stretch regularly, 1 = does not stretch regularly), training pace (MAT = 7.49 ± 0.14 min/mi, Mc = 7.87 ± 0.12 min/mi), and years running (MAT = 13.0 ± 1.48 yrs, Mc = 9.5 ± 0.93 yrs) were significant discriminators ($p < .05$). Although not significant, the injured runners tended to run more miles per week (MAT = 31.3 mi/wk, Mc = 26.7 mi/wk) and trained more often on dirt (12.4%) and less often on asphalt (64.3%) than the control group (10.2% and 73.1%, respectively).

Arch index proved to be the only significant ($p = 0.04$) anthropometric discriminator between the groups (MAT = 0.228 ± 0.01, Mc = 0.250 ± 0.001). The AT group was slightly ($p = 0.08$) older than the C group (MAT = 38.4 ± 1.8 yrs, Mc = 34.5 ± 1.2 yrs).

Although there were several marginally significant muscular strength (60 deg/s) discriminators, plantar flexion peak torque at 180 deg/s (MAT = 13.83 ± 0.93 %BW, Mc = 16.37 ± 0.65 %BW) was the strongest discriminator ($p = 0.008$).

Touchdown angle (MAT = -8.94 ± 1.54 deg, Mc = -6.97 ± 0.73 deg), maximum pronation MAT = 11.98 ± 0.86 deg, Mc = 11.42 ± 0.67 deg), time to maximum pronation (MAT = 37.30 ± 2.31 %, Mc = 40.32 ± 1.38 %) and maximum pronation velocity (MAT = 376.5 ± 43.3 deg/s, Mc = 374.3 ± 23.1 deg/s) were significant discriminators between the AT and C groups.

There were no significant kinetic discriminators between the AT and C groups. Peak ground reaction forces tended to be higher in the AT group (Table 1). This may have due, in large part, to the faster training pace of the AT group.

Table 1. Selected descriptive kinetic data. All forces are normalized to body weight.

Variable	Control	Achilles Tendinitis
1st Vert Peak	1.73±0.04	1.81±0.08
1st Max Loading Rate	54.93±1.74	55.53±2.73
2nd Vert Peak	2.48±0.03	2.62±0.06
Max Propulsive Force	0.31±0.01	0.32±0.01
Max Braking Force	0.39±0.01	0.43±0.02
Max Medial Force	0.11±0.01	0.11±0.01
Max Lateral Force	0.09±0.01	0.13±0.02

A combined discriminant analysis using the significant variables from the previous five analyses revealed that plantar flexion peak torque, touchdown angle, and years running were the strongest discriminators between runners afflicted with AT and runners who had no history of overuse injury. Prediction of individual subjects into their respective groups using a cross validation procedure revealed that these variables were good predictors of the C group (87.2%) but were not good predictors of the AT group (50.0%).

REFERENCES

Brunet, M. E.et al. A survey of running injuries in 1505 competitive and recreational runners. J. Sports Medicine and Physical Fitness. 30(3): 307-315, 1990.

Clarke, T. E.et al. The study of rearfoot movement in running. In: Sport Shoes and Playing Surfaces, E.D. Frederick (Ed.). Champaign, IL: Human Kinetics, 1984, pp 166-189.

Clement, D.B. et al. Achilles tendinitis and peritendinitis: etiology and treatment . Am J. Sports Med. 12(3): 179- 184, 1984.

Clement, D. B. et al. A survey of overuse running injuries. Physician and Sportsmed 9(5): 47- 58, 1981.

Jacobs, S. J.et al. Injuries to runners: a study of entrants to a 10,000 meter race. Am J. Sports Med. 14(2): 151-155, 1986.

James, S. L.et al. Injuries to runners. Am. J. Sports Med. 6: 40-49, 1978.

Janis, L. R. Results of the Ohio runners sports medicine survey. J. Am. Podiatr. Med. Assoc. 10:586-589, 1986.

Krissoff, W. B.et al. Runners' injuries. The Physician and Sportsmed 7(12): 55-63, 1979.

Nelen, G., M. et al. Surgical treatment of chronic Achilles tendinitis. Am. J. Sports Med. 17(6): 754-759, 1989.

Smart, G. W. et al. Achilles tendon disorders in runners - a review. Med. Sci. Sport Exer. 12: 231-243, 1980.

KINEMATIC ANALYSIS OF ANTERIOR-CRUCIATE-LIGAMENT-DEFICIENT SUBJECTS DURING SIDE-STEP CUTTING WITH AND WITHOUT A FUNCTIONAL KNEE BRACE

T. P. Branch, P. A. Indelicato, S. Riley*, G. Miller**

Department of Orthopaedics, Emory University, Atlanta, GA 30322
*Department of Orthopaedics, University of Florida, Gainesville, FL 32611

Introduction

Although functional bracing of the anterior cruciate ligament (ACL) deficient knee has been used since the 1970's, little research has been performed to verify its efficacy[1].

The two purposes of this research were 1) to identify kinematically any differences between athletes with an ACL-deficient knee and normal subjects when performing a side-step cut, and 2) to examine the kinematic changes that occur when two different types of functional knee braces are used by the ACL-deficient athlete.

Subjects with normal knees and with ACL-deficient knees performed a 90° side-step cut while being monitored by a three-dimensional kinematic tracking system. ACL-deficient subjects repeated the test with functional knee bracing. No statistically significant differences were noted when comparing isolated joint rotations. However, differences between the experimental groups were found when we compared total rotation of the planted limb.

Review and Theory

Few studies have looked at the impact of functional knee bracing on the kinematics of ACL-deficient athletes. Knutzsen et al. used electrogoniometry to study ACL-deficient athletes wearing functional knee braces.[2,3] They found that wearing a brace during straight ahead running produced a reduction in sagittal- plane knee flexion of 22% during swing phase and 13% during stance phase. When wearing a brace, mediolateral varus/valgus motion was reduced by 24% and total tibial rotation was decreased by 38%.

Procedures

Ten men with normal knees and ten ACL-deficient men 21 to 42 years old were tested. Each group was verified by history and physical exam including a Lachman and pivot-shift test. A three-dimensional tracking system was utilized for kinematic tracking of subjects while they performed a 90 degree side-step cut.

Each control subject performed the cutting maneuver five times. The ACL-deficient subjects performed three sets of five maneuvers for a total of 15 times (e.g., five times with no brace, five times with the strap-type brace, and five times with the shell-type brace). The order of bracing and non-bracing was random.

The Motion Analysis Corporation (Santa Rosa, CA) three-dimensional tracking system was utilized for kinematic tracking. This system used 25 reflective balls placed on limb segments and four cameras to record the movement of the balls on videotape. A video processor then digitized the location of each ball on each frame and custom software was used to track the movement of each individual ball and interpret that movement as rotation of limb segments.

Statistical comparisons were made between experimental groups for the pelvic angles, hip angles, knee angles, ankle angles, and total rotation of the planted leg.

Results

The time spent during stance phase was the same for all groups ($p < .05$) indicating similar speed during the cut. Statistical analyses failed to show any significant differences between the individual joint rotations across all groups. However, we did find a statistically significant difference ($p < .05$) in the cumulative rotations of the stance-side lower extremity between the control group and the ACL-deficient subjects wearing no brace (Fig. 1). The cumulative external rotation of the hip, knee, and ankle in the ACL-deficient subject translates to a compensatory early turning of the body towards the cut.

A trend was noted that knee rotation in the strap-type of brace was closer to that in control subjects and knee rotation in the shell-type of brace was closer to that in ACL-deficient subjects. When analyzing "total rotation at 50% of the stance phase", these trends were confirmed statistically ($p < .05$).

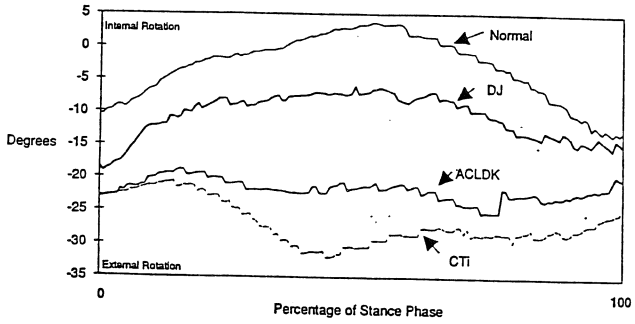

Figure 1: *Total rotation of the planted leg about the Z axis during the stance phase of the side-step cutting maneuver. Normal=Control, DJ=strap-type brace, ACLDK=ACL deficient knee, CTi=shell-type brace.*

Discussion

Compensatory changes observed in the ACL-deficient subject are difficult to measure with accuracy. A subject may employ a complex set of kinematic changes which are significant as a set but not individually. These problems extend to those observations seen when studying the effect of wearing a brace on the kinematics of an ACL-deficient subject. We use "total rotation of the planted leg about the Z axis" as our measure of compensatory techniques.

We believe that the control subject uses his planted leg to stop his forward momentum and to turn his body towards the side of the cut (Fig. 2). The ACL-deficient subject leans his body forward to lessen the impact on the injured limb while starting to turn towards the direction of the cut earlier, apparently minimizing the rotational moment of the injured limb (Fig. 3).

It is interesting that the ACL-deficient subject wearing a strap-type brace cuts in a pattern similar to the control subjects. Either the strap-type of brace provides some increased stability that allows the wearer to cut more like normal, or it only increases their "sense of stability" which "fools" them into not using their normal compensatory motions.

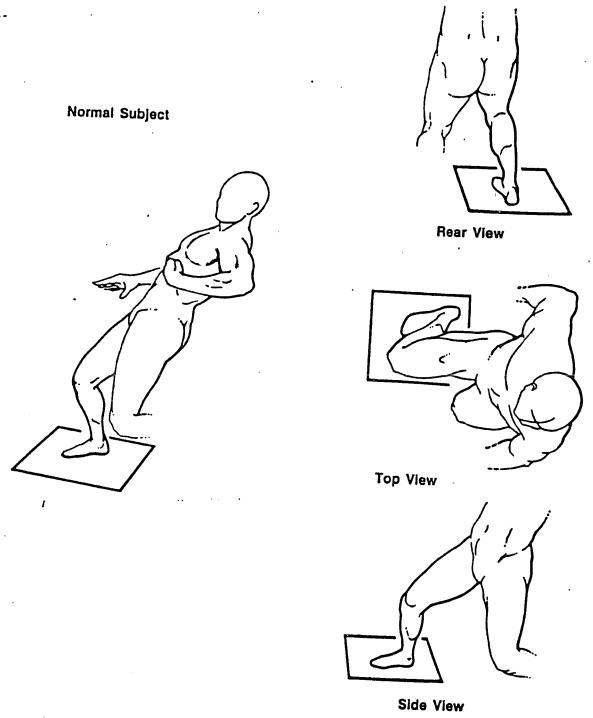

Figure 2: *Kinematics found during mid-stance of a side-step cut performed by a subject with normal knees. Some data (e.g. the forearms in the top view) were not included in order to enhance the reader's ability to identify the rotations between torso and the planted limb.*

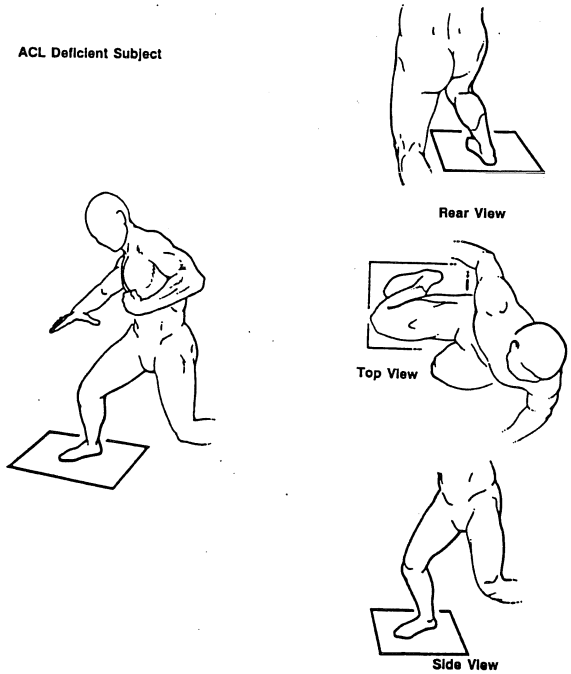

Figure 3: *Kinematics found during mid-stance of a side-step cut in an ACL-deficient subject. Note "compensatory" turning of the torso in the top view compared to the normal subject in Figure 2.*

References

1. *American Academy of Orthopaedic Surgeons. Knee Braces Seminar Report. Chicago, American Academy of Orthopaedic Surgeons, 1985.*
2. *Knutzen, KM; Bates, BT; Hamill, J. Electrogoniometry of post-surgical knee bracing in running. Am J Phys Med 1983;62:172-81.*
3. *Knutzen, KM; Bates, BT; Schot, P; Hamill, J. A biomechanical analysis of two functional knee braces. Med Sci Sports Exerc 1987;19:303-9.*

KINEMATIC AND KINETIC ANALYSES OF GAIT IN SUBJECTS WITH PROXIMAL FEMORAL FOCAL DEFICIENCY

E. FOWLER[1], D. IRVINE[1], R. ZERNICKE[2], Y. SETOGUCHI[3] AND W. OPPENHEIM[4]

Functional Assessment Laboratory[1], Child Amputee Prosthetics Project and Department of Pediatrics[3] Department of Surgery, Division of Orthopaedic Surgery[4], UCLA, Los Angeles, CA 90024
and
Department of Surgery, University of Calgary, Calgary, Alberta, Canada[2]

INTRODUCTION

Proximal femoral focal deficiency (PFFD) is a congenital deformity of the proximal femur associated with varying degrees of hip instability, malrotation, insufficient proximal musculature, and leg length discrepancy. In severe cases, treatment options have included primary prosthetic fitting or secondary prosthetic fitting following Syme amputation with knee fusion. An alternative procedure, initially described by van Nes, involves rotating the tibia 180 degrees allowing the ankle to serve as a surrogate knee joint. Theoretically, this allows the patient to ambulate as a below knee amputee. However, questions have arisen as to whether the latter procedure offers a true biomechanical advantage over the more conventional Syme procedure. In particular, the van Nes rotational osteotomy is controversial in terms of cosmetic appearance and the tendency to derotate requiring additional surgical procedures. It is unknown which of these two procedures produces better results. The purpose of this study is to quantify the gait mechanics and metabolic energy costs for PFFD patients who have received the Syme amputation versus those who have received the van Nes rotationplasty.

METHODS

Subjects were recruited from Shriners Hospital, Los Angeles or the Child Amputee Prosthetics Project at the UCLA Institute for Rehabilitation and Chronic Disease and studies were performed at least 5 years after their surgical procedures. Eight out of a total of 20 subjects have been studied to date, four with Syme amputation and four with a van Nes procedure. Reflective joint markers were placed on the iliac crest, greater trochanter, knee joint center, lateral malleolus, heel, and 5th metatarsal head for the natural limb. For the prosthetic limb, joint markers were placed on the iliac crest, mechanical joint axes at the knee, and estimated from analogous locations on the natural limb for other locations. Movement was recorded from one side by two video cameras at 60 Hz while the subject walked along a walkway. Force plate information was simultaneously acquired from a force plate concealed in the walkway floor and synchronized using timing lights and an analog pulse. Trials were accepted only if the limb being filmed hit the force plate in isolation. Kinematic data were digitized using a PC computer and interactive software to obtain 3 dimensional joint coordinates. Data were digitally filtered with a fourth-order Butterworth filter using a cutoff frequency which preserved 90% of the signal energy as determined from spectral analysis. Anthropometric data were calculated for the uninvolved limb with regression equations using limb segment lengths. Residual limb data were calculated using circumference measurements. Center-of-mass locations were determined for prosthetic components by balancing each component over a

knife-edge. Moments of inertia were determined from the period of oscillation. The lower limb was modeled as a set of interconnected rigid links with frictionless joints. Joint moments were calculated during the stance phase of locomotion using principles of inverse dynamics.

RESULTS

Kinematic data for the involved limb indicate that two van Nes subjects had muscular control of prosthetic knee during stance as indicated by the presence of a loading response. The other subjects, however, kept their knees in extension throughout stance. Kinematics were, therefore, similar to Syme subjects having a mechanical knee joint positioned in extension throughout the stance phase.

GRF vertical component maxima were less on the prosthetic side for both van Nes and Syme subjects. While both braking and propulsive components were observed for all van Nes subjects, propulsive components were absent for three out of four Syme subjects.

Peak joint moments for the prosthetic limb were less than the uninvolved limb for all subjects. On the uninvolved side, hip extensor moments were dominant during the first half of the stance phase while hip flexor moments were usually delayed or absent. Most subjects did not exhibit a stance phase knee extensor moment on the uninvolved side.

On the prosthetic side, stance phase knee extensor moments were present in the two van Nes subjects that exhibited a loading response. Flexor moments dominated the knee joint during the first half of stance for all other subjects.

These preliminary findings indicate that the van Nes procedure may result in a functional "knee" joint for some patients. Factors such as the degree of hip joint pathology and tibial derotation may explain why the other two van Nes subjects were not able to functionally utilize their surrogate "knee".

a)

b)

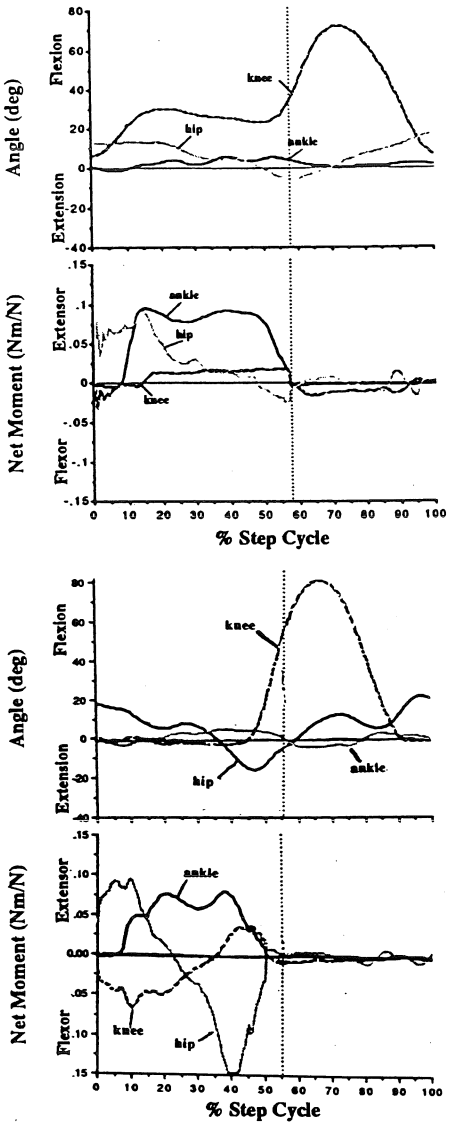

Fig. 1. Kinematic (clinical angles) and kinetic data for a) a van Nes and b) a Syme subject. Data were normalized to 100% of one step cycle (heel contact to the next ipsilateral heel contact). The vertical line denotes toe off.

Supported by Shriners Hospital Grant #15956.

JOINT FORCES AND MOMENTS DURING GAIT INITIATION

Christopher A. Miller & Mary C. Verstraete

Department of Biomedical Engineering
The University of Akron, Akron, OH 44325-0302.

INTRODUCTION

The forces and moments in the hip, knee, and ankle during gait initiation were studied. The forces and moments were computed using the Newton-Euler equations of rigid body motion.

REVIEW & THEORY

Nissan and Whittle (1990) defined gait initiation as, "When a subject is changing his/her mechanical condition from standing at rest to the cyclic movement of walking." Many authors have reported the ground reaction forces applied to the body during gait initiation [Herman et al. (1973); Cook et al. (1976); Mann et al. (1979); Breniere et al. (1986); Nissan et al. (1990); Brunt et al. (1991)].
Only Herman et al. (1973) and Cook et al. (1976) used the ground reaction forces to investigate body dynamics. They utilized equation (1) to calculate the dorsi/plantarflexion torque at the ankle.

$$F_v\ (x_f - x_s) + F_{ls}\ (y_s) = T \qquad (1)$$

Cook et al. (1976) used the computed ankle torque to calculate an ankle "stiffness", defined as the ratio of the change in torque to the change in the ankle's flexion angle. However, no authors have reported on the other joint moments and forces during gait initiation. Thus the objective of this research is to calculate the joint moments and forces during gait initiation.

PROCEDURES

Four subjects were targeted with fourteen retroreflective markers to aid in defining the centers of mass, the joint centers, and the inertial parameters of each body segment. The motion of the markers was recorded by a Vicon motion analysis system (Oxford Metrics) at a sampling rate of 50 Hz. Two AMTI force plates, set in the walking platform, recorded ground reaction forces and moments at a sampling rate of 250 Hz.

Gait events were synchronized using plastic footswitches taped to four locations on the plantar surface of the subject's feet. The footswitch data were also sampled at 250 Hz. All data were collected and time synchronized by a PDP-11 computer implementing Vicon software developed by Oxford Metrics.

The gait initiation event was recorded in successive steps. First, the subject stood astride the edge of the force plate, such that the markered leg was on the plate. Data was recorded for the first step of the markered leg. The next step was recorded with the subject starting one step behind the force plate so the second step began with the markered leg on the force plate. Similarly, the third step of the markered leg was recorded with the subject starting two steps behind the force plate. This method ensured that each step occurred within the calibration volume and had corresponding force data so as to compute joint reaction forces and moments for each step. The entire process was repeated for the contralateral leg.

Each dataset contained data for one full stride. Assuming that the gait initiation event is repeatable, the output of the three datasets for the three successive strides were "spliced" together to form one dataset of the entire event. Employing the Newton-Euler equations of motion, joint reaction forces (F) and moments (M) were calculated at the hip, knee, and ankle.

RESULTS & DISCUSSION

In the literature regarding gait initiation, the swing leg was defined as the leg that took the first step, and the stance leg was the contralateral leg. For this study, a more descriptive nomenclature was used. The leg that took the first step was called the *initiation leg* or the *initiator*, and the contralateral leg was called the *foundation leg*.

Based on an energy and power analysis [Miller (1993)], it was determined that a subject achieves steady state after two steps. Figures 1 and 2 show the anterior/ posterior forces computed for a single subject, for the initiator and foundation legs, respectively. Similar variations were seen in all components for all three joints of the leg. It can be seen that these forces and moments also indicate that steady state is achieved prior to the third step.

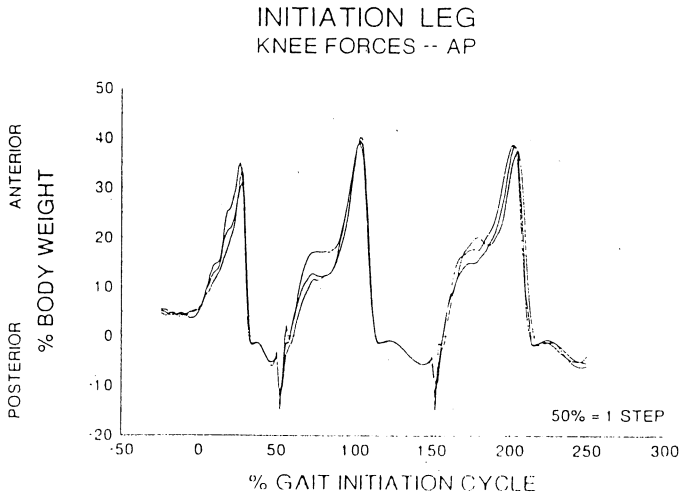

Figure 1. AP Knee Forces - Iniation Leg

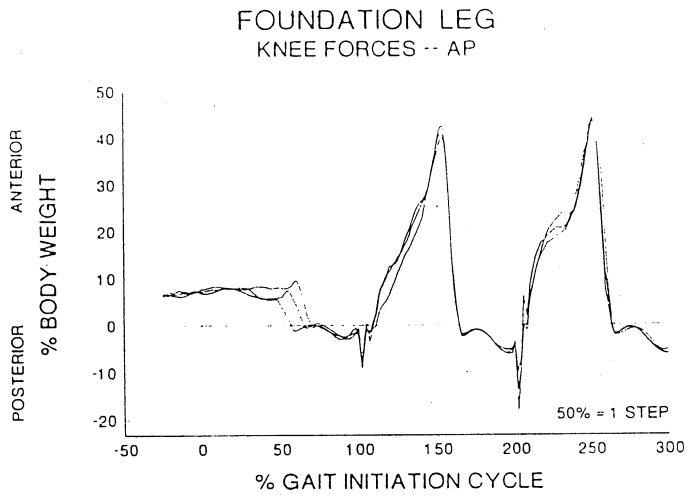

Figure 2. AP Knee Forces - Foundation Leg

REFERENCES

Breniere, Y. et al. *J. Biomech.*, 19(12), 1035-40, 1986.

Brunt, D. et al. *Am. J. of Phys. Med. and Rehab.*, 70(4), 206-12, 1991.

Cook, T. et al. *Neural Control of Locomotion*, (pp. 65-76), Herman, R.M. et al., 1976.

Herman, R. et al. *Control of Posture and Locomotion*, (pp. 232-9), Stein, R.B. et al., 1973.

Mann, R.A. et al. *J. B. J. S.*, 61(2), 232-9, 1979.

Miller, C.A. Master's Thesis, University of Akron (OH), 1993.

Nissan, M. et al. *J. Biomed. Eng.*, 12(2), 165-71, 1990.

STRIDE ADJUSTMENT DURING A RUNNING APPROACH TO A FORCE PLATE

JULIANNE ABENDROTH-SMITH
Utah State University, Dept. of HPER. Logan Utah 84322-7000

INTRODUCTION

Much of the literature on running mechanics has utilized force plates, and often assumed a "normal or typical stride" as a subject struck the plate (e.g. see Miller, 1990). This assumption has not been examined. The purpose of this study was to investigate control characteristics of locomotion when approaching a force plate. More specifically, this study determined that the use of a force plate may result in an artificially induced stride pattern, not reflective of a typical stride pattern. The approach to a force plate was examined using experienced distance runners participating in a U.S. Olympic Training Center Camp. A typical steady state stride of each subject was determined for each trial, by calculating the minimum standard deviation (SD) across five steps during the approach. The mean step length of these five steps was defined as the typical step length for that trial. The normal step length was compared to the steps onto and off of the plate. If the steps deviated more than ± 3 SD from the minimum SD of the five typical steps, then the step lengths at the plate were said to be significantly different. During the data collection, the subjects were successful in striking the force plate 62.8% of the time, on average. Based on the normal step criteria, only 31.9% of the trials were successful (a 49.3% reduction). In addition, a visual control strategy was observed in 10 of 12 subjects while approaching the force plate. The two remaining subjects showed a consistent motor pattern of running, and were most successful in not altering their strides to strike the force plate. They experienced an average 25.3% reduction in successful trials, using the normal step criteria. Five subjects showed enough stride adjustment at the plate to have an 80.0% reduction, on average. The last five were more successful, averaging a 28.4% reduction. These results indicate the assumption of a normal step at plate contact to be questionable, at best. Differences in the targeting strategy need further examination in relation to stride adjustments.

REVIEW AND THEORY

The significance of this study is a "normal or typical stride" has been assumed, as a subject approaches and hits the force plate, during gait analyses. Furthermore, force platforms "must be designed to accommodate foot contact with a minimum necessity of targeting the platform" (Dainty & Norman, 1987, p. 88). However, related research has indicated that stride adjustments do occur when approaching a target (Hay, 1988; Lee, et al., 1982; Warren, Young & Lee, 1986).

Specifically, stride length adjustments have been observed to be produced by changes in vertical impulses (Warren, et al., 1986) or both vertical and horizontal impulses (Patla, Robinson, Samways & Armstrong, 1989). To date, the data gathered from gait studies utilizing force plates have not been examined with respect to stride adjustment-induced reaction forces. Previous literature reporting ground reaction forces for a normal stride (e.g. see Simpson and Bates, 1990) may not reflect a normal stride at all; rather, the data reported may instead indicate an individual's ability to adjust their strides to successfully strike a force plate. While this study did not propose to test the accuracy of the actual force plate measurements, it is proposing a possible indication of potential problems with force plate measurements due to the normal stride assumption.

PROCEDURES

Twelve experienced distance runners were videotaped while running over a force plate (62 cm x 92 cm). The entire approach of six successful trials and all non-successful trials were examined for each subject. Total trials averaged 9.8 trials per subject.

A normal or typical steady state stride of each subject was determined for each trial, using an algorithm to calculate the minimum standard deviation (SD) across five steps during the approach to the force plate. The mean step length of these five steps was defined as the typical step length for that trial. This normal step length was compared to the steps onto and off of the plate. If the steps deviated more than ± 3 SD, using the minimum SD of the five typical steps as a baseline, then the step lengths at the plate were said to be significantly different.

The control characteristics of locomotion during the approach were also examined. A switch from a motor programmed strategy to a visual control strategy would appear to occur in subjects approaching the force plate by examining the standard deviations of their footfall positions across all trials, in relation to the force plate as the runners approached the plate. According to Lee, et al. (1983) and Hay

(1988), during the programmed portion of the run-up, the athletes should demonstrate a consistent stride pattern, showing only small SDs in their step lengths. However, theSD of their footfall position in relation to the plate should rise with each step, due to the cumulative effect of the small inconsistencies in the athlete's stride lengths. At some given support phase, the SD reaches a peak level, and from that point until the plate is struck, the SDs of the footfall positions drop. This drop indicated the subjects were "aiming" for their target, or using visual control.

RESULTS AND DISCUSSION

During the data collection, the subjects were successful in striking the force plate 71 of 113 trials (62.8 %). Based on the normal step criteria, this figure dropped 49.3%, with only 36 of the 113 trials (31.86%) containing "typical" step lengths onto and/ or off of the force plate. The mean minimum SD of the five step lengths across subjects was .030 m, and occurred on average 4.25 support phases (plus four steps back) before plate contact.

A visual control strategy was observed in 10 of 12 subjects during the approach. Seven subjects exhibited an increasing SD of footfall positions, across trials, followed by a decreasing SD before target strike (figure 1). Onset of visual control occurred at the fourth last support phase, on average. Three subjects exhibited a decreasing pattern of SDs, which indicates a visual control strategy also. However, the large variation in the starting positions of these subjects mask where the switch to a visual control strategy takes place. The two remaining subjects showed an increasing pattern of SDs, indicating a consistent motor pattern of running.

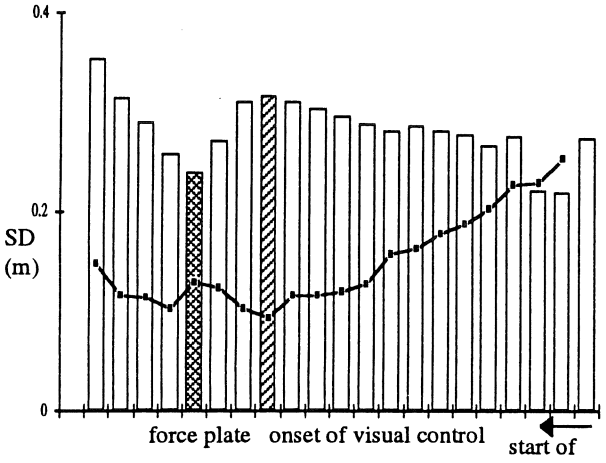

Figure 1. Visual Control Pattern of Approach (bar graph - SD of footfall positions; line graph-SD of step lengths: for seven subjects)

These last two subjects were also most successful in not altering their strides to strike the force plate, experiencing a 25.3% reduction in successful trials, on average, using the normal step criteria. The rest of the subjects were split: five showed enough stride adjustment at the plate to have an 80% reduction, on average, while the other five were more successful, averaging a 28.4% reduction in successful trials.

These results indicate the assumption of a normal step at plate contact to be questionable, at best. To keep this typical stride assumption valid, more stringent requirements during data collection may be necessary. Differences in the targeting strategy need further examination in relation to stride adjustments approaching a force plate.

REFERENCES

Dainty, D.A., & Norman, R.W. (1987) Standardizing Biomechanical Testing in Sport. Champaign, IL: Human Kinetics Publishers, Inc.

Hay, J.G. (1988). Approach strategies in the long jump. International Journal of Sport Biomechanics,4, 114-129.

Lee, D.N., Lishman, J.R., & Thomson, J.A. (1982). Regulation of gait in long jumping. Journal of Experimental Psychology: Human Perception and Performance, 8, 448-459.

Miller, D. I. (1990). Ground reaction forces in distance running. In P.R. Cavanagh (Ed.), Biomechanics of Distance Running (pp. 203-224), Champaign,IL: Human Kinetics Books.

Patla, A., Robinson, C., Samways, M., & Armstrong, C.J. (1989). Visual control of step length during overground locomotion: Task specific modulation of the locomotor synergy. Journal of Experimental Psychology: Human Perception and Performance, 15, 603-617.

Simpson, K. & Bates, B.T. (1990). The effect of running speed on lower extremity joint moments. International Journal of Sport Biomechanics, 6, 309-324.

Warren, W.H., Young, D.S., & Lee, D. N. (1986). Visual control of step length during running over irregular terrain. Journal of Experimental Psychology: Human Perception and Performance, 12, 259 - 266.

ACKNOWLEDGEMENTS

The author wishes to thank Dr. Peter McGinnis, the U.S. Olympic Training Center and the Sport Science Staff for the use of their facilities and resourses.

SELECTION OF A STANDARD CONVENTION FOR ANALYZING GAIT BASED ON THE ANALYSIS OF JOINT TORQUES AND ELECTROMYOGRAPHY

Paul DeVita, Department of Physical Education, Southern Illinois University at Carbondale, Carbondale, Illinois 62901

INTRODUCTION

Gait is usually analyzed with one of two conventions: heel contact starts the cycle and stance is followed by swing or toe-off starts the cycle and swing then stance phases are shown. Presentation of gait descriptors in two formats makes it difficult to compare results between studies. To provide a biomechanical basis for the standardization of gait analyses this study was designed with the purpose of showing that based on joint torque and EMG data, a convention using toe-off as the start of the cycle with swing then stance phases is superior to the convention using heel contact as the start with stance followed by swing.

METHODS

Four males were filmed as they walked and ran along a lane contacting a force plate. Surface EMG was recorded from biceps femoris (BF), semitendinosis (ST), rectus femoris (RF), vastus lateralis (VL), gastrocnemius (GS), and tibialis anterior (TA). Consecutive swing, stance, and swing phases were analyzed to obtain accurate data from both transition points between phases. Inverse dynamics were used to calculate joint torques in the lower extremity. EMGs were rectified and digitally filtered to produce linear envelopes which were normalized to an MVC contraction. Torque and EMG values at the swing to stance and stance to swing transitions were compared. It was assumed that if the majority of the descriptors had greater values during either transition point then this phase would have greater biomechanical importance and it should be retained in the middle of the analysis. The gait cycle would therefore start and end at the other transition point.

RESULTS

Hip and knee torques were 314% and 340% larger in walking and 131% and 30,000% (knee torque was 30 and 0.1 Nm at the transitions) larger in running at swing to stance compared to stance to swing transition (Table 1 & Fig 1). EMG results were similar for both activities. Five muscles had greater EMG levels as the limb approached and contacted the floor compared to when the limb left the surface. EMG values at swing to stance transition were between 130% (RF) and 580% (BF) larger in walking and between 237% (RF) and 2,805% (TA) larger in running compared to those at the stance to swing transition.

DISCUSSION

Joint torques and EMG were used to identify the superior convention since they describe the dynamics of the system and the muscular contributions to these dynamics.

Most reported torque curves for walking and running were in agreement with present results (6,10,11,12) although some showed larger hip torques at the stance to swing transition (1,9). The present torque curves and those of the knee in the literature indicate describing gait with swing followed by stance phases. This position is not unequivical due to some differences in the hip torque in the literature.

EMG results were similar to those presented previously which showed greater activity during late swing and at the transition from swing to stance then at the other transition for all muscles except GS (5,7,8,13). EMG data strongly support the use of toe-off as the start of the cycle showing swing then stance phases.

Results showed the subjects needed to prepare for the initiation of stance and the application of large forces and

torques. This agrees with studies on landing from falls which have shown increases in joint torques (3) and EMG (4) while falling in preparation for floor contact. Transition from stance to swing did not seem to be as critical a point in the cycle since torques and EMG were low. Therefore, the stance to swing transition should be used as the start and end of the gait cycle and the more meaningful transition of swing to stance should occur in the middle of the analysis. An exception to this proposal would be if the research question examined the stance to swing transition or events close to this point.

Table 1. Torque & EMG values at transition times

	Walk		Run	
	SW-ST	ST-SW	SW-ST	ST-SW
Hip	49	16	47	36
Knee	25	7	30	0
BF	160	27	340	100
ST	158	37	342	90
RF	70	54	175	74
VL	85	29	218	58
GS	61	84	75	98
TA	170	68	210	8

SW-ST: swing to stance transition
ST-SW: stance to swing transition
torque in Nm; EMG in % MVC

REFERENCES

1) Cappozzo et al. J. Biomech. 9, 35-43, 1976.
2) DeVita et al. Hum. Movt. Sci., 9, 99-115, 1990.
3) DeVita et al., Med. Sci. in Sports & Exerc., 24, 108-115, 1992.
4) Dietz et al. Brain Res. 142, 576-579, 1978.
5) Limibird et al. J. Orthop. Res., 6, 630-638, 1988.
6) Mann et al. Res Quart. for Exerc. & Sport, 51, 334-348, 1980.
7) Shiavi et al. J. Rehabil. Res. & Dev., 24, 13-23, 1987.
8) Scott et al. Med. Sci. SPorts & Exerc., 22, 357-369, 1990.
9) Simonsen et al. Eur. J. Appl. Physiol., 54, 524-532, 1985
10) Sprague et al. Res. Quart. for Exerc. & Sport, 54, 60-66, 1983.
11) Thornton-trump et al. J. Biomech., 8, 173-178, 1975.
12) Winter. Hum. Movt. Sci., 3, 51-76, 1984.
13) Yang et al. Electroenceph. & Clin Neurophysiol., 60, 485-491, 1985.

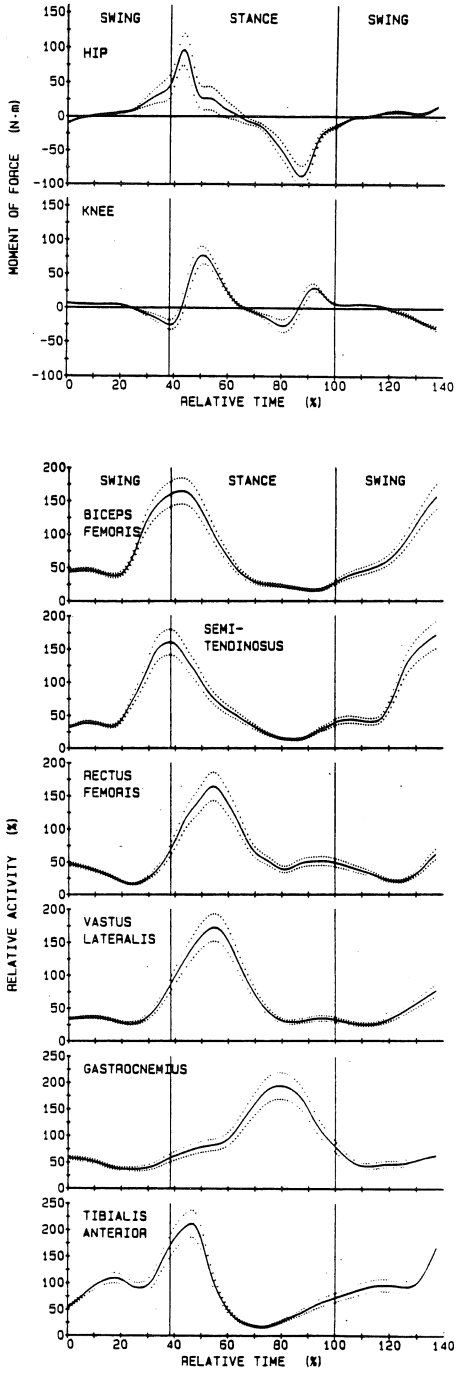

Fig 1. Mean torque & EMG curves from a representative subject during walking. Results for running were similar (Table 1).

VARIATION IN THE JOINT MOMENTS OF THE LOWER EXTREMITIES DURING GAIT DUE TO FOUR INERTIAL MODELS

D.C. Chapman and M.C. Verstraete

Department of Biomedical Engineering,
The University of Akron, Akron, OH, 44325-0302.

INTRODUCTION

Joint moments were calculated for the ankle, knee and hip during gait using four methods of approximating the segment moments of inertia. The data were analyzed to determine whether significant differences occur in the calculated joint moments due to the different inertial approximations. Because there is no standard method of approximating the moments of inertia for the segments of the human body, it is important to understand what effect variations in the inertial parameters can have on the joint moment calculation. This is especially true when the results of such an analysis are used for medical purposes. The results showed that some differences in the calculated joint moments do exist. These differences occur primarily in the flexion/extension moments of the knee and hip during swing phase and terminal stance.

REVIEW AND THEORY

Early investigations of the inertial properties for the limb segments of the human body were conducted using cadavers. Dempster et al. (1955), in a much cited study, determined the segmental moments of inertia for eight male cadavers using a pendulum technique. He then developed linear regression equations that estimated segmental moments of inertia based on height and weight. In a similar study, Chandler et al. (1975) used the same methods to determine the moments of inertia for the segments of six male cadavers. McConville et al. (1980) used biostereometrics, developed by Herron et al. (1975), to determine the inertial properties for the limb segments of 31 live adult male adults.

Given the fact that Ackland et al. (1988) validated the uniform density assumption in determining the inertial parameters for the limb segments of the human body, it is interesting that regression equations based on cadaveric data from studies involving small samples are seemingly still preferred over those based on larger samples of living subjects using biostereometrics.

The purpose of this study was to investigate the variations in joint moments calculated during gait due to four different methods of approximating the inertial parameters of the limb segments. The hypotheses were that the inertial effects are significant in the joint moment calculation and that significant differences exist in the moments calculated using the four methods of estimating the inertial properties.

PROCEDURES

The four methods used to approximate the segmental inertial properties were biostereometrics, geometric modelling, the regression equations developed by McConville et al. (1980) and ignoring them by setting the principle moments of inertia equal to zero. Data were collected for nine subjects. For the biostereometric evaluation, important anatomical landmarks for the lower limb segments were targeted. The subjects were photographed from the front and back using two stereo cameras. The principal moments of inertia of the lower limb segments were then calculated for the biostereometric model. Next, a gait analysis was performed using 14 of the same anthropometric landmarks. Anthropometric measurements were also recorded to provide the dimensions for the geometric model and regression equations. The position data of the targets were

recorded by a Vicon motion analysis system at a rate of 50 Hz. Ground reaction forces were recorded from an AMTI force plate at a rate of 250 Hz.

For the sake of analysis, the limb segments were assumed to be rigid bodies. The joint forces and moments were then determined using the Newton-Euler equations of motion:

$$\Sigma F_x = ma_{cmx}$$

$$\Sigma F_y = ma_{cmy}$$

$$\Sigma F_z = ma_{cmz}$$

$$\Sigma M_x = I_{xx}\alpha_x - \omega_y\omega_z(I_{yy} - I_{zz})$$

$$\Sigma M_y = I_{yy}\alpha_y - \omega_z\omega_x(I_{zz} - I_{xx})$$

$$\Sigma M_z = I_{zz}\alpha_z - \omega_x\omega_y(I_{xx} - I_{yy})$$

The principal moments of inertia for each model were substituted, in turn, for I in the above equations. The remaining values necessary to calculate the joint forces and moments were determined from recorded marker positions, ground reaction forces and from the literature.

RESULTS

Figure 1 shows the flexion/extension moments at the hip. The solid lines represent the mean of the subjects for three of the models. Very little variation was seen in the moments at the ankle. This is due to the small moments of inertia of the foot. Similarly, little variation was seen in the ab/adduction and medial/lateral rotation moments at the knee and hip. Variations between the models are seen, however, for the flexion/extension moments at the knee and hip.

DISCUSSION

Differences do appear to exist between the models and, as expected, these differences are greater during swing phase than during stance phase. This is due to the fact that the ground reaction forces are not present during swing. Work is in progress to include the bio-stereometric model in the analysis. Also, statistical analysis will then be performed to determine the variation in the data. Should no statistical difference be found, it may be possible to decrease the time and cost of clinical gait evaluations. On the other hand, should it be found that statistical differences do exist, it will be important for investigators to report which inertial model was used in order to compare data with other laboratories.

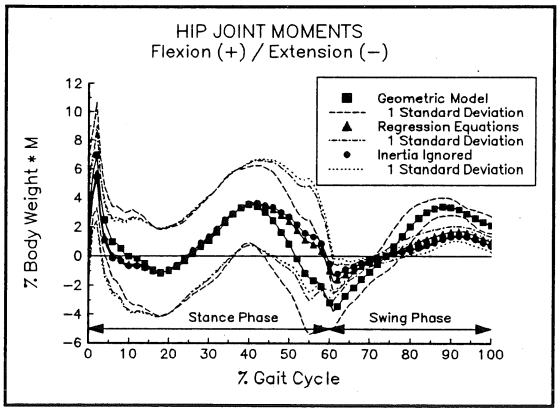

Figure 1. Flexion / extension moment about the hip.

REFERENCES

Ackland, T. et al. Int. J. of Sport Biomech. 4(2), 146-155, 1988.

Chandler, R. et al. U.S. Dept. of Transportation, Report DOT HS-801 430, Washington, D.C., 1975.

Dempster, W. WADC Technical Report, 55-159, WPAFB, Ohio, 1955.

Herron, R. DOT-HS-231-2-397 Final Report, 1974.

McConville, J. AFAMRL Technical Report, 80-119, WPAFB, Ohio, 1980.

ACKNOWLEDGEMENTS

The authors would like to express their appreciation to Dr. D.B. Sheffer, W. Morek,and R. Bartfai for their ongoing assistance with this project.

NOCICEPTION AND IMPACT LOADING DURING RUNNING

M.A. Lafortune, M.J. Lake and J. Hystead

School of Human Biology, University of Guelph, Guelph, Ont. N1G 4C3

INTRODUCTION

It has recently been suggested that the magnitude of the impact observed during running could be attenuated through the use of insoles that produce local plantar deformations. The purpose of the present study was to compare the shock attenuation properties of a regular insole to those of an insole with an heavily profiled top surface. Ground reaction force and tibial acceleration were used to quantify the foot/ground impact in four recreational runners. Ten overground trials were measured before and after a 22 min. long treadmill run. Acceleration measurements were also taken 8 times during the treadmill bout. All four subjects reported severe discomfort less than 10 min. after beginning their run on the treadmill. The present results suggest that nociception resulting from an acute exposure to an irregular insole surface does not modify impact force and shock experienced during running. Future research should investigate the effects of long term habituation to insoles that induce nociception.

REVIEW AND THEORY

Repetitive impact loadings are an integral part of human locomotor activities. Most researchers agree that unless the magnitude of the impact of the foot with the ground is controlled, chronic injuries to the musculo-skeletal structure will likely occur. Some disagreement exists as to the best means for preventing these chronic injuries. Over the last six to seven years, barefoot running has been advocated by Robbins and his colleagues (1989,1991). Barefoot running is believed to induce runners to raise the medial longitudinal arch of their feet, thus, moderating shock (Robbins & Gouw, 1990). Due to social and climatic constraints as well as artificial surfaces, they stated that insoles that produce localised plantar surface deformation are a more satisfactory alternative to barefoot locomotion (Robbins & Gouw, 1990). These authors hypothesized that "avoidance of uncomfortable or painful but locally innocuous plantar cutaneous tactile stimuli moderates shock on subsequent impacts when humans walk, run, or jump repetitively" (Robbins & Gouw, 1991). The purpose of the present study was to determine the effects of insole irregularities upon impact loading in running.

PROCEDURES

Four healthy recreational runners with size 9 feet participated in the present study (averages: 28 yr., 177.3 cm, 70.5 kg). The experimental protocol involved overgound and treadmill running at 3.5 m/s to evaluate a regular shoe insole and a prototype insole that were randomly presented to the subjects on two separate days. The prototype insole consisted of three mm diameter hard plastic rods laid at one cm interval across the heel area of a three mm thick plantex board to produce an irregular surface (Figure 1). Both shoes were fitted with prototype insoles. An AMTI force platform (OR6-5-1) mounted 11 m into an 18 m long runway and a surface mounted Entran (EGA2-C-50D) accelerometer were used to quantify impact loading. Vertical ground reaction force was sampled at 2000 Hz for 10 overground trials recorded before and immediately after a 22 min. treadmill run. During the treadmill trial, tibial acceleration was sampled for 10 s at 0.5, 1.0, 1.5, 2.0, 5.0, 10.0, 15.0 and 20.0 min. Thus, each sampling period provided a minimum of 10 foot/ground contacts.

A fourth order low pass (100 Hz) Butterworth filter was applied to the data. Thereafter, magnitude of the initial peak and rate of loading were obtained from individual force and acceleration signals. Time taken to reach a vertical force of 0.2 BW was also recorded (T2). Two-way analyses of variance were used to determine insole and temporal effects upon these impact variables.

RESULTS

The mean and standard deviation of the force and acceleration variables are presented in tables 1 and 2, respectively. The statistical analysis revealed that the rate of loading (ROL) was reduced (93.7 to 87.5 BW/s) and time to 0.2 BW (T2) increased from pre to post treadmill run (11.7 to 13.2 ms).

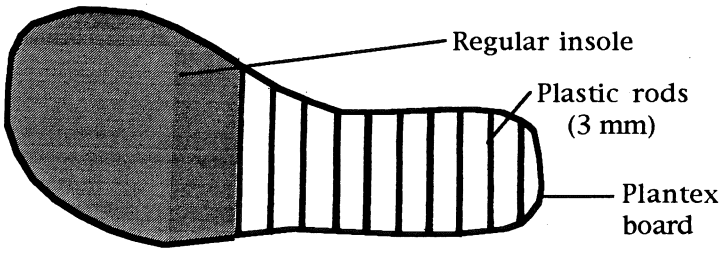

Figure 1. Schematic of irregular insole prototype.

Peak vertical force was unaffected by insole type and itremained unchanged from pre to post treadmill run. Similarly, peak tibial acceleration and acceleration transient rate remained constant during the 22 min. treadmill run and no differences were observed between the two insoles tested.

Finally, all subjects complained of moderate to severe discomfort less than 10 min. after beginning the treadmill run. Bruising of the plantar surface of the feet was still visible three days after the experiment.

Table 1. Means (± SD) of the GRF variables for the irregular test insole and the normal insole before and after the 22 min. treadmill run.

	Pre treadmill run		Post treadmill run	
	Normal	Test	Normal	Test
Initial Peak F_Z (BW)	1.72 (.13)	1.69 (.17)	1.71 (.14)	1.71 (.04)
Loading rate (BW/s)	98.6 (9.4)	88.8 (18.6)	87.9 (21.9)	87.2 (3.2)
Time to 0.2 BW (ms)	11.3 (1.4)	12.1 (2.3)	12.2 (1.6)	14.3 (2.9)

Table 2. Means (± SD) of the acceleration variables for the irregular test insole and the normal insole for the 22 min. treadmill run.

	Normal	Test
Peak Acc. (g)	5.26 (1.3)	5.08 (0.9)
Transient rate (g/s)	81.2 (14.3)	76.3 (15.4)

DISCUSSION

Since the experimental insoles were evaluated with only four subjects, the results of the present study should be interpreted with care. Yet, it must be mentioned that the study was initially designed to analyse the data from 10 subjects. Due to severe discomfort and plantar bruising of the feet the experiment was shortened on ethical grounds. In spite of the low statistical power, temporal variables associated with impact GRF (ROL and T2) were modified after the treadmill run for both insole conditions. These variables indicated a more gradual build up of the external force. This phenomenon can presumably be explained by an adaptation of the subjects to prolonged running and/or an increased temperature of the shoe sole. The latter reduces sole stiffness thereby increasing its shock attenuating properties. This finding points out the importance of adequately warming up both subjects and shoes for comparative *in vivo* evaluation of footwear cushioning properties.

The foot/ground impact measurements, vertical ground reaction force and tibial axial acceleration, obtained in a condition of severe nociception were very similar to those obtained with a regular insole. Consequently, it is unlikely that insoles inducing less discomfort would modify impact loading experienced during running. The present study measured the acute effects of localised plantar surface deformations. The biomechanical response of the lower extremities to long term and/or gradual habituation to insoles that promote nociception remains to be examined.

REFERENCES

Robbins, S. & Hanna, A. Med. Sci. Sp. Exer. 19(2) 148-156, 1987.
Robbins, S. & Gouw, G. Sports Medicine. 9(2) 76-85, 1990.
Robbins, S. & Gouw, G. Med. Sci. Sp. Exer. 23(2) 217-224, 1991.

COMPARISON OF GONIOMETRY AND VIDEO MOTION SYSTEMS FOR GAIT ANALYSIS

E. Growney, T. Cahalan, D. Meglan and K. N. An
Orthopedic Biomechanics Laboratory
Mayo Clinic/Mayo Foundation, Rochester, MN 55905 U.S.A.

INTRODUCTION

Previously, all lower extremity motion during human gait was measured in our lab using the triaxial electrogoniometer. However, a growing number of studies have required the use of a video motion system. The accuracy of kinematic measurements using such a system have been assessed. Therefore, it has become necessary to compare the outputs of both systems in order to understand and account for any differences in measurement between the two. An electrogoniometer and video motion system measured the knee motion of normal subjects during gait. Flexion/extension, abduction/adduction, and internal/external rotation angles measured by both systems were compared. The sagittal plane angles from both systems correlated well, where as the error introduced into "down-stream" angles in Euler angle calculations and goniometer linkage cross-talk are believed to have been the major factors causing poorer correlation for the non-sagittal angles.

REVIEW AND THEORY

The use of the triaxial electrogoniometer with its associated advantages and disadvantages has been previously studied by Chao (1980). In gait analysis, the electrogoniometer allows easy data reduction, is simple to place on a subject, is relatively inexpensive, and provides more gait cycles per trial as compared, for example, to a video motion system viewing a 2 meter walk way. However, the electrogoniometer lacks absolute position and orientation information of the joint segments and multiple joint measurements are, at best, limited. Gait analysis studies involving joint kinetics and multiple joint kinematics must use an alternative method in order to acquire the needed information.

An et al. (1991) assessed the reliability of a video tracking system in calculating the kinematics of ideal joint model motions. It was found that alignment of markers with the true axes of motion of the joint is crucial for accurate joint kinematic determination. This was further confirmed in a later study by Growney et al. (1991), where the measurements of knee motion from a triaxial electrogoniometer and a video motion system were compared. It was believed that the marker set used in that study was the principle source of difference between the two systems. The marker set was developed specifically for the task of system comparison, not for an established protocol of joint motion study. Thus, it was inconvenient for regular use, as well as prone to repeatability errors.

It is important to understand and, if possible, account for differences in motion measurement between the two systems as they are used in clinical and research settings. Therefore, this study compared the electrogoniometer with the video system implementing an established, full body marker set that will be repeatedly used for gait analysis protocols.

PROCEDURES

The right and left knee motions of healthy subjects were monitored for three gait trials using the triaxial electrogoniometer and a four-camera Expert Vision™ video tracking system (Motion Analysis Corporation, Santa Rosa, CA.), described by An et al. (1991). Footswitch and electrogoniometer signals were simultaneously sampled with the video data at a rate of 60 points/s. Marker positions and goniometer signals were low-pass filtered at 8 Hz. Reflective markers were placed on the body and local coordinate systems formed as described by Kadaba et al. (1990). The coordinate system generation and relative joint angle calculations were done using the ANZ software described in detail by Meglan (1991). Both the goniometer and calculated angles follow the sequentially dependent Euler angle convention described by Chao et al. (1983). Gait cycles from each of three trials were collected. The three cycles were normalized to 50 samples, then averaged. The average curves were then compared. The correlation between corresponding pairs of average curves was examined using a linear regression.

RESULTS

Figure 1 is an example of the reduced data for the left side. To enhance the visual comparison, the static offset obtained from the linear regression y-intercept was subtracted out of the data for those graphs. Correlations of the measurements between these systems were also obtained based on the linear regression analysis (Table 1).

Table 1: Results of linear regression.

	Slope		R^2	
	Right	Left	Right	Left
Flexion	1.25	1.17	98	98
AB/AD	2.57	1.21	54	98
Rotation	0.83	0.57	36	19

DISCUSSION

The regression coefficients and R-squared values illustrate a close correlation between the two systems for the flexion angles. The correlation declines for the "down-stream" angles. The knee rotations, the 3rd in the sequentially dependent Euler angle convention as used here, correlates the least between the two systems. Causes for error and error propagation in both systems have been described by Growney et al. (1991). Cumulative errors initially introduced as small offsets in marker placement or goniometer alignment from the true embedded coordinate system can cause "down-stream" errors in each measurement system and thus result in uncorrelated readings between the two. Chao (1980) documented that linkage cross talk introduces an error into "up-stream" goniometer readings, particularly when the range of internal-external rotation exceeds 10 degrees. A set of equations was described that would correct for this effect, however, knowledge of the true joint motion is required to implement them.

The triaxial electrogoniometer and video based motion system are vulnerable to their own sources of error in describing true joint motion. When care is taken to use each system appropriately and account for those error sources, 3 D measurements from both systems are comparable.

REFERENCES

An, K.N. et al. Biomedical Sciences Instrumentation, 27, 245-252, 1991.

Chao, E.Y.S. J. Biomech., 13, 989-1006, 1980.

Chao, E.Y.S. et al. J. Biomech., 16, 219-233, 1983.

Growney, E. et al. Proceedings of the 7th Annual East Coast Clinical Gait Laboratory Conference, Richmond, VA, (sec. 2), 1991.

Kadaba, M.P. et al. J. Orth. Res., 8, 383-392, 1990.

Meglan, D.A. Thesis Dissertation, The Ohio State University, 1991.

ACKNOWLEDGEMENT

The Expert Vision™ system was supported by NIH grant 1S10RR04658. The study was supported by Mayo Foundation.

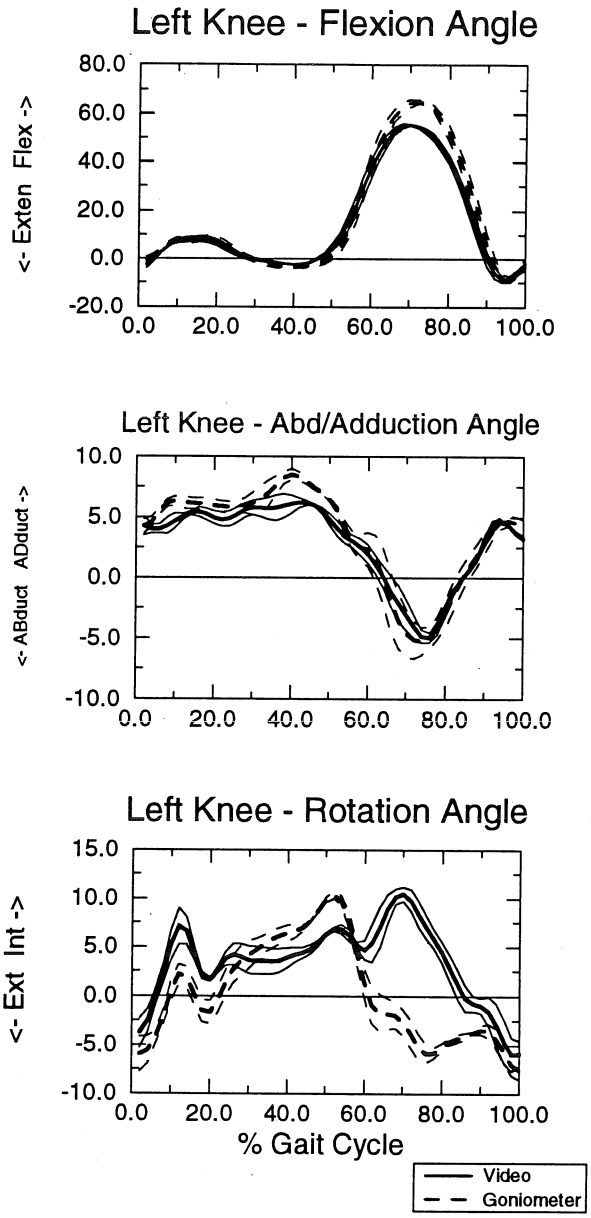

Figure 1: Mean and ± S.D. curves of knee angles from 3 trials normalized to % gait cycle. Angles were measured by video and goniometer systems simultaneously.

DIMENSIONLESS COMPLEXES FOR THE CALCULATION OF THE MASS-INERTIAL PARAMETERS OF THE HUMAN BODY

G. Ariel, A. Guskov, A. Vorobiev, N. Yakunin, J. Probe
International Center for Biomechanical Research, P.O.Box 1169 La Jolla, CA, 92038

INTRODUCTION

Regression relationships are widely used in biomechanics to calculate such anthropometric parameters as segment mass, length, and principal moments of inertia with respect to the segment center of mass. These regression equations contain a small number of parameters and as a rule are linear, thus reducing accuracy of the calculations.

REVIEW AND THEORY

As an example, Zatsiorsky and Seluyanov (1983) used the following regression equation to calculate mass of the body segment m_i:

$$m_i = b_0 + b_1 M + b_2 H \quad (1)$$

where M is a body mass, H is body height and $b_0; b_1; b_2$ are statistically determined coefficients using the measurement results from the representative sampling.

According to the theory of similarity and dimensionality, any functional relationships between determinative parameters should meet the demand of data homogeneity. The number of determinative parameters $\{a_1,...,a_n\}$ constitutes n-k dimensionless complexes $\{\pi_1,...,\pi_{n-k}\}$, where k is the number of independent dimensionalities (Sedov, 1943). Obviously, the relationship (1) doesn't meet requirement of data homogeneity. Only one dimensionless complex m_i / M could be constituted from the list of parameters $\{m_j, M, H\}$ because the body height is not adequate to characterize the body mass correctly.

The aim of the present study was to develop more statistically reliable regression equations to calculate anthropometrical parameters of the human body using theory of the similarity and dimensionality known as a Π-theorem.

PROCEDURES

The following list of variables was considered to determine the body segmental masses:

$$\{m_i, M, H, \sigma, \rho, g, P\} \quad (2)$$

where σ is the average strain characteristic of the living tissues [Pa], ρ is the average density of the human body [kg/m³], g is the gravity acceleration [m/s²], P is the thorax circumference [m]. This set of variables determines four dimensionless complexes:

$$\pi_1 = \frac{H}{P}, \pi_2 = \frac{Mg}{H^2\sigma}, \pi_3 = \frac{M}{\rho H^3}, \pi_4 = \frac{m_i}{M} \quad (3)$$

The relationship for determining m_i is:

$$\pi_4 = f(\pi_1, \pi_2, \pi_3) \quad (4)$$

where type of the function f depends of the type of regression relationship.

RESULTS

Two forms of presentation of function f were chosen to determine the mass of the human head:

$$\pi_4 = -4.31E^{-2} + 5.13E^{-2} / \pi_1^{1/2} + 4.8E^{-6} / \pi_2 - 1.55E^{-3} / \pi_3 \quad (5)$$

or

$$\pi_4 = 1.046 * 10^{-11} * \pi_1^{-0.224} * \pi_2^{-2.83} * \pi_3^{1.804} \quad (6)$$

The tabulated values reported by Zatsiorsky and Seluyanov (1983) were used for calculations. Coefficients of variation for equations (5) and (6) were equal to the 6.25% and 6.26% respectively.

Calculations for determining the segmental mass and length were also performed. The energetic regression equations have been developed in the same way.

DISCUSSION

The application of the theory of similarity allows to make calculations regardless of a system of measurement units and take into account age, sex, body stature and etc. on equations for determining mass-inertial parameters of the segments of the human body.

REFERENCES

Bernstein, N. The coordination and regulation of movements. London Pergamon Press, 1967.

Cappozzo, A. et al. The interplay of muscular and external forces in human ambulation. J.Biomechanics 9, 35-43, 1976.

Dempster, W.T. Space requirements of the seated operator. WADS technical report 55-159. Wright-Patterson Air Force Base , Ohio 1955.

Sedov, L. Method of theory of similarity and dimensionality in mechanics, Moscow, 1946.

Winter, D.A. Biomechanics and motor control of the human movements. A Willey-Interscience Publication, John Willey & Sons, Inc. 1990

Zatsiorsky, V. and Seluyanov, V. The mass and inertia characteristics of the main segments of the human body. In: VIII-b Matsui, H. and Kobayashi ed., Human Kinetics Publishers, Champaign, IL, 1152-1159, 1983.

INEXPENSIVE FOOTSWITCH SYSTEM FOR LONGITUDINAL RECORDING OF THE TEMPORAL PARAMETERS OF GAIT

Jeffrey M. Hausdorff*+, Zvi Ladin*, and Jeanne Y. Wei+
*Department of Biomedical Engineering, Boston University, Boston MA 02215, USA.
+Department of Medicine, Beth Israel Hospital, Boston MA 02215, USA.

INTRODUCTION AND BACKGROUND

Improvements in technology have enabled today's biomechanist to study the kinematics and kinetics of human locomotion with improved accuracy and resolution. Force plates accurately measure components of force and moments while optoelectronic and video cameras provide three dimensional limb trajectories to within 1-2 mm. Notwithstanding, there is still room for enhancing the tools with which we study biomechanics. Today's measurement systems are laboratory bound, limiting the duration and constraining the space in which data can be collected. To augment laboratory bound investigations, we have recently developed a low cost footswitch system that provides repeated, longitudinal measurements of the beginning and end of foot contact.

The benefit of using a force plate is that it permits detailed study of the timing, forces and moments of the foot-ground interaction, one of the crucial elements of both normal and pathological gait. Unfortunately, due to size and economic constraints, a force plate is typically used to capture data of only a single, isolated step in a walk of several steps, while kinematic measurements are obtained for several strides. Although changes in the trajectory of the kinematics may themselves suggest when heel strike occurs, use of kinematic data to identify timing of footfall is based upon circular reasoning that may be inaccurate in the analysis of abnormal gait. Footswitches can supplement the kinematic analysis of these steps by objectively providing data on the timing of footfall for a large number of steps.

Numerous methods have been used for measuring timing of footfall with varying degrees of success (1). One of the limitations of some of the past methods is that duplication of methods and production of the device was often difficult. While some commercial systems are available for this purpose (e.g. EDG, BTE), their cost can be prohibitively expensive. We have endeavored to design a system that could be easily replicated by others at uninhibitive costs. The parts we have used for a single footswitch can be readily combined from commercially available products in a few hours for less than $20.

METHODS

The transducer we use is a conductive polymer layer sensor that changes resistance when loaded (Interlink Electronics, Carpenteria CA). This sensor was chosen because of its thickness (<.05''), commercial availability, temperature insensitivity, ability to withstand overload, and the ease with which it may be interfaced. Wertsch et al. (1992) have used this technology to successfully measure insole pressures. In part because of their interest in measuring insole pressures, their design requires calibration of each sensor before usage, special footwear to accommodate the sensor, stiff metal backing (to reduce hysteresis due to bending), as well as individual testing to determine sensor placement. We hoped to eliminate all of these requirements and use the sensors to provide accurate timing information. To this end, a 1.5 inch square force sensitive resistor is placed under the heel (simply taped to the shoe insole) and another under the big toe. These two sensors are connected in parallel, and essentially act as one larger sensor. This parallel connection is placed in series with a measuring resistor that acts as a voltage divider. The sensors are driven by a battery operated circuit (most DC voltage sources will do just fine) that easily fits in a pants pocket. The voltage across the divider is fed into a follower, whose voltage output increases non-linearly with increasing force. Output switch voltage ranges from 0 volts with no foot contact to 3.5 volts when fully closed. The analog signal is then digitized and analyzed in software.

The original signal is smoothed using a moving average and differentiated. This differentiated signal serves as the guide for determining the temporal parameters of gait. The start of foot contact time, typically heel strike, is defined as the time when the derivative exceeds a threshold value, provided the output voltage of the switch also exceeds a threshold value. A similar definition (using opposite sign for the derivative) is used to define the end of foot contact, typically toe-off.

RESULTS AND DISCUSSION

To evaluate our footswitch system, we compared its timing estimates with that obtained using an AMTI force plate (Newton, MA). The footswitch signal and the force platform force in the vertical direction were collected simultaneously and sampled at 200 Hz as steps were taken across the force plate. An example of the data acquired is shown in Figure 1. The dashed and solid lines correspond to the output voltage of the footswitch sensor and the vertical force measured by the force platform, respectively. A key advantage of the footswitch system can be readily observed. Note how the footswitch system can be used to provide continuous and sequential

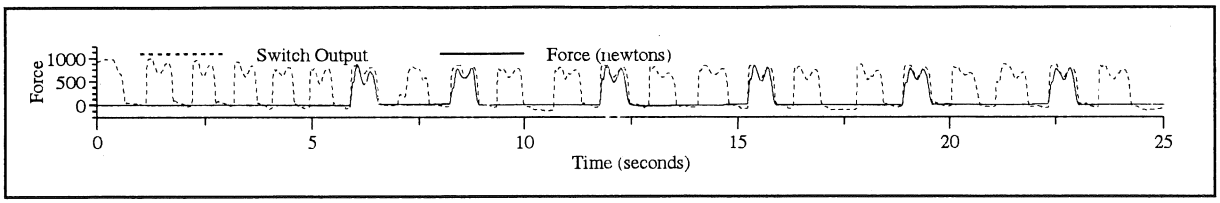

Figure 1: Example of force platform vertical force and switch output for multiple steps.

estimates of the temporal parameters of gait, while the force platform data is limited to isolated steps.

To compare estimates of stance phase derived from the footswitch system with those derived from the force plate, determination of the beginning and end of stance phase was made from the force plate data using a similar algorithm as that used for the switch. Various thresholds (10 - 100 newtons) were used to compare the two timing estimates in order to assess the sensitivity of both systems to the threshold values.

Initially, we studied the effect of sensor placement within the shoe on the timing measures by changing the location of each sensor in the shoe. The sensor under the heel was placed as far back as possible in the shoe and then moved forward in one cm increments up to 6 cm. We found, to our surprise, that timing of heel strike was independent of sensor position, probably because the normal loading is quickly dispersed in the insole. We found similar insensitivity to placement of the sensor under the forefoot when the distance between anterior end and the sensor was less than 4 cm. Beyond that point, large differences occurred, possibly due to bending of the sensor.

Next we compared timing measures as a normal subject repeatedly walked across the force platform at slow, normal, and fast paces. An example of the differentiated signal and its estimate of start and end of heel strike are shown in Figure 2. The dashed lines in this figure mark the beginning and end of stance phase as estimated using the force platform data (top) and the switch data. For this example, both estimates were in complete agreement for both the start and end of stance phase. In general, both estimates for the start of stance phase were in agreement (within the sampling resolution of 5 ms) for normal and fast steps for several switch voltage thresholds when the force threshold was at 20 or 30 newtons. As the force threshold was increased to 50 newtons, the estimates differed from 0 to 15 ms. For the slow steps, sensitivity to thresholds was larger and the range of the differences between the two estimates was slightly larger (0 to 30 ms). This was probably because for these slow steps vertical force at heel strike more closely resembled a slowly rising exponential rather than a step input. Correspondence between the two estimates of toe-off were also generally similar.

We have developed a low cost, easy-to-implement footswitch measuring system that provides accurate estimates of stance phase for longitudinal, sequential steps. The estimates of the beginning and ending of stance phase do not require custom footwear, extensive calibration, or precise placement of the sensor within the shoe. In addition, the estimates coincide with force plate derived estimates for normal gait. It therefore should prove to be a useful tool for augmenting laboratory based investigations. Applicability to the study of pathologic gait remains to be established.

REFERENCES

1. Alexander, I., et al. Foot & Ankle, 11, 152-167, 1990.
2. Wertsch, J. et al. J. Rehab. Res. Dev., 29, 13-18, 1992.

ACKNOWLEDGEMENTS

This work was funded in part by a Boston University Presidential Fellowship and grants from the National Institute on Aging (AG07225, AG08812).

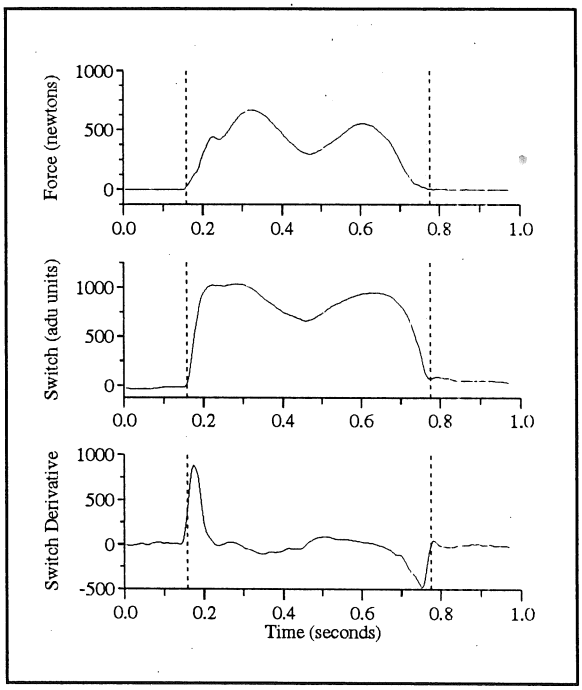

Figure 2: Force platform and switch output with estimates of beginning and end of stance phase (dashed lines).

EVALUATION OF LENS DISTORTION FOR VIDEO-BASED MOTION ANALYSIS

J. Poliner, R.P. Wilmington, and G.K. Klute.

Lockheed Engineering and Sciences Company, C81, Houston, TX 77058
Anthropometry and Biomechanics Laboratory, Johnson Space Center, Houston, TX 77058

INTRODUCTION

Video based motion analysis systems are widely used to study human movement. These systems use computers to aid in the capturing, storing, processing, and analyzing of video data. One of the errors inherent in such systems is that caused by distortions introduced by the camera and lens. Wide angle lenses are often used in environments where there is little space to position cameras to record an activity of interest. Wide angle lenses distort images in a predictable manner. Even "standard" lenses tend to have some degree of distortion associated with them. These lens distortions will introduce errors into any analysis performed with video-based motion analysis systems.

The purposes of this research included: developing methodology to evaluate errors introduced by lens distortion; comparing errors introduced by standard and wide angle lenses; and investigating techniques to minimize lens induced errors.

PROCEDURES

A grid was constructed with thin, black vertical and horizontal lines spaced 3.8 cm apart on a white background. The intersections of eleven horizontal and fifteen vertical lines defined a total of 165 points (see Figure 1). The grid was mounted on a sheet of foam core and attached to a wall. The center point of the grid was marked for easy reference. A Quasar camcorder (model VM-37) was placed on a camera stand perpendicular to the grid, with the center of the lens aligned with the center of the grid. Two lenses were used to record video. The first was a standard 1:1.4 lens. The other was a 0.5X wide angle-lens. For each lens, the camera was positioned at a distance from the grid such that the grid almost completely filled the field of view, paying special attention to the left and right borders. For the standard lens this distance was 88.3 cm; for the wide angle, 50.2 cm. Data collection consisted of videotaping the grid with each of the two lenses.

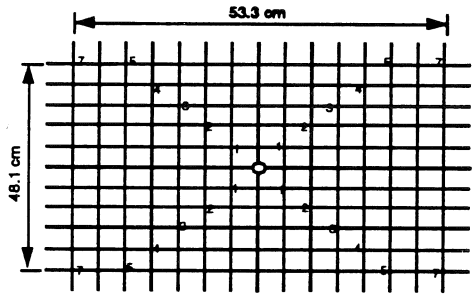

Figure 1. Grid of lines used in the study. Numbers indicate locations of calibration (control) points.

An Ariel Performance Analysis System (APAS) was used to process the video data. Images were played back on a VCR into a personal computer that was equipped to grab and store the images to disk. Using these stored images, two experiments were conducted.

For the first experiment, three operators each digitized all points in the grid twice. Digitizing and subsequent processing resulted in X and Y coordinates for the points. The four points nearest the center of the grid were used as the control (calibration) points (points marked "1" in Figure 1). These were chosen because it was anticipated that errors would be smallest near the center of the image; using control points that were in the distorted region of the image would further complicate the results. The control points were digitized and their known coordinates were used to determine the scaling from screen units to actual coordinates. These coordinates ranged from 0 to ±266.7 mm in the X direction and 0 to ±190.5 mm in the Y direction. Values of the calculated X and Y coordinates for the two trials from each of the three operators were averaged. To remove the dependence of the data on the size of the grid, normalized coordinates were calculated by dividing the calculated X coordinates by 266.7 mm and the Y by 190.5 mm. The error of each point was calculated as the distance between the calculated average location and the known location of that point. These error values were then normalized by calculating them as a percentage of the maximum coordinate in the horizontal direction (266.7 mm). This dimension was chosen to be representative of the size of image.

For the second experiment, the digitized grid of points from one of the three operators was re-processed using six different sets of control points. For the first condition, the control points were at ±1 grid units in the X and Y directions from the center of the grid (i.e., {1,1}, {1,-1}, {-1,1}, and {-1,-1}). For the other conditions, the control points were at 2, 3, 4, and 5 grid units. A final condition was with the control points the furthest from the center (7 grid units in X, 5 in Y). See Figure 1. Normalized coordinates and errors were calculated as they were in the first experiment.

RESULTS

Figure 2 shows contour plots of the average error as a function of the normalized X-Y location in the image for the two lenses. With both lenses it was clear that errors were small near the center of the image and became progressively greater further away from the center. Errors were also evaluated as a function of the radial distance from the center of the image. This distance was normalized by dividing the raw coordinates by the maximum coordinate in the horizontal direction (26.67 cm). Graphs

of these average errors as a function of radial distance from the center of the screen are shown in Figure 3.

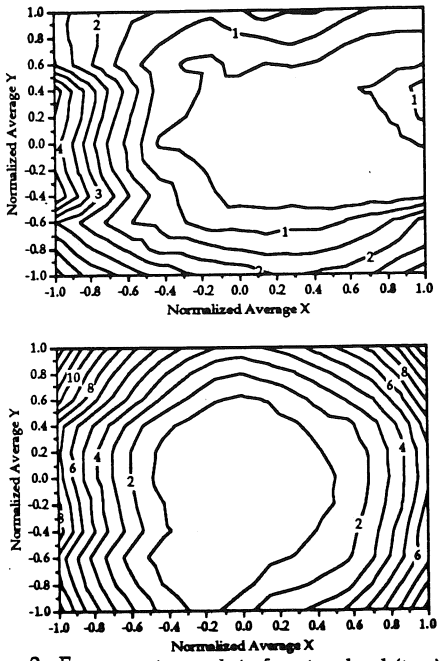

Figure 2. Error contour plots for standard (top) and wide angle (bottom) lenses.

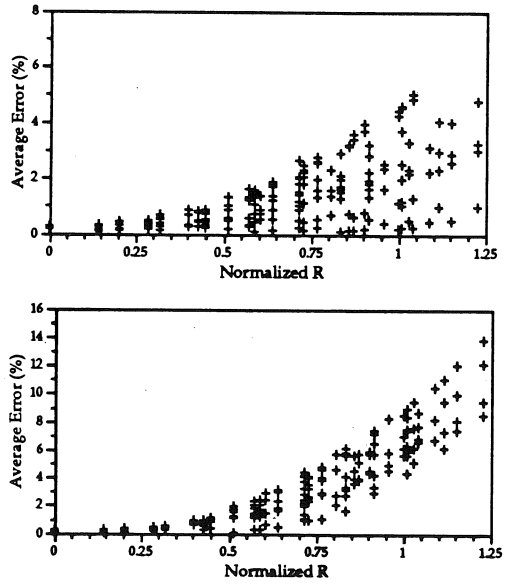

Figure 3. Average error as a function of radial distance (R) from the center of the screen for the standard (top) and wide angle (bottom) lenses.

Linear and binomial regressions were created for the relationship between the error (E) and the normalized radial distance from the center of the image (R). For the standard lens these were:

$E = 2.562R - 0.420$ $(r^2=0.406)$

$E = 1.155R^2 + 1.085R - 0.048$ $(r^2=0.410)$

For the wide angle lens, the relations were:

$Error = -2.722 + 8.811R$ $(r^2=0.765)$

$Error = 10.01R^2 - 3.992R + 0.503$ $(r^2=0.864)$

For the second experiment, similar graphs were created as with the first. Third order polynomial regressions were fit to the error-distance data for each calibration condition. Figure 4 presents these regression curves combined into single graphs for the standard and wide angle lenses. Errors were least for both lenses when the control points were at 5 by 5 grid units. Errors could be kept even smaller if the region of the image greater than half the horizontal image distance (normalized R greater than 1) away from the center were not considered. With this, the absolute maximum error was the smallest when the control points were at four grid units from the center of the screen for both lenses.

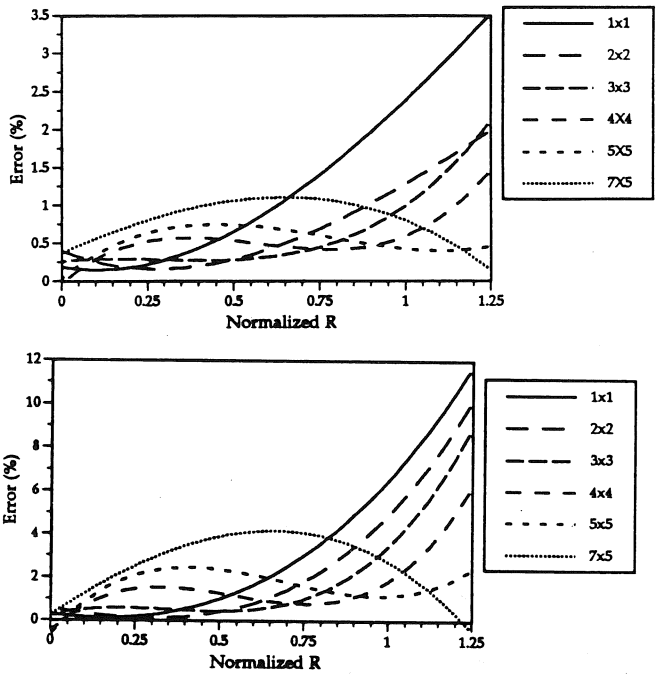

Figure 4. Cubic regression curves for standard (top) and wide angle (bottom) lenses for each of the calibration conditions.

CONCLUSION

This study has taken a thorough look at one of the sources of error in video based motion analysis. A methodology was developed to evaluate lens distortion. It was seen that when using a wide angle lens, errors from lens distortion could be as high as 10% of the size of the entire field of view; 4% with a "standard" lens. It was also found that the choice of calibration points influenced the lens distortion error. By properly selecting the calibration points, and avoiding the outermost regions of a wide angle lens, the error from lens distortion can be kept below approximately 0.5% with a standard lens and 1.5% with a wide angle lens.

TIME-FREQUENCY ANALYSIS APPLIED TO CENTER OF PRESSURE PATHS

Timothy Schumann and Mark S Redfern
Human Movement Analysis Laboratory, University of Pittsburgh

INTRODUCTION

Center of pressure (COP) paths have been used to study the postural control system in humans. Investigators have derived many parameters from the COP paths in an attempt to differentiate between normal and patient populations, (Dichgans et al., 1976). They have also utilized spectral analysis techniques to study the frequency content of the COP signal, (Soames et al., 1982). Most investigations have assumed that the COP is stationary and have used the periodogram for estimating the spectral content of COP paths. It has been shown that this assumption may not be correct, (Harris et al., 1986). When humans are asked to stand quietly with eyes closed, the resultant COP paths appear to exhibit non-stationary characteristics. This is plausible since the postural control system is complex, receiving inputs from the vestibular, visual, proprioceptive and somatosensory systems. If a non-stationary signal is analyzed with a stationary method the results are often confounded, resulting in an incorrect analysis.

Recently developed time-frequency analysis techniques permit study of non-stationary signals. The advantage over stationary techniques is that transient events in the COP such as perturbations can be studied. The purpose of this paper is to demonstrate the use of time-frequency analysis in examining the COP.

REVIEW AND THEORY

Three basic methods for estimating time-frequency distributions are currently utilized; the spectrogram, methods based on the Wigner distribution, and the evolutionary spectrum introduced by Priestly (1988). Each method has drawbacks and all suffer from a time-frequency tradeoff, i.e. to get better time resolution you must give up some frequency resolution.

An evolutionary spectrum method was chosen since 1) it is rooted in sound mathematical theory, 2) it is always positive and can be thought of as an energy distribution (Wigner methods cannot), and 3) the estimators reduce to well understood spectral estimators in the stationary case. The estimator used in this study is the evolutionary periodogram (EP), (Kayhan et al.,1991). This method assumes that at each frequency a time-varying amplitude can be accurately represented by a set of orthonormal basis functions (Legendre, Fourier, Walsh-Hadamard,etc.). The EP is a minimum mean-squared error estimator. Time and frequency resolution can be controlled by changing the number of orthonormal functions used and the length of the FFT. The different basis functions chosen also affect the characteristics of the EP. We found that eight Fourier basis functions provide adequate time and frequency resolution for analysis of COP paths.

PROCEDURES

Subjects (5 normal/ 5 vestibularly-impaired patients) were instructed to stand on a Bertec force plate and to sway about the ankles to the frequency of a metronome as it was decreased from 2 to 1 Hz. We conducted this experiment in order to assess the utility of time-frequency analysis as a technique for studying COP. A second test was performed to compare normals and patients during quiet stance with eyes closed. Normal foot forces and moments were digitized for 60 seconds at a sampling rate of 20 Hz. Center of pressure paths were calculated and zero-meaned. The resultant data was decimated by two and low-pass filtered at a cutoff of 5 Hz with a phaseless filter. The EP was calculated and plotted as a three-dimensional surface and a contour plot for visual analysis.

RESULTS

Figure 1 illustrates the utility of time-frequency analysis for non-stationary signals. The raw anterior-posterior COP data is illustrated in Fig. 1a. The stationary periodogram reveals significant energies from 1-2 Hz but provides no useful temporal information(Fig. 1b). A purposeful movement or perturbation to the postural control system during a test would not be able to be accurately interpreted by this method of analysis. The EP, however, provides temporal, frequency and relative energy information(Fig. 1c & 1d). Changes in amplitude of the raw COP produce energy amplitude changes in the EP. The contour plot permits efficient identification of significant energy contributions in time and frequency. For example, the contour plot shows that the frequency of sway changes from 2 to 1 Hz in a linear fashion for 20 seconds and then remains at 1 Hz for the final 10 seconds(Fig 1d).

In the second experimental condition time-frequency is used to compare normals with various patient groups during quiet stance with eyes closed. Figure 2 illustrates the EP for a typical normal and a vestibularly-impaired individual. The patient exhibits higher energies than the normal and also displays significant energies at higher frequencies. The normal appears to have significant energies at only one frequency. The patient appears to have two to three significant frequencies with the amplitudes changing through time.

DISCUSSION AND CONCLUSIONS

Since control of balance, as measured by COP, is a complex process with inputs from many systems, advantages are gained by utilizing analysis methods which do not assume stationarity. These new non-stationary methods permit a temporal examination of the frequency content of the COP paths and provide investigators with a new tool for studying the postural control system. Transient events in the COP paths and the response of the postural control system to perturbations can be analyzed with the EP. Future work should concentrate on developing methods for statistically analyzing these time-frequency distributions so that they may be utilized as discriminators.

REFERENCES

Dichgans, J. et. al Aggressologie, 17, 15-24, 1976.
Soames, R. et al. European Journal of Applied Physiology, 49, 169-177, 1982.
Harris, G. et al IEEE/Eighth Annual Conference of the Engineering and Biology Society, (pp. 1583-1585), 1986.
Priestly, M., Non-Linear and Non-Stationary Time Series Analysis (pp. 139-153), Academic Press, 1988.
Kayhan, A. et al. International Conference on Acoustics,Speech, and Signal Processing, Toronto (pp. 3165-3168), 1991.

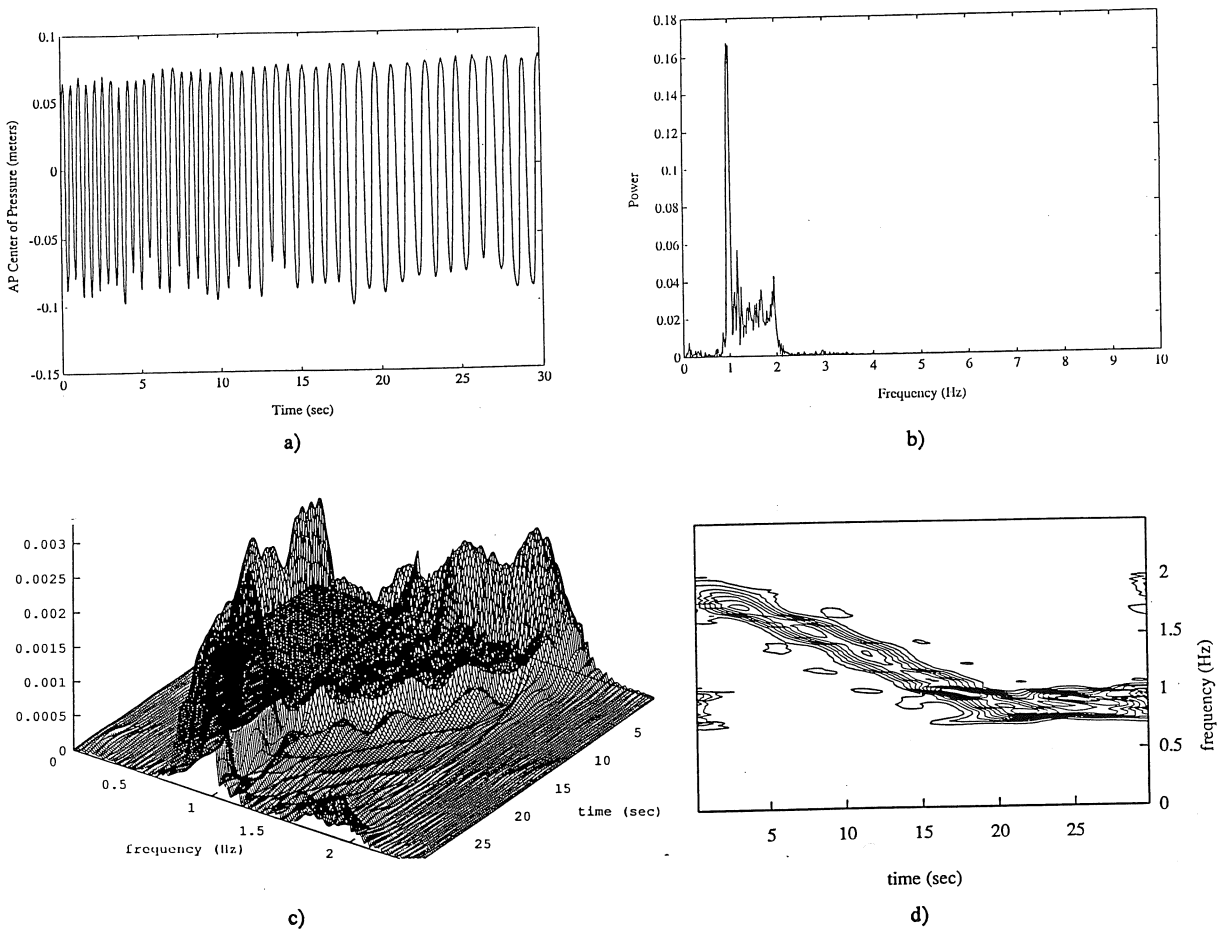

Figure #1 a) Center of pressure paths for subject swaying at same frequency as metronome, b) stationary periodogram of COP, c) surface plot of evolutionary periodogram, d) contour plot of evolutionary periodogram.

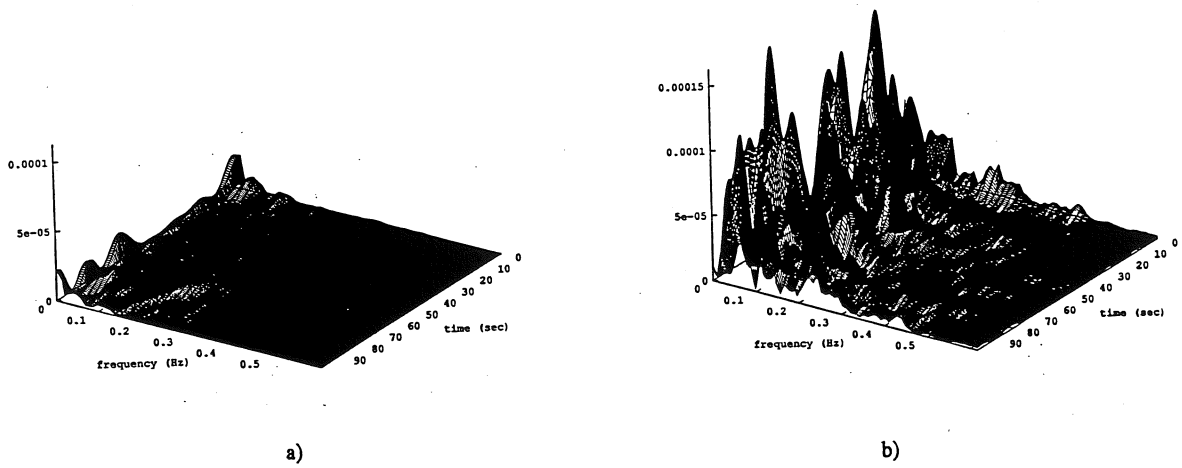

Figure #2 Evolutionary periodogram for subjects during quiet stance with eyes closed. a) Typical normal, b) Vestibularly-impaired subject.

A THREE-DIMENSIONAL DYNAMIC MODEL OF THE LOWER LIMB

Q. Wu and A.B. Thornton-Trump
Department of Mechanical & Industrial Engineering
The University of Manitoba
Winnipeg, Manitoba, Canada, R3T 2N2

INTRODUCTION

A multy-body dynamic formulation has been developed for the purpose of human gait analysis. The equations are derived for a link system with up to three degrees of rotational freedom at each joint which is required by pathological gait. The method is developed from Newtonian and Eulerian principles and is based on the orthogonal complement approach. The approach allows elimination of the internal forces and torques. The method has been tested by simulating large vibration of a two-link system. Good agreement has been shown between the simulation outputs and the desired output profiles.

REVIEW AND THEORY

In the study of dynamics and kinematics of human lower limbs, many models have been developed. Those models usually do not consider three degrees of rotational freedom at the joints since only sagittal motions are considered. Recently, it has been shown that measuring sagittal plane joint angle time histories alone does not fully describe an individual's gait pattern Apkarian et al (1989). Measuring of joint angles in all three planes becomes increasingly important for pathological gait analysis Vaughan et al (1992). Thus, it is imperative to develop a model with three degrees of rotational freedom at each joint, especially for pathological gait analysis. Additionally, for any reasonably complicated model of the human lower extremities, manually deriving the equations of motion is a time consuming process, and becomes an intolerable limitation if a variety of models are to be investigated.

The objective of this work is to develop a method for modelling human lower limbs with up to three degrees of rotational freedom at each joint. At same time, the method should be easily expand to systems of larger dimension.

PROCEDURES

The general dynamic equations of motion for a closed/open kinematic linkage can be written as follow Wong et al (1991).

$$\begin{bmatrix} J & 0 \\ 0 & m \end{bmatrix} \begin{bmatrix} \dot{\omega} \\ \ddot{x} \end{bmatrix} - \begin{bmatrix} f \\ g \end{bmatrix} + \begin{bmatrix} H_1 \\ H_2 \end{bmatrix} \gamma + \begin{bmatrix} N_1 \\ 0 \end{bmatrix} \lambda + \begin{bmatrix} E \\ 0 \end{bmatrix} \tau \qquad (1)$$

where $\mathbf{H_1}$ and $\mathbf{H_2}$ are coefficient matrices for the linear constraint forces; $\mathbf{N_1}$ is the coefficient matrix for the rotational constraint torques, and $\mathbf{E}$ relates the actuator torques to the appropriate coordinate frames; γ, λ and τ are the vectors of constraint forces, constraint torques and actuator torques, respectively; $\mathbf{f}$ and $\mathbf{g}$ are vectors describing the system forces generated by the gyroscopic torques and gravity; $\mathbf{J}$ and $\mathbf{M}$ are block diagonal matrices of inertia and mass.

Orthogonal complement approaches use global Jacobean transformation matrix which projects the system from primitive derivative state space to a reduced independent set of variables. The transformation matrix contains vectors which are perpendicular to the coefficients orienting the constraint forces and torques. As the result, the transformation matrix eliminates the hinge forces and torques. One example of such transformation matrix approaches is Newton-Euler State space method Hemami et al (1982). In such method, a two-step transformation is used to eliminate the constraint forces and torques. First step transformation is to redefine $\mathbf{x}$ as a function of ω using translational, kinematic, hinge constraint equations. The equations for $\mathbf{i}^{th}$ hinge constraint and its second order derivative are:

$$x^i_{i,0} + K^i_{i,i} - x^i_{i-1,0} - A^i_{i-1} l^{i-1}_{i+1,i} = 0 \qquad (2)$$

$$\ddot{x}^i_{i,0} - \ddot{x}^i_{i-1,0} + (\omega^i_{i,0})^2 k^i_{i,i} - A^i_{i-1} (\omega^{i-1}_{i-1,0})^2 l^{i-1}_{i-1,i} - \tilde{K}^i_{i,i} \dot{\omega}^i_{i,0} + A^i_{i-1} \tilde{l}^{i-1}_{i-1,i} \dot{\omega}^{i-1}_{i-1,0} = 0 \qquad (3)$$

where
$\mathbf{x}_{i,0}^{i}$ is the translational displacement of body i (first subscript) measured with respect to the inertial frame **0** (second subscript) and referred to frame **i** (superscript).
$\tilde{\mathbf{k}}_{i,0}^{i}$ is the skew symmetric matrix of vector $\mathbf{k}_{i,i}^{i}$, measured from the centre of mass of body **i** to the $\mathbf{i}^{th}$ hinge and referred to the $\mathbf{i}^{th}$ coordinate frame.
$\tilde{\mathbf{l}}_{i,i+1}^{i}$ is the skew symmetric matrix of vector $\mathbf{l}_{i,i+1}^{i}$ measured from the centre of mass of body **i** (first subscript) to the outboard hinge **i+1** on body **i** (second subscript) and referred to $\mathbf{i}^{th}$ coordinate frame.
$\mathbf{A}_{i-1}^{i}$ is the rotation matrix referring a vector from $\mathbf{i\text{-}1}^{th}$ to $\mathbf{i}^{th}$ coordinate system.

The differentiated hinge constraint equation for the whole system is therefore:

$$\ddot{X} = U^{-1} Q \dot{\omega} + U^{-1} \dot{Q} \omega \qquad (4)$$

The transformation matrix $[U^{-1}Q]$ can be used to eliminate γ in equation (1).

The second step of coordinate transformation is to obtain the matrix to eliminate λ in equation (1) and to convert to the system of relative Euler joint angle acceleration space. The kinematic equation is:

$$\omega^i_{i,0} = A^i_{i-1} \omega^{i-1}_{i-1,0} + \omega^i_{i,i-1} \qquad (5)$$

where $\omega_{i,i-1}^{i}$ is the angular velocity relative to the previous body, but referred to its own coordinate system. $\omega_{i,i-1}^{i}$ is related to the relative joint angle rate through the kinematic differential equations. For the entire system, the kinematic equation is:

$$\omega = C \dot{\theta} \qquad (6)$$

Where matrix C is the angular velocity matrix. The angular acceleration is:

$$\dot{\omega} = C\ddot{\theta} + \dot{C}\dot{\theta} \qquad (7)$$

Substituting equation (4) and (7) into equation (1) and premultiply (1) by the transformation matrix $[C^T (U^{-1}QC)^T]$, the internal forces and torques are eliminated and the equation of motion can be written in the following form:

$$[C^T (U^{-1}QC)^T] \begin{bmatrix} J & 0 \\ 0 & M \end{bmatrix} \begin{bmatrix} C \\ U^{-1}QC \end{bmatrix} \ddot{\theta} = [C^T (U^{-1}QC)^T] \qquad (8)$$
$$\left(\begin{bmatrix} f \\ g \end{bmatrix} - \begin{bmatrix} 0 \\ M^{-1}\dot{Q}\omega \end{bmatrix} - \begin{bmatrix} J \\ M^{-1}Q \end{bmatrix} \dot{C}\dot{\theta} + \begin{bmatrix} E \\ 0 \end{bmatrix} \right)$$

RESULT

The method has been applied to a two-link system for large vibration about one axis at each joint. The desired displacement profile for each link is assumed as a sine function. The torque applied at each joint corresponding to the desired output is calculated using Lagrange Mechanics and shown in Fig.1. This inverse dynamics control the system in an open-loop control mode. Fig.2 shows the error curves for second link which have maximums of 9.26×10^{-4} rad, 3.42×10^{-3} rad/sec and 8.08×10^{-3} rad/sec^2 for displacement, velocity and acceleration of Euler angles. The simulation outputs agree with desired output profiles very well.

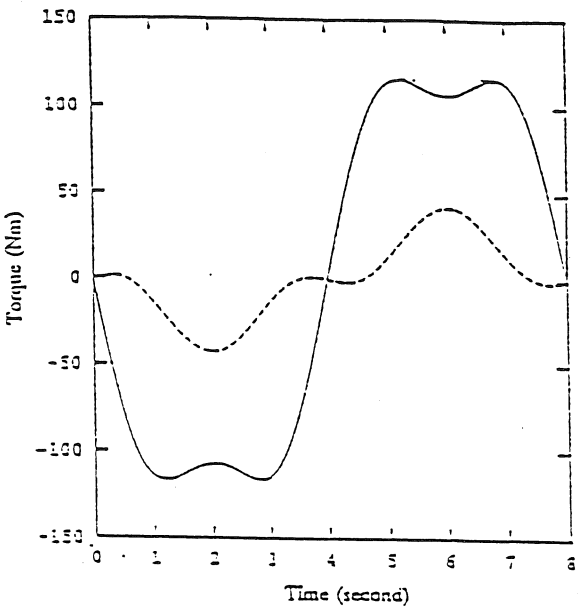

Fig.1: Torque profiles for the joints
——Torque applied at joint 1
- - - -Torque applied at joint 2

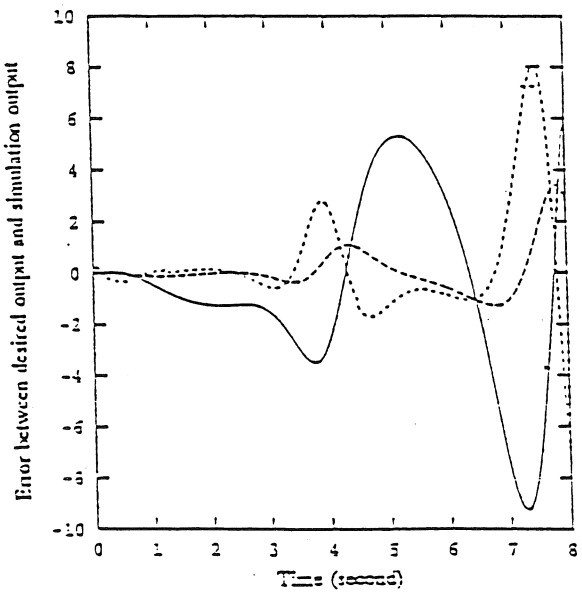

Fig.2: Error profiles for second link
——$\theta_d - \theta$ ($\times10^{-4}$)
- - - -$\dot{\theta}_d - \dot{\theta}$ ($\times10^{-3}$)
·····$\ddot{\theta}_d - \ddot{\theta}$ ($\times10^{-3}$)

DISCUSSION

A state-space formulation for modelling the human lower limbs has been developed. The approach has the advantages, over other existing approaches, in that it is capable of modelling systems with up to three axes of rotation at each joint when pathological gait requires it; it is easy to formulate and to expand to systems of larger dimension, and it allows easier incorporation and implementation of muscular and actuator control. The research is continuing, and further simulations are proceeding.

REFERENCES

Apkarian, J. et al. Journal of Biomechanics, Vol.22, NO. 2,143-155, 1989.

Vaughan, C. et al. Dynamics of Human Gait, Versa Press, 1992.

Wong, D., Ph.D dissertation, Dept. of Elec. Engng., U. B. C., Vancouver, British Columbia, Canada, 1991.

Hemami, H. et al. IEEE Transactions on Automatic Control, Vol. AC-27, NO. 2, 376-382, 1982.

ACKNOWLEDGEMENTS

This work is supported by the Natural Sciences and Engineering Research Council of Canada grant number A 8920.

CONTRIBUTION OF SHANK MUSCLE TO PERFORMANCE IN ELECTRICAL STIMULATION-INDUCED LEG CYCLE ERGOMETRY - A PILOT STUDY

M.M. Rodgers, D. R. Schrag, S. F. Figoni, S.R. Collins, R.A. Shively, R. M. Glaser

VAMC, Dayton, OH, Institute for Rehabilitation Research and Medicine, Wright State University, Dayton, OH

INTRODUCTION

Functional electrical stimulation (FES)-induced contractions of paralyzed lower-limb muscles can be utilized for leg cycle ergometer (LCE) exercise of spinal cord injured (SCI) individuals. This can serve to increase their muscular and cardiopulmonary fitness. However, if more muscle groups can be activated than is presently done, greater metabolic response magnitudes may be achieved which can enhance training effectiveness. The purpose of this study was to investigate the additional utilization of the shank muscles using a specially constructed "prototype" FES-LCE system. For this, metabolic and biomechanical responses were monitored during FES-LCE exercise with and without shank muscle utilization, and in comparison to operating a commercially available FES-LCE without shank muscle utilization. The addition of shank muscle FES increased VO_2 by 18% at 0 W. Joint ranges varied between the ERGYS and the "prototype" systems. Increased hip ab/adduction in the "protype" system indicates the need for additional knee stabilization.

REVIEW AND THEORY

Commercially available FES-LCE systems (i.e., Therapeutic Technologies Incorporated models REGYS and ERGYS) incorporate computer-controlled FES of the quadriceps, hamstrings and gluteal muscle groups. Previous work has demonstrated the efficacy of these systems for improving the integrity of these paralyzed muscles and cardiopulmonary (aerobic) function (Hooker et al., 1991; Ragnarsson et al. 1988). Evidence suggests that power output and physiologic response magnitudes may be limited by several factors including the muscle mass employed and biomechanics utilized. Further study of these factors is needed in order to optimize FES exercise training effects.

Schutte, et al. (1992) developed a mathematical model to predict biomechanical factors which would improve ERGYS FES-LCE operation. Factors considered include seat position back support angle, distance between the seat and pedals, and firing angles to activate the quadriceps, hamstring and gluteal muscle groups. However, it would appear that the utilization of additional muscle groups can improve operation due to the availability of greater muscle mass and improved circulation of blood, which may enhance training effectiveness. But, it would be important to evaluate the biomechanical aspects of this modification to ascertain its safety. It was the purpose of this pilot study to evaluate the metabolic effects and biomechanics of adding the shank muscles (i.e., gastrocsoleus, tibialis anterior) to the FES-LCE exercise.

PROCEDURES

The commercially available ERGYS was utilized for the control test to establish baseline responses. A specially constructed prototype FES-LCE was used to test the addition of shank muscle utilization (Ezenwa, et al.). This device provided 10 channels of computer-controlled FES instead of the 6 channels used by the ERGYS. Four additional channels were used to induce bilateral contractions in the gastrocsoleus and tibialis anterior muscle groups. Surface electrodes placed over motor points of the muscle groups were utilized. Standard ERGYS firing angles were maintained, but the antagonistic shank muscles were set to co-contract with their corresponding hamstring muscles (at a 50% current level) in an attempt to stabilize the ankle and assist knee flexion. In addition, the prototype FES-LCE has strain-gauges built into the leg pedals to permit continuous monitoring of tangential loading. This enables the calculation of power output (PO) by multiplying the tangential force by the pedal velocity. (Although the prototype FES-LCE system also has arm crank exercise capability, only the leg pedal ergometry was used in this study.)

A 17 year old C5 incomplete quadriplegic male participated in this pilot study. The methods and procedures used in this study were approved by the IRB of Wright State University. After signing a statement of imformed consent, the subject participated in three FES-LCE exercise tests performed on separate days, each at 0 W PO (i.e., unloaded flywheel): 1) ERGYS, 2) "prototype" without shank muscle FES, and 3) "prototype" with shank muscle FES.

At rest and during each test, steady-state oxygen uptake (VO_2, L/min) was monitored by open circuit spirometry. A Medical Graphics Corp. System 2001 metabolic gas exchange monitoring system was used for this purpose. This provided information concerning the aerobic energy expended during the various test conditions, the efficiency of the exercise modes and the potential of each exercise mode for cardiopulmonary fitness training. Biomechanical analysis for each exercise mode was accomplished by using a three-dimensional motion analysis sytem (Peak Performance Technologies, Inc., CO). Reflective markers were placed at the shoulder, hip, knee, ankle, and 5th metatarsal locations. Subjects were videotaped at 60 frames/sec.

Detemination of power (in W) for the ERGYS was based on calculations by Figoni et al. (1992) using VO_2 measurements. Power (in W) for the "prototype" system was calculated as the product of the pedal force and crank velocity. Protocol for the graded leg cycling exercise test from rest to peak was as follows. After a 5-min rest period, the leg crank was passively turned for 5 min as a warm-up and to relax excessive spasticity. The subject then pedaled the ergometer without any external resistance applied to the flywheel (the indicated 0 W level) for 3 min at 50 RPM.

RESULTS AND DISCUSSION

An example of the joint ranges as demonstrated in a stick figure obtained from ERGYS exercise is shown in Figure 1. Kinematic results are shown in Table 1. The ankle was maintained in more dorsiflexion and within a more narrow range of motion in the "prototype" system compared to the

ERGYS. Knee ranges were similar among the conditions. The hip was more flexed over a wider range and hip abduction was markedly increased in the "prototype". The addition of shank muscle FES decreased ankle motion and knee flexion. However, the ERGYS incorporates a more extensive leg alignment/stabilization system than the "prototype" FES-LCE which could, to a large extent, account for these biomechanical differences.

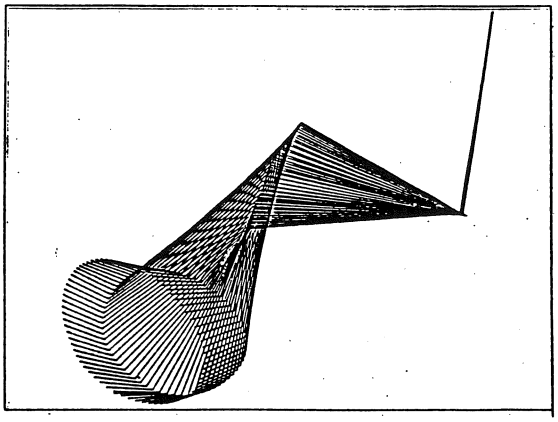

Figure 1. Stick figure showing hip, knee, and ankle motion during ERGYS pedaling.

The kinematic effects seen with the "prototype" system generally would be beneficial to the SCI individual. More ankle dorsiflexion counteracts the "drop-foot" position most often assumed following paralysis. which can cause secondary problems such as interference with shoe fit, creation of pressure areas, and difficulty maintaining the feet on wheelchair foot pedals. The increased hip extension seen in the "prototype" system would be desirable to counteract tight hip flexors. The increased hip abduction, however, poses a potential safety problem as the lack of knee control may increase knee joint stresses. Additional knee stabilization would be recommended.

TABLE 1. Minimum, maximum, and range of motion values (in degrees) for three FES-LCE conditions: ERGYS, "PROTOTYPE" and "PROTOTYPE" plus shank FES.

Motion	ERGYS	Prototype	Prototype + shank FES
ankle flex/ext	97-109 (12)	80-86 (6)	83-86 (3)
knee flex/ext	70-131 (61)	62-126 (64)	71-132 (61)
hip flex/ext	73-112 (39)	42-91 (49)	54-96 (42)
hip ab/ad	61-84 (23)	37-78 (41)	46-84 (38)

Although the ERGYS and "prototype" FES-LCEs were both set to 0 W power output (PO) at their flywheels, the actual POs were greater than 0 W because of internal resistances (e.g., bearing, chains and sprockets). For the ERGYS, Figoni, et al. (1992) calculated that this would be 7.8 W. For the "prototype", PO was determined to be 9.3 W when shank muscles were not used, and 13.1 W when shank muscles were used. VO_2 was found to correspond to these PO levels (Figure 2), and was 18.1% higher when the shank muscles were used with the "prototype" device. This indicates a less efficient transfer of power from the leg to the pedal.

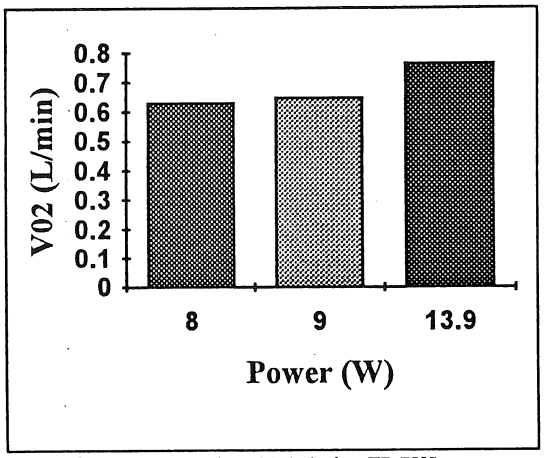

Figure 2. Oxygen uptake (VO_2) during ERGYS, "PROTOTYPE", and "PROTOTYPE"+shank FES exercise conditions.

Metabolic demand was similar for the ERGYS and the "prototype" system without shank FES, however, the addition of shank muscle FES produced the highest VO_2 level of the three exercise conditions. Thus, the cocontraction of the anterior tibialis and gastrocsoleus muscles appears to substantially increase the tangential pedal force while maintaining 0 W PO at the flywheel. This situation decreases the efficiency of power transfer from the pedals to the flywheel even though there was a very limited ankle range of motion. Since the ankle was mechanically braced to limit motion, the muscles were most likely contracting without contributing to the transfer of power. Although mechanically this may be inefficient, it may be advantageous due to the pumping action of the muscles to facilitate the venous return of blood, thereby aiding the circulatory system in meeting exercising muscle demands for O_2 and fuel substrates. Furthermore, the larger muscle mass incorporated can contribute to higher levels of VO_2 than can otherwise be obtained for greater cardiopulmonary training effects. Future work will continue the investigation of FES-LCE exercise systems to further optimize FES exercise training effects and minimize risks to users.

REFERENCES

Hooker S., et al. J. Rehabil. Res. Dev., 29, 1-11, 1992.

Ragnarsson K. et al. Arch. Phys. Med. Rehabil., 69, 672-677, 1988.

Schutte, L. et al. Proceedings of the Second North American Congress on Biomechanics, Chicago, (pp. 565-566), 1992.

Ezenwa, B. et al. Proceedings of the RESNA International '92 Conference, Toronto, (pp. 477-478), 1992.

Figoni, S. et al. Proceedings of the RESNA International '92 Conference, Toronto, (pp. 233-234), 1992.

ACKNOWLEDGEMENTS

This study was supported by the Rehabilitation Research and Development Service of the U.S. Department of Veterans Affairs (B587-RA andB433-RA.

COMPARISON OF CT AND MRI ESTIMATES OF INERTIAL PROPERTIES OF THE HUMAN TRUNK

D.J. PEARSALL and J.G. REID

Department of Anatomy and Cell Biology, and
School of Physical and Health Education, Queen's University, Kingston, Ontario, Canada, K7L 3N6

INTRODUCTION

The purpose of this study was to determine the difference in using Computed Tomography (CT) versus Magnetic Resonance Imagery (MRI) for calculation of inertial properties of the human trunk invivo. Two male subjects had CT and MR transverse images collected at three levels in the trunk (umbilical, +10 cm and +20 cm superiorly). Trunk scan mass, mass centers and moments of inertia were calculated for each image. The MRI-CT differences in mass, volume and density estimates in the abdominal region ranged from -0.3% to -7.6% while thoracic region measures varied from 7.0 to -1.8%. MRI and CT calculations of center of mass locations were found to be within 10 mm of each other. The differences in moment of inertia values were greater, ranging from -14.9% to 18.9%. Although the sample size was limited, these results suggest that MRI technique can be effective for determining trunk segment mass and density properties but greater care is required for moment of inertia evaluation.

REVIEW AND THEORY

Biomechanical modelling of the human body requires accurate measures of body segment inertial properties such as the masses, mass centers and moments of inertia. Most of these parameters have been interpreted from a limited number of cadaver studies such as Clauser et al. (1969) and Chandler et al. (1975). Other techniques, geometric modelling (eg. Hatze, 1980) and volumetric estimations (eg. Jensen,1978), have been introduced to approximate body segment parameters of living people based on the assumption of uniform density distribution within the segments. Another method of determining these parameters has been to reconstruct body segments from CT and MRI (eg Huang et al, 1976; Martin et al., 1989). These latter techniques have the advantage of being used on living subjects and can account for inhomogeneous mass distribution properties. The use of CT however is limited due to the risk of radiation exposure where as MRI has no known health risks. Mungiole et al. (1990) has shown for body limb segments that MR can provide comparable results to cadaver measures. However, it has yet to be determined whether MRI can be used to estimate trunk inertial parameters.

PROCEDURES

Two male subjects (S1 age = 28 yrs, Ht = 167 cm, M = 67 kg; S2 age = 52 yrs, Ht = 180 cm, M = 75 kg) had CT and MRI transverse scans collected at three levels in the trunk. CT and MRI scans were collected within the same week. The first image was collected at the umbilical level. The second and third images were collected 10 cm and 20 cm superior to the umbilicus level, respectively. Both subjects were in a supine position during image acquisition. CT images were collected on a GE CT/T continuum scanner using a window size of 250, CT number of -025, 10 mm thickness and a field of view radius 250 mm. MRI were collect on a Magnetrom 1.5 T with a spin echo sequence of 210 ms, 15 ms echo time and 10 mm thickness. A matrix (256 x 256) within a field of view of 500 mm was used. Digital images were transferred to a PC 486 computer where they were then analyzed. The mass properties in the CT scans were analyzed in a manner similar to Huang et al. (1976). For each image, pixel values were calibrated to known density values derived from tissue composition studies such as Woodward et al. (1986). For cortical bone (1.8 g/cc), muscle (1.06 g/cc), fat (0.96 g/cc) and inflated lung tissue (0.26 g/cc). For the MRI, pixels regions were marked from a set color range identifying different tissues and corresponding densities for cortical and cancellous bone (1.8 and 1.1 g/cc), visceral organs (1.06 g/cc), muscle, fat and lung tissues. Having transformed the images into density profiles and given the pixel volumes, pixel masses, trunk scan mass, mass centers and moments of inertia were calculated.

RESULTS AND DISCUSSION

The comparison of values was expressed in terms of the percent difference of MRI relative to CT (ie. (MRI-CT) / CT * 100). The differences in mass, volume and density estimates are presented in Table 1. At the levels of the umbilicus and 10 cm superior, differences ranged from -0.3% to -7.6%. These differences were small but the MRI technique consistently underestimated CT values. However, at +20 cm level, measure differences varied from 7.0 to -1.8%. Calculation of center of mass locations were found to be within 10 mm. Given the small discrepancy, the MRI technique appears to be as valid an estimator of segment volume, mass and density as CT based analysis.

Table 1. Comparison of CT and MRI Measurements of Mass, Volume and Density at Three Trunk Levels for both Subjects

		MASS (gm)	VOL (cc)	DENS (gm/cc)
S1	Z	%DIF	%DIF	%DIF
	0	-3.9	-2.5	-1.4
	+10	-7.6	-1.4	-6.2
	+20	0.6	-1.8	3.1
S2	Z	%DIF	%DIF	% DIF
	0	-3.7	-2.2	-1.9
	+10	-0.3	-0.9	-0.5
	+20	4.8	-0.2	7.0

The estimates of the moment of inertia are shown in Table 2. The differences between CT and MRI techniques were variable and greater than previously observed with the other parameters. Discrepancies ranged from -12.9% to 18.9% for S1 and -14.9% to 17.6% for S2. These larger variations may have been due to the time period between CT and MRI collection permitting for the rearrangement of abdominal contents. Another factor contributing to these differences was the difficulty in assigning bone regions in the MRI techniques. Furthermore, difficulty with MRI occurs in the thorax where the heart movement creates a considerable amount of image blurring, thus, making identification of cardiac muscle location difficult.

Table 2. Comparison of CT and MRI measurements of Moment of Inertia at Three Trunk Levels for both Subjects

(10 grams * cm^2)		Ixx	Iyy	Izz
S1	Z	% DIF	% DIF	% DIF
	0	5.0	-9.4	-12.9
	+10	2.9	3.8	-4.2
	+20	18.9	7.6	6.8
S 2	Z	% DIF	% DIF	% DIF
	0	8.4	-14.1	-14.9
	+10	9.0	-3.7	-6.1
	+20	-4.3	-9.6	17.6

The above results, although limited in sample size, suggests that MRI technique for determining trunk segment inertial properties can be effective, similar to finding by Mungiole et al. (1990) for limb segments. However, care must be given to identifying bone regions of the spine and rib cage and reducing movement distortions created by the heart to minimize error in moment of inertial estimates. If these limitations can be overcome, then the MRI technique could be employed to determine body segment inertial parameters and permit better biomechanical model representation of various population groups.

REFERENCES

Clauser, C.E. et al. *AMRL- Technical Report 60-70*, Wright-Patterson Air Force Base, OH., 1969.

Chandler, R.F. et al. *Technical Report DOT hs-801 430* Wright-Patterson Air Force Base, OH, 1975.

Hatze, H. *J. Biomech* 13, 833-843, 1980.

Huang, H.K. and Wu, S.C. *Comput. Biol. Med.* 6: 337-343, 1976.

Jensen, R.K. *J. Biomech* 11: 349-358, 1978.

Martin, P.E. et al. *J. Biomech* 22: 367-376, 1989.

Mungiole, M. et al., P.E. *J. Biomech* 23: 1039-1046, 1990.

Woodward, H.Q. et al. *Brit J Radiology* 59: 1209-1219, 1986.

Zatziorski, V. and Seluyanov, V. *Biomechanics VIII-B* 1152-1159, 1983.

ACKNOWLEDGEMENTS

This study was supported by the Natural Sciences and Engineering Research Council of Canada (Project A7154)

TRUNK MUSCULATURE MEASUREMENT OF THIN AND OBESE MALES USING MRI

Wood, S., Pearsall, D.J., Ross, R. and Reid, J.G.

School of Physical and Health Education, and,
Department of Anatomy and Cell Biology, Queen's University, Kingston, Ontario, K7L 3N6

INTRODUCTION

To accurately estimate the forces experienced about the lower back, detailed models of the musculoskeletal system of the human trunk have been proposed [eg. Tracey et al.(1989), McGill et al.(1989)]. The purpose of this study was to compare muscle geometry at the L4/L5 level using transverse Magnetic Resonance Imagry (MRI) of two distinct population groups: obese and thin subjects. The anatomical cross-sectional areas and relative position to the vertebral centroid of the psoas, paraspinals, rectus abdominis, and oblique muscles were calculated. No significant differences in cross-sectional area was found between groups; however, anteroposterior moments for rectus abdominis and obliques were significantly greater for the obese group.

REVIEW AND THEORY

The use of non-invasive techniques to measure the muscular geometry of the lumbar spine; such as CT and MRI. Reid (1985) directly compared muscular area and geometry using CT methods. Reid et al.(1987) used MRI's of 20 males to create regression equations and predictions of muscle areas based on anthropometric measures. McGill et al.(1989) collected values of muscular areas and geometry from 13 active males through CT scans which may be compared to MRI technology. Tracey et al.(1989), in addition to transverse MRI digitization, utilized sagittal scans to measure the angles from the vertical that the lumbar vertebrae describe. These articles have led to the specific inquiry into the special population groups which are analyzed in this study.

PROCEDURES

Ten subjects were selected on the basis of their relative obesity and thinness. Five obese subjects were chosen with body fat percentages (SIRI) greater than 30% and a Body Mass Index of over 29. The SIRI method of fat percent calculation uses lean body mass in junction with under water density values (Ross et al.1992). Five thin subjects were selected who had body fat percentages below 20% and Body Mass Indexes below 25. All subjects were selected from a common age and height group. Mean ages of 39.6 yrs (13.4) and 40.4 yrs (12.4) for obese and thin subjects, respectively. The mean height for the obese group was 177.6 cm (6.1) while the thin group was 171.8 cm (5.0).

Transverse MR images were collected from the level of the L4\L5 vertebral disc. The images were obtained using a Phillips Gyroscan 1.5T whole body scanner. A spin-echo sequence of 500 ms was used. All images were acquired on a 256 X 256 matrix within a 500 mm field of view, giving a 3.81 mm^2 pixel area. Transverse slices were 10 mm. The trunk, vertebral body profiles, and trunk musculature were digitized using a 486 PC with mouse mediated digitization software developed in the laboratory. The digitized musculature included: the right and left psoas, rectus abdominis, quadratus lumborum, and oblique muscle groups.

The superficial, intermediate, and deep groups of trunk extensor muscles were grouped as the right and left paraspinal muscles. From the digitized profiles, cross-sectional areas and centroids were calculated. The anteroposterior and mediolateral distances from the center of each muscle to the vertebral centroid ofvthe vertebreal body subsequently were calculated as a simple estimate of the moment arm lengths of these muscles acting on the spine at the L4/L5 level.

Comparisons between obese and thin groups were made by simple t-tests (pooled variance) to indicate if significant differences in the cross-sectional areas, anteroposterior and transverse moment arm distances were present.

RESULTS AND DISCUSSION

Table 1 presents the mean values for each muscle obtained for the thin and obese groups.

Table 1. Calculated Means of Cross-sectional area, Mediolateral (ML) and Anteroposterior (AP) Moments for the Thin and Obese groups.

	AREA(cm^2)	
	Obese	Thin
Paraspinal	22.2	24.4
Rectus Abd	10.1	7.0
Obliques	25.0	22.7
Psoas	16.3	17.4
Quad Lumb	8.5	5.3
	ML MOMENT ARM(cm)	
	Obese	Thin
Paraspinal	-3.4	-4.1
Rectus.Abd	-3.4	-3.6
Obliques	-12.9	-11.8
Psoas	-5.2	-4.7
Quad Lumb	-7.7	-7.7
	AP MOMENT ARM(cm)	
	Obese	Thin
Paraspinal	6.1	5.1
Rectus Abd	-10.0*	-7.8*
Obliques	-7.0*	-3.9*
Psoas	-1.6	-0.4
Quad.Lumb	2.7	2.5

* $p < 0.05$

No significant differences were found in the cross-sectional area of the trunk musculature between obese and thin subjects. However, given a larger sample size, significant differences may have been found. For example, the mean cross-sectional area of the rectus abdominis for the obese subjects was 10.1 cm^2 versus the 7.0 cm^2 for the thin subjects ($T=2.025, p=0.077, DF=8.0$). The mean areas calculated for the thin subject were less than those reported by Reid (1985) and McGill et al.(1989) while the obese subjects had muscle areas greater than those cited. For instance, the mean areas for the rectus abdominis was calculated to be 10.1 cm^2 and 7.0 cm^2, for obese and thin groups, respectively, while Reid (1985) reported 10.0 cm^2 for the same muscle.

Significant differences were observed for the anteroposterior moments of the rectus abdominis and the oblique muscles, with obese subjects having a greater moment arm distance ($T=2.5, p<0.05$). The distances calculated were similar to those derived by Tracey et al.(1989)and McGill et al.(1989). For example, the anteroposterior moment distance from the centroid of the paraspinal group was 6.1 cm and 5.1 cm for obese and thin groups respectively, while Tracey reported 5.8 cm and McGill observed 6.1 cm.

No significant differences were observed comparing the mediolateral centroid distance of the trunk musculature. Mediolateral distances were consistent with values presented by Tracey et al.(1989). For instance, the mediolateral moment arm calculated the rectus abdominis was 3.4 cm and 3.6 cm for obese and thin groups respectively, while Tracey has reported the same moment arm to be 3.5 cm.

Although cross-sectional area has not been a component of significant variance, these values do not reflect the quality of the measured musculature. The amount of adipose tissue within the muscles of the obese group may be significantly greater than the thin group.

Given that significant differences in AP muscular geometry were observed between thin and obese groups suggests that different muscle group coordinations may exist. Further differences may have been observed had larger sample sizes been compared; for instance, in cross-sectional of the rectus abdominis. If further muscular geometric discrepancies could be resolved, this may help to identify different loading mechanisms on the lumbar spine for specific population groups.

REFERENCES

McGill, S.M. et al. Journal of Biomechanics, Vol.21 No.4, 329-341,1989.

Reid, J.G. et al. Spine, Vol.12 No.3, 273-275, 1987.

Reid J.G. & Costigan P.A., The Journal of Orthopaedic and Sports Physical Therapy, Vol.6 No.5, 278-280, 1985.

Ross, R. et al. Journal of Applied Physiology, 787-795, 1992.

Tracey, M.F. et al. Spine, Vol.14 No.2, 186-193, 1989.

ACKNOWLEDGEMENTS

This study was supported by the Natural Sciences and Engineering Research Council of Canada (Project A7154).

FUNCTIONAL RESERVE AT THE TRUNK OF ELDERLY AND YOUNG FEMALES DURING THE SIT-TO-STAND

Thomas M. Lundin*, Mark D. Grabiner*, Dennis W. Jahnigen**

*Department of Biomedical Engineering
**Department of Geriatric Medicine
The Cleveland Clinic Foundation, Cleveland, OH 44195

INTRODUCTION

Loss of independent mobility is often a cause for institutionalization in elderly people. The sit-to-stand (STS) maneuver is a fundamental mobility activity of daily living which poses a mobility problem to more than 2 million persons older than 64 years of age in the United States (Dawson et al., 1984). However, there have been relatively few biomechanical studies of STS reported in the context of improving mobility deficits in elderly persons. Of those studies that have been reported, one common finding has been related to the trunk. Wheeler et al., (1985) reported that elderly subjects demonstrated greater trunk flexion than young subjects when rising from a standard chair. Alexander et al., (1991) also reported a significantly larger trunk flexion in elderly subjects compared to young subjects and stated that two biomechanical requirements need to be met in order to rise from a seated position. The requirements are: (a) to locate the total body center of mass within the area of foot support and establish postural stability; and (b) to generate the joint torques required to rise. Schultz et al., (1992) suggested that the elderly subjects placed more emphasis on the former by increasing trunk flexion, reasoning that as the trunk rotates forward, the center of mass moves further anteriorly thereby increasing postural stability.

The purpose of the present study was to determine the extent to which the increased trunk flexion observed in an elderly population during STS reflects a strategy selected on the basis of the maximum muscular strength capability of the trunk/hip extensors. This purpose was based on the expectation that as the trunk flexes, the trunk and hip extensor musculature lengthens and thus increases its force producing capability as dictated by the length-tension relationship. Two hypotheses were made: 1) the functional reserve (demands of the STS task on the trunk extensors relative to the maximum isometric trunk strength) of the elderly would be less than that of the young population, and 2) by increasing the trunk flexion angle during STS, elderly subjects would be shown to increase their functional reserve at the trunk.

PROCEDURES

Seven young [22.9 (1.0) years] and seven elderly [74.3 (4.1)] female subjects volunteered to participate in this study. The elderly subjects were all healthy and without neuromuscular or musculoskeletal impairment. There were two components of the data collection, dynamic analysis of STS and measurement of maximum effort trunk extension strength.

The body was modeled as an eight link system with reflective markers defining to the bilateral feet, shanks, and thighs and the pelvis and trunk. Motions of the reflective markers were recorded by four video cameras at a sampling rate of 60 Hz. Ground reaction forces and moments under each foot and chair were collected with three AMTI force plates. Each subject performed five trials of the sit-to-stand maneuver at a self-selected rate and with arms placed across the chest. Subjects were initially positioned on the chair with trunk oriented vertically, feet slightly adducted and shoulder width apart, and knees flexed approximately 110 degrees. The backrest of the chair was located just distal to the inferior angle of the scapula and the front edge of the seat was midway between the greater trochanter and lateral femoral condyle markers. The chair height was adjusted so that the subjects' thighs were parallel with the ground. An inverse dynamics approach was used to calculate ankle, knee, hip, and trunk kinetics. The calculated moment curves were normalized to body weight (BW) and height (BH). Maximum effort isometric trunk extension strength was measured on a Kin-Com isokinetic dynamometer at 45, 30, and 15 degrees flexion, zero degrees (vertical trunk) and 15 degrees extension. The resultant trunk extension moments were normalized to BW and BH.

For the STS variables an initial 2 by 2 by 5 (age by leg by trial) analysis of variance (ANOVA) with repeated measures across leg and trial was performed. The isometric trunk extension data were analyzed using a 2 by 5 (age by trunk angle) ANOVA with repeated measures across trunk angle.

RESULTS AND DISCUSSION

The ANOVA on the STS data revealed that there was no effect of trial thus these data were pooled across trial and can be seen in Table 1. Consistent with expectations, the elderly subjects were observed to perform STS with a greater trunk flexion angle (with respect to vertical) than the young subjects ($p=0.065$). However, in contrast with the report of Schultz et al., (1992) the increase in trunk flexion angle did not result in an anterior shift in center of pressure (relative to the foot center of gravity with positive values reflecting anterior shifts) at liftoff from the chair. The increase in trunk flexion also had no effect on the comparison between peak trunk extensor moments during STS between the two groups.

Table 1

	Trunk flexion angle (degrees)	Center of pressure (cm)	Peak trunk moment (%BW*BH)
Elderly	44.5 (10.8)	-1.11 (3.78)	10.20 (2.02)
Young	35.6 (4.3)	-0.63 (4.42)	11.47 (1.35)

The results of the maximum isometric trunk extension moment values (%BW*BH) at 45, 30, and 15 degrees of flexion are shown in Table 2. As expected, the age-related differences for maximum isometric trunk extension moment at all angles tested were significant ($p<0.001$).

Table 2

	45	30	15
Elderly	18.77 (3.69)	16.08 (3.45)	13.19 (2.99)
Young	32.42 (4.17)	30.38 (6.01)	26.82 (5.09)

From the STS and isometric strength data an estimated functional reserve value can be calculated for each age group. The elderly population (using the isometric value at 45 degrees flexion because it is the isometric angle which is closest to that attained during the STS task) required 54% of their maximum isometric trunk strength for the STS maneuver, their functional reserve therefore was 46%, while the young (using the isometric value at 30 degrees flexion) had a functional reserve of 62%. These results support the first hypothesis that the elderly would have a smaller functional reserve than the young population. Had the elderly population flexed to a lesser extent during STS (30 degrees) they would have been required to generate 63% of their maximum isometric trunk strength to rise from the chair, thus their functional reserve would have decreased to 37%. This result supports the second hypothesis, that by increasing the trunk flexion angle during STS, elderly subjects increase their functional reserve at the trunk.

The present study does not suggest that postural stability during STS is not an important performance factor in successfully executing the STS task, but rather that additional performance elements may play significant roles in the selection of a motor strategy. It is reasonable to assume that as the joint moments required by coordinated motor tasks, such as the STS, approach maximum levels that the task will become more difficult to execute skillfully. The results of this study support the contention that a motor strategy implementing increased trunk flexion during the STS may be selected to increase functional reserve at the trunk by taking advantage of the length-tension relationship of the trunk extensor muscles.

References

Alexander et al., *J. Gerontol. Med. Sci.*. 46:91-98, 1991.

Dawson et al., Advanced Data From Vital and Health Statistics. 133, 1984.

Schultz et al., *J. Biomechanics*. 25:1383-1391, 1992.

Wheeler et al., *Phys. Ther.* 65:22-26, 1985.

The authors appreciate the assistance of L. von Haefen with the data collection.

EFFECTIVENESS OF CONTOUR CUSHIONS IN DISTRIBUTING SEATING PRESSURES

S. Haynes, ME, S. Sprigle, PhD, J. Hale, PhD
Rehabilitation Engineering Center, The University of Virginia, Charlottesville, Virginia, 22903

INTRODUCTION

The occurrence of pressure sores (decubitus ulcers) is a common concern among wheelchair users. To address this concern clinicians search for cushions which will allow the users to maintain a balance between pressure relief and functionality (e.g. dynamic stability and ease of transfer). In this study, fifteen cushions with varying stiffnesses, depths, and contour shapes were loaded using an instrumented buttock model, to quantify the effects of these cushion variables on buttock-cushion interface pressures and cushion deflection. Results showed a strong interaction between the stiffness and depth of contour and between the stiffness and contour shape. Results also indicated that cushions formed into the shape of a mechanically measured (and thereby deformed) contour did not distribute pressure as well as cushions formed into the known (undeformed) shape of the model.

REVIEW AND THEORY

Pressure sores are widely thought to occur when the tissue is deformed or compressed against a bony prominence to the extent that capillary blood flow is restricted long enough to cause tissue necrosis (death). Therefore, the usefulness of a wheelchair cushion in the prevention of pressure sores is based, in part, on its ability to distribute loads which cause deformation in the buttock tissue. It has been shown that contoured cushions are more effective in distributing these loads than flat cushions (Sprigle et al., 1990). Chow (1974) hypothesized that a cushion cut to match the undeformed contour of the buttock would provide hydrostatic loading, which would maximize the pressure distribution and thereby minimize tissue distortion. Because buttock tissue deforms any time a person is seated, devices currently used to measure buttock contours for the purposes of fabricating custom formed cushions, actually measure a "deformed" buttock shape.

The objective of this research was to test the hypothesis that using an undeformed buttock measurement to create a contoured cushion significantly improves the load distribution as compared to a contour cushion based on a deformed buttock contour. Secondary objectives were 1) test how interactions between cushion stiffness, contour depth, and contour shape affect the load distribution, and 2) quantify the relationship between internally and externally measured pressures.

PROCEDURES

To meet these objectives, an axisymmetric model was built, in the shape of a merosphere (section of a hemisphere) with an 8.89 cm (3.5 in.) radius. The model consisted of a solid cylindrical core, surrounded by glycerine-based gel, with a solid top plate to transfer load from a weight bearing shaft to the model as shown in Figure 1. The core, designed to represent the ischial tuberosity while maintaining axisymmetry, was instrumented to measure pressures on the tip and two sides of the core (medial and lateral internal pressures, respectively). The two lateral transducers were designed and fabricated in-house. They consisted of a four strain gage bridge circuit attached to an aluminum shim stock spring with a loading pad mounted flush with the surface of the core in the unloaded condition. Flexible, pneumatic pads (connected to the Oxford Pressure Monitor; Talley Ltd., Hampshire, England) were attached to the surface of the model, at the center and at a 5.08 cm (2 in.) radius from the center, to measure pressure between the cushion and the gel model (medial and lateral external pressures, respectively).

The instrumented model was attached to a weight bearing shaft and placed onto cushions, under a vertical load of 21.5 kg (47.4 lbs.), to simulate the weight bearing load on one buttock of a person weighing approximately 64.5 kg (142.2 lbs.). The cushions were placed onto a contour gage, designed, to measure the surface shape of a loaded cushion. The chair design included an 8 x 8 array of linear potentiometers attached to arrow shafts. These probes pass through pre-drilled holes in the cushion which match the 8 x 8 array. Suction cups were used to keep the top of the probes at the

cushion surface during such that they maintain contact with the surface of the cushion. Five of these potentiometers were used to track the cushion deflection during testing; one directly under the core (medial), and four at a radius of 5.08 cm (2 in.) (lateral).

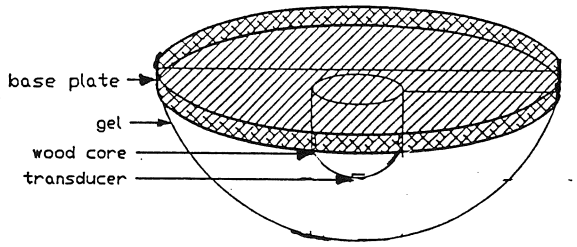

Figure 1: Axisymmetric buttock model.

A total of 15 cushions, each 4" thick, were tested. The following independent variables were varied; cushion stiffness (soft-HR45, medium-HR2855, and hard-HR70), contour depth (flat, 25 mm, and 50 mm), and contour shape (one undeformed and two deformed). The two deformed contours were obtained using two cushions of different stiffness placed in the contour gage described above. To eliminate the effects of contour depth on the deformed cushions, the gel model was weighted into both cushions until a maximum contour depth of 50 mm was reached. The undeformed contour was obtained by using the equation which defined the surface of the merosphere. Each cushion test was repeated three times. During each trial, seven measures were recorded; internal and external medial/lateral pressures, the total vertical deflection of the gel model, and the vertical medial/lateral deflection of the cushion.

RESULTS

The research design permitted analysis of two separate interactions. The interaction between foam stiffness and contour shape (deformed vs. undeformed) was significant for all dependant variables ($p < 0.0005$). Similarly, the interaction between contour depth and foam stiffness was significant for all dependent variables ($p < 0.0005$). Keeping in mind these interactions, the effects which were seen were as follows: 1) greater pressures and cushion deflections were measured using deformed cushions than undeformed cushions; 2) increased cushion stiffness and decreased contour depth both led to increased pressures; 3) increased cushion stiffness and increased contour depth both led to decreased cushion deflection and decreased vertical deflection of the core. There was a strong correlation between internal and external pressures ($r > 0.94$). In 13 out of 15 cases, internal medial pressures averaged 1.25 times higher than external medial pressures.

DISCUSSION

The strong interactions between the stiffness, depth, and contour shape of the cushions prohibit broad generalizations about the effects of any one independent variable on any one dependant variable. For example, the effects of contour shape diminish as the depth of the contour is reduced and the cushion begins to resemble a flat cushion.

As stated in the introduction, there are other factors which must be considered when designing an optimum cushion. The dynamic stability as well as the ease of transfer into or out of a wheelchair is greatly affected by the stiffness of the cushion and the depth of the contour. However, when a deep contour is warranted, this research indicates that an undeformed buttock contour may be better at distributing pressures than a deformed contour.

In conclusion, it can be stated that the use of a contour measuring device to create a custom formed cushion does have a statistically significant effect on factors which contribute to pressure sores. However, these effects interact significantly with contour depth and foam stiffness.

REFERENCES

Chow,WWC, "Mechanical Properties of Gels and Other Materials with Respect to their Use in Pads Transmitting Forces to the Human Body". Ph.D. Dissertation, University of Michigan, Ann Arbor, 1974.

Sprigle,S. et al., "Reduction of Sitting Pressures with Custom Contoured Cushions", J.Rehab. Research, Vol 27 No. 2, 1990: 135-140.

A TECHNIQUE FOR THE CALCULATION AND REPRESENTATION OF THE RANGE OF MOTION AT THE SHOULDER

G. F. Miller and W.G. Darling

Department of Exercise Science, The University of Iowa, Iowa City, IA 52242

INTRODUCTION

The purpose of this study was to develop a method of calculation and representation of the continuous range of motion of the shoulder complex, or more specifically, the complete angular orientation of the humerus relative to the trunk. This includes the ability to measure motion outside of the anatomical planes, as well as the amount of humeral rotation.

REVIEW AND THEORY

The shoulder joint has long been recognized as one of the most complex joints in the body. Research on the function of the shoulder complex dates back over 100 years beginning with the works of Cleland (1881) and Cathcart (1884). Yet there is relatively little complete range of motion (ROM) data for the shoulder joint compared to many of the simpler joints in the body.

Experimental determination of shoulder ROM has been accomplished using several different techniques over the past 40 years. They include goniometric techniques, use of Cybex type machines, video and film analysis, external linkage systems, sonic digitizing, and magnetic tracking devices. Goniometers are probably the most straightforward and easiest to use of these methods, but unfortunately ranges of motion are normally measured in only the three primary anatomical planes of movement of the shoulder. These studies are often incomplete in that they do not measure ranges of all possible rotations of the joint, nor do they provide a continuous ROM representation. Of all the methods previously listed, only the one study involving sonic digitizing (An et al. 1991) measured the continuous ROM at the shoulder including the amount of humeral rotation. In that study the angular orientation of the humerus relative to the scapula was determined in cadavers. Three Euler angles were used that defined the amount of humeral elevation, the plane of humeral elevation, and the amount of humeral rotation.

PROCEDURES

Determination of the angular orientation of the humerus relative to the trunk was accomplished by fixing one coordinate system in the right humerus, R_H, and a second in the trunk, R_T. With the arm in anatomical position, the X_H, Y_H,and Z_H axes of the humerus were directed anteriorly, laterally, and distally, respectively, and were parallel with the X_T, Y_T,and Z_T axes of the trunk coordinate system. The positional data was collected using a three-camera WATSMART system (Northern Digital, Waterloo , Canada) that recorded the 3-D coordinates of small infrared light emitting diodes. The diodes were fixed to rigid components attached to the trunk and right arm, and allowed definition of a coordinate system in each segment.

A y-x-z Cardan rotation sequence was used to define and represent the angular orientation of the humerus relative to the trunk. The coordinate systems were not parallel initially: The Z_H axis was parallel with the X_T axis. The X_H axis was parallel with the negative Y_T axis. The Y_H axis was parallel to the negative Z_T axis. From this initial orientation, the Cardan angles were defined by the following rotations of the R_H system:

1. A rotation of the humerus through θ about the negative superiorly directed $Z_T=Y_{H1}$ axis, resulting in an initial intermediate system R_{H1} (X_{H1},Y_{H1},Z_{H1});
2. A rotation through ϕ about the positive $X_{H1}=X_{H2}$ axis, resulting in a second intermediate humeral system R_{H2} (X_{H2},Y_{H2},Z_{H2});
3. A rotation through ψ about the positive $Z_{H2}=Z_H$ axis, resulting in the final position of R_H relative to R_T.

The first rotation, θ, defined the plane of elevation of the humerus. The angle θ may be thought of as the angle that the projection of the Z_H axis on the transverse plane of the trunk makes with the X_T axis. For brevity, the plane of elevation θ was also referred to as the yaw angle. The second rotation, ϕ, defined the angle of elevation of the humerus relative to the trunk. The third rotation, ψ, defined the amount of rotation about the longitudinal axis of the humerus.

When the second rotation approaches $\pm 90°$ in an ordered rotation sequence such as this, the first and third rotations are about parallel axes, and cannot be distinguished separately. For the defined sequence, this position corresponds to the humerus being oriented vertically at the side or above the head. This problem was avoided, however, due to the nature of the protocol (discussed below).

Four subjects were used to test the method, two male and two female members of the University swim teams. The protocol involved the subject elevating the arm in a series of vertical planes by tracing specified vertical target strips of paper with a beam that was emitted from a laser pen fixed to the humeral cuff component. This provided experimental control over the plane of elevation of the humerus. Thus even at elevations (second rotation) which the first and third rotations could not be distinguished, the value of the first rotation (yaw angle) was known, allowing calculation of the third rotation (humeral rotation), and the singularity problem discussed earlier was avoided. As the arm was elevated, the subjects were asked to maintain the maximum possible amount of internal or external humeral rotation.

Several angles were chosen as being representative of the limits of a subject's ROM: the maximum elevation within each plane of elevation, and the amount of internal or external humeral rotation at the point of maximum elevation; the maximum amount of internal or external rotation within each plane of elevation, and the elevation at which maximum rotation occurred. The reliability of the data collection technique was established using intraclass correlation coefficients (ICC) on these angles.

RESULTS AND DISCUSSION

The validity of the method was checked by computing the correlation coefficients between the angles calculated from the segment position data and angles determined from precision potentiometers mounted over the three rotation axes on a physical model. Coefficients were above 0.98 for all three angles calculated.

Based on the ICC analysis of angles representative of ROM limits, the method of data collection and analysis was shown to be highly reliable from trial to trial within days (Table 1).

Table 1. Intraclass correlation coefficients for trial to trial reliability of angles of interest, for each subject, each day.

			Internal	Rotation				
Sub	MIR		MIREL		MEL		MELRO	
	D1	D2	D1	D2	D1	D2	D1	D2
JJ	.97	.98	.99	.95	.99	.99	.89	.99
MY	.99	.99	.99	.98	.97	.99	.96	.99
SM	.93	.99	.96	.98	.99	.99	.98	.99
TG	.96	.95	.14	.89	.99	.99	.99	.99
			External	Rotation				
Sub	MER		MEREL		MEL		MELRO	
	D1	D2	D1	D2	D1	D2	D1	D2
JJ	.89	.91	.99	.99	.99	.99	.85	.97
MY	.80	.78	.89	.91	.99	.96	.92	.77
SM	.97	.95	.95	.99	.99	.99	.91	.97
TG	.97	.96	.97	.99	.99	.99	.98	.98

MIR = MAXIMUM INTERNAL ROTATION
MIREL = ELEVATION AT MIR
MER = MAXIMUM EXTERNAL ROTATION
MEREL = ELEVATION AT MER
MEL = MAXIMUM ELEVATION
MELRO = ROTATION AT MAXIMUM ELEVATION

Day to day reliability coefficients of these angles ranged from 0.63 to 0.96, with the highest values for maximum elevation (> 0.89, Figure 1) and internal rotation at maximum elevation (> 0.80, Figure 1). Thus these measures could be used to develop range of motion profiles of an individual (Figure 2). There were no apparent differences in reliability estimates of males versus females or of individuals with varied body sizes. The reliability of all measures would probably be improved by providing subjects with more sessions in which to practice and become used to the rather complex task of elevating the arm in a specific plane of elevation while maintaining maximal humeral rotation.

The Cardan rotation sequence used has several advantages over the currently used terminology for describing the orientation of the shoulder complex. Combining plane of elevation (yaw angle) of the humerus with the angle of elevation provides a simple and easily visualized description of where the longitudinal axis of the humerus is relative to the trunk. Adding the third rotation in the sequence completes the information necessary to completely represent and visualize this orientation.

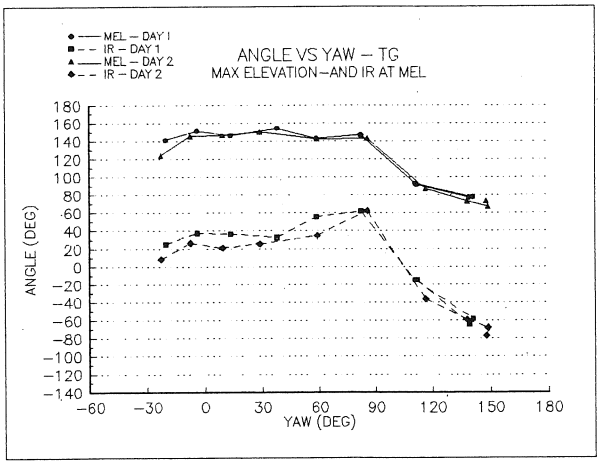

Figure 1. Maximum elevation (MEL) and humeral rotation at maximum elevation (IR) vs. plane of elevation, while maintaining internal rotation. Values from day 1 and day 2 are shown for one subject.

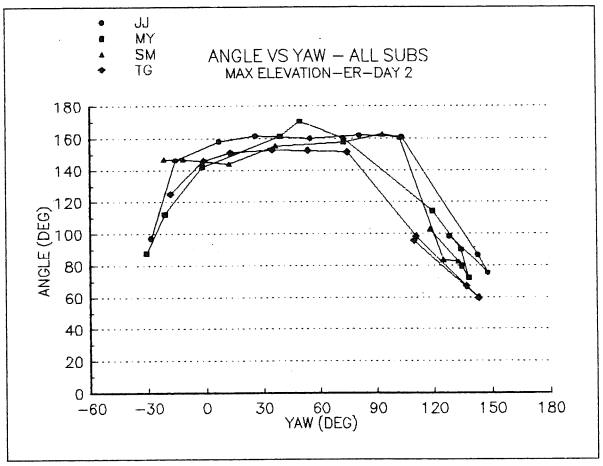

Figure 2. Maximum elevation vs. plane of elevation. Values for all subjects shown for maintenance of external rotation while elevating.

REFERENCES

An K.-N. et al. J. Ortho. Res., 9, 143-149, 1991.
Cathcart, C. J. Anat. Physiol., 18, 211-218, 1884.
Cleland J. Lancet, 1, 283-284, 1881.

KINETIC CHARACTERISTICS OF WHEELCHAIR PROPULSION UTILIZING THE SMART^{Wheel}

R.N. Robertson and R.A. Cooper

Human Engineering Laboratory, California State University, Sacramento, Sacramento, CA, 95819

INTRODUCTION

The ability of an individual to push a wheelchair efficiently and without injury is in large part related to the way in which the user applies force to the push rim. A number of factors influence the interaction between wheelchair user and chair. These include level of spinal cord injury, design of the wheelchair, fit between user and chair, stroke mechanics, user fitness levels, and history of upper extremity injury. Understanding forces are applied to the push rim will allow the clinician to recommend changes in these factors, which will allow a wheelchair user to push a chair more efficiently and without producing trauma to the upper extremity. A device called the Smart^{Wheel} has been developed (Watanabe et al., 1991; Cooper et al., 1992) which allows the measurement of push rim forces. The 2-dimensional Smart^{Wheel} allows measurement of push rim forces in the plane of the wheel and the turning moment about the hub axis. This paper describes the forces and torques applied by the wheelchair user to the push-rim. Understanding how forces generated by the individual are applied to the push rim will provide insight into how these forces are related to optimizing efficiency, improving performance, identifying mechanisms of injuries (such as carpal tunnel syndrome, elbow tendonitis, and shoulder rotator cuff injuries), developing injury prevention techniques and implementing changes in wheelchair design.

REVIEW AND THEORY

No study to date has investigated the actual forces and torques being applied to the push rim during wheelchair propulsion, although several studies have measured various aspects of force production. Cooper and Cheda (1989) described a technique for measuring forces and torques applied to the push rim of racing wheelchairs. Van der Woude et al. (1989) measured forces employing a force transducer mounted in the wheel center. Tupling et al. (1986) used a force plate during initiation of wheelchair movement, while Brauer and Hertig (1981) measured static torque with a spring system and linear potentiometers. Brubaker et al. (1982) measured static forces applied to the push rim by utilizing strain gauged beams attached to a moveable seat. The present study is intended to investigate realistic push rim forces and torque during wheelchair propulsion. This information will be used to institute changes in propulsion mechanics and wheelchair design in order to reduce the potential for injury and make the wheelchair user more efficient.

PROCEDURES

Each of the eleven individuals (4 ambulatory men, 4 ambulatory female, and 3 male wheelchair users) gave informed consent to participate in this study. Subjects were asked to push a Quickie 1 wheelchair secured to the CSUS dynamometer (Cooper, 1989a; Cooper, 1989b) and fitted with the 3-channel wheel (Smart^{Wheel}) on its right side. Each subject was asked to propel the wheelchair at 1.34 to 1.79 m/s for 3 minutes for accommodation. Subjects monitored his/her speed by viewing a digital tachometer mounted at the front of the dynamometer. Data were collected at 75 Hz per channel for approximately 10 complete strokes. Processing of the signals from the beam mounted strain gauges resulted in a determination of forces in the x and y direction and moment about the z-axis (x - anterior-posterior; y - superior-inferior; z - medial-lateral)

RESULTS

Five propulsive strokes were analyzed for each subject. Discrete variables were determined for the forces in the x and y directions. Tables 2 and 3 depicts the mean and standard deviations of these variables for each group (F-NWC female non-wheelchair user; M-NWC male non-wheelchair user; M-WC male). An impact spike was analyzed for both magnitude and rate of rise. The wheelchair users demonstrated a more rapid rise in the x-

direction than in the y-direction, and the non-wheelchair users had considerably higher rates of rise in the y-direction. Peak forces were higher for wheelchair users in the x-direction but lower in the y-direction and the peak forces were maintained for longer periods of time for the wheelchair users. The duration of propulsion was longer for wheelchair users.

1A.

	Impact Spike (N)	Peak Force (N)	Impulse (N·s)
F-NWC	17.4 (6.3)	22.8 (4.6)	4.07 (1.31)
M-NWC	16.7 (12.1)	23.8 (19.7)	4.68 (3.79)
M-WC	20.7 (1.1)	29.1 (2.0)	8.61 (2.23)

1B.

	Rate of Rise (N/s)	Duration of Propul. (sec)	Duration of Peak Values (sec)
F-NWC	186.6 (49.4)	.366 (.006)	.155 (.035)
M-NWC	164.7 (106.8)	.248 (.231)	.154 (.032)
M-WC	193.3 (74.1)	.662 (.143)	.269 (.101)

Table 1 A) and B) Magnitude and Duration of X Forces.

2A.

	Impact Spike (N)	Peak Force (N)	Impulse (N·s)
F-NWC	35.6 (6.5)	71.9 (16.8)	12.50 (3.70)
M-NWC	49.0 (11.4)	81.9 (6.0)	15.70 (1.70)
M-WC	39.5 (10.4)	51.5 (11.3)	18.10 (5.00)

2B.

	Rate of Rise (N/s)	Duration of Peak Values (sec)
F-NWC	396.7 (36.0)	.155 (.035)
M-NWC	399.4 (75.4)	.154 (.032)
M-WC	178.6 (159.0)	.269 (.101)

Table 2 A) and B) Y Forces

DISCUSSION

Push rim forces were shown to differ in the x and y directions and between wheelchair and non-wheelchair user. The rapid rate of rise of the impact spike for the non-wheelchair users in the y-direction indicates that structures in the upper extremity may be experiencing a rapid force loading. This may be a possible cause for injury particularly over repeated strokes. The wheelchair users appeared to maintain peak forces at moderate levels for longer periods of time, whereas the non-wheelchair user had rapid rises to high force levels (in the y-direction), with these forces being maintained for shorter time periods. The effect of these forces applied to the push rim on injury to the upper extremity and on efficiency of propulsion needs further investigation. The force data needs to be analyzed in the 3 orthogonal directions and combined with 3-dimensional kinematic information in order to get a more complete understanding of these processes. It may be that the experienced wheelchair user produces a stroking pattern which reduces the potential for injury over repeated strokes, while producing a less than optimal application of force to the push rim.

REFERENCES

Brauer, R. et al. Proceedings of the 1981 Biomechanics Symposium, ASME/ASCE Mechanics Conference, (pp. 113-116), 1981.

Brubaker, C. et al. Proceedings of the 5th Annual Conference on Rehabilitation Engineering, (pp. 111), 1982.

Cooper, R. et al. Proceedings of the. IEEE-EMBS 11th International Conference, Seattle, (pp. 530-1531), 1989.

Cooper R.A. J. Rehab. Res. Develop., 26, 63-70, 1989a,

Cooper R.A. Proceedings of the 12th Annual RESNA Conference, New Orleans, (pp. 450-451), 1989b.

Cooper, R.A. Adapt. Phys. Act. Quart., 7, 74-85, 1990.

Cooper R.A. et al. Proceedings of the 14th Annual IEEE/EMBS International Conference, Paris, (pp. 1544-1545), 1992.

Tupling, S. et al. Ergonomics, 29, 303-311, 1986.

Van Der Woude, L. et al. J. Med. Engr. Tech., 13, 136-141, 1989.

Watanabe, K. et al. Proceedings of the IEEE-EMBS 13th International Conference, Orlando, (pp. 1817-1818), 1991.

SONIC COORDINATE TRACKING SYSTEM FOR 3D DYNAMIC POSTURE ACQUISITION

U. Raschke, J. Foulke and D.B. Chaffin
Center for Ergonomics, The University of Michigan, Ann Arbor, MI 48109

INTRODUCTION

Most typical work tasks require complex and dynamic 3D movements. Recently, 3D computer biomechanical models have been introduced to estimate the internal forces on individuals as they perform these typical work tasks. However, a major obstacle toward the widespread use of these models is the accurate representation of the postures, both statically and dynamically. Chaffin et al. (1991) showed that the internal force estimations of these biomechanical models can be very sensitive to posture. As these motions in industry typically involve walking and twisting, a system is needed to obtain data from both body sides and over a large (often greater than 2m) volume. This escalates the cost of 3D video based systems as cameras and image processing hardware are added. Therefore, it was desired to develop a cost effective system easily configured and accurate enough to dynamically capture work tasks.

The sonic coordinate tracking system fulfills these requirements. It uses a parallel hardware architecture providing redundant information from multiple body sites with minimal penalty to the sampling rate. Coupled with error reducing data analysis techniques, this system is able to reduce the marker detection dropout and noise interference problems common in complex tasks.

Both static and dynamic accuracy laboratory tests were performed. The results indicate that the system is able to dynamically capture the motion of joint markers at typical material handling speeds.

REVIEW AND THEORY

Sonic based systems have been described to capture dynamic hand movements (Youm et al. (1978), Fleischer et al. (1983)) and static postures (Hsiao et al. 1990). These systems all use the time of flight of a sonic pulse, emitted from a device attached to a point of interest on a subject to microphones located in the room. This time is translated into a distance from the speed of sound in air. Given at least four distances to non-coplanar receivers at known locations, the spatial coordinates of the emitter can be triangulated. In contrast to the current system, minimum systems use only three distance readings which are augmented with some *a priori* information about the environment to solve for a unique 3D spatial location. In order to increase the configuration flexibility of the new system, the triangulation equations were solved requiring four distance readings, but omitting the necessity for *a priori* information.

In order to capture dynamic motions, the receivers in the environment must be able to listen for an emitted sonic pulse in parallel. Similar to the system described by Youm et al. (1978), this design uses parallel hardware architecture, dedicating a timing counter to each receiver. When the location of a given emitter is to be determined, the receiver counters are all reset and started with the emission of the sonic pulse from the emitter. Each receiver channel stops its counter when it receives the pulse. Thus, the pulse time of flight to each receiver is found in parallel, allowing for rapid sampling. The current system is configured such that all of the receivers receive the emitted sound before another emitter is fired. This requirement limits the sampling rate of the system to the sonic time of flight over the environmental test volume. Given a 2 meter volume and the speed of sound of 344m/sec, the system can sample at approximately 344/2=172 samples/sec/emitter.

A characteristic of sonic devices used is that they are fairly directional. This means that the sound energy is highest along the acoustic axis (the axis out of the center of the emitter) and falls off sharply toward the sides. Hsiao et al. (1990) found this to only minimally effect the accuracy of their static system, however this characteristic is undesirable when tracking objects, as the direction of the acoustic axis of the emitter may change drastically as the object moves (emitter is attached to the object). If the acoustic axis deviates too far from the direction of the receivers, the signal may fail to be detected. In order to reduce this type of error, a sonic source which radiates in all directions is desirable. Youm et al. (1978) used a spark gap emitter which has these characteristics. However, the signal energy is very broadly distributed across the frequency spectrum using this type of emitter (white noise), and therefore the receivers, which tend to be sensitive to a narrow frequency range, receive only a fraction of the total energy output. In contrast, for the system described here, narrow band emitters (matched to the receivers in frequency) were enhanced with hemispherical reflectors to distribute the emitted energy. The hemisphere is mounted such that the signal energy out of the emitter bounces against the convex hemisphere and is spread. This increased the amount of directional change the emitter can have while still having its signal detected by a receiver.

A test of the parallel receiving sonic tracking system under laboratory conditions was performed.

PROCEDURES

The sonic system was implemented on an 16MHz 386 PC computer. Custom hardware was developed including the parallel receiver detection amplifiers and counters, emitter firing electronics and associated hardware multiplexing. The receiver counters were set to count at 1MHz. The conversion from receiver counts (in μsec) to distance was found empirically by regressing known distances against system counts. This regression equation has a non-zero intercept which is in contrast to the assumption made by Hsiao et al. (1990). However, it can be explained as there is overhead in the setup of the hardware before the counting actually begins and a minimal amount of energy which must be received before a pulse is detected. Although the system is to work with multiple sets of receivers and emitters, one emitter and five receivers were used for the test case. Custom software was written to control the hardware, collect the data and solve the triangulation equations. As part of the software package, a calibration routine locates the receivers in the room. As it is difficult to accurately measure the relative location of the receivers in 3D using tape measures, a reverse calculation technique is used to find the receiver locations based on the locations of emitters on a pre measured calibration fixture. Five receivers were mounted on a rectangular frame 1 meter from the ground and 1.3 by 0.64 meters in size. Both static and dynamic accuracy tests were performed using the system. For both cases, the system collected readings at 20 Hz. The emitters emitted a 42kHz sonic pulse with a wavelength of approximately 8mm.

For the static experiments, an emitter was mounted to a fixture moved to ten separate locations in the environment. The orientation of the emitter was held constant throughout the positions. At each location, the system collected 50 position samples. The known and measured positions were then compared to give an indication of system repeatability and accuracy.

For the dynamic experiments, a pendulum was used to produce a consistent single frequency dynamic reference motion. The emitter was attached to a heavy weight at the end of a 1.35m line. The pendulum was set up 1.9m from the receiver array and swung parallel to the array. The starting height of the pendulum was chosen to allow the swing velocities and accelerations to fall within the ranges observed for materials handling workers. Marras (1991) observed mean maximum torso extension accelerations in industry of 5 rads/sec^2. This corresponds to a marker at the shoulder moving at approx. 2.5m/sec^2. Resnick (1992) observed maximum velocities of approx. 1.5m/sec in individuals manipulating materials handling devices. A starting angle of 24 degrees was calculated to have the pendulum swing at a maximum rate of 1.5 m/sec and have a maximum acceleration of 3.95m/sec^2. An acceleration of 2.5m/sec^2 occurs at approx. 15 degrees. For the pendulum experiments the data was smoothed using a FFT based smoothing algorithm with an approximate cutoff frequency of 5 Hz.

RESULTS AND DISCUSSION

As it is difficult to measure the exact location of emission of the emitters (resides somewhere within the 1.3cm housing), the location of the holding fixture was measured accurately instead for the static tests. The relative distances between the positions were then used in the comparison between the actual and observed readings. The minimum distance of the emitter from the receivers was 70cm and the maximum was 3m. Over all readings, the mean distance error was 0.54cm (std. dev. of 0.27cm).

For the dynamic pendulum tests, the expected motion of the pendulum was calculated using the standard equations assuming no friction. These theoretical curves were then shifted in time to match the period of the observed motion. The observed was then subtracted from the theoretical curve to highlight the differences. Figure 1 shows the observed, theoretical and difference velocity curves while figure 2 shows the acceleration curves. For the velocities, the deviation of the maximum observed values from the theoretical was on average 1% while for the accelerations it was on average 1.1%. The mean peak velocities observed over the five seconds of data shown in figures 1 and 2 was 164.3cm/sec (std. dev. 2.6cm/sec) compared to the theoretical peak of 165.8cm/sec. For the accelerations, the mean was 435.3cm/sec^2 (std. dev. 13.1cm/sec^2) compared to the theoretical peak of 440.0 cm/sec^2.

The small errors found in the static experiments and the close agreement of the velocity and acceleration curves for the dynamic experiments provides evidence that the sonic system represents an alternative to video based systems for capturing 3D dynamic postures in large areas. Laboratory tests to confirm this are currently being planned using subjects performing typical materials handling tasks.

REFERENCES

Chaffin, D.B. et al. IIE Transactions, 23(3):215-227,1991
Fleischer, A.G et al. Ergonomics, 26(6):555-564, 1983
Hsiao, H. et al. Ergonomics, 33(9):1089-1114, 1990
Resnick, M. et al. Proceedings of H.F.S. Conference, Atlanta, pp. 644-648, 1992
Youm, Y. et al. J. of Bioengineering, 2:359-367, 1978

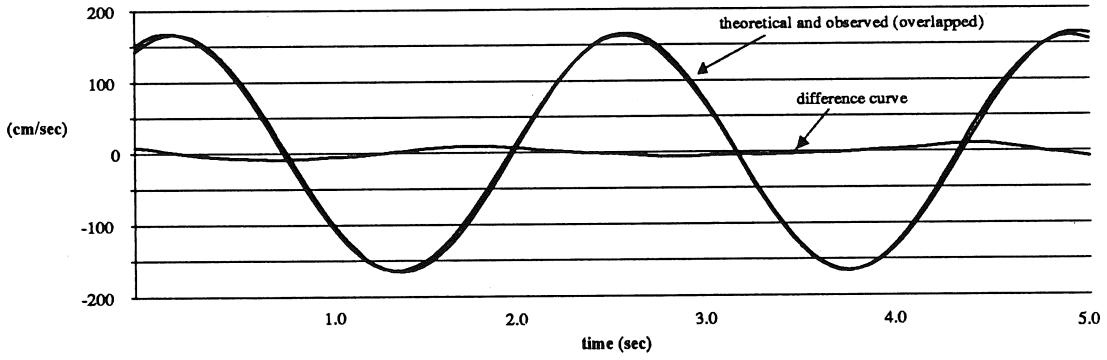

Figure 1. Pendulum Velocity curves (measured vs. theoretical and difference)

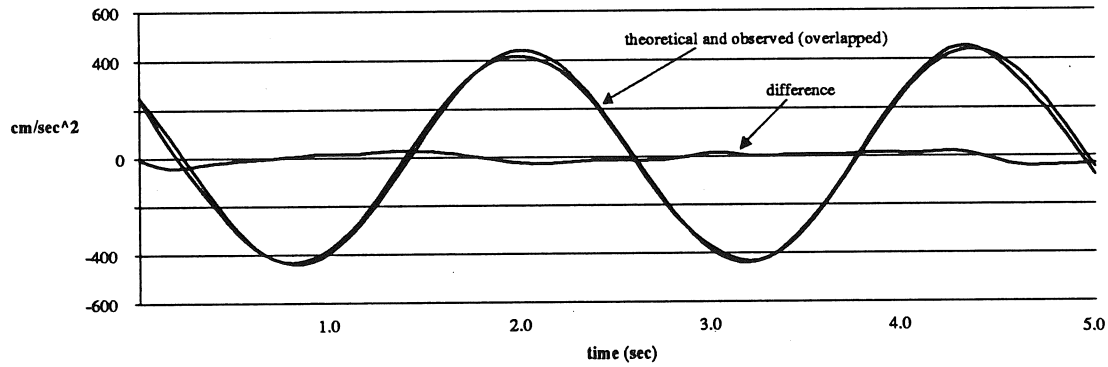

Figure 2. Pendulum Acceleration curves (measured vs. theoretical and difference)

THE EFFECTS OF ACCELERATION AND CREST FACTOR ON HUMAN MECHANICAL IMPEDANCE RESPONSE DURING WHOLE-BODY VIBRATION

S. D. Smith

Armstrong Laboratory, Wright-Patterson Air Force Base, Dayton, OH 45433-7901

INTRODUCTION

Human subjects were exposed to sinusoidal and quasi-random whole-body vibration to evaluate the effects of acceleration level and crest factor on the mechanical impedance frequency response. Up to four regions of resonance were observed. Significant reductions in the identified resonance frequencies occurred at the higher acceleration level. The appearance of the second and fourth resonance peaks was most obvious for the second highest crest factor. At the highest crest factor, identified by the subjects as producing the most discomfort, a second peak was not observed. At the lowest acceleration level, the fourth peak was noticeably diminished and approached the response of a dampened mass. It appears that nonlinear behavior in the impedance response can occur by varying the acceleration level as well as the magnitude of the crest factor.

REVIEW AND THEORY

Current whole-body vibration standards and recommended exposure limits assume that the human body responds as a linear vibration system. Several studies have indicated that the resonance behavior of the human is dependent on the input acceleration level (Hinz and Seidel, 1987; Fairley and Griffin, 1989; Smith, 1992a) but the significance of these acceleration effects are still under investigation. Questions have also been raised about the effects of the type of vibration (sinusoidal, quasi-random or random) and the crest factor (ratio of peak acceleration to root-mean-square (rms) acceleration) on human biodynamic and subjective responses. The crest factor (CF) can be physically described as the impulsiveness of the motion; quasi-random and random vibrations being more impulsive than sinusoidal vibration. Bastek et al. (1977), Cohen et al. (1977) and Manninen (1987) have all observed that the mean transmissibility between the seat and head was greater for sinusoidal vibration as compared to quasi-random or random vibration in the vicinity of the primary resonance frequency (about 4-6 Hz). The objective of this study was to use both the transmissibility and driving-point mechanical impedance techniques to study the effects of the type of vibration, frequency bandwidth, acceleration level and crest factor on nonlinear human response to vibration. This paper compares the mechanical impedance response to sinusoidal and quasi-random vibrations and evaluates the effects of acceleration level and crest factor for the frequency range 3-21 Hz. Emphasis is placed on evaluating the frequency response characteristics, particularly any changes occurring in the resonance behavior. An assessment of relative discomfort is also presented.

PROCEDURES

Three male and two female subjects weighing between 64 and 86 Kg (140 - 190 lbs) were exposed to sinusoidal vibration and to three quasi-random signals generated using the sum-of-sines technique. The three signals were defined as RAN1, CF=2.7; RAN2, CF=3.8; and RAN3, CF=4.9. (The crest factor for sinusoidal vibration is always 1.4.) The frequency exposures were from 3 to 21 Hz in one-Hz increments. Two overall acceleration levels were used for the signals; 1.0 and 2.0 ms^{-2} rms (.102 and .204 g_{rms}). The method used for collecting the vibration data and for calculating the mechanical impedance frequency response is described in Smith (1992a, b). The sum-of-sines technique was used to generate quasi-random acceleration time profiles using the following equation:

$$A(t) = \Sigma[a_i \, SIN(\omega_i t + \theta_i)] \quad (1)$$

where i equals the number of frequency components (19) and a_i equals 0.229 or 0.458 ms^{-2} rms depending on the overall acceleration level. The crest factor was varied by changing the phase profile, θ_i. Figure 1 illustrates two of the quasi-random signals. Two tests were conducted on each subject. Each test

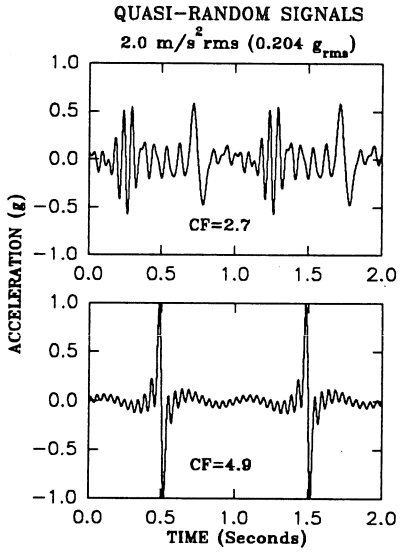

Figure 1 RAN1 and RAN3 Signals

consisted of collecting the sinusoidal and quasi-random data at the two acceleration levels in a single testing session. Ten impedance magnitude and phase frequency response profiles were generated for each type of exposure (sinusoidal and three quasi-random signals) and at each acceleration level (1.0 and 2.0 ms^{-2} rms). During the tests, the subjects were asked to rate the relative level of discomfort for the three quasi-random.

RESULTS

Up to four regions of resonance were identified in the impedance response between 3 and 21 Hz, similar to the regions described in Smith (1992a). For the results of this study, the regions were defined as follows: Region One, 5-7 Hz; Region Two, 7-9 Hz;

Region Three, 10-14 Hz; and Region Four, 16-19 Hz. The magnitude results were noticeably lower for one male and the two females who weighed 30-50 lbs less than the remaining male subjects. In general, differences between the types of exposures were observed as variations in the appearance of resonance behavior. Resonance peaks were more prevalent and more clearly delineated in the responses to quasi-random vibration, particularly for Regions Two, Three and Four. More specifically, the responses to RAN2 revealed better defined resonance behavior in the four regions including the observation of the second region of resonance (7-9 Hz) in all but one subject at the lower acceleration level, and the consistent appearance of the fourth resonance peak (16-19 Hz) at both acceleration levels. The third region of resonance was easily identified for RAN3, while the fourth region was more apparent at the higher acceleration level. The most distinguishing feature for RAN3 was the elimination of the second resonance peak and the relatively dampened and mass-like appearance of the fourth resonance region, particularly at the lower acceleration level. Figure 2 depicts the response of a subject to RAN2 and RAN3. The second and fourth resonance peaks are clearly observed for RAN2 while the response above 15 Hz for RAN3 approaches that of a dampened mass. The paired t-statistic indicated that,

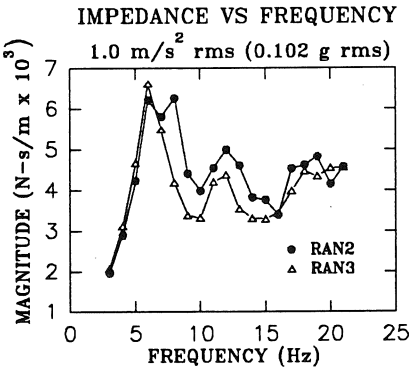

Figure 2 Impedance Magnitude Profiles

for many of the profiles, there was a significant lowering of the resonance frequencies (1-2 Hz) at the higher acceleration level (2.0 ms^{-2} rms) (5% confidence level). Figure 3 depicts the percentage of tests which showed reductions in Regions One, Three and Four. Reductions in 50% of the tests or greater were significant. The sinusoidal data did not reveal a significant lowering of the first resonance peak. The paired t-statistic also indicated that the impedance magnitude associated with the first resonance peak was significantly lower for the sinusoidal

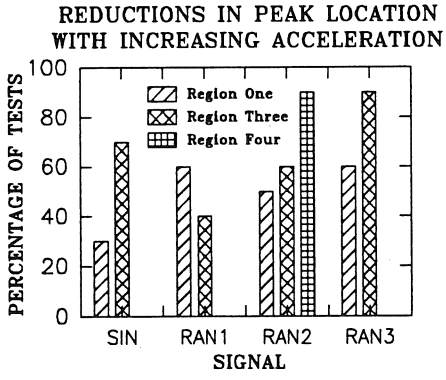

Figure 3 Resonance Frequency Reductions

exposures. The difference between the mean sinusoidal data and mean quasi-random data was less than 21%. For both acceleration levels, the subjects overwhelmingly ranked RAN3 (CF=4.9) as the most uncomfortable while RAN1 (CF=2.7) was consistently ranked the least uncomfortable. Several of the subjects indicated that the higher crest factors, particularly RAN3, were quite annoying and uncomfortable.

DISCUSSION

The decline in the resonance frequency with increasing acceleration level was consistent with the trends described by Hinz and Seidel (1987), Fairley and Griffin (1989) and Smith (1992a), however, the higher magnitudes associated with the quasi-random exposures at the first resonance peak contradicted the transmissibility results of previous investigators. Both Fairley and Griffin (1989) and Smith (1992a) concluded that the musculoskeletal system was less stiff at higher acceleration levels. The preliminary modeling results of Smith (1992a) indicated that, in general, the reduction in the occurrence of observable resonance peaks appeared to be the result of the combination of reduced stiffness and/or increased damping in the associated anatomical structures. The responses to RAN2, in particular, indicated that there may be higher stiffness and/or lower damping in the anatomical structures associated with Region Two and Region Four as compared to the response to RAN3. For sinusoidal vibration, Smith (1992a) observed the generation of resonance peaks in all four regions at 0.347 ms^{-2} rms (0.05 g peak). If the sinusoidal exposures in this study had been conducted at the same acceleration level as the corresponding frequency components in RAN2 (0.229 and 0.458 ms^{-2} rms) and not at the overall rms level, the resonance behavior may have been quite similar between the two types of exposures at the lower crest factors. In summary, the results of this study suggest that, while the impedance response to quasi-random vibration may be similar to that observed for sinusoidal exposures at relatively lower acceleration levels than used in this study, the responses at different crest factors display nonlinear behavior. It appears that the stiffness and damping characteristics of certain anatomical structures are affected; the most obvious behavior being increased damping. The significance of changes in the stiffness and damping characteristics of specific anatomical structures is not easily delineated from the impedance data collected for a multi-degree-of-freedom system without the use of a model. Application of a model and the evaluation of the transmissibility data collected for specific anatomical regions may provide a more quantitative correlation between the biodynamic behavior and the assessment of discomfort.

REFERENCES

Bastek R. et al. Int. Arch. Occup. Environ. Hlth., 39, 143-152, 1977.

Cohen, H. et al. Ergonomics, 20, 207-216, 1977.

Farley, T. and Griffin, M. J. Biomechanics, 22, 81-94, 1989.

Hinz, B. and Seidel, H. Industrial Health, 25, 169-181, 1987.

Manninen, O. J. Low Freq. Noise and Vibration, 6, 133-146, 1987.

Smith, S. Proceedings of the 63rd Shock and Vibration Symposium, Las Cruces, NM, 13-22, 1992.

Smith, S. 1992 Advances in Bioengineering, ASME Winter Annual Meeting, Anaheim, CA, 561-564, 1992.

WITHDRAWN

WITHDRAWN

ELECTROMYOGRAPHY STUDY OF THE PATIENTS WITH ANKYLOSING SPONDYLITIS

C.K. Cheng, S.W. Lin, Y.H. Tsuang and P.Q. Chen

Department of Orthopaedic Surgery and Center for Biomedical Engineering, National Taiwan University, Taipei, Taiwan, R.O.C.

INTRODUCTION

The trunk of the patients with ankylosing spondylitis (AS) has a tendency to lean forward owing to the structural change of the spine. As the center of gravity gradually shifts to the anterior, the Back and hip muscle groups tend to keep sagittal balance. The objective of this study is to demonstrate this muscle abnormal activity which has been considered the secondary factor to cause the low back pain of the patients with ankylosing spondylitis.

MATERIALS AND METHOD

Ten normal subjects and ten patients with ankylosing spondylitis were studied. Six paired surface electrodes were put on the right and left Multifidus, Iliocostalis, and Hamstring muscles on each subject. Every subject were asked to perform three different postures, prone lying, sitting and standing. IEMG was calculated and used to represent the outcomes of the muscle activities from the electromyography (EMG) [1].

RESULTS AND DISCUSSION

The results showed that in the normal subjects, the electromyographic activities of the erector spinae and hip extensors were very low (Figure 1). These may suggest that the trunk was in a state of extreme balance. There was no significant difference of the outcomes of EMG activities of erector spinae muscles in the standing and lying positions. However, the activities were significantly increased in the sitting position. This is consistent with previous investigations and can be explained why in the prolong sitting position has higher incidence of the low back pain. In patients with ankylosing spondylitis, they need more back muscle activities to keep balance of the trunk. From the results of the patients with ankylosing spondylitis showed that they have much higher EMG activities than normal subjects. Also, in the AS patients, their EMG results showed in the standing position performed higher activities than the sitting position. In conclusion of this pilot study, the back pain of the AS patients can be reduced greatly after the surgical operation not only due to the primary correction of the spinal deformities but the muscle activity reduced.

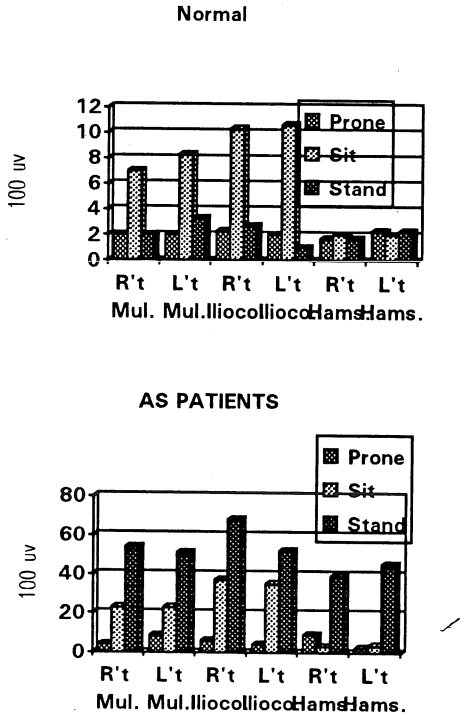

Figure 1

REFERENCE

[1] McGill, S.M., J. of Ortho. Res. 9:91-103, 1991.

THE EFFECT OF AXIAL ROTATION ON THE GEOMETRY OF THE TRUNK MUSCULATURE A THREE DIMENSIONAL CT BASED MODEL

D. Hooper, V. Goel, H. Chang*, Z. Zhang

Department of Biomedical Engineering, The University of Iowa, Iowa City, IA, 52242
*Catholic University Medical College, Seoul, Korea

INTRODUCTION

Computer aided tomography (CT) scans were acquired for two patients in both neutral and axially rotated postures in an effort to understand how axial rotation effects the geometrical parameters of the muscles between T12 and the sacrum. It was discovered that the moment arms, cross-sectional area and lines of action are dependent on axial rotation. These data are to be used to create a three dimensional optimization model to approximate the forces generated by the trunk muscles during tasks involving axial rotation.

REVIEW AND THEORY

For the past fifteen years, models of the lumbar spine during lifting tasks have been steadily evolving. We have been developing a three dimensional model for the purpose of determining the resultant forces and moments at the L3/L4 disc during asymmetric lifts. This information is then to be applied to an optimization model to assess the force contributions of individual muscles in the trunk during these complex loadings. In order to complete such a model, the cross-sectional area, point of application and line of action of each muscle must be quantified. In the past, researchers have gathered this data for subjects in a neutral posture using techniques such as computer aided tomography (Han et al. 1992, Nemeth et al 1986, Kumar 1988), magnetic resonance imaging, ultrasonic recordings and cadaver dissection (Dumas et al. 1988).

In an effort to broaden the scope of application of our model to include twisting, we are investigating the behavior of the trunk muscles from T12 to the sacrum during right axial rotation. This study will provide us with information relating the amount of twist in the lumbar spine to the resulting muscular geometry. We believe that an axial rotation will affect the cross-sectional area, and location of various muscle groups. It is further hypothesized that these effects will be prominent in muscles that are located furthest from the spine and in the higher levels with respect to the sacrum.

PROCEDURES

Data was collected for two Korean subjects, one 50 year old male and one 27 year old female. Transverse (T12-S1) and sagittal CT scans were recorded on film for each subject and posture, Figure 1. The rotated position was attained by asking the subject to twist to the right as far as possible. Each transverse scan was taken such that the plane of the image passed through a vertebra, bisecting the angle formed by the endplates of that vertebra. The sagittal image displayed the T12 through S1 vertebrae along with dotted lines representing the transverse image planes. In order to determine the lateral translation of a vertebra relative to the sacrum, two reference markers were created from radio-opaque bone cement. The markers consisted of two thin rods made from the polymer and were mounted side by side between two wooden boards. The markers and boards were placed on the bed of the CT machine so that the rods ran axially along the patient's spine. These rods appeared on the transverse scans as two small dots which could be used to align the scan while digitizing the film and also to determine the lateral translation of the vertebra. These points of reference proved valuable in our analysis.

Measurements of the area and centrode were made from the transverse slices for the left and right rectus abdominus, internal and external obliques, transversus, latissimus dorsi, iliocostalis, longissimus dorsi, multifidus, quadratus lumborum, psoas, illiacus, gluteus medius and vertebral body. This allowed for the determination of the area and centrode of each muscle with respect to a local reference frame located at the centrode of the vertebral body and oriented with the transverse slice. The local reference frame was located and oriented relative to the sacrum in the sagittal plane by locating the center of the vertebral body, and measuring the inclination of the line representing the transverse slice. The lateral coordinate of the local reference frame was recovered using the radio-opaque markers present in the transverse image. The coordinates of all muscles were transformed to a global coordinate system located at the center of the sacrum, aligned such that the X, Y, and Z axes defined left lateral, cranial and ventral directions, respectively. In the rotated posture the sacrum was always rotated a finite angle from the neutral posture. In order to compare the data for the two postures the global reference frame of the rotated sacrum was transformed so that the global Z axis pointed anteriorly out of the sacrum. This ensured that the global reference frame for each case was based at the center of the sacrum, and defined left lateral, cranial and ventral directions.

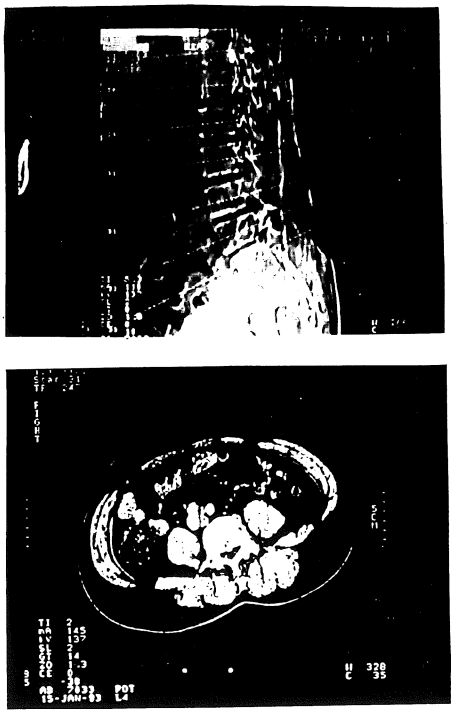

Figure 1. Sagittal slice and transverse slice through the L4 vertebral body. Images taken following right axial rotation.

The direction cosines of a muscle as it crossed a transverse plane bisecting a disc were determined by connecting the centrodes of the muscles at adjacent levels. The direction cosines of this vector, directed cranially, were determined with respect to the global frame at the sacrum. The point of application of the muscle on the transverse disc was determined by averaging the centrodes of the muscle at adjacent levels. The true cross-

sectional area along the line of action of the muscle was determined from the average of the measured areas across adjacent levels and the line of action. This method is described by Han et al, 1992.

Difficulties in determining the outlines of the muscles were encountered at various levels for select muscles. In cases when a muscle was not well defined it was not evaluated at that level. This problem was most frequent with the oblique muscles at levels above L3. This difficulty detracts from the completeness of our muscle model but is not critical when considering the motivation of this project, since our primary interest is the L3/L4 disc level. There were occasionally ambiguities in detecting any connective tissue that would indicate separation of adjacent muscles. This was encountered primarily with the deep back muscles (illiocostalis, longissimus and multifidus). In such situations, we referred to the anatomy literature, consulted with an orthopedic surgeon and tried to be consistent.

RESULTS AND DISCUSSION

The lordosis of the lumbar spine resulted in three-dimensional displacements of the vertebrae during rotation. The T12 vertebral body was found to be displaced as much as 2.5 centimeters in the right lateral direction. This fact indicates that the inclusion of the radio-opaque rod markers were a necessary component of the experimental protocol. The rotation measured between T12 and S1 while the subject was fully twisted was about thirteen degrees.

It is evident that the cross-sectional area of the muscles is dependent on the presence of axial rotation, Table 1. The true cross-sectional area of the muscles tended to decrease for muscles that rotated away from their line of action, thus stretching the muscle. This conclusion is stated cautiously as the data is merely a trend for some muscles.

Table 1. Change in physiological cross-sectional area for muscles crossing the L3/L4 disc level for the male subject, (area units: cm^2).

Muscle	Neut. Area	Rot. Area	% Change
R. Rec. Abd.	5.59	5.47	-2.15
L. Rec. Abd.	5.79	5.99	3.45
R. Ext. Obl.	6.13	8.05	31.32
L. Ext. Obl.	5.39	7.37	36.73
R. Int. Obl.	9.16	8.03	-12.34
L. Int. Obl.	8.55	8.49	-0.70
R. Trans.	3.87	3.24	-16.28
L. Trans.	3.72	4.00	7.53
R. Lat. Dor.	3.93	3.50	-10.94
L. Lat. Dor.	3.00	3.32	10.67
R. Multifidus	4.95	6.23	25.86
L. Multifidus	4.80	5.11	6.46
R. Long. D.	7.14	5.44	-23.81
L. Long. D.	7.31	7.93	8.48
R. Illio.	9.66	8.08	-16.36
L. Illio.	11.82	11.70	-1.02
R. Quad. L.	3.77	4.45	18.04
L. Quad. L.	4.77	4.79	0.42
R. Psoas	10.53	11.67	10.83
L. Psoas	11.64	11.90	2.23

The change in location of the muscle centrodes and verterbral bodies is presented graphically in Figure 2. The magnitudes of displacement of the muscle centrodes due to rotation increased for disc levels that are higher in the spine relative to the sacrum. Centrodes of the muscles generally translated in a manner associated with a right axial rotation, meaning the posterior muscles tended to move to the left and the anterior muscles to the right. Notice that the symmetry of the muscles present in the transverse and sagittal planes of the reconstructed torso during the neutral posture is lost following rotation. Centrode coordinates of the oblique muscles are questionable, as was expected. This is due to diffucluties measuring the centrodes of these thin, curved muscles.

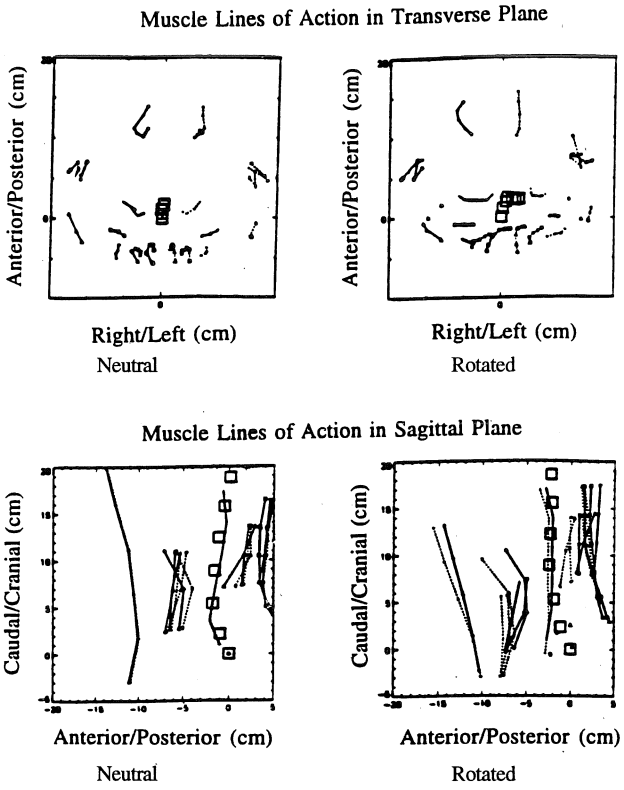

Figure 2. Muscle centrodes and lines of action for the male subject. Solid lines represent muscles on the right, dotted lines represent muscles on the left.

It is well known that the fibers of the obliques and transversus muscles are not directed as the centrode method dictates. We are attempting to use magnetic resonance imaging to detect the direction of these fibers and incorporate this data into our model. As of this time we have successfully recorded MRI images in which we can visualize the fiber direction of the abdominal muscles and are in the process of developing appropriate software for processing these images.

REFERENCES

Dumas, G. et al. Spine, 13, 532-541, 1988.
Han, J. et al. J. Spinal Dis., 5, 448-458, 1992.
Kumar, S. Clin. Biomech., 3, 137-144, 1988.
Nemeth, G. et al. Spine, 11, 158-160, 1986.
Reid, J. et al. Spine, 12, 273-275, 1987.

ACKNOWLEDGEMENT

Work supported in part by a grant from the NIH (AR-40166-02).

SMOOTHING THREE-DIMENSIONAL RECONSTRUCTIONS OF THE SPINE WITH DUAL KRIGING: CONTROL OF THE NUGGET EFFECT

Bernard André[1,2], François Trochu[1], Jean Dansereau[1,2]

[1]:Dept. Mech. Eng. École Polytechnique, P.O. Box 6079, St. "A", Montréal, Québec, Canada H3C 3A7
[2]: Research Center, Hôpital Sainte-Justine, 3175 Côte Ste-Catherine, Montréal, Québec, Canada, H3T 1C5

INTRODUCTION

This paper presents a new interpolation method, based on dual kriging, allowing the smoothing of three-dimensional (3D) reconstructions of the spine. The interpolation model adapts itself to the geometry of each particular spine and allows to control the amount of smoothing performed on raw data. Results obtained so far (15 subjects) are promising.

REVIEW AND THEORY

In numerous situations, 3D reconstructions of the spine are represented as curves in space with the vertebral centroids as control points. Interpolation functions such as cubic splines (Mc Neice et al., 1975), polynomials or Fourier series (Labelle et al., 1990) are used to minimize measurement errors and to perform specific calculations.

A more general approach is presented in this paper: dual kriging, which is an extension of usual interpolation functions. The principal equations will be briefly presented. More details may be found in Trochu (1992).

A function U(x) may be expressed as $U(x) \approx U'(x) = A(x) + B(x)$ where A(x), called the drift, is an approximation of the general shape of U(x). B(x), the generalized covariance, is a representation of the error made by stating U'(x) = A(x). For example, given N experimental data points (x_i, u_i), where u_i are observed values of function U(x) at location x_i, $1 \le i \le N$, A(x) a 2^{nd} order polynomial and B(x) expressed as $\Sigma b_i K(|x-x_i|)$ we have

$$U'(x) = a_1 + a_2 x + a_3 x^2 + \Sigma b_i K(|x-x_i|).$$

Assuming that measurement errors on u_i may be estimated, the above equation becomes

$$U'(x) = a_1 + a_2 x + a_3 x^2 + \Sigma b_i K(|x-x_i|) + \Sigma b_i \sigma_i^2.$$

σ_i^2 is called the "nugget effect" and is associated with the variance of the measurement error made on each u_i. A nugget effect equal to zero produces an interpolation function passing by each control point (as it is the case with spline functions) and a large σ_i^2 produces a best fit interpolation function (as least square functions are). Coefficients a_i and b_i are found by stating that the model fits the data points and adding the conditions of unbiasedness (Trochu, 1992).

In the case of three-dimensional (3D) curves, it is more suitable to express each coordinate as a function of a parameter t, giving:

$$x = f_1(t); \quad y = f_2(t); \quad z = f_3(t)$$

with $t_i = t_{i-1} + \sqrt{(x_i - x_{i-1})^2 + (y_i - y_{i-1})^2 + (z_i - z_{i-1})^2}$

The purpose of this study was to develop a kriging model which adapts itself to the geometry of each spine and which allows the control of the nugget effect.

PROCEDURES

In order to quantify the nugget effect, a study regarding reconstruction errors on vertebral centroids was conducted. Posterior-Anterior (PA) and 20° angled down PA radiographs of five subjects were digitized and reconstructed four times according to the procedure described in André *et al.* (1992). Centroids of vertebrae in each reconstruction were calculated as well as the most probable value (MPV = $\Sigma x_i/n$) and the estimated error (EER = x_i - MPV). A model of error distribution was then deduced.

Fifteen reconstructed spines of scoliotic patients (different from those of the error study) were used to develop the model. Since the shape of the spine varied for each patient, it was not possible to fix the drift and covariance in the kriging model. Five drift models (1- constant; 2- linear; 3- quadratic; 4- cubic and 5- trigonometric) and four covariance models (1- K(h) = h; 2- $K(h) = h^2 \ln(h)$; 3- $K(h) = h^3$ and 4- $K(h) = \sin(2\pi h)$, with $h = t_i - t_j$) were investigated and the best kriging model was determined with a cross validation algorithm. Briefly, the technique consisted of taking a sample of N data and one by one removing each data to form N samples of N-1 data. The kriging model was then applied to each sample, the removed data interpolated and the resulting error calculated. The "best" model was the one giving the smallest error.

Once the kriging model has been determined for a specific spine, the nugget effect was applied. First, the initial values were calculated using the coefficients of the cross validated model. A new kriging model with a nugget effect was then calculated and the new positions of control points were compared with the previous ones. If the displacements were larger than a certain control volume, a new solution was calculated with smaller nugget effects. This was repeated as long as all displacements were larger than the control volume. This volume was determined with the error study done previously.

RESULTS AND DISCUSSION

Results show that the variance of errors on vertebral centroids was of the same order of magnitude for the five subjects investigated. Furthermore, with the exception of

the fifth vertebral level (L5), the variance of error was almost identical for all vertebral levels. Therefore, errors were plotted globally for all five subjects for each coordinate (X, Y and Z), showing a normal distribution in each case. Confidence intervals were calculated using these distributions and they showed that with a probability of 99%, all errors were included between ±0.8mm for both X and Y coordinates and between ±3.2mm for Z. Although of slightly less magnitudes, these results were in agreement with error studies already published (Rab and Chao, 1977; André *et al*, 1992).

Results of cross validation for various drift and covariance models are shown in table 1. This indicates that among the functions investigated, linear polynomials were the best estimation for X and Y coordinates and that cubic polynomials were more suitable for Z. Excluding K(h)=h which was never chosen, there were no real preferences for covariance functions. The "preferred" kriging models were, for X, linear drift and cubic covariance (33% of the time), for Y, linear drift and logarithmic covariance (25%) and for Z, cubic drift and trigonometric covariance (20%). Therefore, there was no real winning combination of drift and covariance. This emphasizes the need for a flexible algorithm when interpolating and smoothing 3D reconstructed data from scoliotic spines.

Table 1. Distribution of drift and covariance for 15 subjects

Drift	X	Y	Z	Covariance	X	Y	Z
Constant	0	0	1	h	0	0	0
Linear	7	8	1	$h^2 \ln(h)$	5	5	4
Quadratic	4	5	3	h^3	9	5	6
Cubic	3	2	8	$\sin(2\pi h)$	1	5	5
trigono.	1	0	2	———	—	—	—

Smoothing of vertebral centroid positions was done for each of the 15 subjects using results of cross validation and by controlling the nugget effect within the confidence intervals previously calculated.

In all cases, differences between smoothed and raw centroid positions were well within the confidence intervals, validating the control algorithm. Figure 1 shows smoothing results with dual kriging for 3D reconstruction of a spine. This is typical for 8 of the 15 spines investigated. It can be seen that the interpolated spine (solid line) is smoother than the raw spine (dots), especially in the lateral and top views. On the other hand, for some vertebral levels (T5 and T6 for example) a larger control volume would have produced a better smoothing.

For 7 of the 15 spines, smoothed results show almost no differences with raw data. This suggests that the confidence intervals previously calculated underestimate the errors and that larger values may be taken (±5.0mm for Z) as suggested in Rab and Chao (1977) or André *et al*, (1992).

It should be noted that this error study was done with four repetitions on five subjects limiting the investigation to a global error model. A larger sample should provide a more accurate estimation of the control volume for each vertebral level and therefore improve the control of nugget effect.

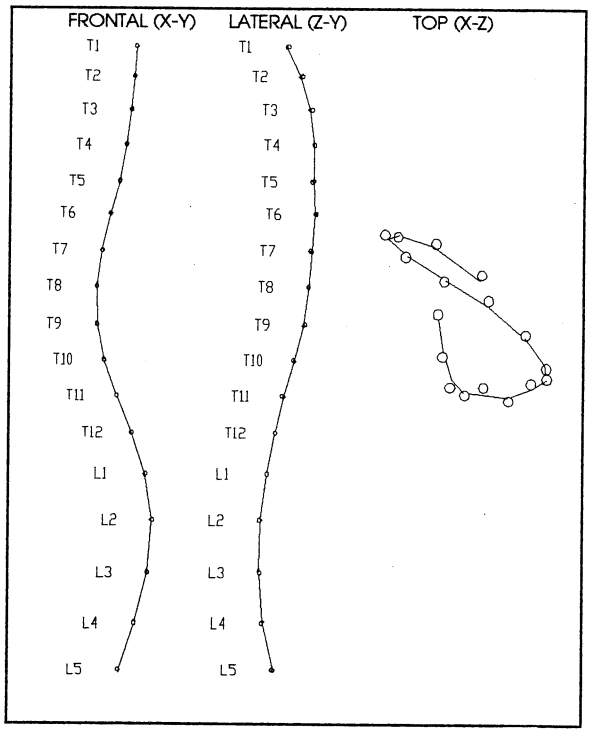

Figure 1. Smoothed 3D reconstruction of a spine with dual kriging. Raw position of vertebral centroids are represented by dots. The solid line shows the interpolated data. Top view is scaled by a factor of 2 for clarity.

CONCLUSION

A smoothing interpolation method based on dual kriging was presented in this paper. Given different drift and covariance functions, the algorithm builds the most suitable interpolation model for specific spine geometries. It is also possible to control the amount of smoothing performed on raw data.

REFERENCES

André, B. et al., Medical. & Biological. Engineering. & Computing, 30, 569-575, 1992.

Labelle et al., 7th Interntl. Cong. on Cotrel-Dubousset Instr., Montpellier, France, pp. 15-19, 1990

Mc Neice et al., Advance in Engineering, ASME winter Annual Meeting, Houston, p 76, 1975

Rab, G.T. and Chao, E.Y., Spine, 2, 287-293, 1977.

Trochu, F., A Contouring Program Based on Dual Kriging Interpolation, accepted in Engineering with Computers, 1992.

ACKNOWLEDGMENTS

The authors wish to thank the Institut de Recherche en Santé et Sécurité du Travail du Québec and the Natural Science and Engineering Research Council of Canada for their financial support.

THREE DIMENSIONAL KINEMATIC ANALYSES OF CONTROL AND WHIPLASH SUBJECTS USING INSTANTANEOUS HELICAL AXIS PARAMETERS

T. Ribaudo[1], K. Long[2], P. Osterbauer[2], G. Yamaguchi[1], A. Fuhr[2]

[1]Department of Chemical, Bio and Materials Engineering, [2]Whiplash Analysis
[1]Arizona State University, Tempe, AZ 85283; [2] Phoenix, AZ 85018

INTRODUCTION

Difficulty in determining whiplash injuries has led to assessments based largely on subjective, clinical data. New non-invasive methods of analysis are being developed to describe head and neck movement patterns using Instantaneous Helical Axis (IHA) parameters.

The study investigates whether the motion of the head with respect to the trunk is indicative of neck injuries, and if so, to quantify the differences with kinematic parameters. Three head motions, designed to simulate activities of daily living, are studied: (i) flexion/extension, (ii) axial rotation and (iii)oblique movements (combine flexion/extension and axial rotation). The (IHA), calculated from three dimensional motion analysis, are computed at one degree intervals to describe the motion of the head with respect to the trunk.

Differences in the Instantaneous Helical Axes parameters in the cervical and thoracic spine area, during specified head movement patterns are quantified for 52 control and 28 injured individuals.

A scoring system based on observed biomechanical parameters is developed to show evidence and severity of injury in whiplash patients. Scoring is based on path deviations observed in the Z level piercing point (PPZ) , degree of curvature of the PPZ, height of PPZ's and lack of symmetry in oblique movement patterns. Clinical measurements including: active cervical range of motion (ROM), neck pain via a visual analog scale (VAS) and neck disability index (NDI) are used in conjunction with biomechanical parameters to formulate a composite score.

Results indicate that biomechanical parameters may be useful in assessing both evidence and severity of neck injuries.

REVIEW AND THEORY

Because the head is the final link in the kinematic chain of the spinal column, it is possible to analyze head motion using an equivalent rotation to represent the combined translation and rotation of the head. Previous work by Winters & Peles (1990) has shown that Finite Helical Axes (FHA) data, calculated from three dimensional motion analysis may provide an objective tool to distinguish between asymptomatic (control) subjects and injured patients. Unfortunately, noisy, unsmoothed data necessitates finding the FHAs over large angular intervals.

The "Instantaneous" Helical Axes (IHA; actually small interval FHAs) give a better indication of small rotational movements. According to Woltring et al (1993) IHA's estimated from low pass smoothed video data are not restrained by smaller rotation velocities ω as seen in the FHA.

Of the many descriptors available from the IHA (eg. unit direction vector, helical attitude angle, piercing point coordinates, etc.). The Z level piercing point (PPZ) of the IHA projected onto the mid-sagittal plane appears to be the most useful in discriminating between injured and asymptomatic persons during flexion/extension and oblique movements.

PROCEDURES

Equipment in the lab consists of the ExpertVision™ system from *Motion Analysis*, two NEC T1-23A CCD cameras with Comiscar 8 mm lenses, two Panasonic AG-6300 VCR units, a SparcStation IPC and other DOS based PCs.

To reproduce movements which are similar to activities of daily living (ADL) the subject generates flexion/extension, axial rotation and oblique motions. The subject moves over a range of 100° for the vertical movement, ±50°.

Similar procedures are then repeated for horizontal and oblique movements. A small laser diode affixed to the top of a lightweight helmet, worn by the subject, provides visual feedback for these movements insuring analysis of head, rather than eye movement.

Data are collected via three markers rigidly attached to the helmet (the distal body), one marker placed on the skin over the spinous process of T1 (anatomical reference point) and four markers bolted to a board strapped on the torso of the subject (proximal body).

After processing the data and obtaining the 3-D coordinates, IHA estimation is executed by a unique program designed at Whiplash Analysis, Inc. Calculation of the IHA is accomplished using the distal segment's coordinates with respect to the proximal segment's coordinates. The smoothing parameters are determined by monitoring the rigid-body fit to the smoothed data. Oversmoothing results in fitting errors which are too large and undersmoothing results in a noisy appearance of the IHA in graphical representation. The conclusion reached, after examination of many graphs with similar movement frequencies, that a smoothing parameter of 0.1 yields an acceptable balance between minimizing noise and signal distortion.

Data is further reduced by interpolation to obtain a single value for each degree over the complete range of movement. Data is analyzed from ±35° in order to remove startup and end effects. Analysis of the PPZ of the IHA onto the mid-sagittal plane yields an "envelope"; consisting of the control subjects' mean bounded by ± one/two standard deviations. Data from a whiplash patient is then superimposed on this envelope for analysis.

Z axis piercing point data is further analyzed to determine the degree of curvature for each individual whiplash subject. Data is fit it to a third order polynomial equation and the first and second derivatives are taken; finding the slope and degree of curvature respectively. End and turn around points are disregarded during this analysis. A maximum second derivative value as determined from the normal population, is used for comparison.

Symmetry of opposing oblique movements are analyzed based on number of inflection points, opposing concavities and differing vertical levels.

RESULTS AND DISCUSSION

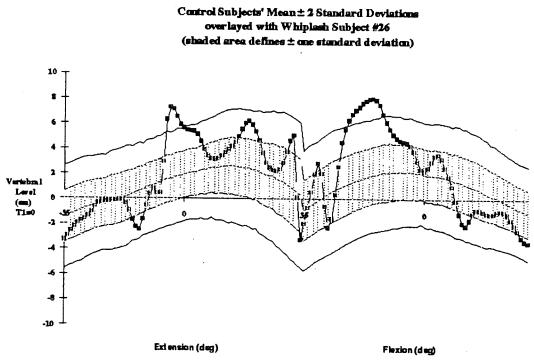

Figure 1. Moderately injured whiplash patient's PPZs superimposed over the normal envelope.

The increased curvature exhibited is only evident in whiplash patients (maximum degree of curvature for control subjects being 0.046). Ten whiplash patients exceeded this level with a maximum value of 13.95.

Scoring using the PPZ is based on: number of inflection points, vertical level deviations , differing concavities and degree of curvature. Oblique movement patterns are evaluated for symmetry with respect to the mid-sagittal plane.

The four previously mentioned parameters are used in conjunction with existing range of motion, neck pain and neck disability index to formulate a composite score ranging from 0 to 7.

Results suggest that biomechanical parameters are useful in assessing both evidence and severity of neck injury

REFERENCES

Winters et al. Spine, (accepted for publication) 1993.
Winters, J.M. & Peles, J.D. Multiple Muscle Systems - Biomechanics and Movement Organization, (pp. 461-480), Springer, 1990.
Woltring et al. Journal of Biomechanics, (accepted for publication)1993.

ACKNOWLEDGEMENTS

The authors wish thank Doctor Donald G. and Joan C. Kimble for their support of this project.

THE INFLUENCE OF TORSO ORIENTATION ON HYBRID III NECK LOADING

W. Lu and P.J. Bishop
Biomechanics Impact Laboratory
Department of Kinesiology
University of Waterloo
Ontario, Canada

INTRODUCTION

Axial compressive loading leading to cervical spine injury remains an important problem in automotive, sport and recreational accidents. A considerable amount of literature has been devoted to injury mechanics, injury simulation and injury prevention. Such injuries occur because of human tissue failure caused by impact forces which exceed the tolerance of the cervical vertebrae.

REVIEW AND THEORY

Early studies (Torg, et al., 1990) have postulated that the most dangerous configuration of the cervical spine occurs when the impact force is transmitted along the straightened axis of the spine. In such cases, most of the torso energy will be transferred to the cervical spine in the form of strain energy which causes spinal column buckling and vertebral dislocation.

Other studies related to different conditions of head constraint have shown that neck loading accompanied by restricted head motion greatly increased the stiffness of the vertebral column and the compressive force applied to the neck (Hodgson and Thomas, 1980; Myers, et al. 1991; Bishop and Lu, 1992). These results suggest that the risk of cervical injury may be strongly dependent on the degree of head and neck constraint imposed by the contact surfaces.

While some studies have considered the influence of the head constraint conditions on cervical spine injury, few have been performed to consider the effects of torso conditions. Because most of the energy causing axial compressive failure comes from the torso, the effect of torso posture on neck loading becomes important. Hodgson and Thomas (1980) measured vertebral strain in human cadavers subjected to crown impacts with the torso aligned with the head or positioned above it. Vertebral strain was lowest for a straight torso and head alignment and increased as the torso was elevated. The force acting on the vertebral elements was not measured. Because other torso postures were not considered, the purpose of this study was to simulate head first collisions with the torso below the head using a Hybrid III Anthropometric Test Dummy (ATD).

METHODS

The methods of simulation and analysis were similar to those used in other studies (Bishop and Wells 1986; Li and Bishop, 1991). Essentially, the ATD was placed in a prone position , then attached to a swing bar suspended from the ceiling. This permitted the ATD to be released from a given height, thereby controlling the impact speed. Four torso conditions were simulated in this study: torso aligned with the impact axis(0^{o}); torso inclined 6^{o} and 12^{o} below the impact axis; and impact without a torso (Hybrid III head neck and only).

A force and moments of force transducer(Denton Electroncs) measured three orthogonal forces and moments of force about the Atlanto-Occipital junction (AOJ) of the ATD head and neck. The force and moment signals were digitized via a 12 bit A/D board and were stored in an IBM computer for further analysis.

Using this system, six trials of each condition were conducted in which the ATD was propelled at 2 m/s into a movable barrier consisting of a wooden box, closed at the front with canvas, and filled with sand to a mass of 75 Kg. The sand bag was suspended from the ceiling with wire cables and was able to swing freely.

High speed film(500fps) and video were recorded on some trials so that the ATD neck movement could be observed.

RESULTS AND DISCUSSION

Table 1 summarizes the average(SD) peak forces and moments of force at the AOJ under four impact conditions. Since the Mx, Mz and Fy were much smaller compared to the forces and moments in other directions, they were not listed in the Table. Figure 2 and 3 displays a typical force-time and a moment-time history of the different trial conditions.

The results indicate that the torso posture before head first impact did influence the loads on the cervical spine. In this study, the compressive forces at AOJ were decreased from 4.5 KN at straight alignment impact to 3.7 KN at the 12 degree impact. Statistical analysis (ANOVA) disclosed that the four impact conditions differed significantly(p-value< 0.001). These

results were similar to those of Hodgson and Thomas (1980) who found the maximum force on the head but the least vertebral strain when the torso was aligned with the head. The 6° and 12° impacts produced intermediate and minimum forces, a condition similar to that of Hodgson and Thomas (1980) for two elevated torso positions. Of note, as well, is the relatively small compressive neck load without the torso (1463 N) which illustrates the influence of the torso mass on neck loading.

As the compressive forces were reduced, which may reduce the risk of compression injuries, the shear forces and the flexion moments were substantially increased in our test series. These increased shear forces (> 800 N) and moments (> 140 N.m.) may lead to bilateral facet dislocation or intervertebral disk disruption in the human cervical spine. From high speed film and the force-deformation history, condition I produced axial compression with no motion of the head. This corresponds to a fully constrained end condition. For condition II and III there was head motion after impact leading to a semi-constrained condition. These results were comparable to other studies (McElhaney, et al. 1983; Myers et al. 1991) where they found that full constraint produced large axial loads and comparatively small flexion moments, while rotational constraint produced moderate axial loads and comparatively large flexion moments.

To summarize, torso posture does influence the loading on the cervical spine. However, additional research is required before recommending a change in torso posture as a strategy for reducing the risk of neck injury under head first collision.

REFERENCES

Bishop, P. Wells, R. 1986, Pass. Comf. Conve. and Saf. Test Tools and Proced., P-174, SAE.

Bishop, P. & Lu, W., 1992, Proceedings of NACOB II, pp. 205-206.

Hodgson V.R. and Thomas, L.M. 1980, Mechanisms of Cervical... 24th STAPP.

Li, Y; Bishop, P.J. et al, 1991, 35th STAPP.

McElhaney, J.H. et al. 1983, Cervical Spine Compression Resopnes. 27th STAPP.

Myers, B.S. et al.1991, The Inf. of End Cond... 35th STAPP.

Torg, J.S. et al., 1990, The Ame. J. of Spo. Med. Vol18, No.1.

ACKNOWLEDGEMENTS

The authors wish to thank Sport Canada for its support of this work.

Table 1. Average(SD) Peak Forces and Moments at AOJ. n=6, I=0°, II=6°, III=12°, IV=Head&Neck (H&N)

	My(N.m) (SD)	Fx(N)* (SD)	Fy(N)** (SD)
I	39 8	-267 67	-4541 169
II	102 12	-547 61	-4285 116
III	147 17	-830 73	-3712 77
IV	15 28	-46 291	-1463 110

* A-P Shear force; ** Compressive force.

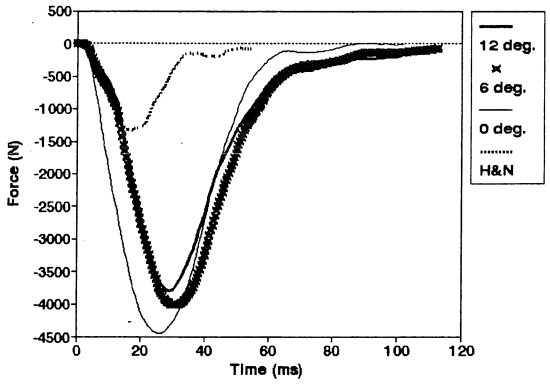

Fig.1 Compressive Force at AOJ

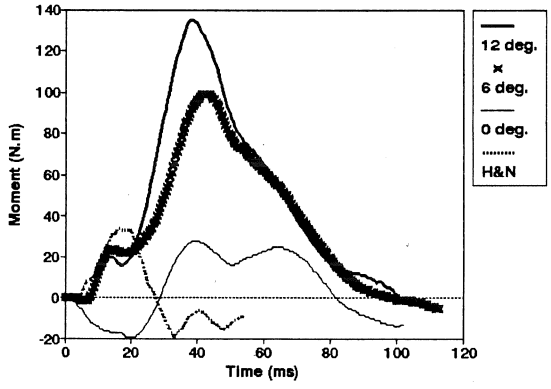

Fig.2 Moment (My) at AOJ

DEVELOPMENT OF A NINE DEGREE OF FREEDOM, 3 DIMENSIONAL MODEL FOR KINEMATIC NECK ANALYSIS

David A. Morgan and Gary T. Yamaguchi

Department of Chemical, Bio & Materials Engineering
Arizona State University, Tempe, AZ 85281-6006

INTRODUCTION

One problem in the field of head and neck biomechanics is determining, non-invasively, the location and orientation of the vertebrae. The information available to researchers in this field is very limited, and often is extrapolated from data collected from cadavers which may be inappropriate.

In order to better understand movements of the upper cervical spine, we developed a three segment, nine degree of freedom (DOF), three dimensional model to simulate intervertebral movements. Given the 3-D locations of the head as a function of time, the problem is one of determining the positions and orientations of the intermediate vertebrae. The model solves for these variables via a dynamic method. This dynamic model includes passive springs and dashpots to model the intervertebral disks, and torques and forces to control for the aggregate effects of muscles and ligaments. A graphical computer interface was also developed to display the kinematics, and to better quantify the assessment of neck injuries.

REVIEW AND THEORY

In the past, there have been several studies done on the cervical spine, and various attempts have been made to model this region. However, most of the research has been directed towards anatomical properties of the vertebrae (Moroney *et al.*, 1988; Panjabi *et al.*, 1988; Panjabi *et al.*, 1991; Pelker *et al.*, 1991). These studies of mechanical properties use cadavers for their *in-vitro* tests. These publications, as well as White and Panjabi's *Clinical Biomechanics of the Spine* (1985) provide a great deal of biomechanical properties, such as relevant anatomy, stiffness, movements, and load-displacement comparisons. One study produced a significant amount of information regarding the normal and injured cervical spine (Goel *et al.*, 1984). In this study, rotations between segments were described, again using cadavers for the tests.

The literature also discusses the use of the Instantaneous Helical Axis (IHA) to describe the relative motion between rigid bodies (Woltring *et al.*, 1985; Fioretti *et al.*, 1990; Amevo *et al.*, 1991). In our study, the IHA was measured experimentally in order to quantify the positions and orientations of the head relative to T1 in more than 60 normal and whiplash-injured subjects. The model described herein uses the IHA to determine endpoint (i.e. skull) position and orientation. Thereafter, a damped, dynamic simulation solves for the intermediate positions and orientations of the "vertebrae".

PROCEDURES

The cervical spine, C1 through C7, was grouped into three vertebral body segments (B, C, and D) and stacked upon a segment designated as T1. T1, in this study, was the reference body, where all other body motions (both rotation and translation) were described about. The model has nine degrees of freedom (DOF), as follows: two angular and one translational DOF about the origins of each moving body (B, C, and D) (Figure 1). The two angular DOF represent forward flexion/extension and lateral flexion/extension. The translational DOF for each body allows the neck to expand or compress if necessary. This model can easily be expanded to model the entire cervical spine.

The mathematical equations of motion for the model were then derived using Kane's method (Kane and Levinson, 1985). By this method, a FORTRAN program was created to output the resulting system configuration when given initial parameters (segment lengths, masses, initial angles, etc.) As mentioned above, the position of the top body (D) was prescribed using the IHA. After verifying that the dynamic model conserved energy, viscoelastic forces due to the intervertebral disks

were added. These springs and dashpots were placed and configured so as to appropriately mimic a compressible, cylindrical disk to obtain the desired characteristic. A torque and a force were also added to each appropriate body to control for the aggregate effects of muscles and ligaments.

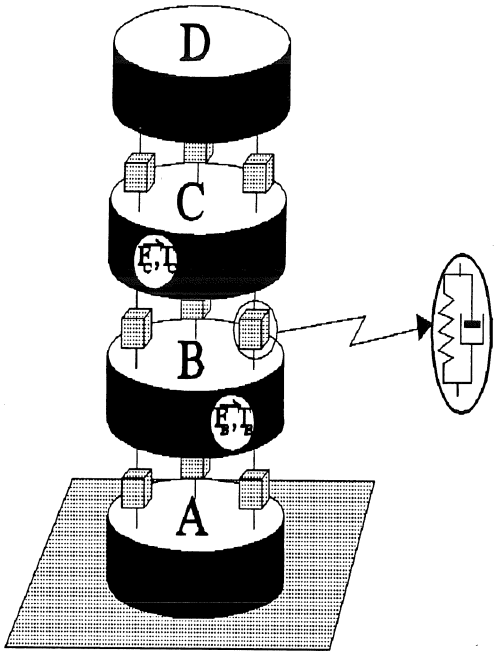

Figure 1. The nine degree of freedom model. The intervertebral disk is modeled as a spring-dashpot system and muscle/ligament aggregate effects as torques and forces. Three degrees of freedom are present at each joint.

RESULTS AND DISCUSSION

The forward dynamic simulation allows us to predict, using energy as the cost function, the equilibrium positions of the intermediate body segments when given the orientation and position of the end body (D). If only two intermediate bodies are used to model the entire cervical spine (C1 through C7), the angular deviations can be subdivided and then displayed graphically, allowing researchers and doctors to easily show the biomechanical movement of the neck in animated form. We propose this method as a possible means of visualizing the internal motions of the vertebrae, and possibly as an method to assess and evaluate neck injuries.

REFERENCES

Amevo, B. *et al.,Clinical Biomechanics*, **6**, 31-37, 1991.

Fioretti, S. *et al., IEEE Trans. Biomed. Engrg.*, **37**, 398-409, 1990.

Goel, V.K. *et al., J. Biomechanics*, **17**, 363-376, 1984.

Kane, T. and Levinson, D.A., *Dynamics: Theory and Applications*, Mc-Graw-Hill, 1985.

Moroney, S.P. *et al., J.Biomechanics*, **21**, 769-779, 1988.

Panjabi, M. *et al., Spine*, **13**, 726-730, 1988.

Panjabi, M. *et al., Spine*, **16**, 861-869, 1991.

Pelker, R.R. *et al.,Spine*, **16**, 117-122, 1991.

White, A.A. and Panjabi, M.M., *Clinical Biomechanics of the Spine, Second Edition*, J.B. Lippinott, 1990.

Woltring, H.J. *et al., J. Biomechanics*, **18**, 379-389, 1985.

ACKNOWLEDGEMENTS

The authors wish to thank Doctors Donald G. and Joan C. Kimble for their support of this project and Whiplash Analysis, Inc. for its role in supplying experimental data.

PULSATILE FLOW IN A THREE-DIMENSIONAL MODEL OF LARYNX

Fariborz Alipour and Chenwu Fan

Department of Speech Pathology and Audiology
The University of Iowa, Iowa City, IA 52242.

INTRODUCTION

The airflow in the larynx is pulsatile and three-dimensional with moving boundaries. It is known that the oscillation of vocal folds are induced by the airflow in the glottal constriction and the valve-like action of the vocal folds makes the airflow pulsatile. The pressure distribution and flow pattern in the larynx and glottis are essential in the studies of voice acoustics and biomechanics.

Because of the complexity of the airflow, geometry and boundary conditions, the early studies of laryngeal airflow included many simplifying assumptions such as one-dimensional flow and extending the results of pressure and flow measurements in static models to the oscillatory flow. Only in recent years, using the method of computational fluid dynamics (CFD), more accurate analyses of the laryngeal airflow were performed and minute details of the airflow in the larynx were revealed. Iijima et al. (1988), Liljencrants (1991), Alipour & Patel (1991,1992) studied airflow in the static models of glottis and reported velocity profiles and pressure distributions in three major shapes (convergent, divergent & parallel). Alipour & Ni (1992) also Ni & Alipour (1993) studied the airflow in two-dimensional model of larynx with moving boundaries and presented results of the pulsatile flow with frames of the streamline and pressure maps.

In this study the state of the art (CFD) was employed to obtain a three-dimensional solution for the airflow in a model of the larynx with moving boundaries (vocal fold).

METHOD

The 3D geometry was build upon 2D model of larynx in xy plane and projected in the z direction for the amount of channel width.

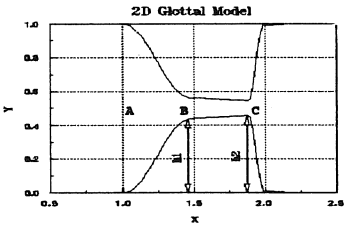

Figure 1. Design of Moving Boundaries

The glottis was constructed with two sinusoidal curves connected with a straight line (Figure 1). The height of the first sinusoid (h1) was fixed but the height of the second was varied as a sinusoidal function of time,

$$h2 = h1 + ACos(\omega t) \qquad (1)$$

where A is amplitude and $\omega = 2\pi f$ gives h2 a time variation with frequency of f. At any time step, h2 is updated and the sinusoidals were connected by a straight line that was tangent to them and its points of contact were calculated analytically.

Sine in real phonation, as the vocal folds open, airflow rate increases and vice versa, a sinusoidal time varying velocity

with the same frequency was applied to the inlet flow as

$$u(y,z) = u_0 \sin(\omega t) \qquad (2)$$

Where u_0 is the amplitude of inlet velocity that is also used for the calculation of Reynolds number.

Solutions for airflow were obtained by the Phoenics package, a CFD computer program that is based on the finite volume numerical method. Using this code the unsteady Navier -Stokes equations for laminar flow was solved and velocity components were obtained by iterations and successive over-relaxation. The pressure was calculated from the continuity using Simpler's algorithm on the staggered grids. Computations were performed on a DEC-Station 5000 workstation. Computational domain was discretized into a non-uniform grid of 60x30x11 in x, y, and z directions respectively. Higher density grid points were chosen near the vocal folds. To apply a moving boundary in the fixed grid domain, a so-called `shadow method` with big source terms in the governing equation was used to enforce zero velocities below and on the walls at any time instant.

RESULTS AND DISCUSSION

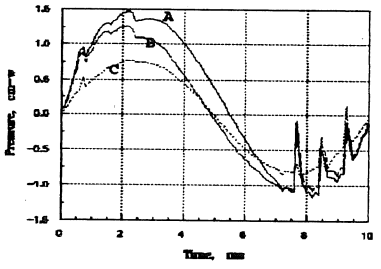

Figure 2. Pressure Waveforms within the Glottis.

Figure 2 shows pressure waveforms at centerline of glottal model at three locations A, B, C in the glottis at Frequency of 100 Hz and Strouhal number of 5. The pressure drop between points A, B, and C changes periodically with time with a maximum drop near 1/4 T (period).

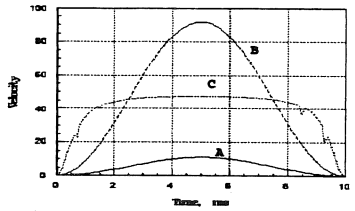

Figure 3. Mean Velocities in the Glottis

The mean velocity waveforms at locations A, B, and C across the x axis are shown in Fig. 3. Location A has a velocity waveform similar to the inlet flow. Location B reaches a high velocity of 91.6 at the half period, but location C has an almost flat velocity for a major portion of the period. These velocity and pressure waveforms are similar to those of two-dimensional flow but flow pattern is more complex particularly at low channel aspect ratios.

REFERENCES

Alipour, F. et al. Advances in Bio-engineering, (pp. 111-114), 1991.

Alipour, F. et al. Proc. Int. Conf. Eng. Appl. Mech. (pp. 93-100), 1992

Alipour, F. et al. J. Acoust. Soc. Am. 92(4) pt. 2 (pp. 2391), 1992.

Iijima, H. et al. The Second joint ASA & ASJ meeting, Nov. 1988.

Liljencrants, J. Vocal Fold Physiology Vol 3, Raven Press 1991.

Ni, J. et al. J. Acoust. Soc. Am. (in review).

ACKNOWLEDGMENTS

The study was supported by NIDCD, Grant No. DC00831-02.

CLOSING SOUND ENERGY LEVEL OF MECHANICAL HEART VALVE PROSTHESES IN WATER TANK TESTER

G. X. Guo, P. Adlapavar, C. Kingsbury and R. C. Quijano
Baxter-Edwards CardioVascular Group, CVS Division, Irvine, CA 92714

INTRODUCTION

When implanted, a heart valve prosthesis is a source of sound. The total sound depends not only on the sound source (valve), but also on the structural influences and the reverberant environment. To quantitatively evaluate the valve closing sound, we developed a cylindrical water tank test system measuring 5 ft. in diameter and 6 ft in height. The structural influences and background noise were thus minimized. Valves were mounted in three point suspension to ensure an acoustically transparent mounting structure. A linear motor was used to maintain controllable and repeatable valve motion.

Five types of mitral valves, size 29 mm, were tested including: 3 each of Edwards-Duromedics™ Original Specification (EDOS), Edwards-Duromedics™ Modified Specification (EDMS), St. Jude Medical (SJM), and Björk-Shiley (BS), and 2 Medtronic-Hall (MH). The FFT spectral analyzer was used for data processing. Upper limit of the analysis was 25 KHz. The "A-weighted" total power spectra level (dBA) is displayed graphically. The distances between the valve and the hydrophone were 8" (near field) and 32" (far field) respectively.

Comparisons of the EDOS and EDMS show approximately 5 dBA less energy. The results demonstrate a significant improvement in audible acoustic characteristics due to the modification of the Edwards-Duromedics™ valves.

REVIEW AND THEORY

Both the circulatory system noise and complex structural influences affect valve sound analysis. Structural influences can include contacts with the valve housing due to suturing, complex reflection of the sound in the body, and surface coupling with respect to acoustic wave propagation between blood and muscle as well as between skin and air. These influences will affect both the sound pressure and the frequency content, creating strong low frequency sounds which have been the subject of earlier valve sound studies.

To quantitatively evaluate the acoustic characteristics of a mechanical heart valve prosthesis both the environment noise and structural influence must be controlled or minimized. *In vivo* testing provides information with respect to the total sound. However, due to the structural variability from patient to patient, the contribution of the sound source will be difficult to quantify. Although the structural variability can be better controlled in *in vitro* testing, the contribution of the sound source may still be difficult to quantify due to the complex acoustic behavior between sound source and system structure.

In this study, to quantitatively evaluate the fluid born acoustic characteristics of mechanical heart valve prostheses the structural influences were minimized by means of a water tank test system.

PROCEDURES

Figure 1 schematically shows the water tank system used in this study. A cylindrical water tank, measuring 5 ft. in diameter and 6 ft. in height, was used to allow a 1 msec (maximum) reflection free time window for data collection.

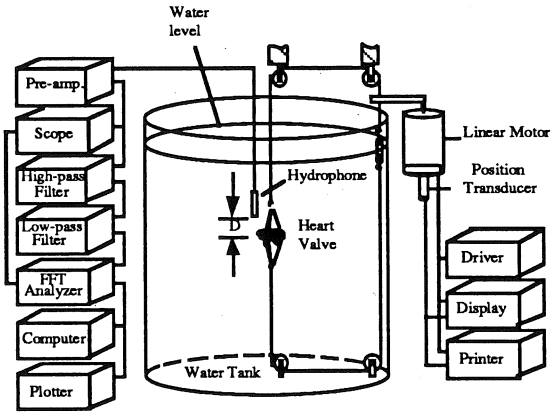

Figure 1. Testing Apparatus

The drive system consists of a linear motor that moves the valve through a 2" stroke via a line mounted on four Delrin pulleys. The driving velocity of the valve was maintained at 1.5 meters/sec during valve closure. The driving frequency was set at 0.5 Hz (equivalent to a heart rate of 30 beats/min) to allow for restablization of the test fluid between strokes.

Distances between sound source and receiver of 32 inches and 8 inches were selected for far field and near field analyses, respectively. The distance between the valve and the bottom of the tank was equal to the distance between the hydrophone and the top surface of the water. The hydrophone was kept 2" off the center axis of the tank to reduce the focusing effects of the circular wall.

The valves were mounted in three point suspension to provided balanced driving relatively symmetrical motion

of the valve. The three point suspension mounting also provided an acoustically transparent structure to avoid structural effects of solid body contact.

The acoustic data acquisition system consisted of a Brüel & Kjær 8103 hydrophone, a Brüel & Kjær (B&K) 2032 frequency analyzer, a B&K 2635 charge preamplifier, a Kron Hite filter, a computer based data storage, and a plotter for documentation. The sound signal was analyzed over the frequency range from DC to 25 kHz. The power spectra were based on 64 spectral averages. A-weighted total spectral levels (in dBA) were used to present the sound energy.

Five types of 29 mm mitral clinical quality valves were tested including: three Edwards-Duromedics Original Specification (EDOS), three Edwards-Duromedics Modified Specification (EDMS), three St. Jude Medical (SJM), three Björk-Shiley (BS), and two Medtronic-Hall (MH). Each valve was tested at both far and near field distances.

RESULTS

The "A-weighted" total power spectra levels (dBA) are listed in the following table.

Valve Type	Far Field Testing (dBA)	Near Field Testing (dBA)
SJM (N=3)	118.9	129.8
EDMS (N=3)	121.4	132.2
EDOS (N=3)	126.5	137.5
BS (N=3)	126.2	137.7
MH (N=2)	124.6	136.8

These results are also presented Graphically in Figures 2 and 3.

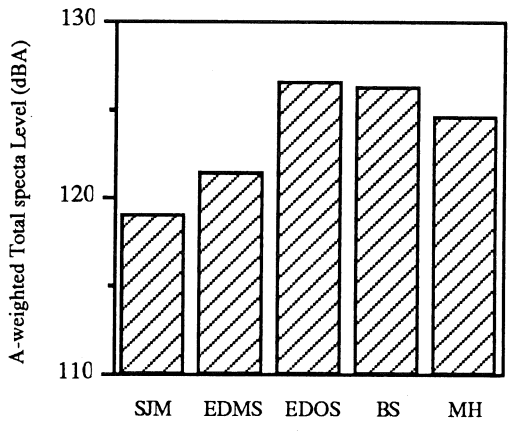

Figure 2. Far Field Testing

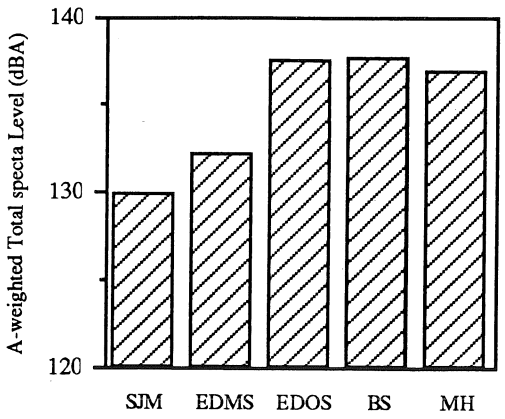

Figure 3. Near field Testing

DISCUSSION

The results indicated that the SJM valves showed the lowest sound energy. The EDOS, BS and MH exhibited similar energy levels that were approximately two times higher than those of SJM. A comparison of EDOS and EDMS shows an approximate 5 dBA reduction corresponding to a factor of 1/3.16.

The results demonstrate a significant improvement of the audible acoustic characteristics due to the modification of the Edwards-Duromedics valves. In both the far field and near field measurements, we see a significant drop in sound energy between the Original and Modified Specification ED valves. The results also show that mechanical valves do have considerable high frequency content in their acoustic output.

REFERENCES

Foale, R. et al. IEEE Transactions on Biomedical Engineering, vol. 30: pp. 110-118, 1983.

Sabbah, H. et al. The American Journal of Cardiology, vol. 50: pp. 53-58, 1982.

Stein, P. et al. The American Journal of Cardiology, vol. 46: pp. 48-52, 1980.

Yoganathan, A. et al. Medical and Biological Engineering, vol. 14: pp. 69-73, 1976.

Yoganathan, A. et al. Medical and Biological Engineering, vol. 14: pp. 455-460, 1976.

Moritz, A. et al. Br Heart J, vol. 67: pp. 460-5, 1992.

Donnerstein, R. et al. J Thorac Cardiovasc Surg, vol. 101: pp. 1060-8, 1991.

Kagawa, Y. et al. J Thorac Cardiovasc Surg, vol. 79: pp. 671-9, 1980.

Schondube, et al. F. J Thorac Cardiovasc Surg, vol. 86: pp. 136-41, 1983.

Wieting, D. et al. Baxter Healthcare Corporation, Mechanical Valve Technical Bulletin, Vol. 5: pp. 238-41, 1987.

DYNAMIC HINGE FLOW VISUALIZATION OF BILEAFLET MECHANICAL HEART VALVE PROSTHESES

G. Guo, J. Roy, P. Adlparvar, R. Kafesjian, D. Ward, C. Kingsbury, R. C. Quijano
Baxter-Edwards CardioVascular Group, CVS Division, Irvine, CA. 92714

INTRODUCTION

An unique flow visualization technique was devised to understand mechanisms of hinge flow in bileaflet mechanical heart valves. By utilizing hydrogen micro bubbles, high speed video, and transparent molds of cardiac prostheses housings, flow through the hinge device of both a 29mm Edwards-Duromedics™ (ED) and a 29mm St. Jude Medical (SJM) mitral heart valve were visualized. Preliminary results indicate hinge washing occurred during both the closing and closed phase of the ED mitral valve while primarily only during the closing phase for the SJM mitral valve. The diastolic phase of the cardiac cycle was not analyzed.

REVIEW AND THEORY

Inadequate washing of the hinge flow region has been suggested as a major cause of thrombotic complications particularly during valve closure (Bokros et al. 1991). Nunez et al. (1980) pointed out that small amounts of thrombus formation in the hinge area could lead to malfunction of a cardiac valve prosthesis. Various hinge washing mechanisms for bileaflet mechanical heart valves have been proposed (figures 1 and 2) yet never fully explored. Difficulties lied in the space and time fields wherein the localized, dynamic motion of hinge flow as well as limitations in testing technique prevented proper corroboration. This study utilized hydrogen micro bubbles at the hinge locale to serve as flow tracers enabling detailed flow visualization.

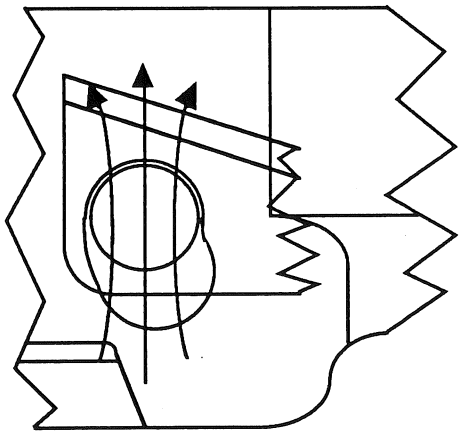

Figure 1: Schematic diagram showing proposed backflushing through hinge of Edwards-Duromedics™ prosthesis (Bokros, 1991).

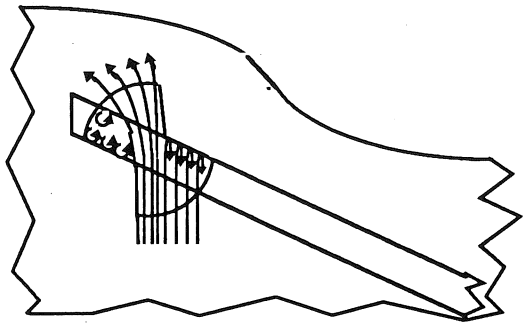

Figure 2: Schematic diagram showing proposed backflushing through hinge of St. Jude Medical prosthesis (Bokros, 1991).

PROCEDURE

Due to the opaque nature of the pyrolytic carbon housing of both the SJM mitral and the ED mitral cardiac prostheses, a clear epoxy mold was made for each size 29mm mitral housing design. The pyrolytic carbon leaflets of each valve were then refitted into their functional/dimensionally accurate epoxy housing. An 0.08 mm thick wire was positioned approximately 2 mm from the outflow end of one of the valve's four hinges. Combined with a 30 volt power source, the wire served as a cathode to produce hydrogen micro bubbles. Each valve was placed individually into the mitral position of a cardiac pulse duplicator.

A Kodak EcktaPro 1000 Imager high speed video camera was positioned to view the hinge flow through the epoxy housing under simulated physiologic dynamic conditions in a 37°C blood analog solution. The high speed video recorded frame by frame motion of the hydrogen bubbles through the hinge area at a rate of 1 ms per frame.

RESULTS

Due to the placement of the cathode on the outflow end of the hinge, localized flow was only qualitatively analyzed during the systolic phase of the mitral valves, namely during dynamic leaflet closure and during complete valve closure. The ED pivot ball hinge during complete valve closure exhibited a streaking white pattern showing the hydrogen micro bubbles as they passed between the housing and the pivot ball as shown schematically in figure 3. A comparable condition for the SJM hinge showed a substantially lower degree of hydrogen micro bubble motion (figure 4). In the dynamic portion of leaflet closure the SJM's 29mm

mitral valve relied primarily on the rotational closing/opening phase for the hinge washing effect. The same size ED mitral valve relied mainly on the translational sliding of the pivot ball in the elongated hinge while the subsequent rotational motion of the leaflets also had a minor washing effect.

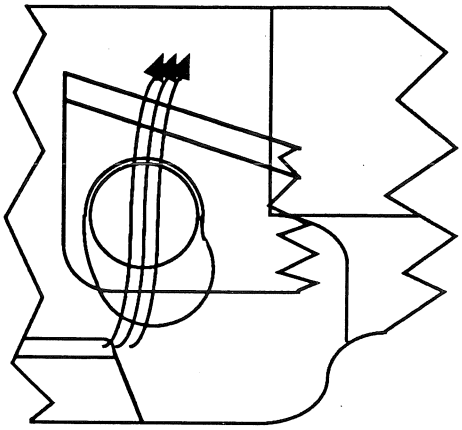

Figure 3: Schematic diagram showing measured backflushing through hinge of Edwards-Duromedics™ prosthesis.

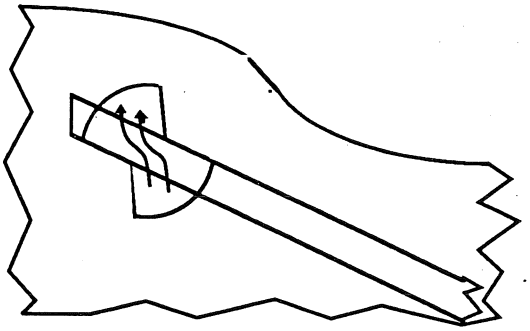

Figure 4: Schematic diagram showing measured backflushing through hinge of St. Jude Medical prosthesis.

DISCUSSION

It has been pointed out that designs of bileaflet mechanical heart valves should encompass sufficient washing of the hinge mechanism to prevent thromboembolism. Results show that both the SJM and the ED mitral valves have unique hinge washing mechanisms during the dynamic leaflet motion of valve closure for their respective design. During complete valve closure, however, the ED mitral valve demonstrated a higher rate of hinge washing compared to the SJM's hinge mechanism. It has been suggested by Austin et al. (1987) that the unloaded pivot ball of the ED during valve closure allows for proper washing, thereby responsible for low clinical thromboembolic rates. Overall, the SJM relied on the short dynamic phase of leaflet closure for its washing mechanism while the ED mitral hinge showed a more continuous washing through the pivot ball during both the dynamic leaflet closing phase and the static, longer closed phase.

This preliminary flow visualization study analyzed flow fields in the vicinity of the mitral valve hinge, concentrating on the systolic phase of the cardiac cycle. It successfully overcame the testing limitations of the localized and dynamic setting of hinge flow for properly understanding the relationship of hinge flow and thromboembolic events in cardiac valve prostheses. This *in vitro* test could now support the substantiation or refutation of proposed heart valve hinge flow mechanisms in mechanical bileaflet valves.

REFERENCES

Austin, E.H. et al. Cardiac Surg. State of Art Rev., Vol. 1, No. 2, Feb. 1987.

Nunez, L. et al. Ann. Thorac. Surg. Entrapment of Leaflets of St. Jude Medical Cardiac Valve Prosthesis by Miniscule Thrombus. 29:567, 1980.

Bokros, J. et al. Trends in Prosthetic Heart Valve Design. Replacement Cardiac Valves. Bodnar and Frater (eds.) Peramon Press, (pp. 333-355), 1991.

THE EFFECTS OF RADIOGRAPHIC CONTRAST INJECTION ON INTRACORONARY PRESSURE DURING TRANSFEMORAL CORONARY ANGIOGRAPHY

K.A. Herman, J.D. Rossen, and M. Siebes

Department of Biomedical Engineering
Department of Internal Medicine
The University of Iowa, Iowa City, IA 52242

INTRODUCTION

Transfemoral coronary angiography was performed in healthy animals in order to assess the effects of contrast injection on intracoronary pressure. Initial results suggest that the rapid administration of contrast material results in substantial artificial elevation of the coronary pressure during the injection. This pressure increase appears to depend on the method and rate of administration, as well as on the pre-injection pressure in the coronary artery.

REVIEW AND THEORY

Coronary angiography has become a gold standard for the quantitative assessment of coronary stenosis severity. This method allows visualization of the coronary arteries via x-ray image acquisition. Since the blood and arterial walls have similar x-ray absorption characteristics, coronary vessel appearance is enhanced by temporarily replacing arterial blood with a radiographic contrast agent that is administered through a catheter via either manual or pump injection. While the cardiovascular effects of contrast agents have been studied in detail (Dawson, 1989), the mechanical effects of the injection have not been evaluated.

Estimates of coronary dimensions based on conventional visual analysis do not correlate with the physiological effect of coronary stenoses (White et al., 1984). Computerized techniques have been implemented to obtain absolute dimensions of coronary arterial diameter, which provides the basis for evaluation of the physiologic significance of the analyzed stenosis (Siebes et al., 1985). If the injection of contrast material during coronary angiography alters intracoronary pressure, the coronary diameters on the angiogram would not be representative of the true pre-injection dimensions. The present study was conducted to test the above hypothesis, and preliminary data are presented in this report.

PROCEDURES

Standard transfemoral coronary angiography was performed using Hypaque-76® as contrast material. Anesthetized pigs were chosen as the animal model, since their coronary anatomy is comparable to that of humans. To obtain the necessary pressure measurements, a micro-tip catheter pressure transducer (Millar Inc., Houston, TX) (2F, 0.67 mm o.d.) was inserted inside the injection catheter and advanced into the left circumflex coronary artery. Femoral arterial pressure was measured with a fluid-filled pressure transducer (Gould-Statham, Oxnard, CA). A three-lead ECG was also recorded.

Injections of contrast material were performed both by hand and via a power injector (Medrad Mark IV, Medrad Inc, Pittsburg, PA). A 5 V signal from the power injector was used to mark the beginning and end of injection and was recorded together with the pressures. All signals were sampled at a rate of 100 Hz for a period of 20 seconds. The voltages were digitized into a 386/25 MHz PC using a 12 bit A/D board and stored for later analysis.

Injections were performed using the following modes of administration:
1) 8cc hand injection
2) 8cc power injection at 2cc/sec
3) 8cc power injection at 3cc/sec
4) 8cc power injection at 4cc/sec
5) 8cc power injection at 6cc/sec

Intracoronary pressure was recorded at 0,1,2, and 2.5 cm distal to the tip of the injection catheter. The sampled pressure data were converted to physical units and then smoothed with a 3-point moving average filter in order to minimize the effects of noise.

RESULTS AND DISCUSSION

Figure 1 shows the intracoronary pressure during an 8cc hand injection into the LCX of a healthy 50 kg male pig. It is evident that the pressure during the injection is increased by about 30 mmHg. The pulse pressure was present, but decreased.

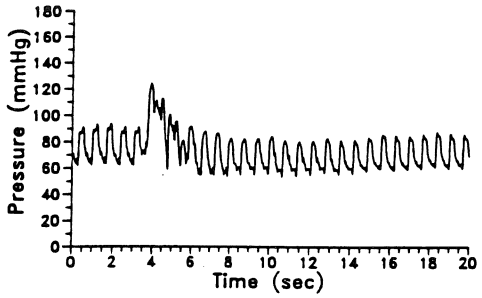

Figure 1. Coronary Pressure during an 8cc hand injection.

Hand injections had the largest effect on intracoronary pressure. With decreasing injection rate, the magnitude of the pressure rise decreased progressively, as shown in Figure 2. The results also show that, for the same rate of injection, the pressure rise decreased with decreasing distance from the tip of the catheter. Since the elastic modulus of the artery is a nonlinear function of intravascular pressure (Cox, 1978), the increased compliance of the arterial wall at lower intraluminal pressures may serve to buffer effects of rapid volume loading during contrast injection. However, the data at

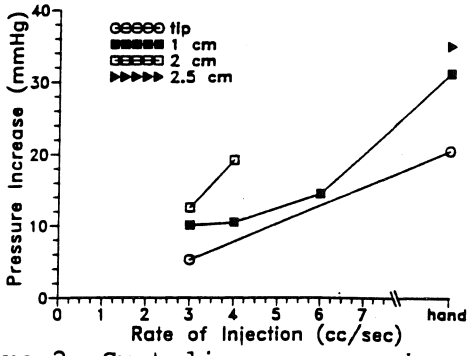

Figure 2. Systolic pressure increase vs. rate of contrast administration.

shorter distances were obtained later in the experiment, at which time the mean arterial pressure had dropped by about 20 mmHg due to prolonged anesthesia.

While these results only represent preliminary data from a limited number of experiments, they point to potentially important clinical implications regarding the administration of contrast material and the selection of angiographic frames for quantitative analysis. The above findings suggest that it may be necessary to determine "optimal" conditions under which to acquire and analyze clinical coronary angiograms. We are currently expanding the experimental protocol to include acquisition of cineangiograms in order to obtain pressure-diameter relationships during contrast injection under a variety of experimental conditions.

REFERENCES

Cox, R.H., Am. J. Physiol, 234:H533-H541, 1978.

Dawson, P. Am. J. Cardiol, 64:2E-9E, 1989.

Siebes, M. et al., Comp. Meth & Prog Biomed 21:143-152, 1985.

White, C.W. et al. N Engl J Med 310:819-824, 1984.

ACKNOWLEDGEMENTS

This research was supported in part by a grant from The Whitaker Foundation and a G.E. Foundation Faculty Fellowship.

PHYSICAL MODEL OF A COMPLIANT ARTERIAL PLAQUE

D. Elizondo and M. Siebes

Department of Biomedical Engineering
The University of Iowa, Iowa City, IA, 52242

INTRODUCTION

Although many atherosclerotic plaques are compliant, they are usually modeled as rigid obstructions to flow. This paper describes the modeling of a compliant atherosclerotic plaque using a synthetic vinyl plastisol material. Mechanical testing of this artificial tissue was performed to characterize its mechanical properties. The results indicate that it possesses nonlinear mechanical relationships similar to those of natural arteries. Plaque models made from this material will be used to represent compliant arterial stenoses in future flow studies.

REVIEW AND THEORY

Kragel et al.(1989) have shown that atherosclerotic plaques actually consist of lipids, collagen, elastin, and in later stages, calcium deposits. This composition suggests that the plaque may exhibit compliant behavior when subjected to stresses caused by pressure variations during the cardiac cycle. Very few data exists on the mechanical properties of atherosclerotic plaque (Borne et al., 1990). However, it appears that a realistic model of an atherosclerotic plaque should include the compliant properties.

PROCEDURES

An artificial compliant material resembling the appearance of fat (Spenco Skin Care Pads, Spenco Medical Corp., Waco, TX) was used. The mechanical properties of two cylindrical samples of 36 mm diameter and 17 mm height were determined by subjecting the samples to progressive axial loading on a Material Testing System (MTS) over a range from 0 to 10 mm at a rate of 10 mm/min. The compression tests were videotaped for later dimensional analysis. Approximately 30 video frames throughout the displacement range of the compression tests were digitized on a Macintosh IIfx computer. For each frame the magnitude of axial displacement and the width of each sample at five axial locations were obtained using mouse-directed markers. An average circular cross-section for each loading condition was determined from the five width measurements (Figure 1). The corresponding force during compression was found by matching the measured axial displacement with the force/displacement curves obtained from the MTS testing.

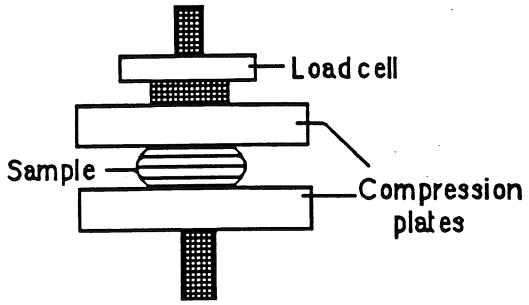

Figure 1: Setup of compression test

The stress, strain, Poisson's ratio, and incremental elastic modulus of each specimen were calculated (Byars et al., 1975).

$$\text{Transverse Strain } (\varepsilon_x) = \ln(Lf_x/Lo_x)$$

$$\text{Axial Strain } (\varepsilon_y) = \ln(Lf_y/Lo_y)$$

$$\text{Stress}(\sigma) = \text{Force/Cross-sectional Area}$$

$$\text{Poisson's ratio } (\upsilon) = \varepsilon_x / \varepsilon_y$$

$$E_{inc} = (\Delta\sigma/\Delta\text{height}) * \text{mean height}$$

where Lf = final height of sample
Lo = initial height of sample
mean height = $(L_i + L_{i+1})/2$

RESULTS

The stress-strain relationship for each of the samples is shown in Figure 2. It is nonlinear with a significant increase in stress for higher magnitudes of strain.

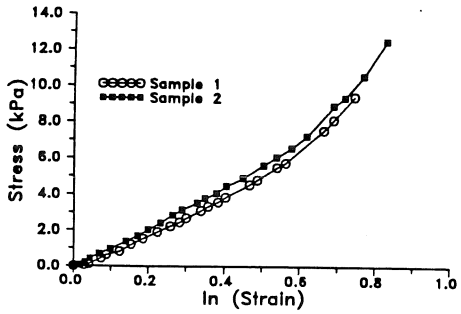

Figure 2: Stress-strain relationship

Figure 3 illustrates that the Poisson's ratio initially increases sharply and converges to a stable value of about 0.4 at pressures above 40 mmHg. The pressure applied to the material was obtained from the calculated stresses.

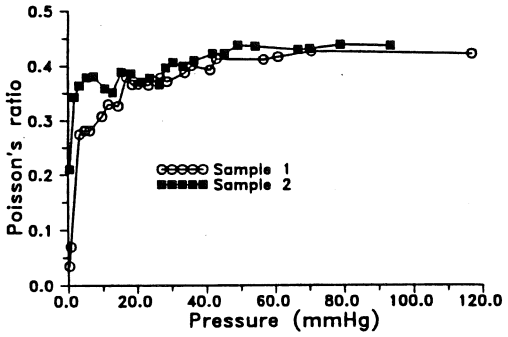

Figure 3: Poisson's ratio

The incremental elastic modulus increases nonlinearly with an increase in applied pressure from about 0.05 to 0.4 x10^6 dynes/cm^2 at a pressure of approximately 100 mmHg (Fig.4).

DISCUSSION

Due to the lack of comparable data for human atherosclerotic plaque, the results obtained for the artificial fat tissue were compared to the mechanical properties of dog arteries. The Poisson's ratio of the artificial plaque material was

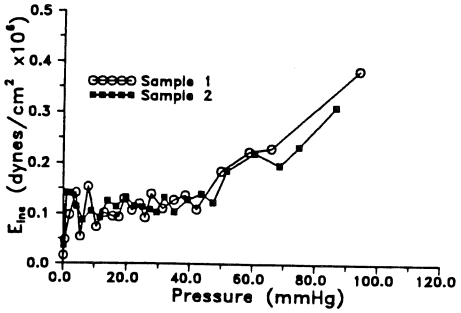

Figure 4:Incremental elastic modulus

close to the value of 0.5 found by Dobrin (1986) for dog carotid arteries under physiological conditions. Compared to data reported by Bergel (1961) and Dobrin (1986), the incremental elastic modulus of arteries exhibits a similar nonlinear relationship to pressure, although the absolute values are an order of magnitude smaller for the material used in this study. The mechanical testing was performed on the same two samples four months later and similar results were found. Our results indicate that this material may be suitable for modeling a compliant fatty plaque. It can be easily molded into desired shapes of known dimensions to serve as a model for a compliant arterial stenosis in future flow studies.

REFERENCES

Bergel, D. J. Physiology, 156, 445-457, 1961.

Born, G.V.R. and Richardson, P.D. In Pathobiology of Human Atherosclerotic Plaque (Glagov et al., eds.), Springer Verlag, (pp.413-423), 1990.

Byars, E.F. et al. Engineering Mechanics of Deformable Bodies, Harper & Row Publishers, 1975.

Dobrin, P.B. J. Biomechanics, 19:5, 351-358, 1986.

Kragel, A.H. et al. Circulation, 80, 1747-1756, 1989.

ACKNOWLEDGEMENTS

This project was supported by a grant from The Whitaker Foundation.

STEADY FLOW THROUGH A RIGID ECCENTRIC AND CONCENTRIC STENOSIS IN SERIES

B. John and M. Siebes

Department of Biomedical Engineering, The University of Iowa, Iowa City

INTRODUCTION

A major proportion of the coronary stenoses is eccentric. In addition, multiple stenoses may be present in the same coronary artery. The pressure drop-flow relationship of a 90% rigid eccentric stenosis in series with a concentric stenosis in collapsible tubing was studied under steady flow conditions. The severity of the downstream stenosis was varied between 50, 80, and 90% and the distance between the stenosis was varied in steps of 1, 2, 4, and 6 times the unobstructed tube diameter. The overall pressure drop increased as the downstream severity was increased. For a severe downstream stenosis, the pressure drop decreased with increasing distance between the stenoses. This may be due to an additional pressure drop caused by the complicated flow path through the stenoses. This additional loss was higher at high Reynolds numbers and at smaller distances between the stenoses.

REVIEW AND THEORY

Based on flow experiments carried out on two concentric stenoses of equal severity in series in rigid tubing, Seeley and Young (1976) have shown that the pressure drop across the two stenoses was equal to the sum of the losses only when the distance between the stenoses exceeded a critical length, which depended on the Reynolds number. Siebes et al. (1983) found in flow experiments involving two concentric stenoses of different severity that the presence of a mild downstream stenosis in close distance to a severe upstream stenosis reduced the overall pressure drop to levels below that of the severe stenosis alone. An eccentric stenosis in series with a concentric downstream stenosis was used in the present study to determine whether the eccentricity of the upstream stenosis would alter this relationship.

PROCEDURES

Four blunt ended stenosis models were made from 6.35 mm Plexiglas rods with a length-to-diameter ratio of two. Models 5C, 8C, and 9C were concentric with 50, 80, and 90% area reduction, respectively. Model 9E was an eccentric 90% stenosis with one third of the tube wall circumference not attached to the plug (Fig. 1). The stenoses were inserted into thin-walled latex tubing of 6.35 mm i.d. Model 9E was created by applying epoxy glue to the outer wall of the latex tubing (at 110 mmHg) at the location where the plug had been glued into place. The concentric stenoses were tied into place using silk sutures. Three sequential stenoses configurations 5R, 8R, and 9R consists of model 9E in series with model 5C, 8C, or 9C, respectively. The distance between the stenoses, S, was varied between 1, 2, 4, and 6 times the unobstructed tube diameter, D. Pressure losses across all single and sequential stenoses configurations were measured in a recirculating steady flow system over a range of Reynolds numbers, Re, from about 70 to 2000 using two different fluids (27% glycerin in water and distilled water). Calculated Poiseuille losses across the unobstructed test section were subtracted from the measured pressure drop to obtain the pressure loss across the stenoses alone. The pressure drop and flow were converted the non-dimensional Euler number, Eu, and Reynolds number, Re, respectively. A least-squares nonlinear regression of the form

Figure 1: Stenosis cross-sections

$Eu=A/Re+B$ was carried out through all the data sets. In this relationship the coefficients A and B are related to viscous and to inertial exit losses, respectively, and are constant for a given stenosis geometry. Based on these coefficients, the sum of the Eu-Re relationship for two individual stenoses was calculated for comparison to the experimentally determined data.

RESULTS

In general, the pressure drop across the sequential stenoses increased as the severity of the downstream stenosis was increased. For configuration 5R, the overall pressure drop increased with increasing distance between the stenoses. However, this relationship was reversed for configurations 8R and 9R (Fig. 2). Furthermore, at $Re>200$, the overall pressure drop at $S/D=1$ was higher than the sum of the pressure losses across the individual stenoses. Since the inertial losses associated with flow separation dominate the overall losses at higher Reynolds numbers, the regression coefficient B was plotted as a function of S/D for all combinations (Fig. 3). With a mild downstream stenosis (5R), B increased from a value below that for the single eccentric model (9E) to a value slightly above. With a severe downstream stenosis (8R, 9R), however, B decreased with increasing distance, most notably so between $S/D=1$ and $S/D=2$. In addition, B was higher than the value calculated for the sum of the corresponding models for configurations 8R and 9R at $S/D=1$ and $S/D=2$.

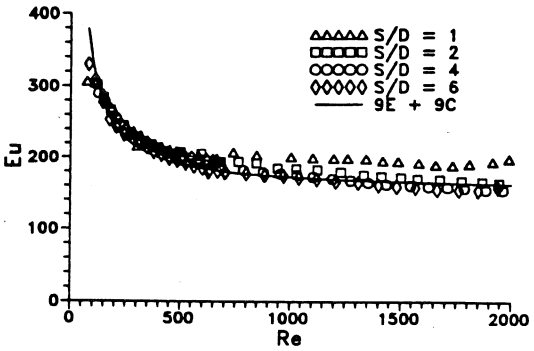

Figure 2: Variation of Eu with Re for configuration 9R.

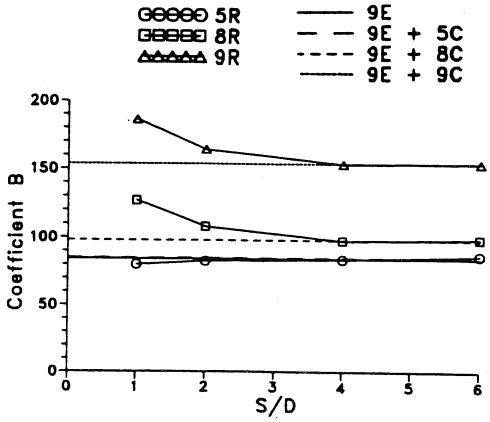

Figure 3: Variation of regression coefficient B with S/D.

DISCUSSION

In general, the results obtained in the present study are similar to previous findings on flow through sequential concentric stenoses. However, our results indicate that the pressure losses decreased with an increase in stenosis spacing in the presence of a severe downstream stenosis, which is in contrast to findings by Seeley and Young (1976) and Siebes (1983). Furthermore, the overall pressure loss was larger than the sum of the individual pressure losses when the stenoses were closer together. The eccentricity of the upstream stenosis may account for the differences. The flow through an eccentric stenosis in close proximity to a concentric stenosis is more tortuous than that through two concentric stenoses, causing additional pressure losses. This effect would be more pronounced at higher Re, with a severe downstream stenosis and at smaller distances between the stenoses.

REFERENCES

Seeley, B.D. and Young, D.F. J. Biomechanics, 9, 439-448, 1976.

Siebes, M. et al. J. Am. Coll. Cardiol., 1, 684, 1983.

ACKNOWLEDGMENTS

This work was supported by NSF Research Initiation Award BCS-9011761.

AUTHOR INDEX